Lithium-Rich Anti-Perovskites: Understanding the Structure and its Influence on Ion Mobility

TAVLEEN SINGH ATTARI

Lithium-Rich Anti-Perovskites: Understanding the Structure and its Influence on Ion Mobility

Tavleen Singh Attari

A thesis presented for the degree of Doctor of Philosophy at Durham University

Department of Chemistry
Durham University

2022

Abstract

The rechargeable lithium-ion (Li-ion) battery is considered the technology of choice for energy storage in a wide range of portable electronic devices, including mobile phones and laptop computers. Despite the many advantages of the Li-ion battery, its application is limited by its use of liquid electrolytes, which are known to pose serious fire and safety risks. Hence, suitable alternatives are urgently required. In recent years there has been considerable interest in the development of all-solid-state batteries (ASSBs), with a particular focus on novel solid electrolyte materials.

Recent literature suggests that Li-rich anti-perovskites (LiRAPs) could be suitable solid electrolyte materials. LiRAPs have the general formula ABX_3, where A is a monovalent anion, B is a divalent anion, and X is a strongly electropositive monovalent cation. The LiRAPs Li_3OCl and Li_3OBr have been reported to possess ionic conductivities on the order of 10^{-3} S cm^{-1}. However, the precise conduction mechanisms and pathways that lead to such conductivities are poorly understood. Hence, studies are needed that can probe ion mobility within these materials.

The work presented in this thesis focuses on the synthesis and structural characterisation of LiRAPs, including Li_3OCl, Li_3OBr and their hydrated analogues, Li_2OHCl and Li_2OHBr. The samples produced were analysed extensively via laboratory XRD, NPD and multinuclear SSNMR spectroscopy. Initial investigations focused on synthesising phase pure samples of Li_3OCl and Li_3OBr. Due to their extremely hygroscopic nature, air-sensitive techniques were required for their synthesis. Several synthetic methods were attempted, and reaction variables, including the time and temperature, were varied systematically to optimise the reaction conditions. Despite testing numerous synthetic conditions, producing phase pure samples of Li_3OCl and Li_3OBr remained a challenge.

The focus of the investigation then shifted towards the hydrated LiRAP Li_2OHCl, which is considerably easier to synthesise. Li_2OHCl was suc-

cessfully synthesised via conventional solid-state and mechanical milling methods. Li_2OHCl is reported to exist in two different phases; a room-temperature phase believed to be orthorhombic and a high-temperature cubic ($Pm\bar{3}m$) phase. Several structural suggestions have been made in the literature for the room-temperature phase of Li_2OHCl, but a structural model is yet to be agreed upon. Hence, considerable effort was dedicated to evaluating the structures reported in the literature and determining an accurate structure for the room-temperature phase of Li_2OHCl. Moreover, the phase transition in Li_2OHCl and the associated structural changes were also explored.

As LiRAPs are proposed as candidate solid electrolyte materials, probing ion mobility within this system is of significant interest. Thus, Li_2OHCl was extensively analysed via variable-temperature $^{1/2}H$ and ^{7}Li NMR spectroscopy to investigate the proton and lithium-ion mobility as a function of temperature. Additionally, AIMD simulations were completed by our collaborators to support our experimental findings. These complementary techniques led to an understanding of a highly correlated mechanism for proton and Li-ion movement in Li_2OHCl. Furthermore, LiRAP samples were also analysed via VT ^{35}Cl NMR spectroscopy to investigate the changes in the local environment of Cl as a function of temperature.

As with perovskites, the LiRAPs exhibit extreme structural flexibility. Hence, the composition of Li_2OHCl was modified by varying the proton and, consequently, the lithium content to synthesise $Li_{3-x}OH_xCl$ (x = 0.25 – 1), and via fluorine doping and halide mixing to synthesise $Li_2(OH)_{0.9}F_{0.1}Cl$ and $Li_2OHCl_{1-x}Br_x$ (x = 0 – 1), respectively. The influence of compositional variation on the structure and ion mobility in the system was studied extensively via XRD and multinuclear SSNMR spectroscopy.

Declaration

The work described in this thesis was undertaken under the supervision of Dr Karen E. Johnston at the Department of Chemistry, Durham University between January 2016 and March 2019. This work was supported by the UK Engineering and Physical Sciences Research Council (EPSRC). This is the original work of the author and has not previously been submitted for a degree at this or any other university. All of the work reported is my own, except where specifically stated otherwise.

Statement of Copyright

I dedicate this thesis to my mother and father.

Acknowledgements

The journey toward a PhD is never completed in isolation; this one is no exception. First and foremost, I would like to thank my supervisor, Dr Karen E. Johnston, for her continued support and guidance throughout this process. I appreciate all her efforts and endless patience during my journey to become a real scientist. I am truly thankful for all that I have learned.

All members of the KEJ group (past and present) have also been very helpful. I would like to thank Dr Russell Taylor for his advice regarding the use of laboratory equipment. Dr David Apperley assisted with the NMR experiments, and Mr Gary Oswald provided XRD training. Mr Aaron Brown and Mr Malcolm Richardson were particularly helpful. They made all the glassware I ever needed and devised creative solutions for handling air-sensitive samples.

I would also like to thank Dr Alexandra Gibbs for assisting with the NPD experiments at HRPD and Dr Theodosios Famprikis for preparing the samples. The ^{7}Li PFG-NMR experiments were completed by Professor Clare P. Grey and Dr Steffen P. Emge, and the ^{1}H PFG-NMR experiments were completed by Professor Laurent Le Polles and Dr Claire Roiland. The AIMD simulations were completed by Dr James A. Dawson and Professor Saiful Islam.

I could not have completed this arduous journey without the encouragement and warmth of Ms Lauren Turner, who taught me to believe in myself. I would also like to thank Ms Cathy Earley for her kindness and support.

Along this journey, I have gotten to know some incredible people, including Dr Jessica Andrews, Dr Yuexian Hong, Dr Melissa Goodwin, Dr Melissa Walden, Dr Laura Dearlove, Dr Tharindi Udalagama, Ms Natalia Wojcik, Ms Claire Fairish and Ms Emma Knighton. I am grateful for their friendship. A special thanks goes to Dr Charlotte (Lottie) Ayres, from whom I have learned the value of goodness and kindness.

Fortunate are those who can find a true friend like Ms Jiayin Zhao. Thank you, Jiayin, for always being there for me. Of course, I never would have managed without Ms Pat Palmer, who is always kind, understanding

and wise.

Most importantly, I would like to thank my family for their constant support and encouragement. Thank you, Joginder and Gurtek, for always believing in me. Your hard work has helped me to realise my dreams and goals. Special thanks to Arjun and Shivam for their love and kindness.

Contents

Publication

J. A. Dawson, T. S. Attari, H. Chen, S. P. Emge, K. E. Johnston and M. S. Islam, Elucidating lithium-ion and proton dynamics in anti-perovskite solid electrolytes, *Energy Environ. Sci.*, 2018, **11**, 2993 – 3002, DOI: 10.1039/c8ee00779a

List of Symbols and Abbreviations

Symbols

mA	MilliAmpere
h	Hour
g	Gram
V	Volt
°C	Degree Celsius
cm	Centimetre
σ	Ionic conductivity
S	Siemens
M	Molar
t	Tolerance factor
r_A	Ionic radius of A
r_B	Ionic radius of B
r_X	Ionic radius of X
□	Vacancy
eV	Electronvolt
E_a	Activation energy
nm	Nanometre
atm	Atmosphere
Å	Angstrom, 1×10^{-10} metres
r_{ion}	Ionic radius
a, b, c	Lattice parameters
K	Kelvin
meV	Millielectronvolt
d_{hkl}	d-spacing between Miller planes
hkl	Miller indices
θ	Angle of incident and diffraction
n	Integer
λ	Wavelength
f_i	Scattering factor or form factor

F_{hkl}	Structure factor
I_{hkl}	Intensity of a particular reflection
kg	Kilogram
MeV	Megaelectronvolt
t	Time
m_n	Mass of a neutron
h	Plank's constant
L	Flight Path
m	metres
S_y	Structural refinement residual
y_{oi}	Observed intensity
y_{ci}	Calculated intensity
R_P	R-profile
wR_P	R-weighted profile
χ^2	Parameter determining the quality of fit
$\mathbf{I}$	Intrinsic spin angular momentum
$\hbar$	$h/2\pi$
I	Spin quantum number
m_I	Magnetic quantum number
$\boldsymbol{\mu}$	Magnetic dipole moment
γ	Gyromagnetic ratio
$\mathbf{B}_0$	Magnetic field strength
E	Energy
μ_Z	Projection of the magnetic dipole moment onto the z-axis
ΔE	Change in energy
ν_0	Frequency
ω_0	Larmor frequency in rad s^{-1}
σ	Shielding constant
δ	Deshielding parameter
ω	Resonance frequency
ω_{ref}	Reference frequency
$\mathbf{M}_0$	Bulk magnetisation vector

ω_{rf}	Frequency of the radiofrequency radiation
$\mathbf{B}_1$	Strength of an applied pulse
τ_P	Duration of a pulse
Ω	Offset frequency
$\mathbf{B}_0^{eff}$	Effective magnetic field
T_2	Transverse or spin-spin relaxation
$\Delta\nu$	Peak width at half height
T_1	Longitudinal or spin-lattice relaxation
f(t)	Time-domain signal
$\mathbf{B}_\mu$	Localised magnetic field
ω_D	Dipolar splitting parameter
ω_D^{PAS}	Dipolar splitting parameter in the PAS
μ_0	Vacuum permeability
r_{ij}	Distance between spins i and j
δ	Chemical shift
δ_{iso}	Isotropic chemical shift
Δ_{CSA}	Magnitude of the CSA interaction
η_{CSA}	Asymmetry parameter of the CSA interaction
eQ	Nuclear quadrupolar moment
eq	Electric field gradient
V_{XX},V_{YY},V_{ZZ}	Principal components in the PAS
η_Q	Asymmetry parameter of the quadrupolar interaction
C_Q	Quadrupolar coupling constant
ω_Q	Quadrupolar splitting parameter
ω_Q^{PAS}	Quadrupolar splitting parameter in the PAS
mm	millimetre
kHz	kilohertz
MHz	Megahertz
τ	Duration
g	Magnetic field gradient
ω_{tot}	Total larmor frequency
δ	Duration

Δ	Time period between two gradient pulses
Λ	Pitch
I	Intensity
D	Diffusion coefficient
I_0	Intensity at the lowest gradient strength
τ_m	Mixing period
e	Electron charge
hrs	Hours
GPa	GigaPascals
kJ	Kilojoules
mol	Mole
mbar	Millibar
mins	Minutes
T	Tesla
µs	Microsecond
s	Second
V	Volume
U(iso)	Isotropic thermal displacement parameter
D_{Li}	Diffusion coefficient for Li
ps	picosecond
n	No. of charge carriers
q	Electron charge
k	Boltzmann constant
T	Temperature
H_R	Haven ration
R	Gas constant
R^2	Parameter determining the quality of fit
Hz	Hertz

Abbreviations

Li-ion	Lithium-ion
PC	Propylene Carbonate

DC	Diethyl Carbonate
LCO	$LiCoO_2$
LNO	$LiNiO_2$
LMO	$LiMnO_2$
SEI	Solid Electrolyte Interface
LMO′	$LiMn_2O_4$
NCA	$LiNi_{0.8}Co_{0.15}Al_{0.05}O_2$
NMO	$Li(Ni_{0.5}Mn_{0.5})O_2$
NMC	$LiNi_{1-x-y}Co_xMn_yO_2$
LFP	$LiFePO_4$
LMP	$LiMnPO_4$
LTO	$Li_4Ti_5O_{12}$
ASSBs	All-Solid-State-Batteries
ALD	Atomic Layer Deposition
ABX_3	General formula for perovskites
LLTO	$Li_{3x}La_{(2/3)-x}\square_{(1/3)-2x}TiO_3$
RT	Room temperature
LSTZ	$LiSr_{1.65}Ta_{1.7}Zr_{1.3}O_9$
NASICON	Na Super Ionic Conductor
LATP	$Li_{1.3}Al_{0.3}Ti_{1.7}(PO_4)_3$
LAGP	$Li_{1.5}Al_{0.5}Ge_{1.5}(PO_4)_3$
LISICON	Li Super Ionic Conductor
$A_3B_2C_3O_{12}$	General formula for garnets
LLZO	$Li_7La_3Zr_2O_{12}$
LiPON	Lithium Phosphorus Oxynitride
RF	Radiofrequency
IBAD	Ion Beam Assisted Deposition
MOCVD	Metalorganic-Chemical Vapour Deposition
Li_6PS_5X	General formula for argyrodites (X = Cl, Br or I)
LiRAP	Lithium-Rich Anti-Perovskites
AIMD	*Ab Initio* Molecular Dynamics
PLD	Pulsed Layer Deposition

XRD	X-ray Diffraction
TOF	Time-of-Flight
HRPD	High Resolution Powder Diffractometer
cif	Crystallographic information file
GSAS	General Structural Analysis System
ICSD	Inorganic Crystal Structure Database
NMR	Nuclear Magnetic Resonance
ppm	Parts per million
FID	Free Induction Decay
FT	Fourier transform
CSA	Chemical Shift Anisotropy
PAS	Principal Axis System
SSNMR	Solid-State NMR
EFG	Electric Field Gradient
MAS	Magic-Angle Spinning
DOR	Double rotation
DAS	Dynamic-Angle Spinning
MQMAS	Multiple-Quantum Magic-Angle Spinning
FWHM	Full Width at Half Maximum
VT	Variable-Temperature
PFG	Pulse-Field Gradient
EXSY	Exchange Spectroscopy
rpm	Revolutions per minute
SOLA	Solids Line Shape Analysis
NPD	Neutron Powder Diffraction
EIS	Electrochemical Impedance Spectroscopy
DFT	Density Functional Theory
CCR	Closed Cycle Refrigerator
EVT	Enhanced Variable-Temperature
VASP	Vienna *Ab initio* Simulation Package
MSD	Mean Square Displacement
ICP-MS	Inductively Coupled Plasma Mass Spectrometry

XRF	X-ray Fluorescence
SEM	Scanning Electron Microscopy
TEM	Transmission Electron Microscopy

1 Introduction and Background

1.1 Current Challenges in Energy

At present, virtually all of the energy we use is produced via the burning of fossil fuels. These non-renewable resources are known to emit greenhouse gases and contribute to global warming.[1] Following the industrial revolution, the atmospheric levels of CO_2 have increased by more than 30%, resulting in considerable environmental concerns.[2] The declining world reserves of fossil fuels, as well as the environmental issues associated with their use, have resulted in the growing demand for alternative energy sources. As such, many potential solutions have been suggested, including reducing the usage of fossil fuels altogether, increasing the use of biofuels and adopting carbon capture methods.[3,4] One increasingly popular alternative is the use of renewable energy sources such as solar, wind and tidal power.[5] However, these are notoriously intermittent in their ability to provide energy on demand, owing to their dependency on the weather. An obvious solution to this issue is to develop methods for storing the energy they provide in order to use that energy at a later date. Batteries are a convenient and reliable method of energy storage that could provide a suitable means for storing renewable energy.[6] Recent improvements in battery technology have revolutionised the technology and communications industry.[7] Can the same be done for the current energy crisis?

Batteries are used to convert chemical energy to electrical energy via redox reactions.[6,8] They consist of multiple electrochemical cells that are connected in series or in parallel. Each cell contains a positive (cathode) and a negative (anode) electrode that are separated by an electrolyte, which is responsible for transferring charge between the two electrodes. The electrolyte is an electronically insulating material. Hence, during operation, the electrons are forced to flow through the external circuit. Batteries are divided into two principal categories; primary and secondary.[6,8] Primary batteries are single use and are therefore discarded after use, as the electrochemical reactions taking place in the cell are irreversible. A popular example is the Zn/alkaline/MnO_2

battery, also known as the alkaline battery.[8] Secondary batteries such as the lead-acid battery are used extensively in the automotive industry as they can be recharged and used multiple times.[9]

At present, one of the most popular and influential rechargeable batteries is the lithium-ion (Li-ion) battery. This technology has revolutionised global communication and the technology industry, with its application in virtually all handheld portable electronics.[10]

1.2 The Lithium-ion Battery

Lithium has many properties that make it appealing for use in portable electronics. For example, it is the lightest metal with an atomic mass of 6.94, making it ideal for the construction of lightweight batteries. Lithium also has the lowest reduction potential of any element, allowing for large cell potentials and therefore a high theoretical voltage.[10,11] Li-ion batteries have several advantages, including their high specific energies, meaning a cell is able to store a large amount of electricity. They also have low self-discharge rates, resulting in long shelf lives and long cycle lives, so they can be recharged many times. Furthermore, they can operate over a broad temperature window and offer rapid charge capabilities, meaning they can be charged relatively quickly. They are also energy efficient, *i.e.*, the energy produced is close to the theoretical value.[12]

The first Li-ion battery was commercialised by SONY in 1991.[13] Following numerous trials, the final product was composed of a mixed metal oxide cathode, lithium cobalt oxide ($LiCoO_2$), and a graphite anode, a schematic representation of which is shown in Figure 1.1. The electrolyte was lithium salts (lithium hexafluorophosphate, $LiPF_6$) dissolved in a mixture of propylene carbonate (PC) and diethyl carbonate (DC).

Li-ion batteries make use of intercalation chemistry, a process in which Li ions are reversibly incorporated into a material without causing a significant change in the structure.[10] In the case of Li-ion batteries, both the anode and the cathode can act as a host for the guest ions (Li^+). During charge (lithiation), Li^+ ions are generated at the cathode, leading to the oxidation of the positive

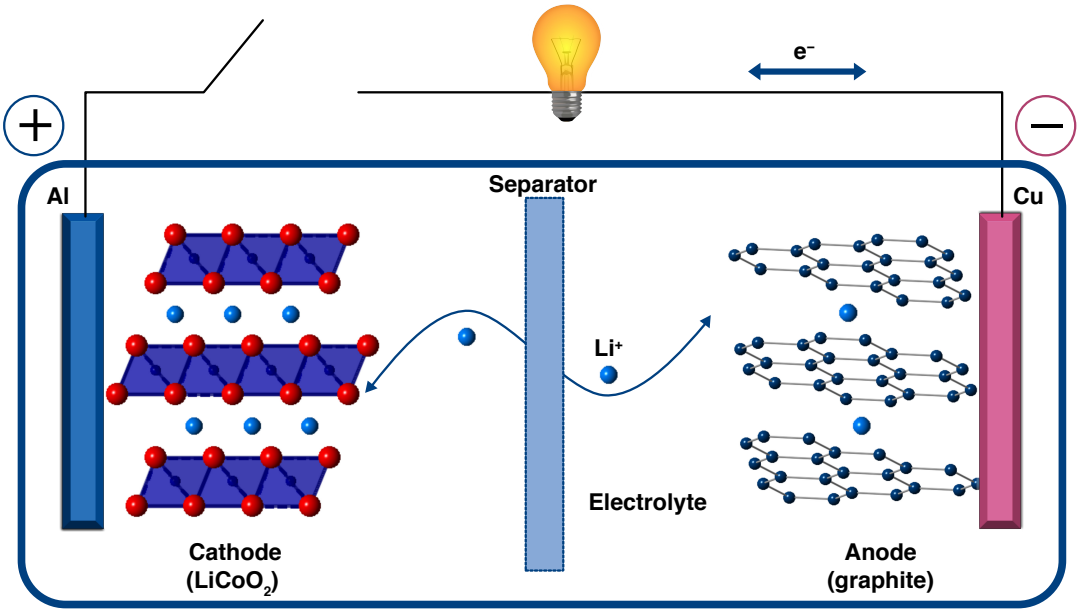

Figure 1.1: Schematic representation of a commercial Li-ion battery, detailing the composition of both the cathode ($LiCoO_2$) and the anode (graphite). Also shown is the relevant electrochemical process that takes place.

electrode material. The Li^+ ions then migrate through the liquid electrolyte and are intercalated into the graphite structure which is, in turn, reduced. During discharge (delithiaton), the ions move back to the cathode. The redox reactions taking place at the cathode and anode are summarised by Equations 1.1 and 1.2, respectively.

$$LiCoO_2 \longleftrightarrow Li_{1-x}CoO_2 + xLi^+ + xe^- \,, \tag{1.1}$$

$$6C_{(graphite)} + Li^+ + e^- \longleftrightarrow C_6Li \,. \tag{1.2}$$

1.2.1 Electrode Materials in Li-ion Batteries

Numerous materials have been studied extensively as potential electrode materials in Li-ion batteries. To be successfully used as an electrode, they must fulfil certain criteria.[14] For example, they must readily undergo redox chemistry, thereby enabling the intercalation process to take place. Moreover, they should be able to incorporate large amounts of lithium and offer high Li-ion diffusivity. The material should be a good electrical conductor, and it

should be stable, *i.e.*, the structure should not distort, change or decompose during operation. Other factors to consider include the ease of fabrication, cost, toxicity and any environmental issues associated with using the materials.

1.2.2 Cathode Materials

Cathodes should be efficient oxidising agents and comply with the conditions stated above. During the development of Li-ion batteries, several options were considered for the cathode, including $LiNiO_2$ and $LiCoO_2$.[13] Cathode materials typically contain transition metals as they can readily undergo redox reactions. This allows them to act as a solid host network that can accommodate guest ions reversibly. Specific capacities for cathode materials typically range between 100 – 200 mA h g^{-1} and the average voltage is between 3 – 5 V vs. Li metal.[14] Current commercial cathode materials are based on transition metal oxides and polyanion compounds.

1.2.2.1 Transition Metal Oxide Cathodes

Many lithium-based metal oxides adopt a layered structure that is suitable for intercalation chemistry. $LiCoO_2$ (LCO), shown in Figure 1.2, was first developed by Goodenough and Mizushima and has a layered structure in space group $R\bar{3}m$.[15] In the LCO structure, Li is located in the octahedral sites between the layers of edge sharing CoO_6 octahedra. LCO is reported to have a specific capacity of 155 mA h g^{-1}, making it a suitable cathode material.[8] Other advantages of LCO include good cycling performance, a high discharge voltage (3.9 V) and low self-discharge.[16]

Despite the many advantages of LCO, it is costly to produce and suffers from capacity fade at high cycling rates and during deep cycling (when more than 50% Li^+ is extracted). During deep cycling the structure undergoes a phase transition from hexagonal to monoclinic symmetry, causing the cycling performance to deteriorate.[18] This can, however, be resolved by using metal oxide coatings.[19] One major disadvantage of LCO is its low thermal stability.[20] As the temperature is raised and approaches 200 °C, oxygen is re-

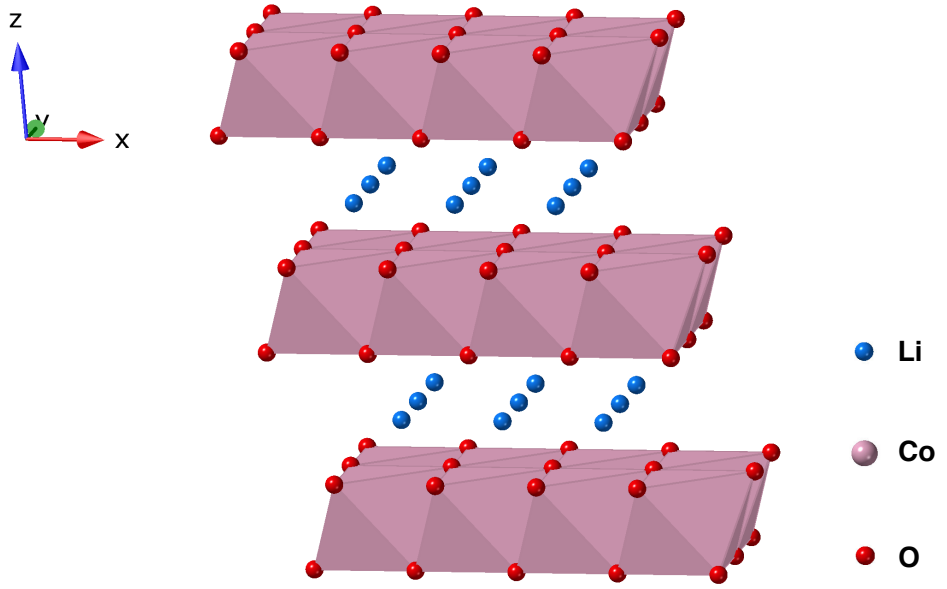

Figure 1.2: The layered structure of $LiCoO_2$, in space group $R\bar{3}m$, showing Li located between the layers formed by the CoO_6 octahedra.[17]

leased from LCO. When used as a cathode inside a cell, the oxygen released reacts with the organic components of the electrolyte. This is a thermal runaway reaction which can cause the cell to catch fire.

Another transition metal oxide considered as a possible cathode material is lithium nickel oxide, $LiNiO_2$ (LNO), which is isostructural to LCO with the Co being substituted by Ni.[20,21] The substitution of Co in $LiCoO_2$ is desirable due to its high cost and toxicity. This lowers the manufacturing costs and reduces the toxicity of the material. LNO has a comparable theoretical capacity of 275 mA h g^{-1}.[22] However, it exhibits a low thermal stability and Ni^{2+} can substitute onto the Li^+ sites, thereby blocking the Li^+ diffusion pathways.[23]

Another layered structure is lithium manganese oxide, $LiMnO_2$ (LMO), shown in Figure 1.3.[14] Again, the substitution of Co with Mn is desirable, as Mn has a higher natural abundance and its use is environmentally friendly. The specific capacity and the voltage operation window of LMO is comparable to LCO. However, the use of Mn does have some disadvantages. Specifically, during Li^+ ion extraction, the structure of LMO changes to that of a $LiMn_2O_4$–type spinel (*vide infra*).[24] Unfortunately, all cathodes containing Mn

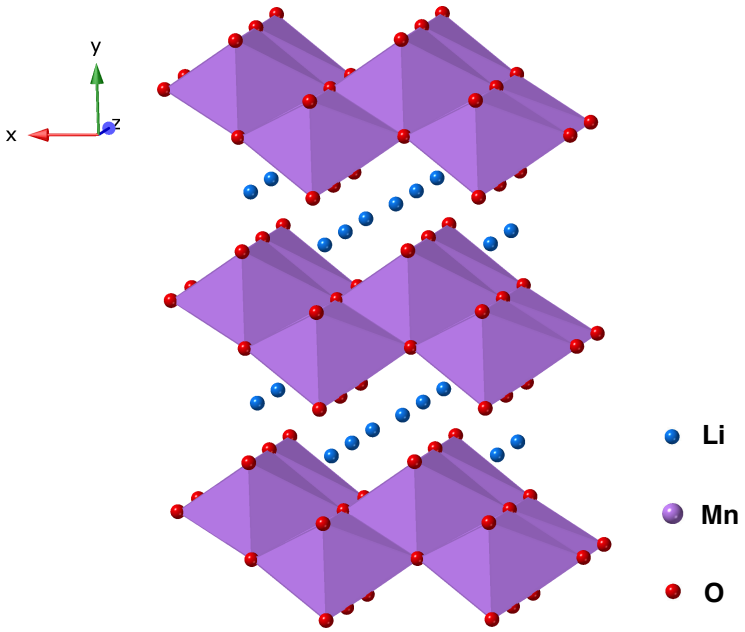

Figure 1.3: The layered structure of $LiMnO_2$, in space group *Pmnm*, showing Li residing between the layers formed by the MnO_6 octahedra.[25]

suffer from this issue of Mn dissolution, the underlying cause being the disproportionation of Mn^{3+} to Mn^{2+} and Mn^{4+}.[26] It is believed that Mn^{2+} is soluble in the electrolyte. Hence, it can migrate to the negative electrode and destabilise the solid electrolyte interface (SEI) layer formed. A SEI layer is a thin layer that forms on the anode surface upon contact with the electrolyte.[27] The layer is believed to be composed of insoluble or partially soluble reduction products of the electrolyte and is usually a good ionic conductor. Research suggests that its presence is essential in order for the battery to operate.[28] However, to date, very little is known regarding the composition and/or functionality of the SEI. As such, considerable research into the SEI is currently underway. The LMO structure can be stabilised by cationic doping.[29] However, it still suffers from poor cycle stability.

A variation of lithium manganese oxide is $LiMn_2O_4$ (also called LMO but denoted as LMO') which adopts a spinel structure in space group $Fd\bar{3}m$, as shown in Figure 1.4.[30,31] The structure consists of a cubic close packed array of oxygen anions, where Li occupies the tetrahedral sites, and Mn occupies the octahedral sites. Li^+ ions diffuse via vacant tetrahedral and octahedral interstitial sites. Unfortunately, LMO' does not perform as well as LCO as a

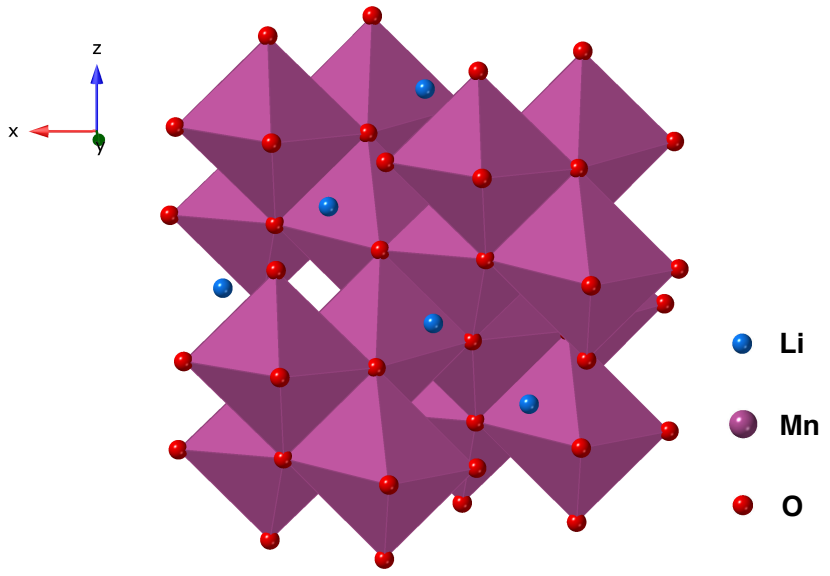

Figure 1.4: The spinel structure of $LiMn_2O_4$, in space group $Fd\bar{3}m$, showing Li occupying the tetrahedral sites between the MnO_6 octahedra.[32]

cathode material and also suffers from Mn dissolution. Other issues include irreversible side reactions with the electrolyte and the loss of oxygen during delithiation.

All of the cathode materials discussed have been compositionally doped with various different metals in order to try and improve their performance and produce safer materials. For example, LNO has been doped with Co and Al to produce $LiNi_{0.8}Co_{0.15}Al_{0.05}O_2$ (NCA) which is currently used in Panasonic batteries for Tesla electric vehicles.[20] NCA has a high capacity of 200 mA h g^{-1} and a longer storage calendar life when compared to other Co-based cathodes. Doping the structure with Co and Al results in a higher thermal stability than LNO and a reduction in the Ni^{2+} content lowers the obstruction of the Li^+ diffusion pathway. However, NCA is known to suffer from capacity fade at higher temperatures (40 – 70 °C) which can limit its use.[33,34]

Attempts to modify the LMO structure include doping with Ni and Co, generating $Li(Ni_{0.5}Mn_{0.5})O_2$ (NMO) and $LiNi_{1-x-y}Co_xMn_yO_2$ (NMC).[35,36] NMO is cheaper than LCO and offers a comparable energy density.[37] Furthermore, doping with Ni enables greater quantities of Li to be extracted. The pres-

ence of Ni and Co in NMC stabilises the structure, resulting in a similar specific capacity and operating voltage to LCO. NMC is also cheaper than LCO and, at present, the most popular composition used is $LiNi_{0.33}Co_{0.33}Mn_{0.33}O_2$.[36] However, one concern is that mixing the cations leads to low Li^+ diffusivity, resulting in lower rate capabilities.[35]

1.2.2.2 Polyanion Compounds as Cathodes

Polyanion compounds are another class of cathode materials. These compounds contain large polyanions $(XO_4)^{3-}$, where X can be S, P, Si, As, Mo and W. Commercialised polyanion compounds include $LiFePO_4$ (LFP) and $LiMnPO_4$ (LMP), both with the olivine structure, as shown in Figure 1.5.[38,39] In this structure type, P occupies one-eighth of the tetrahedral sites whilst Li and Fe/Mn occupy half of the octahedral sites in a hexagonal close packed oxide array. LFP has good thermal stability and high power capability. It is reported to have a specific capacity of 165 mA h g^{-1}, which is higher than that of LCO. However, it also has a low average voltage (3.4 V) and low electronic and ionic conductivities. LMP, on the other hand, has a slightly higher average voltage than LFP (3.8 V, the same as LCO), and a reported specific capacity of 168 mA h g^{-1}. However, a major disadvantage of LMP is its low conductivity.[40]

So far, many different cathode materials have been described, and their

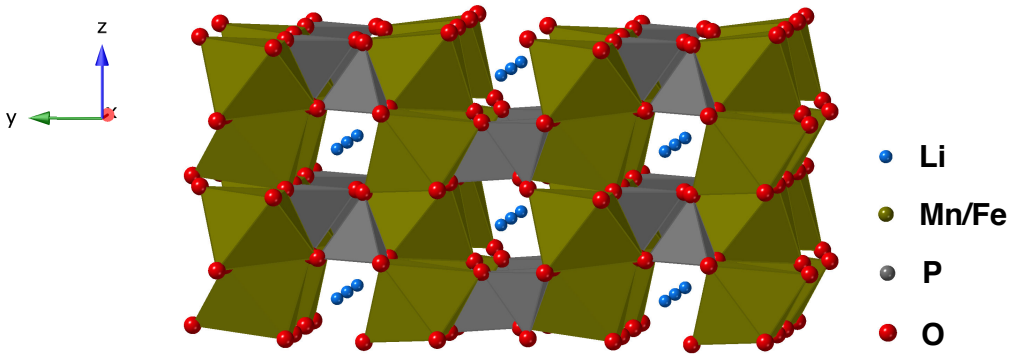

Figure 1.5: The olivine structure of $LiMPO_4$ (M = Mn or Fe), in space group *Pnma*, showing Li in the channels formed by the interconnected MO_6 octahedra and PO_4 tetrahedra.[41]

advantages and disadvantages have been noted. The first commercialised Li-ion batteries used LCO as the cathode material. However, partly due to the high costs associated with using Co, materials with a reduced Co content, such as NMC and NCA, are becoming increasingly popular and have gained a larger market share.[8,42,43]

1.2.3 Anode Materials

The ideal choice for an anode would be lithium metal due to its high specific capacity.[44] However, it was deemed unsuitable due to a series of safety concerns. The formation of dendrites during cycling was found to be of particular concern.[13] Dendrites have been shown to rupture the separator that sits between the two electrodes, thereby short circuiting the cell. As a result, cells were at risk of overheating and exploding. Since then, efforts have focused on using intercalation materials as the anode, as batteries produced using these materials are altogether safer, albeit at the expense of the energy density.

1.2.3.1 Carbon

The first commercial batteries contained carbon-based anodes. These continue to be a popular choice based on their low cost and high abundance.[8,45] Carbon is a good electrical conductor and has a low delithiation potential vs. Li metal. During the intercalation of Li into the structure there is a minor change (10%) in the volume of the electrode. Carbon has a high gravimetric density, but the volumetric capacity is on the lower side (330 – 430 mA h cm^{-3}).[20] Carbon anodes can generally be divided into two categories; soft and hard carbons, a schematic representation of which is shown in Figure 1.6.

Soft carbons, also known as graphitic carbons, have large graphitic grains and very high charge capacities. However, they do not work well with electrolytes containing PC, because PC tends to intercalate in the graphite layers along with the Li^+ ions, resulting in graphite exfoliation and a loss in capacity.[46] In contrast, hard carbons have small graphitic grains with disordered orientations. Hard carbons offer high capacities and a long cycle life. Moreover, they do not exfoliate easily, and the structure contains nanovoids, which

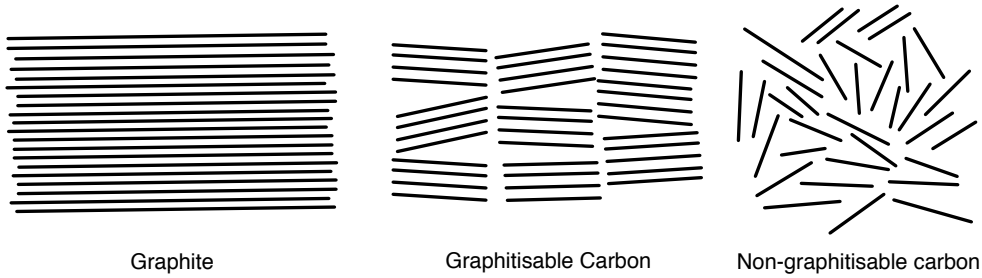

Figure 1.6: Schematic representations of the different morphologies of graphite, graphitisable carbon (soft) and non-graphitisable carbon (hard).[13]

reduce any volume expansion during intercalation and offer better gravimetric capacity (372 mA h g^{-1}).[47] The high surface area of hard carbons is also a disadvantage. The voids result in a material which is not very dense and, hence, has a lower volumetric capacity.

1.2.3.2 Lithium Titanium Oxide

Lithium titanium oxide, $Li_4Ti_5O_{12}$ (LTO), is a non-carbon-based material commercialised as an anode, the structure of which is shown in Figure 1.7.[48,49] LTO has very good thermal stability, together with a high volumetric capacity and a long cycle life. LTO is referred to as a "zero-strain" material, as the change in volume during Li^+ intercalation and de-intercalation is only 0.2%.[50,51] LTO has a potential of ~1.55 V vs. Li metal. Operating at this po-

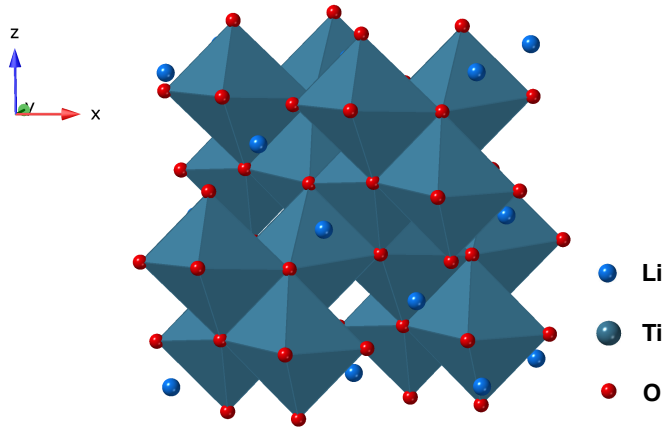

Figure 1.7: The spinel structure of $Li_4Ti_5O_{12}$, in space group $Fd\bar{3}m$, showing Li in the tetrahedral sites between TiO_6 octahedra.[52]

tential avoids the formation of a SEI layer on the anode, which typically takes place below 1 V. Disadvantages of LTO include the high cost of Ti, a lower cell voltage when compared with carbon and a lower theoretical capacity (175 mA h g^{-1} and 600 mA h cm^{-3}). LTO also exhibits slower lithium diffusion and is a good electrical conductor. Hence, LTO is suitable for stationary storage applications due to its high power and long cycle lives. However, it can only be used in lower energy Li-ion batteries.

1.2.4 Electrolytes in Li-ion Batteries

In a Li-ion battery, the purpose of the electrolyte is to transfer the Li^+ ions between the electrodes during charge and discharge. For the electrolyte to function well, it must possess a high ionic conductivity to transport the ions efficiently. It must also be electronically insulating, forcing the electrons to flow outside the cell, thus avoiding an internal short circuit. Current commercial electrolytes consist of lithium salts dissolved in organic solvents.[8,13,45] The conventional choice is $LiPF_6$ dissolved in ethylene carbonate. This combination has high ionic conductivity (σ >10^{-3} S cm^{-1}) and is compatible with the operating voltage window of current Li-ion batteries. Another lithium salt that can be used is $LiBF_4$ which delivers better performance over a broader temperature range when compared to $LiPF_6$. However, the ionic conductivity is 2- to 3-folds lower.[53]

As an alkali metal, lithium is highly reactive towards water; hence non-aqueous electrolytes are required. Carbonate solvents are a good option owing to their ability to solvate lithium salts at high concentrations (>1 M). Carbonate solvents are aprotic, polar and have high dielectric constants. The organic solvent mixtures currently used in commercial liquid electrolytes are based on ethylene carbonate, but they can vary in composition. Typical co-solvents used include linear alkyl carbonates, such as dimethyl carbonate, diethyl carbonate and ethyl methyl carbonate. Ethyl carbonate is essential, as it facilitates reversible reactions at the anode. More specifically, it undergoes a reductive decomposition, and the resulting products form a SEI layer at the anode. As stated earlier, this layer can be hugely beneficial, as it inhibits un-

wanted molecules from intercalating into the graphite structure along with the Li^+ ions.[27]

At present, there are many safety concerns surrounding Li-ion batteries owing to their use of liquid electrolytes, which are known to be corrosive, flammable, irritants and have the potential to leak.[54,55] Furthermore, liquid electrolytes are not compatible for use with metallic lithium anodes due to the formation of dendrites during cycling (*vide supra*).[13] All of these issues have led to an increased demand for safer alternatives, resulting in the development of all-solid-state batteries.

1.3 All-Solid-State Batteries

1.3.1 Introduction

In contrast to conventional Li-ion batteries, all-solid-state batteries (ASSBs) use a solid electrolyte. Since ASSBs are composed of solely solid materials, *i.e.*, no liquid components, they generally have longer cycle lives when compared to traditional Li-ion batteries, as the liquid electrolytes used can facilitate the degradation of the batteries.[54,55] Furthermore, since the electrodes are separated by a solid electrolyte, there is no need for a separator, which leads to a reduction in the net weight and volume of the battery. Other advantages of ASSBs include a low self-discharge rate and a uniform output voltage. As a result of their many advantages, ASSBs are already being used in a variety of applications including cardiac pacemakers where a low power output is required. Moreover, they have been demonstrated to be safe, whilst offering a reasonable lifetime and sufficient energy density.[56]

Undoubtedly, the use of solid electrolytes is key in the development of ASSBs. Many Li-based solid electrolytes have the potential to work well with Li metal anodes, thereby offering high energy densities. In general, solid electrolytes tend to be stable over a large voltage window and have good thermal stability. Moreover, the use of solely solid materials can make packaging simpler, and miniaturisation for small scale applications more realistic when compared to current commercial battery designs. ASSBs could also offer bet-

ter resistance towards wear and tear as well as shock and vibrational changes when compared to current conventional batteries.[54]

Despite their many advantages, there are several challenges which limit the use of ASSBs in commercial applications. One major issue is that solid electrolytes typically have lower ionic conductivities (~10^{-5} – 10^{-9} S cm^{-1}) than their liquid counterparts (>10^{-3} S cm^{-1}). They also tend to offer lower power and current outputs at low temperatures, caused by the high resistance of the solid oxides used. In addition, the stress created at the interface of the electrolyte and the electrodes can have an adverse effect on the lifetime of the battery.[57] The manufacturing costs are also typically very high because expensive techniques such as atomic layer deposition (ALD) are often needed to form thin layers of electrolytes during device fabrication.[57] Hence, research into suitable solid electrolyte materials is still very much ongoing and several candidate systems that are of considerable interest are discussed in greater detail in the following sections.

1.3.2 Requirements for Solid Electrolyte Materials

There are several essential criteria that a material must meet in order to be considered for use as a solid electrolyte, let alone actually being prepared for use in a device.[54,58,59] Most importantly, the material must exhibit a high ionic conductivity, that either matches or exceeds the performance of current liquid electrolytes. This is the ultimate driving force for future commercialisation. Candidate systems must also have a low electronic conductivity and be functional over large voltage and current windows. For example, being operational up to 5 V is desirable as high voltage cathodes usually operate at or close to 4 V. The electrolyte should also be able to maintain its functionality over a broad temperature range, typically −100 to 300 °C. The grain boundary resistance should also be negligible, and the electrolyte must be compatible with the electrode materials used. In addition to this, no side reactions should occur during operation, as they can produce undesirable products at the interface, thereby reducing the conductivity. Furthermore, to avoid deterioration of the battery, there should be no leakage of the electrolyte and very little cor-

rosion of the electrode (*i.e.*, the electrolyte needs to be stable and compatible with the electrodes used). Ideally, the materials should be lightweight to enable their use in portable applications. Sufficient thermomechanical strength is also required for easy packaging and survival in harsh conditions. In addition, self-discharge should be minimal in order to preserve the shelf life. Other desirable qualities include a low cost and toxicity of the materials used, and where possible, recyclable materials, thereby making their production cheap and their use environmentally friendly.

1.3.3 Candidate Solid Electrolyte Materials

Numerous materials have been studied in recent years for use as electrolytes in all-solid-state batteries. These include perovskites, lithium and sodium superionic conductors (LISICON and NASICON), garnets, LiPON, Li_3N and argyrodites. It is noted that this list is by no means exhaustive as many different systems have been explored as potential solid electrolytes. In the following sections those exhibiting the best performance to date will be discussed.

1.3.3.1 Perovskite-type Systems

Perovskites have the general formula ABX_3, where A is a rare earth or alkali earth metal, B is a transition metal, and X is an anion, typically O^{2-} or F^-.[60] The ideal perovskite structure has a cubic unit cell, although most perovskites are distorted owing to the relative sizes of the A- and B-site cations. The extent of the distortion exhibited is dependent on the radii of the ions present in the structure, and it can be expressed via the tolerance factor (t), given by,

$$t = \frac{r_A + r_X}{\sqrt{2}(r_B + r_X)}\,, \tag{1.3}$$

where r_A, r_B and r_X are the radii of the ions A, B and X, respectively.[61] When t = 1, the perovskite adopts a perfect cubic structure. Deviations from this value lead to structural distortions, most commonly caused by cation displacements and/or tilting of the BX_6 octahedra.[62] The compositional flexibility of the per-

ovskite structure allows for various A- and/or B-site substitutions, leading to the development of different perovskite-based systems with varying compositions, many of which often display interesting and tuneable physical properties, including piezoelectricity, ferroelectricity and pyroelectricity.[62]

Perovskite-based Li-ion conductors can be described as A-site deficient solid solutions. One of the most popular examples of a perovskite-based Li-ion conductor is lithium lanthanum titanate, $Li_{3x}La_{(2/3)-x}\square_{(1/3)-2x}TiO_3$ (LLTO) ($0 < x < 0.16$), shown in Figure 1.8.[63] LLTO has a tetragonal structure, with a large A-site vacancy concentration that allows Li ions to move via a vacancy mechanism. More specifically, Li ions move through a square planar configuration formed by the four O^{2-} ions and the A-site cations. The ionic conductivity of LLTO is dependent on the Li concentration, and when $x = 0.11$, the bulk conductivity of LLTO can reach up to 10^{-3} S cm^{-1} at room temperature (RT), with an activation energy of 0.40 eV for the migration of Li ions.[64,65]

Whilst LLTO offers a comparable ionic conductivity to conventional liquid electrolytes (>10^{-3} S cm^{-1}), it does have some disadvantages. Most notably, during sample preparation it is particularly challenging to control the Li content, as very high temperatures are required for synthesis, leading to significant losses of Li_2O. Moreover, the use of high temperatures can result in grain boundary resistance, which reduces the conductivity to <10^{-5} S cm^{-1}.[64] Attempts to improve the ionic conductivity of LLTO have included doping the A-sites with Sr. For example, LLTO doped with 5% Sr on the A-site, $(Li_{0.5}La_{0.5})_{0.95}Sr_{0.05}TiO_3$, has a reported ionic conductivity of 1.5×10^{-3} S cm^{-1} at 27 °C. It is noted that doping the A-site results in a reduction of Li concentration; hence, if the doping level is too high (in this case >0.1) the conductivity will start to decrease.[67] As stated earlier, it is envisaged that Li metal anodes will be used in ASSBs. Hence, solid electrolytes must be compatible with their use. Unfortunately, one major drawback of LLTO is its inability to be used with a metallic lithium anode, as Li insertion is known to result in the reduction of Ti^{4+} to Ti^{3+}, which increases the electronic conductivity of LLTO, causing short-circuiting of the cell.[68]

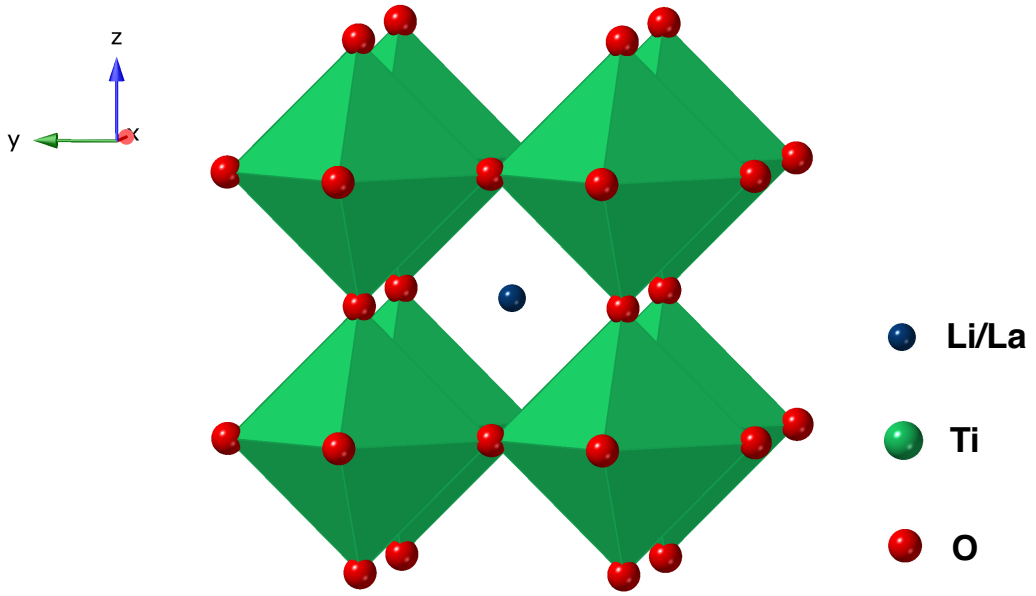

Figure 1.8: The perovskite structure of LLTO, in space group $Pm\bar{3}m$, showing Li in the cavities formed via the TiO_6 octahedra.[66]

Another well known example of a perovskite-based solid electrolyte is $LiSr_{1.65}Ta_{1.7}Zr_{1.3}O_9$ (LSTZ), which is known to be stable in contact with Li, as Zr^{4+} and Ta^{5+} do not undergo reduction during the intercalation process. However, the reported ionic conductivity is 1.3×10^{-5} S cm^{-1}, which is lower than that of LLTO.[69] In order to improve the ionic conductivity of this material, differing compositions have been investigated and $Li_{0.375}Sr_{0.438}Ta_{0.75}Zr_{0.25}O_3$ is reported to have an ionic conductivity of 1.33×10^{-4} S cm^{-1}, higher than that of the parent LSTZ system.[70] Similar or related modifications have included substituting Zr with Hf, forming $Li_{0.375}Sr_{0.438}Ta_{0.75}Hf_{0.25}O_3$. This material is reported to exhibit an ionic conductivity of 3.8×10^{-4} S cm^{-1} at RT.[71] Hence, this suggests that compositional modifications are a good method for improving the ionic conductivity of perovskite-based materials, making them a good candidate for solid electrolytes. However, their ionic conductivities remain lower than those of current liquid electrolytes. Also, it is noted that the synthesis of these materials requires very high temperatures (>1300 °C) making them economically less viable for large scale processing.

1.3.3.2 NASICON-type Conductors

In recent years, NASICON (NA Super Ionic CONductor)-type systems have gained considerable interest as solid electrolyte materials.[72] NASICON refers to $NaA_2(PO_4)_3$ (A = Ge, Ti and Zr), the structure of which is shown in Figure 1.9. One example of a NASICON-type material is $Na_{1+x}Zr_2Si_xP_{3-x}O_{12}$ ($0 < x < 3$), with an ionic conductivity on the order of 10^{-3} S cm^{-1} at RT.[73] Typically, NASICON has a rhombohedral structure in space group $R\bar{3}c$. When $1.8 < x < 2.2$ NASICON adopts a monoclinic structure with space group $C2/c$. The NASICON structure consists of a framework of interconnected AO_6 octahedra and PO_4 tetrahedra, with two different Na sites within the framework. Ion diffusion occurs via the movement of Na ions from one site to another. The Na-ion mobility is dependent upon both the value of x and the activation energy, E_a, for Na ion transport. When x = 0, only one Na site is preferentially filled and when x > 0, the second site begins to be filled and the ionic con-

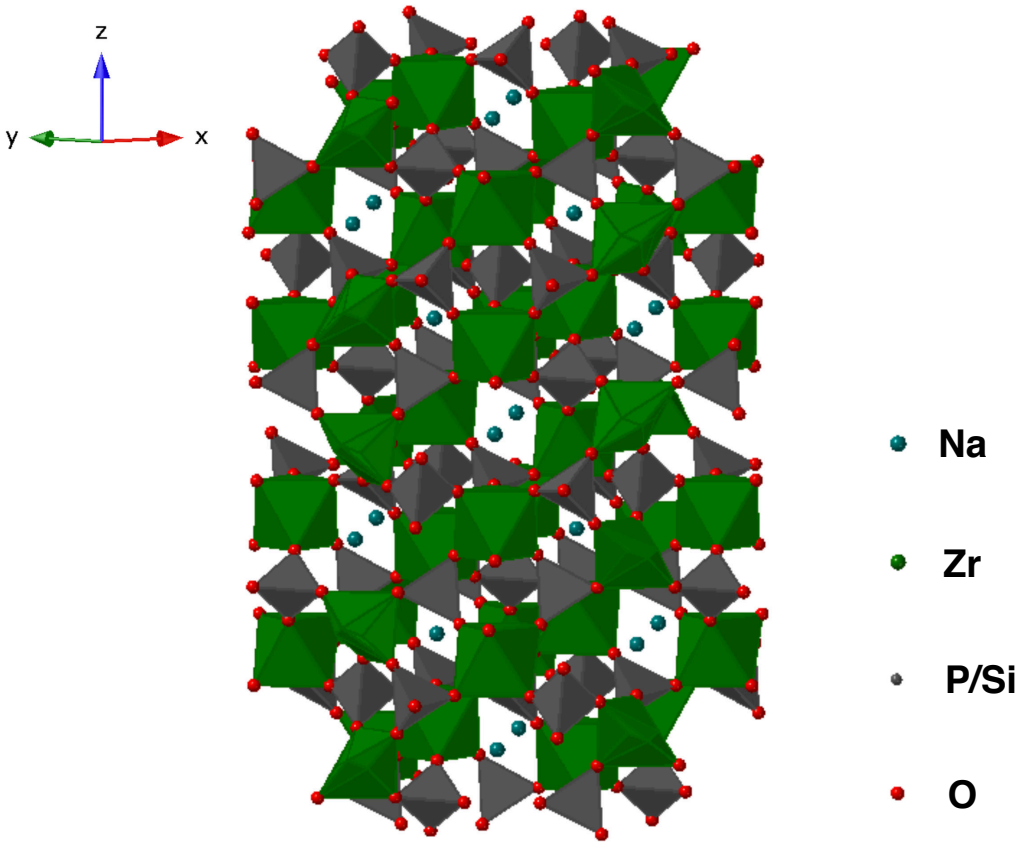

Figure 1.9: The structure of NASICON, in space group $R\bar{3}c$, showing Na in the framework formed via chains of interconnected ZrO_6 octahedra and P/SiO_4 tetrahedra.[74]

ductivity increases. Changing the framework ions in order to provide more space for the Na ions to move can increase the ionic conductivity. One popular example is $Na_3Zr_2PSi_2O_{12}$, which is reported to display an ionic conductivity of 2.0×10^{-1} S cm^{-1} at 300 °C.[75] This value alone makes NASICON an attractive candidate for use in sodium-ion batteries and, as such, has inspired the synthesis of Li-based structures for use in Li-ion batteries.

One type of Li-based equivalent is $Li_{1.3}Al_{0.3}Ti_{1.7}(PO_4)_3$ (LATP), the structure of which is shown in Figure 1.10. LATP has a reported ionic conductivity of 3.0×10^{-3} S cm^{-1} at RT.[54] In a similar manner to the perovskite-based systems, the composition of LATP has been modified in order to improve performance, *e.g.*, $Li_{1+x}Ti_{2-x}M_x(PO_4)_3$, where M is Ga, In or Sc. Such compositional modifications have resulted in an ionic conductivity of 7.0×10^{-4} S cm^{-1}.[76] This ionic conductivity is lower than LATP, and in a similar manner to the perovskite LLTO, a significant drawback of this material is the presence of Ti^{4+}, which is susceptible to reduction. Hence, like LLTO, LATP is also unsuitable

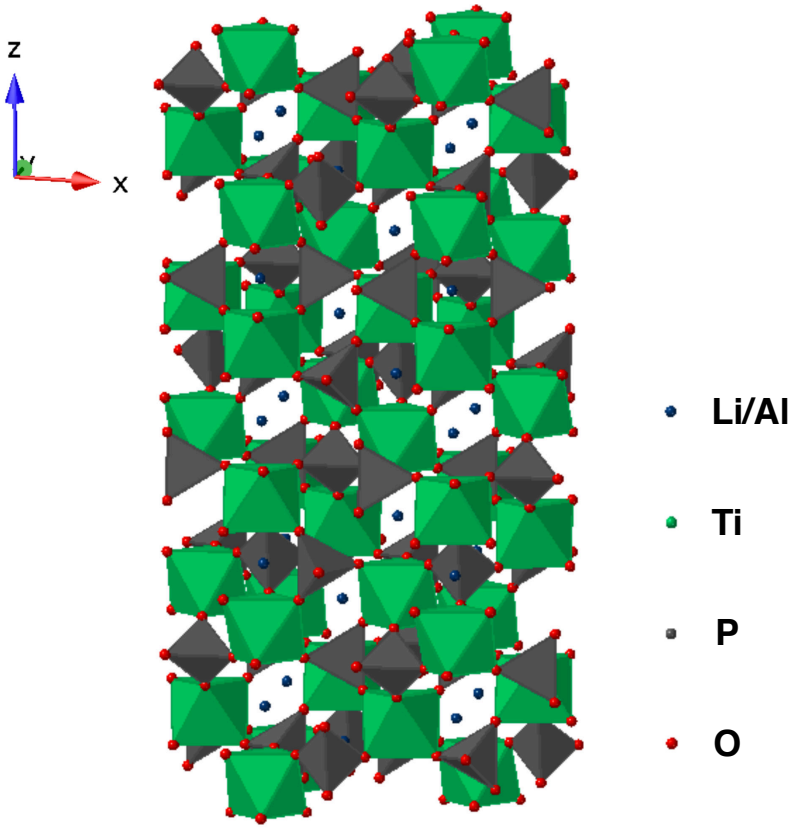

Figure 1.10: The structure of LATP, in space group $R\bar{3}c$, showing Li in the framework formed via chains of interconnected TiO_6 octahedra and PO_4 tetrahedra.[77]

for use with a metallic lithium anode. Another Li-based NASICON material is $Li_{1.5}Al_{0.5}Ge_{1.5}(PO_4)_3$ (LAGP), which is reported to exhibit an ionic conductivity of 4.0×10^{-4} S cm^{-1} at RT.[78] This can be improved to 6.65×10^{-3} S cm^{-1} by partially substituting Al with Cr, forming $Li_{1.5}Al_{0.4}Cr_{0.1}Ge_{1.5}(PO_4)_3$.[79] Unlike LATP, LAGP does not contain Ti and therefore does not have the issue of being reduced during cycling. Moreover, LAGP is known to be electrochemically stable between 0.85 – 7.0 V vs. Li metal.[80] However, it is noted that although LAGP is stable and has a good ionic conductivity, it is expensive to produce owing to the costs associated with its precursors, namely GeO_2.[81] Hence, this is a limiting factor when considering its potential use in future applications.

1.3.3.3 LISICON-type Materials

LISICON (LI Super Ionic CONductor), first reported by Hong *et al.* in 1978, refers to $Li_{14}Zn(GeO_4)_4$.[82] The structure of LISICON, shown in Figure 1.11, is based on the γ-Li_3PO_4 framework. It is widely known that γ-Li_3PO_4 is not a good ion conductor, hence, the composition must be modified in order to improve the ionic conductivity.[83,84] In γ-Li_3PO_4, Li can only move via a vacancy mechanism, as Li does not occupy any interstitial sites. However, when P^{5+} is replaced and Li is partially substituted with Ge^{4+} and Zn^{4+}, the resulting LISICON, $Li_{14}Zn(GeO_4)_4$, contains both vacant Li sites and Li located in interstitial sites. The structure therefore consists of a framework of $[Li_{11}Zn(GeO_4)]^{3-}$ with the remaining three Li ions occupying the interstitial sites within the framework. These Li ions are then able to move through the structure in two dimensions via both vacancy and interstitial mechanisms. At present, the reported ionic conductivity of LISICON is 1.3×10^{-6} S cm^{-1} at 33 °C. This has been shown to increase to 1.25×10^{-1} S cm^{-1} at 300 °C, making LISICON an excellent high temperature conductor.[55]

In LISICON, the Li-ion mobility is dependent on the size of the bottleneck formed via O^{2-} ions and on the bonding energy between the Li and O^{2-} ions in the framework. In a similar manner to earlier discussions, different compositional modifications have been made in order to obtain a material with good ionic conductivity. For example, O^{2-} ions have been partially substi-

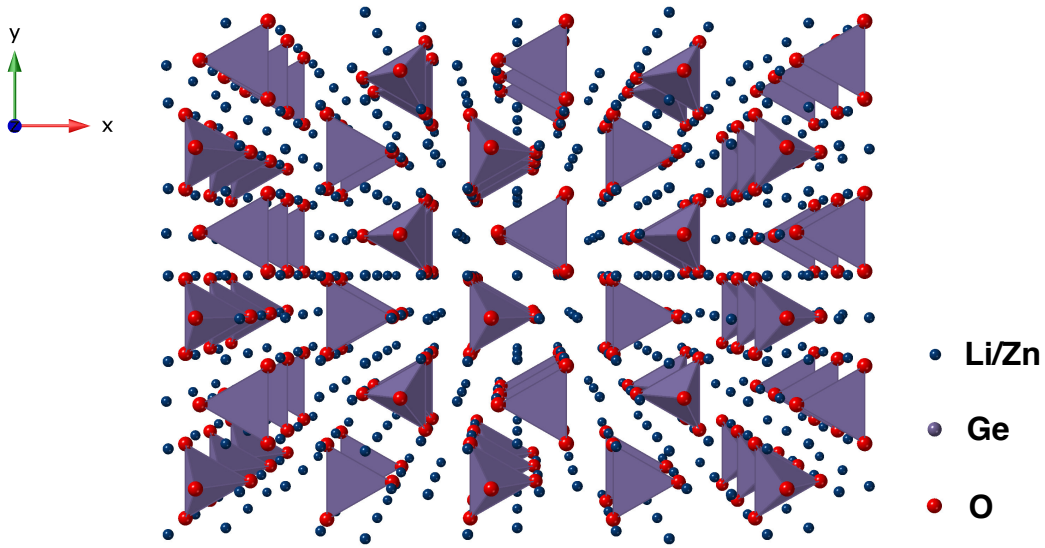

Figure 1.11: The structure of LISICON, in space group *Pnma*, showing Li located in channels formed via the GeO_4 tetrahedra.[82]

tuted with Cl^- ions to form the composition $Li_{10.42}Ge_{1.5}P_{1.5}Cl_{0.08}O_{11.92}$.[85] This material is reported to have an ionic conductivity of 3.7×10^{-5} S cm^{-1} at 27 °C, which is higher than that of LISICON. This improvement is believed to be due to the larger ionic radius of Cl^- which leads to a larger bottleneck, providing more room for Li to move. Furthermore, Cl^- has a lower electronegativity than O^{2-}so it does not bond as strongly to the mobile Li as O^{2-}, enabling Li to move with greater ease.

Another material based on this structure type is $Li_{3+x}Ge_xV_{1-x}O_4$ (x = 0 – 1), which is a solid solution between γ-Li_3VO_4 and Li_4GeO_4.[86] In a similar manner to γ-Li_3PO_4, γ-Li_3VO_4 does not have any Li occupying the interstitial sites within the structure. Hence, forming a solid solution with Li_4GeO_4 is a good way of introducing Li onto the interstitial sites and therefore producing a good Li-ion conductor. When x = 0.5, an ionic conductivity of 4.0×10^{-5} S cm^{-1} at 18 °C is reported which is an order of magnitude higher than LISICON. A solid solution between Li_4SiO_4 and Li_3PO_4 has also been reported, $Li_{4-x}Si_{1-x}P_xO_4$ (x = 0 – 1), with an ionic conductivity of $\sim 10^{-6}$ S cm^{-1} at RT for x = 0.5, which is similar to LISICON, but not comparable to liquid electrolytes.[87] Whilst the LISICON structure has been extensively investigated, the ionic conductivities of all the compositions remain too low for these systems

to be effectively used in commercial applications.

1.3.3.4 Garnets

Garnets have the general formula $A_3B_2C_3O_{12}$, where the A-, B- and C-cations occupy the dodecahedral, octahedral and tetrahedral sites, respectively.[62] In the context of battery-related research, garnets containing an excess of Li have been extensively investigated. These garnets are known as Li-stuffed garnets and one popular example is $Li_5La_3M_2O_{12}$ (M = Ta or Nb), shown in Figure 1.12. It is reported to have a cubic structure in space group $Ia\bar{3}d$, with the La and M occupying the octahedral sites.[88] In this particular system, Li is situated in both the octahedral and tetrahedral sites owing to an excess of Li within the system. The tetrahedra and octahedra are connected by a shared face, which is believed to facilitate the movement of Li ions through the structure. The octahedral sites are known to promote Li-mobility, whilst the tetrahedral sites trap the Li ions and restrict their movement.[89] Although Li is able to move in three-dimensions through the structure, the ionic conductivity of this material remains low at around 10^{-6} S cm^{-1} at RT. Attempts to improve the ionic conductivity have included doping with Ba to form $Li_6BaLa_2Ta_2O_{12}$, which gives an ionic conductivity of 4.0×10^{-5} S cm^{-1} at RT.[90] This material was also found to be stable when in contact with molten Li and is stable up to 6 V vs. Li metal.

Another potential Li-based garnet-type solid electrolyte is $Li_7La_3Zr_2O_{12}$ (LLZO), which also adopts a cubic structure.[92] Here, the framework is formed via interconnected LaO_8 dodecahedra and ZrO_6 octahedra, and in a similar manner to $Li_5La_3M_2O_{12}$ (M = Ta or Nb), Li is located on both the octahedral and tetrahedral sites. LLZO is reported to be a better ion conductor than $Li_5La_3M_2O_{12}$, with an ionic conductivity of 3.0×10^{-4} S cm^{-1} at RT. LLZO is also reported to be stable when in contact with Li metal and has an electrochemical stability window of up to 9 V vs. Li metal. Attempts to increase the ionic conductivity have included doping Nb^{5+} with Zr^{4+}, forming $Li_{6.75}La_3Zr_{1.75}Nb_{0.25}O_{12}$, which is reported to display an ionic conductivity of 8.0×10^{-4} S cm^{-1} at RT, which is higher than LLZO.[93]

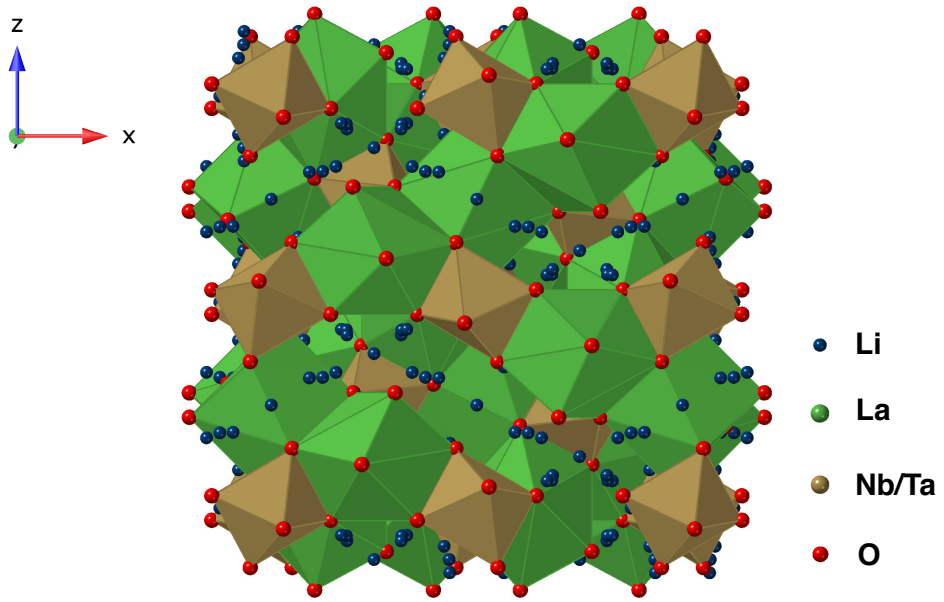

Figure 1.12: The garnet structure of $Li_5La_3(Nb/Ta)_2O_{12}$, in space group $Ia\bar{3}d$, showing Li in channels formed via chains of interconnected Nb/TaO_6 octahedra and the LaO_8 dodecahedra.[91]

Whilst Li-based garnets are stable in contact with Li metal and have the potential to be modified via doping, the ionic conductivities reported to date remain low. It has also been suggested that the distribution of Li between the two sites is dependent on the annealing process.[89] Furthermore, a significant proportion of the Li ions are immobile within the structure as the tetrahedral sites restrict Li ion movement which leads to a reduction in the ionic conductivity.[88] Hence, these materials are not suitable for use as solid electrolytes at present.

1.3.3.5 LiPON-type Materials

Lithium phosphorus oxynitride, known as LiPON, has the general formula $Li_xPO_yN_z$, where the amount of Li, O and N can be controlled during synthesis and can also be used to influence and/or control the ionic conductivity of the material.[94] The LiPON structure consists of cross-linked PO_4 chains and doubly and triply coordinated nitrogen to the bridging and non-bridging oxygen ions in the glass network. It has been suggested that the PO_4 chains promote mobility, but the conduction pathways are yet to be specified.[94]

A thin film of LiPON with composition $Li_{3.1}PO_{3.8}N_{0.16}$ was first synthesised by Bates *et al.*, using radiofrequency (RF) magnetron sputtering with Li_3PO_4 as the target in a pure N_2 atmosphere.[95] This material had an ionic conductivity of 2.0×10^{-6} S cm^{-1} at RT and was found to be stable up to 5 V vs. Li metal. Further studies have focused on modifying the composition and using different synthetic techniques to increase the ionic conductivity. For example, Li_3PO_4 has been mixed with Li_2O in a 1:2 ratio in order to introduce more Li into the system. This particular composition, Li_3PO_4:Li_2O (1:2), is reported to exhibit an ionic conductivity of 6.4×10^{-6} at RT, which is higher than that of the original composition.[96] LiPON thin films have also been synthesised using ion beam assisted deposition (IBAD) and metalorganic-chemical vapour deposition (MOCVD).[78,97] During IBAD, the nitrogen content can be controlled using the flow ratio of N_2 and Ar, with the resulting material displaying an ionic conductivity of 4.5×10^{-6} S cm^{-1} at RT. The thin film produced using MOCVD (thickness = 190 nm) is reported to display a slightly higher ionic conductivity (5.9×10^{-6} S cm^{-1}) than that of a film with a thickness of 95 nm (5.3×10^{-6} S cm^{-1}). Hence, LiPON is a good candidate for use as a thin-film solid electrolyte however, the ionic conductivity is too low for it to realistically compete with liquid electrolytes for use in ASSBs.[98]

1.3.3.6 Li_3N-type Materials

The lithium nitride, Li_3N, structure is composed of two alternating layers, shown in Figure 1.13. One layer in Li_3N consists of N anions coordinated to 6 Li cations. The other layer is composed of solely Li cations.[99] Li_3N has been synthesised by reacting pure Li ribbon with N_2 followed by sintering at 650 °C under a nitrogen atmosphere. The density of the resulting material was 80% of its theoretical value, and the reported ionic conductivity was 3.7×10^{-8} S cm^{-1} at 25 °C.[100] The ionic conductivity reported for this "as-synthesised" Li_3N is lower than that of commercially available 96% Li_3N, which exhibits an ionic conductivity of 3.0×10^{-7} S cm^{-1} at 25 °C.[55] It has been suggested that, in order to improve the ionic conductivity of the "as-synthesised" samples, the sintering temperature should be increased to 750 °C and heating should take

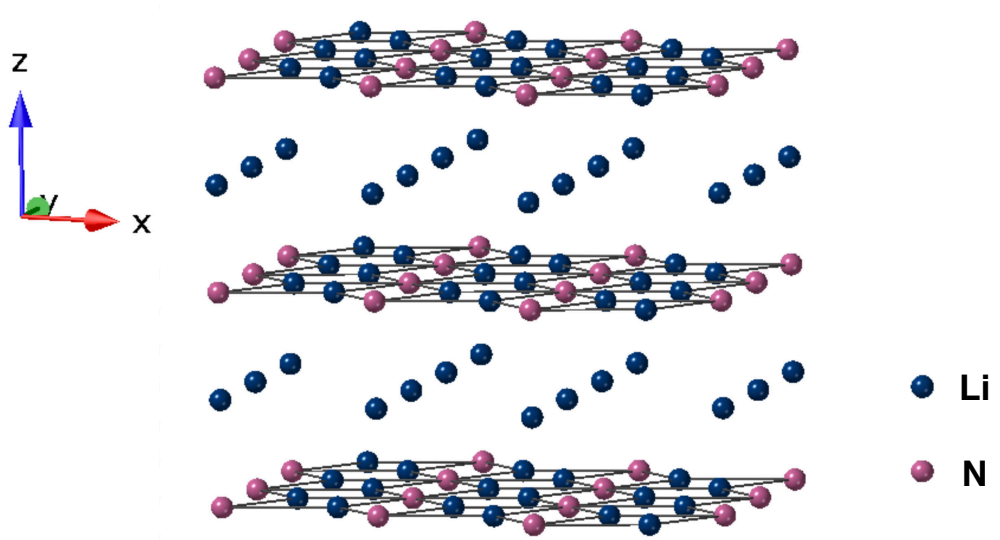

Figure 1.13: The hexagonal structure of Li_3N, in space group *P6/mmm*, showing two alternating layers of Li_6N and Li atoms.[99]

place under 1 atm of N_2. The samples produced under these conditions are reported to display an ionic conductivity of 2.0×10^{-4} S cm^{-1} at 25 °C, which is a considerable improvement in performance.[101] This is believed to be the result of an increase in the Li/N ratio.

Additional studies into the Li_3N system have included the synthesis of lithium nitride halides, *e.g.*, Li_3N–LiCl. Kitahama *et al.*, investigated samples with compositions ranging from $2Li_3N$–3LiCl to $9Li_3N$–11LiCl.[102] In all cases, a cubic antifluorite structure was produced. However, a new non-cubic phase, $Li_9N_2Cl_3$, was also observed that was reported to display an ionic conductivity of $>10^{-7}$ S cm^{-1} at RT, which was higher than all of the other samples prepared. Additional investigations by Hatake *et al.*, focused on 3LiN–MI (M = Li, Na, K and Rb) systems prepared via solid-state synthesis at 600 °C.[103] Here, the reported ionic conductivities ranged from 7.0×10^{-5} S cm^{-1} to 1.1×10^{-4} S cm^{-1} at RT. However, unfortunately, these samples were susceptible to decomposition at voltages ranging from 2.5 – 2.8 V.

Additional structural modifications have been undertaken by partially substituting Li in Li_3N with cations such as Al, Si and Ca.[104–106] Li_3AlN_2 is re-

ported to adopt a cubic antifluorite structure and has an ionic conductivity of 5.0×10^{-8} S cm^{-1} at RT, which is lower than that of Li_3N. In a similar manner to 3LiN–MI systems, Li_3AlN_2 undergoes decomposition at low voltages (0.85 V) at 104 °C. The ionic conductivity can be marginally improved by doping with Ca and Si, as samples of $Li_{0.85}Ca_{0.075}Si_2N_3$ are reported to display an ionic conductivity of 1.6×10^{-7} S cm^{-1} at RT. Although the Li_3N system can be easily modified via changing the composition or by cation doping, the ionic conductivities typically remain low at ambient temperatures. Furthermore, samples of Li_3N are susceptible to decomposition at low voltages, which limits their use in commercial applications.

1.3.3.7 Sulphide-based Electrolytes

Sulphide-based electrolytes are typically referred to as thio-LISICON electrolytes in the literature and are prepared by replacing the O^{2-} in LISICON with S^{2-}.[107,108] Thio-LISICON electrolytes tend to exhibit higher ionic conductivities than LISICON-based electrolytes as the interaction between the S^{2-} and Li^+ is weaker than O^{2-} and Li^+. This is believed to promote Li-ion mobility and, hence, result in high ionic conductivities. Thio-LISICON electrolytes can be divided into three categories: ceramics, glasses and glass-ceramics.

Several ceramic thio-LISICON materials have been synthesised using Li_4GeS_4 as the parent material, the composition of which can be intentionally modified in order to create either more vacancies or more interstitial Li.[109] For example, partially substituting Li^+ with Zn^{2+} and Ge^{4+} with Ga^{3+}, results in the compositions Li_2ZnGeS_4, $Li_{4-2x}Zn_xGeS_4$ and $Li_{4+x+\delta}(Ge_{1-\delta'-x}Ga_x)S_4$ being produced, with $Li_{4+x+\delta}(Ge_{1-\delta'-x}Ga_x)S_4$ (which contains interstitial Li) exhibiting the highest ionic conductivity (6.5×10^{-5} S cm^{-1}) at 25 °C when x = 0.25.[110] It is also reported to be stable up to 5 V vs. Li metal. Li_4GeS_4 can also be modified by partially substituting Ge^{4+} with P^{5+} to produce $Li_{4-x}Ge_{1-x}P_xS_4$ ($0 < x < 1$), which contains vacant Li sites.[111] Its structure is based on that of LISICON (*vide supra*) with the main difference being that O^{2-} has been replaced by S^{2-}. The ionic conductivity is reported to increase with increasing x, reaching a maximum when x = 0.75. $Li_{3.25}Ge_{0.25}P_{0.75}S_4$ is reported to exhibit an ionic

conductivity of 2.17×10^{-3} S cm^{-1} at RT, which is comparable to current commercial liquid electrolytes. Furthermore, this material is also stable up to 5 V vs. Li metal, making it is a promising candidate.

As stated previously, sulphide-based electrolytes also produce glasses, and these have also been researched extensively. Glasses have an amorphous structure as opposed to crystalline materials; therefore, they are expected to display high ionic conduction as the movement of ions is likely to be easier. In order to investigate the influence of glass and ceramic structures on the ionic conductivity, Mizuno *et al.*, synthesised $70Li_2S$–$30P_2S_5$ in both glass and glass-ceramic forms using a melt-quench method in addition to a ceramic sample prepared via a solid-state route.[112] The ionic conductivities reported for the glass and glass-ceramics are 5.4×10^{-5} S cm^{-1} and 3.2×10^{-3} S cm^{-1} at RT, respectively. In contrast, the ceramic sample exhibits an ionic conductivity of 2.6×10^{-8} S cm^{-1} at RT, which is considerably lower than the conductivities reported for the glassy samples. These findings suggest that samples composed of both glass and ceramic are suitable candidates for further exploration. These glass-ceramic materials, xLi_2S–$(100-x)P_2S_5$, have also been reported via mechanical milling at RT, which can enable values of x up to 80 to be reached.[113] In contrast, the melt-quench method could only produce compositions with $x \leq 70$. It has been reported that the Li-ion conductivity increases with increasing Li content and for xLi_2S–$(100-x)P_2S_5$, the conductivity reaches a maximum at x = 75. The reported ionic conductivity is 2.0×10^{-4} S cm^{-1} at RT, which is higher than that for samples produced using the melt-quench method.

Hayashi *et al.*, have also reported the synthesis of the 80-Li_2S–$20P_2S_5$ glass-ceramic via mechanical milling and heating.[114] Samples prepared using this method are reported to exhibit an ionic conductivity of 9.0×10^{-4} S cm^{-1} at RT, which is, again, higher than that of a glassy sample. The ceramic phase observed in this sample is Li_7PS_6, which is reported to have an ionic conductivity of 8.0×10^{-5} S cm^{-1} at RT in its pristine ceramic form.[114] It has been suggested that the Li_7S_6 phase in the glass-ceramic sample is different to that in the ceramic phase, which is believed to result in a higher ionic conductivity. Some studies have indicated the presence of additional phases in 80-Li_2S–

$20P_2S_5$, such as Li_3PS_4 and Li_7PS_6 in addition to other, unidentified, phases. It has been suggested that the ionic conductivity is dependent on the crystalline phases formed, which are, in turn, dependent on the temperatures used during synthesis. The reaction temperatures used during synthesis have been optimised by Seino *et al.*, to produce a Li_2S–P_2S_5 glass-ceramic, containing $Li_7P_3S_{11}$ as a ceramic phase.[115] Investigations into the structure of the Li_2S–P_2S_5 glass-ceramic indicated that samples exhibited few or no grain boundaries, and an ionic conductivity of 1.7×10^{-2} S cm^{-1} was reported at 25 °C. To date, the data obtained for the glass-ceramic thio-LISICON materials indicates that they are a better conductor than current commercial liquid electrolytes. Furthermore, the ionic conductivity at lower temperatures (−35 °C) is reported to be on the order of 10^{-3} S cm^{-1}.[115]

There is no doubt that sulphide-based materials are excellent solid electrolyte candidates. However, there are some serious drawbacks to their potential use. For example, these materials are extremely moisture sensitive, meaning they cannot be handled in an ambient atmosphere, making large scale applications extremely challenging. Furthermore, upon exposure to moisture, these materials react to form H_2S gas. Hence, when considering these materials for use in commercial applications, this is a major safety concern.

1.3.3.8 Argyrodite-type Materials

The synthesis of Li-based argyrodite-type materials was first reported by Deiseroth and co-workers in 2008.[116] These materials have a general formula of Li_6PS_5X, where X can be Cl, Br or I, and the structure of Li_6PS_5Cl is shown in Figure 1.14. Here, the sulphur and halogen atoms form 136 tetrahedral holes, out of which, four are made by sulphur atoms (S1) and are occupied by P atoms, forming PS_4 tetrahedra. The rest of the 132 tetrahedral holes are formed by the remaining sulphur (S2) and halogen atoms. These tetrahedral holes are partially filled by Li atoms. The structure is also influenced by the halogen used; for example, Li_6PS_5I has a fully ordered structure, Li_6PS_5Br has partially disordered S and Br sites and Li_6PS_5Cl exhibits complete disorder on the S and Cl sites. For Li_6PS_5Br, there is 84% S and 16% Br on the S2 sites

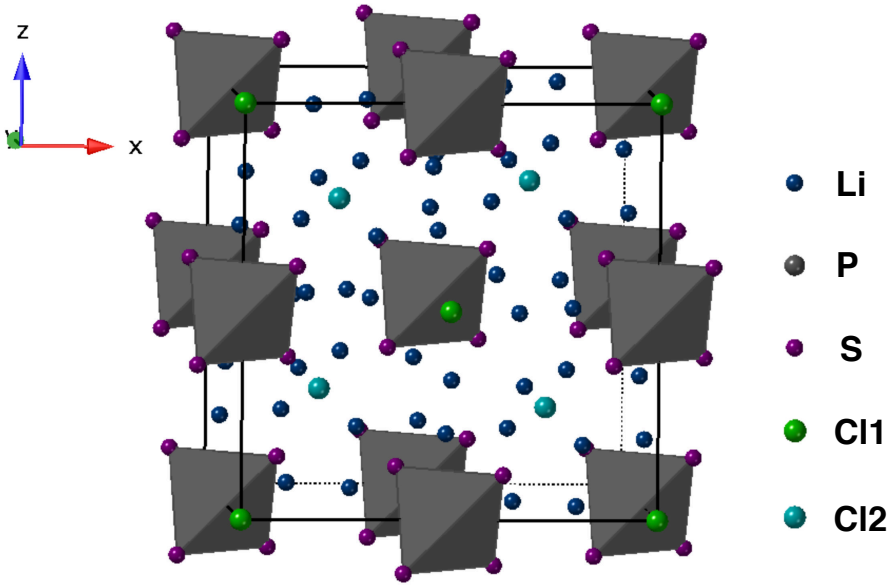

Figure 1.14: The cubic structure of Li_6PS_5Cl, in space group $F\bar{4}3m$, displaying PS_4 tetrahedra and two different Cl sites.[117]

and 60% Br and 40% S on the X sites. The reported ionic conductivity at RT for Li_6PS_5I synthesised via conventional solid-state routes is 3.6×10^{-7} S cm^{-1}, whereas for the Br analogue it is in the range of 10^{-3} – 10^{-2} S cm^{-1}.[118,119]

These materials have also been synthesised using mechanical milling followed by annealing. After mechanical milling, the crystallite size of the samples produced was around 15 nm. The reported ionic conductivities at RT for Li_6PS_5Cl, Li_6PS_5Br and Li_6PS_5I are 4.6 x 10^{-4}, 6.2 x 10^{-4} and 1.9 x 10^{-4} S cm^{-1}, respectively.[120] Following heat treatment, the crystallite size of the samples increased to ~90 nm, and there was no significant change in the ionic conductivities for Li_6PS_5Cl and Li_6PS_5Br. However, for Li_6PS_5I, the ionic conductivity decreased to 10^{-7} S cm^{-1}. These differences are believed to be caused by structural disorder. In Li_6PS_5Cl and Li_6PS_5Br the S/Cl and S/Br disorder promotes Li-ion mobility, resulting in high ionic conductivities whereas, in Li_6PS_5I, there is no disorder and, hence, a very low ionic conductivity is observed. These samples were also tested to determine their electrochemical stability and were found to be stable between 0 – 7 V vs. Li metal.

Additional attempts to produce samples with high ionic conductivities have included synthesis via solid-state sintering methods and using an excess of Li_2S. Zhang *et al.*, found that samples prepared using these methods exhibited higher ionic conductivities than the samples produced using mechanical milling.[121] The reported values at RT are 1.8×10^{-3} and 1.3×10^{-3} S cm^{-1} for Li_2PS_5Cl and Li_2PS_5Br, respectively. This makes Li-based argyrodites a suitable candidate for further investigation. However, in a similar manner to sulphide-type materials, Li-based argyrodites are moisture sensitive, making it challenging to successfully incorporate them into commercial applications.

All the materials discussed so far have their advantages and disadvantages, and, an ideal solid electrolyte candidate material is yet to be found. Hence, many different materials are still under intensive investigation. The following section discusses another candidate solid electrolyte material, lithium-rich anti-perovskites, which are the main focus of this thesis.

1.4 Lithium-Rich Anti-Perovskites

1.4.1 Introduction

Recently, a class of materials called lithium-rich anti-perovskites (LiRAPs) attracted considerable attention in the field of solid electrolytes, based on their reportedly high ionic conductivities. These "electrochemically-inverted" perovskites were initially inspired by the high temperature superionic perovskite conductors, $NaMgF_3$ and $(K,Na)MgF_3$.[122,123] Anti-perovskites have the general formula $A^-B^{2-}X^+_3$, where the A-site contains a monovalent anion (*e.g.*, F, Cl, Br, I), the B-site is a divalent anion (typically O) and the X-site is an electropositive cation (*e.g.*, Li or Na).[124] Typically, for ease and in keeping with the convention for conventional perovskites, LiRAPs are written as X_3BA, *e.g.*, Li_3OCl. In a similar manner to perovskites, anti-perovskites exhibit extreme structural flexibility, making them an excellent candidate for exploration as useful functional materials. As with perovskites, the composition can be modified with relative ease, meaning a wide range of systems can be synthesised with varying compositions.

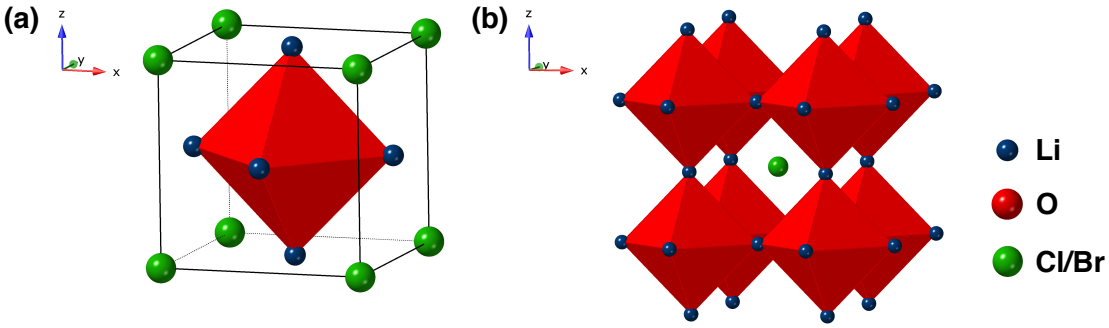

Figure 1.15: (a) The cubic unit cell of Li_3OCl/Br, in space group $Pm\bar{3}m$, displaying Li_6O octahedra surrounded by Cl ions, and (b) the structure of Li_3OCl/Br displaying Cl/Br residing in the cavities formed via corner sharing Li_6O octahedra. [125]

The LiRAPs Li_3OCl and Li_3OBr (Figure 1.15) were recently reported by Zhao and Daeman and it was this study that highlighted their potential as possible solid electrolyte materials.[124] LiRAPs are lightweight, have a high Li content (60% Li by composition and 29 wt%) and are reported to exhibit very high ionic conductivities. At room temperature the ionic conductivity is reported to be $>10^{-3}$ S cm^{-1}, which increases to $\sim10^{-2}$ S cm^{-1} at temperatures close to the melting point of the LiRAP. They are also reported to have low activation energies ~0.2 – 0.3 eV, low electronic conductivity, and a large potential voltage and current window over which they can safely operate. Moreover, LiRAPs are reported to be stable up to 400 °C and are able to conduct in the molten state. Their composition makes them environmentally friendly and, hence, recyclable. Furthermore, the reagents required for synthesis are inexpensive, making them cheap to produce. All of these qualities make LiRAPs a worthy candidate for further investigation as a solid electrolyte.

1.4.2 Structure of LiRAPs

The LiRAPs Li_3OCl and Li_3OBr are reported to adopt a cubic structure, in space group $Pm\bar{3}m$, with lattice parameters a = 3.91 and 4.02 Å, respectively. Li_3OBr has a larger unit cell owing to the larger size of the Br^- ions ($r_{ion}Br^-$ = 1.96 Å) relative to Cl^- ($r_{ion}Cl^-$ = 1.81 Å).[124,126] The tolerance factors for Li_3OCl and Li_3OBr are 0.85 and 0.91, respectively, indicating a less distorted structure

for Li_3OBr.

It is well known and widely reported in solid-state chemistry that perfect crystals are not good ion conductors, as there is no mechanism by which the ions can move through the structure. Hence, structural defects are typically required to effectively introduce ion migration pathways and achieve ionic conductivity.[127] As stated earlier, the anti-perovskite structure is extremely flexible and can be modified with relative ease in a variety of ways, including:

$$(1 - x)LiX + xLiX' + 2LiOH \rightarrow Li_3OX_{1-x}X'_x + H_2O, \quad (1.4)$$

$$(1 - y)LiX + (y/2)MX_2 + 2LiOH \rightarrow Li_{3-y}M_{y/2}OX + H_2O, \quad (1.5)$$

$$(1 - z)LiX + 2LiOH \rightarrow Li_{3-z}OX_{1-z} + H_2O. \quad (1.6)$$

Halogen doping (Equation 1.4) results in a mixed composition, *e.g.*, Li_3OCl can be doped with Br^- to produce $Li_3OCl_{1-x}Br_x$. Zhao and Daeman recently reported that $Li_3OCl_{0.5}Br_{0.5}$ exhibits a higher ionic conductivity than the parent Li_3OCl at room temperature.[124] This is believed to be caused by the introduction of very specific structural distortions (*vide infra*). Hence, halogen doping can be hugely beneficial.

LiRAPs can also be doped with divalent metals to form $Li_{3-y}M_{y/2}OX$-type compositions (Equation 1.5). Zhang *et al.*, recently reported the synthesis of the LiRAP $Li_{3-x}Ca_{x/2}OCl$.[128] Doping with a divalent metal, *e.g.*, Ca^{2+}, produces a Li vacancy in order to balance the charge.[124] Hence, cationic doping is a good method for creating additional vacancies, which are known to be required for Li^+ ion conduction. At present, it is believed that the vacant Li sites in $Li_{3-x}Ca_{x/2}OCl$ facilitate the movement of ions via a Schottky mechanism, *i.e.*, via the vacancies present, which increases the ionic conductivity of the material.

Further modifications to the anti-perovskite structure include the synthesis of depleted materials (Equation 1.6), *i.e.*, purposely reducing the amount of halogen species present in order to increase the number of vacant Li sites present. For example, Zhao and Daeman, synthesised selected LiRAPs with 5,

10, 15 and 20% Cl depletion, containing 1.66, 3.33, 5 and 6.66% Li vacancies, respectively.[124] Doing this can reduce the structural distortion, whilst creating defects in the structure. As a result, Li^+ ion conduction can be improved by creating a pathway for the ions to move throughout the three-dimensional structure. Theoretically, it is also possible to combine all of the aforementioned modifications to create a highly conductive material with a stable structure.

1.4.3 Stability of LiRAPs

The stability of LiRAPs has been studied extensively via computational methods. However, to date very little has been reported experimentally. With respect to their decomposition products (*e.g.*, LiCl and Li_2O), LiRAPs are reported to be thermodynamically metastable. Hence, in order to successfully synthesise LiRAPs and prevent them from decomposing, the kinetic formation of Li_2O must be stopped.[59,127] Mouta *et al.*, recently reported that Li_3OCl is metastable at all temperatures up to 550 K.[129] It has been suggested that Li_3OCl and its decomposition products are separated by a high Gibbs energy barrier. More recently, there have been further suggestions that Li_3OCl is entropically stabilised above 480 K.[130]

Emly and co-workers have investigated the phase stability of Li_3OCl and Li_3OBr in considerable detail using first-principles calculations and have suggested that both Li_3OCl and Li_3OBr are only stable in the absence of Li_2O, hence, the synthetic method used is extremely important.[59] Emly *et al.*, have also suggested that additional anti-perovskite structures could form during synthesis, including $Li_{17}O_6Cl_5$ and Li_5O_2Cl, the structures of which are shown in Figure 1.16.[59] When examined, it is unsurprising that these phases could form, as the structures can be directly derived from the Li_3OCl structure with relative ease by simply removing LiCl units.

Zhang *et al.*, calculated the band gap for Li_3OCl via density of states calculations and determined that it exceeds 5 eV, suggesting that Li_3OCl is suitable for use in high voltage batteries.[127] This is in stark contrast to Emly *et al.*, who reported Li_3OCl not to be stable above an applied voltage of 2.5 V

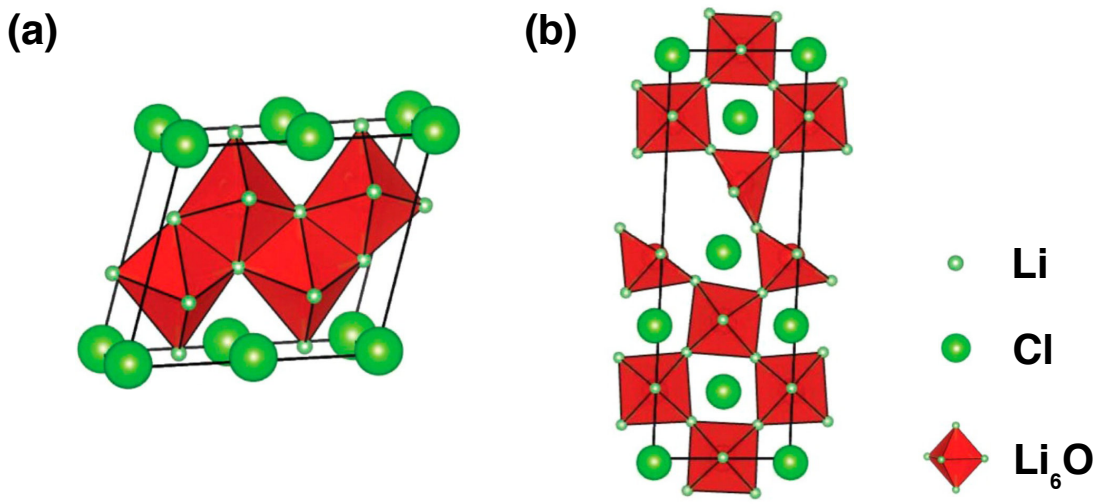

Figure 1.16: The structures of (a) Li_5O_2Cl, displaying distorted edge sharing Li_6O octahedra, and (b) the structure of $Li_{17}O_6Cl_5$, displaying corner sharing Li_6O octahedra owing to two vacant LiCl units.[59] Reprinted with permission from A. Emly, E. Kioupakis and A. Van der Ven, *Chem. Mater.*, 2013, 25, 4663 – 4670. Copyright 2013 American Chemical Society.

unless the formation of Li_2O is prevented.[59] Above 2.5 V, Li_3OCl is susceptible to decomposition to Li_2O_2, LiCl and LiO_4Cl. Hence, this suggests that Li_3OCl is only suitable for low-voltage battery applications and cannot be used in high voltage batteries. It is noted that all of the stability studies published to date are solely computational. Hence, detailed experimental studies that monitor decomposition products and rates are still needed.

1.4.4 Ionic Conductivity and Li-ion Transport Mechanisms

The bulk conductivity of LiRAPs is reported to be highly dependent on temperature. An Arrhenius-type relationship is reported to exist at high temperatures, meaning Li^+ ion conductivity increases exponentially with temperature.[124] However, it is noted that the conductivity of a material is also dependent on both the concentration and mobility of the mobile species, *e.g.*, the ions present. Typically, ions conduct through a material either via a vacancy (Schottky) or interstitial mechanism (Frenkel).[11,62] The precise mechanism for conduction will depend heavily on both the composition of the material and its structure.

Li_3OCl is reported to exhibit an ionic conductivity of 0.85×10^{-3} S cm^{-1} at RT, which increases to 4.82×10^{-3} S cm^{-1} at 250 °C.[124] Whereas a mixed composition sample, $Li_3OCl_{0.5}Br_{0.5}$, is reported to exhibit an ionic conductivity of 1.94×10^{-3} S cm^{-1} at RT, which increases to 6.05×10^{-3} S cm^{-1} at 250 °C.[124] These values are considerably higher than Li_3OCl and Li_3OBr at both RT and 250 °C. A specific ionic conductivity value has not been reported for Li_3OBr by Zhao and Daeman, although it is indicated to be lower than Li_3OCl and $Li_3OCl_{0.5}Br_{0.5}$.[124] This change in conductivity is believed to be an attribute of the unit cell size and the associated changes in structure. For example, in Li_3OBr, the size of the A-site anion results in an almost ideal cubic structure, *i.e.*, very little structural distortions present. As a result, there is no space for Li^+ ion movement, making Li_3OBr a relatively poor ion conductor. In contrast, because Li_3OCl has a smaller A-site anion, the structure contracts and the coordination of the Cl reduces from 12 to 8. This causes the Li_6O octahedra to tilt and, in doing so, limits the ability of the Li^+ ions to move. The mixed halogen composition, $Li_3OCl_{0.5}Br_{0.5}$, has two different anions on the A-site. This results in a larger unit cell with less distortion, thereby providing sufficient interstitial space in the chlorine-containing A-sites for Li^+ ions to pass, while the A-sites containing Br^- help to stabilise the structure. Hence, when compared, the mixed compositions produce the highest conductivities. However, it is noted that very few experimental studies have been completed to date for both the mixed and non-mixed compositions. Hence, there is still considerable scope for investigation.

The values stated above seem very promising however, it must be noted that they are heavily dependent on the method of sample preparation. It is possible that the samples used for the conductivity measurements had non-ideal stoichiometries owing to the presence of defects. As with all conductivity studies, the samples were annealed at high temperatures for several days prior to undertaking the measurements. Hence, it is possible that the samples were depleted of Li during the annealing process. In all of the studies completed to date, no post synthetic analysis has been undertaken for the samples investigated. Hence, there is no firm evidence to suggest that the samples have re-

tained their exact composition after annealing, and to confirm this, additional analysis is required.

Based on the initial experimental study of $Li_3OCl_{1-x}Br_x$ by Zhao *et. al.*,[124] computational methods such as first-principles calculations and percolation theory have been used to try and establish the optimal composition responsible for the highest Li^+ ion conductivity. It is believed that when $0.235 \leq x \leq 0.395$ a higher ionic conductivity will be observed. *Ab initio* molecular dynamics (AIMD) simulations completed by Deng and co–workers suggest that when $x = 0.25$, $Li_3OCl_{0.75}Br_{0.25}$, a higher conductivity will be observed than that of $Li_3OCl_{0.5}Br_{0.5}$.[131] Mixed halide compositions are believed to have low mixing energies, suggesting that the halides could be disordered at RT. However, the formation energies are small and positive indicating that a solid-solution could also form at RT. At present, the mixed halide sublattice structure in LiRAPs is unknown. Hence, again there is considerable scope for further investigation.

Many of the theoretical studies published to date have attempted to understand the mechanisms involved in Li^+ ion transport and to determine whether it occurs via a vacancy or interstitial mechanism or, indeed, a combination of the two. Zhang *et al.*, suggested that Li^+ ions move along the Li_6O octahedron edge.[127] It has also been suggested that the Li sublattice melts at lower temperatures when compared to the anion sublattice. Hence, the melted Li sublattice will enable faster Li^+ ion movement, as the cell volume will expand, allowing extra interstitial space for the Li^+ ions to migrate. Meanwhile, the anions will remain in their local positions, meaning that only the Li^+ ions are mobile throughout the structure. During AIMD simulations, sublattice melting temperatures of 206.85 and 176.85 °C were used for Li_3OCl and Li_3OBr, respectively. The proposed differences in melting temperatures of the two sublattices appears to explain the dramatic increase in conductivity observed closer to the melting point of the product.

Emly and co-workers have proposed that movement of the Li ions occurs via a dumbbell interstitial mechanism, involving three Li atoms (Figure

1.17).[59] Energy barriers for Li^+ ion movement via both a vacancy route and an interstitial route were calculated during the study, and for both Li_3OCl and Li_3OBr, the energy barriers for the interstitial route were found to be much lower than those calculated for vacancy migration. Hence, this suggests that interstitial movement is the dominant process taking place during conduction. Based on their simulations, Emly *et al.* proposed that, during conduction, an interstitial Li coordinates with a Li bound in the Li_6O octahedra to form a dumbbell (Figure 1.17(a)).[59] This dumbbell then displaces both of the Li atoms such that the centre of the dumbbell is at the centre of the octahedron corner, the original position of the bound Li (Figure 1.17(b)). One Li in the dumbbell moves into an octahedral site and the second Li forms a dumbbell with the next Li (Figure 1.17(c)). This results in a coordinated movement of the dumbbell throughout the structure.

In a similar manner to Emly *et al.*,[59] Deng and co-workers also calculated the energy barriers for vacancy migration in Li_3OCl and Li_3OBr and obtained values of 328 and 361 meV, respectively.[131] These values are lower than those initially reported by Emly *et al.*[59] However, both studies suggest Li_3OBr is a poorer conductor than Li_3OCl.

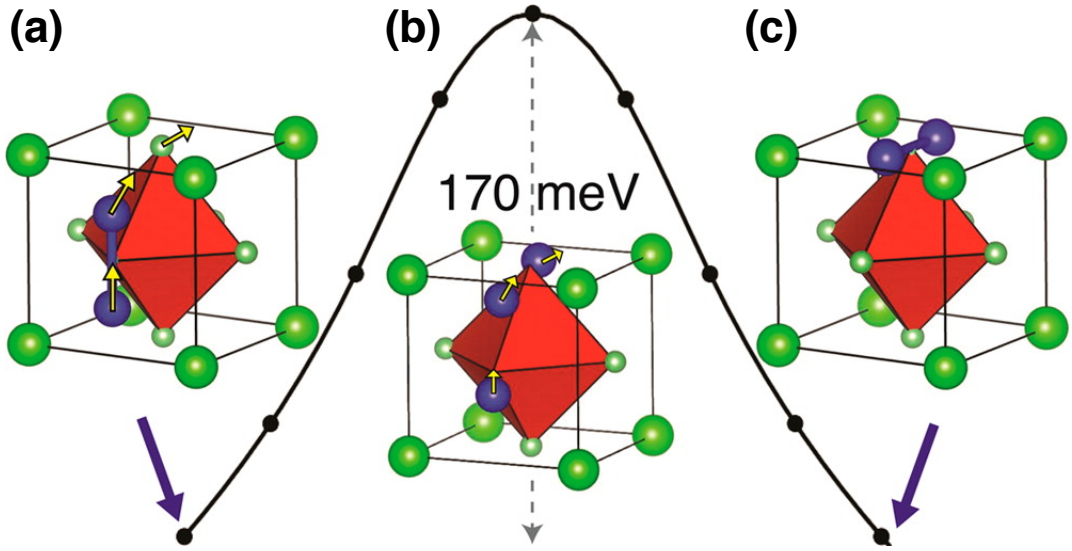

Figure 1.17: A schematic representation of Li movement via a dumbbell interstitial mechanism proposed by Emly and co-workers.[59] Reprinted with permission from A. Emly, E. Kioupakis and A. Van der Ven, *Chem. Mater.*, 2013, 25, 4663 – 4670. Copyright 2013 American Chemical Society.

Li-ion transport mechanisms in LiRAPs have also been investigated by Mouta and co-workers.[129] They determined, via classical atomistic calculations, that the concentration of Schottky vacancies is 1×10^{-7} at any given temperature and the migration enthalpy is 0.30 eV above RT. For Frenkel defects, the formation energy was found to be higher, meaning the concentration of defects at any given temperature is 1×10^{-13} and the migration enthalpy is 0.133 eV. This suggests that the dominant conduction process in stoichiometric and in divalent doped materials is via a vacancy mechanism, which is in contrast to the findings of Emly *et al.*[59] However, it must be noted that non-stoichiometric samples, *i.e.*, those with LiCl deficiency, can undergo a mechanism that results in interstitial Li sites to balance the charges. In such situations, this could easily increase the concentration of Frenkel defects above 1×10^{-7}, causing the Li to move via the interstitial mechanism with a lower enthalpy.

A LiCl vacancy is created when a Cl^- ion is removed for each Li vacancy, and similarly, a Li_2O vacancy is created when an O^{2-} ion is removed for every 2 Li vacancies. Li_2O interstitials have a lower formation energy when compared to LiCl interstitials, most likely due to the size of Cl^- ions.[59] Lu *et al.*, recently completed a theoretical study of the different types of charge neutral defects.[132] Interestingly, their findings regarding Li Frenkel pair defects agree with those of Emly *et al.*[59] They calculated the formation energy of the Li Frenkel pairs to be 2.02 eV. The formation energies of LiCl Schottky vacancies, Li_2O Schottky vacancies and Li interstitials stabilised by replacing O on the Cl site were found to be 1.41, 1.60 and 1.67 eV, respectively. These values suggest LiCl Schottky vacancies are the most common, as they have the lowest formation energy. Hence, Lu *et al.* propose that, in Li deficient LiRAPs, Li moves predominantly via a Schottky mechanism.[132]

Work by Mouta *et al.*, suggests that in LiCl deficient LiRAPs the interstitial mechanism is the dominant process for Li transportation.[133] By calculating the Gibbs energy of structures with vacancies and interstitials, they determined that structures with interstitials are energetically favourable. In fact, there are far more interstitial defects when compared with vacancy defects. Hence, they must be the charge carriers. This implies that Li depleted

samples would make better conductors than cation doped samples. Hence, they are worth investigating further.

1.4.5 Methods for Improving Ionic Conductivity

In an attempt to increase the ionic conductivity, LiRAPs have been synthesised as thin films using pulsed laser deposition (PLD) methods.[134] Thin films are essential for battery miniaturisation and very specific applications such as for use in medical devices. Hence, methods for successfully producing thin films of LiRAPs are needed which are economically viable. It is widely reported in the literature that thin films exhibit higher conductivities than bulk materials.[135] To produce thin films of Li_3OCl, the bulk ceramic was used as the source material. The bulk ceramic had a conductivity of 5.8×10^{-7} S cm^{-1} at RT, whilst the thin film had a conductivity of 8.9×10^{-6} S cm^{-1} at RT. This further increases to 3.5×10^{-4} S cm^{-1} at 140 °C. Compositional modifications can also be made to LiRAP thin films using a composite target for deposition of the film. For example, the composite target can consist of a mixture of Li_2O and LiCl, which results in an enhanced ionic conductivity of 2.0×10^{-4} S cm^{-1} at RT and an even greater increase to 5.9×10^{-3} S cm^{-1} at 140 °C.[135] Moreover, the activation energy of conduction for bulk Li_3OCl is 0.59 eV whereas for the Li_3OCl thin films it is 0.36 eV. The lower activation energy for thin films is likely due to structural differences between the bulk and the thin film. It is noted that some of the most recent studies of bulk Li_3OCl quoted much higher conductivity values 0.85×10^{-3} S cm^{-1} at RT.[124] However, as discussed earlier, heat treatment and the possible presence of impurities could have contributed to the values obtained (*vide supra*).

The synthesis of glass-based LiRAPs has recently been reported by Braga *et al*.[136] The general formula is $Li_{3-2x}M_xOX$, where M is a divalent metal and X is a halogen. For $Li_{3-2x}Ba_xOCl$ (x = 0.005), conductivity values of 2.5×10^{-2} and 24×10^{-2} S cm^{-1} have been reported at RT and 100 °C, respectively. These glassy LiRAPs are also reported to be stable over a large voltage range (8 V). It is believed that conduction occurs via a vacancy mechanism and the amorphous nature of a glass assists the migration of ions, leading to a high

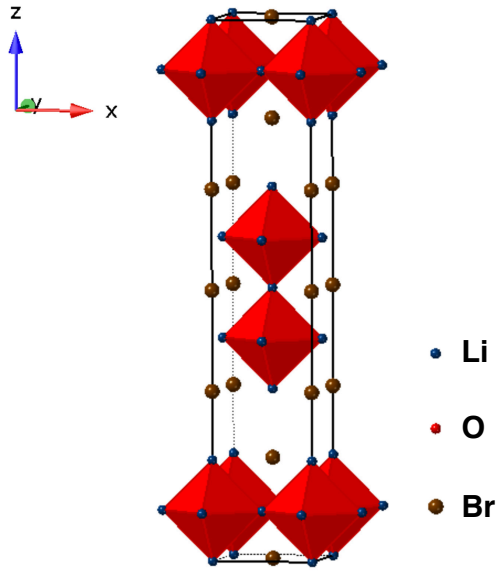

Figure 1.18: The tetragonal unit cell of $Li_7O_2Br_3$, in space group *I*4/*mmm*, displaying Li_6O octahedra surrounded by Br ions.[137]

ionic conductivity. However, further investigation into these materials is required to gain additional structural and performance-based information.

Zhu *et al.*, recently reported the presence of the phase $Li_7O_2Br_3$ in samples of Li_3OBr.[138] The structure of $Li_7O_2Br_3$ is shown in Figure 1.18. $Li_7O_2Br_3$ is a Li_2O deficient form of Li_3OBr. When the phase is present, an increase in ionic conductivity is observed. For example, the reported conductivity of $Li_7O_2Br_3$:Li_3OBr (44:56) is 0.24×10^{-4} S cm^{-1} at RT, which is higher than that of Li_3OBr (10^{-5} – 10^{-6} S cm^{-1}). Hence, this suggests the phase is contributing to the enhancement of the ionic conductivity.

1.5 Thesis Overview

This thesis is focused on the synthesis of LiRAPs and understanding the precise mechanisms for ion mobility within the anti-perovskite structure. As discussed earlier, at present, the mechanism for Li-ion transport in LiRAPs is not well understood, despite the many recent investigations. In order for LiRAPs to be effectively used as solid electrolytes in Li-ion batteries and future ASSBs, it is essential to study Li-ion migration and the transport mechanisms within them. An understanding of these mechanisms will enable

suitable modifications of the structure to be made via, for example, compositional doping, in order to increase the overall ionic conductivity. Several solid-state synthetic methods have been explored, and the samples obtained have been characterised via X-ray and neutron powder diffraction and multinuclear solid-state NMR spectroscopy. The fundamentals of these techniques are discussed in Chapter 2.

Initially, the project began with attempts to synthesise the LiRAPs Li_3OCl and Li_3OBr via melt recrystallisation methods using high temperature annealing. Several synthetic methods were attempted with reaction variables including the time and temperature being modified in order to determine the optimal synthetic conditions required. Chapter 3 discusses the findings of these investigations in detail.

Based on our initial studies of Li_3OCl and Li_3OBr, our research efforts changed to focus on the hydrated LiRAP Li_2OHCl. Considerably easier to synthesise, Li_2OHCl is known to undergo a phase transition to the cubic phase $Pm\bar{3}m$ at ~50 °C. Despite several recent theoretical and experimental studies of Li_2OHCl, the room-temperature structure of Li_2OHCl is still somewhat of a mystery. Numerous space groups have been suggested, but few studies have provided detailed structural information, complete with crystallographic information. Hence, we focused our efforts on accurately determining the room-temperature phase of Li_2OHCl. To do so, X-ray and neutron powder diffraction have been used in conjunction with multinuclear solid-state NMR spectroscopy. The results of which are presented in Chapter 4.

As the synthesis of Li_2OHCl proved to be a much easier task than Li_3OCl, the synthesis of LiRAPs with varying Li and, in turn, H content was attempted to produce samples in the series $Li_{3-x}OH_xCl$ (x = 0.25, 0.5 and 0.75). The resulting findings are detailed in Chapter 5.

Also of significant interest is the ion mobility in Li_2OHCl, and, in particular, the precise source of ion mobility. Using variable-temperature X-ray and neutron powder diffraction, alongside solid-state NMR spectroscopy, the phase transition in Li_2OHCl has been probed, and the associated structural

changes monitored. Using a variety of complementary techniques, a very intimate structure-mobility relationship has been identified, the details of which are discussed in Chapter 6.

Finally, the flexibility of the LiRAP structure and its influence on the potential functionality and ion mobility of the system was investigated via compositional doping. Like many other perovskite-based systems, compositional doping has a substantial effect on the structure. This was investigated by substituting OH^- with F^- and Cl^- with Br^- in Li_2OHCl, to produce $Li_2(OH)_{0.9}F_{0.1}Cl$ and $Li_2OHCl_{1-x}Br_x$ (x was varied from 0.1 to 1). The resulting findings are discussed in Chapter 7.

Chapter 8 summarises the findings presented and discusses the potential for LiRAPs to be used as solid electrolytes in future ASSBs. Based on the findings presented, suitable directions for future work are also suggested.

2 Experimental Techniques

2.1 X-ray Diffraction

2.1.1 Introduction[62,139,140]

X-ray diffraction (XRD) is a technique used to investigate the long-range order in crystalline materials. The phenomenon of diffraction can be easily described by thinking of a crystalline material as consisting of layers or planes of atoms. These layers are called Miller planes and are separated by a distance d_{hkl}, known as the d-spacing, and are labelled using integers known as Miller indices (hkl). X-rays are electromagnetic radiation with wavelength ~1 Å, which is comparable to the interatomic distances within crystalline materials. Hence, an incident X-ray beam will be reflected by these planes, as shown in Figure 2.1. It can be seen that the beam reflected by the second layer has a longer path (XY + YZ). For constructive interference to occur between the two reflections, the path difference must be an integer number of wavelengths.

Diffraction-based methods can be described using Bragg's Law and the Bragg equation,

$$n\lambda = 2d_{hkl}\sin\theta, \tag{2.1}$$

where d_{hkl} is the distance between the planes, θ is the angle of incident and diffraction, n is an integer and λ is the wavelength of the radiation used. It

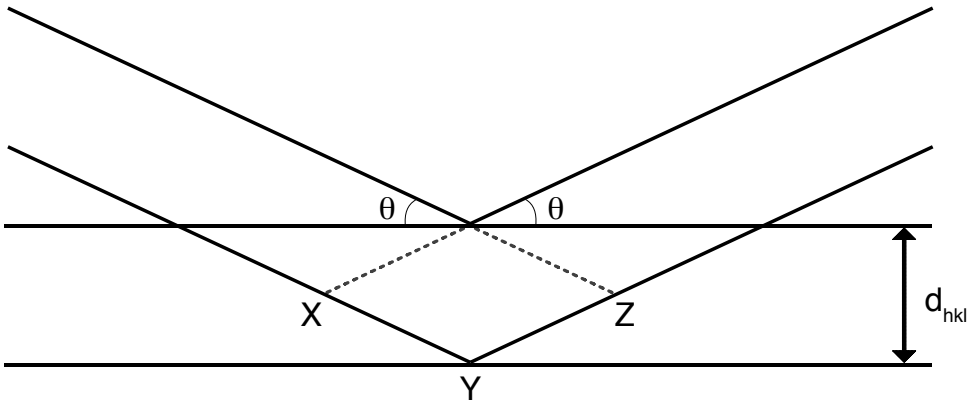

Figure 2.1: A schematic representation of X-rays being reflected from adjacent planes.

must be noted that the Miller planes used for the derivation of Bragg's Law are merely a concept used to understand and explain the diffraction process. In reality, crystal structures are composed of a lattice formed via a regularly repeating unit cell, where atoms are rarely located on sites corresponding to such layers.

2.1.2 Generation of X-rays[62,140,141]

Laboratory X-rays are produced using an X-ray tube. In this tube, a beam of accelerated electrons strikes a metal target, typically Cu or Mo. The electrons decelerate as they penetrate the metal target and produce radiation, called Bremsstrahlung or 'white radiation', shown in Figure 2.2, which consists of a continuous range of wavelengths.[142] More specifically, this particular type of radiation is not useful for diffraction-based experiments. Instead, the radiation generated from electrons being expelled from the atoms within the metal can be used. The electrons produced can lead to ionisation of the metal, and an electron from the core shell is removed and is replaced by an electron from a higher energy orbital. This change in the energy is emitted in the form of X-ray radiation.

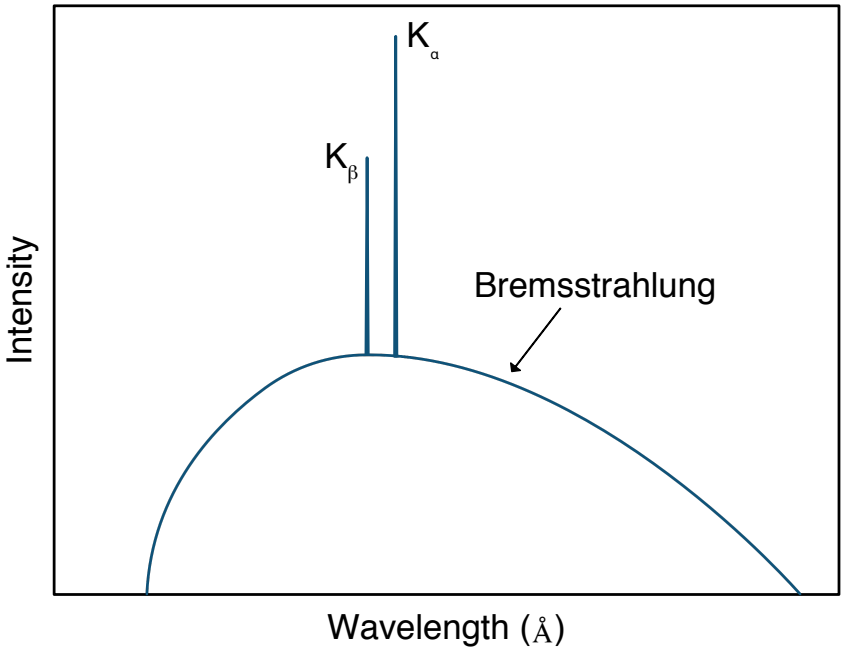

Figure 2.2: A schematic representation of Bremsstrahlung, K_α and K_β radiation.

The work presented here used X-rays generated via a Mo source. For Mo, 2p → 1s transitions produce $K_{\alpha 1}$ and $K_{\alpha 2}$ radiation, with wavelengths of 0.7093 and 0.7135 Å, respectively. Two different wavelengths are produced as the electrons in the 2p orbital have two possible spin states. A transition from a 3p to 1s orbital produces K_β radiation with a wavelength of 0.6323 Å. X-ray diffraction requires monochromatic radiation, therefore to isolate the K_α radiation Nb foil is used to absorb the K_β radiation. Since K_α consists of both $K_{\alpha 1}$ and $K_{\alpha 2}$ radiation, X-ray diffraction patterns obtained using both of these wavelengths can exhibit poor resolution. Hence, a suitable monochromator can be used to isolate a single wavelength.

2.1.3 Powder Diffraction[62,139,140]

The X-rays generated in an X-ray diffraction experiment will interact with the electrons present in matter and, upon contact with a powdered crystalline sample, the X-rays will be scattered by the electron density in various directions. As the powdered sample contains a large number of tiny crystallites oriented in different directions, the result is many cones of diffracted radiation, as shown in Figure 2.3. These cones are formed by closely spaced dots from diffraction by each of the individual crystallites within the sample. A large number of crystallites results in the dots joining together to form a continuous cone. A moving detector traces a line through all of the cones to

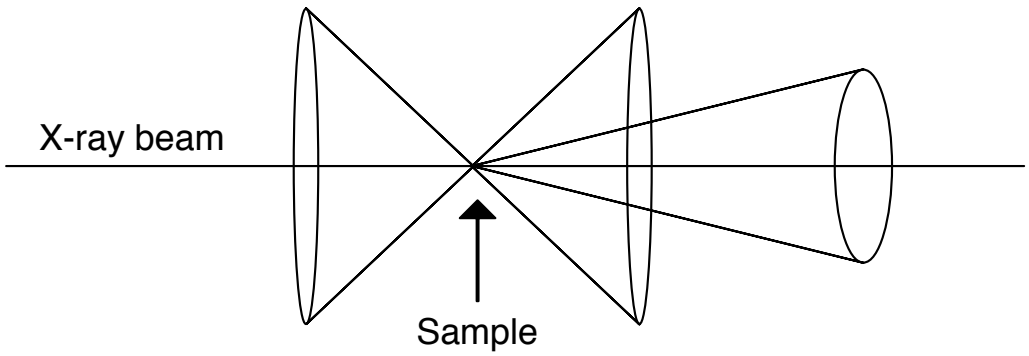

Figure 2.3: A schematic representation of the cones of radiation produced during a powder X-ray diffraction experiment.

produce a diffraction pattern.

Compounds containing atoms with a high atomic number scatter more intensely than those containing atoms with a low atomic number. The scattering is dependent on the number of electrons present in the sample so it is proportional to the scattering factor, f_i. The scattering factor, also known as the form factor is dependent on the scattering angle. The scattering power decreases at higher angles due to the finite size of the electron cloud. A schematic representation of the fall off in scattering power for Ca^{2+} and F^- is shown in Figure 2.4. The structure factor, F_{hkl}, is related to the scattered intensity in a diffraction pattern and a particular reflection can be defined by,

$$F_{hkl} = \sum_{i=1}^{N} f_i \exp\left(2\pi i(hxi + kyi + lzi)\right), \tag{2.2}$$

where hkl are the miller indices and (xi, yi and zi) are the fractional coordinates. The intensity of this reflection can be written as,

$$I_{hkl} = F_{hkl}^2 \, . \tag{2.3}$$

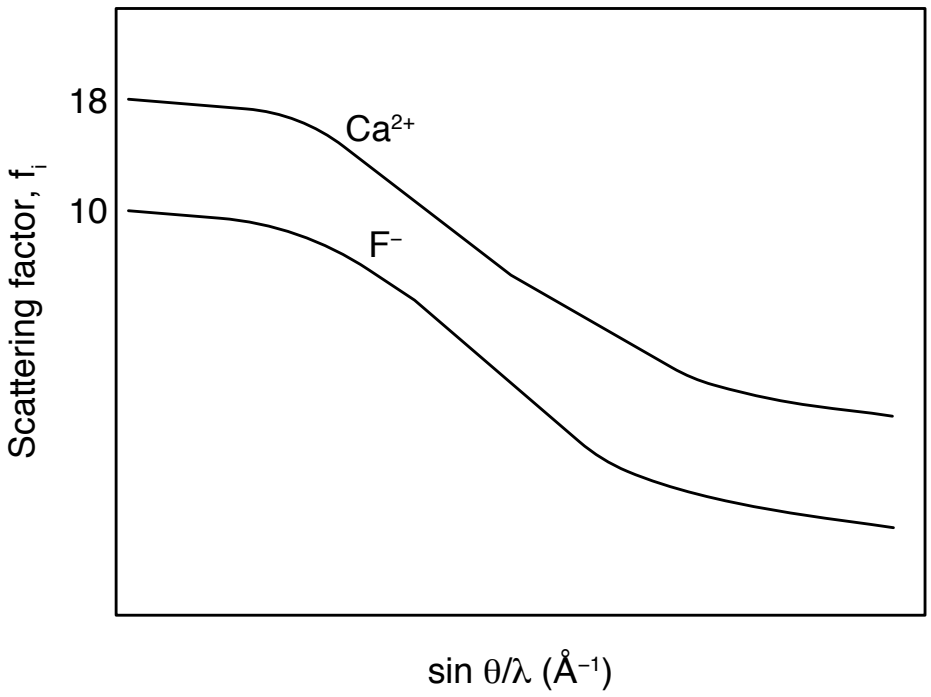

Figure 2.4: A schematic representation of the form factors of Ca^{2+} and F^- showing the fall off in scattering power with increasing angle (θ).

2.2 Neutron Diffraction[62,140,143]

2.2.1 Introduction

Neutrons are uncharged subatomic particles with spin-1/2 and a mass of 1.67×10^{-27} kg. Neutrons also have comparable wavelengths to atomic spacings in crystalline materials, enabling diffraction experiments to be performed. Unlike X-rays, neutrons are scattered by the nucleus of an atom instead of the electron cloud. Hence, the scattering power (cross-section) of neutrons does not reduce with increasing angle, as it does in X-ray diffraction (*vide supra*). This gives neutron diffraction a few advantages over conventional X-ray diffraction. Specifically, it is easier to detect light atoms, *i.e.*, hydrogen, in the presence of heavier atoms. It is also easier to distinguish between neighbouring elements in the periodic table and different isotopes of the same element as they are likely to have substantially different cross-sections. However, this technique also has some disadvantages, predominantly the high costs required to run and maintain neutron diffraction facilities, as well as the large sample quantities needed for such experiments. Furthermore, the user time allocation is becoming increasingly competitive due to high demand. Hence, it is harder to get experimental time at these facilities.

2.2.2 Generation of Neutrons[62,140]

Neutrons can be generated either via a nuclear reactor or a spallation source. In a nuclear reactor, neutrons are produced via chain reactions of neutron-induced fission of a heavy nucleus such as ^{235}U. The neutrons produced by fission are fast neutrons meaning they have high energies (MeV range). However, for neutron-induced fission slow neutrons are needed, with energies in the meV range. So, in order to maintain the fission process, the neutrons must be slowed down. This is achieved using a moderator. The neutrons produced via a nuclear reactor need to be passed through a monochromator to produce a beam with a fixed wavelength that is suitable for diffraction experiments. During such experiments, since a fixed wavelength is used, the detector is moved.

In a spallation source, neutrons are produced by firing a beam of high energy protons at a heavy metal target. This high energy proton beam is obtained via a linear particle accelerator and a synchrotron. The interaction between the protons and the target metal emits neutrons, and this is called the spallation process. The neutrons produced are then moderated to ensure that they are suitable for neutron scattering. In a spallation source, the neutron flux produced is pulsed, as accelerator-based sources are typically pulsed. This is ideal for completing time-of-flight (TOF) neutron diffraction experiments. During TOF experiments, the time taken (t) for a neutron to travel from the moderator to the detector (via the sample) is measured. This allows us to calculate the neutron wavelength (assuming that elastic scattering is taking place) as follows,

$$t = \frac{m_n}{h} L\lambda \,, \tag{2.4}$$

where m_n is the mass of a neutron, h is Plank's constant, L is the flight path of the neutron and λ is the neutron wavelength. The TOF technique does not require a monochromatic neutron beam. Hence, a moving detector is not required, and fixed detector banks positioned at different angles are used instead.

2.2.3 The High Resolution Powder Diffractometer (HRPD)[144,145]

HRPD is one of the highest resolution neutron powder diffractometers in the world, and it is located at ISIS neutron spallation source, Rutherford Appleton Laboratories, Didcot, UK. HRPD has a long flight path, located ~96 m from the target at the end of a neutron guide, which ensures a greater resolution, making HRPD suitable for studying materials that exhibit subtle structural changes such as phase transitions. HRPD has three fixed detector banks, the backscattering ($158.46° < 2\theta < 176.11°$), 90° ($80.41° < 2\theta < 99.59°$) and low angle ($27.47° < 2\theta < 32.22°$). The backscattering and 90° banks use ZnS scintillator detectors, whereas the low angle bank uses ^{3}He gas tubes for detectors. The resolution of a diffractometer is highest when $\Delta d/d$ is at a minimum. A low value of $\Delta d/d$ means that the spread in a Bragg reflection has been minimised. On HRPD the highest resolution is obtained via the backscattering

bank as it has the lowest $\Delta d/d$ ($\sim 6 \times 10^{-4}$) of all the banks and d-spacings of up to 4 Å can be examined.

2.3 Rietveld Analysis[62,140,146]

The Rietveld method was originally proposed by Hugo Rietveld in 1969,[147–149] and it is a popular method for the analysis of powder diffraction data. This method requires some prior knowledge of the structural model, as the diffraction pattern obtained is compared to a model generated via a crystallographic information file (cif). In the current study, all structural refinements were completed using a program called the General Structural Analysis System (GSAS),[150] where parameters such as the background, detector zero point, lattice parameters, profile coefficients and thermal coefficients can be varied to generate a profile that is compared to the experimentally obtained XRD pattern.

Polycrystalline samples often produce many overlapping peaks, making it extremely challenging to fit each peak individually. The Rietveld method does not attempt to index and fit individual peaks. Instead, the whole pattern is fitted at once to the structural model using a least-squares minimisation method. The parameters listed above are refined until the residual (S_y) is minimised. S_y is calculated as follows,

$$S_y = \sum_i \frac{1}{y_i}(y_{oi} - y_{ci})^2 \,, \tag{2.5}$$

where y_{oi} is the observed intensity and y_{ci} is the calculated intensity. The parameter $\frac{1}{y_i}$ is required so that all the peaks are fitted with equal preference. This avoids peaks with higher intensities being fitted preferentially. The 'goodness of fit' is characterised via R-factors such as the R-profile (R_p) and R-weighted profile (wR_p), given by,

$$R_P = \frac{\sum_i |y_{oi} - y_{ci}|}{\sum_i y_{oi}} \,, \tag{2.6}$$

$$wR_P = \sqrt{\frac{\sum_i \frac{1}{y_i}(y_{oi} - y_{ci})}{\sum_i \frac{1}{y_i}(y_{oi})^2}} \,. \tag{2.7}$$

Another parameter used to determine the quality of fit is χ^2, given by,

$$\chi^2 = \frac{\sum_i \frac{1}{y_i}(y_{oi} - y_{ci})^2}{N - P + C}\,, \tag{2.8}$$

where N corresponds to the number of observations, P is the number of parameters refined, and C is the number of constraints applied. A χ^2 value of 1 corresponds to a perfect fit. All of the cifs used in the work presented were obtained from the Inorganic Crystal Structural Database (ICSD), and all structural refinements were completed using GSAS.[150]

2.4 Nuclear Magnetic Resonance

Nuclear magnetic resonance (NMR) spectroscopy is a technique used to investigate the local structure of a material. NMR is a non-destructive technique that does not require a material to possess any long-range ordering. It is therefore suitable for ordered, disordered and amorphous systems.

2.4.1 Introduction[151–156]

All nuclei possess an intrinsic spin angular momentum, **I**, the magnitude of which can be described by,

$$|\mathbf{I}| = \hbar\sqrt{I(I+1)}\,. \tag{2.9}$$

I is the corresponding spin quantum number and is determined by the number of unpaired protons and neutrons. When $I = 0$, the nuclei are said to be NMR inactive. Therefore, only nuclei possessing spin greater than zero ($I > 0$) can be investigated via NMR spectroscopy. The spin angular momentum is a vector quantity, meaning it has both direction and magnitude, both of which are quantised. The projection of this angular momentum vector onto the z-axis is given by,

$$I_z = m_I\hbar, \tag{2.10}$$

where m_I is the magnetic quantum number with integer values ranging from $+I$ to $-I$. This results in $2I + 1$ states that are degenerate in energy. Nuclei

possess a magnetic dipole moment, $\boldsymbol{\mu}$, given by,

$$\boldsymbol{\mu} = \gamma \mathbf{I}, \tag{2.11}$$

where γ is the gyromagnetic ratio of the nucleus. The value of γ differs for each nucleus. If γ is positive then the magnetic dipole moment is parallel to the spin angular momentum, and if γ is negative then the magnetic dipole moment is antiparallel to the spin angular momentum.

In the absence of an external magnetic field, $\mathbf{B}_0$, all $2I + 1$ orientations of I are degenerate. However, upon the application of a magnetic field this degeneracy is broken because an axis of quantisation has been defined and the nuclear spins align themselves relative to $\mathbf{B}_0$. This is known as the Zeeman interaction and the energy of each state can be described by,

$$\mathrm{E} = -\mu_Z \mathbf{B}_0, \tag{2.12}$$

where μ_Z is the projection of the magnetic dipole onto the z-axis. Hence, the energy of a state with magnetic quantum number $\mathrm{m_I}$, is given by,

$$\mathrm{E} = -\gamma \mathrm{m_I} \hbar \mathbf{B}_0. \tag{2.13}$$

This leads to the $2I + 1$ states of a spin I nucleus losing their degeneracy, resulting in equally spaced energy levels, as shown in Figure 2.5. The change in energy (ΔE) between the nuclear energy levels relates to the frequency (ν_0) of the transition and can be described by,

$$\omega_0 = 2\pi\nu_0 = \frac{\Delta \mathrm{E}}{\hbar} = -\gamma \mathbf{B}_0, \tag{2.14}$$

where ω_0 is the Larmor frequency, also known as the resonance frequency. Allowed transitions follow the spectroscopic selection rule, $\Delta \mathrm{m_I} = \pm 1$.

The frequency at which the nuclei resonate is not solely dependent on the gyromagnetic ratio and the magnetic field, it is also affected by the environment experienced by the nuclei. The applied magnetic field causes the electrons in the sample to circulate, resulting in an internal field. If the internal field is parallel to the applied field, then the nucleus is deshielded as the internal field augments the external field. Conversely, if the internal field is

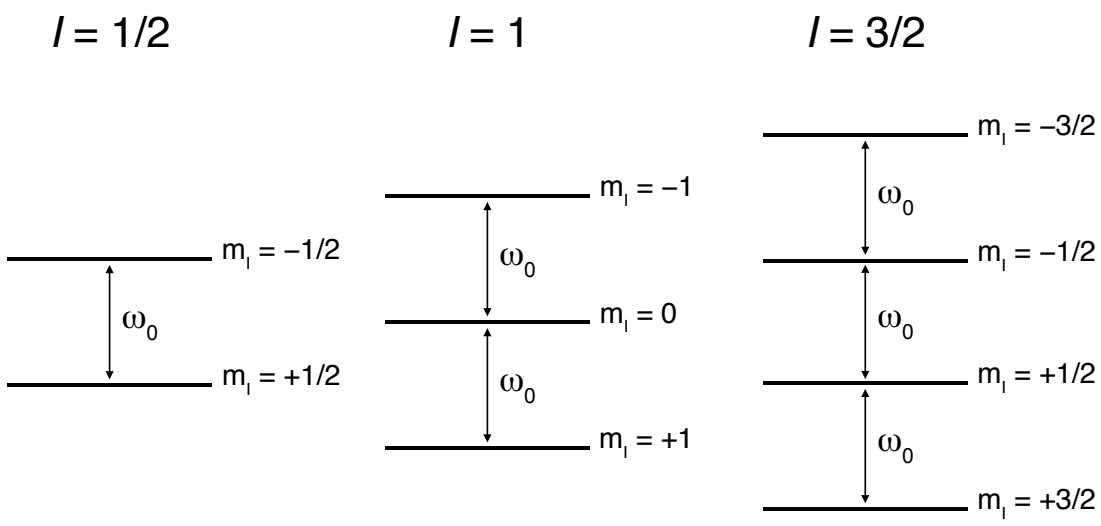

Figure 2.5: A schematic representation of the effect of the Zeeman interaction on the nuclear energy levels of nuclei with spin = 1/2, 1 and 3/2.

perpendicular to the applied field, then the nucleus is shielded as the internal field opposes the external field. Hence, the actual resonance frequency is given by,

$$\omega' = -\gamma \mathbf{B}_0(1 - \sigma), \tag{2.15}$$

where σ is the shielding constant. This changes the resonance frequency of the nucleus, thereby allowing for the characterisation of different environments within a single sample. However, the shielding is a relatively inconvenient method for measuring the chemical shift of a nucleus. Instead, a deshielding parameter, δ, is used,

$$\delta = 10^6((\omega - \omega_{\text{ref}})/\omega_{\text{ref}}), \tag{2.16}$$

where ω is the resonance frequency and ω_{ref} is the reference frequency. ω_{ref} is determined using a standard sample, the chemical shift of which, is set at 0 ppm. The deshielding parameter, δ, also known as the chemical shift, is quoted in parts per million (ppm). It is specific to the sample under investigation and is independent of the magnetic field used.

2.4.2 The Vector Model[151–153,157]

The vector model is a convenient model for understanding the basic principles of an NMR experiment. It can be described using classical mechanics, therefore, it is easier to comprehend. When a sample is placed in a magnetic field, the nuclear spin magnetic moment interacts with the magnetic field. The system has the lowest energy when the spins are aligned parallel to the applied field, though this alignment is disrupted owing to the random thermal motion. However, a Boltzmann population difference between the aligned and anti-aligned spins results in a net alignment of the spins, giving rise to a bulk magnetisation vector, $\mathbf{M}_0$.

In an NMR experiment, a pulse of intense RF radiation is applied to a sample. The frequency of this radiation, ω_{rf}, is close to the resonance frequency, ω_0, of the nucleus of interest. The pulse that is applied has a strength $\mathbf{B}_1$ and duration τ_P. When the pulse is applied it simultaneously excites all resonances within a sample. This, in turn, affects the orientation of $\mathbf{M}_0$. It is easiest to visualise this interaction in the 'rotating frame' rather than a static frame of reference. The rotating frame is a frame of reference which is itself rotating about the z-axis at frequency ω_{rf}. In this frame, $\mathbf{M}_0$ precesses around $\mathbf{B}_0$ at frequency Ω, with an effective magnetic field, $\mathbf{B}_0^{eff}$, along z,

$$\Omega = \omega_0 - \omega_{rf}, \tag{2.17}$$

$$\mathbf{B}_0^{eff} = \frac{\Omega}{\gamma} = -\mathbf{B}_0 - \frac{\omega_{rf}}{\gamma}. \tag{2.18}$$

In the rotating frame, a pulse can be described as a static field, $\mathbf{B}_1$, that is applied perpendicular to $\mathbf{B}_0$. If a pulse is applied along x, $\mathbf{M}_0$ nutates into the xy plane. Once removed, $\mathbf{M}_0$ undergoes free precession at frequency Ω. This is shown schematically in Figure 2.6. The bulk magnetisation vector will return to equilibrium via relaxation mechanisms such as spin-spin relaxation (transverse) or spin-lattice relaxation (longitudinal). Spin-spin relaxation is the loss of magnetisation from the xy plane, and it is described via the time constant, T_2. This relaxation process leads to the decay observed in the NMR signal which is, in turn, responsible for peak broadening. Hence, the peak width at

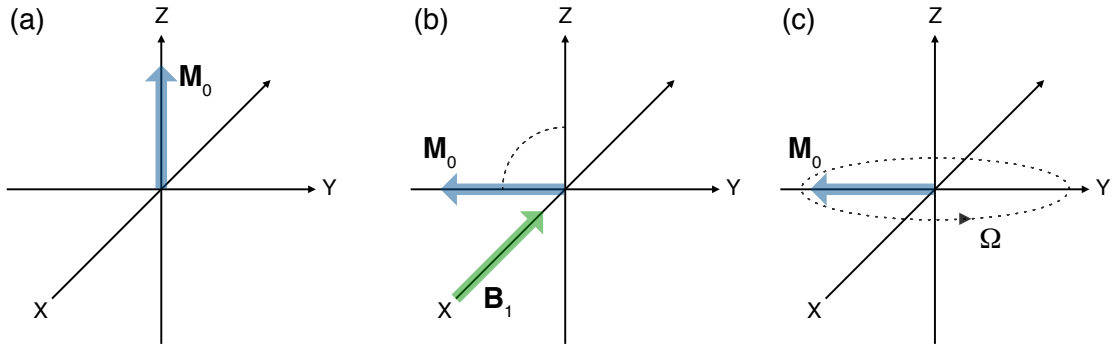

Figure 2.6: Vector model representations of (a) the bulk magnetisation vector, M_0, aligned along the z-axis of the rotating frame, (b) a radiofrequency pulse, B_1, applied along the x-axis, resulting in the nutation of M_0 into the xy-plane and (c) following nutation, M_0 undergoes free precession in the xy-plane at frequency Ω.

half maximum ($\Delta\nu$) is given by,

$$\Delta\nu = \frac{1}{\pi T_2}. \tag{2.19}$$

Spin-lattice relaxation is the return of the z component of the magnetisation to equilibrium and is described via the time constant T_1. This process essentially determines the duration of time needed before another radiofrequency pulse can be applied in order to repeat the experiment. In general, T_1 values tend to be greater than T_2, although both are sample dependent. Any change in the environment of the nuclei under investigation, *i.e.*, a phase transition or ion mobility will have a significant impact on the relaxation processes. Hence, measuring these time constants can provide in-depth information regarding the environment of the nuclei being investigated, and can be incredibly useful for studying structural changes in samples on the local scale.

The relaxation process results in a free induction decay (FID), an oscillatory signal which decays over time. This signal is then Fourier transformed (FT) to produce a frequency-based spectrum, as shown in Figure 2.7. The Fourier transform enables conversion between time-domain and frequency-

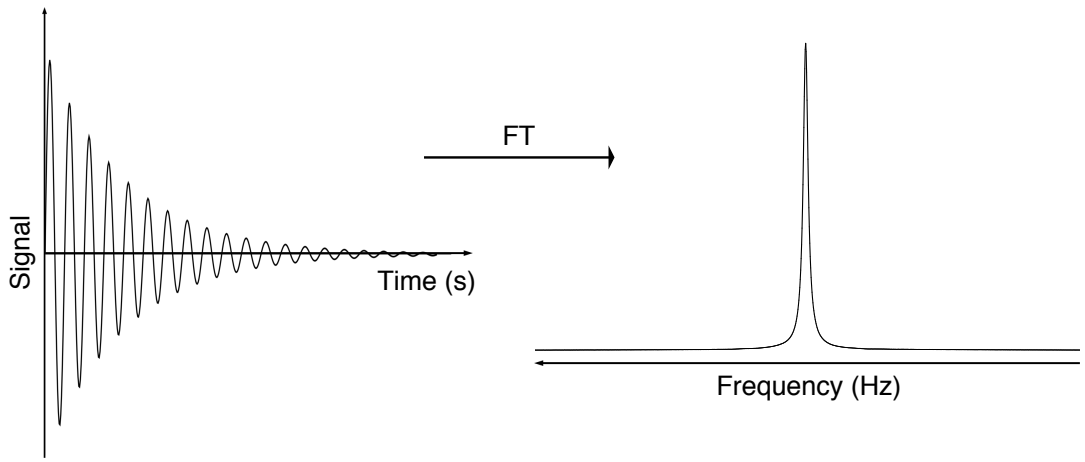

Figure 2.7: A schematic representation of an FID signal and the spectrum produced following Fourier transformation.

domain data and can be described by,

$$F(\omega) = \int_0^\infty f(t) e^{i\omega t} dt, \tag{2.20}$$

where f(t) is a time-domain signal. If the signal acquired were to oscillate indefinitely, a sharp peak at the oscillation frequency would be obtained. In reality, the signals obtained do not oscillate indefinitely but decay over time, resulting in peak broadening.

2.5 Interactions in NMR[153,157–162]

Solution-state NMR spectra commonly exhibit sharp and narrow lineshapes. As a result, it is possible to obtain detailed structural information from interactions such as the scalar couplings. This is because, in solution, orientationally-dependent, or anisotropic interactions are averaged to their isotropic value due to rapid molecular tumbling. In solids, however, there is no such motion. Hence, the presence of anisotropic interactions, gives rise to very broad resonances, thereby making the extraction of structural information quite challenging. Anisotropic interactions that take place between different spins are known as dipolar couplings, and those that can occur between spins and their environment include the chemical shift anisotropy (CSA) and the quadrupolar interaction. Many of these interactions are described using a three-dimensional tensor (*vide infra*) and, in many cases, it is convenient to

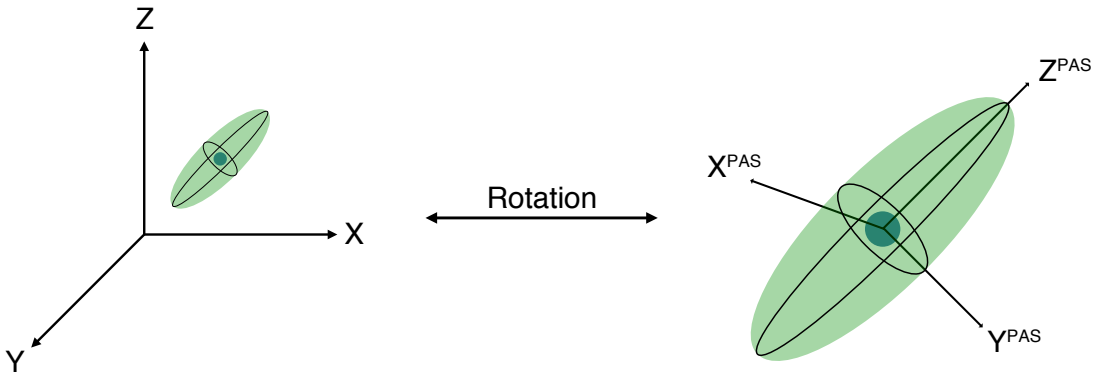

Figure 2.8: A schematic representation of conversion between the laboratory frame and the Principal Axis System (PAS) via rotation.

use a frame defined by the magnitude and shape of the interaction. This frame is known as the Principal Axis System (PAS). A schematic representation of the conversion between the laboratory frame and PAS via rotation is shown in Figure 2.8.

2.5.1 Scalar Couplings

Scalar couplings, also referred to as *J*-couplings, are a through-bond interaction that provide information regarding the connectivity of the system. Scalar couplings are prominent in solution-state NMR with couplings typically on the order of a few tens of hertz. For example, solution-state spectra often exhibit multiplet splitting patterns resulting from *J*-couplings. However, in solid-state NMR (SSNMR), they are typically dominated by much larger interactions such as the quadrupolar interaction.

2.5.2 Dipolar Couplings

Dipolar couplings are through-space anisotropic interactions. The magnetic dipole moments of nuclei produce small, localised magnetic fields, $\mathbf{B}_\mu$, which interact with the dipole moments of neighbouring nuclei. This is shown schematically for three different spins in Figure 2.9(a). The effect of spin i on spins j and k is different due to the anisotropic nature of this interaction. This interaction is affected by the strength of the dipole moments, the distance between and the geometry of the spins, as demonstrated in Figure 2.9(b) for spins

i and j. The dipolar interaction, ω_D, can be characterised as follows,

$$\omega_D = \omega_D^{PAS}\frac{1}{2}(3\cos^2\theta_{ij} - 1), \tag{2.21}$$

where ω_D^{PAS} is the dipolar coupling constant and is described by,

$$\omega_D^{PAS} = -\frac{\mu_0}{4\pi}\frac{\gamma_i\gamma_j\hbar}{r_{ij}^3}, \tag{2.22}$$

where μ_0 is the vacuum permeability and r_{ij} is the distance between the spins i and j. As described in these equations, the dipolar interaction depends upon the gyromagnetic ratios of nuclei i and j and the distance between them. Dipolar couplings tend to be quite large, typically on the order of a few kilohertz.

Dipolar couplings can occur between heteronuclear and homonuclear spins. In the case of the heteronuclear dipolar interaction between two spins, the spectrum would consist of a doublet centred around the Larmor frequency with a splitting of $2\omega_D$, as shown in Figure 2.10(a). In a polycrystalline sample, numerous different orientations exist, and a range of splittings are observed. This results in a complex lineshape called a Pake doublet, as shown in Figure 2.10(b). For homonuclear dipolar coupling, a similar spectrum is observed but with a splitting of $3\omega_D$. Similar to heteronuclear dipolar couplings, a powdered sample will produce a Pake doublet lineshape.

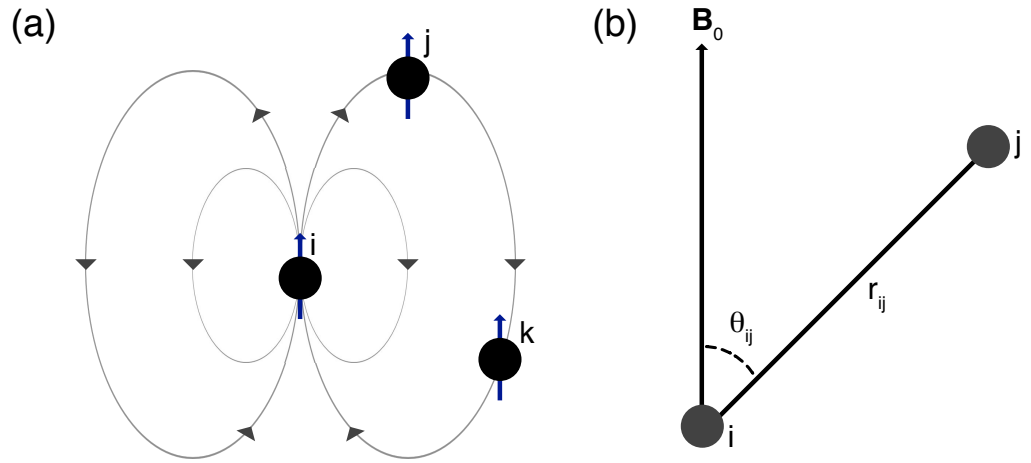

Figure 2.9: (a) A schematic representation of the dipolar interaction between spins i, j and k and (b) the geometry between spins i and j, with respect to the external magnetic field, B_0.

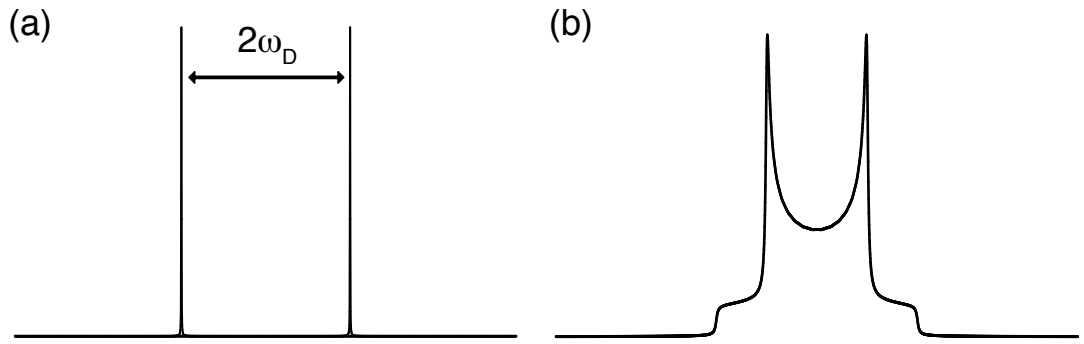

Figure 2.10: (a) Simulated lineshape for a heteronuclear dipolar coupled nucleus with a splitting of $2\omega_D$ and (b) the Pake doublet lineshape expected for a powdered crystalline sample.

2.5.3 Chemical Shift Anisotropy (CSA)

As discussed previously, the exact frequency at which a nucleus resonates is dependent upon the degree of shielding or deshielding experienced by the nucleus, resulting in the chemical shift interaction. In a solid sample, the shielding is orientationally-dependent, as the electron distribution around a nucleus is anisotropic. Hence, the chemical shift is given by,

$$\delta = \delta_{iso} + \frac{1}{2}\Delta_{CSA}(3\cos^2\theta - 1 \ + \eta_{CSA}\sin^2\theta \cos 2\phi), \tag{2.23}$$

where δ_{iso} is the isotropic component, Δ_{CSA} is the magnitude of the anisotropic component and η_{CSA} is the asymmetry, with values ranging between 0 and 1. In solution-state NMR, the anisotropic component is removed due to rapid molecular tumbling and $\delta = \delta_{iso}$. In the solid-state, however, the anisotropic interaction remains, and the shielding can be described by a three-dimensional tensor, which can be visualised as an elongated ellipsoid, as shown schematically in Figure 2.11. The length of the ellipsoid corresponds to the magnitude of the anisotropy, and the cross-sectional shape represents the asymmetry. The angles θ and ϕ describe the orientation of the ellipsoid, with respect to $\mathbf{B}_0$.

In a powdered sample, there will be many different molecular orientations, each with a distinct chemical shift. Hence, the overall spectrum ob-

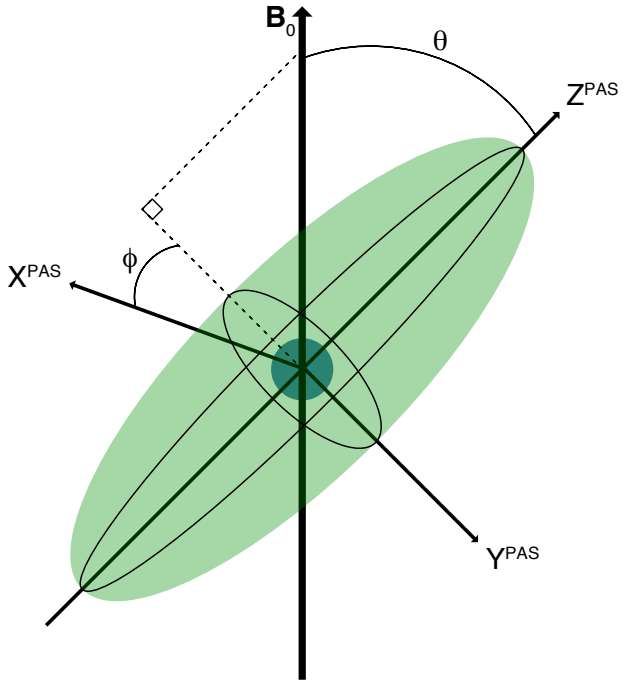

Figure 2.11: A schematic representation of the shielding tensor in the PAS. The angles θ and ϕ describe the orientation of the tensor with respect to the external magnetic field, B_0.

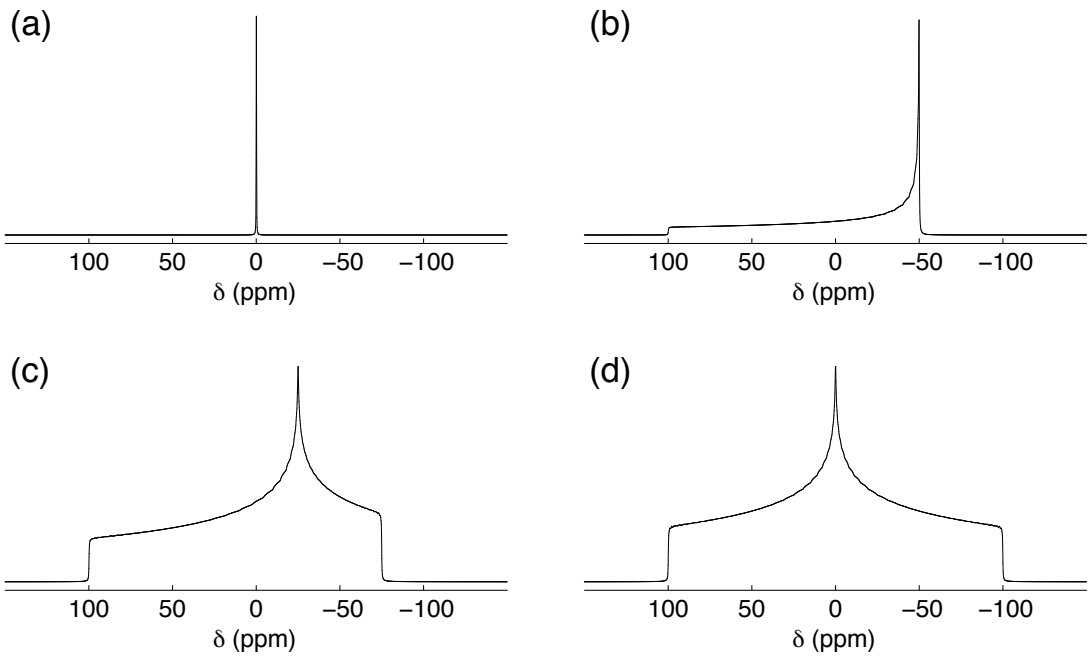

Figure 2.12: Simulated CSA lineshapes for (a) a cubic system and a spin I = 1/2 nucleus with Δ_{CSA} = 100 ppm and η_{CSA} of (b) 0, (c) 0.5 and (c) 1.

tained for the sample will consist of a broad resonance, the shape of which will be representative of the number of each different type of orientation present. The CSA lineshapes obtained are characteristic of the asymmetry of the tensor. Figure 2.12 shows the expected lineshapes for a cubic system where there is no anisotropy, an axially symmetric system ($\eta = 0$) and an axially asymmetric system ($\eta \neq 0$).

2.5.4 Quadrupolar Couplings

Nuclei with a spin quantum number greater than 1/2 exhibit quadrupolar interactions as they possess a nuclear electric quadrupole moment, eQ, which interacts with the electric field gradient (eq or EFG) generated at the nucleus by the other atoms present in the sample. This interaction is anisotropic, and the magnitude of the interaction depends both on the local environment and the nuclear electrical quadrupolar moment of the nucleus under investigation. In most cases, this interaction is very large and results in inhomogeneous broadening of the spectrum on the order of megahertz. Similar to the CSA, the anisotropy of this interaction can be described by an ellipsoid, and in its PAS it can be described by three principal components; V_{XX}, V_{YY} and V_{ZZ}. The magnitude of the EFG is given by $eq = V_{ZZ}$ and its cross-sectional shape can be described by an asymmetry parameter, η_Q, given by

$$\eta_Q = \frac{V_{XX} - V_{YY}}{V_{ZZ}}, \tag{2.24}$$

and ranges between 0 and 1. The magnitude of the quadrupolar interaction can be described by the quadrupolar coupling constant, C_Q, in hertz by,

$$C_Q = \frac{eQV_{ZZ}}{h} = \frac{e^2qQ}{h}. \tag{2.25}$$

The value of C_Q can provide information regarding the symmetry of the nucleus under investigation. For a perfectly symmetrical system, C_Q would be 0 as the charge will be spherically distributed. However, for systems with reduced symmetry, the value of C_Q will be much higher.

The quadrupolar interaction can be described using a first- or second-order approximation. Even though the quadrupolar interaction is quite large,

the Zeeman interaction remains the dominant interaction. Hence, the quadrupolar interaction is described as a perturbation of the Zeeman energy levels. The effects of the first-order interaction on $I = 1$ and $I = 3/2$ nuclei is shown in Figure 2.13(a). To a first-order approximation the energy levels are perturbed, and the transitions are split into $2I$ transitions. The resulting resonances are all equally spaced by $2\omega_Q$, as shown in Figure 2.13(b). The quadrupolar splitting parameter, ω_Q, can be described by,

$$\omega_Q = \frac{\omega_Q^{PAS}}{2}(3\cos^2\theta - 1 + \eta_Q(\sin^2\theta\cos 2\phi)), \tag{2.26}$$

where the angles θ and ϕ describe the orientation of the PAS with respect to $\mathbf{B}_0$ and ω_Q^{PAS}, in rad s^{-1} is given by;

$$\omega_Q^{PAS} = \frac{3\pi C_Q}{2I(2I-1)}\,. \tag{2.27}$$

As a powdered sample will have many different orientations, the resulting spectra will contain a lineshape akin to those shown in Figure 2.13(c).

It is also observed that for half-integer spins the central transition is not affected by the first-order interaction, resulting in a sharp peak. The satellite transitions, however, are broadened by this interaction, as demonstrated in Figure 2.13. For integer spins, there is no central transition, and all transitions are affected by the first-order interaction. The shape of the resulting powder pattern will vary depending on the value of η_Q. Figure 2.14 shows simulated lineshapes for a spin-1 nucleus with a C_Q of 25 kHz and values of η_Q ranging between 0 and 1, under static conditions. As η_Q is varied the lineshape changes, thus demonstrating that an analysis of the lineshape obtained allows for the extraction of quadrupolar parameters which describe the environment of the nucleus under investigation.

Typically, the quadrupolar interaction is considerably larger and requires a second-order approximation. The effects of the second-order interaction on the energy levels of a spin $I = 3/2$ nucleus are shown schematically in Figure 2.15. As this interaction is so large, even the central transition is perturbed, and the satellite transitions are often not observed as they are broadened. The effect of this perturbation on a transition frequency $m_I \longleftrightarrow -m_I$ can

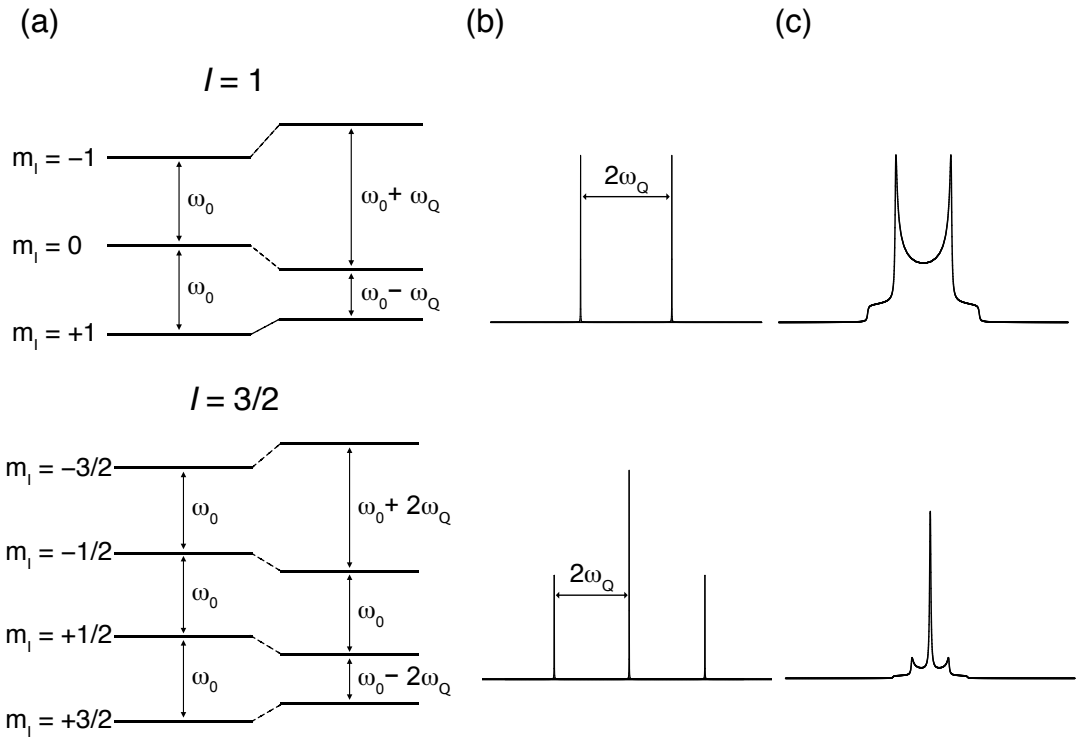

Figure 2.13: (a) First-order perturbation of the Zeeman energy levels by the quadrupolar interaction for spin-1 and 3/2 nuclei. (b) The corresponding simulated spectra with a splitting of $2\omega_Q$ and (c) the expected simulated lineshapes for powdered crystalline samples.

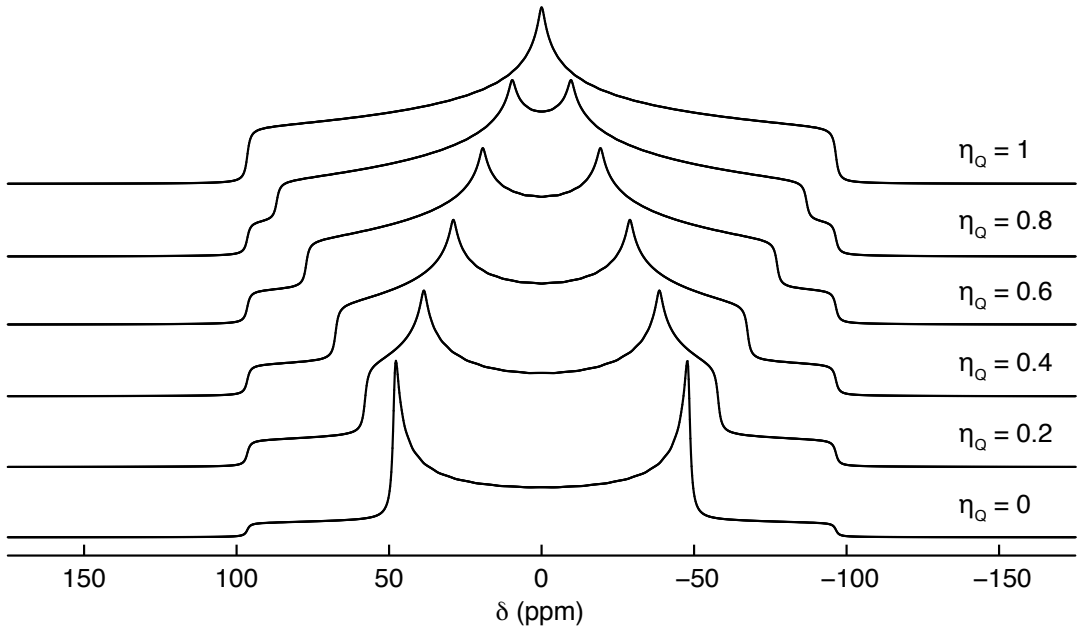

Figure 2.14: Simulated lineshapes for a spin-1 nucleus under static conditions with C_Q = 25 kHz and η_Q ranging between 0 and 1.

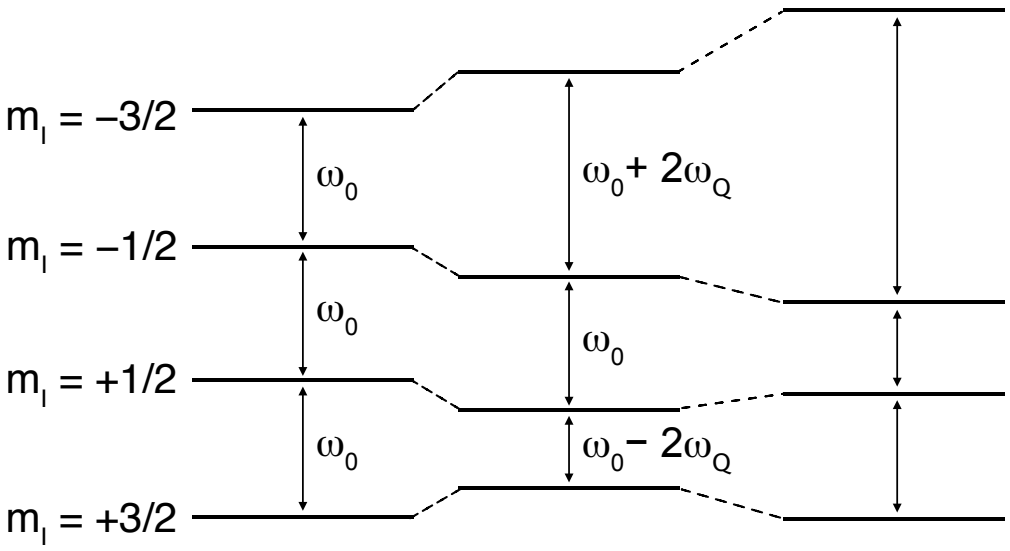

Figure 2.15: First- and second-order perturbations of the Zeeman energy levels arising from the quadrupolar interaction for a spin-3/2 nucleus.

be described by,

$$E^{(2)}_{|m_I\rangle} - E^{(2)}_{|-m_I\rangle} = \frac{(\omega_Q^{PAS})^2}{\omega_0}[A^0(I, m_I) + A^2(I, m_I)\, d^2_{00}(\theta)d^2_{00}(\chi) + A^4(I, m_I)\, d^4_{00}(\theta)d^4_{00}(\chi)], \quad (2.28)$$

where $A^n(I,m_I)$ are coefficients that are dependent upon spin and energy levels, θ and χ describe the orientation of the crystallite and the rotor with respect to the applied field. The second order interaction consists of an isotropic shift proportional to $A^0(I,m_I)$ and second- and fourth-rank anisotropic terms proportional to $A^2(I, m_I)\, d^2_{00}(\theta)d^2_{00}(\chi)$ and $A^4(I, m_I)\, d^4_{00}(\theta)d^4_{00}(\chi)$, respectively. Figure 2.16 shows the effects of the second-order perturbation on the lineshape observed for a spin $I = 3/2$ nucleus with a C_Q of 2 MHz, where η_Q is varied from 0 to 1. The central transition exhibits a complex lineshape, which is in contrast to that observed for a first-order approximation (Figure 2.13), where the central transition was a single sharp line.

For a spin $I = 3/2$ nucleus with an η_Q of 0, Equation 2.28 can be sim-

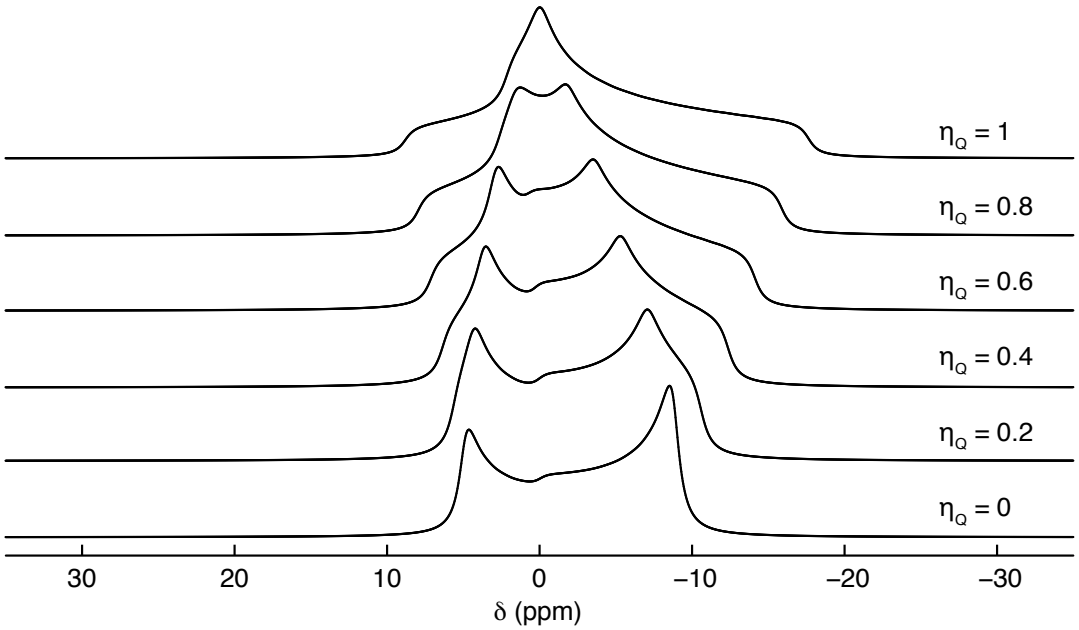

Figure 2.16: Simulated lineshapes for a spin-3/2 nucleus under static conditions with C_Q = 2 MHz and η_Q ranging between 0 and 1.

plified to,

$$E^{(2)}_{|\frac{1}{2}\rangle} - E^{(2)}_{|-\frac{1}{2}\rangle} = \frac{(\omega_Q^{PAS})^2}{\omega_0}\left[-\frac{2}{5} - \frac{8}{7}d^2_{00}(\theta)d^2_{00}(\chi) + \frac{54}{35}d^4_{00}(\theta)d^4_{00}(\chi)\right]. \tag{2.29}$$

Here, the first term represents the isotropic component, and d^2_{00}(second-rank interaction) and d^4_{00}(fourth-rank interaction) represent the anisotropic components, and the orientational dependence of these interactions on θ can be described by,

$$d^2_{00}(\theta) = \frac{1}{2}(3\cos^2\theta - 1), \tag{2.30}$$

$$d^4_{00}(\theta) = \frac{1}{8}(35\cos^4\theta - 30\cos^2\theta + 3). \tag{2.31}$$

2.6 Magic-Angle Spinning[153,158]

As discussed previously, in the solution-state, anisotropic interactions are averaged to their isotropic value due to rapid molecular tumbling. Hence, solution-state NMR spectra commonly exhibit very narrow lineshapes with complex multiplet splitting patterns. In contrast, in the solid state, all of the interactions detailed previously (*vide supra*) are present simultaneously, resulting in very broad resonances, making it extremely challenging to extract useful

structural information. It is possible to suppress the anisotropic interactions present by the introduction of artificial motion on solids. This technique is called magic-angle spinning (MAS) and is widely used in solid-state NMR experiments.

During an experiment, the sample is oriented at an angle of 54.736° relative to the external magnetic field, $\mathbf{B}_0$, and spun at various rates. This process is demonstrated schematically in Figure 2.17. Whilst spinning does not entirely replicate the isotropic motion of a liquid, it does ensure that all the spins adopt a similar orientation. This particular angle is chosen as the dipolar coupling, CSA and the first-order quadrupolar interaction show a dependence on $(3\cos^2\theta - 1)$ and when $\theta = 54.736°$ this term is 0, and the interactions are averaged to their isotropic values. In general, MAS NMR spectra display higher resolution when compared to static NMR spectra.

The rate of spinning is extremely important, it must be greater than or equal to the magnitude of the interaction(s) being removed. A slow spinning rate will result in a manifold of spinning sidebands that are evenly spaced from the isotropic signal. When the spinning speed is varied, the position of

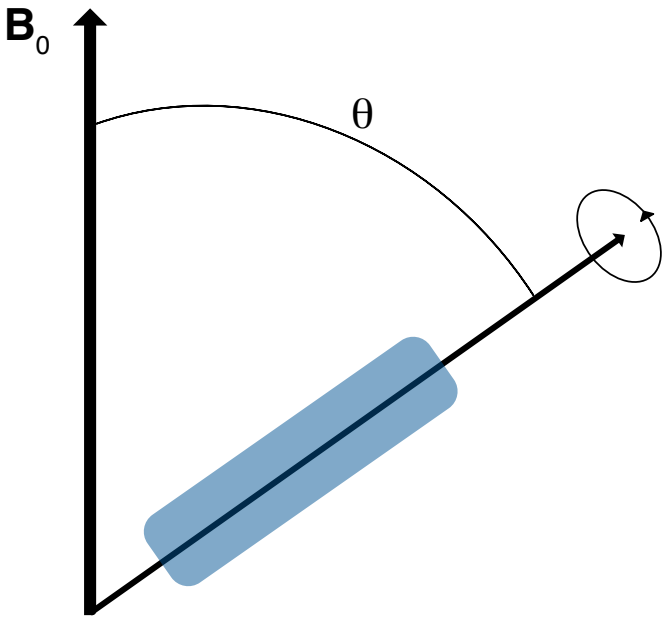

Figure 2.17: A schematic representation of a rotor inclined at the magic angle, $\theta = 54.736°$, with respect to the external magnetic field, B_0.

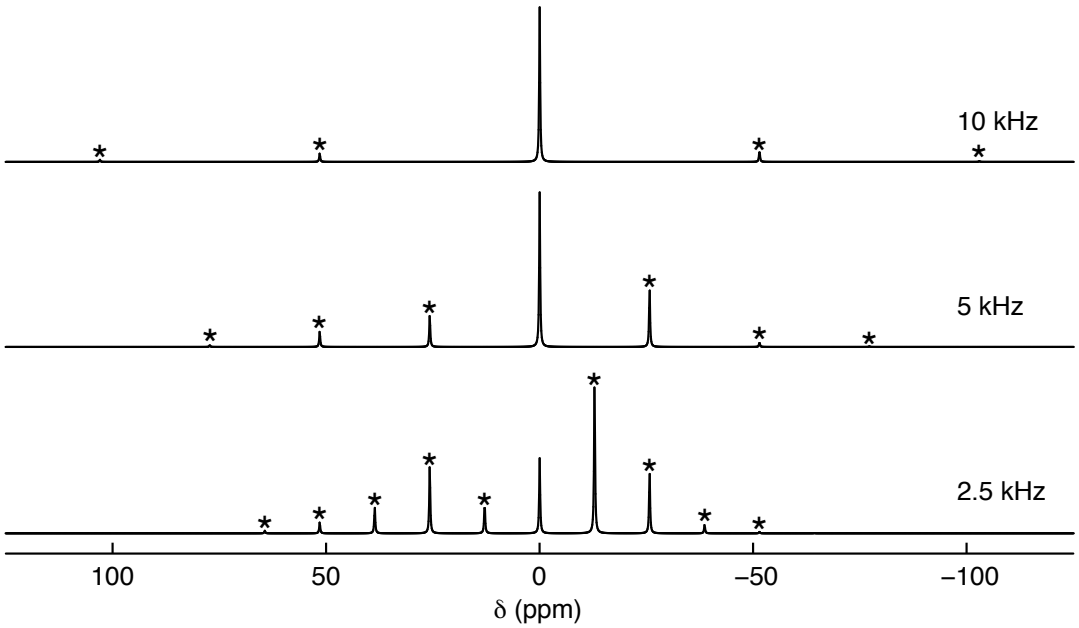

Figure 2.18: Simulated lineshapes for a spin-1/2 nucleus at MAS rates of 2.5, 5 and 10 kHz. The isotropic signal is at δ = 0 ppm and the spinning sidebands are denoted by *.

the sidebands will change, whereas the position of the isotropic signal will remain the same. This is demonstrated in Figure 2.18, where the spinning sidebands move further away from the isotropic signal, and their intensities decrease with increasing spinning rate.

The rate of spinning is also dependent upon the size of the rotor. Rotors used for NMR experiments are commonly made of ZrO_2, BN or SiN, and they are available in a range of different sizes. In this study, rotors with a diameter of 3.2, 4 and 5 mm were used. Smaller rotors can reach much higher spinning speeds in comparison to larger rotors, although the sample volume is in turn reduced. For example, for 2.5 mm rotors, spinning rates of 30 – 35 kHz can be used.

2.7 Dipolar Decoupling[153,158]

As discussed previously, dipolar couplings are a through-space interaction that are often very large, resulting in very broad lineshapes. This makes it challenging to analyse the spectra obtained. Hence, removing the effects of this interaction can be extremely beneficial. In order to effectively remove the

dipolar interaction using MAS, very fast MAS rates would be required, which is not always feasible. Hence, dipolar interactions are usually removed using decoupling methods. Heteronuclear dipolar interactions can be removed via high-power decoupling which can be used under static or MAS conditions, which are usually more effective. Consider a system where there is a dipolar interaction between nuclei I and S, and nucleus S is being detected. Dipolar decoupling involves the application of a high-power pulse at the Larmor frequency of nucleus I whilst acquiring the FID of nucleus S. Initially, a pulse is applied on S, and then the FID is acquired in the presence of a long pulse on I. A schematic illustrating this process is shown in Figure 2.19. Homonuclear dipolar interactions, on the other hand, cannot be removed using this method and often requires the use of very fast MAS rates. Again, this is not always feasible, meaning alternative methods are needed. Typically, a "windowed" approach can be used where decoupling pulses are alternated with "windows" where decoupling is not applied, and FID data points are collected instead. However, it is noted that these experiments can be quite challenging.

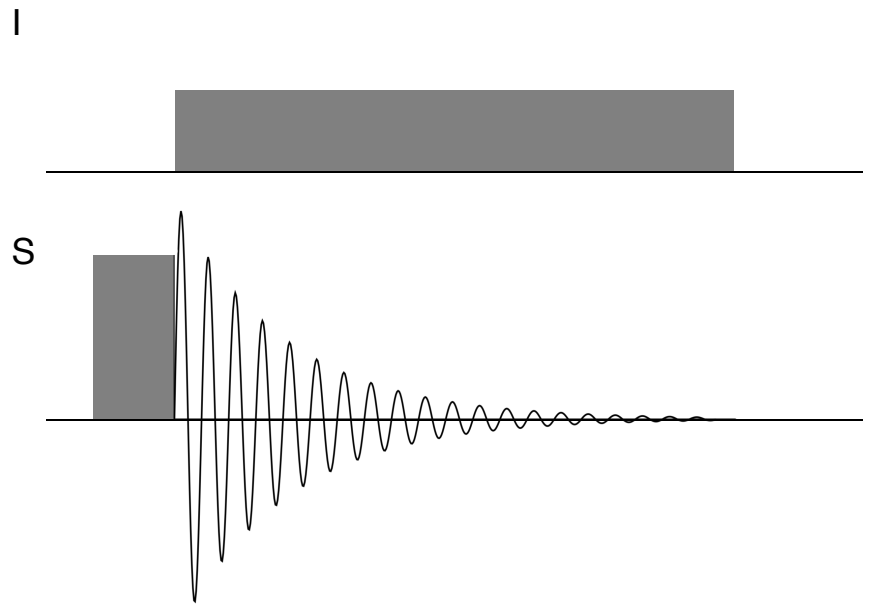

Figure 2.19: A schematic representation of continuous wave decoupling, where a continuous pulse is applied at the Larmor frequency of nucleus I whilst acquiring the FID for nucleus S.

2.8 Removing the Effects of Second-Order Quadrupolar Interaction[153,158]

Second-order quadrupolar broadening can make the analysis of the spectra obtained quite challenging, *i.e.*, it can be difficult to determine the number of crystallographically different sites observed. Thus, it is desirable to remove the effects of this interaction. MAS cannot remove the second-order quadrupolar interaction. This is due to the second and fourth-rank terms, which can only be removed when θ is 30.56° or 70.12°. Hence, alternative techniques are required to obtain high-resolution spectra. These techniques include double rotation (DOR), dynamic-angle spinning (DAS) and multiple-quantum (MQ) MAS. DOR involves spinning the sample around two angles simultaneously using a double rotor. This is achieved by placing the sample inside an inner rotor inclined at 30.56° or 70.12° with respect to the outer rotor, which is, in turn, inside an outer rotor inclined at 54.736°, with respect to the external magnetic field, $\mathbf{B}_0$. DAS is a two-dimensional technique where the isotropic signal is acquired in one dimension, and the quadrupolar broadened anisotropic powder patterns are acquired in the other. MQMAS is also a two-dimensional technique where single- and multiple-quantum coherences which cannot be observed directly are correlated under MAS.

2.9 Probing Dynamics in Solids via NMR[151,158,163–165]

Investigating dynamics and molecular motion in solid materials is of great interest, particularly in the field of solid electrolytes. NMR is a very useful technique for studying motion in solids as all the nuclear interactions present are anisotropic and are therefore greatly influenced by the local environment of the nucleus being studied. Thus, any changes occurring in the system can be probed via NMR.

Dynamics in solid crystalline materials can be divided into two general categories; reorientation and translation. During reorientation, the movement of the atoms is limited, whereas translation allows for diffusion to occur throughout the crystalline structure. In order to differentiate between the type

of motion present in a sample, the linewidth of the resonance observed in a spectrum can be used. As stated earlier, the linewidth of a resonance is dependent on T_2, which is in turn, determined by the local environment of the nucleus being studied. Reorientation of the nucleus will result in a small degree of line narrowing, typically three to four orders of magnitude. Whereas translational motion usually results in an extreme line narrowing and, depending on the degree of motion, the line can narrow by several orders of magnitude. The convention is to measure the peak width of a resonance observed at half maximum, termed full width at half maximum (FWHM). In this study, variable-temperature (VT) NMR experiments have been completed, and the FWHM has been plotted as a function of temperature.

Another method for investigating motion in solid materials is to measure the relaxation rates, in particular the time constant, T_1. As stated earlier, T_1 is used to describe the return of the z component of the bulk magnetisation to equilibrium. This process is dependent on the local fields present in a sample due to the magnetic moments of other nearby spins. These local fields mediate the relaxation process, and any motion in the system will cause these local fields to fluctuate, and thus, change the rate of relaxation. Therefore, T_1 measurements can prove to be useful in studying motion in solids. One standard method of measuring T_1 is via saturation recovery, where two 90° pulses are applied with a time interval of τ. The signal obtained is proportional to $M_z(\tau)$, which is described as

$$M_z(\tau) = M_0 \left(1 - e^{-\tau/T_1}\right) . \tag{2.32}$$

T_1 is determined by repeating the experiment as a function of τ. M_0 is the magnetisation at equilibrium and is taken to be the signal obtained after a time $>5T_1$. In the current study, T_1 measurements have been recorded as a function of temperature.

2.10 Pulsed-Field Gradient (PFG) NMR Spectroscopy[166–170]

PFG-NMR spectroscopy is a technique typically used for investigating diffusion. As stated earlier, placing a sample in a magnetic field, $\mathbf{B}_0$, results in

a net alignment of the spins, producing a bulk magnetisation vector, $\mathbf{M}_0$. As previously discussed, the Larmor frequency of the nucleus under investigation can be described as a function of its gyromagnetic ratio and the strength of the magnetic field (Equation 2.14). When a constant magnetic field gradient is applied along the z-axis, g(z), the total Larmor frequency, ω_{tot}, is described by,

$$\omega_{tot}(z) = -\gamma(\mathbf{B}_0 + g(z)) = \omega_0 - \gamma g(z). \tag{2.33}$$

It is noted that that the Larmor frequency is now dependent on the spatial position of the nucleus.

Here, PFG-NMR spectroscopy has been used to study ion diffusion in LiRAPs. The PFG-NMR spectra presented in this work were acquired using the stimulated echo PFG pulse sequence shown in Figure 2.20. Initially, a 90° RF pulse is applied to excite the spins, and the bulk magnetisation vector, $\mathbf{M}_0$, nutates into the xy-plane. A gradient pulse of strength, g, is then applied for a duration, δ, to ensure spatial encoding of the spins. This creates a helical pattern of the tips of the magnetisation vectors at various positions in the sample. Essentially, a phase shift of the spins is created, and another gradient pulse with the same strength and duration must be applied to cancel this shift. Thus, unwinding the helical pattern, and bringing all of the spins in-phase again. However, if the spins move during the time period between the two gradient pulses, Δ, then rewinding of the helix is not perfect, causing a reduction in the signal intensity. The loss of signal is dependent on the intensity of the gradient pulse and its duration. This is because the magnetisation at various positions in the sample has a pitch (Λ) given by,

$$\Lambda = \frac{2\pi}{\gamma g(z)\delta}\,. \tag{2.34}$$

The relationship between the signal intensity (I) and the diffusion coefficient (D) is described by the Stejskal and Tanner[171] equation,

$$\frac{I}{I_0} = \exp\left[-(\gamma\ \delta\ g)^2\ D\left(\frac{\Delta - \delta}{3}\right)\right], \tag{2.35}$$

where I is the measured intensity, I_0 is the intensity at the lowest gradient strength, γ is the gyromagnetic ratio, δ the effective gradient length, g the gra-

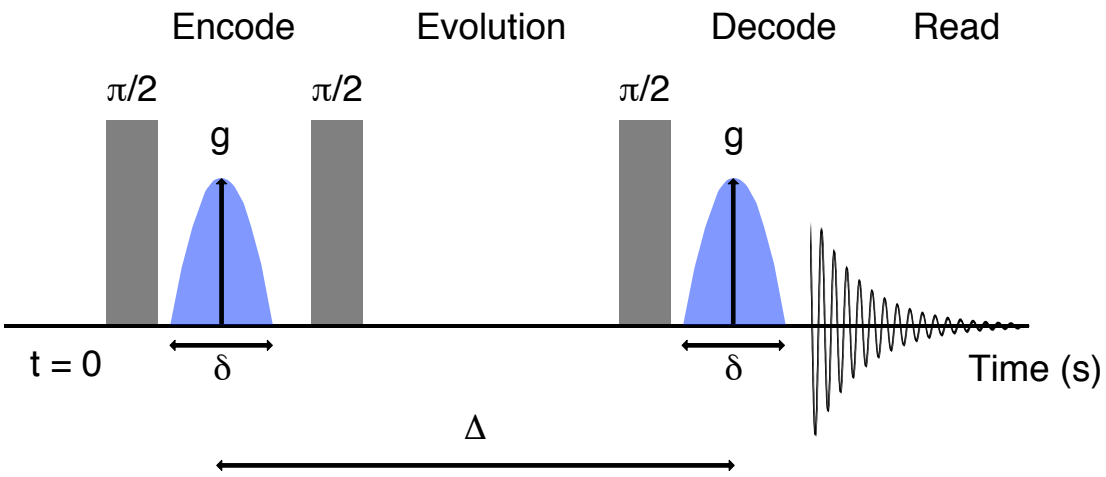

Figure 2.20: A schematic representation of the stimulated echo diffusion pulse sequence typically used for the acquisition of PFG-NMR spectra of solid materials when $T_1 >> T_2$.

dient strength, Δ is the diffusion time between the two gradient pulses and D is the apparent diffusion coefficient of the observed nucleus.

2.11 Exchange Spectroscopy (EXSY) NMR[151,158,172]

Exchange spectroscopy NMR is an excellent method for obtaining information regarding any dynamic processes occurring within a material. EXSY NMR experiments are most commonly used for investigating conformational changes or chemical exchange within a sample. The EXSY pulse sequence is shown in Figure 2.21(a). Consider a system where a spin undergoes exchange between two different positions, A and B. In this experiment, the first 90° pulse prepares the spins by rotating their bulk magnetisation vector into the xy-plane, where the spins are allowed to evolve for a duration t_1. The next phase of the experiment (90° – τ_m – 90°) is responsible for the transfer of magnetisation from A to B and this takes place during the mixing period (τ_m). The 90° pulses before and after τ_m are used to interconvert between transverse and longitudinal magnetisation, $M_{x,y}(A)$ to $M_z(A)$ and $M_z(B)$ to $M_{x,y}(B)$, respectively. The results obtained are presented in a 2D spectrum, a schematic of which is shown in Figure 2.21(b). The spectrum consists of peaks both on and off the diagonal. The off-diagonal peaks are termed cross-peaks and are only

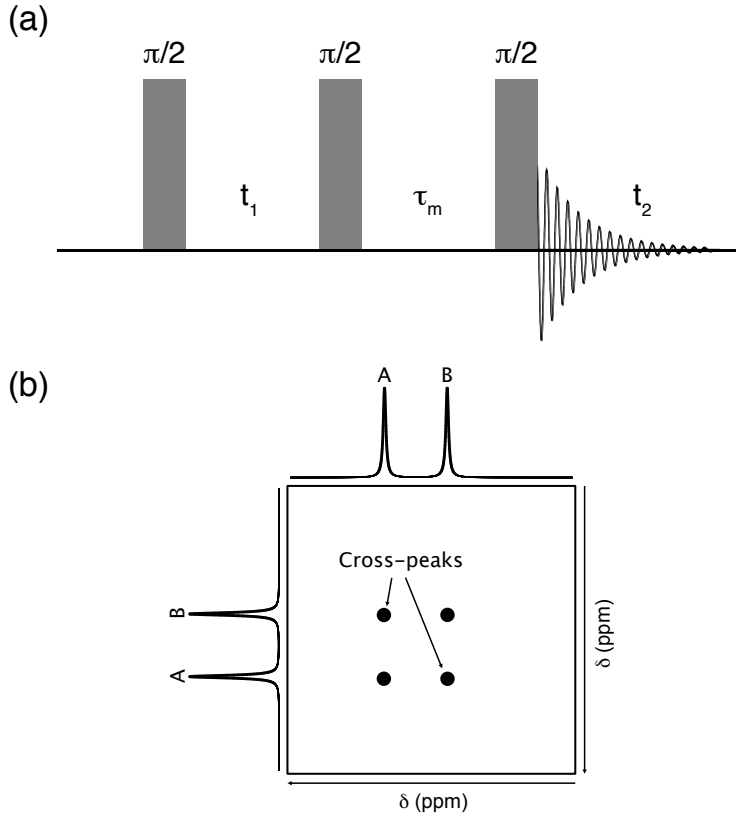

Figure 2.21: (a) A schematic representation of the pulse sequence used for EXSY NMR experiments, and (b) a schematic representation of a 2D EXSY NMR spectrum displaying cross-peaks between spins A and B.

observed in the event of an exchange of magnetisation between two species.

2.12 Nuclei Probed in this Study

In the current study, multinuclear SSNMR spectroscopy has been used extensively to characterise and probe ion mobility within the LiRAP samples. Several different nuclei were investigated, and each nucleus has its specific set of properties, *e.g.*, spin, natural abundance etc., that determine its usefulness for NMR spectroscopy. This section discusses the nuclei studied and the specific challenges associated with each species.

2.12.1 ^{1}H NMR[163]

^{1}H ($I = 1/2$) has an abundance of 99.985% and is one of the most commonly studied nuclei. ^{1}H nuclei usually exhibit strong homonuclear dipolar

couplings, the effects of which cannot be removed via moderate MAS rates. However, in inorganic materials, the ^{1}H nuclei tend to be relatively distanced, which reduces the magnitude of the ^{1}H–^{1}H dipolar interaction. Thus, a high-resolution spectrum can usually be acquired using moderate MAS rates. Crystalline materials can incorporate protons in their structure as stoichiometric hydroxyl groups or intact water molecules. It is not easy to differentiate between them based on their chemical shift as the shift range for ^{1}H is ~20 ppm, which often results in an overlap of the resonances observed. The two species are usually distinguished by inspecting the spinning sidebands observed. The protons in hydroxyl groups usually result in 1 or 2 pairs of sidebands whereas intact water molecules tend to produce a large manifold of sidebands extending over ~100 kHz.[173–175] This difference is due to the different dipolar coupling interactions taking place in each case. Typically, ^{1}H NMR spectra are acquired using background suppression experiments as ^{1}H background signals can arise from moisture or polymer parts present in the probe.[176]

2.12.2 ^{2}H NMR[158,177–179]

In NMR spectroscopy, ^{2}H (I = 1) is a commonly exploited quadrupolar nucleus for studying molecular dynamics and motion in solids. ^{2}H has a reasonably small quadrupole moment (2.8×10^{-31} e m^{2}) making the acquisition of a spectrum relatively easy as the resulting lineshapes are not exceptionally broad. However, its very low natural abundance (0.012%) makes isotopic enrichment necessary, which can, in some cases, be quite challenging. The most common method for extracting dynamic information using ^{2}H NMR is to record the powder pattern for a stationary sample using a spin-echo experiment. In the absence of motion, a well-defined Pake doublet with a quadrupolar splitting is obtained. In the presence of motion, the lineshape will become distorted, which will be influenced by the precise geometry and rate of the motion observed. In some cases, it can be challenging to derive the underlying types of motion from static ^{2}H NMR experiments. In such circumstances, MAS NMR experiments can be used, where the manifold of spinning sidebands outlines the shape of the static powder pattern.

2.12.3 $^{6/7}$Li NMR[163]

^{6}Li (I = 1) and ^{7}Li (I = 3/2) are both suitable nuclei for NMR spectroscopy. However, ^{7}Li is usually favoured owing to its high natural abundance (92.5%) when compared to ^{6}Li (7.5%). ^{7}Li has a much higher quadrupole moment (-4.01×10^{-30} e m^2) than ^{6}Li (-0.08×10^{-30} e m^2), meaning that Li in non-symmetrical environments usually result in relatively broad lineshapes. Furthermore, there is little variation in ^{7}Li chemical shift which makes the identification of different species challenging. In such circumstances, ^{6}Li NMR may be used as it generally produces narrower, better resolved lineshapes.[180] However, its low natural abundance, less favourable receptivity and often very long relaxation times render it difficult to complete ^{6}Li NMR experiments. Both ^{6}Li and ^{7}Li NMR have been used extensively to study the structure of and Li ion mobility in various inorganic systems, including solid electrolytes such as lithium lanthanum titanate.[181–183] The work presented in this study includes both ^{7}Li MAS and static NMR spectra. During experiments, dipolar decoupling was used to remove the effects of the ^{1}H–^{7}Li heteronuclear dipolar coupling.

2.12.4 ^{19}F NMR[163]

^{19}F is a spin-1/2 nucleus and has a natural abundance of 100%. In a similar manner to ^{1}H (I = 1/2), ^{19}F also displays strong homonuclear dipolar couplings, meaning that moderate MAS rates are insufficient for obtaining high-resolution spectra. However, materials with spatially dilute ^{19}F can result in good spectra.[184,185] One material that has been studied extensively via ^{19}F is CaF_2 due to its significance in dental sciences.[186,187] It has been demonstrated that increasing the MAS rate also increases the resolution and sufficiently good spectra can be acquired at MAS rates ca. 15 kHz. Hydroxyl groups in crystalline materials can be easily substituted via F^-.[188] Hence, ^{19}F NMR can be extremely beneficial for investigating such substitutions.

2.12.5 $^{35/37}$Cl NMR[163,189–191]

Both ^{35}Cl ($I = 3/2$) and ^{37}Cl ($I = 3/2$) nuclei are suitable for NMR spectroscopy and have similar quadrupole moments (^{35}Cl = -8.71×10^{-30} e m^2 and ^{37}Cl = -6.46×10^{-30} e m^2). However, ^{35}Cl is preferred owing to its higher natural abundance (75.77%) when compared to ^{37}Cl (24.23%). Typically, Cl in symmetrical or near-symmetrical environments results in reasonably narrow lineshapes that are easy to acquire. However, Cl in asymmetrical environments can result in broadened lineshapes which can be difficult to acquire in full and may therefore need to be acquired in segments. These lineshapes can be simulated to determine the number of crystallographically distinct sites present in a sample and to extract the corresponding quadrupolar parameters, *i.e.*, C_Q and η_Q. In this study, several ^{35}Cl MAS NMR spectra have been acquired using spin-echo experiments.

2.12.6 $^{79/81}$Br NMR[189,192,193]

Both ^{79}Br ($I = 3/2$) and ^{81}Br ($I = 3/2$) can be studied via NMR spectroscopy. Both nuclei have a similar natural abundance (^{79}Br = 50.69% and ^{81}Br = 49.31%), so neither isotope is favoured. However, the quadrupole moments of both isotopes are extremely large (^{79}Br = 31.30×10^{-30} e m^2 and ^{81}Br = 26.15 $\times 10^{-30}$ e m^2) meaning that Br in non-symmetrical sites will result in incredibly broad lineshapes. Most often, the degree of broadening makes it challenging to detect a signal at all. Hence, $^{79/81}$Br are not very popular nuclei to be studied via NMR. However, there are a few reports of $^{79/81}$Br NMR studies of alkali metal bromides and cubic salts, for example, AgBr, CuBr and TlBr.[194,195] In these systems, bromine exists in a symmetrical or near-symmetrical environment meaning that the quadrupolar interaction is either zero or very small. Thus, reasonably narrow resonances can be observed. In this study, ^{79}Br MAS NMR experiments were completed for samples adopting a cubic structure.

3 Li_3OCl and Li_3OBr

3.1 Introduction

As stated in Chapter 1, LiRAPs have been suggested as candidate solid electrolyte materials and, as a result, this thesis is focused on both their synthesis and characterisation. LiRAPs are extremely hygroscopic. Hence, they must be synthesised using air-sensitive methods. Zhao and Daemen initially reported the synthesis of Li_3OCl, Li_3OBr and the related mixed compositions by heating LiCl, LiBr and LiOH between 330 – 360 °C under vacuum.[124] Li_3OCl and Li_3OBr were reported to adopt a cubic structure in space group $Pm\bar{3}m$ with lattice parameter a = 3.91 and 4.02 Å, respectively. However, it must be noted that the specific reaction conditions used were not fully reported. In the same publication, the synthesis of Li_3OCl was also attempted using high-pressure and high-temperature methods, using LiCl and Li_2O as precursors. However, again, no specific reaction details regarding the exact pressures or temperatures used were stated. In addition, it was reported that very little of the desired phase was produced using this method. Hence, it was not explored in any great detail by Zhao and Daemen.[124] In this initial LiRAPs study, the samples prepared were analysed to determine their physical properties and, more specifically, their ionic conductivities. The values reported were on the order of 10^{-3} S cm^{-1}, which are comparable to current commercial liquid electrolytes. However, subsequent studies of the same systems by other researchers in the field have noted reduced Li-ion conductivities. These include reports by Lu and co-workers,[134,135] and Li and co-workers (*vide supra*).[196]

The synthesis of Li_3OCl was also recently reported by Reckeweg and co-workers.[126] Here, Li_3OCl was prepared by heating LiCl and Li_2O at 350 °C for 40 hrs. Characterisation of the sample produced agrees with that initially reported by Zhao and Daemen,[124] confirming that Li_3OCl is cubic in space group $Pm\bar{3}m$ with a lattice parameter of 3.907 Å. However, the samples prepared were not phase pure and were reported to contain a hydrated form of LiCl, $LiCl{\cdot}H_2O$, as an impurity phase.[126] This suggests it is particularly chal-

lenging to synthesise a phase pure sample of Li_3OCl via conventional solid-state methods.

Zhang and co-workers have also reported the synthesis of Li_3OCl, Li_3OBr and Ca-doped Li_3OCl, $Li_{3-x}Ca_{x/2}OCl$ (x = 0.1 and 0.2), via high-pressure and high-temperature methods using Li_2O, CaO, LiCl and LiBr as precursors.[128] Samples of Li_3OCl and $Li_{3-x}Ca_{x/2}OCl$ (x = 0.1 and 0.2) were prepared via mechanical milling of the reagents for two hours and heating of the reagent mixtures at temperatures ranging between 127 and 152 °C under a pressure of 0.5 GPa. For Li_3OBr, the reagents were milled for three hours and the mixture was heated at 177 °C under 3.0 GPa. Specific details regarding the reaction times were not specified. This synthetic method involved using an indirect route in which the hydrated version of the desired LiRAP, $Li_{2x+1}(OH)_{2y}Cl/Br$ (x = y), was first prepared and then dehydrated to remove water and produce Li_3OCl/Br.

Additional reports regarding the synthesis of LiRAPs include work by Li and co-workers.[196] Samples of Li_3OCl and Li_3OBr were synthesised under an inert atmosphere, where the entire sample preparation process took place inside an argon-filled glovebox. Li metal and LiH were used as reducing agents to break the OH bond in LiOH. It is widely known that the OH bond is hard to break, given its large mean bond enthalpy (463 kJ mol^{-1}).[11] This undoubtedly makes the synthesis of Li_3OCl/Br quite challenging. Hence, the use of a reducing agent can assist in facilitating the synthesis. The samples were prepared using LiCl, LiBr, LiOH and Li/LiH as precursors that were mechanically milled for two hours prior to annealing. The reagent mixture containing Li was heated at 600 °C for ten hours, whereas the mixture containing LiH was heated at 480 °C for one hour. In both cases, the samples were reground and reheated to obtain phase pure samples.

This chapter focuses on the synthesis of Li_3OCl and Li_3OBr, and characterisation of the samples produced via XRD and SSNMR spectroscopy. All of the samples discussed in this chapter have been synthesised either under vacuum using a conventional Schlenk line or in the inert atmosphere of an Ar-

filled glovebox. The following sections detail the precise synthetic procedures and characterisation methods used, followed by a discussion of the findings. The chapter concludes with a summary of the results obtained.

3.2 Experimental

3.2.1 Synthesis

During this project, three different solid-state synthetic techniques were used: (1) heating under vacuum using a conventional Schlenk line apparatus, (2) heating reagents inside the inert atmosphere of an Ar-filled glovebox and (3) mechanical milling of reagents using a planetary ball-mill. The specific experimental procedures used are outlined in the following sections.

3.2.2 Schlenk Line Method

To prepare samples of Li_3OCl and Li_3OBr using the Schlenk line method, stoichiometric amounts of LiOH (Acros Organics, anhydrous, 98%) or Li_2O (Alfa Aesar, 99.5%) and LiCl (Alfa Aesar, anhydrous, 99%) or LiBr (Acros Organics, anhydrous, 98%) were ground together using an agate mortar and pestle and placed into an alumina crucible. All reagents were used as purchased without further purification or drying, unless otherwise stated. The sample preparation took place either on a benchtop using reagents stored in the open air or inside an Ar-filled glovebox using reagents stored under an inert atmosphere. For clarity, the specific method used in each case has been specified in the relevant figure captions. The alumina crucible was placed inside a borosilicate or quartz glass tube, connected to a conventional Schlenk line apparatus and evacuated to 10^{-3} mbar for 1 hr. The reagents were then heated under vacuum between 330 – 360 °C for as little as 30 mins and up to 4 days before removing the tube from the furnace and allowing it to cool to room temperature. The precise time and temperature of the heating varied depending on the specific reaction taking place. An extensive range of temperatures and times were analysed. Again, specific details are given in the relevant figure captions. Once cooled, the glass tube was taken inside an Ar-filled glovebox, where the

sample was recovered. In some cases, reagents were mechanically milled prior to heating using a Retsch planetary PM100 ball mill. Details regarding the specific milling times and speeds used are given in the relevant figure captions.

3.2.3 Muffle Furnace Method

Samples of Li_3OCl and Li_3OBr were also prepared using a muffle furnace located inside an Ar-filled glovebox. Stoichiometric amounts of LiCl (Alfa Aesar, ultra dry, 99.9%) or LiBr (Alfa Aesar, anhydrous, 99.99%) and Li_2O (Alfa Aesar, 99.5%) were weighed out inside the glovebox and ground together using an agate mortar and pestle. The reagent mixtures were placed into either an alumina or zirconia crucible, and heated between 300 – 500 °C for 1 – 4 days using a KLS-1100X muffle furnace inside an Ar-filled glovebox. In all cases, samples were slow cooled to room temperature before being removed from the furnace. In some cases, reagents were mechanically milled prior to heating using a Retsch planetary PM100 ball mill. The reagents were added to the milling jar inside an Ar-filled glovebox and the jar was subsequently sealed shut, enabling the reagent mixture to remain under air-sensitive conditions. Specific details regarding heating times, temperature, as well as milling times and speeds are given in the relevant figure captions.

3.2.4 X-ray Diffraction

All samples were prepared for XRD studies inside the inert atmosphere of an Ar-filled glovebox. Samples were ground using an agate mortar and pestle and packed into 0.7 mm special glass capillaries. All XRD patterns were recorded on a Bruker d8 diffractometer using Mo radiation (λ = 0.71073 Å). All scans were acquired for 2θ = 5 – 35°, with a step size of 0.01° and a step time of 2 seconds. During all scans, the capillary was continually rotated at 60 revolutions per minute (rpm) to reduce the effects of preferred orientation. Rietveld analysis was performed using the General Structure Analysis System Version 2 (GSAS-II) software.[150] Parameters including the background, unit cell size, isotropic thermal coefficients, phase fractions and peak profile coefficients were refined.

3.2.5 Solid-State NMR

All solid-state NMR spectra were acquired using a Bruker 500 Avance III HD spectrometer, equipped with a wide-bore 11.7 T Oxford magnet, using Larmor frequencies of 499.69 MHz for ^{1}H (I = 1/2) and 194.20 MHz for ^{7}Li (I = 3/2). Powdered samples were packed into conventional 4.0 mm ZrO_2 rotors under an Ar atmosphere and placed into a Bruker 4.0 mm HX probe. A MAS rate of 10 kHz was employed. ^{1}H chemical shifts were referenced to neat tetramethylsilane, by setting the resonance from a sample of adamantane to δ_{iso} = 1.9 ppm. ^{7}Li chemical shifts were referenced to 1 M $LiCl_{(aq)}$.

To check for hydration effects, ^{1}H MAS NMR spectra were acquired for Li_3OBr using a background suppression experiment (DEPTH)[197] with typical $\pi/2$ and π pulse lengths of 4 and 8 μs, respectively. An optimised recycle interval of 1650 s was used and 16 transients were acquired. ^{7}Li MAS NMR spectra were obtained using single pulse experiments with a pulse duration of 1.5 μs. For Li_3OCl and Li_3OBr, optimised recycle intervals of 700 and 200 s were used to acquire 4 and 16 transients, respectively. ^{1}H decoupling was applied during the acquisition of ^{7}Li MAS NMR spectra using SPINAL-64[198] and the pulse duration was 7.8 μs. RF fields of 80 and 65 kHz were employed for ^{1}H and ^{7}Li, respectively. Unless otherwise stated all measurements were conducted at ambient temperatures. Selected NMR spectra were fitted using the Solids Line Shape Analysis (SOLA) tool in Topspin 4.0.

3.3 Results and Discussion

3.3.1 Li_3OCl

3.3.1.1 Schlenk Line Method

The LiRAP samples discussed in this study have been synthesised via the molten synthesis method reported by Zhao and Daemen,[124] which involved heating stoichiometric amounts of LiCl and LiOH as follows,

$$LiCl + 2LiOH \longrightarrow Li_3OCl + H_2O\,. \tag{3.1}$$

The method involves heating the reagent mixture above the melting point of

the desired phase, in this case Li_3OCl, which is then crystallised from the melt. The melting point of Li_3OCl is reported to be 282 °C.[124] To ensure that the sample remains moisture free, the synthesis was completed under vacuum, with the water produced being continually removed using a condensation trap. Thereby helping to drive the reaction forward.

Initial efforts to synthesise Li_3OCl focused on using a conventional Schlenk line apparatus with various reaction conditions attempted, as detailed in Table 3.1. Initial investigations used the "procedure" outlined by Zhao and Daemen.[124] However, it is noted that this was extremely vague and lacking in experimental detail. More specifically, the method reported did not state the precise temperature and/or time required for the synthesis. Hence, to find the optimal synthetic conditions, several preliminary experiments were completed that varied the reaction temperature and/or time. Initially, the temperature was held constant at 360 °C and the reaction time was varied between 1 and 4 days to determine the effect of reaction time and establish whether short or long reaction times favoured the synthesis of Li_3OCl. In accordance with the method stated by Zhao and Daemen,[124] the reagent mixture was prepared on a benchtop in the open air, *i.e.*, the reagents were not added under

Table 3.1: Details of the specific reaction conditions used for the synthesis of Li_3OCl via the Schlenk line method.

Reagents and Location	Temperature (°C)	Time
LiCl + LiOH (Benchtop)	360	1, 2, 3 and 4 days
LiCl + LiOH (Benchtop)	330	24 hrs
LiCl + LiOH (Benchtop)†	400	15 mins
LiCl + LiOH (Benchtop)‡	360	24 hrs
LiCl + LiOH (Glovebox)	350	30 mins and 24 hrs
LiCl + Li_2O (Glovebox)	350	24 hrs

† The reagent mixture was dried at 150 °C for 48 hrs prior to heating at 400 °C.

‡ The reagent mixture was mechanically milled at 300 rpm for 1 hr and pressed into a pellet prior to heating.

inert conditions. The samples synthesised were then analysed via XRD and the patterns obtained are shown in Figure 3.1(a). As stated earlier, Li_3OCl is reported to have a cubic unit cell, in space group $Pm\bar{3}m$ with a unit cell parameter of 3.91 Å.[124] An initial inspection of the XRD patterns obtained (Figure 3.1(a)) suggests the presence of a species with considerably lower symmetry, as indicated by the large number of reflections observed. Hence, the XRD data obtained suggests that the samples prepared are not phase pure. At present, no cif has been reported for Li_3OCl. Hence, in order to have a suitable structural model for comparison, a cif was generated using one available for Li_3OBr, in which the Br was substituted for Cl.[125] Since Li_3OCl and Li_3OBr are both reported to be cubic in space group $Pm\bar{3}m$ and have a similar unit cell, this is an appropriate method for obtaining a suitable structural model for Li_3OCl. The calculated diffraction pattern for Li_3OCl and the XRD patterns obtained for the dry reagents, LiCl and LiOH, are also shown for comparison in Figure 3.1(a). All diffraction patterns corresponding to the starting materials in this thesis were obtained for the dry reagents stored under an inert atmosphere. It was not possible to record a diffraction pattern for the reagents stored in open-air due to their hygroscopic nature. It is clear that the XRD patterns obtained for each of the reactions completed contain numerous reflections, in addition to those corresponding to the expected phase Li_3OCl. Thus, confirming initial suggestions that the samples are not phase pure.

Further assessment of the diffraction patterns obtained suggests that the sample heated for 1 day contains a considerable amount of Li_3OCl, in addition to LiCl. Based on the reflections observed, there does not appear to be any LiOH present in the sample. However, there are numerous additional reflections in the diffraction pattern that do not correspond to either the desired phase or the starting materials. Hence, these additional reflections most likely correspond to impurities arising from side reactions. Unfortunately, it was not possible to identify the impurity phases as the corresponding reflections could not be indexed to any known structures or the structural models available on the ICSD.[200] The XRD pattern obtained for the sample heated for 2 days is very similar to that of the sample heated for 1 day. Both diffraction patterns

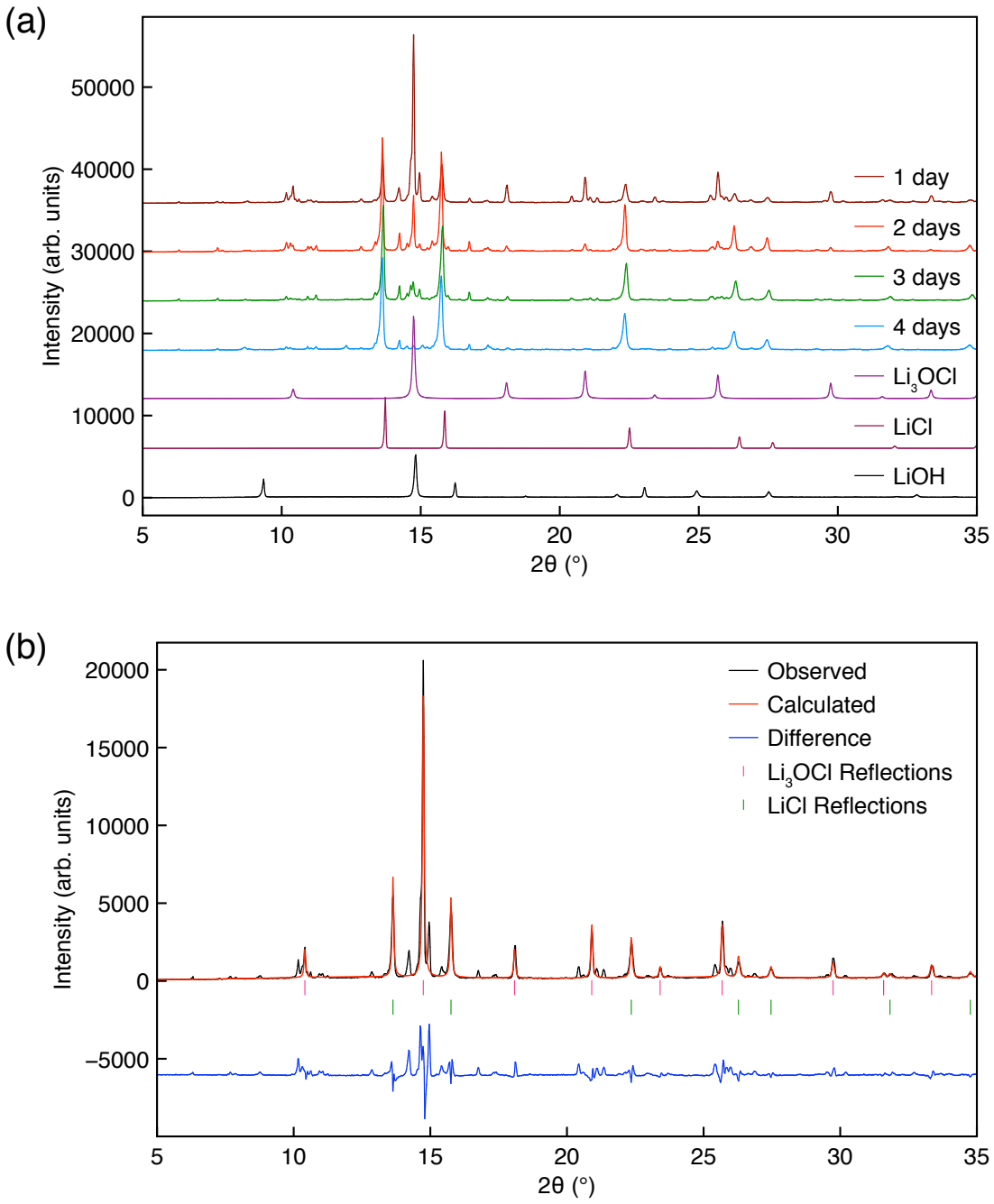

Figure 3.1: (a) X-ray diffraction patterns obtained for samples of Li_3OCl synthesised via the Schlenk line method. The reagent mixture was prepared on a benchtop and, in all cases, the reaction temperature was fixed at 360 °C, and the reaction time was varied between 1 – 4 days. A calculated diffraction pattern for Li_3OCl[125] and the XRD patterns obtained for the dry reagents, LiCl and LiOH, are also shown for comparison. (b) Multiphase Rietveld refinement for the XRD data obtained for the sample of Li_3OCl heated for 1 day, using the $Pm\bar{3}m$ (Li_3OCl)[125] and $Fm\bar{3}m$ (LiCl)[199] structural models. χ^2 = 44.97, wR_P = 31.78%, R_P = 23.65%.

contain reflections at the same 2θ positions, although their relative intensities differ. The reflections corresponding to the desired phase have a lower intensity than those of the starting reagent, LiCl, suggesting that less Li_3OCl has been produced when compared to the sample heated for 1 day. This sample also appears to contain the same impurity phases as those present in the sample heated for 1 day.

The XRD pattern obtained for the sample heated for 3 days appears to be quite different to those obtained for the samples heated for 1 and 2 days. The intensity of the reflections corresponding to LiCl is markedly higher than all other reflections, whilst the reflections corresponding to Li_3OCl are barely noticeable. This indicates that the sample contains almost solely LiCl and very little of the desired Li_3OCl phase. This sample also appears to contain the same impurity phases as those present in the samples heated for 1 and 2 days. As the reaction time is increased further to 4 days, the diffraction pattern obtained mainly consists of reflections belonging to LiCl, indicating that the sample is predominantly composed of LiCl. This sample also contains a number of unidentified impurity phases. However, the intensity of the reflections corresponding to these impurity phases is extremely low, suggesting that very small amounts have been formed.

Investigating different reaction times at a reaction temperature of 360 °C revealed that the amount of Li_3OCl produced decreases with increasing reaction time. Whereas, the opposite is true for the amount of LiCl present in the sample. At a first glance, this seems to suggest that, at longer reaction times, the reaction does not actually proceed, as significant quantities of the starting reagent remain. However, this is unlikely to be the case, as heating for 1 day appears to produce a considerable amount of Li_3OCl. Hence, it is possible that heating for longer results in additional reactions where Li_3OCl is not the final product. The XRD data presented in Figure 3.1(a) indicates that shorter reaction times, such as 1 day, favour the synthesis of Li_3OCl. As a result, the diffraction pattern obtained for the sample heated for 1 day was analysed further.

A multiphase Rietveld refinement was completed using the $Pm\bar{3}m$ and $Fm\bar{3}m$ structural models[125,199] for Li_3OCl and LiCl, respectively, and is shown in Figure 3.1(b). The corresponding refined parameters, including the isotropic thermal coefficients, are shown in Table 3.2. A χ^2 of 44.97 and wR_p of 31.78% were obtained, highlighting the poor quality of the fit. A lattice parameter of 3.9170(2) Å was obtained for Li_3OCl, which is in good agreement with the literature value of 3.91 Å.[124] A multiphase refinement includes fitting the diffraction pattern to two or more structural models. During such a refinement, phase fractions can be determined to establish the relative amounts of each phase present in the sample. In cases where all phases present in a sample are known, the precise composition of the sample can be determined. However, in this instance, only two of the phases present have been identified. Hence, the phase fraction values can only be used as an indication of the ratio between the two phases. A ratio of 87.54:12.46 is obtained for Li_3OCl to LiCl, suggesting the sample contains considerably more of the desired Li_3OCl than the starting material LiCl.

During the refinement, the thermal coefficients for both Li and Cl in LiCl were constrained to a default value of 2.5×10^{-2} Å^2 as they could not be refined to sensible values. In addition to this, the thermal coefficient obtained for Li in Li_3OCl is unusually large. Typically, such an issue occurs due to the use of inaccurate structural models, *i.e.*, inaccurate crystallographic informa-

Table 3.2: Structural parameters obtained for a sample of Li_3OCl heated for 1 day, from Rietveld refinement of the XRD data using isotropic thermal coefficients. The thermal coefficients for atoms in the LiCl phase were constrained to a default value of 2.5×10^{-2} Å^2. Li_3OCl: space group $Pm\bar{3}m$, a = 3.9170(2) Å, V = 60.100(9) Å^3, phase fraction = 87.54(33)%. LiCl: space group $Fm\bar{3}m$, a = 5.1852(4) Å, V = 139.413(33) Å^3, phase fraction = 12.46(33)%. χ^2 = 44.97, wR_P = 31.78%, R_P = 23.65%.

Atom	x	y	z	U(iso) × 100 (Å^2)
Li	0.5	0.5	0.0	15.6(13)
O	0.5	0.5	0.5	3.8(4)
Cl	0.0	0.0	0.0	3.5(3)

tion may have been reported in literature or the phase(s) present in the sample may have been misidentified. Either way, the model selected for refinement does not truly represent the phase being refined. Hence, it is possible that the structural model used for Li_3OCl in space group $Pm\bar{3}m$ is not entirely correct. Interestingly, Zhao and Daemen have suggested the $Li_3OCl_{1-x}Br_x$ system to be pseudo-cubic, meaning that while the lattice parameters correspond to a cubic unit cell, the actual symmetry of the system may be lower than initially assumed. It is also noted that the $Pm\bar{3}m$ structural model used during the refinement was adapted from a model originally reported for Li_3OBr, as Li_3OCl and Li_3OBr are believed to be isostructural. There is, in fact, no structural model for Li_3OCl in the ICSD.[200] In addition to this, Li_3OCl is reported to be a Li-ion conductor. Hence, Li may be exhibiting some ion mobility at room temperature. Thus, the thermal coefficients obtained may include some contribution from movement of the ions. Alternatively, both of the above-stated situations may be occurring at the same time, *i.e.*, if Li exhibits subtle motion and deviates from its crystallographic position, it can be said to not occupy a special position. Thus, making the structure proposed in the literature inaccurate.

Moreover, a closer inspection of the XRD patterns obtained for samples of Li_3OCl (Figure 3.1(a)) shows that the reflections corresponding to LiCl in the samples are fairly broad and exhibit a slight shift to lower 2θ values, when compared to those corresponding to the dry reagent (LiCl). The samples also contain additional impurity phases. Hence, some of the reflections corresponding to LiCl may be a product of multiple reflections that are overlapped. In turn, making it difficult to accurately refine the thermal coefficients. It is possible that constraining the thermal coefficients for the LiCl phase has an impact on the thermal coefficients obtained for atoms in the Li_3OCl phase. Thus, also contributing towards unusually large values. Unfortunately, the laboratory XRD does not offer sufficient resolution to determine the precise cause of the large thermal coefficient obtained for Li_3OCl. Furthermore, the sample investigated is not phase pure and does not contain enough of the desired phase for accurate structural determination. Hence, further investigations were not undertaken on this particular sample. Instead, our focus was to optimise the

reaction conditions in order to obtain a phase pure sample of Li_3OCl.

As stated earlier, shorter reaction times appear to be favoured for the synthesis of Li_3OCl. Hence, a reaction time of 1 day was used to evaluate the temperature range reported by Zhao and Daemen (330 – 360 °C).[124] A sample was prepared using a reaction temperature of 330 °C and a reaction time of 1 day via the Schlenk line method. Again, the reagent mixture was prepared on a benchtop. Figure 3.2 shows the XRD pattern obtained for this sample, in addition to the XRD pattern for the sample heated at 360 °C for 1 day. A calculated pattern for Li_3OCl and the XRD patterns obtained for the reagents LiCl and LiOH are also shown for comparison. The diffraction pattern obtained suggests that Li_3OCl has been successfully formed. However, the sample produced is not phase pure and appears to contain the same impurity phases as those produced in earlier samples synthesised via the Schlenk line method (Figure 3.1(a)). Unlike the sample heated at 360 °C, this sample does not contain any starting reagents. A comparison of the relative peak intensities of

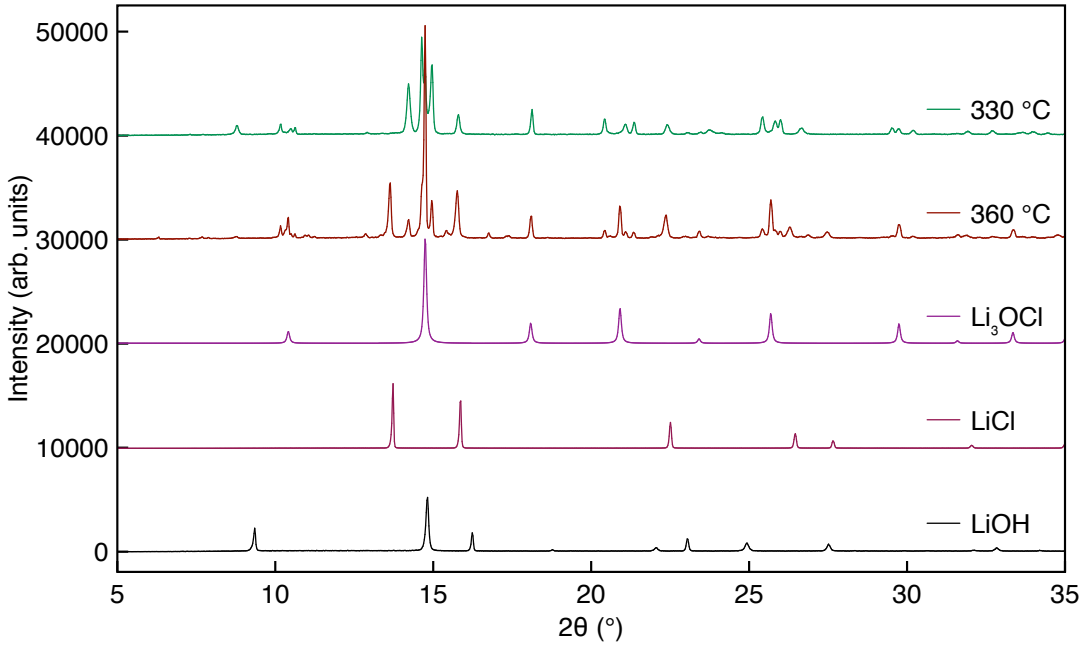

Figure 3.2: X-ray diffraction patterns obtained for samples of Li_3OCl synthesised via the Schlenk line method. The reagent mixture was prepared on a benchtop. The reaction time was fixed at 1 day and the reaction temperature was either 330 °C (green) or 360 °C (red). A calculated diffraction pattern for Li_3OCl[125] and the XRD patterns obtained for the dry reagents LiCl and LiOH are also shown for comparison.

the reflections corresponding to Li_3OCl and impurity phases for both samples suggests that the sample heated at 330 °C contains more of the impurity phase relative to Li_3OCl. Thus, suggesting that higher reaction temperatures result in an increased phase purity as more of the desired phase is formed.

Analysis of the results obtained thus far indicates that high reaction temperatures and short reaction times are preferred for the synthesis of Li_3OCl. The sample prepared using a reaction time of 1 day and a temperature of 360 °C contained the greatest amount of Li_3OCl. However, it is noted that a phase pure sample was not obtained. Hence, additional attempts were made using different synthetic methods.

Schroeder *et al.*, recently reported the synthesis of Li_3OBr, in which the reagents were dried at 150 °C for 48 hrs prior to use and then heated at 400 °C for 15 mins.[201] Since Li_3OCl is reported to be isostructural to Li_3OBr, the synthesis of Li_3OCl using this procedure was attempted via the Schlenk

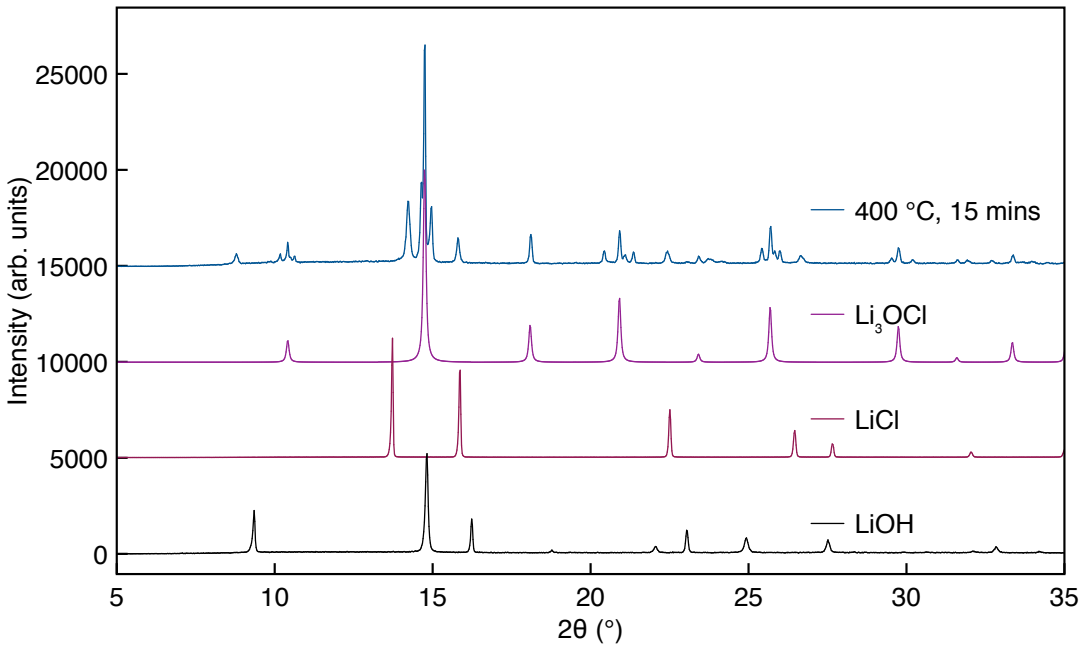

Figure 3.3: X-ray diffraction pattern obtained for a sample of Li_3OCl synthesised via the Schlenk line method. The reagent mixture was prepared on a benchtop. The reagent mixture was initially heated at 150 °C for 48 hrs and then the temperature was increased to 400 °C over 2 hrs and held at that temperature for 15 mins. The sample was slow cooled to room temperature. A calculated diffraction pattern for Li_3OCl[125] and the XRD patterns obtained for the dry reagents LiCl and LiOH are also shown for comparison.

line method. The reagent mixture was prepared on a benchtop before heating under vacuum. The XRD pattern obtained for this sample is shown in Figure 3.3. Also shown are the calculated diffraction pattern for Li_3OCl and the diffraction patterns obtained for the reagents. The sample appears to contain a considerable amount of Li_3OCl and no starting reagents. When compared to the XRD patterns obtained for the earlier samples prepared via the Schlenk line method (Figure 3.1(a) and 3.2) there are some similarities, *i.e.*, there are numerous additional reflections present, indicating that the sample is not phase pure. Closer inspection of these additional reflections suggests this sample contains the same impurity phase(s) as the earlier samples. Hence, this method and set of conditions are not conducive to preparing a phase pure sample of Li_3OCl.

Mechanical Milling and Pellet Pressing

Additional attempts to prepare a phase pure sample of Li_3OCl included using techniques popular in conventional solid-state chemistry, for example, mechanical milling and pressing the reagent mixture into a pellet. In recent years, mechanical milling (mechanochemical) methods have become increasingly popular in many areas, including metal alloys,[202,203] metal hydrides,[204,205] metal oxides[206,207] and the preparation of pharmaceuticals.[208] Mechanical milling can be quite advantageous as it can allow unusual phases and/or different polymorphic forms to be accessed that would otherwise be missed.[62] Furthermore, mechanical milling methods typically produce samples with smaller particle sizes, again enabling different phases with different crystallite sizes to be accessed. Pressing the reagents into a pellet ensures greater contact between them, thereby encouraging the reaction to proceed more easily. Additionally, both techniques can be combined in order to maximise the chances of success.

A sample of Li_3OCl was synthesised by mechanically milling the reagents for 1 hr at 300 rpm. The reagents were added to the milling jar on a benchtop. The resulting reagent mixture was then pressed into a pellet and heated at 360 °C for 24 hrs via the Schlenk line method. The XRD pattern obtained for this sample is shown in Figure 3.4(a), along with a calculated diffraction

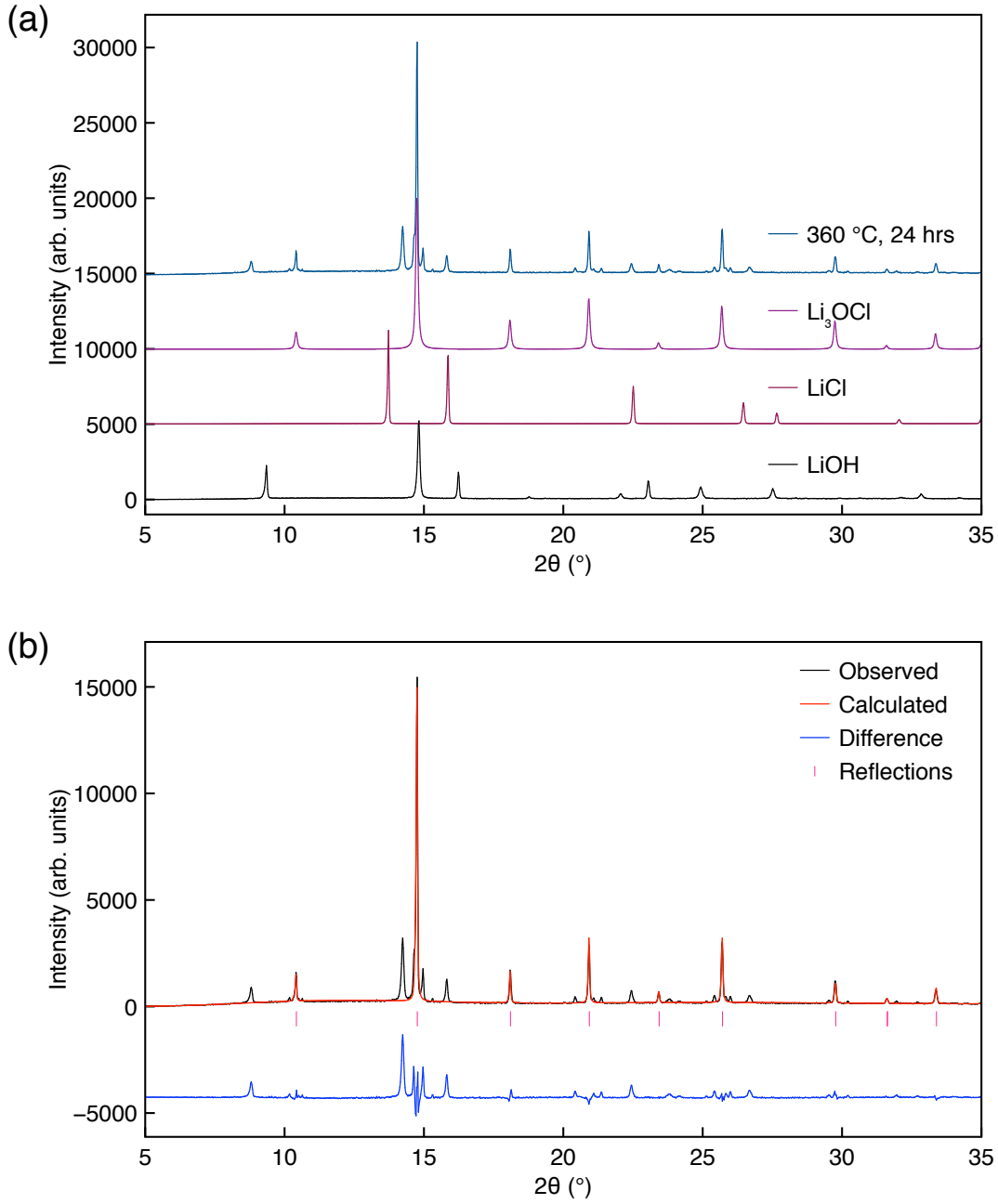

Figure 3.4: (a) X-ray diffraction pattern obtained for a sample of Li_3OCl synthesised via the Schlenk line method. The reagent mixture was prepared on a benchtop. The reagents were mechanically milled for 1 hr at 300 rpm and the resulting mixture was pressed into a pellet and heated at 360 °C for 24 hrs. A calculated diffraction pattern for Li_3OCl [125] and the XRD patterns obtained for the dry reagents LiCl and LiOH are also shown for comparison. (b) Rietveld refinement for the XRD data obtained for the Li_3OCl sample prepared using mechanical milling and pellet pressing methods, using the $Pm\bar{3}m$ structural model. [125] χ^2 = 19.85, wR_P = 28.97%, R_P = 19.25%.

pattern for Li_3OCl and the diffraction patterns obtained for the starting materials, LiCl and LiOH. When compared to the theoretical diffraction pattern for Li_3OCl and the XRD patterns of the reagents, it is clear that there is a considerable amount of Li_3OCl present, and the sample does not contain any of the starting materials. However, the presence of numerous additional reflections indicates that the sample is not phase pure, and the same impurity phases as those present in the earlier samples have also been formed here.

A Rietveld refinement was completed for the XRD pattern obtained using the $Pm\bar{3}m$ structural model for Li_3OCl.[125] The results are shown in Figure 3.4(b), and the corresponding structural parameters, including the isotropic thermal parameters, are shown in Table 3.3. A lattice parameter of 3.9124(1) Å is obtained which agrees with the literature value[124] and the value obtained from refinement of the diffraction pattern for the sample of Li_3OCl heated at 360 °C for 1 day (Figure 3.1(b)). The sample appears to contain a substantial amount of Li_3OCl, suggesting that the use of techniques such as mechanical milling and pellet pressing aids the synthesis of Li_3OCl. However, it is noted that, in a similar manner to the refinement presented earlier in Figure 3.1, the thermal coefficient corresponding to Li in Li_3OCl is unusually large. As stated previously, this is most likely caused by Li-ion mobility in the sample and/or inaccuracies in the structural model used.

Thus far, several reaction conditions have been tested. These include heating for 1 to 4 days at 360 °C, heating for 1 day at 330 °C, drying the reagent

Table 3.3: Structural parameters for a sample of Li_3OCl, prepared using mechanical milling and pellet pressing methods, obtained from Rietveld refinement of the XRD data using isotropic thermal coefficients. Li_3OCl: space group $Pm\bar{3}m$, a = 3.9124(1) Å, V = 59.885(5) Å^3. χ^2 = 19.85, wR_P = 28.97%, R_P = 19.25%.

Atom	x	y	z	U(iso) × 100 (Å^2)
Li	0.5	0.5	0.0	14.7(10)
O	0.5	0.5	0.5	3.3(3)
Cl	0.0	0.0	0.0	3.6(2)

mixture at 150 °C for 48 hrs prior to heating at 400 °C for 15 mins and pressing the mechanically milled reagent mixture into a pellet and heating for 1 day at 360 °C. It appears that, despite changing many of the reaction variables, a phase pure sample of Li_3OCl could not be produced. For all of the samples discussed so far, the reagent mixtures were prepared on a benchtop using the reagents stored in the open air. This was in accordance with the procedures reported in the literature.[124,201] However, the reagents used are known to be extremely hygroscopic. Therefore, they will likely have absorbed some water during sample preparation, meaning that the stoichiometry of the reagents may not have been as intended. This is not ideal for producing a phase pure sample. Hence, additional synthesis attempts were made where the reagents were mixed inside an Ar-filled glovebox using dry reagents that had been stored under an inert atmosphere.

Dry Reagents

Samples of Li_3OCl were synthesised via the Schlenk line method where the reagent mixture was prepared under the inert atmosphere of an Ar-filled glovebox, using dry reagents that had not been exposed to moisture. The samples were heated at 350 °C for 30 mins and 24 hrs, and the XRD patterns obtained are shown in Figure 3.5. A calculated diffraction pattern for Li_3OCl and the XRD patterns obtained for the dry reagents, LiCl and LiOH, are also shown for comparison. In both cases, it appears that the desired phase has been produced, with no starting reagents present. However, the samples are not phase pure and appear to contain the same impurity phases as the earlier samples (Figures 3.1(a), 3.2, 3.3 and 3.4(a)). This is interesting as it suggests that using dry reagents alone is not sufficient to form a phase pure sample of Li_3OCl. A comparison of the relative peak intensities for Li_3OCl and the impurity phases in both samples suggests that the sample heated for 24 hrs contains more of the desired Li_3OCl than the sample heated for 30 mins. This is similar to earlier observations, where a reaction time of 1 day resulted in samples containing large quantities of the desired phase. Thus, indicating that too short a reaction time is not ideal for the synthesis of Li_3OCl and instead, a reaction time of 1

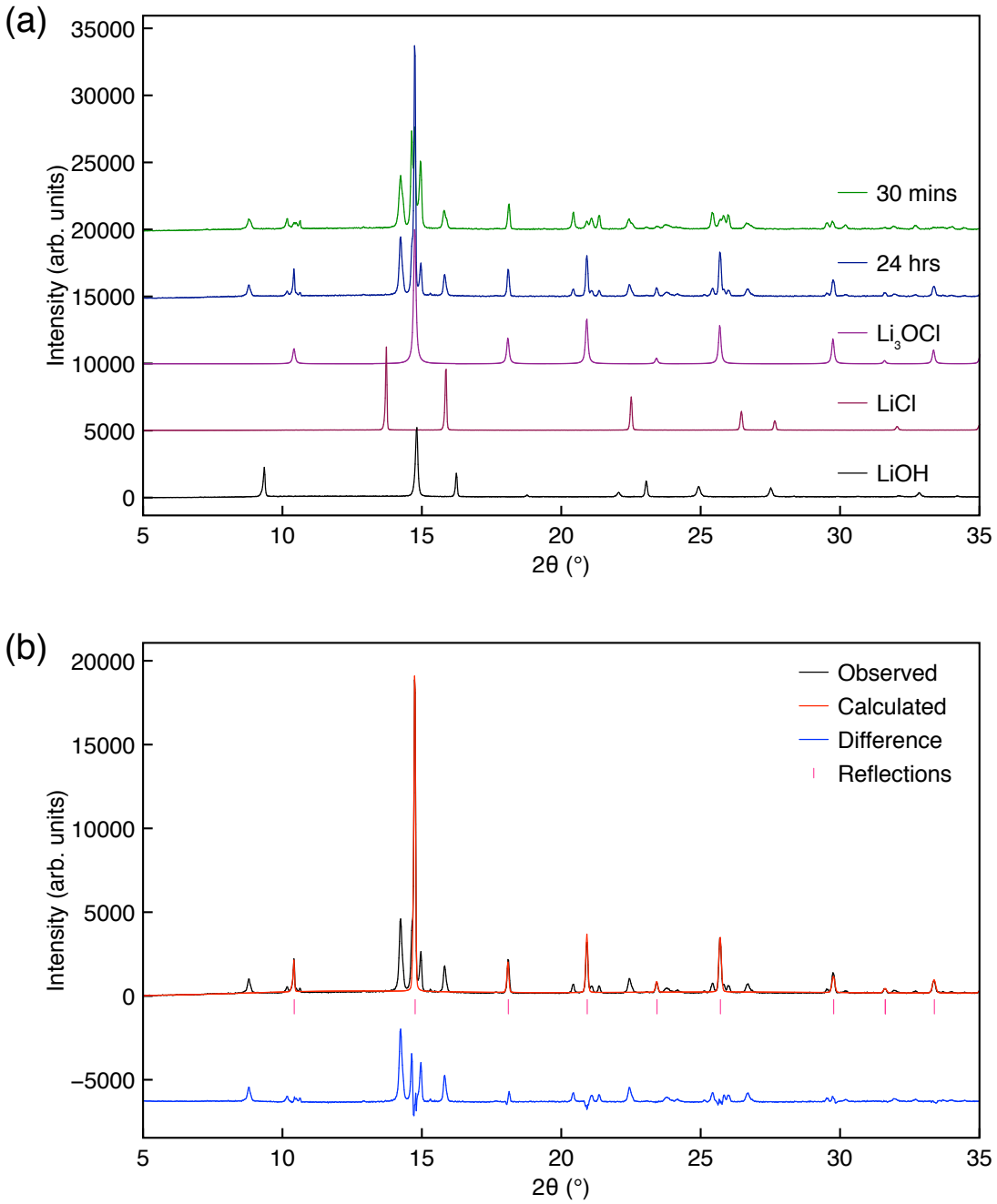

Figure 3.5: (a) X-ray diffraction patterns obtained for samples of Li_3OCl synthesised via the Schlenk line method. The reagent mixture was prepared inside an Ar-filled glovebox using dry reagents. The reaction temperature was fixed at 350 °C and the reaction time was varied between 30 mins and 24 hrs. A calculated diffraction pattern for Li_3OCl[125] and the XRD patterns obtained for the dry reagents LiCl and LiOH are also shown for comparison. (b) Rietveld refinement for the XRD data obtained for the Li_3OCl sample heated at 350 °C for 24 hrs, using the $Pm\bar{3}m$ structural model.[125] χ^2 = 40.14, wR_P = 35.51%, R_P = 24.09%.

Table 3.4: Structural parameters for a sample of Li_3OCl, prepared using dry reagents, obtained from Rietveld refinement of the XRD data using isotropic thermal coefficients. Li_3OCl: space group $Pm\bar{3}m$, a = 3.9127(2) Å, V = 59.902(7) Å^3. χ^2 = 40.14, wR_P = 35.51%, R_P = 24.09%.

Atom	x	y	z	U(iso) × 100 (Å^2)
Li	0.5	0.5	0.0	15.1(12)
O	0.5	0.5	0.5	3.1(3)
Cl	0.0	0.0	0.0	3.2(2)

day appears to best suited.

A Rietveld refinement was completed using the XRD data obtained for the Li_3OCl sample heated at 350 °C for 24 hrs and the $Pm\bar{3}m$ structural model for Li_3OCl.[125] The results are shown in Figure 3.5(b), and the structural parameters obtained, including the isotropic thermal parameters, are shown in Table 3.4. A χ^2 = 40.14 and wR_P = 35.51% suggest a moderately good fit. This is to be expected for a sample containing a significant quantity of impurity phases. It is noted that, similar to earlier refinements, the thermal coefficient calculated for Li in Li_3OCl is quite large (*vide supra*). A lattice parameter of 3.9127(2) Å is obtained, which is in good agreement with the literature value[124] and the values obtained from earlier refinements (Figures 3.1 and 3.4).

Li_2O as a Precursor

Finally, a different combination of reagents was tested. The samples discussed so far have all been synthesised using stoichiometric amounts of LiCl and LiOH to form Li_3OCl and H_2O. However, it is also possible to synthesise Li_3OCl using LiCl and Li_2O as precursors, as follows,

$$LiCl + Li_2O \longrightarrow Li_3OCl\,. \tag{3.2}$$

Hence, a sample of Li_3OCl was prepared via the Schlenk line method using these reagents. The reagent mixture was prepared inside an Ar-filled glovebox using reagents stored under an inert atmosphere. The sample was heated at 350 °C for 24 hrs and the XRD pattern obtained for this sample is shown in

Figure 3.6(a), along with the diffraction pattern for a sample of Li_3OCl synthesised under identical reaction conditions using LiCl and LiOH. A calculated diffraction pattern for Li_3OCl and the XRD patterns obtained for the dry reagents are also shown for comparison. Once again, a phase pure sample is not produced. However, unlike the earlier samples there are no unidentified impurities present. The sample appears to contain solely Li_3OCl and the reagents LiCl and Li_2O. The presence of the starting materials suggests that the reaction did not reach completion. It is noted that Zhao and Daemen also attempted the synthesis of Li_3OCl using LiCl and Li_2O via high-pressure and high-temperature methods.[124] They reported that very little of the desired phase was formed (*vide supra*). Hence, they did not pursue this method any further.

A multiphase Rietveld refinement was completed using the XRD data for the Li_3OCl sample synthesised using LiCl and Li_2O, and the $Pm\bar{3}m$ (Li_3OCl)[125] and $Fm\bar{3}m$ (LiCl and Li_2O)[199,209] structural models. The results are shown in Figure 3.6(b). The corresponding structural parameters, including isotropic thermal coefficients, are detailed in Table 3.5. A χ^2 = 5.80 and a wR_p = 14.20% is obtained, suggesting a good fit is achieved. Upon closer inspection of the refinement, it appears that the fit may not be as good as initially thought. In particular, the calculated intensities for Li_2O are lower than those experimentally observed. Here too, the thermal coefficient corresponding to Li in Li_3OCl is quite large. This is similar to what was observed in previous refinements (Figures 3.1(b), 3.4(b) and 3.5(b)). All phases present in this sample have been identified, making it possible to determine the corresponding phase fractions and therefore establish the precise sample composition. The sample contains 48.86(35)% Li_3OCl, 23.17(21)% LiCl and 27.97(35)% Li_2O. Interestingly, the ratio of LiCl and Li_2O present in the sample is not 1:1 as expected. There appears to be a slight excess of Li_2O. However, this is most likely due to a slight mismatch between the observed and calculated intensities of the reflections corresponding to Li_2O. The phase fractions obtained indicate the reaction is far from reaching completion. Overall, these findings suggest that the combination of LiCl and Li_2O is not ideal for producing a phase pure sample of Li_3OCl via the

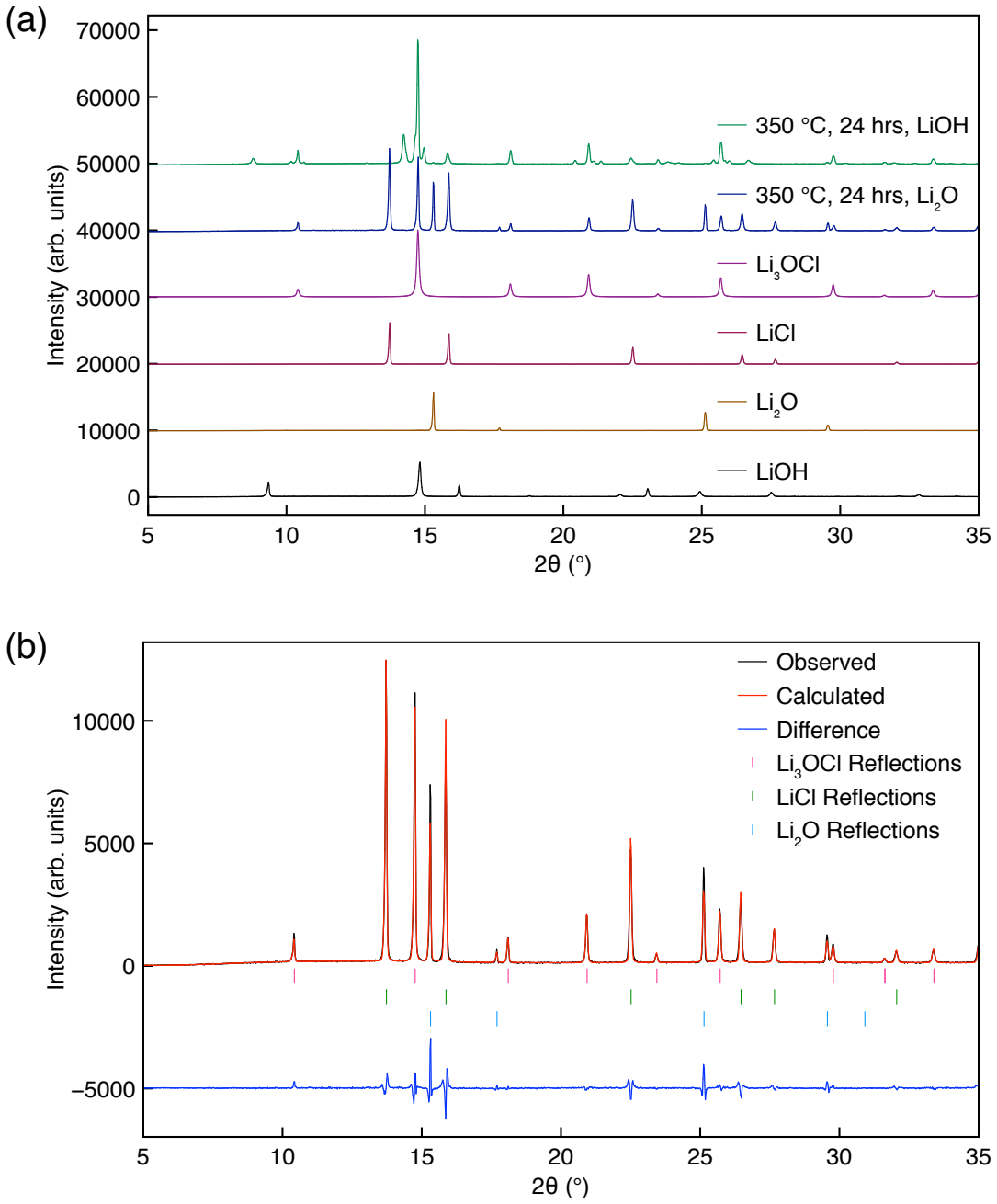

Figure 3.6: (a) X-ray diffraction patterns obtained for samples of Li_3OCl synthesised via the Schlenk line method. The samples were prepared using different starting reagents (LiCl and LiOH shown in green and LiCl and Li_2O shown in blue). In both cases, the reagent mixture was prepared inside an Ar-filled glovebox, the reaction temperature was fixed at 350 °C and the reaction time was fixed at 24 hrs. A calculated diffraction pattern for Li_3OCl[125] and the XRD patterns obtained for the reagents, LiCl, Li_2O and LiOH, are also shown for comparison. (b) A multiphase Rietveld refinement for the XRD data obtained for the Li_3OCl sample prepared using LiCl and Li_2O, and the $Pm\bar{3}m$ (Li_3OCl)[125] and $Fm\bar{3}m$ (LiCl and Li_2O)[199,209] structural models. χ^2 = 5.80, wR_P = 14.20%, R_P = 10.39%.

Table 3.5: Structural parameters for a sample of Li_3OCl, prepared using LiCl and Li_2O via the Schlenk line method, obtained from Rietveld refinement of the XRD data using isotropic thermal coefficients. Li_3OCl: space group $Pm\bar{3}m$, a = 3.9113(1) Å, V = 59.837(4) Å^3, phase fraction = 48.86(35)%, LiCl: space group $Fm\bar{3}m$, a = 5.1480(1) Å, V = 136.434(6) Å^3, phase fraction = 23.17(21)%. Li_2O: space group $Fm\bar{3}m$, a = 4.6188(1) Å, V = 98.536(9) Å^3, phase fraction = 27.97(35)%. χ^2 = 5.80, wR_P = 14.20%, R_P = 10.39%.

Atom	x	y	z	U(iso) × 100 (Å^2)
Li_3OCl				
Li	0.5	0.5	0.0	14.8(7)
O	0.5	0.5	0.5	2.5(2)
Cl	0.0	0.0	0.0	2.6(1)
LiCl				
Li	0.0	0.0	0.0	3.8(3)
Cl	0.5	0.5	0.5	2.1(1)
Li_2O				
Li	0.25	0.25	0.25	0.6(2)
O	0	0	0	0.2(1)

Schlenk line method.

Summary

Several different reaction conditions were tested for the synthesis of Li_3OCl using the Schlenk line method. The method reported by Zhao and Daemen was initially used to determine the optimal reaction temperature and time.[124] This method was found to favour high reaction temperatures and short reaction times and the sample heated at 360 °C for 1 day appeared to contain the greatest quantity of Li_3OCl. However, the sample was not phase pure, as it contained both the starting reagent LiCl and unidentified impurity phases. Additional attempts included using the method reported by Schroeder *et al.*,[201] which produced similar results to those obtained using the method reported by Zhao and Daemen.[124] The sample contained a considerable amount of Li_3OCl and no starting reagents. However, the sample was not phase pure as it contained the same impurity phases as those synthesised via the method

reported by Zhao and Daemen.[124]

Attempts to increase the phase purity of samples included using techniques such as mechanical milling and pellet pressing. Some very promising results were obtained by combining these techniques with the Schlenk line method. The sample produced using these methods contained greater amounts of Li_3OCl than any of the other samples synthesised via the Schlenk line method. However, again, the sample was not phase pure and appeared to contain the same impurity phases as the earlier samples. Samples of Li_3OCl were also synthesised where the reagent mixtures were prepared under the inert atmosphere of an Ar-filled glovebox using dry reagents, instead of on a benchtop in the open air. Whilst Li_3OCl was produced successfully, the same impurity phases as earlier were also observed here. Thus, suggesting that using dry reagents alone is not sufficient to produce a phase pure sample.

Finally, the synthesis of Li_3OCl was attempted using LiCl and Li_2O as precursors. Li_3OCl was synthesised successfully using this combination of reagents. However, the sample produced was not phase pure as it contained considerable quantities of the starting reagents, indicating that the reaction did not reach completion. This is in stark contrast to the sample prepared using LiCl and LiOH under the same reaction conditions, which did not contain any of the starting materials. Thus, suggesting that the combination of LiCl and Li_2O is not ideal for the synthesis of Li_3OCl via the Schlenk line method.

Several XRD patterns corresponding to the samples containing a considerable amount of Li_3OCl were analysed via Rietveld refinements. In all cases, a reasonable fit was achieved, and similar values were obtained for the lattice parameter corresponding to the desired phase. It was noted that the thermal coefficients obtained for Li in Li_3OCl during all refinements were unusually large. Thus, suggesting the structural model used to complete the refinement may not be quite correct. In the current study, the cubic structural model in space group $Pm\bar{3}m$ has been used to characterise Li_3OCl. It is noted that the model used is adapted from the one originally proposed for Li_3OBr, as Li_3OCl is believed to be isostructural to Li_3OBr. Moreover, Li_3OCl is sug-

gested to be pseudo-cubic by Zhao and Daemen,[124] meaning that the actual symmetry of the structure may be lower than initially assumed. Alternatively, the large thermal coefficients may be a consequence of Li-ion mobility. As discussed previously in Chapter 1, Li_3OCl is a known Li-ion conductor. Hence, Li may be exhibiting subtle movement that is being interpreted as thermal motion during Rietveld analysis. Thus, resulting in rather large thermal parameters. Moreover, if Li exhibits subtle motion and deviates from its crystallographic position, it can be said to not occupy a special position. In turn, making the proposed structure in the literature inaccurate. In order to determine the precise cause of these large thermal parameters, high-resolution diffraction data would be required. Unfortunately, laboratory XRD data does not offer sufficient resolution for such detailed investigations. Hence, the exact cause of these high thermal coefficients currently remains unknown. This avenue was not investigated any further, as our efforts focused on optimising the reaction conditions to synthesise a phase pure sample of Li_3OCl.

All of the Li_3OCl samples prepared using LiCl and LiOH appear to contain the same impurity phases, as evidenced by the XRD data shown. At present, these phases have not been identified. As discussed in Chapter 1, Emly *et al.*, have reported that additional phases may be formed when trying to synthesise Li_3OCl.[59] These include Li_5O_2Cl and $Li_{17}O_6Cl_5$ (Figure 1.16). However, the specific structural and crystallographic details for these phases, *i.e.*, the lattice parameters, atomic positions or space groups have not yet been reported as they were only identified as possible structures via a computational study. Hence, it was not possible to confirm the presence of these phases in the Li_3OCl samples discussed. As stated earlier, the synthesis of Li_3OCl has also been reported by Reckeweg and co-workers using LiCl and Li_2O as precursors.[126] They reported the presence of $LiCl{\cdot}H_2O$ as an impurity phase. However, the samples produced during the current study, using LiCl, LiOH and/or Li_2O as precursors, do not contain any $LiCl{\cdot}H_2O$. Recently, Hanghofer and co-workers reported the synthesis of barium-doped Li_3OCl and the hydrated analogue of Li_3OCl, Li_2OHCl.[210] The Ba-doped Li_3OCl sample synthesised was found to contain LiCl and $Li_4(OH)_3Cl$ as impurities. However, the

diffraction patterns shown here do not indicate the presence of $Li_4(OH)_3Cl$. Hence, it appears there are considerable differences between each synthetic study.

Li_3OCl is known to be extremely hygroscopic and is reported to have a favourable hydration enthalpy (-71.40 kJ mol^{-1}), indicating that proton uptake in Li_3OCl is readily feasible.[211] Also, as discussed earlier, it is difficult to break strong OH bonds, as a large amount of energy is required to do so, making it particularly challenging to form Li_3OCl. Therefore, it is entirely feasible that several hydrated LiRAP species may be formed when synthesising Li_3OCl using LiCl and LiOH as precursors. Hanghofer and co-workers have suggested that the hydrated compositions could include, $Li_5(OH)_3Cl_2$, $Li_5(OH)_2Cl_3$, $Li_3(OH)_2Cl$ and $Li_3(OH)Cl_2$.[210] However, again, no structural information was provided for any of these compositions, making it challenging to identify their presence in the samples discussed. Furthermore, the samples discussed thus far were synthesised under vacuum using a standard laboratory vacuum pump which enables the pressure to reach only $\times 10^{-3}$ mbar. This vacuum may be insufficient in removing all of the water produced during the reaction. Hence, the presence of water could be influencing the reaction pathways and therefore producing unwanted phases. Zhao and Daemen reported the use of a 'high vacuum pump', although specific details regarding the pressure used were not stated.[124] Unfortunately, during the course of this study, it was not possible to evaluate the effects of lower pressures on the reaction conditions tested due to limitations in the equipment available within our laboratory. However, this is certainly an area that warrants further investigation.

3.3.1.2 Muffle Furnace Method

The synthesis of Li_3OCl was also attempted via conventional solid-state reactions completed inside an Ar-filled glovebox. Here, the mixing of reagents and the reaction itself were carried out under an inert atmosphere, ensuring that the samples remained moisture free throughout the whole process. For these reactions, it was necessary to use LiCl and Li_2O as precursors, instead of LiCl and LiOH, as there is no mechanism inside a glovebox to re-

move the water produced during synthesis. The starting materials used were stored under an inert atmosphere, meaning the reagents were truly dry and, therefore, the corresponding stoichiometries were as intended. The various reaction conditions attempted are detailed in Table 3.6. Initially, the reaction time was fixed at 1 day, whilst the reaction temperature was varied between 300 and 500 °C. The XRD patterns obtained for each of the samples prepared are shown in Figure 3.7. A calculated diffraction pattern for Li_3OCl and the XRD patterns obtained for the reagents, LiCl and Li_2O, are also shown for comparison.

From initial inspections, it is apparent that the XRD patterns are considerably "cleaner" than those obtained for samples of Li_3OCl synthesised using the Schlenk line method, *i.e.*, they contain considerably fewer reflections, which is in line with what would be expected for a high symmetry phase. Initially, a reaction temperature of 350 °C was used as this was similar to that used for the Schlenk line synthesis and that reported by Zhao and Daemen.[124] Thus, allowing for a direct comparison with the sample produced using the same reagents via the Schlenk line method. The XRD pattern obtained for the sample heated at 350 °C seems to exhibit the presence of Li_3OCl. However, it is also clear that the sample produced is not phase pure, as evidenced by the presence of several additional peaks.

These additional reflections appear to correspond to the starting rea-

Table 3.6: Details of the specific reaction conditions used for the synthesis of Li_3OCl using LiCl and Li_2O via the muffle furnace method.

Reagents and Location	Temperature (°C)	Time (days)
LiCl + Li_2O (Glovebox)	300, 350, 450 and 500	1
LiCl + Li_2O (Glovebox)	350	4
LiCl + Li_2O (Glovebox)†	350	1
LiCl + Li_2O (Glovebox)‡	350	1

† Sample was reground and reheated at 350 °C for 1 day.

‡ Reagent mixture was mechanically milled at 300 rpm for 1 hr.

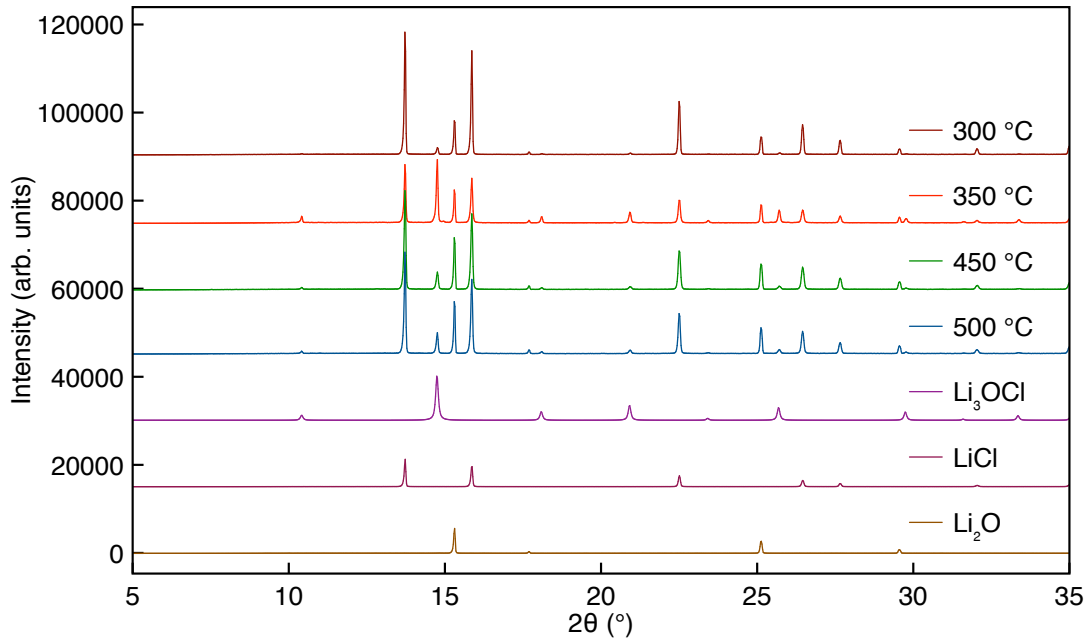

Figure 3.7: X-ray diffraction patterns obtained for samples of Li_3OCl synthesised via the muffle furnace method. In all cases, the reaction time was fixed at 24 hrs and the reaction temperature was varied between 300 – 500 °C. A calculated diffraction pattern for Li_3OCl[125] and the XRD patterns obtained for the dry reagents, LiCl and Li_2O, are also shown for comparison.

gents, LiCl and Li_2O, indicating that the reaction has not reached completion. This is similar to what was observed previously for the sample synthesised using the same precursors via the Schlenk line method. To probe the reaction further and to try and produce a phase pure sample of Li_3OCl, a range of different temperatures (300, 450 and 500 °C) were tested. The XRD patterns obtained for the samples prepared using these conditions appear to be very similar. In all cases, only a small amount of the desired phase is formed and the starting materials are still present in the sample. The data presented indicates that a change in reaction temperature, whether it is an increase or a decrease, does not improve the phase purity of the sample produced. In fact, the amount of Li_3OCl formed appears to decrease in both cases. This indicates that varying the reaction temperature is not a suitable method for increasing the phase purity of the Li_3OCl samples.

The XRD data presented in Figure 3.7 suggests that the sample heated at 350 °C for 24 hrs contains the greatest quantity of the desired phase. How-

ever, the presence of residual starting reagents suggested the reaction time could be increased. Hence, a longer reaction time of 4 days was tested at 350 °C to determine whether the reaction could be forced to completion. The XRD pattern obtained for this sample is shown in Figure 3.8 alongside that of the sample heated at 350 °C for 1 day. The calculated diffraction pattern for Li_3OCl and the XRD patterns obtained for the reagents, LiCl and Li_2O, are also shown for comparison. It is clear from the data presented that a longer reaction time does not result in any improvement. In fact, many of the peaks corresponding to Li_3OCl appear to decrease in intensity when compared to the pattern obtained for the sample heated for 1 day. Thus, suggesting that, in a similar manner to the Schlenk line method, shorter reaction times are favoured for the synthesis of Li_3OCl via the muffle furnace method.

In an attempt to increase phase purity, the Li_3OCl sample heated at 350 °C for 1 day was reground and reheated at 350 °C for an additional 24 hrs. The XRD pattern obtained for this sample after additional heating is shown in Figure 3.9(a) and is denoted as (R). Figure 3.9(a) also shows the diffraction pattern

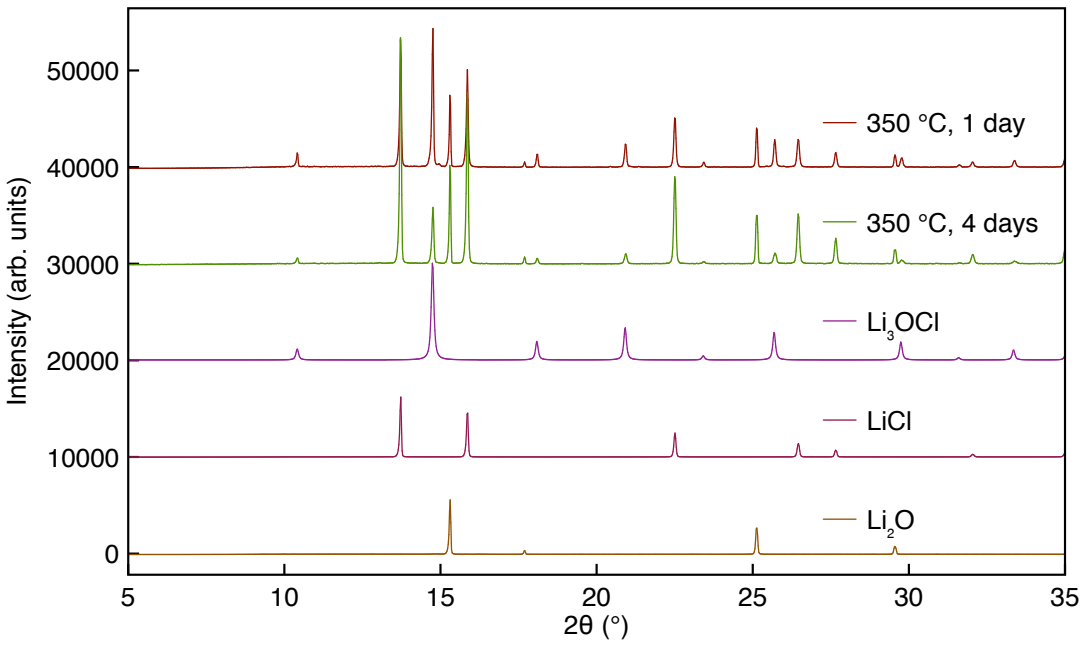

Figure 3.8: X-ray diffraction patterns obtained for samples of Li_3OCl synthesised via the muffle furnace method. The reaction temperature was fixed at 350 °C and reaction times of 1 (red) and 4 days (green) were tested. A calculated diffraction pattern for Li_3OCl [125] and the XRD patterns obtained for the dry reagents, LiCl and Li_2O, are also shown for comparison.

for the sample before the regrinding and reheating process and the calculated diffraction pattern for Li_3OCl, along with the XRD patterns obtained for the reagents, LiCl and Li_2O. As stated earlier, regrinding samples can assist reactions in reaching completion, as the act of regrinding exposes new surfaces, thereby enabling the reaction to proceed further. In doing so, it was expected that the amount of the desired phase present in the sample would increase, causing the peaks corresponding to Li_3OCl to increase in intensity. However, after this additional treatment, no significant or noticeable differences were observed between the two XRD patterns, indicating that the reaction did not proceed any further.

When the Schlenk line method was combined with mechanical milling methods, some very promising results were obtained. As a result, mechanical milling methods were also combined with the muffle furnace method. As stated earlier, mechanical milling methods are particularly useful as the reagents can be ground for much longer than by hand and smaller crystallites are obtained, enabling the reaction to proceed further, as a larger surface area is available for reaction. For the synthesis of Li_3OCl, the reagents LiCl and Li_2O were milled for 1 hr at 300 rpm, and the resulting mixture was heated at 350 °C for 1 day. The XRD pattern obtained for this sample is shown in Figure 3.9(a) and is denoted as (M). When compared to the sample prepared via heating at 350 °C for 1 day using the same muffle furnace method and the calculated pattern for Li_3OCl, it is clear that only a very small amount of Li_3OCl is produced. Again, the reaction has not gone to completion, *i.e.*, all of the additional reflections observed correspond to the starting reagents.

The Li_3OCl sample produced via heating at 350 °C for 1 day using the muffle furnace method appears to contain the greatest amount of Li_3OCl. Hence, the XRD pattern for this sample was analysed further via a multiphase Rietveld refinement using the $Pm\bar{3}m$ (Li_3OCl)[125] and $Fm\bar{3}m$ (LiCl and Li_2O)[199,209] structural models. The results are shown in Figure 3.9(b), and the structural parameters obtained, including the isotropic thermal coefficients are detailed in Table 3.7. A χ^2 = 5.12 and wR_p = 13.16% are obtained, suggesting a good fit. Inspection of the refinement also indicates a good fit, except for

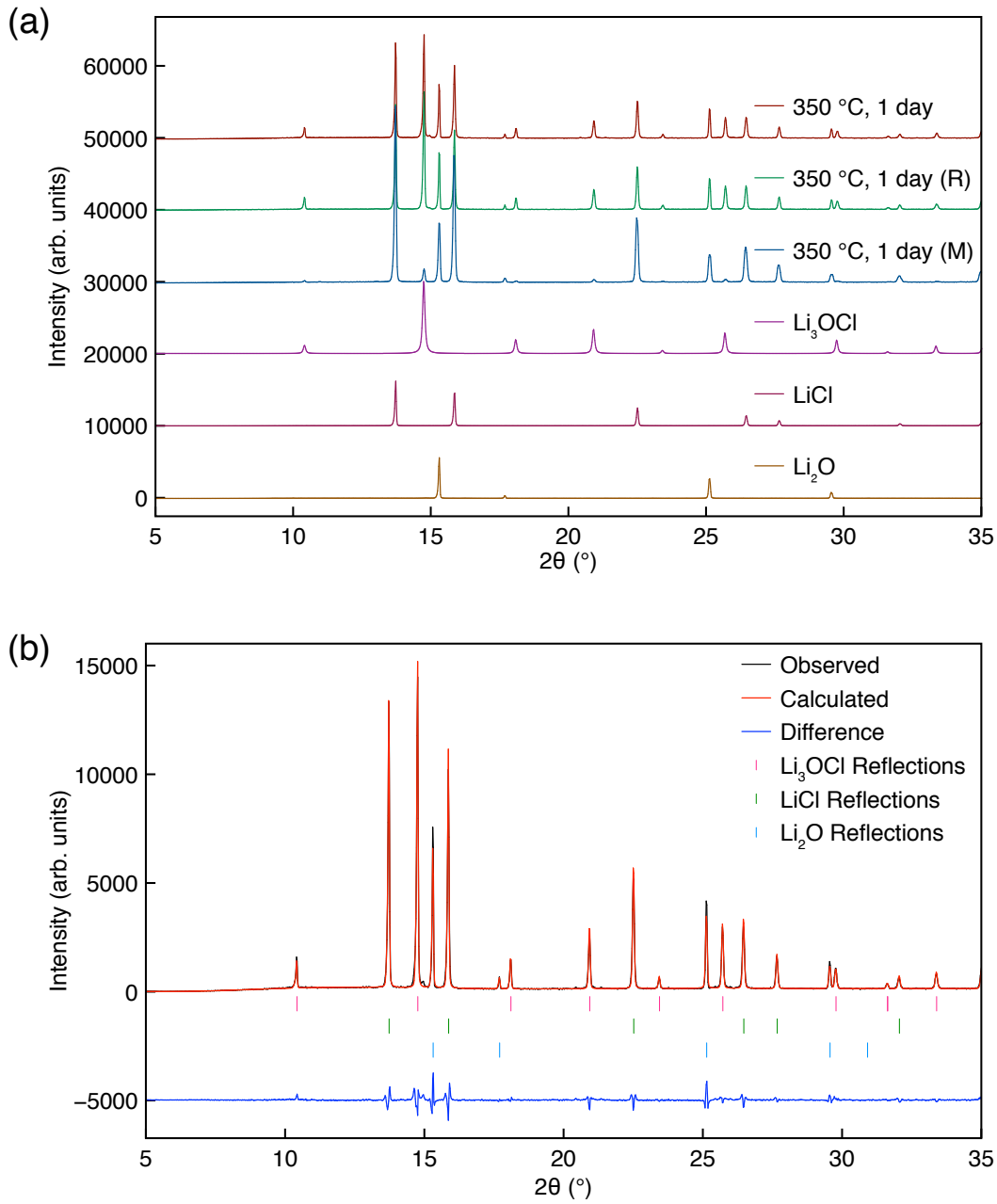

Figure 3.9: (a) X-ray diffraction patterns obtained for samples of Li_3OCl synthesised via the muffle furnace method. The reaction temperature was 350 °C and reaction time was 1 day. A sample was reground and reheated at 350 °C for an additional 24 hrs, denoted by (R), and another sample was prepared by mechanically milling the reagent mixture for 1 hr at 300 rpm prior to heating, denoted by (M). A calculated diffraction pattern for Li_3OCl[125] and the XRD patterns obtained for the dry reagents, LiCl and Li_2O, are also shown for comparison. (b) A multiphase Rietveld refinement for the XRD data obtained for the Li_3OCl sample prepared via heating at 350 °C for 1 day, using the $Pm\bar{3}m$ (Li_3OCl)[125] and $Fm\bar{3}m$ (LiCl and Li_2O)[199,209] structural models. χ^2 = 5.12, wR_P = 13.16%, R_P = 9.67%.

Table 3.7: Structural parameters for a sample of Li_3OCl, prepared via the muffle furnace method by heating at 350 °C for 1 day, obtained from Rietveld refinement of the XRD data using isotropic thermal coefficients. Li_3OCl: space group $Pm\bar{3}m$, a = 3.9112(1) Å, V = 59.833(3) Å^3, phase fraction = 53.05(31)%. LiCl: space group $Fm\bar{3}m$, a = 5.1477(1) Å, V = 136.411(5) Å^3, phase fraction = 20.66(17)%. Li_2O: space group $Fm\bar{3}m$, a = 4.6189(1) Å, V = 98.538(7) Å^3, phase fraction = 26.29(30)%. χ^2 = 5.12, wR_P = 13.16%, R_P = 9.67%.

Atom	x	y	z	U(iso) × 100 (Å^2)
Li_3OCl				
Li	0.5	0.5	0.0	14.6(5)
O	0.5	0.5	0.5	2.8(1)
Cl	0.0	0.0	0.0	2.9(1)
LiCl				
Li	0.0	0.0	0.0	3.4(3)
Cl	0.5	0.5	0.5	2.0(1)
Li_2O				
Li	0.25	0.25	0.25	1.0(2)
O	0	0	0	0.2(1)

the reflections corresponding to Li_2O, where the calculated peak intensities are lower than those observed. This is similar to earlier findings (Figure 3.6) for the refinement completed using the XRD data corresponding to the sample of Li_3OCl, synthesised via the Schlenk line method, using LiCl and Li_2O as precursors. A lattice parameter of 3.9112(1) Å is obtained for Li_3OCl, which is in good agreement with the literature value[124] and those obtained earlier for Li_3OCl. A closer inspection of the refinement shows that the XRD pattern also contains a few additional reflections (2θ = 14.97, 20.44, 21.35, 25.42 and 25.97°) that have not been indexed by any of the structural models. Thus, suggesting that, in addition to the desired phase and the starting materials, the sample contains an impurity phase. The peaks observed are extremely low in intensity, meaning that a very small amount is present. However, this does make it quite challenging to identify the additional phase.

An inspection of the structural parameters obtained indicates that, once again, the thermal coefficient of Li in Li_3OCl is unusually high (*vide supra*). As

this sample contains multiple phases, the corresponding phase fractions were also refined to determine the composition. The sample contains 53.05(31)% Li_3OCl, 20.66(17)% LiCl and 26.29(30)% Li_2O, indicating a substantial amount of the desired phase has been produced. However, the reaction has not reached completion as a considerable amount of the starting reagents are still present in the sample. It is noted that this is not the exact composition of the sample owing to the presence of an unidentified impurity phase. However, the impurity phase appears to be present in a very small quantity. Hence, the phase fractions obtained are good indicators of the actual sample composition. Overall, these findings indicate that the muffle furnace method produces slightly better results than the Schlenk line method, as the latter resulted in only 48.86(35)% of the desired phase. Interestingly, here too, the sample appears to contain slightly more Li_2O than LiCl. However, as mentioned earlier this could be due to a slight mismatch between the observed and calculated peak intensities for the reflections corresponding to Li_2O.

^{7}Li MAS NMR Spectroscopy

This sample appears to contain a considerable amount of Li_3OCl, and the composition of this sample has been determined from the XRD data. Hence, this sample was deemed to be a good candidate for further analysis via SS-NMR. After considering the composition of this sample, it was analysed via ^{7}Li MAS NMR spectroscopy, and the spectrum acquired is shown in Figure 3.10. The spectrum appears to display two distinct resonances that are overlapped; one of which is sharp and centred around -1.16 ppm. The other resonance, centred around 2.67 ppm, is relatively broad. Given the composition of this sample, at least three distinct Li sites were expected. However, as discussed previously, ^{7}Li has a very small chemical shift range.[163] Moreover, all phases present in this sample adopt a cubic structure and, therefore, are likely to all have very similar chemical shifts. Hence, an overlap of resonances is to be expected.

In order to determine the distinct number of Li sites present, the lineshape observed was simulated, and a minimum of three distinct sites were

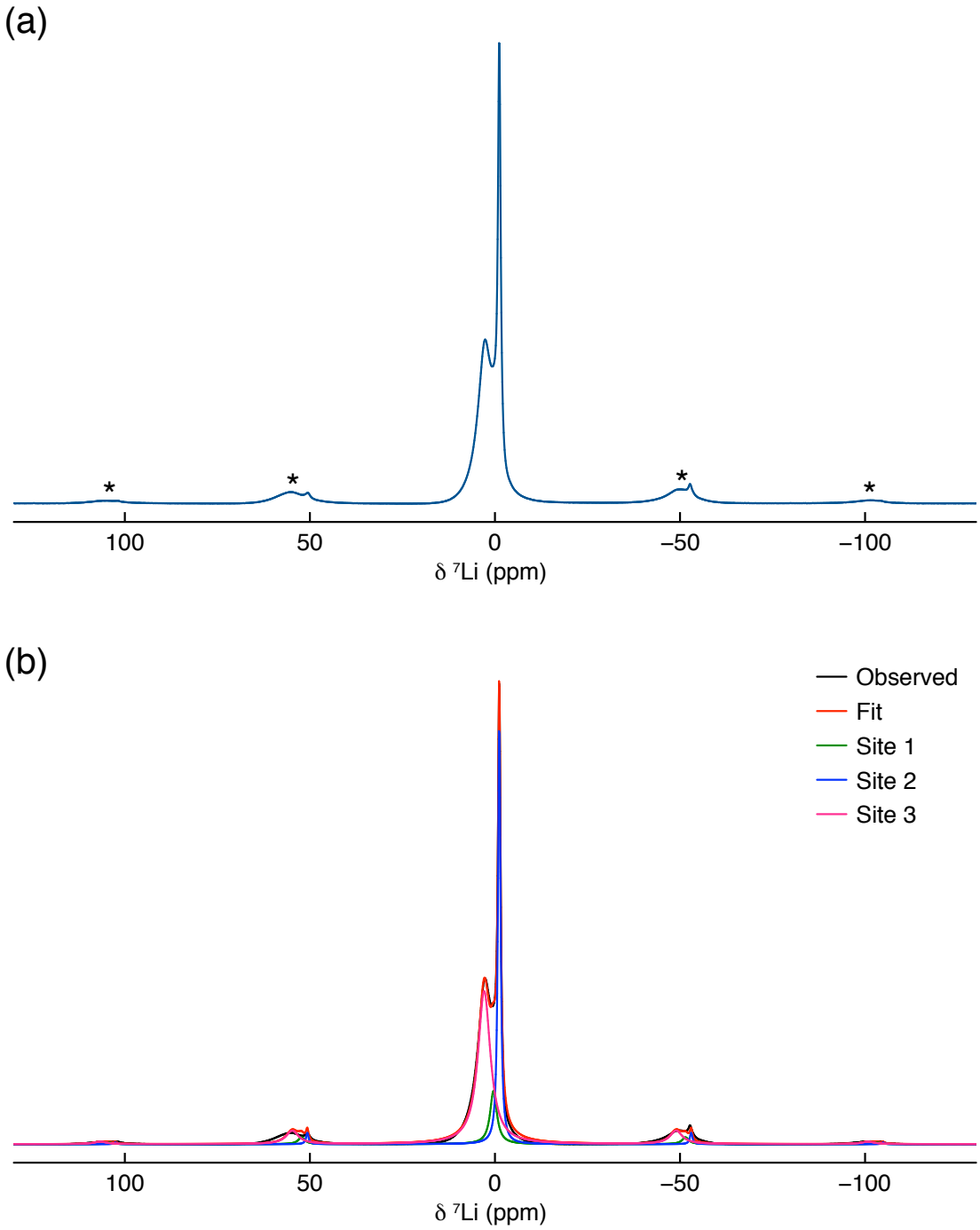

Figure 3.10: (a) ^{7}Li (11.7 T) MAS NMR spectrum acquired for a sample of Li_3OCl, prepared via the muffle furnace method by heating at 350 °C for 1 day. The MAS rate used was 10 kHz and spinning sidebands are denoted by *. A recycle delay of 700 s was used to acquire 4 transients. (b) Simulation of the spectrum using three distinct sites.

required to obtain a good fit. The simulated spectrum displaying individual Li sites is shown in Figure 3.10(b). All sites have a C_Q = ~0 MHz and an η_Q of 0. These parameters are typical of species within highly symmetrical envi-

ronments such as cubic structures.[163] The three sites have a chemical shift of 0.41(1), −1.15(1) and 2.92(3) ppm. In the literature, the reported ^{7}Li chemical shifts of LiCl and Li_2O are −1.1 and 2.8 ppm, respectively.[212] These are relatively close to the chemical shifts of sites 2 and 3. Thus, suggesting that these sites correspond to LiCl and Li_2O, respectively. Additionally, the lineshapes observed for site 2 is sharp and narrow and for site 3 is relatively broad. This is in line with the lineshapes reported in the literature for LiCl and Li_2O. The XRD data obtained for this sample (Figure 3.9(b)) also indicated the presence of Li_3OCl. Thus, suggesting that site 1 corresponds to Li_3OCl.

Summary

Multiple reaction conditions were tested for the synthesis of Li_3OCl via the muffle furnace method. LiCl and Li_2O were used as precursors and reaction temperatures ranging between 300 to 500 °C were tried using a reaction time of 1 day. A reaction temperature of 350 °C was found to be optimal, and in all cases, a modest amount of the desired phase was produced, but starting materials were still present. Further attempts to synthesise Li_3OCl included increasing the reaction time to 4 days. However, no improvement was observed, as the amount of Li_3OCl produced appeared to decrease with increasing reaction time, suggesting that shorter reaction times were favoured. The Schlenk line method produced similar results, *i.e.*, short reaction times were preferred.

Further attempts included using techniques such as regrinding and reheating, and mechanically milling the reagents prior to heating. However, regrinding and reheating the sample did not result in any significant improvement. Similarly, very little of the desired phase was produced using mechanical milling methods. This is in contrast to the Schlenk line method where mechanical milling resulted in a sample with the greatest quantity of the desired phase. It is noted that the samples synthesised via the muffle furnace method only appeared to contain the desired phase and the starting materials. A very small amount of an unidentified impurity phase was present in the sample synthesised using a reaction temperature of 350 °C and a reaction time of 1 day. This is also in contrast to the findings obtained for the Schlenk

line method, where samples appeared to contain several impurity phases in considerable quantities. It is noted that Rietveld analysis of the XRD data obtained for a sample of Li_3OCl synthesised via the Muffle furnace method indicates similar thermal parameters to those obtained for samples prepared via the Schlenk line method. A sample of Li_3OCl synthesised via the muffle furnace method, using a reaction temperature of 350 °C and a reaction time of 1 day, was analysed via ^7Li MAS NMR spectroscopy. A simulation of the resulting spectrum exhibited the presence of three distinct Li sites. The corresponding quadrupolar parameters indicated a highly symmetrical environment for all three sites, as expected for cubic structures. Two of the sites determined were assigned to the starting materials LiCl and Li_2O, as their chemical shifts and respective lineshapes were in agreement with those reported in the literature.[212] The remaining site was assigned to the desired phase as the XRD analysis of the sample showed the presence of three phases, Li_3OCl, LiCl and Li_2O. It is noted that the sample was also observed to contain traces of an impurity phase. However, it only appears to be present in small quantities. Thus, no distinct signal could be observed via NMR.

In summary, the synthesis of Li_3OCl has been attempted using two different synthetic methods, and several reaction conditions were tried to produce a phase pure sample. Whilst some of the samples were found to contain a considerable amount of the desired phase, a phase pure sample was not produced. Samples produced via the Schlenk line method using LiCl and LiOH were found to contain impurity phases. The samples produced using LiCl and Li_2O, both via the Schlenk line methods and the muffle furnace method, contained considerable amounts of the starting materials, indicating that the reactions did not reach completion.

Based on the data presented thus far, it is believed that the stability of Li_3OCl and its extremely hygroscopic nature could be hugely influential when considering whether it is actually feasible to produce a phase pure sample of Li_3OCl. As discussed previously, proton uptake in Li_3OCl is readily feasible and breaking the OH bond in LiOH is extremely difficult. Therefore, several hydrated LiRAPs with various compositions may be formed, mak-

ing it extremely challenging to produce a phase pure sample of Li_3OCl using LiCl and LiOH. When attempting the synthesis of Li_3OCl using LiCl and Li_2O, the relative stabilities of the reagents and the product must be considered. As discussed in Chapter 1, recent computational studies have suggested that LiRAPs are thermodynamically metastable when compared to their decomposition products, LiCl and Li_2O.[129] It has also been suggested that in order to successfully synthesise LiRAPs, the kinetic formation of Li_2O must be stopped.[59,127] This explains why reactions using LiCl and Li_2O have not reached completion. Hence, it is extremely challenging to produce a phase pure sample of Li_3OCl. The findings presented in this study strongly disagree with those initially reported by Zhao and Daemen, making the accuracy of their reports questionable.[124] Recent follow up reports from the same research group have insinuated that the Li_3OCl samples discussed in the original study may have been the hydrated analogues of Li_3OCl, Li_2OHCl.[196] In turn, implying that both the sample compositions and the corresponding ionic conductivities initially reported are inaccurate. The findings detailed in the current study are in agreement with these latest reports. Thus, providing sufficient evidence to indicate that phase pure samples of Li_3OCl cannot be synthesised.

3.3.2 Li_3OBr

3.3.2.1 Schlenk Line Method

As the synthesis of a phase pure sample of Li_3OCl had proven to be extremely challenging, the synthesis of the related anti-perovskite, Li_3OBr, was also attempted during this study to determine whether a phase pure sample could be produced. Samples of Li_3OBr were prepared via the Schlenk line method using the procedure reported by Schroeder *et al.*[201] The reagents, LiBr and LiOH, were initially dried at 150 °C for 48 hrs, before being heated to 400 °C over a 2 hr period and held there for 15 mins. The sample was then slow cooled to room temperature. The mixing of reagents either took place on a benchtop using reagents stored in the open air or under the inert atmosphere of an Ar-filled glovebox using dry reagents stored inside an Ar-filled glovebox. The XRD patterns obtained for these samples are shown in Figure

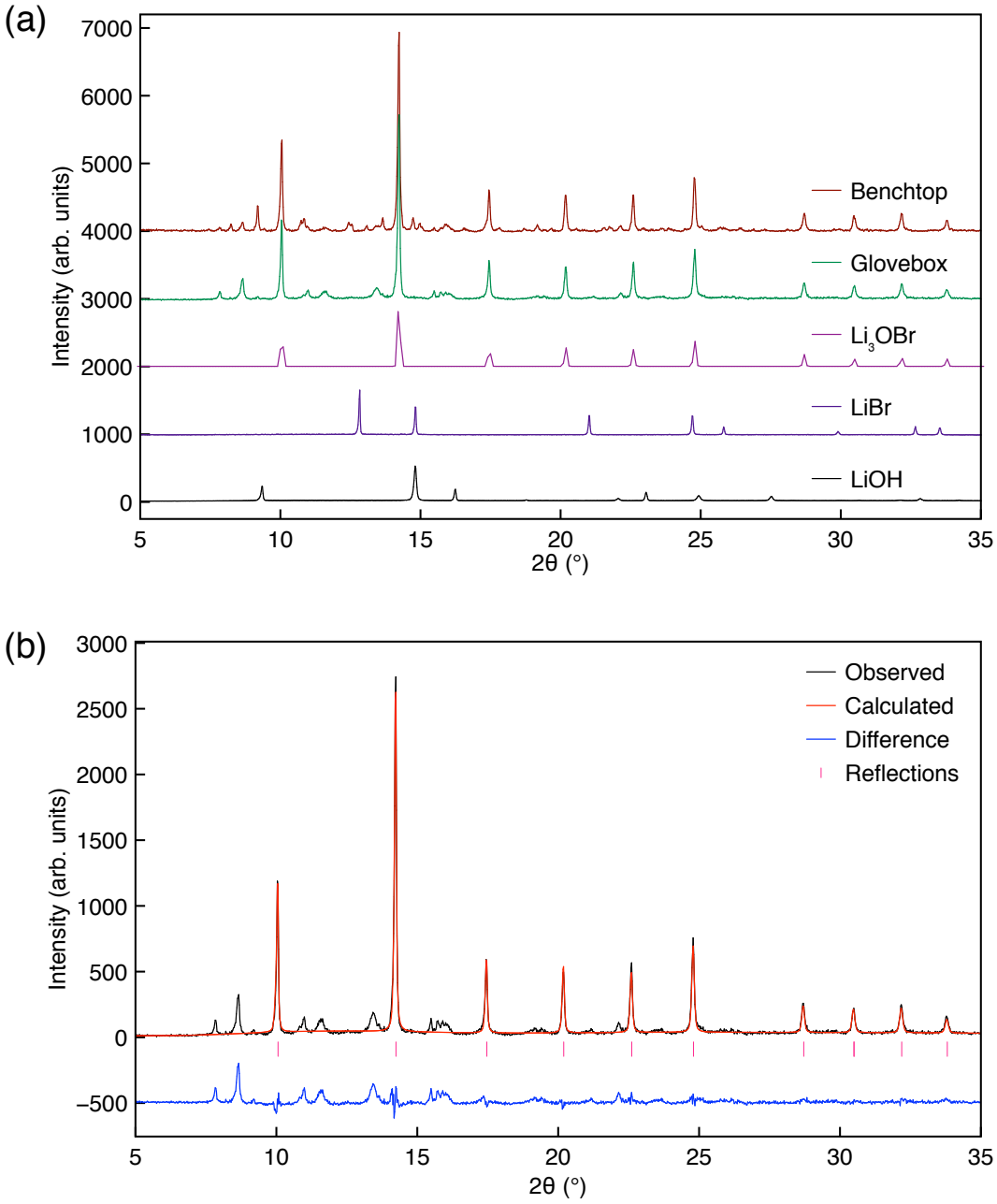

Figure 3.11: (a) X-ray diffraction patterns obtained for samples of Li_3OBr synthesised via the Schlenk line method. The reagent mixture was either prepared on a benchtop (red) or inside an Ar-filled glovebox (green). The reagent mixture was initially dried at 150 °C for 48 hrs and then heated to 400 °C over 2 hrs and held there for 15 mins. The sample was slow cooled to room temperature. A calculated diffraction pattern for Li_3OBr[125] and the XRD patterns obtained for the dry reagents, LiBr and LiOH, are also shown for comparison. (b) Rietveld refinement of the XRD data obtained for the Li_3OBr sample, where sample preparation took place inside an Ar-filled glovebox, using the the $Pm\bar{3}m$ structural model.[125] χ^2 = 4.98, wRp = 29.34%, Rp = 20.35%.

3.11(a). The calculated diffraction pattern for Li_3OBr and the XRD patterns obtained for the dry reagents, LiBr and LiOH, are also shown for comparison. In a similar manner to Li_3OCl, the Li_3OBr samples produced are very clearly not phase pure. However, upon initial inspection, the samples appear to contain considerably more of the desired phase than the Li_3OCl samples. Both of the samples appear to contain predominantly Li_3OBr, with no reflections corresponding to the starting reagents observed. There are, however, numerous additional reflections present that do not correspond to the desired phase or the starting reagents. The XRD pattern for the sample where the reagent mixture was prepared under an inert atmosphere appears to contain fewer of these additional reflections when compared to the XRD pattern for the sample where the reagent mixture was prepared on a benchtop. Unfortunately, these additional reflections could not be indexed to any known structures or any of the structural models available on the ICSD.[200] Hence, the impurity phases present in these samples have not been identified. Earlier, for Li_3OCl samples, several compositions were mentioned that could potentially be formed when trying to synthesise Li_3OCl. Therefore, it is reasonable to assume that the Br analogues of those compositions could also form when synthesising Li_3OBr. Hence, the impurity phases present are most likely non-stoichiometric and/or hydrated LiRAPs based on Li_3OBr.

A Rietveld refinement was completed using the XRD data obtained for the sample of Li_3OBr prepared under an inert atmosphere and the $Pm\bar{3}m$ (Li_3OBr) structural model.[125] The results obtained are shown in Figure 3.11(b), and the corresponding structural parameters, including the isotropic thermal coefficients are shown in Table 3.8. A $\chi^2 = 4.98$ and $wR_p = 29.34\%$ is obtained, suggesting a reasonably good fit. A lattice parameter of 4.0535(1) Å is obtained, which is very close to the value of 4.02 Å reported in the literature for Li_3OBr.[124] The lattice parameter for Li_3OBr is significantly larger than that of Li_3OCl, likely owing to the larger ionic radius of the bromide ion. Inspection of the structural parameters obtained indicates that, in a similar manner to the refinements completed for Li_3OCl, a large thermal coefficient is obtained for Li. As stated earlier, this is likely due to Li-ion mobility, pseudo-symmetry

Table 3.8: Structural parameters obtained for a sample of Li_3OBr, where the reagent mixture was prepared inside an Ar-filled glovebox, from Rietveld refinement of the XRD data using isotropic thermal coefficients. Li_3OBr: space group $Pm\bar{3}m$, a = 4.0535(1) Å, V = 66.602(7) Å^3. χ^2 = 4.98, wRp = 29.34%, Rp = 20.35%.

Atom	x	y	z	U(iso) × 100 (Å^2)
Li	0.5	0.5	0	11.3(15)
O	0.5	0.5	0.5	3.6(5)
Br	0	0	0	2.6(1)

and/or inaccuracies in the structural model proposed in the literature. Interestingly, Li_3OBr is reported to exhibit lower Li-ion conductivity when compared to Li_3OCl.[124] It is noted that that the thermal coefficient obtained is smaller than that obtained for Li_3OCl. Thus, suggesting that Li-ion mobility may be contributing towards the unusually large value obtained for the thermal coefficient corresponding to Li.

^{1}H and ^{7}Li MAS NMR Spectroscopy

The Li_3OBr sample prepared using the Schlenk line method, where the reagents were mixed under an inert atmosphere, was also analysed via ^{1}H and ^{7}Li MAS NMR spectroscopy. It is noted that a phase pure sample of Li_3OBr is not expected to have any ^{1}H species present and, therefore, does not need to be studied via ^{1}H NMR spectroscopy. However, the sample obtained is not phase pure, and as previously discussed, the impurity phases present may contain ^{1}H species. The ^{1}H MAS NMR spectrum obtained is shown in Figure 3.12(a), where a broad resonance centred around δ = 0 ppm is observed. From the diffraction data, it is clear that the sample does not contain any LiOH. Therefore, the signal must be due to the impurity phases present in the sample. This suggests that the impurity phases must contain protons. As previously discussed, the appearance of the spinning sidebands in a ^{1}H NMR spectrum can assist in differentiating between the different types of ^{1}H species present in a sample. For example, hydroxyl groups would produce a limited number of spinning sidebands, whereas intact water molecules result in a large manifold

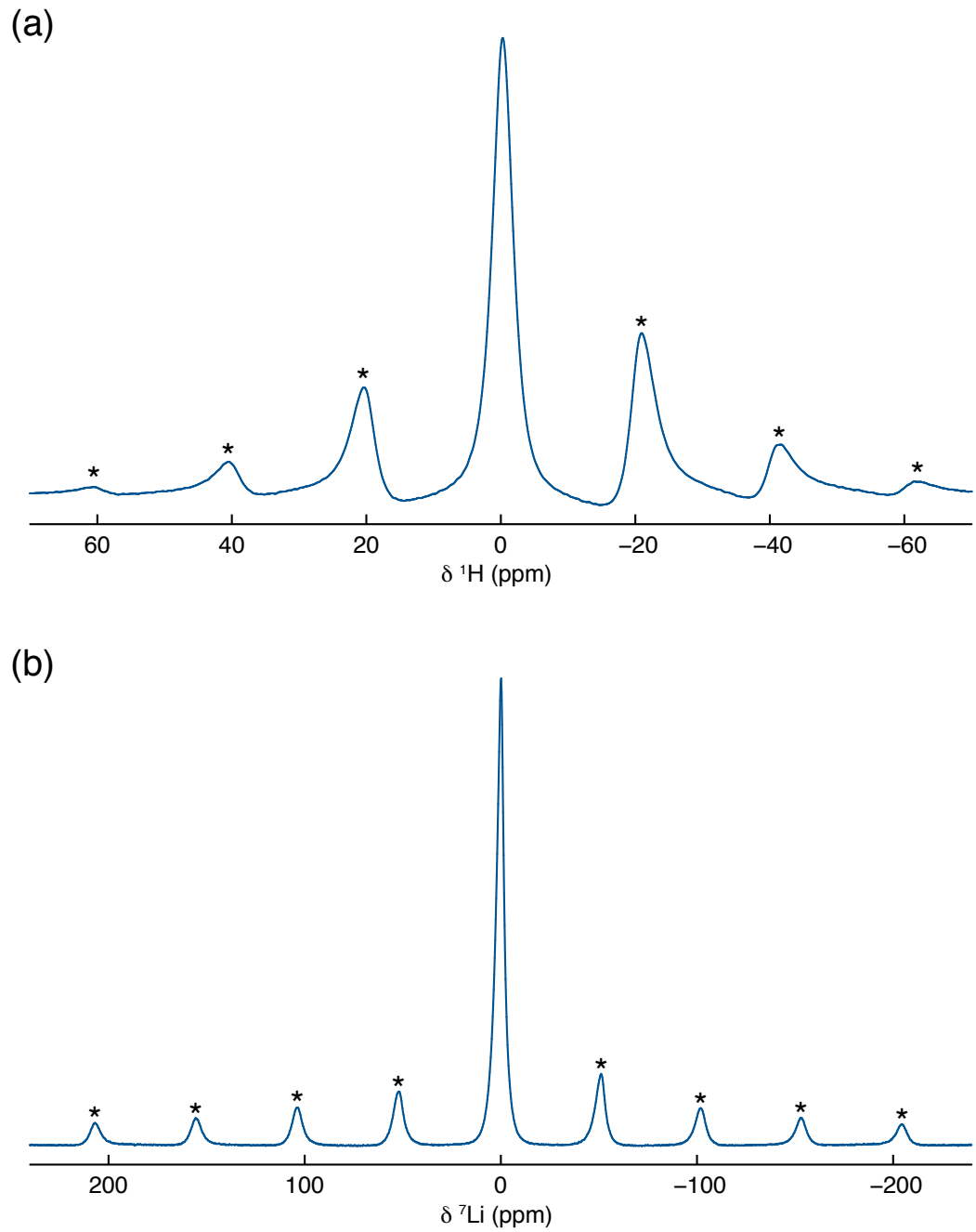

Figure 3.12: (a) ^{1}H and (b) ^{7}Li (11.7 T) MAS NMR spectra acquired for a sample of Li_3OBr prepared via the Schlenk line method, where the reagent mixture was prepared inside an Ar-filled glovebox. The MAS rate used was 10 kHz and spinning sidebands are denoted by *. A recycle delay of (a) 1650 and (b) 200 s was used to acquire 16 transients.

of spinning sidebands. Here, only a few sidebands are observed, indicating that the sample contains hydroxyl species and does not contain any adsorbed water. Hence, the impurity phases present must be hydrated species, most

likely non-stoichiometric hydrated LiRAPs based on Li_3OBr. The ^7Li MAS NMR spectrum, shown in Figure 3.12(b), also displays a single broad resonance centred around δ = 0 ppm. As stated earlier, ^7Li has a small chemical shift range.[163] Hence, resonances often overlap, making it difficult to distinguish between different sites. This suggests that all of the Li species present within the sample have very similar local environments. From the diffraction data, it is clear that the sample contains more than one phase. However, it has not been possible to accurately identify the different phases from the current data alone. It is not possible to determine the number of crystallographically distinct Li sites present from the ^7Li MAS NMR spectrum. To accurately do this two-dimensional methods such as MQMAS would be needed. However, in this case, based on the broadening observed and the obvious similarity in chemical shift, it is highly unlikely that MQMAS methods would be able to differentiate the extremely similar sites. Hence, MQMAS methods were not attempted for this sample.

Summary

Samples of Li_3OBr were synthesised via the Schlenk line method, where the reagent mixture was prepared either on a benchtop using reagents stored in the open air or under the inert atmosphere of an Ar-filled glovebox using reagents stored inside an Ar-filled glovebox. In both cases, a considerable amount of Li_3OBr was formed. However, the samples were not phase pure. As discussed earlier, the impurity phases present in these samples are most likely hydrated compositions based on Li_3OBr owing to its extremely hygroscopic nature and the difficulties in breaking the OH bond in LiOH. Unlike samples of Li_3OCl, no starting reagents were observed in the Li_3OBr samples. In the case where the reagent mixture was prepared under an inert atmosphere, fewer impurities were formed. Thus, indicating that the method of sample preparation influences the sample purity and, in this case, preparation under an inert atmosphere is preferred. However, preparation under an inert atmosphere using dry reagents was not enough to produce a phase pure sample. The diffraction pattern for the corresponding Li_3OBr sample was analysed

via Rietveld refinement and, again, the thermal coefficient obtained for Li was unusually large. As discussed previously, this is most likely a consequence of Li motion and/or inaccuracies in the structural model. The sample produced using the reagent mixture prepared inside a glovebox was analysed via ^{1}H and ^{7}Li MAS NMR spectroscopy. In both cases, a single resonance was observed. The ^{1}H signal obtained is characteristic of hydroxyl groups, indicating that the impurity phases are hydrated species. However, it was not possible to distinguish between the various Li species present in the sample.

3.3.2.2 Muffle Furnace Method

The synthesis of Li_3OBr was also attempted via the muffle furnace method using LiBr and Li_2O as precursors. The various reaction conditions attempted are detailed in Table 3.9. In a similar manner to Li_3OCl, the reaction time was initially fixed at 1 day, and the reaction temperature was varied from 300 to 500 °C. The XRD patterns obtained for the samples are shown in Figure 3.13. A calculated diffraction pattern for Li_3OBr and the XRD patterns obtained for the reagents, LiBr and Li_2O, are also shown for comparison. In all cases, the diffraction patterns predominantly consist of reflections corresponding to the starting reagents, indicating that the reaction has not reached completion. A few additional reflections, albeit of very low intensity, are also

Table 3.9: Details of the specific reaction conditions used for the synthesis of Li_3OBr, using LiBr and Li_2O, via the muffle furnace method.

Reagents and Location	Temperature (°C)	Time
LiBr + Li_2O (Glovebox)	300, 350, 450 and 500	1 day
LiBr + Li_2O (Glovebox)	350	4 days
LiBr + Li_2O (Glovebox)†	480	16 hrs
LiBr + Li_2O (Glovebox)‡	480	16 hrs

† Sample was reground and reheated three times at 480 °C for 16 hrs.

‡ Sample was reground via mechanical milling at 300 rpm for 1 hr and reheated three times 480 °C for 16 hrs.

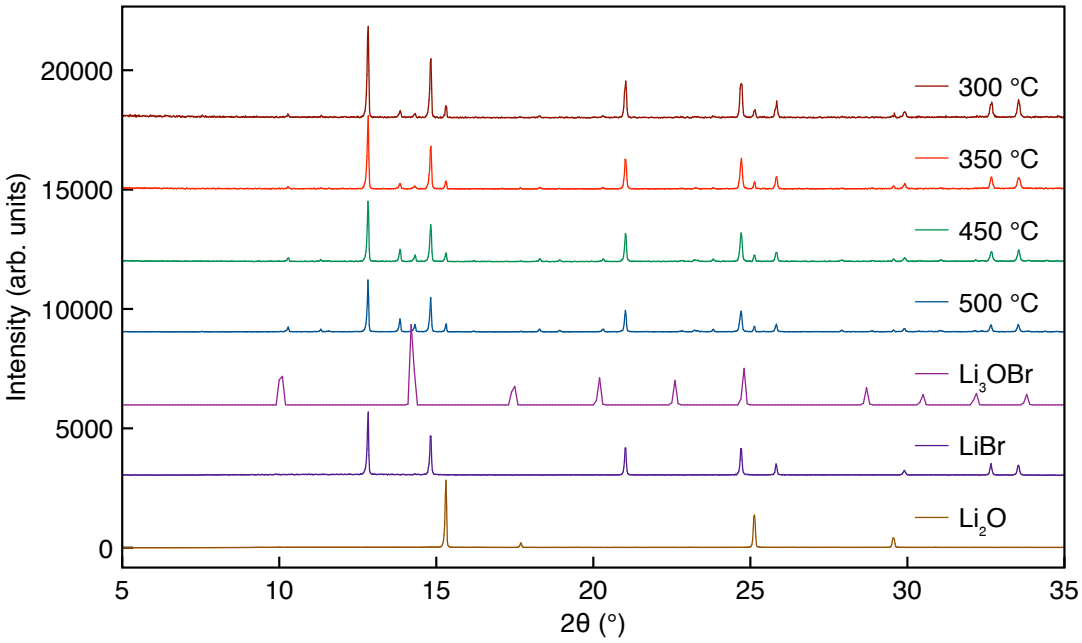

Figure 3.13: X-ray diffraction patterns obtained for samples of Li_3OBr synthesised via the muffle furnace method. The reaction time was fixed at 24 hrs and the reaction temperature was varied from 300 to 500 °C. A calculated diffraction pattern for Li_3OBr[125] and the XRD patterns obtained for the reagents, LiCl and Li_2O, are also shown for comparison.

observed. These additional reflections do not appear to correspond to the desired phase, indicating that the samples produced do not contain any Li_3OBr. Instead, a small amount of an impurity phase has been formed (*vide infra*). Moreover, a change in the reaction temperature does not appear to have a significant impact on the sample composition.

In an attempt to drive the reaction forward and produce Li_3OBr, a longer reaction time was tested. A sample was heated for 4 days at 350 °C, and the XRD pattern obtained is shown in Figure 3.14(a). Initial inspection of the XRD pattern suggests that the sample is predominantly composed of the starting reagents, LiBr and Li_2O. The sample does not appear to contain any Li_3OBr. However, the same impurity phase observed in the earlier samples synthesised via the same method (Figure 3.13) has again been formed. As discussed previously in Chapter 1, Zhu *et al.*, have reported the presence of $Li_7O_2Br_3$ (Figure 1.18) in samples of Li_3OBr synthesised using Li_2O as a precursor.[138] Hence, the XRD pattern obtained was analysed further to determine whether $Li_7O_2Br_3$ is also present in this sample.

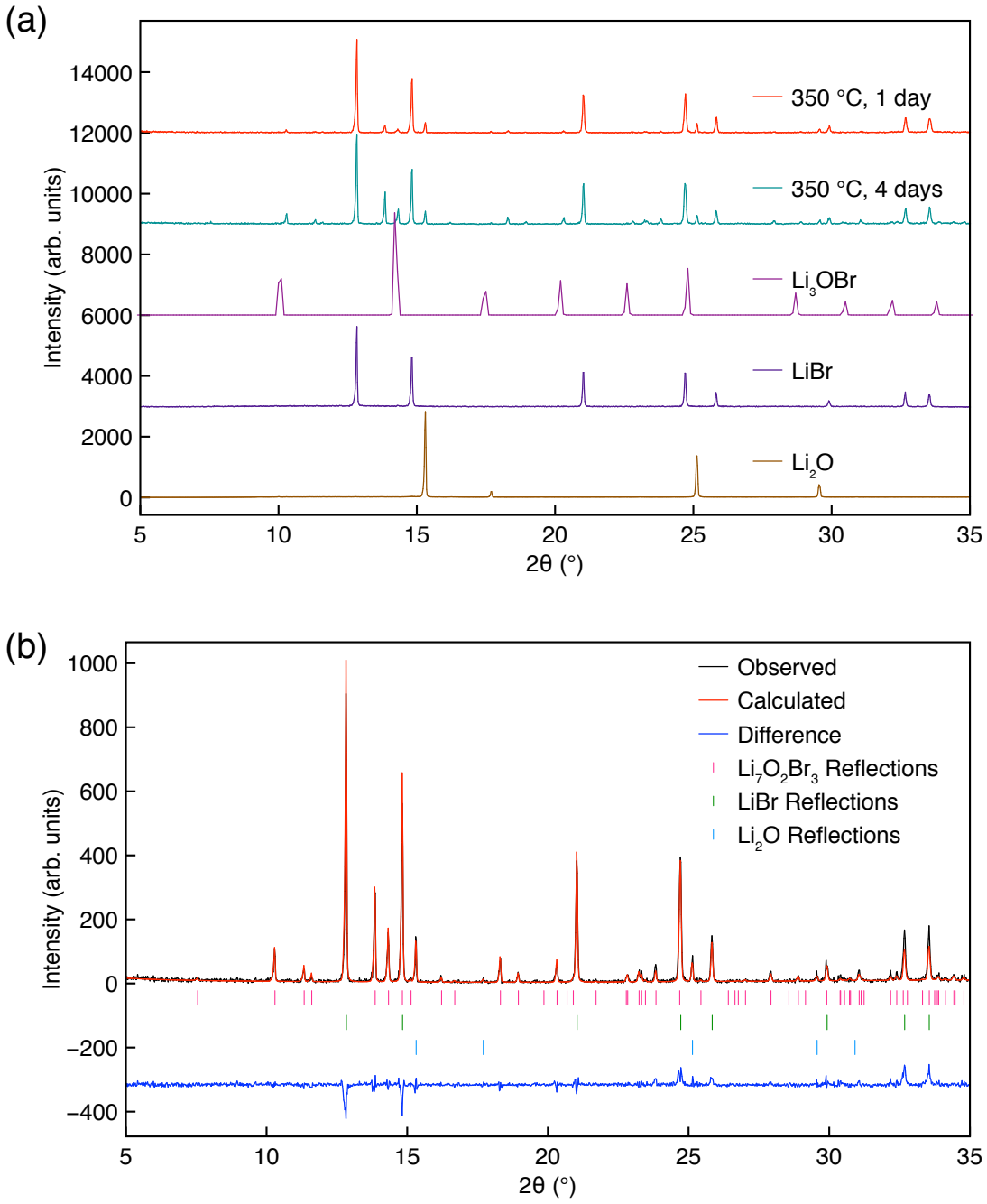

Figure 3.14: (a) X-ray diffraction patterns obtained for samples of Li_3OBr synthesised via the muffle furnace method. The reaction temperature was fixed at 350 °C and the reaction time was varied between 1 and 4 days. A calculated diffraction pattern for Li_3OBr[125] and the XRD patterns obtained for the reagents, LiCl and Li_2O, are also shown for comparison. (b) Multiphase Rietveld refinement of the XRD data for the Li_3OBr sample heated at 350 °C for 4 days using the *I*4/*mmm* ($Li_7O_2Br_3$)[137] and $Fm\bar{3}m$ (LiBr and Li_2O)[199,209] structural models. χ^2 = 1.72, wR_P = 31.44% and R_P = 23.77%.

A Rietveld refinement was completed using the XRD data obained for the sample of Li_3OBr heated at 350 °C for 4 days, and the $I4/mmm$ structural model reported for $Li_7O_2Br_3$ and $Fm\bar{3}m$ structural models for LiBr and Li_2O.[137,199,209] The refinement is shown in Figure 3.14(b) and the corresponding structural parameters are listed in Table 3.10. An inspection of the refinement shows that a reasonable fit has been achieved with a χ^2 = 1.72 and wR_p = 31.44%. The additional reflections observed in the Li_3OBr samples have been successfully indexed using the tetragonal structural model for $Li_7O_2Br_3$ in space group $I4/mmm$. Thus, demonstrating that the Li_3OBr samples produced via the muffle furnace method do in fact contain $Li_7O_2Br_3$, as well as the starting materials, LiCl and Li_2O. During the refinement, the thermal coefficients for all atoms were constrained to 2.5×10^{-2} Å^2 as that was the only way a stable, fully converged refinement could be obtained. This was the only parameter constrained, the other usual parameters were refined as normal. As all the phases present in this sample have been identified, the phase fractions were refined to determine the relative quantity of each phase. The sample contains 8.41(22)% $Li_7O_2Br_3$, 29.45(69)% LiBr and 62.14(87)% Li_2O. Thus, confirming the initial observation that the sample predominantly contains the starting reagents, LiBr and Li_2O, and the desired phase has not been produced. Interestingly, in a similar manner to Li_3OBr, $Li_7O_2Br_3$ is also believed to be a

Table 3.10: Structural parameters for a sample of Li_3OBr, prepared via the muffle furnace method by heating at 350 °C for 4 days, obtained from Rietveld refinement of the XRD data. The thermal coefficients for all atoms were constrained to 2.5×10^{-2} Å^2. χ^2 = 1.72, wR_P = 31.44% and R_P = 23.77%.

Phase	a (Å)	c (Å)	Vol (Å^3)	Phase fraction (%)
$Li_7O_2Br_3$ *$I4/mmm$*	4.0279(2)	21.5870(17)	350.235(39)	8.41(22)
LiBr *$Fm\bar{3}m$*	5.5056(1)	–	166.887(13)	29.45(69)
Li_2O *$Fm\bar{3}m$*	4.6185(6)	–	98.516(37)	62.14(87)

metastable phase.[138] In fact, Zhu *et al.*[138] believe $Li_7O_2Br_3$ to be even less stable than Li_3OBr. As such, their attempts to obtain a phase pure sample of $Li_7O_2Br_3$ were unsuccessful as they could only synthesise a phase mixture of Li_3OBr and $Li_7O_2Br_3$. This contrasts with the findings presented in this study, as all the samples discussed thus far do not contain any Li_3OBr.

Further attempts to synthesise Li_3OBr included following the procedure reported by Zhu and co-workers as they successfully synthesised Li_3OBr using LiBr and Li_2O as precursors.[138] Their method involved heating the reagent mixture at 480 °C for 16 hrs. The sample was then mechanically milled and reheated three additional times at 480 °C for 16 hrs. In this study, the samples produced were reground both manually and via mechanical milling before reheating. This was done to see if mechanical milling has any significant impact on the sample produced. The XRD patterns obtained are shown in Figures 3.15 and 3.16(a), respectively. The XRD patterns obtained for the manually reground samples appear to be similar to those shown in Figures 3.13 and 3.14, suggesting the presence of $Li_7O_2Br_3$ and the starting materials, LiBr and Li_2O. In a similar manner to the earlier samples, no Li_3OBr has been formed. Moreover, all the diffraction patterns shown in Figure 3.15 appear to be very similar, indicating that the composition of the sample has not changed. Hence, multiple cycles of manual regrinding and reheating do not help to drive the reaction forward.

The XRD patterns obtained for the samples that were mechanically milled are also very similar to those shown in Figures 3.13 and 3.14, suggesting that, once again, the sample produced contains the starting reagents and a small amount of $Li_7O_2Br_3$. The XRD pattern for the sample mechanically milled and heated for a third time is slightly different to the previous diffraction patterns obtained for the same sample. Here, reflections corresponding to the desired phase, Li_3OBr, are observed. However, it is noted that this sample still contains the starting reagents, indicating that the sample is not phase pure and the reaction has not reached completion. It is also noted that this sample does not contain any $Li_7O_2Br_3$. Thus, suggesting that $Li_7O_2Br_3$ may be an intermediary phase when synthesising Li_3OBr. A Rietveld refinement

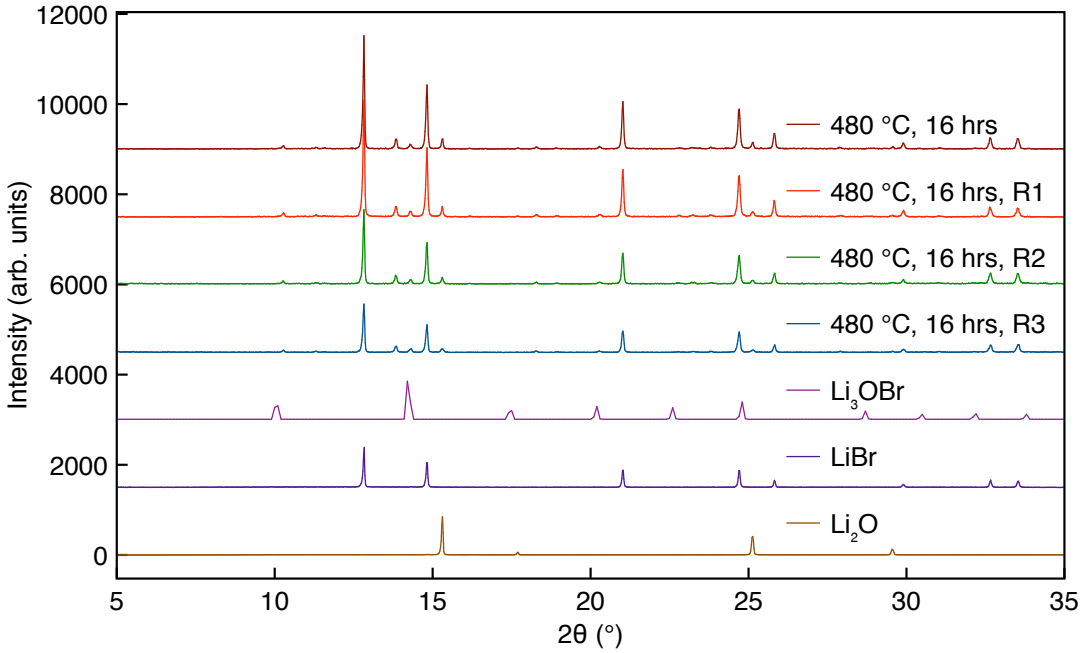

Figure 3.15: X-ray diffraction patterns obtained for samples of Li_3OBr synthesised via the muffle furnace method. The reaction time was fixed at 16 hrs and the reaction temperature was 480 °C. The sample was reground and reheated three times, denoted R1, R2 and R3, respectively. A calculated diffraction pattern for Li_3OBr[125] and the XRD patterns obtained for the reagents, LiCl and Li_2O, are also shown for comparison.

was completed using the XRD data obtained for the final sample (denoted as R3, (M)) and the $Pm\bar{3}m$ (Li_3OBr)[125] and $Fm\bar{3}m$ (LiBr and Li_2O)[199,209] structural models. The results obtained are shown in Figure 3.16(b) and the corresponding structural parameters are detailed in Table 3.11. The fit obtained appears to be reasonable with a $\chi^2 = 2.01$ and $wR_p = 22.92\%$. However, in a similar manner to the earlier sample, the thermal coefficients for all atoms had to be constrained to 2.5×10^{-2} Å^2. As all of the phases present in the sample have been identified, the phase fractions were refined to determine the relative quantities of each phase. The sample contains 17.61(34)% Li_3OBr, 28.30(41)% LiBr and 54.09(64)% Li_2O. These phase fractions confirm initial suggestions that the sample predominantly consists of the starting materials, and the desired phase is present in very small quantities. Unfortunately, despite multiple regrinding and reheating cycles, only a very small quantity of Li_3OBr was produced, indicating that, in a similar manner to Li_3OCl, obtaining a phase pure sample of Li_3OBr is extremely challenging.

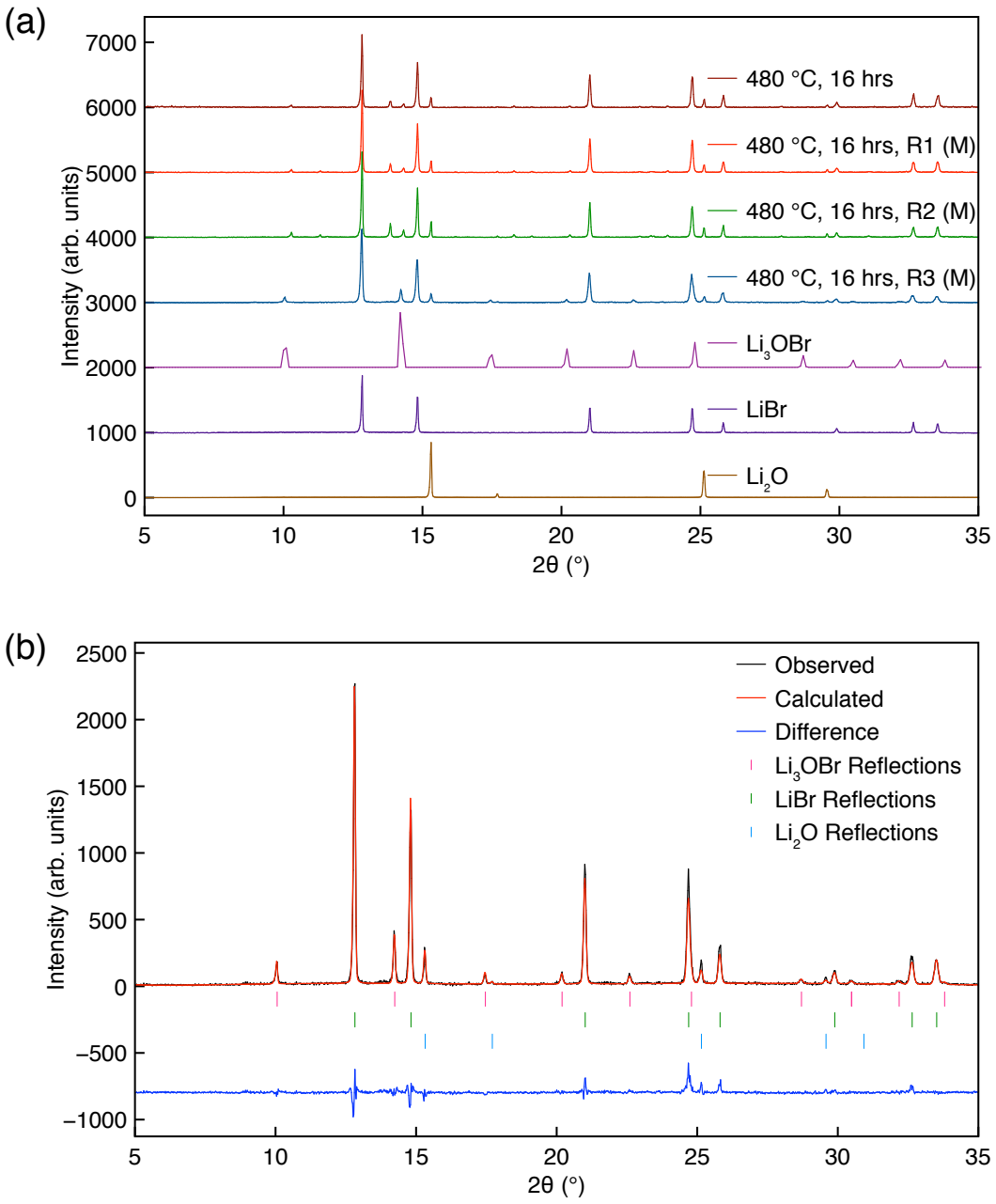

Figure 3.16: (a) X-ray diffraction patterns obtained for samples of Li_3OBr synthesised via the muffle furnace method. The reaction time was 16 hrs and the reaction temperature was 480 °C. The sample was mechanically milled at 300 rpm for 1 hr and reheated three times, denoted by R1, R2 and R3, respectively. The notation (M) indicates that the sample was mechanically milled during the regrinding. A calculated diffraction pattern for Li_3OBr[125] and the XRD patterns obtained for the reagents, LiCl and Li_2O, are also shown for comparison. (b) Multiphase Rietveld refinement of the XRD data for R3 Li_3OBr sample using the $Pm\bar{3}m$ (Li_3OBr)[125] and $Fm\bar{3}m$ (LiBr and Li_2O)[199,209] structural models. χ^2 = 2.01, wRp = 22.92%, Rp = 16.72%.

Table 3.11: Structural parameters for a sample of Li_3OBr, prepared via the muffle furnace method by heating at 480 °C for 16 hrs and regrinding (via mechanical milling) and reheating three times, from Rietveld refinement of the XRD data. The thermal coefficients for all atoms were constrained to 2.5×10^{-2} Å^2. χ^2 = 2.01, wRp = 22.92%, Rp = 16.72%.

Phase	a (Å)	Vol (Å^3)	Phase fraction (%)
Li_3OBr *$Pm\bar{3}m$*	4.0544(3)	66.648(14)	17.61(34)
LiBr *$Fm\bar{3}m$*	5.5116(1)	167.433(11)	28.30(41)
Li_2O *$Fm\bar{3}m$*	4.6168(7)	98.406(43)	54.09(64)

Summary

The synthesis of Li_3OBr was attempted using LiBr and Li_2O as precursors, via the muffle furnace method. Initially, the reaction time was fixed at 1 day, and the reaction temperature was varied from 300 to 500 °C. In all cases, the samples predominantly contained the starting reagents and a small amount of $Li_7O_2Br_3$. No Li_3OBr was formed in any of the samples. A longer reaction time of 4 days was tested at 350 °C to determine if it would assist in driving the reaction forward. In this case, the amount of $Li_7O_2Br_3$ produced increased slightly, but no Li_3OBr was formed. The method reported by Zhu *et al.* was also attempted, with the sample heated at 480 °C for 16 hrs and reground and reheated three times.[138] The samples were reground both manually and via mechanical milling. Again, the samples contained a small amount of $Li_7O_2Br_3$, but none of the desired Li_3OBr. The sample synthesised using mechanical milling methods was the only one that contained a small amount of Li_3OBr after regrinding and reheating three times.

In summary, all samples produced using the muffle furnace method contained a large amount of starting reagents, and in most cases, the desired phase was not formed at all. Instead, a related composition, $Li_7O_2Br_3$, was formed. Thus, indicating that the muffle furnace method is not optimal for

the synthesis of Li_3OBr. As discussed earlier, the stability of the reagents versus the desired phase is worth considering. Computational studies have suggested that the starting materials, LiBr and Li_2O, are more stable than Li_3OBr, making it challenging to form Li_3OBr.[59,129] This potentially explains why, in most cases, Li_3OBr has not been produced. However, the presence of $Li_7O_2Br_3$ in the samples was quite surprising as Zhu *et al.*, claimed that the stability of $Li_7O_2Br_3$ is, in fact, lower than Li_3OBr.[138]

3.4 Conclusions

This chapter has detailed the numerous experiments undertaken to synthesise Li_3OCl and Li_3OBr. The synthesis has been carried out under vacuum via a conventional Schlenk line apparatus, as well as under the inert atmosphere of an Ar-filled glovebox using a muffle furnace. Despite numerous attempts, phase pure samples of Li_3OCl and Li_3OBr could not be produced. Several different reaction temperatures and times were tested to find the optimal reaction conditions. For Li_3OCl, a reaction temperature of 360 °C and a reaction time of 1 day, using LiCl and LiOH as precursors, resulted in the best sample using the Schlenk line method, as the sample contained a considerable amount of the desired phase, despite the presence of LiCl and some unidentified impurity phases. Attempts to increase the phase purity included preparing the reagent mixture under an inert atmosphere before heating via the Schlenk line method. A phase pure sample was not produced, although, the sample did contain fewer impurities.

Further attempts included the use of techniques such as mechanical milling and pellet pressing. The reagent mixture was mechanically milled and then pressed into a pellet before heating. A significant improvement was observed using these methods, as the sample produced appeared to contain a large amount of Li_3OCl, and very little of the impurity phases. All of the Li_3OCl samples synthesised via the Schlenk line method appear to contain the same impurity phases. At present, these impurity phases have not been identified as the corresponding reflections could not be indexed using any known

structures or any of the structural models currently available on the ICSD.[200] Additional phases that may be formed when trying to synthesise Li_3OCl include Li_5O_2Cl and $Li_{17}O_6Cl_5$.[59] However, the presence of these phases could not be confirmed as detailed crystallographic information has not been reported for either phase. Furthermore, Li_3OCl is reported to have a high hydration enthalpy making it extremely challenging to form proton-free samples. Moreover, the OH bond is extremely difficult to break owing to its high bond enthalpy, which presents additional challenges when trying to obtain a phase pure sample of Li_3OCl from LiOH. This could result in the formation of several hydrated LiRAPs with varying compositions based on Li_3OCl (*vide supra*).

Samples of Li_3OCl were also synthesised using LiCl and Li_2O as precursors. Synthesis using this combination of starting materials was carried out via the Schlenk line and the muffle furnace method using reagents stored inside an Ar-filled glovebox. In both cases, Li_3OCl was produced successfully. However, the samples obtained were not phase pure and contained the starting materials as impurities. Thus, the reactions did not reach completion. Additional attempts to drive the reaction forward included using longer reaction times, regrinding and reheating and mechanical milling of the reagents. However, unfortunately, no improvement was observed using any of these techniques.

Samples of Li_3OBr were also synthesised via the Schlenk line method. The reagent mixtures were prepared on a benchtop in the open air or under the inert atmosphere of an Ar-filled glovebox. The latter obtained better results, as the sample contained predominantly the desired phase, and only small quantities of the impurity phases were present. The Li_3OBr samples appear to contain more of the desired phase when compared to Li_3OCl synthesised via the same method. Hence, the Schlenk line method appears to be a good approach for the synthesis of Li_3OBr.

On the other hand, the muffle furnace method does not appear to be suitable for the synthesis of Li_3OBr. Many different reaction temperatures and times were tested using LiBr and Li_2O as precursors. Unfortunately, it was

not possible to form the desired phase. The samples synthesised were found to contain the starting materials, LiBr and Li_2O, and $Li_7O_2Br_3$. Additional attempts to form Li_3OBr included regrinding and reheating the sample three times. The samples were either reground manually or mechanically milled. A similar outcome to the earlier samples was also observed here, with the exception of the sample that had been mechanically milled and reheated three times. Here, a small amount of Li_3OBr was produced, although the sample was not phase pure and mostly contained the starting reagents. This contrasts with the Li_3OCl samples synthesised via the muffle furnace method, where a significant amount of the desired phase was produced.

Despite numerous efforts, the synthesis of phase pure samples of both Li_3OCl and Li_3OBr has proven to be hugely challenging. Samples containing a considerable amount of the desired phase have been produced in both cases. However, the samples always contained impurities, be it the starting materials or products of a side reaction. The difficulties associated with the synthesis of a phase pure sample can be attributed to the fact that the desired phases are extremely hygroscopic. Hence, many hydrated LiRAPs can be formed when trying to synthesise Li_3OCl/Br. Additionally, Li_3OCl/Br are believed to be metastable phases compared to the starting reagents, LiCl/Br and Li_2O. Therefore, Li_3OCl/Br can only be formed when the formation of Li_2O is kinetically stopped.[129] The inability to prepare samples of Li_3OCl and Li_3OBr is a direct contradiction of the work by Zhao and Daemen[124] and brings their reported findings into question and doubt. Furthermore, subsequent reports by the same group have stated that the samples discussed in the original study were most likely hydrated analogues of Li_3OCl/Br.[196] These reports support the findings presented in this study which demonstrate that phase pure samples of Li_3OCl and Li_3OBr cannot be synthesised via conventional solid-state routes. Thus, making it difficult to assess their suitability as solid electrolytes in ASSBs.

4 Li_2OHCl: A Structural Study

4.1 Introduction

As detailed in Chapter 3, numerous attempts were made to synthesise Li_3OCl and obtain a phase pure sample. However, these were limited in their success. As a result, our efforts shifted towards synthesis of the hydrated analogue, Li_2OHCl, which is believed to be easier to prepare than Li_3OCl.[213] Two phases have been reported for Li_2OHCl; a room-temperature phase (believed to be orthorhombic) and a high-temperature cubic ($Pm\bar{3}m$) phase (believed to be analogous to Li_3OCl).[213] A reversible phase transition from the room- to high-temperature phase is reported to occur at ~35 °C.[213,214] Initially, it was believed that studying Li_2OHCl could provide insight into why the non-hydrated phase could not be prepared. However, since then, it has become apparent that Li_2OHCl itself is worthy of exploration as a solid electrolyte, as it is expected to be a good ion conductor owing to a third of the Li sites being vacant, which can enable the movement of ions via a vacancy mechanism. Hence, Li_2OHCl is of considerable interest as a potential ion conductor.

In 1997, Eilbracht and co-workers reported that the high-temperature phase of Li_2ODX (X = Cl, Br) adopts a structure similar to the widely known perovskite $CaTiO_3$, now known as an anti-perovskite structure type.[215] They reported Li_2ODCl/Br to exist as a cubic structure, in space group $Pm\bar{3}m$, where Li, O and Cl/Br occupy 3d, 1a and 1b Wyckoff positions, respectively (Table 4.1 details the atomic coordinates corresponding to these Wyckoff positions). Li was reported to have an occupancy of 2/3 to reflect the composition of the material and H/D, were described as pointing towards the faces of the Li_6O octahedra. However, the corresponding Wyckoff positions or exact atomic coordinates were not reported. Notably, there appears to be a distinct lack of information in the current literature regarding the crystallographic positions of the protons in the cubic phase of Li_2OHCl. In 2018, Hanghofer and co-workers reported the synthesis of barium-doped Li_3OCl, $Li_{2.99}Ba_{0.005}OCl$ and Li_2OHCl (*vide infra*).[210] They had intended to form a proton-free sample of

$Li_{2.99}Ba_{0.005}OCl$. However, neutron powder diffraction (NPD) analysis of the sample indicated a composition of $Li_{1.84}OH_{1.16}Cl$, which is closer to Li_2OHCl than Li_3OCl. This is not surprising as their synthetic method involved mixing the reagents with distilled water prior to heating, and as stated earlier, a phase pure sample of Li_3OCl is extremely difficult to obtain. As such, the sample contained LiCl and $Li_4(OH)_3Cl$ as impurity phases. Additionally, the sample contained a very small amount of Ba. Hence, its atomic coordinates were not determined. Interestingly, at room temperature $Li_{1.84}OH_{1.16}Cl$ adopts a cubic structure in space group $Pm\bar{3}m$ and VT NPD analysis indicated that cooling the sample to 4 K does not affect the symmetry, *i.e.*, no phase transition was observed. The structure reported at 300 K is shown in Figure 4.1 and the corresponding structural parameters reported at 300 and 4 K, including the proton positions, are detailed in Table 4.1. So far, this is the only study that reports the atomic coordinates of protons in a system close to Li_2OHCl. However, it is noted that the sample was intended to be Li_3OCl, not Li_2OHCl, and the authors did not report any crystallographic information for the cubic structure of Li_2OHCl.

To date, there is considerable confusion regarding the room-temper-

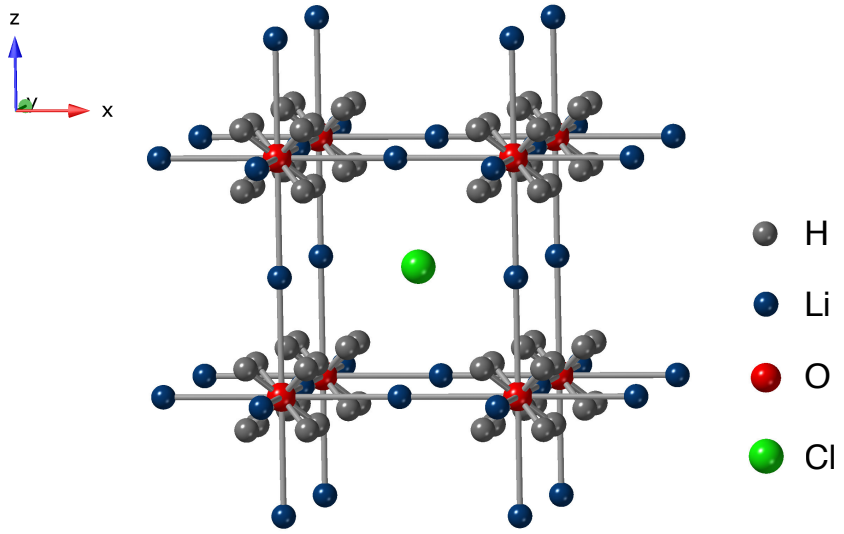

Figure 4.1: The structure of $Li_{1.84}OH_{1.16}Cl$ in space group $Pm\bar{3}m$, proposed by Hanghofer and co-workers.[210]

Table 4.1: Crystallographic details for the cubic phase of $Li_{1.84}OH_{1.16}Cl$ (space group $Pm\bar{3}m$), proposed by Hanghofer and co-workers at 300 and 4 K.[210] a = 3.89442 and 3.86466 Å at 300 and 4 K, respectively.

Atom	Wyckoff	x	y	z	Occ.	U(iso) × 100 (Å²)†
300 K						
Li	3d	0.5	0	0	0.614‡	9.63
O	1a	0	0	0	1	2.03
H	8g	0.1279	0.1279	0.1279	0.145	5.09
Cl	1b	0.5	0.5	0.5	1	2.52
4 K						
Li	3d	0.5	0	0	0.592	7.35
O	1a	0	0	0	1	0.99
H	8g	0.1389	0.1389	0.1389	0.153	5.08
Cl	1b	0.5	0.5	0.5	1	0.98

† The thermal coefficients were originally reported as B(iso) values. These were converted to U(iso) for ease of comparison to the data reported in the current study.

‡ The actual value quoted in the paper is 6.14. However, this is most likely a typographical error as the composition determined during the study, $Li_{1.84}OH_{1.16}Cl$, can only be obtained if the fractional occupancy for Li is 0.614.

ature phase of Li_2OHCl. As such, a structural model is yet to be agreed upon, although several suggestions have been made in the literature. In 2003, Schwering and co-workers reported the synthesis of several samples in the series $Li_{3-x}OH_xCl/Br$, where x was varied from 0.83 to 2.[213] The samples prepared were reported to exhibit ionic conductivities on the order of 10^{-4} S cm^{-1}, although specific conductivity values were not reported for any sample. At room temperature, Li_2OHCl was reported to adopt an orthorhombic structure in space group *Amm*2, with lattice parameters a = 3.8220 Å, b = 7.9968 Å and c = 7.7394 Å. The high-temperature cubic phase, in space group $Pm\bar{3}m$, is reported to have a lattice parameter of a = 3.9103 Å. However, it is noted that detailed crystallographic information, *i.e.*, atomic coordinates, were not reported for either phase. Hence, it is challenging to confirm the accuracy of the reported structures as there is insufficient structural information available to generate a suitable model.

Hood and co-workers have also investigated Li_2OHCl and have tested different cooling rates post-synthesis, with Li_2OHCl either fast or slow cooled.[214] The fast cooled sample of Li_2OHCl was reported to adopt an orthorhombic structure, whereas the slow cooled sample was cubic in space group $Pm\bar{3}m$. Again, no specific crystallographic details were reported for either structure. Electrochemical impedance spectroscopy (EIS) data presented in the same study indicated that fast cooled samples of Li_2OHCl exhibit higher Li-ion conductivities at elevated temperatures when compared to slow cooled samples. Fast cooled Li_2OHCl is reported to exhibit a conductivity of 2.8×10^{-3} S cm^{-1} at 195 °C, with an activation energy of 0.56 eV. It was suggested that fast cooling results in structural defects that aid the movement of ions in the structure, resulting in samples exhibiting higher ionic conductivity.

Attempts to obtain additional information regarding the room-temperature phase of Li_2OHCl have included the use of computational methods. In 2017, Howard and co-workers determined, via density functional theory (DFT) calculations, the ground state structure of Li_2OHCl to be tetragonal in space group $P4mm$. A metastable orthorhombic structure, in space group $Pmc2_1$, was also predicted.[216] The synthesis of Li_2OHCl was also reported in the same study. According to their experimental findings, at room temperature, Li_2OHCl adopted an orthorhombic structure in space group $Pmc2_1$, with their predicted model providing a good fit for their XRD data. The predicted ground state tetragonal structure, however, was not observed experimentally. More recently, Howard *et al.* published an additional computational study in which it was suggested that Li_2OHCl could adopt an orthorhombic structure, in space group $Cmcm$.[217] However, it must be noted that this structure has not been evaluated against experimental data. The structural models proposed by Howard and co-workers[210] are shown in Figure 4.2 , and the corresponding crystallographic details are listed in Table 4.2.

Additional structural suggestions have included a study carried out by Song and co-workers who investigated $Li_{3-x}OH_xCl$, where x was between 0.3 and 1.[218] They proposed that, at room temperature, Li_2OHCl adopts an orthorhombic structure in space group $Pmmm$ and the transition to a cubic

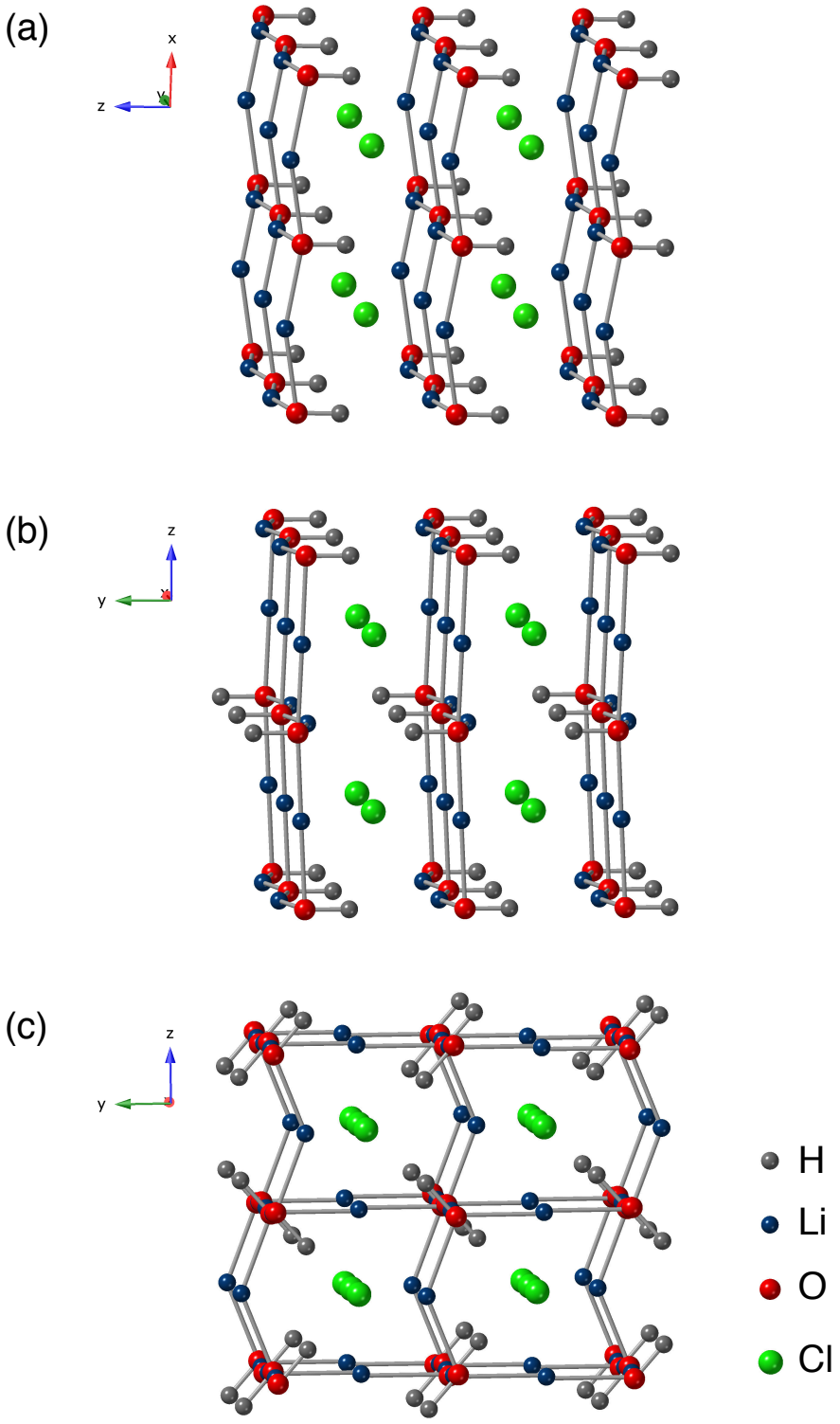

Figure 4.2: The structures of Li_2OHCl proposed by Howard and co-workers in space group (a) *P4mm*, (b) $Pmc2_1$ and (c) *Cmcm*.[216,217]

Table 4.2: Crystallographic details for the tetragonal and orthorhombic phases of Li_2OHCl (in space groups *P4mm*, *Pmc*2_1 and *Cmcm*), proposed by Howard and co-workers.[216,217] Space group *P4mm*, a = b = 3.794 Å and c = 3.578 Å. Space group *Pmc*2_1, a = 3.831 Å, b = 3.617 Å and c = 7.985 Å. Space group *Cmcm*, a = 7.91 Å, b = 7.74 Å and c = 7.42 Å.

Atom	Wyckoff	x	y	z
***P4mm*†**				
Li	2c	0.5	0	0.015
O	1a	0	0	0.925
H	1a	0	0	0.654
Cl	1b	0.5	−0.5	0.439
***Pmc*2_1**				
Li1	2a	0	0.001	0.25
Li2	2b	0.5	0.086	0
O1	2a	0	−0.024	0
H1	2a	0	0.699	0
Cl1	2b	0.5	0.5	0.25
Cmcm				
Li1	8d	0.25	0.25	0
Li2	4b	0	0.5	0
Li3	4c	0	0.167	0.25
O1	8f	0	0.747	0.510
H1	8f	0	0.831	0.407
Cl1	8g	0.75	0.487	0.25

† The data was originally reported using non-standard coordinates (x → x, y → z and z → −y), which were converted to standard coordinates for ease of comparison to the data reported in the current study.

structure in space group $Pm\bar{3}m$ proceeds via an intermediate phase, which is believed to be tetragonal in space group $P4/mmm$. However, as with many of the studies relating to Li_2OHCl, detailed crystallographic information was not provided for any of the structures proposed by Song *et al.*[218] Hence, it is challenging to confirm these claims as the structural models proposed cannot be generated and validated against experimental data.

As stated earlier, Hanghofer and co-workers have published a study in which they investigated the structure of barium-doped "Li_3OCl" and Li_2OHCl

via X-ray and NPD.[210] Samples of Li_2OHCl were synthesised at 400 °C, and two different dwell times were tested. One sample was heated for 30 minutes, whilst another was cooled immediately after reaching 400 °C. The sample heated for 30 minutes was reported to adopt a cubic structure in space group $Pm\bar{3}m$ at room temperature, whereas the sample immediately cooled adopted an orthorhombic structure. The sample with the cubic structure was not discussed in any great detail, whereas the sample exhibiting an orthorhombic structure was studied extensively via VT NPD. Indexing the NPD pattern obtained at 300 K produced an orthorhombic unit cell with lattice parameters a = 7.74574 Å, b = 7.99730 Å and c = 3.82298 Å. These lattice parameters are in agreement with those reported previously by Schwering *et al.*[213] and appear to correspond to a 2a × 2b × c configuration when compared to the $Pm\bar{3}m$ unit cell of Li_3OCl and Li_2OHCl. Analysis of the extracted intensities by Hanghofer *et al.*, indicated that Li_2OHCl most likely adopts a primitive unit cell as *C*- *F*- and *I*- centred orthorhombic cells were not suitable.[210]

During the study, Hanghofer *et al.* tested numerous space groups to determine the room-temperature structure of Li_2OHCl.[210] They found that their data could be refined reasonably well using several different space groups, including *Amm*2, *Cmcm*, *Pmma*, *Pmm*2, *Pmmm* and *Pban*. This explains the confusion surrounding the structure of the room-temperature phase of Li_2OHCl. Structural models in space groups *Pmmm* and *Pban* were reported to provide particularly good fits for their NPD data. The structural model in space group *Pban* was favoured as the authors reasoned that it provided a better description of the Li positions when compared to the *Pmmm* model and a sample composition of $Li_{2.00}OH_{1.00}Cl$ was reported. Moreover, they reported that when Li_2OHCl is cooled to 4 K, the structure remains orthorhombic in space group *Pban* and an additional Li site appears. An additional Li site was also reported for the *Pmmm* structure at 4 K. However, this was not discussed in any great detail by Hanghofer *et al.*[210] Hence, the precise nature and cause of the structural changes taking place at low temperatures are not known. The structures proposed in space groups *Pmmm* and *Pban* at 300 and 4 K are shown in Figure 4.3, and the corresponding crystallographic details are listed in Table 4.3.

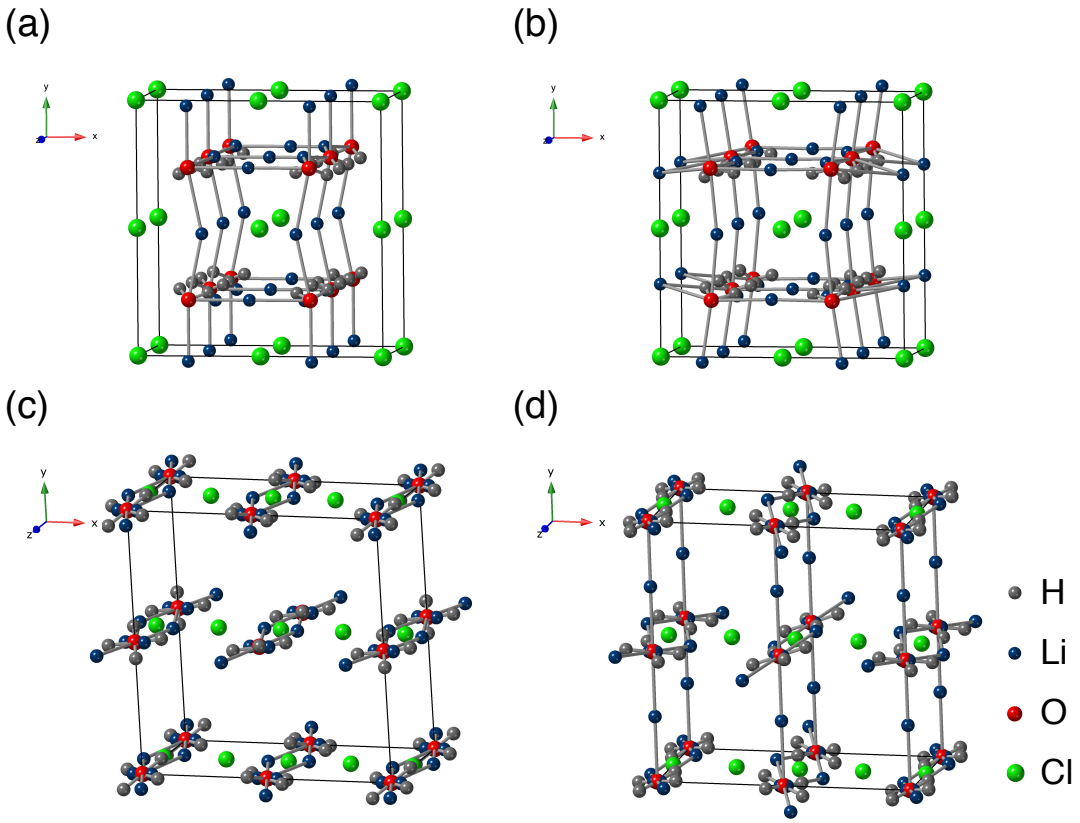

Figure 4.3: The structures of Li_2OHCl proposed by Hanghofer and co-workers in space groups (a,b) *Pmmm* and (c,d) *Pban* at (a,c) 300 and (b,d) 4 K.[210]

Table 4.3: Crystallographic details for the orthorhombic phase of Li_2OHCl (in space groups *Pmmm* and *Pban*) proposed by Hanghofer and co-workers.[210] Space group *Pmmm*: T = 300 K, a = 7.74898 Å, b = 8.00215 Å and c = 3.82511 Å. T = 4 K, a = 7.69718 Å, b = 7.99502 Å and c = 3.77307 Å. Space group *Pban*: T = 300 K, a = 7.74898 Å, b = 8.00248 Å and c = 3.82528 Å. No information regarding the lattice parameters was reported for the *Pban* structure at 4 K.

Atom	Wyckoff	x	y	z	Occ.	U(iso) × 100 (Å^2)†
Pmmm						
300 K						
Li1	2j	0.2480	0	0.5	0.250	3.55
Li2	2l	0.3077	0.5	0.5	0.250	1.18
Li3	2p	0.5	0.2410	0.5	0.228	4.94
Li4	4y	0.3178	0.2189	0	0.263	0.89
O1	4z	0.2517	0.2413	0.5	0.500	1.63
H1	8α	0.1974	0.2750	0.2880	0.253	4.43
H2	8α	0.3185	0.2640	0.3620	0.253	4.43
Cl1	1a	0	0	0	0.125	2.05
Cl2	1b	0.5	0	0	0.125	1.85
Cl3	1e	0	0.5	0	0.125	3.14

Cl4	1f	0.5	0.5	0	0.125	1.08
Pmmm						
4 K						
Li1	2j	0.2129	0	0.5	0.250	0.86
Li2	2l	0.2770	0.5	0.5	0.250	4.69
Li3	2p	0.5	0.2470	0.5	0.219	4.69
Li4	4y	0.3148	0.2390	0	0.255	4.69
Li5	2m	0	0.2830	0	0.154	4.69
O1	4z	0.2521	0.2426	0.5	0.500	2.33
H1	8α	0.2133	0.2840	0.3128	0.222	1.52
H2	8α	0.3389	0.2630	0.3852	0.222	1.52
Cl1	1a	0	0	0	0.125	1.53
Cl2	1b	0.5	0	0	0.125	1.33
Cl3	1e	0	0.5	0	0.125	0.73
Cl4	1f	0.5	0.5	0	0.125	3.50
Pban						
300 K						
Li1	4g	0.0373	1	0	0.500	3.08
Li2	4i	1	−0.0049	0	0.218	4.66
Li3	8m	0.0741	0.0037	0.4540	0.297	3.76
O1	4e	0	0	0	0.500	2.08
H1	8m	0.0834	0.0016	0.1296	0.244	3.12
H2	8m	0.0399	0.4681	0.2168	0.244	3.12
Cl1	2d	1	1	0.5	0.250	3.03
Cl2	2c	0.75	1	0.5	0.250	1.28
Pban						
4 K						
Li1	4g	0.0136	1	0	0.500	1.71
Li2	4i	1	−0.0041	0	0.188	1.71
Li3	8m	0.0867	0.0367	0.4750	0.261	1.71
Li4	2b	1	0.75	0	0.052	1.71
O1	4e	0	0	0	0.500	1.61
H1	8m	0.0895	0.0209	0.1220	0.252	1.63
H2	8m	0.0459	0.4870	0.1960	0.252	1.63
Cl1	2d	1	1	0.5	0.250	3.09
Cl2	2c	0.75	1	0.5	0.250	0.37

† The thermal coefficients were originally reported as B(iso) values, which were converted to U(iso) for ease of comparison to the data reported in the current study.

The aim of this investigation was to synthesise a phase pure sample of Li_2OHCl and accurately determine the structure of the room-temperature phase. The reported phase transition to cubic symmetry ($Pm\bar{3}m$) has also been studied. Samples of Li_2OHCl have been prepared both via conventional solid-state and mechanical milling methods. X-ray and neutron powder diffraction experiments, in conjunction with multinuclear SSNMR experiments, have been completed to gain an insight into the structure of Li_2OHCl. The resulting findings are discussed in the following sections.

4.2 Experimental

4.2.1 Synthesis

Samples of Li_2OHCl

The synthetic methods previously detailed in Chapter 3 have also been used to synthesise samples of Li_2OHCl. All samples were prepared using stoichiometric amounts of LiCl (Alfa Aesar, Ultra dry, 99.99%) and LiOH (Acros Organics, anhydrous, 98%). The reagents were mixed and ground in an agate mortar and pestle inside an Ar-filled glovebox. The powdered sample was placed in a zirconia crucible and heated at 350 °C for 30 mins. A sample of Li_2OHCl was also prepared via mechanical milling methods, using a Retsch PM100 ball mill, where the reagents were milled at 500 rpm for 9 hrs. A sample of Li_2OHCl was deuterated for ^2H NMR experiments using the glovebox procedure outlined above, and the deuterated starting reagent LiOD. Exactly the same reaction conditions were used for the deuterated and non-deuterated samples. ^2H NMR spectroscopy was used to confirm that the samples had been successfully deuterated. This was done by acquiring a ^2H NMR signal with a relatively good signal-to-noise ratio. The ^2H MAS NMR spectrum acquired for LiOD is shown in the Appendix (Figure A2).

To prepare LiOD, 5 g of LiOH (Acros Organics, anhydrous, 98%) was mixed with 5 ml of D_2O (Sigma-Aldrich, 99.9 atom% D) inside a round bottom

flask to allow the protons to be exchanged for deuterons. The solution was heated at 110 °C for 1 hr whilst stirring continuously using a magnetic stirrer and a hotplate. The flask was allowed to cool to room temperature after all the water had evaporated. The flask was then connected to a Schlenk line and evacuated to 10^{-3} mbar for 12 hrs to dry the reagent completely. The flask was then sealed and taken inside an Ar-filled glovebox. An XRD pattern obtained for LiOD was identical to that of LiOH, indicating that no unexpected changes had occurred during the deuteration process. The XRD pattern is shown in the Appendix (Figure A1).

Samples of Li_2OHCl used for NPD Experiments

Deuterated samples of Li_2OHCl used for NPD experiments via HRPD at ISIS Neutron and Muon Source, Oxford, UK (*vide supra*), were prepared by our collaborator, Dr Theodosis Famprikis (Professor Christian Masquelier Group) at Université de Picardie Jules Verne (UPJV), Laboratoire de Réactivité et de Chiemie des Solids (LRCS), Amiens, France.

A deuterated sample of Li_2OHCl was synthesised using LiCl and LiOD, and a 5% excess of LiOD was used to ensure that no residual LiCl remained in the sample. The reagents were ground together thoroughly using a mortar and pestle inside an Ar-filled glovebox. The reagent mixture was then pressed into a pellet, placed in a gold crucible, and sealed inside a steel reactor using a copper gasket. The steel reactor was then placed inside a furnace and heated at 350 °C for 6 hrs and then cooled to 250 °C in 100 mins and held there for 18 hrs. The sample was then cooled to room temperature in ~2 hrs. A deuterated sample of Li_2OHCl was also produced via mechanical milling. The reagents were initially ground together using a mortar and pestle inside an Ar-filled glovebox, and the resulting mixture was sealed inside a ZrO_2 milling jar. The reagent mixture was milled at 500 rpm for 15 hrs using a planetary ball mill (Pulverisette 7 premium, Fritsch). The corresponding XRD patterns are shown in the Appendix (Figure A4).

LiOD was prepared using lithium metal and water as precursors as

follows:

$$Li + 2D_2O \longrightarrow LiOD{\cdot}D_2O + \frac{1}{2}D_2. \tag{4.1}$$

In order to remove any dissolved gases (N_2, O_2, CO_2 etc.) D_2O was bubbled with argon gas for 30 mins. Additionally, the surface layer of Li metal was removed inside an Ar-filled glovebox to remove any impurities such as nitride, hydroxide, carbonate etc. The lithium metal was then sealed inside a reaction flask and removed from the glovebox. The flask was then placed inside an ice bath and D_2O was added slowly using a syringe. The H_2/D_2 gas generated during the reaction was allowed to escape via an oil bubbler. A 3-fold stoichiometric excess of D_2O was required to form a slurry that was stirred overnight to complete the reaction. Subsequently, the slurry was placed in a heat bath at 120 °C to remove any supernatant water. The precipitated $LiOD{\cdot}D_2O$ was then scraped off and placed inside a vacuum oven (Büchi) which was evacuated to 10^{-3} mbar. The reagent was heated at 200 °C for 3 hrs for dehydration. The corresponding XRD patterns are shown in the Appendix (Figure A3).

4.2.2 X-ray Diffraction

All samples were ground using an agate mortar and pestle and packed into 0.7 mm special glass capillaries, inside an Ar-filled glovebox. All XRD patterns were recorded on a Bruker d8 diffractometer using Mo (λ = 0.71073 Å) radiation. All scans were acquired for $2\theta = 5 - 45°$, with a step size of 0.01° and a step time of 2 seconds. During all scans, the capillary was continually rotated at 60 rpm to reduce the effects of preferred orientation. VT XRD patterns were also acquired using a Bruker d8 diffractometer, where the temperature was increased at 2 °C per hr from 25 to 50 °C, whilst continuously recording the diffraction pattern. The experimental temperatures were controlled via an Oxford Cryosystems Cryostream and set using the Cryopad control software. Rietveld analysis was performed using the GSAS-II software.[150] Parameters including the background coefficients, lattice parameters, isotropic thermal coefficients and the profile coefficients were refined.

4.2.3 Neutron Powder Diffraction

For neutron diffraction experiments, deuterated samples of Li_2OHCl were prepared by our collaborator, Dr Theodosis Famprikis. The samples were synthesised using either a solid-state melt method or mechanical milling and were analysed using HRPD at ISIS Neutron and Muon Source, Oxford, UK. The samples were packed into a 5 mm aluminium-framed slab can with vanadium windows. The body of the can and fixing screws were masked with Cd foil, and the can containing the Li_2OHCl sample was sealed using gold wire, whereas the can containing the mechanically-milled Li_2OHCl was sealed using indium wire. The can was then mounted into a top-loading Closed Cycle Refrigerator (CCR) and diffraction patterns were recorded at temperatures ranging from −263.15 °C (10 K) to 300 °C (573 K). Specific details regarding the number of counts acquired are provided in the relevant figure captions. Rietveld analysis was performed using the GSAS-II software.[150] Parameters including the background coefficients, instrumental parameters, lattice parameters, isotropic thermal factors, atomic positional coordinates and the profile coefficients were refined.

4.2.4 Solid-State NMR

All solid-state NMR spectra were acquired using a Bruker 500 Avance III HD spectrometer, equipped with a wide-bore 11.7 T Oxford magnet, using Larmor frequencies of 499.69 MHz for ^{1}H (I = 1/2), 194.20 MHz for ^{7}Li (I = 3/2) and 49.00 MHz for ^{35}Cl (I = 3/2). Powdered samples were packed into conventional 4.0 mm ZrO_2 rotors under an Ar atmosphere and placed into a Bruker 4.0 mm HX probe. ^{1}H chemical shifts were referenced to neat tetramethylsilane, by setting the resonance from a sample of adamantane to δ_{iso} = 1.9 ppm. ^{7}Li and ^{35}Cl chemical shifts were referenced to 1 M $LiCl_{(aq)}$ and 1 M $NaCl_{(aq)}$, respectively. Standard VT ^{1}H, ^{7}Li and ^{35}Cl MAS NMR experiments were completed between 33 and 52 °C using conventional hardware. Static ^{7}Li NMR experiments, completed at 24 and 54 °C, were undertaken using a Bruker 400 Avance III HD spectrometer, equipped with a wide-bore 9.7 T magnet, using a Larmor frequency of 155.5 MHz for ^{7}Li. The sample was packed into a

5.0 mm ceramic rotor inside an Ar-filled glovebox and placed into a Bruker 5.0 mm static-HX probe.

Typically, a broad background signal is observed in the ^{1}H MAS NMR spectra of samples with a low concentration of ^{1}H, as is the case for Li2OHCl samples. To overcome this, a "depth" pulse sequence was used for background suppression. Hence, ^{1}H MAS NMR spectra were acquired using a background suppression (DEPTH)[197] experiment with typical $\pi/2$ and π pulse lengths of 4 and 8 μs, respectively. Conventional ^{7}Li MAS NMR spectra were obtained using a single-pulse experiment with a typical pulse length of 1.5 μs. During acquisition, proton-decoupling was applied using SPINAL-64,[198] with a RF field of 32 kHz. Typical RF fieldstrengths of 62 – 166 kHz were employed. ^{35}Cl MAS NMR spectra were acquired using a hahn-echo ($90°_{x} - \tau - 180°_{y} - \tau$) experiment with a pulse length of 4 μs. Specific details regarding the recycle delays and MAS rates used are provided in the relevant figure captions. In all cases, quoted temperatures have been calibrated and reflect the true temperature of the sample during the experiment. Selected NMR spectra were fitted using the SOLA tool in Topspin 4.0.

Temperature Calibration

During a NMR experiment, the set temperature rarely reflects the true temperature of a sample, especially under MAS conditions as spinning generates additional heat. Hence, to determine and monitor the true temperature of the sample, a temperature calibration was completed for the 4 mm probe using neat methanol. ^{1}H MAS NMR spectra were acquired at temperatures ranging from 25 to 100 °C. The ^{1}H MAS NMR spectrum for neat methanol consists of two ^{1}H signals, and the chemical shift of the two signals is temperature dependent.[219] The chemical shift difference between the two signals was measured, and the true temperature was calculated using the following equation,

$$T = 409.0\ K - 36.54\ K \times(\Delta\delta(ppm)) - 21.85\ K \times(\Delta\delta(ppm))^{2}\ . \qquad (4.2)$$

The temperature calibration curve obtained shows a linear relationship (y = 1.0852x + 8.23) between the actual and set temperature (Figure A5). This tem-

perature calibration was therefore used to determine the true sample temperature during all variable-temperature SSNMR experiments.

4.3 Results and Discussion

4.3.1 Li_2OHCl

4.3.1.1 Synthesis of Li_2OHCl and the Phase Transition

In a similar manner to the LiRAPs discussed earlier, Li_2OHCl is known to be hygroscopic. Hence, air-sensitive methods are required for its synthesis. In this study, Li_2OHCl was synthesised under an inert atmosphere using a muffle furnace inside an Ar-filled glovebox. The whole sample preparation process, including the mixing of reagents and heating, was completed inside a glovebox. Li_2OHCl was synthesised by grinding together stoichiometric amounts of LiCl and LiOH and heating the reagent mixture at 350 °C for 30 mins, as per the reaction conditions reported in the literature.[196] In a similar manner to Li_3OCl, the sample was heated at a temperature higher than the melting point of the desired phase and Li_2OHCl was crystallised from the melt. The XRD pattern obtained for a sample of Li_2OHCl prepared using this method is shown in Figure 4.4. Also shown for comparison are the diffraction patterns of the starting materials, LiCl and LiOH. An initial inspection of the diffraction pattern indicates it is quite different from the diffraction patterns of the starting materials, indicating that a reaction has taken place. When the patterns are compared there appear to be reflections corresponding to LiCl, suggesting the presence of residual LiCl in the sample. However, there are no reflections corresponding to LiOH. At this point, it was challenging to confirm the precise composition of the sample produced, as the structure of the room-temperature phase of Li_2OHCl has not been confirmed.

As previously discussed, Li_2OHCl is known to undergo a phase transition to cubic symmetry ($Pm\bar{3}m$) upon heating and this high-temperature phase has been extensively studied.[213–216,218] Hence, in order to confirm the identity of the sample produced in this study, a VT XRD experiment was completed where the sample temperature was slowly increased from 30 to 50 °C. The

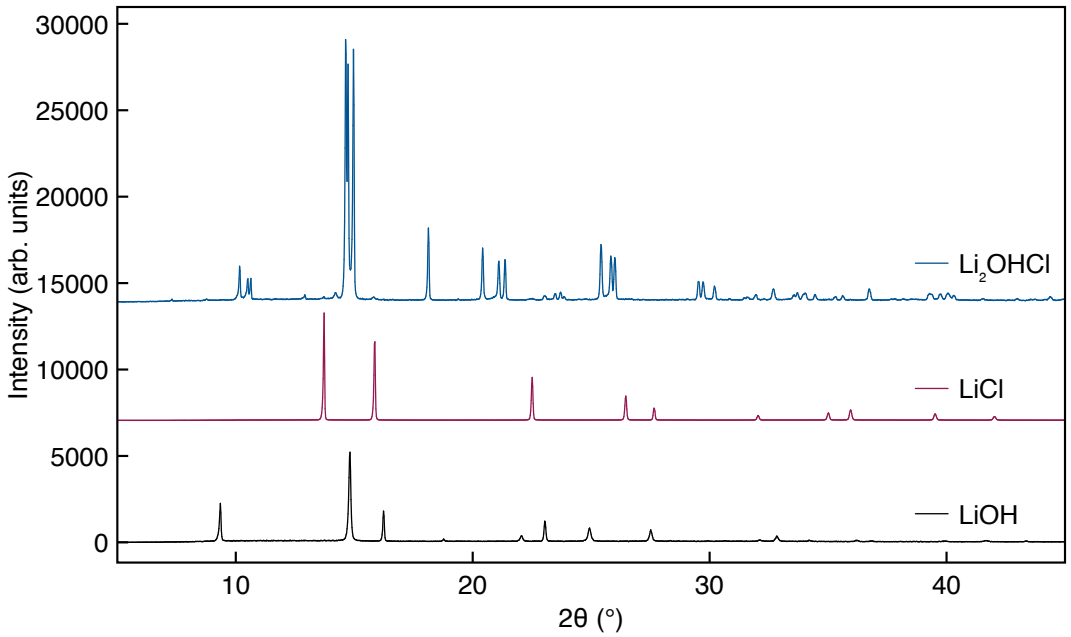

Figure 4.4: X-ray diffraction pattern obtained for a sample of Li_2OHCl synthesised via a conventional solid-state reaction completed inside an Ar-filled glovebox. The reaction temperature was 350 °C and the reaction time was 30 mins. Also shown for comparison are the diffraction patterns obtained for the reagents LiCl and LiOH.

corresponding XRD patterns are shown in Figure 4.5. The patterns acquired at 30 and 35 °C appear identical, indicating that no structural change occurs between these temperatures. As the temperature increases to 40 °C fewer reflections are observed. As the temperature is increased further to 45 °C and then 50 °C fewer reflections are again observed. The patterns obtained at 45 and 50 °C are the same, indicating the phase transition has occurred. These observations indicate that, in this sample, the phase transition starts at 35 °C and is complete at 45 °C. This is in agreement with the literature reported thus far.[213–216,218] The diffraction pattern obtained at 50 °C contains far fewer reflections than that at 30 °C, which is in line with an increase in symmetry. Hence, it is likely the sample is Li_2OHCl as it is known to adopt a cubic structure at high temperatures.

The XRD pattern obtained at 50 °C was analysed via a multiphase Rietveld refinement using the $Pm\bar{3}m$ (Li_2OHCl) and $Fm\bar{3}m$ (LiCl) structural models.[199,210] The $Pm\bar{3}m$ model reported by Hanghofer *et al.* has been used to refine the Li_2OHCl phase as it contains crystallographic information regarding the

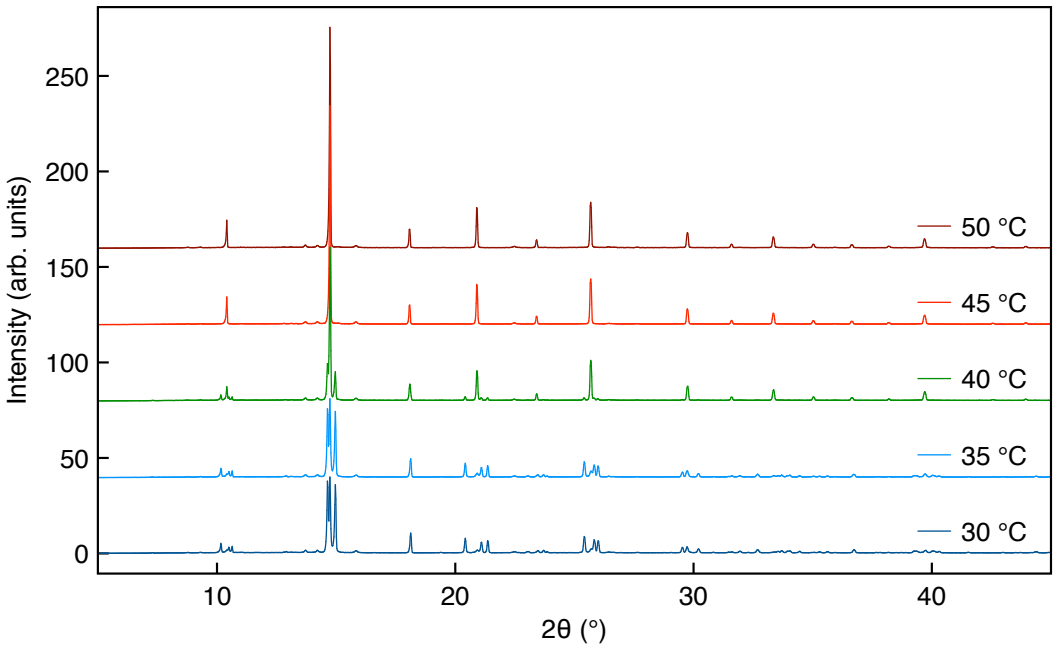

Figure 4.5: X-ray diffraction patterns obtained for a sample of Li_2OHCl during a variable-temperature study in which the temperature was gradually increased from 30 to 50 °C. The sample was synthesised via a conventional solid-state reaction completed inside an Ar-filled glovebox. The reaction temperature was 350 °C and the reaction time was 30 mins.

protons.[210] The thermal coefficients of O and H were constrained to be equivalent, as is commonly done for hydroxyl groups when refining laboratory XRD data. The refinement is shown in Figure 4.6, and the corresponding structural parameters are detailed in Table 4.4. A χ^2 = 2.77 and a wR_p = 10.71% are indicative of a very good fit. This appears to confirm that the sample prepared is indeed that of Li_2OHCl, as the diffraction pattern obtained after the phase transition can be indexed using the $Pm\bar{3}m$ structural model, in good agreement with the literature.[213–216] A lattice parameter of 3.91854(2) Å was obtained for Li_2OHCl, which is again in good agreement with values previously reported in the literature.[213–216] As the sample contains two phases, Li_2OHCl and LiCl, phase fractions were refined to determine the relative quantity of each phase. The sample contains 99.44(3)% of the desired Li_2OHCl and 0.56(3)% of residual LiCl. Hanghofer *et al.*, also reported the presence of LiCl as an impurity in Li_2OHCl samples.[210] Thus, suggesting that obtaining a completely phase pure sample of Li_2OHCl is somewhat challenging. However, when compared to our synthetic efforts for the non-hydrated Li_3OCl this is considerably bet-

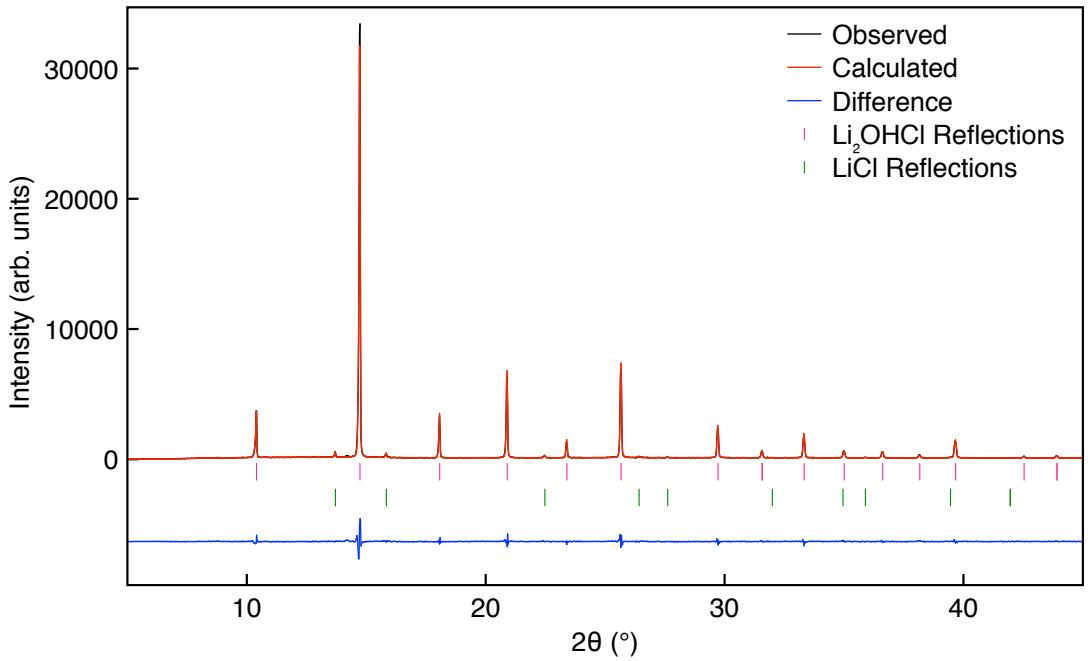

Figure 4.6: A multiphase refinement of the XRD data obtained for a sample of Li_2OHCl at 50 °C, using the $Pm\bar{3}m$ (Li_2OHCl)[210] and $Fm\bar{3}m$ (LiCl)[199] structural models. The sample was synthesised via a conventional solid-state reaction completed inside an Ar-filled glovebox. The reaction temperature was 350 °C and the reaction time was 30 mins. χ^2 = 2.77, wR_P = 10.71%, R_P = 8.15%.

Table 4.4: Structural parameters for a sample of Li_2OHCl at 50 °C, obtained from Rietveld refinement of the XRD data using isotropic thermal coefficients. The sample was synthesised via a conventional solid-state reaction completed inside an Ar-filled glovebox. Li_2OHCl: space group $Pm\bar{3}m$, a = 3.91854(2) Å, V = 60.169(1) Å^3, phase fraction = 99.44(3)%. LiCl: space group $Fm\bar{3}m$, a = 5.15728(36) Å, V = 137.171(29) Å^3, phase fraction = 0.56(3)%. χ^2 = 2.77, wR_P = 10.71%, R_P = 8.15%.

Atom	x	y	z	Occ.	U(iso) × 100 (Å^2)
Li_2OHCl					
Li	0.5	0	0	0.667	7.45(21)
O	0	0	0	1	2.43(6)
H	0.1279	0.1279	0.1279	0.125	2.43(6)
Cl	0.5	0.5	0.5	1	2.88(3)
LiCl					
Li	0	0	0	1	3.08(189)
Cl	0.5	0.5	0.5	1	2.55(47)

ter, as the sample is predominantly composed of the desired phase. It is noted that the VT XRD data and the Rietveld analysis of the diffraction pattern obtained at 50 °C demonstrate that Li_2OHCl *gradually* transitions from the room temperature phase to a cubic phase in space group $Pm\bar{3}m$. Earlier, it was mentioned that Song and co-workers propose that this phase transition occurs via an intermediary tetragonal phase.[218] However, the findings presented in this study contrast those of Song *et al.*,[218] as no intermediary phase is observed via XRD. Interestingly, Song *et al.*[218] report the formation of a small amount of LiCl upon gradually heating Li_2OHCl from 26 to 60 °C to observe the phase transition. The formation of LiCl was found to be irreversible, and LiCl was still present upon cooling the sample. According to a computational study by Lu and co-workers,[132] defects based on LiCl vacancies would be the most energetically favourable in Li_3OCl. Song *et al.*[218] believe that this could also be true for Li_2OHCl. Thus, explaining the formation of LiCl upon heating the sample. This could also explain the presence of residual LiCl in the current study, especially since no residual LiOH is detected.

It is noted that the thermal coefficient obtained for Li in Li_2OHCl is quite large. Hanghofer *et al.* also reported an unusually large thermal coefficient for Li (Table 4.1).[210] This is also similar to the refinements presented earlier in Chapter 3 where unusually large thermal coefficients were obtained for Li in Li_3OCl and Li_3OBr. However, it is noted that, the thermal coefficient for Li in Li_2OHCl is smaller than that obtained for Li in Li_3OCl and Li_3OBr. Earlier, it was suggested that possible causes could include Li-ion mobility in the samples that is being interpreted as thermal motion during the refinement. This could also be occurring here as Li_2OHCl is a known Li-ion conductor, and therefore, is likely to exhibit some Li-ion mobility. As discussed previously, Zhao and Daemen have suggested that Li_3OCl/Br is pseudo-cubic.[124] As Li_2OHCl is analogous to Li_3OCl, the same could also be true for Li_2OHCl, resulting in unusual parameters. However, no such suggestions are made for Li_2OHCl in the literature. In addition to this, the XRD data used for the refinement was obtained at 50 °C, where the atoms are likely to exhibit an increased degree of thermal motion. Additionally, constraining the thermal co-

efficients for O and H could also have an impact on the thermal coefficients corresponding to other atoms in the system. However, refining the coefficients freely for all atoms returned an unreasonably large coefficient for H. Moreover, it must be noted that in the current refinement, the thermal motion is being treated as isotropic, whereas, in reality, the thermal motion is most likely to be anisotropic. However, laboratory XRD data is not of sufficient quality to obtain anisotropic thermal coefficients. Lastly, it is noted that the thermal coefficient obtained for Li in LiCl has a large error. This may be because LiCl is present in a very small quantity, making it challenging to accurately determine the thermal coefficients. It could also be due to the large thermal coefficient obtained for Li in Li_2OHCl that is affecting the value obtained for Li in LiCl.

Finally, it is noted that there are low intensity reflections at 2θ = 8.78 and 14.21° that do not correspond to the desired phase or the starting materials, LiCl and LiOH. Thus, suggesting the presence of an impurity phase in the sample, albeit in a very small quantity. These reflections are present in all the diffraction patterns shown in Figure 4.5. This suggests that, in a similar manner to the residual LiCl, the impurity phase also remains unchanged with increasing temperature. As the intensities of these peaks are extremely low, it is challenging to investigate the nature of the impurity phase any further. However, this does imply that the phase fractions calculated during the refinement are not fully correct, as the refinement did not account for the presence of an impurity phase. Hence, the actual phase fractions will likely vary slightly from the values stated.

4.3.1.2 The Room-Temperature Phase of Li_2OHCl

As previously discussed, the structure of the room-temperature phase of Li_2OHCl has not yet been confirmed, although several suggestions have been made. To investigate the structure of the room-temperature phase, the models proposed in the literature were used to refine the laboratory XRD data obtained in this study. Unfortunately, the *Amm*2 model proposed by Schwering *et al.*,[213] and the *Pmmm* and *P*4/*mmm* models proposed by Song *et al.*,[218] could not be evaluated as complete crystallographic details were not reported,

meaning that a suitable cif could not be generated to test these models. However, the *P*4*mm*, *Pmc*2_1 and *Cmcm* models reported by Howard *et al.*,[216,217] and the *Pmmm* and *Pban* models reported by Hanghofer *et al.*,[210] have all been tested.

Initially, the XRD data for Li_2OHCl obtained at room temperature was refined using the *P*4*mm* model reported by Howard *et al.*, for the ground state tetragonal structure of Li_2OHCl.[216] The refinement is shown in Figure 4.7. It is noted that, in order to simplify the refinement and focus on Li_2OHCl, the reflections corresponding to the impurity phase and LiCl were excluded and are denoted by *. For completeness, this has been done for all refinements in this section. At first, the model placed calculated reflections where there was no experimental data, requiring the lattice parameters to be heavily refined in order to index the reflections observed. In doing so, the lattice parameters a = b = 3.8712(6) Å and c = 3.9945(9) Å were obtained. Notably, these are very

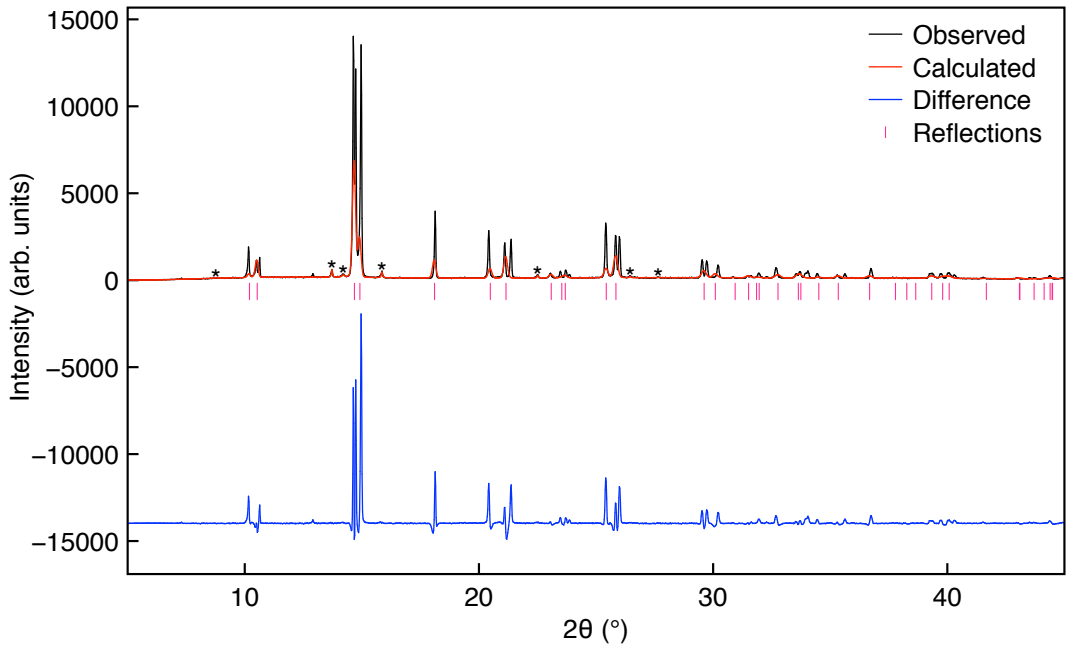

Figure 4.7: Attempted Rietveld refinement of the XRD data obtained for a sample of Li_2OHCl, synthesised via a conventional solid-state reaction completed inside an Ar-filled glovebox, using the *P*4*mm* structural model proposed by Howard *et al.*[216] The reaction temperature was 350 °C and the reaction time was 30 mins. Reflections corresponding to an unidentified impurity phase and LiCl were excluded and are denoted by *. a = b = 3.8712(6) Å, c = 3.9945(9) Å, V = 59.862(17) Å^3. χ^2 = 67.62, wR_P = 49.25%, R_P = 36.24%.

different from those originally reported (a = b = 3.794 Å and c = 3.578 Å) by Howard *et al.*[216] Unfortunately, not all reflections were indexed. Thus, suggesting that the model is not fully correct. Therefore, no additional parameters, *i.e.*, the fractional occupancies or thermal coefficients were refined and they were fixed at 1 and 2.5×10^{-2} Å^2, respectively, for all atoms. Attempts to refine these parameters did not result in sensible values. Unsurprisingly, the fit obtained is quite poor. Hence, this model could not be used to describe the structure of the room-temperature phase of Li_2OHCl. This seems to be in agreement with Howard *et al.*, that the ground state tetragonal structure is not observed experimentally.[216]

In the same study, Howard *et al.* also reported the orthorhombic $Pmc2_1$ model, and stated that it provided a good fit for their XRD data.[216] Hence, it was also used here to complete the Rietveld refinement of the XRD data for Li_2OHCl. The refinement is shown in Figure 4.8, and the corresponding structural parameters are detailed in Table 4.5. In this case, a reasonably good fit is obtained with a χ^2 = 5.86 and wR_p = 14.49%. All of the major reflections observed in the diffraction pattern can be indexed using this model, suggesting that $Pmc2_1$ is a promising model for describing the room-temperature structure of Li_2OHCl. However, it must be noted that some of the lower intensity reflections at 2θ = 7.30 and 12.90° have not been indexed. Additionally, the reflection at 2θ = 15.83° that has been indexed is believed to correspond to the starting material LiCl. Moreover, the calculated intensity for a number of reflections does not match with the experimental data. This could be suggesting inaccuracies in the atomic positions reported. However, as discussed previously, it is quite challenging to detect lighter atoms such as Li and H via laboratory XRD. Hence, the atomic coordinates were not refined as it would be difficult to obtain reliable values. The lattice parameters obtained (a = 3.87987(7) Å, b = 3.83163(7) Å and c = 8.01418(14) Å) are in general agreement with those initially reported (a = 3.831 Å, b = 3.617 Å and c = 7.985 Å). It is noted that parameter b exhibits a slight variation from the reported value. However, such differences are not unexpected when comparing calculated models proposed in computational studies with experimental data. Lastly, the thermal coefficients

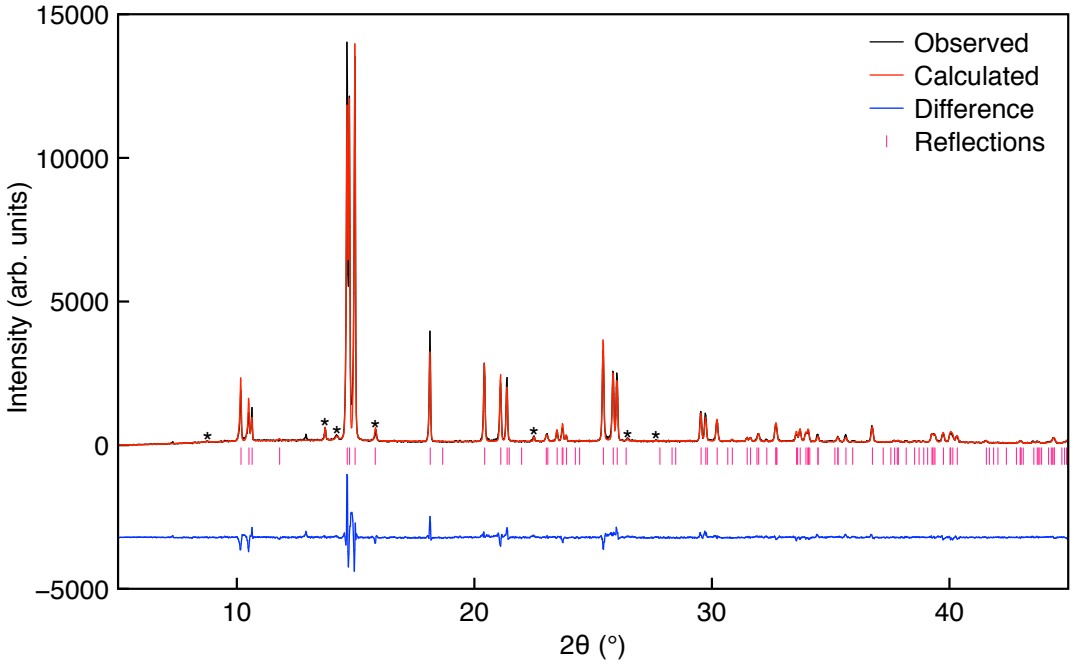

Figure 4.8: Rietveld refinement of the XRD data obtained for a sample of Li_2OHCl, synthesised via a conventional solid-state reaction completed inside an Ar-filled glovebox, using the $Pmc2_1$ structural model proposed by Howard *et al.*[216] The reaction temperature was 350 °C and the reaction time was 30 mins. Reflections corresponding to an unidentified impurity phase and LiCl were excluded and are denoted by *. χ^2 = 5.86, wR_P = 14.49%, R_P = 10.87%.

obtained for Li are very large, which could again be indicating the model is not quite right. In particular, the thermal coefficient for Li2 is extremely large with a similarly large error. The presence of such a large value on one particular

Table 4.5: Structural parameters for a sample of Li_2OHCl, synthesised via a conventional solid-state reaction completed inside an Ar-filled glovebox, obtained from Rietveld refinement of the XRD data using isotropic thermal coefficients. Li_2OHCl: space group $Pmc2_1$, a = 3.87987(7) Å, b = 3.83163(7) Å, c = 8.01418(14) Å, V = 119.141(3) Å^3. χ^2 = 5.86, wR_P = 14.49%, R_P = 10.87%.

Atom	x	y	z	Occ.	U(iso) × 100 (Å^2)
Li1	0	0.001	0.25	1	4.73(30)
Li2	0.5	0.086	0	1	29.87(136)
O1	0	−0.024	0	1	1.55(9)
H1	0	0.699	0	1	1.55(9)
Cl1	0.5	0.5	0.25	1	2.74(5)

site could be indicating structural inconsistencies with that site, *i.e.*, the symmetry around that site is not quite right in this model. However, this model is quite promising with regards to the fact that it successfully indexes many of the observed reflections and the fit obtained appears to be quite reasonable.

In a follow-up study, Howard *et al.* suggested another orthorhombic structure for Li_2OHCl, in space group *Cmcm*.[217] This model was also used to refine the XRD data. The refinement is shown in Figure 4.9 and the corresponding structural parameters are shown in Table 4.6. Again, this model appears to provide a relatively good fit with a $\chi^2 = 7.90$ and $wR_p = 16.82\%$, and can index almost all of the reflections, including those at $2\theta = 7.30$ and 12.90°, which were not indexed using the $Pmc2_1$ model. However, the calculated peak intensities do not appear to match well with those observed experimentally. Additionally, in some places, the model appears to place calculated intensities where there is no experimental data (2θ = 9.03, 11.76, 15.57, 16.58, 21.75, 24.08, 26.56,

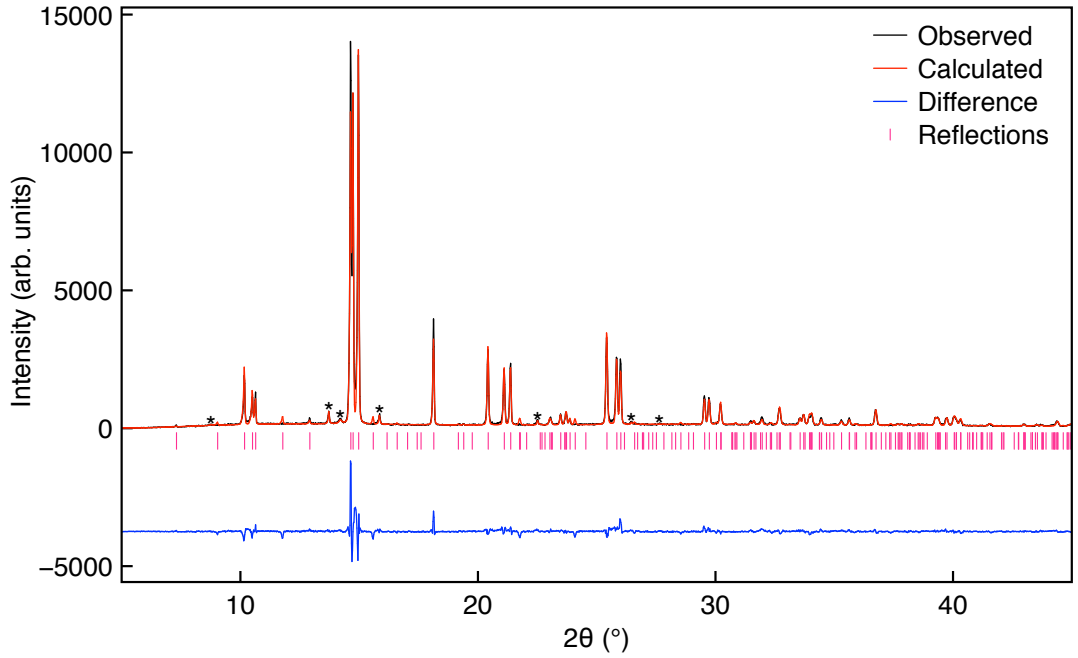

Figure 4.9: Rietveld refinement of the XRD data obtained for a sample of Li_2OHCl, synthesised via a conventional solid-state reaction completed inside an Ar-filled glovebox, using the *Cmcm* structural model proposed by Howard *et al.*[217] The reaction temperature was 350 °C and the reaction time was 30 mins. Reflections corresponding to an unidentified impurity phase and LiCl were excluded and are denoted by *. $\chi^2 = 7.90$, $wR_P = 16.82\%$, $R_P = 11.20\%$.

Table 4.6: Structural parameters for a sample of Li_2OHCl, synthesised via a conventional solid-state reaction completed inside an Ar-filled glovebox, obtained from Rietveld refinement of the XRD data using isotropic thermal coefficients. Li_2OHCl: space group *Cmcm*, a = 8.01433(16) Å, b = 7.75981(16) Å, c = 7.66315(16) Å, V = 476.569(12) Å^3. χ^2 = 7.90, wR_P = 16.82 %, R_P = 11.20%.

Atom	x	y	z	Occ.	U(iso) × 100 (Å^2)
Li1	0.25	0.25	0	1	4.03(33)
Li2	0	0.5	0	1	4.60(70)
Li3	0	0.167	0.25	1	33.76(284)
O1	0	0.747	0.510	1	1.44(11)
H1	0	0.831	0.407	1	1.44(11)
Cl1	0.75	0.487	0.25	1	2.48(6)

28.53, 30.02 and 37.37°). Thus, suggesting possible issues with the atomic coordinates and/or fractional occupancies. The lattice parameters obtained are in reasonable agreement with those reported. Moreover, in a similar manner to the *Pmc*2$_1$ model, the thermal coefficients obtained are quite large, particularly for Li3, which also has a large error. Also, it is noted that the goodness of fit is slightly lower than that obtained using the *Pmc*2$_1$ model. Hence, again, the model is good, but it is perhaps not entirely correct.

As discussed previously, Hanghofer *et al.* tested many space groups to determine the correct space group for the room-temperature phase of Li_2OHCl, and structural models in space groups *Pmmm* and *Pban* were reported as possible structures for Li_2OHCl.[210] The latter was believed to be more suitable. As stated earlier, two different structures were reported in each space group, one at 300 K and another at 4 K containing an additional Li site. In the current study, all of these models have been used to refine the XRD data for Li_2OHCl and the refinements completed using the *Pmmm* models are shown in Figure 4.10. The corresponding structural parameters obtained are detailed in Table 4.7. In the first instance, the fit obtained using the model proposed at 300 K appears to be relatively good with χ^2 = 5.17 and wR_p = 13.64%. All reflections corresponding to the desired phase are indexed. However, in a similar manner

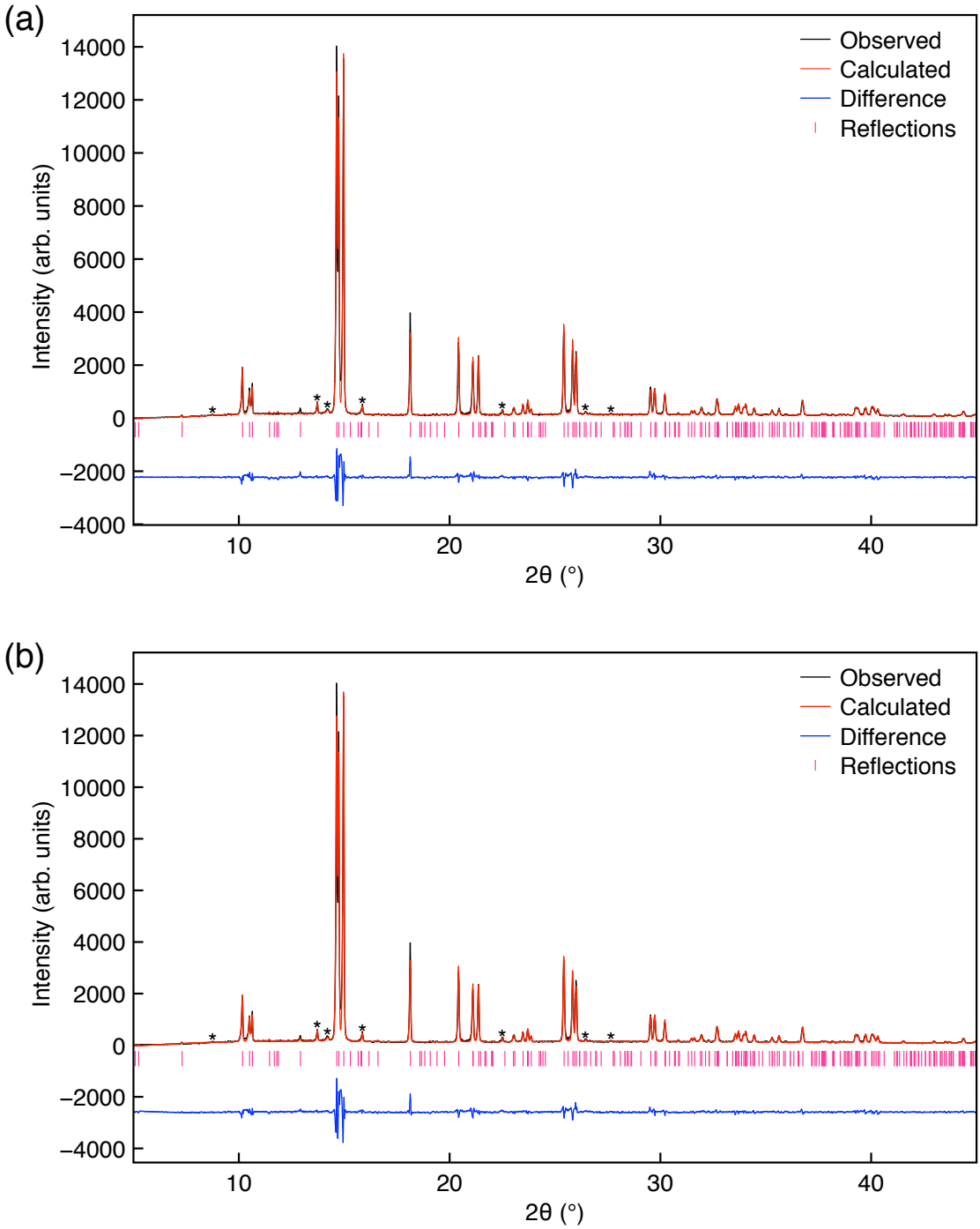

Figure 4.10: Rietveld refinement of the room temperature XRD data obtained for a sample of Li_2OHCl, synthesised via a conventional solid-state reaction completed inside an Ar-filled glovebox, using the *Pmmm* structural model proposed at (a) 300 and (b) 4 K by Hanghofer *et al.*[210] The reaction temperature was 350 °C and the reaction time was 30 mins. Reflections corresponding to an unidentified impurity phase and LiCl were excluded and are denoted by *. (a) χ^2 = 5.17, wR_P = 13.64%, R_P = 10.06%. (b) χ^2 = 5.93, wR_P = 14.57%, R_P = 10.36%.

Table 4.7: Structural parameters for a sample of Li_2OHCl, synthesised via a conventional solid-state reaction completed inside an Ar-filled glovebox, obtained from Rietveld refinement of the room temperature XRD data using isotropic thermal coefficients. Li_2OHCl: 300 K: space group *Pmmm*, a = 7.75968(13) Å, b = 8.01395(13) Å, c = 3.83160(6) Å, V = 238.271(5) Å^3. χ^2 = 5.17, wR_P = 13.64%, R_P = 10.06%. 4 K: space group *Pmmm*, a = 7.75973(13) Å, b = 8.01400(14) Å, c = 3.83162(7) Å, V = 238.275(5) Å^3. χ^2 = 5.93, wR_P = 14.57%, R_P = 10.36%.

Atom	x	y	z	Occ.	U(iso) × 100 (Å^2)
300 K					
Li1	0.2480	0	0.5	0.226(4)	2.5
Li2	0.3077	0.5	0.5	0.198(4)	2.5
Li3	0.5	0.2410	0.5	0.127(4)	2.5
Li4	0.3178	0.2189	0	0.100(4)	2.5
O1	0.2517	0.2413	0.5	0.242(1)	2.5
H1	0.1974	0.2750	0.2880	0.145(6)	2.5
H2	0.3185	0.2640	0.3620	0.007(6)	2.5
Cl1	0	0	0	0.245(1)	2.5
Cl2	0.5	0	0	0.210(1)	2.5
Cl3	0	0.5	0	0.241(1)	2.5
Cl4	0.5	0.5	0	0.228(1)	2.5
4 K					
Li1	0.2129	0	0.5	0.244(17)	2.18(44)
Li2	0.2770	0.5	0.5	0.203(17)	2.18(44)
Li3	0.5	0.2470	0.5	0.168(8)	2.18(44)
Li4	0.3148	0.2390	0	0.101(5)	2.18(44)
Li5	0	0.2830	0	0.019(7)	2.18(44)
O1	0.2521	0.2426	0.5	0.252(4)	2.45(21)
H1	0.2133	0.2840	0.3128	0.166(17)	2.45(21)
H2	0.3389	0.2630	0.3852	0.011(15)	2.45(21)
Cl1	0	0	0	0.241(3)	2.63(5)
Cl2	0.5	0	0	0.259(2)	2.63(5)
Cl3	0	0.5	0	0.261(2)	2.63(5)
Cl4	0.5	0.5	0	0.229(3)	2.63(5)

to the previous refinements, there appears to be some variation between the calculated and observed intensities of the reflections. Thus, suggesting that the model is not completely accurate. The structural parameters determined show that the lattice parameters obtained are in excellent agreement with those

initially reported. However, a detailed inspection of the crystallographic information (Table 4.3) reported by Hanghofer *et al.*[210] revealed that the reported occupancy values correspond to a sample composition of $Li_{2.508}O_2H_{4.05}Cl_{0.5}$ and not Li_2OHCl. Thus, suggesting that the sample investigated by Hanghofer *et al.*[210] may not have had the correct stoichiometry. Hence, the fractional occupancies were refined, and a sample composition of $Li_{1.502}O_{0.968}H_{1.216}Cl_{0.924}$ was obtained. This formula is not quite charge-balanced. However, it is much closer to the intended composition of Li_2OHCl. It is noted that the fractional occupancy corresponding to H2 has a relatively large error, meaning a reliable value could not be determined. This could be indicating possible inaccuracies within the structure. During the refinement, the thermal coefficients for all atoms were fixed at 2.5×10^{-2} Å^2. Attempts to refine any thermal coefficients resulted in negative (and therefore meaningless) values. Thus, suggesting possible errors within the structural model. In a similar manner to the refinements presented earlier, here too, the atomic positions were not refined as reliable values cannot be obtained using the laboratory XRD data. Overall, the refinement presented suggests that this model is unsuitable for Li_2OHCl. This is in contrast to the findings of Hanghofer *et al.*,[210] who obtained a very good fit for their NPD data using this model and were able to successfully refine the thermal coefficients (Table 4.3).

Hanghofer *et al.*[210] proposed the *Pmmm* 4 K model as a possible structure for Li_2OHCl at 4 K as they believe the structure of Li_2OHCl at very low temperatures differs from the room-temperature structure. To date, the study reported by Hanghofer *et al.*[210] is the only one to offer this suggestion. In order to confirm that an additional Li site is not present at room temperature and only appears at low temperatures, both *Pmmm* models (300 and 4 K) have been tested using the XRD data acquired at room temperature. A slightly lower goodness of fit was achieved (χ^2 = 5.93 and wR_p = 14.57%) using the *Pmmm* model proposed at 4 K when compared to the *Pmmm* model proposed at 300 K. As expected, the lattice parameters obtained are similar to those determined using the 300 K model and in excellent agreement with the reported values.[210] It is noted that the lattice parameters determined via the

XRD data obtained at room temperature can only be compared to those reported at 300 K and not 4 K. Here too, the fractional occupancies for all atoms were successfully refined, and the values obtained indicate a sample composition of $Li_{1.672}O_{1.000}H_{1.416}Cl_{0.990}$. Again, this is not quite charge-balanced, but it is closer to Li_2OHCl than the composition corresponding to the data reported by Hanghofer *et al.*[210] at 4 K ($Li_{2.766}OH_{3.552}Cl$). Unfortunately, the fractional occupancy for H2 has an error that is bigger than the actual value obtained. Additionally, the fractional occupancy for Li5 is quite low, with a relatively large error. Thus, suggesting possible errors in the model. Moreover, refining the thermal coefficients presented some difficulties, and a sensible outcome could only be obtained when multiple constraints were introduced. Alongside the thermal coefficients for O and H, those for light atoms such as Li and Cl were also constrained to be equivalent. The coefficients obtained appear to be reasonable when compared to some of the earlier refinements. Overall, this model appears to provide a reasonable fit for the XRD data, but it does not appear to be wholly accurate. Unfortunately, it is unclear whether this is due to inaccurate atomic coordinates, the absence of Li5 or if the model is altogether incorrect. Hence, it cannot be said for certain that an additional Li site only appears at low temperatures and is not already present at room temperature.

Finally, the orthorhombic *Pban* models proposed by Hanghofer *et al.*[210] were used to refine the XRD data acquired for Li_2OHCl and the "refinement" attempted using the *Pban* model proposed at 300 K is shown in Figure 4.11. Inspection of the allowed reflections indicates that there are many possible reflections allowed. The refinement was attempted, however, there were some significant issues in getting the experimental pattern to be "recognised" by the model. As a result, the refinement could not be completed as no sensible refined parameters could be obtained. Thus, suggesting that this is not a suitable structural model for Li_2OHCl. This is highly surprising as Hanghofer *et al.*[210] reported the structure in space group *Pban* as the correct model for Li_2OHCl. The crystallographic details reported by Hanghofer *et al.*[210] were examined further and two key observations were made.

Firstly, the fractional occupancies reported at 300 K by Hanghofer *et*

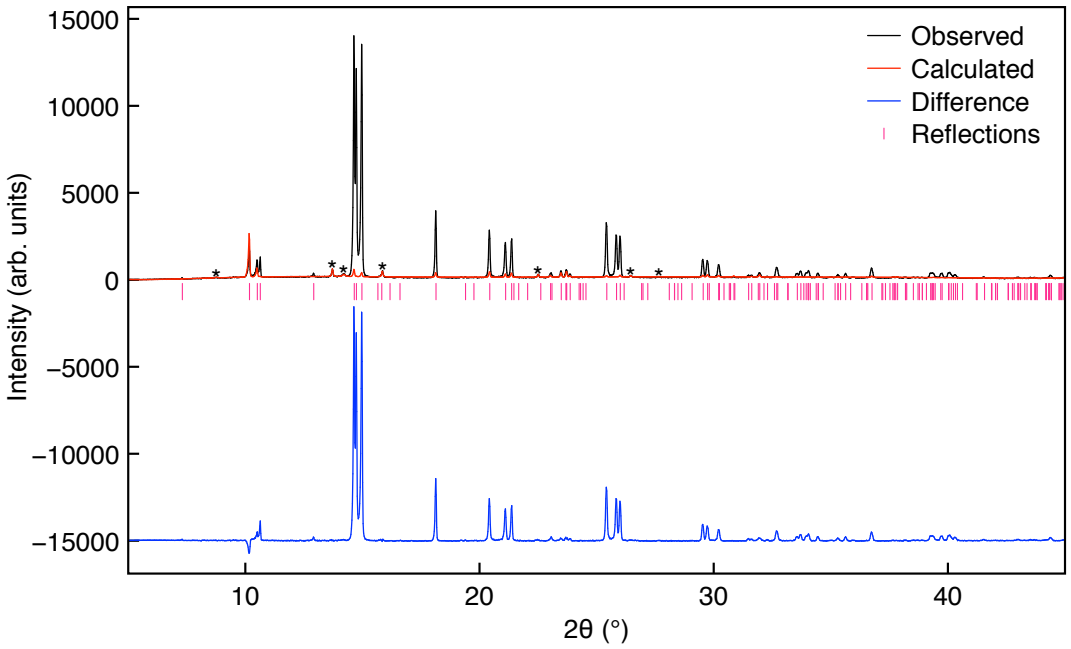

Figure 4.11: Rietveld refinement of the XRD data obtained for a sample of Li_2OHCl, synthesised via a conventional solid-state reaction completed inside an Ar-filled glovebox, using the *Pban* structural model proposed by Hanghofer *et al.* at 300 K.[210] Reflections corresponding to an unidentified impurity phase and LiCl were excluded and are denoted by *. a = 7.7582(34) Å, b = 8.0124(14) Å, c = 3.8330(16) Å, V = 238.27(14) Å^3. χ^2 = 116.68, wR_P = 64.70%, R_P = 53.65%.

al.[210] correspond to a composition of $Li_{4.1}OH_{1.952}Cl$. Interestingly, this is in contrast to the statements made in their publication, as their refinement was reported to indicate a sample composition of $Li_{2.00}OH_{1.00}Cl$. However, the crystallographic information detailed in the publication indicates otherwise. Thus, in a similar manner to the *Pmmm* models discussed earlier, the reported occupancies do not correspond to a sample composition of Li_2OHCl. Thus, further suggesting that the sample investigated by Hanghofer *et al.*[210] did not have the correct stoichiometry, in turn, making the reported crystallographic information somewhat unreliable.

Secondly, corroborating the crystallographic information reported by Hanghofer *et al.*[210] using the International Tables for Crystallography,[220] reveals that the reported atomic positions for Li1, Li2, Cl1 and Cl2 are not in agreement with the Wyckoff positions assigned for those atoms. Table 4.8 shows the allowed coordinates for the assigned Wyckoff positions along with

Table 4.8: A comparison of the atomic coordinates allowed for space group *Pban* as detailed in the International Tables for Crystallography[220] and those reported by Hanghofer and co-workers[210] for Wyckoff positions 4g, 4i, 2d and 2c.

Atom	Wyckoff	Allowed Coordinates	Reported Coordinates
Li1	4g	(x, 0.25, 0), (−x+0.5, 0.25, 0), (−x, 0.75, 0), (x+0.5, 0.75, 0)	0.0373, 1, 0
Li2	4i	(0.25, y, 0), (0.25, −y+0.5, 0), (0.75, −y, 0), (0.75, y+0.5, 0)	1, −0.0049, 0
Cl1	2d	(0.25, 0.25, 0.5), (0.75, 0.75, 0.5)	1, 1, 0.5
Cl2	2c	(0.75, 0.25, 0.5), (0.25, 0.75, 0.5)	0.75, 1, 0.5

those reported by Hanghofer *et al.*[210] It appears that an atomic position of 1 has been specified in place of 0.25. It is noted that positions such as 0.25 and 1 are special positions and therefore cannot be altered, as doing so, will produce a different structure. This was initially believed to be a typographical error. However, the "error" appears to be repeated for all 4 atoms mentioned above, as well as for the model reported at 4 K (Table 4.3). It is noted that the convention for space group *Pban* is to use the origin setting 2. For space group *Pban*, origin setting 1 denotes that the origin lies at a site with a $222/n$ symmetry and exhibits a shift of 0.25, 0.25, 0 from origin 2. Conversely, the origin setting 2 denotes that the origin lies at a site with a $\overline{1}$ symmetry and exhibits a shift of −0.25, −0.25, 0 from origin 1. The origin setting 2 allows the origin to be placed at an inversion centre which is preferable as it provides a more accurate description of the structure and makes the task of structural refinement easier. To check whether the discrepancy in the atomic positions reported by Hanghofer *et al.*[210] was due to an incorrect origin setting, the origin setting 1 was also investigated. However, in this origin setting the atomic positions reported did not agree with the assigned Wyckoff positions. Interestingly, Hanghofer *et al.*[210] stated that they used an origin setting of 2 (the standard setting for space group *Pban*). Yet, their reported crystallographic data does not appear to agree with either origin setting. It is difficult to tell whether this is a case of a repeated typographical error or whether the atomic coordinates reported by

Hanghofer *et al.*[210] are altogether incorrect.

In an attempt to refine the XRD data using the structural model in space group *Pban* with the correct crystallographic details, the model initially reported by Hanghofer *et al.*[210] was modified by altering the atomic positions for Li1, Li2, Cl1 and Cl2. The new model generated is shown in Figure 4.12(a) and the corresponding crystallographic details are listed in Table 4.9. This structure appears to be quite different from that initially proposed by Hanghofer *et al.*[210] (Figure 4.12(b)). The refinement completed using the new model generated is shown in Figure 4.13(a). The fit appears to be considerably improved, with χ^2 = 4.44 and wR_p = 12.59%, suggesting this is the best fit yet. The lattice parameters obtained are in good agreement with those initially reported by Hanghofer *et al.*[210] During the refinement, the fractional occupancies of O1, Cl1 and Cl2 were fixed at 0.25 to reflect the composition of Li_2OHCl, and the fractional occupancies of all Li and H atoms were refined. The values obtained suggest a sample composition of $Li_{1.924}OH_{1.616}Cl$. The formula is not charge-balanced but it is close to the intended composition of Li_2OHCl. Also, it is much closer to Li_2OHCl than $Li_{4.1}OH_{1.952}Cl$, which was reported by Hanghofer *et al.*[210] Unlike the previous refinement (Figure 4.11), the thermal coefficients for all atoms were successfully refined using this model. Thus, suggesting that this *Pban* model is closer to the actual structure of Li_2OHCl than the one reported by Hanghofer *et al.*[210] The thermal coefficients for O1, H1 and H2 were constrained to be equivalent. In most cases, the thermal coefficients obtained appear to be quite reasonable. However, the thermal coefficient obtained for Li2 is quite large and has a very large error, whereas the one for Li3 is rather small and has an error equal to the value obtained. Thus, suggesting some possible inaccuracies in the model. These could include inaccurate atomic positions and/or the fractional occupancies for Li2, Li3 and other atoms. Hence, it is possible that refining the atomic positions may improve the thermal coefficients and the fractional occupancies. However, atomic positions were not refined for any of the atoms as laboratory XRD data is not sufficiently reliable for this.

In a similar manner to the *Pban* model reported at 300 K, the atomic

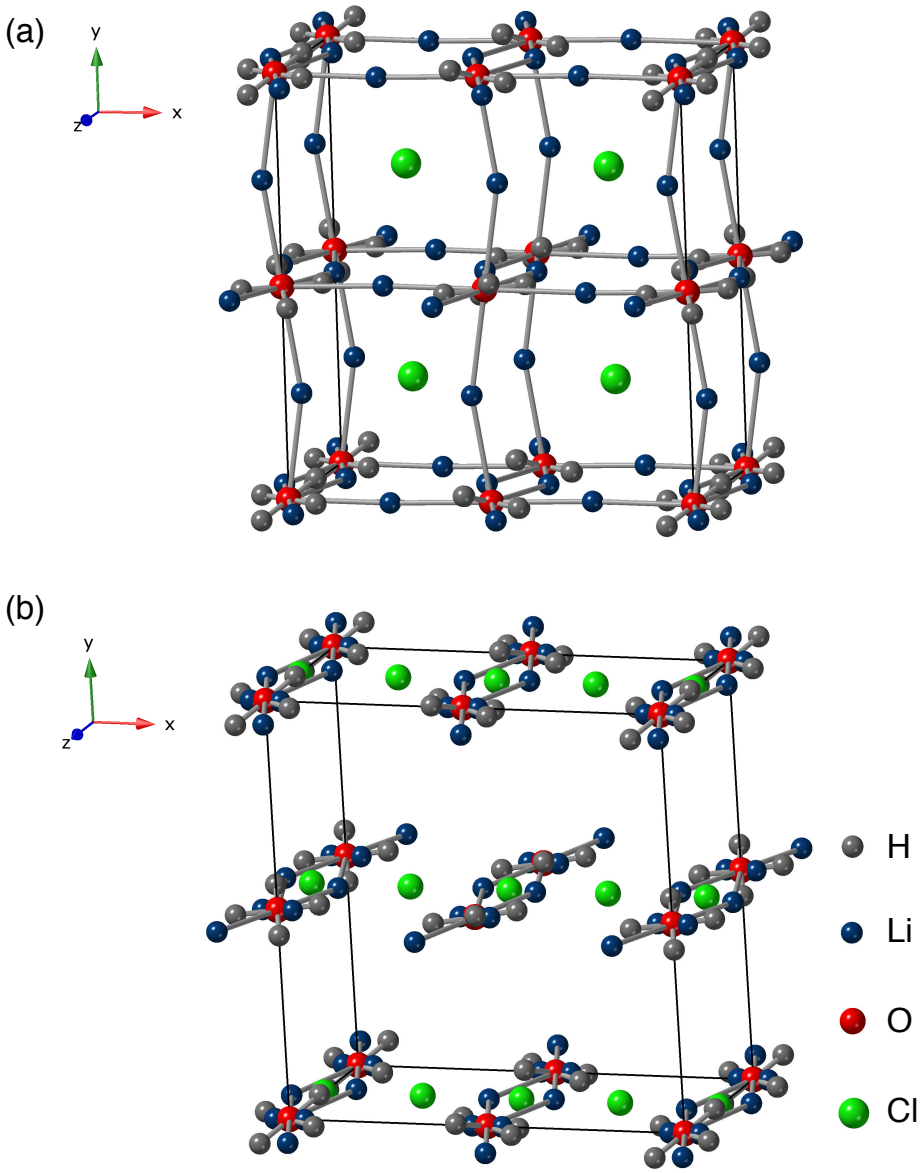

Figure 4.12: The structure of Li_2OHCl in space group *Pban* (a) generated using atomic positions as stated in the International Tables for Crystallograhy[220] and (b) as proposed by Hanghofer and co-workers.[210]

coordinates reported initially for some of the atoms at 4 K (Table 4.3) did not comply with the guidelines specified for this space group in the International Tables for Crystallography.[220] Hence, the atomic coordinates for Li1, Li2, Li4, Cl1 and Cl2 had to be altered, and the new atomic coordinates are listed in Table 4.9. This new *Pban* model was also tested, and the refinement completed is shown in Figure 4.13(b), and the corresponding structural parameters are detailed in Table 4.9. The goodness of fit (χ^2 = 4.43 and wR_p = 12.59%) is

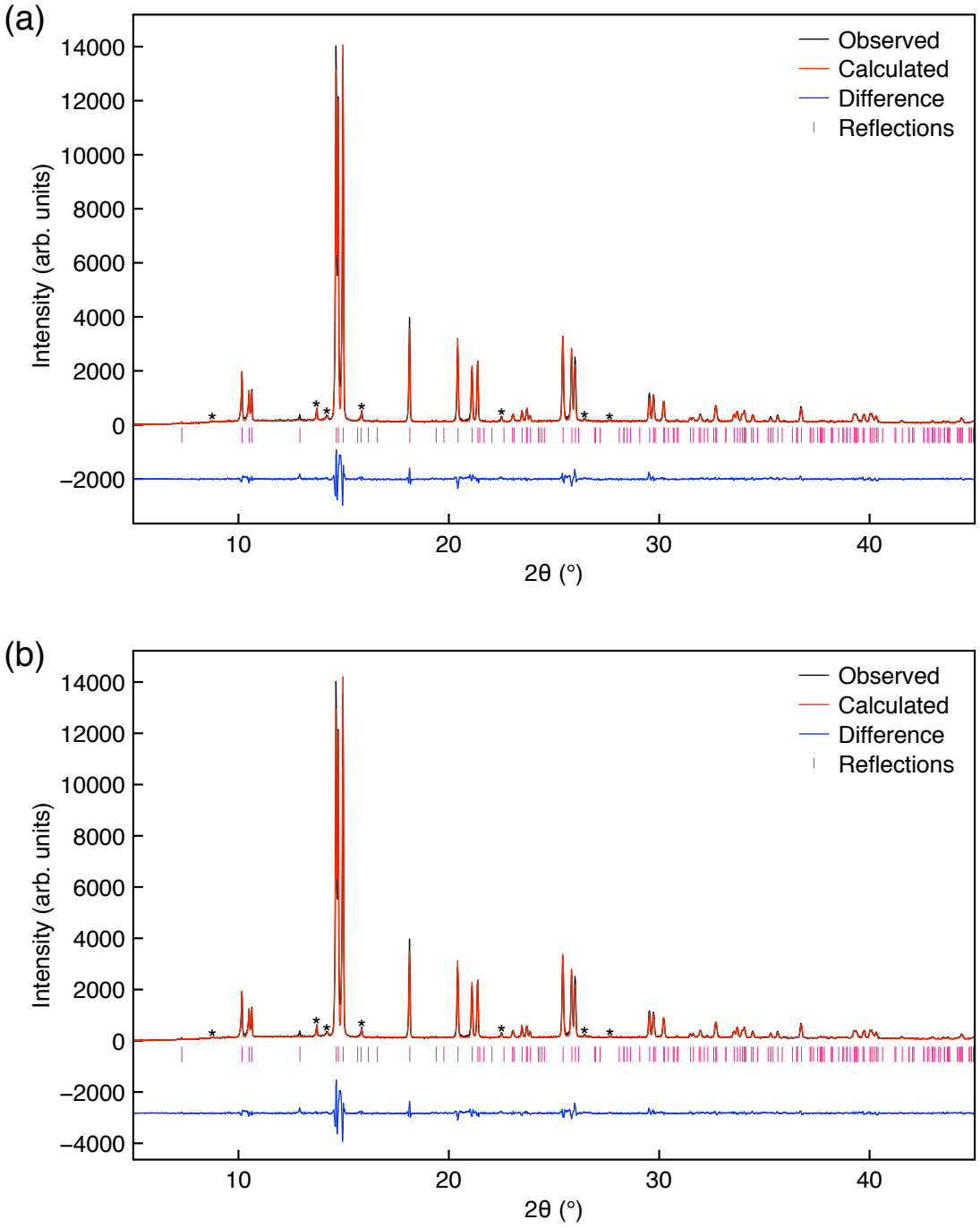

Figure 4.13: Rietveld refinement of the XRD data obtained for a sample of Li_2OHCl, synthesised via a conventional solid-state reaction completed inside an Ar-filled glovebox, using the new *Pban* models adapted from those initially reported by Hanghofer *et al.* at (a) 300 and (b) 4 K.[210] The reaction temperature was 350 °C and the reaction time was 30 mins. Reflections corresponding to an unidentified impurity phase and LiCl were excluded and are denoted by *. (a) χ^2 = 4.44, wR_P = 12.59%, R_P = 9.16%. (b) χ^2 = 4.43, wR_P = 12.59%, R_P = 9.23%.

Table 4.9: Structural parameters for a sample of Li_2OHCl, synthesised via a conventional solid-state reaction completed inside an Ar-filled glovebox, obtained from Rietveld refinement of the XRD data using isotropic thermal coefficients. Li_2OHCl: 300 K: space group *Pban*, a = 7.75963(12) Å, b = 8.01401(12) Å, c = 3.83160(6) Å, V = 238.271(4) Å^3. χ^2 = 4.44, wR_P = 12.59%, R_P = 9.16%. 4 K: space group *Pban*, a = 7.75966(12) Å, b = 8.01409(12) Å, c = 3.83158(6) Å, V = 238.273(4) Å^3. χ^2 = 4.43, wR_P = 12.59%, R_P = 9.23%.

Atom	x	y	z	Occ.	U(iso) × 100 (Å^2)
300 K					
Li1	0.0373	0.25	0	0.244(5)	2.56(42)
Li2	0.25	−0.0049	0	0.113(7)	5.62(112)
Li3	0.0741	0.0037	0.4540	0.062(4)	0.92(92)
O1	0	0	0	0.25	2.28(9)
H1	0.0834	0.0016	0.1296	0.093(17)	2.28(9)
H2	0.0399	0.4681	0.2168	0.109(17)	2.28(9)
Cl1	0.25	0.25	0.5	0.25	2.82(15)
Cl2	0.75	0.25	0.5	0.25	2.43(13)
4 K					
Li1	0.0136	0.25	0	0.243(5)	3.82(40)
Li2	0.25	−0.0041	0	0.113(4)	3.82(40)
Li3	0.0867	0.0367	0.4750	0.072(3)	3.82(40)
Li4	0.25	0.75	0	0.013(6)	3.82(40)
O1	0	0	0	0.25	2.29(9)
H1	0.0895	0.0209	0.1220	0.055(16)	2.29(9)
H2	0.0459	0.4870	0.1960	0.149(15)	2.29(9)
Cl1	0.25	0.25	0.5	0.25	2.08(16)
Cl2	0.75	0.25	0.5	0.25	3.21(19)

very similar to the refinement completed using the *Pban* model adapted from the one reported at 300 K. Additionally, the lattice parameters obtained agree with those reported and are similar to those determined via the previous refinement. This is unsurprising as both models are very similar. As with the previous refinement, the fractional occupancies for O and Cl atoms were fixed at 0.25, and those for Li and H atoms were refined freely. The resulting values indicate a composition of $Li_{2.03}OH_{1.632}Cl$, similar to the composition obtained via the previous refinement. However, unlike the previous refinement, the

thermal coefficients for Li atoms could not be refined freely and had to be constrained to be equivalent to avoid negative values. The thermal coefficients for O and H atoms were also constrained to be equivalent. The resulting values, however, appear to be quite reasonable. Overall, both *Pban* models appear to provide a very good fit. Therefore, it is challenging to rule out the presence of an additional Li site using the current data alone. In order to determine the exact number of Li sites present in the room-temperature phase of Li_2OHCl high resolution diffraction techniques would be required.

4.3.1.3 NPD Studies of Li_2ODCl

Li_2OHCl was further investigated via NPD using HRPD at ISIS.[144] As previously discussed in Chapter 2, neutron diffraction provides better resolution than laboratory XRD. Additionally, the lighter elements are more easily detected via neutron diffraction when compared to laboratory XRD, which is of particular importance in the case of Li_2OHCl. It is common practice to deuterate samples prior to neutron diffraction analysis because, in a neutron diffraction experiment, the scattering power is dependent on the nucleus, unlike in XRD, where the scattering power is dependent on the number of electrons. Deuterons have a higher scattering power than protons, making it easier to probe their position within a structure. In this study, a deuterated sample of Li_2OHCl was prepared by our collaborator and was analysed via neutron diffraction. The sample was prepared using a conventional solid-state reaction, and to ensure that no residual LiCl remained in the sample, a 5% excess of LiOD was used during the synthesis. This synthesis method differs from that used for the Li_2OHCl sample discussed earlier. Therefore, a sample of Li_2OHCl synthesised by our collaborator via the same method was also analysed via VT XRD for comparison to assess the effects of different reaction conditions. The corresponding diffraction patterns obtained at 30 and 50 °C are shown in Figure 4.14. They appear to be very similar to those shown earlier (Figure 4.5). However, closer inspection of the diffraction patterns reveals that the pattern acquired at 30 °C contains reflections that appear to correspond to the high-temperature cubic ($Pm\bar{3}m$) phase. Thus, suggesting the

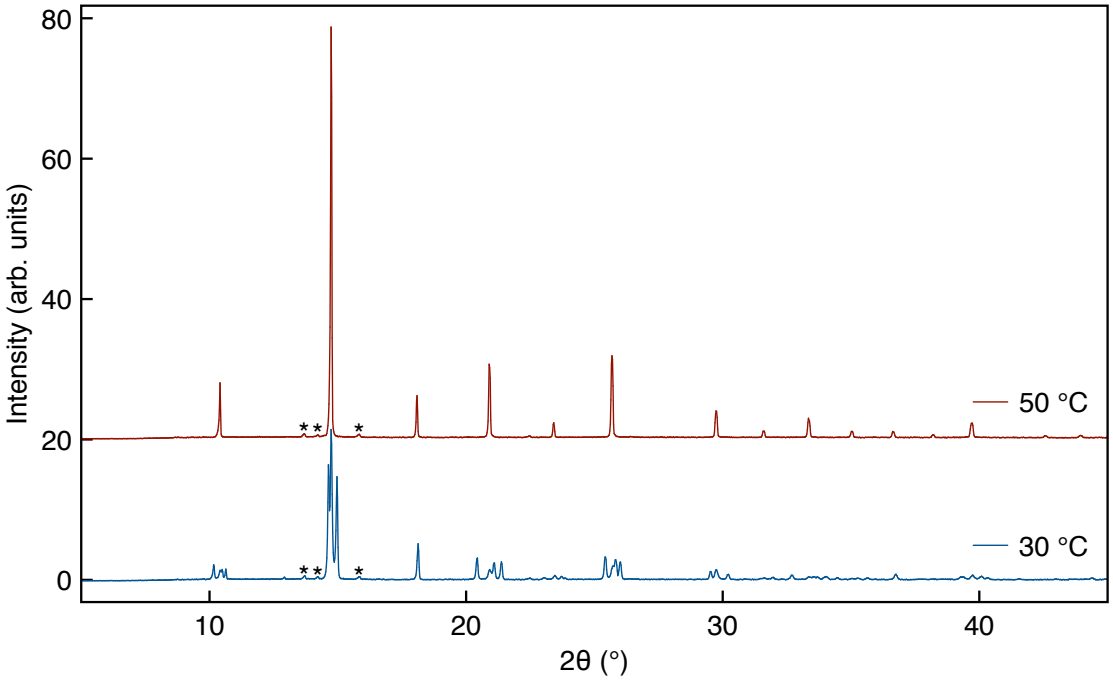

Figure 4.14: Variable-temperature X-ray diffraction patterns acquired at 30 (blue) and 50 °C (red), for a sample of Li_2ODCl, synthesised using a conventional solid-state synthesis by our collaborator. The reflections corresponding to residual LiCl and an unidentified impurity phase are denoted by *.

synthesis method used produces a sample that contains a small amount of the high-temperature cubic ($Pm\bar{3}m$) phase, in addition to the room-temperature phase. Moreover, the sample is not phase pure as the same additional reflections present in the patterns shown earlier (Figure 4.5) are also observed here. These reflections are denoted by * and suggest the presence of residual LiCl and an unidentified impurity phase in the sample. These findings suggest that it is very difficult to obtain an entirely phase pure sample of Li_2OHCl, as small amounts of impurities always seem to be present. Also, the presence of residual LiCl suggests that a 5% excess of LiOD is not sufficient. An XRD pattern obtained (using a Co source) for the deuterated sample of Li_2OHCl investigated via NPD is shown in the Appendix (Figure A4).

The HRPD instrument allows a much wider temperature range to be probed when compared to a conventional laboratory X-ray diffractometer. In turn, allowing for a comprehensive investigation of Li_2ODCl as a function of temperature. The data obtained using the backscattering bank was deemed

the most useful as it contained the greatest number of reflections corresponding to the sample when compared to the other two banks. Hence, it is the only one shown and discussed here. Initially, the Li_2ODCl sample was cooled to −263 °C (10 K), the lowest temperature permitted by the apparatus used. The NPD pattern acquired at −263 °C (10 K) is shown in Figure 4.15(a). The sample was then heated to 20 °C, and the corresponding diffraction pattern is very similar to that obtained at −263 °C (10 K), as it appears to contain the same reflections. The reflections exhibit a slight shift to higher d-spacing, suggesting an increase in the lattice parameters. This is to be expected with increasing temperature. It is noted that, in a similar manner to the XRD pattern obtained for a sample synthesised using this method (Figure 4.14), the NPD pattern recorded at 20 °C also exhibits several low intensity peaks that appear to correspond to the cubic ($Pm\bar{3}m$) phase of Li_2ODCl. Thus, suggesting that at 20 °C, the sample contains a small amount of the high-temperature cubic ($Pm\bar{3}m$) phase of Li_2ODCl alongside the room-temperature phase of Li_2ODCl. This is noteworthy because the sample was initially cooled to −263 °C (10 K) and was reheated to 20 °C. There were no reflections corresponding to the $Pm\bar{3}m$ phase at −263 °C (10 K). The presence of these reflections at 20 °C demonstrates that upon reheating, the structure of Li_2OHCl reverts to its original state, which includes a small amount of the cubic ($Pm\bar{3}m$) phase alongside the orthorhombic phase. As the sample temperature is increased to 50 °C, the diffraction pattern changes significantly, and considerably fewer reflections are observed, suggesting a substantial change in the structure. This is in agreement with the XRD data shown earlier where Li_2OHCl was shown to adopt a cubic structure in space group $Pm\bar{3}m$ at 50 °C (Figure 4.6). A further increase in temperature to 150 °C does not appear to induce any significant changes in the structure of Li_2OH/DCl as the diffraction pattern remains largely unchanged. There is, however, a shift in the reflections to higher d-spacings, suggesting an increase in the lattice parameter with increasing temperature. Again, this is to be expected as cell volumes typically increase with increasing temperature.

As stated earlier, considerably higher temperatures can be probed using HRPD when compared to a conventional laboratory X-ray diffractometer.

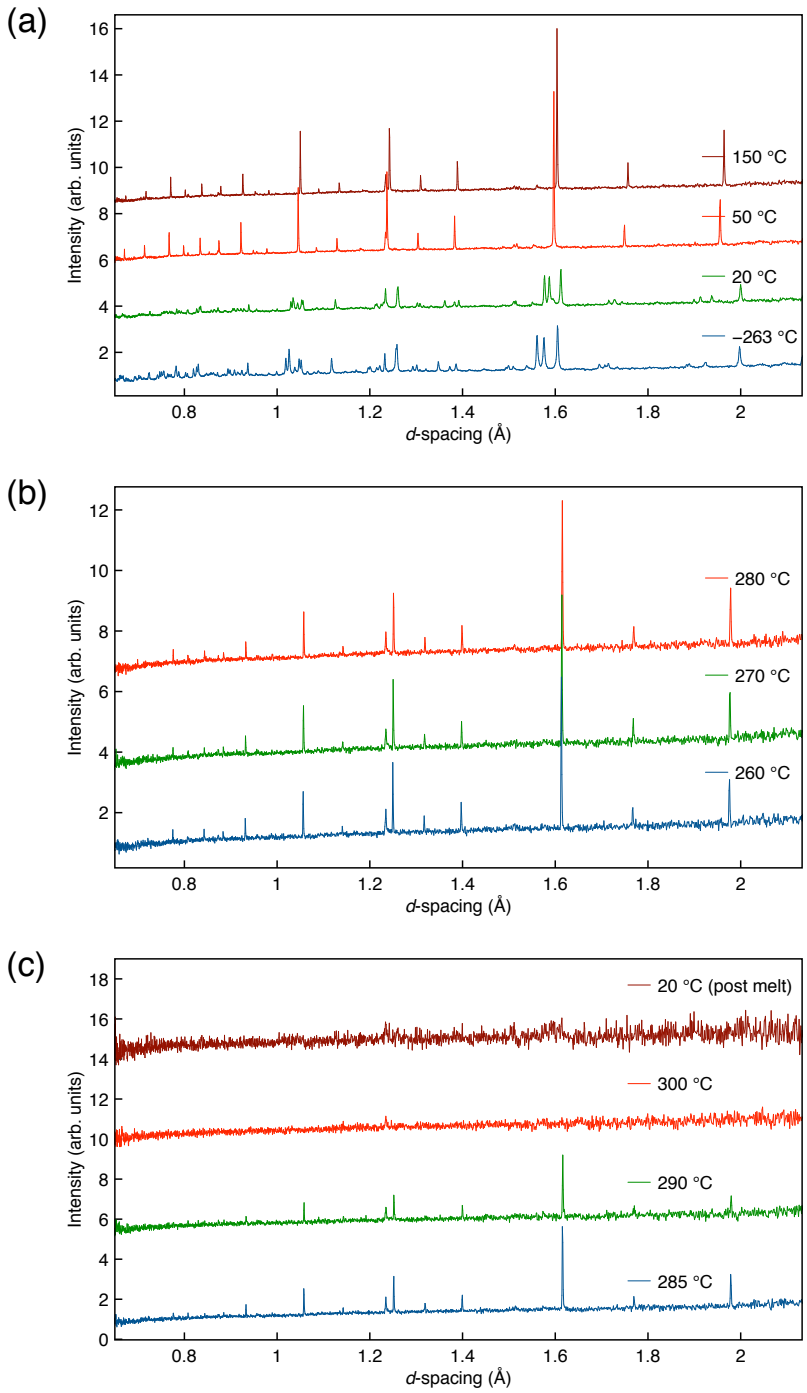

Figure 4.15: Variable-temperature NPD patterns obtained for a sample of Li_2ODCl, synthesised using a conventional solid-state reaction, at (a) −263, 20, 50 and 150 °C, collected for 644.97, 322.89, 320.04 and 237.44 μA, respectively, using the backscattering bank at HRPD. (b) The sample was then heated to 260, 270 and 280 °C and the data was collected for 40.02, 40.02 and 46.96 μA, respectively. (c) The sample was further heated to 285, 290 and 300 °C, where the data was collected for 3.11, 3.59 and 3.50 μA, respectively. Also shown in (c) is the NPD pattern of the sample after it was cooled down to 20 °C post-melt, and the data was collected for 21.12 μA.

Hence, Li_2ODCl was also investigated at 260, 270 and 280 °C. The corresponding NPD patterns are shown in Figure 4.15(b). The diffraction patterns appear to be similar to those obtained at 50 and 150 °C. Thus, suggesting that the structure of Li_2OH/DCl remains cubic with increasing temperature. As observed earlier, here too, an increase in temperature results in a shift of each reflection to higher d-spacing. Finally, higher temperatures were cautiously probed as the temperature approached the melting point of Li_2OH/DCl (Figure 4.15(c)). Zhao and Daemen reported the melting point of their "Li_3OCl" sample to be 282 °C.[124] During the current study, the melting point of Li_2OHCl was measured via a capillary method using a conventional melting point analysis apparatus and, the sample was observed to melt between 285 – 289 °C. At 285 °C, a diffraction pattern is still observable, and it appears that the cubic structure is still intact. The pattern obtained at 290 °C also exhibits reflections corresponding to the cubic structure. However, the intensity of the reflections is significantly lower, and the level of noise is noticeably higher when compared to the pattern obtained at 285 °C. Both patterns were recorded for a similar number of counts. Thus, this suggests that the sample was beginning to melt. Finally, no reflections were observed at 300 °C, suggesting the sample had completely melted. The sample was then cooled back to 20 °C, and the corresponding diffraction pattern does not show any reflections. Thus, suggesting that the sample is no longer crystalline.

The Low-Temperature Phase of Li_2OH/DCl

As discussed earlier, the precise structure of the room-temperature phase of Li_2OHCl is not known, although several models have been proposed. In some cases, adequate structural information to generate a cif was reported, and those models were tested using the XRD data obtained for Li_2OHCl (*vide supra*). Of all the models tested, the *Pban* model adapted from the one reported in the literature by Hanghofer *et al.*[210] at 300 K, provided the best fit. However, as mentioned earlier, the atomic coordinates could not be refined for any of the models as the laboratory XRD data does not offer sufficient resolution to do so. In order to obtain a precise structure, it is necessary to determine accurate

atomic coordinates. In such cases, high-resolution diffraction data acquired at extremely low temperatures can be beneficial as atoms exhibit very little thermal motion. Thus, making it easier to determine their precise location. Hence, in this study, a sample of Li_2ODCl was analysed via NPD at −263 °C (10 K) and the corresponding diffraction pattern was used to evaluate the *Pmc*2_1, *Cmcm*, *Pmmm* and the new *Pban* models discussed earlier. The *P*4*mm* model was not tested as it provided an extremely poor fit for the laboratory XRD data (Figure 4.7).

Initially, the *Pmc*2_1 model proposed by Howard *et al.*[216] was tested, and a multiphase refinement was completed using the *Pmc*2_1 (Li_2ODCl)[216] and *Fm*$\bar{3}$*m* (LiCl)[199] models (Figure 4.16). It was noticed that all NPD patterns acquired exhibited several additional reflections at d = 0.81, 0.87, 0.95, 1.23, 1.24, 1.31, 1.50, 1.51 and 1.88 Å, which are known to correspond to the sample holder. The reflections at d = 1.23 and 1.24 Å are known to correspond to the vanadium windows, and those at d = 1.50 and 1.51 Å are due to the aluminium can be used. All of these reflections were excluded during the refinement and are denoted by *. This has been done for all refinements completed for this dataset. Additionally, it is noted that the XRD pattern corresponding to the Li_2OHCl sample discussed earlier, and the one for the NPD sample, indicate the presence of an impurity phase, albeit in a very small quantity. The impurity phase has not been included in any of the refinements as its precise composition is currently unknown. This is unlikely to pose any significant issues, as it appears to be present in very small quantities.

An assessment of the refinement shows that most of the reflections observed have been indexed. However, there is a substantial difference between the calculated and observed intensities. The model also appears to place intensities where there is no experimental data (e.g., d = 0.95, 1.06, 1.11, 1.28, 1.43, 1.44, 1.47, 1.68, 1.77 and 1.89 Å). As such, the quality of the fit obtained is relatively poor, with a χ^2 = 48.20 and wR_p = 7.24%. The lattice parameters determined for Li_2ODCl are a little shorter than those obtained via the XRD analysis (Figure 4.8). This is to be expected with decreasing temperature. Unfortunately, structural parameters such as the atomic coordinates,

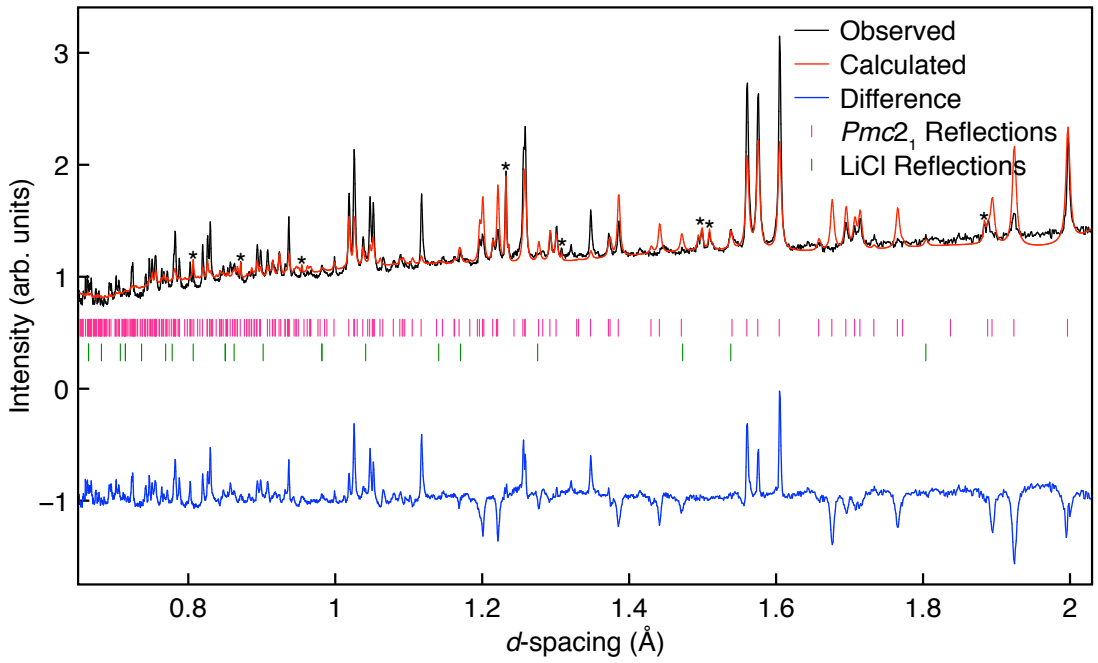

Figure 4.16: Rietveld refinement of the NPD data collected at −263 °C (10 K) for 644.97 μA using the backscattering bank, for a sample of Li_2ODCl, synthesised using a conventional solid-state reaction, using the *Pmc*2$_1$ (Li_2ODCl) structural model proposed by Howard *et al.*[216] and the $Fm\bar{3}m$ (LiCl)[199] model. Reflections corresponding to the sample holder were excluded and are denoted by *. Li_2ODCl: a = 3.84719(24) Å, b = 3.77582(29) Å, c = 7.98632(53) Å, V = 116.012(10) Å^3, phase fraction = 97.73(41)%. LiCl: a = 5.10190(258) Å, V = 132.799(201) Å^3, phase fraction = 2.27(41)%. χ^2 = 48.20, wR_p = 7.24%, R_p = 4.91%.

fractional occupancies and thermal coefficients could not be refined to satisfactory values. Attempts to refine the atomic coordinates produced an unstable refinement and refining the fractional occupancies resulted in values greater than 1 for several atoms. It was hoped that refining the thermal coefficients would improve the fit. As stated earlier, during the XRD analysis, the thermal motion was treated as isotropic, owing to limitations of the technique. In some instances, it was reasoned that treating the thermal motion as isotropic may have resulted in some coefficients being unusally high because, in reality, the thermal motion is likely to be anisotropic. Hence, determining anisotropic thermal coefficients will provide a more accurate representation of the structure. It was hoped that the higher resolution offered by HRPD would aid in determining anisotropic thermal coefficients. However, attempts to obtain anisotropic thermal coefficients were unsuccessful as many of them were

extremely large and/or negative. Consequently, the thermal motion had to be treated as isotropic. Unfortunately, even then sensible values could not be obtained, particularly for Cl, which had a negative (and therefore meaningless) coefficient. Hence, all thermal coefficients were fixed at 2.5×10^{-2} Å^2. In addition to this, the thermal coefficients for atoms in the LiCl phase were also fixed at 2.5×10^{-2} Å^2, as any attempts to refine them resulted in a negative value for Li. These findings strongly suggest that $Pmc2_1$ is not an appropriate model to describe the structure of Li_2OH/DCl at −263 °C (10 K), as very few parameters could be accurately refined. Finally, the phase fractions obtained suggest that the sample contains 97.73(41)% Li_2ODCl and 2.27(41)% LiCl. However, given the quality of the fit, these estimates are unlikely to be accurate.

The *Cmcm* model proposed by Howard and co-workers[217] was also tested and the multiphase refinement completed using the *Cmcm* (Li_2ODCl)[217] and $Fm\bar{3}m$ (LiCl)[199] models is shown in Figure 4.17. The corresponding structural parameters are detailed in Table 4.10. A χ^2 = 24.04 and wR_p = 5.11% suggest a moderate quality of fit which is much better when compared to the previous refinement. However, a considerable difference between the observed and calculated intensities remains. In a similar manner to the previous refinement, this model places calculated intensity where there is no experimental data (d = 0.88, 0.99, 1.13, 1.33, 1.53, 1.69, 1.73, 1.78 and 1.86 Å). An inspection of the structural parameters obtained shows that, as expected at low temperatures, the lattice parameters are slightly shorter than those determined from the XRD data and those reported in the literature at room temperature.[217] The atomic coordinates for Li3, O1 and D1, were successfully refined, and the resulting values are in good agreement with those proposed by Howard *et al.*[217] Unfortunately, attempts to refine the atomic coordinates for Cl1 were less successful, as doing so changed the x = 0.75 coordinate. As x = 0.75 is a special position, it cannot be altered. Hence, the atomic coordinates for Cl1 were not refined. Moreover, attempts to refine the fractional occupancies for all atoms were ineffective, as for most atoms, values greater than 1 were obtained. In a similar manner to the refinement completed using the $Pmc2_1$ model, here too, the thermal motion had to be treated as isotropic to avoid extremely large and

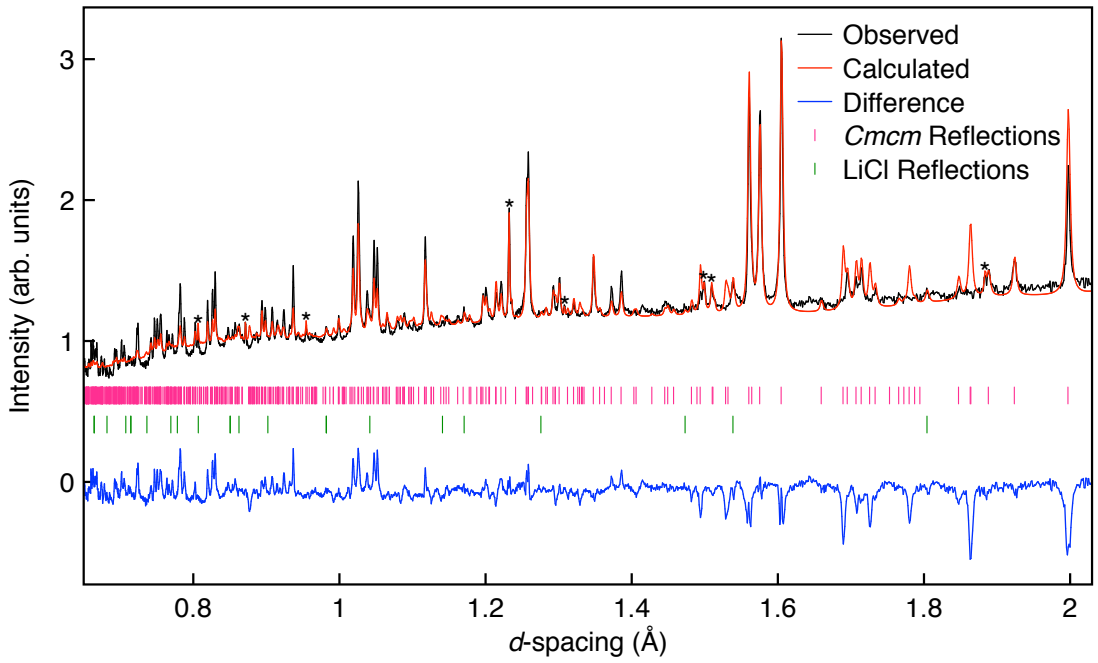

Figure 4.17: Rietveld refinement of the NPD data collected at −263 °C (10 K) for 644.97 μA using the backscattering bank, for a sample of Li_2ODCl, synthesised using a conventional solid-state reaction, using the *Cmcm* (Li_2ODCl) structural model proposed by Howard *et al.*[217] and the $Fm\bar{3}m$ (LiCl)[199] model. Reflections corresponding to the sample holder were excluded and are denoted by *. χ^2 = 24.04, wR_p = 5.11%, R_p = 3.84%.

negative thermal coefficients. Unfortunately, sensible isotropic thermal coefficients could not be obtained as attempts at refinement resulted in negative coefficients for Li1 and Cl1. To avoid this, thermal coefficients for all Li atoms were constrained to be equivalent. Even then, a sensible value could not be obtained for Cl1. Hence, all thermal coefficients were fixed at 2.5×10^{-2} Å^2. In addition to this, the thermal coefficients for atoms in the LiCl phase could not be refined to reliable values and were also fixed at 2.5×10^{-2} Å^2. Moreover, the phase fractions obtained suggest the sample contains 90.74(76)% Li_2ODCl and 9.26(76)% LiCl. However, these estimates are unlikely to be accurate owing to the quality of the fit achieved. Additionally, they differ considerably from the phase fractions determined earlier via the XRD data analysis, where the sample was found to contain a very small amount of residual LiCl (0.56(3)%). It is noted that the samples analysed via XRD and NPD were prepared differently. However, the corresponding XRD patterns are very similar (Figures 4.5 and 4.14). Thus, suggesting a similar sample composition. Overall, considering

Table 4.10: Structural parameters for a sample of Li_2ODCl, synthesised using a conventional solid-state reaction, obtained from Rietveld refinement of the NPD data collected at −263 °C (10 K) using isotropic thermal coefficients. Li_2ODCl: space group *Cmcm*, a = 7.98809(28) Å, b = 7.69451(37) Å, c = 7.55219(34) Å, V = 464.191(22) Å^3, phase fraction = 90.74(76)%. LiCl: space group $Fm\bar{3}m$, a = 5.10278(116) Å, V = 132.868(91) Å^3, phase fraction = 9.26(76)%. χ^2 = 24.04, wR_P = 5.11%, R_P = 3.84%.

Atom	x	y	z	Occ.	U(iso) × 100 (Å^2)
Li1	0.25	0.25	0	1	2.5
Li2	0	0.5	0	1	2.5
Li3	0	0.1618(41)	0.25	1	2.5
O1	0	0.7522(16)	0.4987(15)	1	2.5
D1	0	0.8358(9)	0.4092(9)	1	2.5
Cl1	0.75	0.487	0.25	1	2.5

these findings and the quality of the fit achieved, it is evident that the *Cmcm* model is a better model when compared to the $Pmc2_1$ model. However, it is not entirely correct and therefore is not adequate for describing the structure of Li_2OH/DCl at −263 °C (10 K).

As stated earlier, Hanghofer and co-workers[210] proposed two different models for Li_2OHCl in space group *Pmmm*, one at 300 K and another at 4 K. According to Hanghofer *et al.*,[210] at 4 K, an additional Li site appears in the structure. To date, the study reported by Hanghofer *et al.*[210] is the only one to suggest the presence of an additional Li site in Li_2OHCl at very low temperature. Hence, to verify this claim, both models proposed in space group *Pmmm* at 300 and 4 K were tested using the NPD data acquired at −263 °C (10 K). The refinements completed using the *Pmmm* (300 and 4 K)[210] and $Fm\bar{3}m$ (LiCl)[199] models are shown in Figure 4.18, and the corresponding structural parameters are detailed in Table 4.11.

A moderate fit was obtained using the 300 K model with χ^2 = 15.64 and wR_p = 4.11%. All reflections corresponding to Li_2ODCl were successfully indexed. However, the difference between observed and calculated intensities is significant. As with earlier models, this model places intensity at several

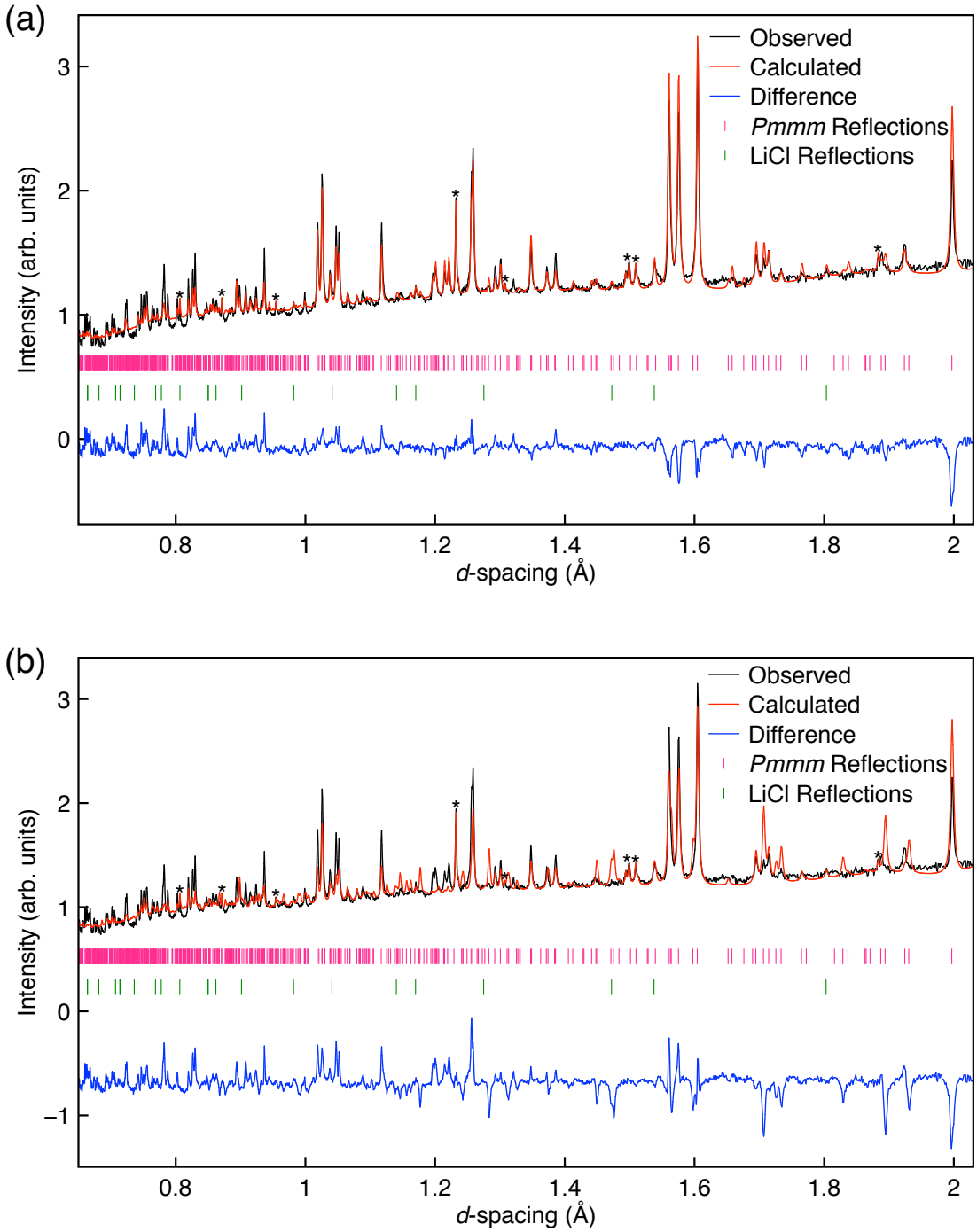

Figure 4.18: Rietveld refinement of the NPD data collected at −263 °C (10 K) for 644.97 μA using the backscattering bank, for a sample of Li_2ODCl, synthesised using a conventional solid-state reaction, using the *Pmmm* (Li_2ODCl) structural model proposed at (a) 300 and (b) 4 K by Hanghofer *et al.*[210] and the $Fm\bar{3}m$ (LiCl)[199] model. Reflections corresponding to the sample holder were excluded and are denoted by *. (a) χ^2 = 15.64, wR_p = 4.11%, R_p = 3.14%. (b) χ^2 = 44.58, wR_p = 6.95%, R_p = 4.81%.

Table 4.11: Structural parameters for a sample of Li_2ODCl, synthesised using a conventional solid-state reaction, obtained from Rietveld refinement of the NPD data collected at −263 °C (10 K) using isotropic thermal coefficients. 300 K model: Li_2ODCl: space group *Pmmm*, a = 7.55195(25) Å, b = 7.98781(21) Å, c = 3.84741(12) Å, V = 232.090(8) Å^3, phase fraction = 99.74(2)%. LiCl: space group $Fm\bar{3}m$, a = 5.10086(87) Å, V = 132.718(68) Å^3, phase fraction = 0.26(2)%. χ^2 = 15.64, wR_P = 4.11%, R_P = 3.14%. 4 K model: Li_2ODCl: space group *Pmmm*, a = 7.54914(53) Å, b = 7.98724(44) Å, c = 3.84865(24) Å, V = 232.061(17) Å^3, phase fraction = 99.68(5)%. LiCl: space group $Fm\bar{3}m$, a = 5.09942(220) Å, V = 132.606(172) Å^3, phase fraction = 0.32(5)%. χ^2 = 44.58, wR_P = 6.95%, R_P = 4.81%.

Atom	x	y	z	Occ.	U(iso) × 100 (Å^2)
Pmmm					
300 K					
Li1	0.2446(34)	0	0.5	0.611(14)	2.5
Li2	0.4130(53)	0.5	0.5	0.154(27)	2.5
Li3	0.5	0.1105(83)	0.5	0.126(19)	2.5
Li4	0.2927(23)	0.2449(46)	0	0.258(16)	2.5
O1	0.2506(18)	0.2485(12)	0.5	0.267(3)	2.5
D1	−0.1555(15)	0.2543(33)	0.3251(32)	0.083(4)	2.5
D2	0.3685(23)	−0.2053(19)	0.3714(43)	0.071(4)	2.5
Cl1	0	0	0	0.248(10)	2.5
Cl2	0.5	0	0	0.208(10)	2.5
Cl3	0	0.5	0	0.205(10)	2.5
Cl4	0.5	0.5	0	0.212(11)	2.5
Pmmm					
4 K					
Li1	0.2129	0	0.5	0.250	2.5
Li2	0.2261(70)	0.5	0.5	0.250	2.5
Li3	0.5	0.3311(70)	0.5	0.219	2.5
Li4	0.2412(45)	0.2716(53)	0	0.255	2.5
Li5	0	0.3161(87)	0	0.154	2.5
O1	0.2521(19)	0.2518(15)	0.5	0.250	2.5
D1	0.1842(10)	0.3181(9)	0.3595(25)	0.222	2.5
D2	0.3433(10)	0.2684(10)	0.3532(20)	0.222	2.5
Cl1	0	0	0	0.250	2.5
Cl2	0.5	0	0	0.250	2.5
Cl3	0	0.5	0	0.250	2.5
Cl4	0.5	0.5	0	0.250	2.5

points where there is no experimental data (d = 0.88, 0.99, 1.83, 1.84 and 1.89 Å). An inspection of the structural parameters obtained shows that the lattice parameters obtained exhibit a slight variation from those reported at 4 K. The lattice parameter a is much shorter, b is about the same, and c is a little longer when compared to the parameters reported at 4 K for the *Pmmm* model (Table 4.3) . It is noted that the model currently being discussed is the one proposed at 300 K. However, lattice parameters vary with temperature. Hence, they are compared to those reported at 4 K. Comparing these parameters to those determined at room temperature via the XRD data, it appears that a and b exhibit a noticeable decrease whilst c exhibits a small increase. Although, the overall cell volume is observed to decrease significantly with decreasing temperature, as expected.

The atomic coordinates for Li, O and D atoms were successfully refined, and the values obtained appear to vary from those reported in the literature (Table 4.3). The fractional occupancies were also refined for all atoms, and the values obtained indicate the composition of desired phase to be $Li_{2.814}O_{1.100}D_{1.232}Cl_{0.873}$. This deviates significantly from the desired composition. It is also quite different from the composition determined earlier via XRD analysis using this model ($Li_{1.502}O_{0.968}H_{1.216}Cl_{0.924}$) and that initially reported by Hanghofer and co-workers[210] ($Li_{2.508}O_2H_{4.05}Cl_{0.5}$). In hopes of achieving a better fit, several attempts were made to refine the thermal coefficients. These included treating the thermal motion as isotropic, anisotropic, and constraining the coefficients of like atoms to be equivalent. However, sensible values could not be obtained in any case. Hence, they were all fixed at 2.5×10^{-2} Å^2. Notably, this was also the case for the XRD refinement completed using this model (Figure 4.10). Again, suitable thermal coefficients could not be obtained for atoms in the LiCl phase. Hence, they were also fixed at 2.5×10^{-2} Å^2. Lastly, the phase fractions obtained suggest the sample consists of 99.75(2)% "Li_2ODCl" and 0.26(2)% LiCl. Unfortunately, given the quality of the fit, these estimates are unlikely to be highly accurate. Overall, the fit obtained is moderate at best, meaning that this model does not accurately describe the structure of Li_2OH/DCl at −263 °C (10 K).

Interestingly, a significant decrease in the goodness of fit was observed when using the *Pmmm* model proposed at 4 K. A χ^2 = 44.58 and wR_p = 6.95% indicate a relatively poor fit. Inspection of the tick marks denoting possible reflections indicates that all reflections are indexed using this model. However, not all reflections have been fitted. Moreover, there is a substantial difference in the observed and calculated intensity for many of the reflections. The structural parameters obtained show that most atomic coordinates were refined successfully and a majority of them differ significantly from those reported. However, the atomic coordinates for Li1 could not be refined as attempts to do so produced an unstable refinement. Unfortunately, the fractional occupancies could not be refined to sensible values and any attempts to do so consistently resulted in a negative fractional occupancy value for Li5. Hence, the exact composition of the desired phase could not be determined. As stated earlier, the fractional occupancies reported by Hanghofer and co-workers, used during the refinement, correspond to a sample composition of $Li_{2.766}OH_{3.552}Cl$, which deviates from the desired Li_2OHCl composition. Hence, a poor fit is to be expected when using these values. Moreover, any attempts to refine the isotropic and anisotropic thermal coefficients resulted in multiple negative values. Hence, the thermal motion was treated as isotropic and all coefficients were all fixed at 2.5×10^{-2} Å^2. Additionally, the phase fractions obtained suggest that the sample is composed of 99.68(5)% "Li_2ODCl" and 0.32(5)% LiCl. These phase fractions are very similar to those obtained using the *Pmmm* model proposed at 300 K, despite a poorer fit. Considering the refinements completed using both *Pmmm* models, it is apparent that neither model is fully correct. Though, the *Pmmm* model proposed at 300 K provides a better fit. Additionally, the inability to refine the fractional occupancies for the 4 K without a negative value for Li5 suggests that an additional Li site may not be present in Li_2OH/DCl at −263 °C (10 K).

Earlier, the crystallographic details reported by Hanghofer and co-workers[210] for the *Pban* models were demonstrated to be incorrect as they did not comply with the guidelines specified in the International Tables for Crystallography.[220] Hence, the models reported were edited, and the new models

provided an excellent fit for the XRD data, especially the new *Pban* model at 300 K, which resulted in the best fit out of all of the models evaluated in the current study. The new *Pban* models have also been tested using the NPD data acquired at −263 °C (10 K), and the refinements completed using these models (in conjunction with the $Fm\bar{3}m$ (LiCl) model[199]) are shown in Figure 4.19, and the corresponding structural parameters are detailed in Table 4.12.

Surprisingly, the fit obtained using the new *Pban* 300 K model is not as good as initially hoped. In fact, it is relatively poor with a χ^2 = 24.00 and wR_p = 5.10%. An inspection of the refinement shows that all reflections were successfully indexed. However, in some instances, the model placed intensity where there was no experimental data (d = 0.95, 1.11, 1.28, 1.31, 1.36, 1.43, 1.77 and 1.89 Å). Additionally, there is a considerable difference between the observed and calculated intensities, particularly at smaller d-spacings. The corresponding structural parameters show that the lattice parameters a and b exhibit a decrease, and the lattice parameter c exhibits a slight increase when compared to those obtained from the XRD data and those reported in the literature at 300 K.[210] As expected, the overall cell volume decreases. As stated earlier, Hanghofer *et al.*[210] did not report any lattice parameters for the *Pban* model at 4 K. Hence, a direct comparison was not possible. As for the atomic coordinates, all of them were successfully refined. The resulting values are observed to vary significantly from those originally reported. However, this may be due to a difference in temperature as this diffraction pattern was collected at −263 °C (10 K). Also, there is a large error in some cases, suggesting that the values determined may not be as reliable. In a similar manner to the Rietveld analysis completed for the XRD data using this model, here too, the fractional occupancies for O and Cl atoms were fixed at 0.25, and those for Li and D were allowed to refine freely. The values obtained differ from those determined using the XRD data and correspond to a composition of $Li_{2.871}OD_{1.416}Cl$. This formula is not charge-balanced and deviates from the intended composition of Li_2ODCl, whereas the XRD data analysis had suggested a composition of $Li_{1.924}OH_{1.616}Cl$ which is much closer to Li_2OHCl. Moreover, all isotropic thermal coefficients, including those for atoms in the LiCl phase, were fixed at 2.5

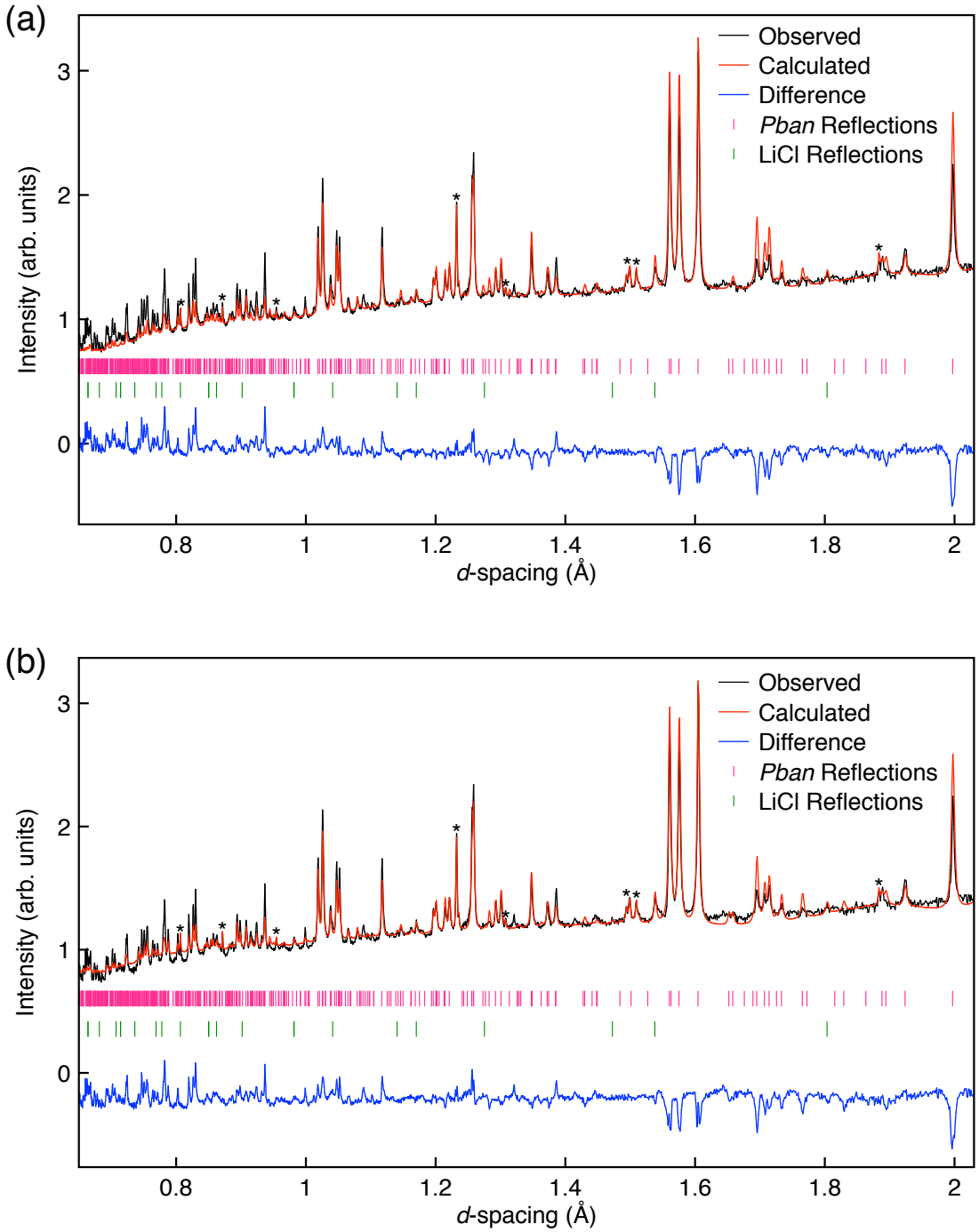

Figure 4.19: Rietveld refinement of the NPD data collected at −263 °C (10 K) for 644.97 μA using the backscattering bank, for a sample of Li_2ODCl, synthesised using a conventional solid-state reaction, using the *Pban* (Li_2ODCl) structural model adapted from that proposed at (a) 300 and (b) 4 K by Hanghofer *et al.*[210] and the $Fm\bar{3}m$ (LiCl)[199] model. Reflections corresponding to the sample holder were excluded and are denoted by *. (a) χ^2 = 24.00, wR_p = 5.10%, R_p = 3.73%. (b) χ^2 = 16.12, wR_p = 4.17%, R_p = 3.19%.

Table 4.12: Structural parameters for a sample of Li_2ODCl, synthesised using a conventional solid-state reaction, obtained from Rietveld refinement of the NPD data collected at −263 °C (10 K) using isotropic thermal coefficients. 300 K model: Li_2ODCl: space group *Pban*, a = 7.55205(30) Å, b = 7.98817(26) Å, c = 3.84722(15) Å, V = 232.091(9) Å^3, phase fraction = 99.69(3)%. LiCl: space group $Fm\bar{3}m$, a = 5.10091(99) Å, V = 132.722(77) Å^3, phase fraction = 0.31(3)%. χ^2 = 24.00, wR_P = 5.10%, R_P = 3.73%. 4 K model: Li_2ODCl: space group *Pban*, a = 7.55226(26) Å, b = 7.98783(22) Å, c = 3.84734(13) Å, V = 232.095(8) Å^3, phase fraction = 99.70(2)%. LiCl: space group $Fm\bar{3}m$, a = 5.10092(91) Å, V = 132.723(71) Å^3, phase fraction = 0.30(2)%. χ^2 = 16.12, wR_P = 4.17%, R_P = 3.19%.

Atom	x	y	z	Occ.	U(iso) × 100 (Å^2)
Pban					
300 K					
Li1	−0.0326(17)	0.25	0	0.388(12)	2.5
Li2	0.25	−0.2511(393)	0	0.077(12)	2.5
Li3	0.0592(22)	0.0227(47)	0.5108(120)	0.129(10)	2.5
O1	0	0	0	0.250	2.5
D1	0.1153(24)	0.0539(16)	0.1203(39)	0.078(4)	2.5
D2	0.0885(15)	0.4995(31)	0.1923(32)	0.100(3)	2.5
Cl1	0.25	0.25	0.5	0.250	2.5
Cl2	0.75	0.25	0.5	0.250	2.5
Pban					
4 K					
Li1	0.0214(25)	0.25	0	0.338(11)	2.5
Li2	0.25	0.1300(95)	0	0.062(11)	2.5
Li3	0.0564(16)	0.0062(71)	0.5127(106)	0.142(8)	2.5
Li4	0.25	0.75	0	0.108(18)	2.5
O1	0	0	0	0.250	2.5
D1	0.0922(15)	−0.0021(30)	0.1755(34)	0.092(3)	2.5
D2	0.1198(26)	0.4510(18)	0.1350(54)	0.063(4)	2.5
Cl1	0.25	0.25	0.5	0.250	2.5
Cl2	0.75	0.25	0.5	0.250	2.5

$\times 10^{-2}$ Å^2 as it was not possible to obtain sensible values. Any attempts to refine them resulted in several negative values, especially for the Cl atoms. As for the composition of the sample, the refined phase fractions suggest it contains 99.69(3)% "Li_2ODCl" and 0.21(3)% LiCl. However, the quality of the fit

obtained means that these values may not be exact.

Although this model provided an excellent fit for the room temperature laboratory XRD data, it does not appear to be suitable for describing the structure of Li_2OH/DCl at −263 °C (10 K). This may be due to several reasons. For example, the structure of Li_2OH/DCl at very low temperatures may be different from that at room temperature, *e.g.*, there may be an additional Li site present as claimed by Hanghofer and co-workers.[210] Another factor to consider is the relative resolution of the two diffraction techniques, laboratory XRD and NPD at HRPD. As mentioned previously, NPD offers considerably better resolution when compared to laboratory XRD. Hence, it is possible that the proposed *Pban* model is very close to the actual structure of Li_2OHCl but is not entirely correct. Therefore, it provides a good fit for the XRD data where it is challenging to detect light elements but provides a less good fit for the NPD data where these atoms are more easily detected.

Lastly, the new *Pban* model adapted from the one proposed at 4 K by Hanghofer *et al.*[210] was also tested to determine whether there is indeed an additional Li site present at low temperatures. It appears that the inclusion of an additional Li site significantly improves the goodness of fit (χ^2 = 16.12 and wR_p = 4.17%). As with the *Pban* 300 K model, here too, all reflections have been indexed, and the difference between observed and calculated intensities has somewhat decreased. However, this model also places intensity where no experimental data exists (d = 1.43, 1.83 and 1.89 Å). The lattice parameters obtained are very similar to those obtained using the new *Pban* 300 K model. The structural parameters obtained show that the atomic coordinates for Li and D atoms were successfully refined, and they appear to vary considerably from those reported by Hanghofer *et al.*[210] Additionally, the fractional occupancies for Li and D were refined, and the values obtained correspond to a composition of $Li_{2.952}OH_{1.242}Cl$. Again, this differs significantly from the intended composition and that obtained via the XRD data analysis completed using this model ($Li_{2.03}OH_{1.632}Cl$). As with the previous refinement completed using the new *Pban* 300 K model, the thermal coefficients could not be refined, as any attempts to do so produced negative values for several atoms.

Finally, the phase fractions obtained suggest the sample consists of 99.70(2)% of the desired phase and 0.30(2)% LiCl. Unfortunately, neither of the new *Pban* models provide a particularly good fit for the NPD data acquired at −263 °C (10 K). Therefore, it is unclear from the data presented whether the structure of Li_2OH/DCl at −263 °C (10 K) actually differs from the room-temperature structure. Thus, making it difficult to ascertain the presence of an additional Li site.

The Room-Temperature Phase of Li_2OH/DCl

The Li_2ODCl sample was also analysed at 20 °C via NPD to further investigate the room-temperature phase of Li_2OH/DCl. As stated earlier, the synthetic method used to produce this sample resulted in a mixture of phases. At 20 °C, the sample appears to be composed of the room-temperature phase of Li_2OH/DCl, the high-temperature cubic ($Pm\bar{3}m$) phase of Li_2OH/DCl, residual LiCl and an unidentified impurity. All refinements completed using the NPD data recorded at 20 °C are done so using a candidate orthorhombic model, the $Pm\bar{3}m$ (Li_2ODCl)[210] and $Fm\bar{3}m$ (LiCl)[199] models. The impurity phase has not been included as it is currently unknown. However, it is hoped that this will not cause any significant issues, as the impurity phase is present in a very small quantity.

Initially, the $Pmc2_1$ model proposed by Howard *et al.*[216] was tested, and a multiphase refinement was completed using the $Pmc2_1$ (Li_2ODCl),[216] $Pm\bar{3}m$ (Li_2ODCl)[210] and $Fm\bar{3}m$ (LiCl)[199] models (Figure 4.20). The fit obtained appears to be much improved (χ^2 = 10.94 and wR_p = 4.81%) when compared to the refinement completed at −263 °C (10 K) using the $Pmc2_1$ model (Figure 4.16). However, a significant mismatch between the observed and calculated intensities remains. Additionally, the model places calculated intensity where there is no experimental data (d = 0.74, 0.82, 1.07, 1.09, 1.11, 1.17, 1.45, 1.48, 1.68, 1.69, 1.77 and 1.90 Å). The lattice parameters obtained are similar to those determined earlier via the XRD data analysis (Figure 4.8), which were noted to differ slightly from those reported in the literature.[216] As with the refinement completed for the NPD data acquired at −263 °C (10 K) using this model, here

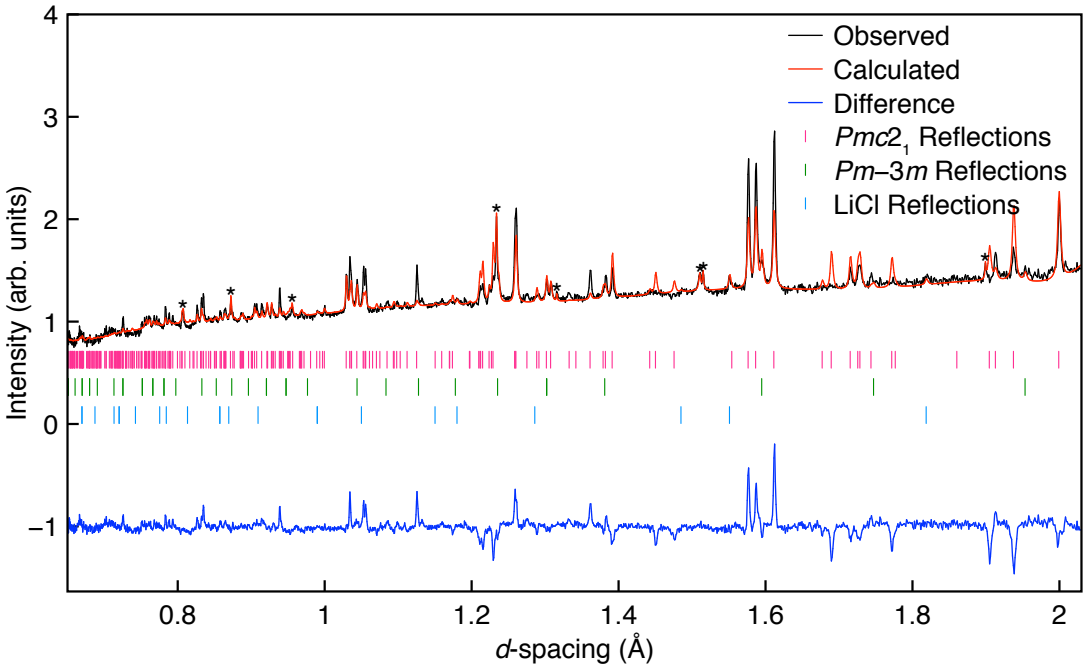

Figure 4.20: Rietveld refinement of the NPD data collected at 20 °C for 322.89 μA using the backscattering bank, for a sample of Li_2ODCl, synthesised using a conventional solid-state reaction, using the $Pmc2_1$ (Li_2ODCl) structural model proposed by Howard *et al.*,[216] the $Pm\bar{3}m$ (Li_2ODCl)[210] and $Fm\bar{3}m$ (LiCl)[199] models. Reflections corresponding to the sample holder were excluded and are denoted by *. Li_2ODCl: space group: $Pmc2_1$, a = 3.87482(18) Å, b = 3.82568(22) Å, c = 7.99624(39) Å, V = 118.535(8) Å^3, phase fraction = 82.50(101)%. Li_2ODCl: space group: $Pm\bar{3}m$, a = 3.90645(68) Å, V = 59.614(31) Å^3, phase fraction = 15.41(97)%. LiCl: a = 5.14384(187) Å, V = 136.101(148) Å^3, phase fraction = 2.09(33)%. χ^2 = 10.94, wR_p = 4.81%, R_p = 3.91%.

too, sensible values could not be obtained for the atomic coordinates and fractional occupancies. Attempts to refine atomic coordinates produced an unstable refinement, whereas refining the fractional occupancies resulted in values greater than 1. Once again, the thermal motion had to be treated as isotropic to avoid extremely large and negative values. Even then, it was difficult to obtain sensible thermal coefficients as any attempts at refinement consistently produced a negative coefficient for Cl. Hence, all thermal coefficients were fixed at 2.5×10^{-2} Å^2. Moreover, the lattice parameter obtained for the $Pm\bar{3}m$ phase is in good agreement with the values reported in the literature.[210,213] However, structural parameters such as the atomic coordinates for D, the fractional occupancies for Li and D and the thermal coefficients for all atoms, could not be refined to sensible values. Additionally, the thermal coefficients for the

LiCl phase could not be refined, as attempts to do so resulted in a negative value for Li. Hence, the thermal coefficients for all atoms in the $Pm\bar{3}m$ and LiCl phase were fixed at 2.5×10^{-2} Å^2. Lastly, the phase fractions obtained suggest the sample contains 82.50(101)% $Pmc2_1$ phase, 15.41(97)% $Pm\bar{3}m$ phase and 2.09(33)% LiCl phase. However, these phase fractions are unlikely to be completely accurate owing to the quality of the fit obtained. Overall, this refinement strongly suggests that the $Pmc2_1$ model is not a good candidate for describing the structure of the room-temperature phase of Li_2OH/DCl.

The *Cmcm* model proposed by Howard *et al.*[217] was also tested, and a multiphase refinement completed using the *Cmcm* (Li_2ODCl),[217] $Pm\bar{3}m$ (Li_2ODCl),[210] and $Fm\bar{3}m$ (LiCl)[199] models is shown in Figure 4.21. The corresponding structural parameters are listed in Table 4.13. A $\chi^2 = 3.33$ and $wR_p = 2.66\%$ suggest that the quality of fit obtained is much better than that obtained using the $Pmc2_1$ model. All peaks are successfully indexed, and the observed and calculated intensities appear to match reasonably well. However, in some instances, the model places intensities where there is no experimental data (d = 0.82, 0.95, 1.01, 1.48, 1.54, 1.70, 1.79 and 1.88 Å). Thus, suggesting that the fit may not be as good as initially believed. Inspection of the structural parameters obtained indicates that, in this case, most parameters could be refined to satisfactory values. The lattice parameters obtained are similar to those determined earlier via the XRD data and in reasonable agreement with those reported in the literature.[217] The atomic coordinates obtained are also in good agreement with those reported in the literature.[217] However, the coordinates for Cl1 could not be refined as attempts to do so changed the x = 0.75 coordinate. As 0.75 is a special position, it cannot be changed. Hence, the atomic coordinates for Cl1 were not be refined. Additionally, attempts to refine the fractional occupancies resulted in values greater than 1 for most atoms. So, they were all fixed at 1. As with the earlier refinements, it was not possible to determine anisotropic thermal coefficients. Hence, the thermal motion was treated as isotropic to obtain somewhat reasonable thermal coefficients. The thermal coefficients for O and D were constrained to be equivalent to avoid unreasonable values. Notably, the values obtained are better than those determined using the labora-

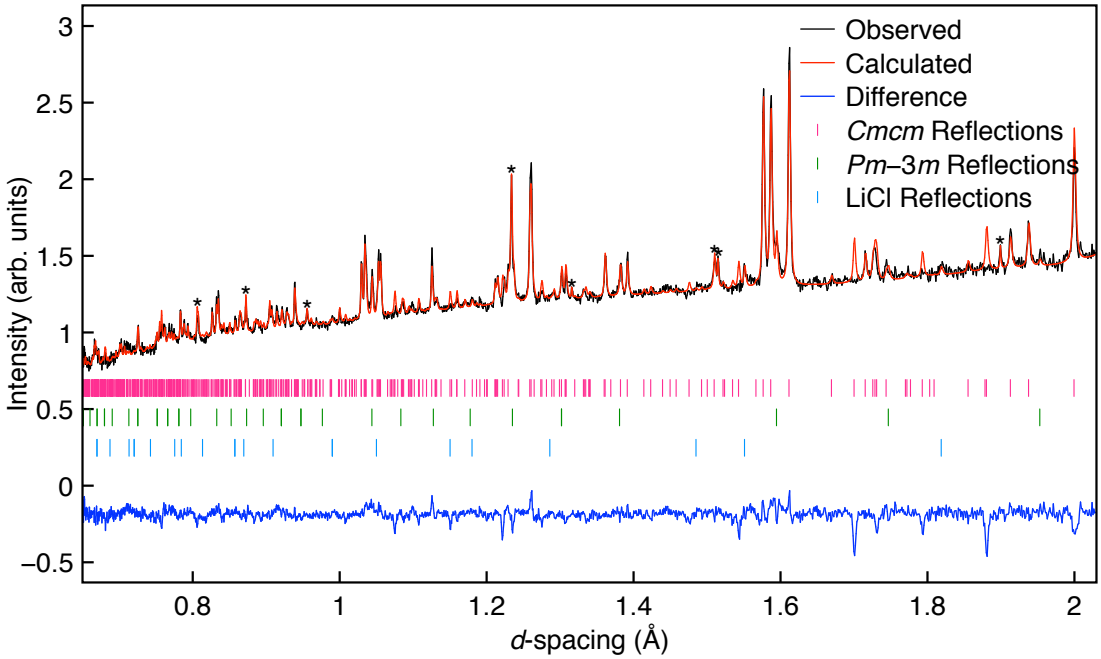

Figure 4.21: Rietveld refinement of the NPD data collected at 20 °C for 322.89 μA using the backscattering bank, for a sample of Li_2ODCl, synthesised using a conventional solid-state reaction, using the *Cmcm* (Li_2ODCl) structural model proposed by Howard *et al.*,[217] the *Pm*$\bar{3}$*m* (Li_2ODCl)[210] and *Fm*$\bar{3}$*m* (LiCl)[199] models. Reflections corresponding to the sample holder were excluded and are denoted by *. χ^2 = 3.33, wR_p = 2.66%, R_p = 2.02%.

tory XRD data. However, the thermal coefficient corresponding to Li2 is quite large. As for the *Pm*$\bar{3}$*m* phase, the lattice parameter is similar to the one determined via the previous refinement. Additionally, the atomic coordinates for D were also refined. However, the coordinates obtained (x = y = z = 0.1691(106)) differ significantly from those reported by Hanghofer *et al.* (x = y = z = 0.1279) for a similar composition ($Li_{1.84}OH_{1.16}Cl$).[210] In order to determine the exact composition of the *Pm*$\bar{3}$*m* phase, refinement of the fractional occupancies for Li and D atoms was attempted. However, sensible values could not be obtained, especially for D which had a negative occupancy value. In addition to this, attempts to refine the thermal coefficients for the *Pm*$\bar{3}$*m* and LiCl phase were unsuccessful, as numerous negative values were obtained. Hence, they were all fixed at 2.5×10^{-2} Å^2. Finally, phase fractions were also refined to determine the precise composition of the sample. The sample appears to contain 51.00(15)% *Cmcm* phase, 43.19(11)% *Pm*$\bar{3}$*m* phase and 5.81(51)% LiCl. However, given the quality of fit obtained these phase fractions are unlikely to be

Table 4.13: Structural parameters for a sample of Li_2ODCl, synthesised using a conventional solid-state reaction, obtained from Rietveld refinement of the NPD data collected at 20 °C using isotropic thermal coefficients. Li_2ODCl: space group *Cmcm*, a = 7.99770(16) Å, b = 7.75022(21) Å, c = 7.65125(20) Å, V = 474.255(13) Å^3, phase fraction = 51.00(105)%. Li_2ODCl: space group *Pm*$\bar{3}$*m*, a = 3.90572(35) Å, V = 59.580(16) Å^3, phase fraction = 43.19(113)%. LiCl: space group *Fm*$\bar{3}$*m*, a = 5.14401(93) Å, V = 136.115(73) Å^3, phase fraction = 5.81(51)%. χ^2 = 3.33, wR_P = 2.66%, R_P = 2.02%.

Atom	x	y	z	Occ.	U(iso) × 100 (Å^2)
Cmcm					
Li1	0.25	0.25	0	1	0.97(20)
Li2	0	0.5	0	1	6.64(94)
Li3	0	0.1767(42)	0.25	1	3.86(78)
O1	0	0.7459(14)	0.5017(13)	1	1.71(9)
D1	0	0.8207(6)	0.4219(7)	1	1.71(9)
Cl1	0.75	0.487	0.25	1	0.21(5)
Pm*$\bar{3}$*m					
Li1	0.5	0	0	0.667	2.5
O1	0	0	0	1	2.5
D1	0.1691(106)	0.1691(106)	0.1691(106)	0.125	2.5
Cl1	0.5	0.5	0.5	1	2.5

exact and the true sample composition will likely vary. Overall, the *Cmcm* model provides a fairly good fit for the data, making it a very likely candidate structure for the room-temperature phase of Li_2OH/DCl. However, the model does not appear to be entirely correct as some structural parameters could not be refined to reasonable values.

The *Pmmm* models proposed by Hanghofer and co-workers[210] at 300 and 4 K were also tested, and the refinements completed using the *Pmmm* (Li_2ODCl),[210] *Pm*$\bar{3}$*m* (Li_2ODCl)[210] and *Fm*$\bar{3}$*m* (LiCl)[199] models are shown in Figure 4.22. The corresponding structural parameters are listed in Table 4.14. The fit obtained using the 300 K model appears to be quite good with a χ^2 = 1.74 and wR_p = 1.91%. It is noticed that the goodness of fit obtained is much higher when compared to that obtained for the −263 °C (10 K) data with the same model. Almost all reflections have been indexed, and the calculated

and observed peak intensities appear to match quite well. An inspection of the structural parameters obtained shows that the lattice parameters for the *Pmmm* phase are similar to those determined earlier via the XRD analysis (Figure 4.10) and in good agreement with those reported in the literature.[210] Moreover, the atomic coordinates for all Li and D atoms were successfully refined, and the coordinates obtained are largely in agreement with those reported by Hanghofer *et al.*[210] However, the coordinates determined for Li2 appear to deviate from those reported. The structure generated using the refined atomic coordinates is shown in Figure 4.23. Also shown for comparison is the structure initially proposed by Hanghofer *et al.*[210] Overall, the refined structure does not exhibit much change. However, the positions of the Li2 and Li3 atoms (labelled in the Figure) have shifted considerably. Additionally, the deuterons have also changed their orientation. Moreover, the fractional occupancies differ drastically from those reported and those determined earlier using the XRD data. The fractional occupancies determined here indicate a composition of $Li_{4.28}O_{1.548}D_{1.528}Cl_{1.518}$. Notably, this formula is not quite charge-balanced and deviates from the intended composition. Isotropic thermal coefficients were also determined. The coefficients corresponding to O1, D1 and D2 and all Cl atoms were constrained to be equivalent, whereas the thermal coefficients for all Li atoms could be refined freely. In general, the coefficients obtained appear to be quite reasonable, except for Li4, where an unusually large value is obtained. Also the coefficient for Li1 is quite small and has an error larger than the coefficient itself. Unfortunately, for the $Pm\bar{3}m$ phase, parameters such as the atomic coordinates, fractional occupancies and thermal coefficients could not be refined to reasonable values. The atomic coordinates for D consistently alternated between two very different values. A negative fractional occupancy was determined for Li whereas for D it was >1. Also, the thermal coefficients for O and D returned negative values. Hence, thermal coefficients for all atoms in the $Pm\bar{3}m$ phase were fixed at 2.5×10^{-2} Å^2. This was also done for the LiCl phase to avoid a negative value for Li. Furthermore, the phase fractions obtained suggest the sample contains 93.35(18)% *Pmmm* phase, 5.70(17)% $Pm\bar{3}m$ phase and 0.95(5)% LiCl phase. These values appear to be more reasonable

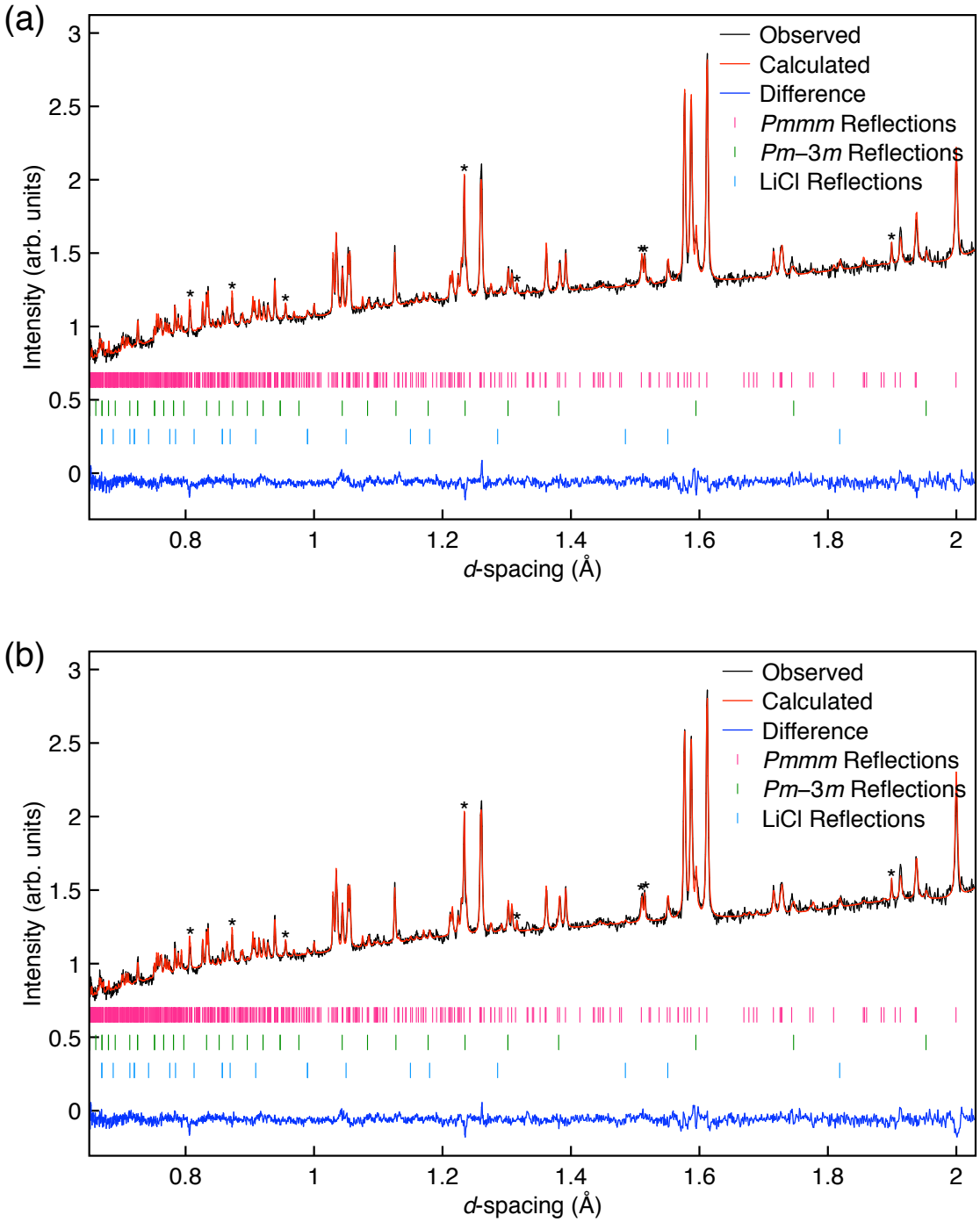

Figure 4.22: Rietveld refinement of the NPD data collected at 20 °C for 322.89 μA using the backscattering bank, for a sample of Li_2ODCl, synthesised using a conventional solid-state reaction, using the *Pmmm* (Li_2ODCl) structural model proposed at (a) 300 and (b) 4 K by Hanghofer *et al.*,[210] the *Pm*$\bar{3}$*m* (Li_2ODCl)[210] and *Fm*$\bar{3}$*m* (LiCl)[199] models. Reflections corresponding to the sample holder were excluded and are denoted by *. (a) χ^2 = 1.74, wR_p = 1.91%, R_p = 1.56%. (b) χ^2 = 1.67, wR_p = 1.88%, R_p = 1.54%.

Table 4.14: Structural parameters for a sample of Li_2ODCl, synthesised using a conventional solid-state reaction, obtained from Rietveld refinement of the NPD data collected at 20 °C using isotropic thermal coefficients. 300 K model: Li_2ODCl: space group *Pmmm*, a = 7.75004(14) Å, b = 7.99781(11) Å, c = 3.82553(7) Å, V = 237.119(4) Å^3, phase fraction = 93.35(18)%. Li_2ODCl: space group $Pm\bar{3}m$, a = 3.90591(26) Å, V = 59.589(12) Å^3, phase fraction = 5.70(17)%. LiCl: space group $Fm\bar{3}m$, a = 5.14337(56) Å, V = 136.064(44) Å^3, phase fraction = 0.95(5)%. χ^2 = 1.74, wR_P = 1.91%, R_P = 1.56%. 4 K model: Li_2ODCl: space group *Pmmm*, a = 7.74992(14) Å, b = 7.99789(11) Å, c = 3.82551(7) Å, V = 237.116(4) Å^3, phase fraction = 97.53(8)%. Li_2ODCl: space group $Pm\bar{3}m$, a = 3.90557(26) Å, V = 59.573(12) Å^3, phase fraction = 2.12(8)%. LiCl: space group $Fm\bar{3}m$, a = 5.14320(56) Å, V = 136.050(44) Å^3, phase fraction = 0.35(2)%. χ^2 = 1.67, wR_P = 1.88%, R_P = 1.54%.

Atom	x	y	z	Occ.	U(iso) × 100 (Å^2)
Pmmm					
300 K					
Li1	0.2421(46)	0	0.5	0.397(75)	0.63(105)
Li2	0.2214(35)	0.5	0.5	0.524(99)	2.15(128)
Li3	0.5	0.2375(111)	0.5	0.276(59)	3.80(168)
Li4	0.3205(19)	0.2475(62)	0	0.466(57)	5.95(100)
O1	0.2439(13)	0.2527(16)	0.5	0.387(10)	0.81(15)
D1	0.1638(13)	0.2663(16)	0.3330(27)	0.118(6)	0.81(15)
D2	0.2979(22)	0.2580(34)	0.3769(48)	0.073(5)	0.81(15)
Cl1	0	0	0	0.252(14)	0.26(6)
Cl2	0.5	0	0	0.408(16)	0.26(6)
Cl3	0	0.5	0	0.546(13)	0.26(6)
Cl4	0.5	0.5	0	0.312(15)	0.26(6)
Pmmm					
4 K					
Li1	0.2169(83)	0	0.5	0.158(34)	2.49(33)
Li2	0.2636(40)	0.5	0.5	0.480(36)	2.49(33)
Li3	0.5	0.2492(170)	0.5	0.127(13)	2.49(33)
Li4	0.3238(20)	0.2541(74)	0	0.127(13)	2.49(33)
Li5	0	0.0709(33)	0	0.314(25)	2.49(33)
O1	0.2497(19)	0.2503(15)	0.5	0.25	1.06(8)
D1	0.1802(16)	0.2232(16)	0.3180(32)	0.067(3)	1.06(8)
D2	0.3364(20)	0.2529(51)	0.3711(41)	0.045(3)	1.06(8)
Cl1	0	0	0	0.25	0.83(5)
Cl2	0.5	0	0	0.25	0.83(5)
Cl3	0	0.5	0	0.25	0.83(5)

Cl4	0.5	0.5	0	0.25	0.83(5)
Pm$\bar{3}$m					
Li1	0.5	0	0	0.667	2.5
O1	0	0	0	1	2.5
D1	0.1512(82)	0.1512(82)	0.1512(82)	0.125	2.5
Cl1	0.5	0.5	0.5	1	2.5

than those obtained from the refinement completed using the *Cmcm* model (Figure 4.21). Overall, the *Pmmm* model proposed at 300 K appears to provide a good fit. However, the structural parameters obtained indicate that the model is not fully correct. For example, the composition determined deviates from Li_2ODCl, and the thermal coefficients had to be severely constrained to obtain somewhat reasonable values. Hence, this model is likely to be close to the true structure of the room-temperature phase of Li_2OHCl, but it is not fully correct.

A good fit was also obtained with the *Pmmm* model proposed at 4 K[210] (Figure 4.22(b)). A χ^2 = 1.67 and wR_p = 1.88% suggest a marginally better fit than that obtained using the 300 K model. All reflections have been indexed, with little difference between the observed and calculated intensities. As expected, the lattice parameters obtained are very similar to those obtained using the 300 K model. The refined atomic coordinates for all Li and D atoms appear to be in agreement with those originally reported in the literature,[210] except for Li5 which differs significantly. Again, the proposed and refined structures are shown in Figure 4.23 for ease of comparison. For this model, the fractional occupancies could not be refined freely for all atoms, as doing so produced an unstable refinement. Hence, the fractional occupancies for O and D were fixed at 0.25 to reflect the composition "Li_2ODCl". The fractional occupancies obtained for the Li and D atoms appear to differ significantly from those obtained via the XRD data and the NPD data acquired at −263 °C (10 K). The values obtained indicate a composition of $Li_{2.852}OD_{0.896}Cl$, quite different from the intended composition. In order to obtain somewhat reasonable thermal coefficients, multiple constraints were required. The coefficients for

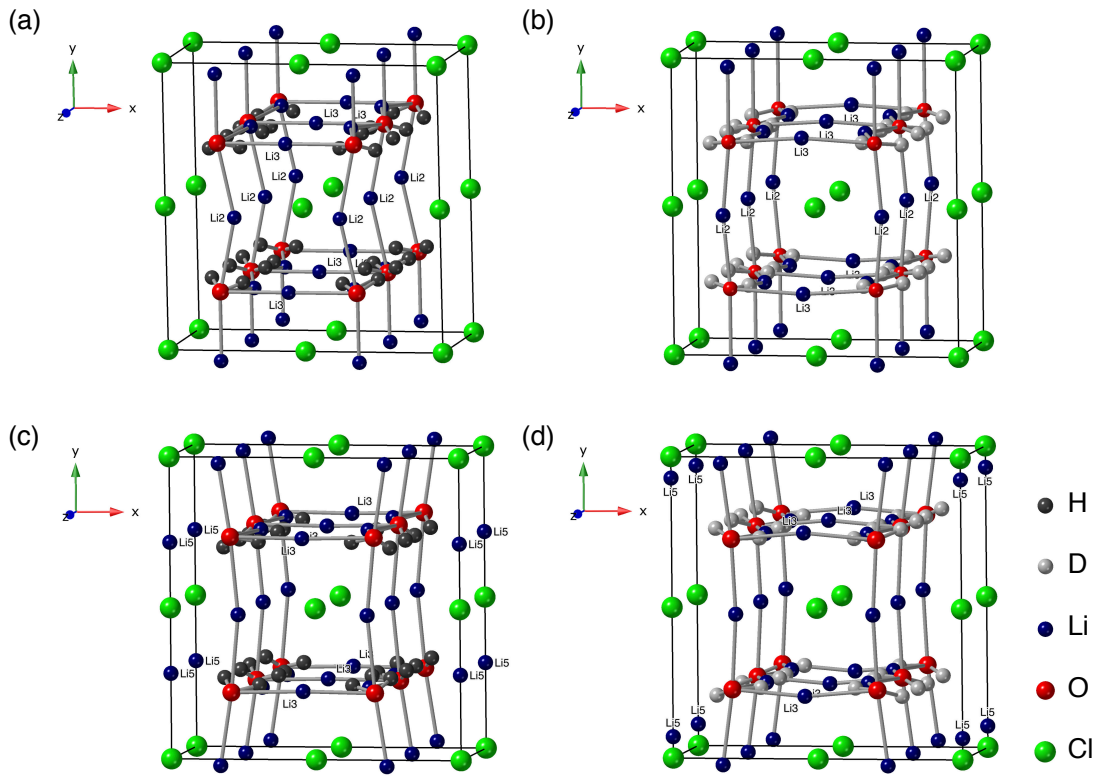

Figure 4.23: The structure of Li_2OHCl in space group *Pmmm* proposed by Hanghofer and co-workers[210] at (a) 300 and (c) 4 K. Also, shown is the refined structure of Li_2ODCl in space group *Pmmm* obtained via Rietveld analysis of the NPD data acquired at 20 °C during the current study using the (b) 300 and (d) 4 K models.

all like atoms and O and D were constrained to be equivalent. The resulting coefficients, however, seem quite sensible. For the $Pm\bar{3}m$ phase, the atomic coordinates obtained for D are quite different from those reported in the literature.[210] Additionally, the fractional occupancies and thermal coefficients for the $Pm\bar{3}m$ phase could not be refined to sensible values. The thermal coefficients for atoms in the LiCl phase could not be refined either. Therefore, thermal coefficients for all atoms in the $Pm\bar{3}m$ and LiCl phase were fixed at 2.5×10^{-2} Å^2. Lastly, the phase fractions obtained suggest the sample is composed of 97.53(8)% *Pmmm* phase, 2.12(8)% $Pm\bar{3}m$ phase and 0.35(2)% LiCl phase. It is noted that these phase fractions vary significantly from those determined earlier using the 300 K model. Overall, the model appears to provide a reasonable fit. However, in a similar manner to the *Pmmm* model proposed at 300K, it does not appear to be fully correct. Thus, it is challenging to confirm the presence or lack of an additional Li site within the structure.

Lastly, the new *Pban* models adapted from those proposed by Hanghofer and co-workers[210] at 300 and 4 K were also tested. Multiphase refinements completed using the *Pban* (Li_2ODCl), $Pm\bar{3}m$ (Li_2ODCl)[210] and $Fm\bar{3}m$ (LiCl)[199] models are shown in Figure 4.24. The corresponding structural parameters are detailed in Table 4.15. A very good fit is obtained using the 300 K model with a χ^2 = 1.83 and wR_p = 1.96%. All reflections have been successfully indexed, and a relatively good match is achieved between the observed and calculated intensities. The lattice parameters obtained for the *Pban* phase are similar to those obtained earlier via XRD analysis and are in agreement with those reported in the literature.[210] Compared to the lattice parameters determined at −263 °C (10 K), the lattice parameter a exhibits an increase, b remains similar, and c decreases. The overall cell volume increases with increasing temperature. The atomic coordinates were successfully refined for the *Pban* phase, and the coordinates obtained exhibit a noticeable difference from those initially reported.[210] As such, the proposed and refined structures are shown in Figure 4.25 for comparison, where the difference between them can be clearly seen. As with the earlier refinements completed using this model, the fractional occupancies for O and Cl were fixed at 0.25, and those for Li and D were refined freely. The occupancies obtained differ somewhat from those determined from the XRD data. The desired phase is suggested to have a composition of $Li_{2.560}OD_{1.216}Cl$, which is not charge-balanced and deviates from Li_2ODCl. Here too, only isotropic thermal coefficients could be determined and to avoid negative and extremely large values, the coefficients for the Li, D and Cl atoms had to be constrained to be equivalent. The resulting coefficients obtained appear to be quite reasonable. For the $Pm\bar{3}m$ phase, the atomic coordinates for D were successfully refined. Although, the coordinates obtained are different from those reported in the literature.[210] Conversely, the fractional occupancies and thermal coefficients could not be refined for any of the atoms in this phase. The thermal coefficients for atoms in the LiCl phase could not be refined either. Hence, thermal coefficients for all atoms in the $Pm\bar{3}m$ and LiCl phase were fixed at 2.5×10^{-2} Å^2. Lastly, the phase fractions obtained indicate that the sample contains 96.89(10)% the *Pban* phase, 2.68(10)% $Pm\bar{3}m$ and

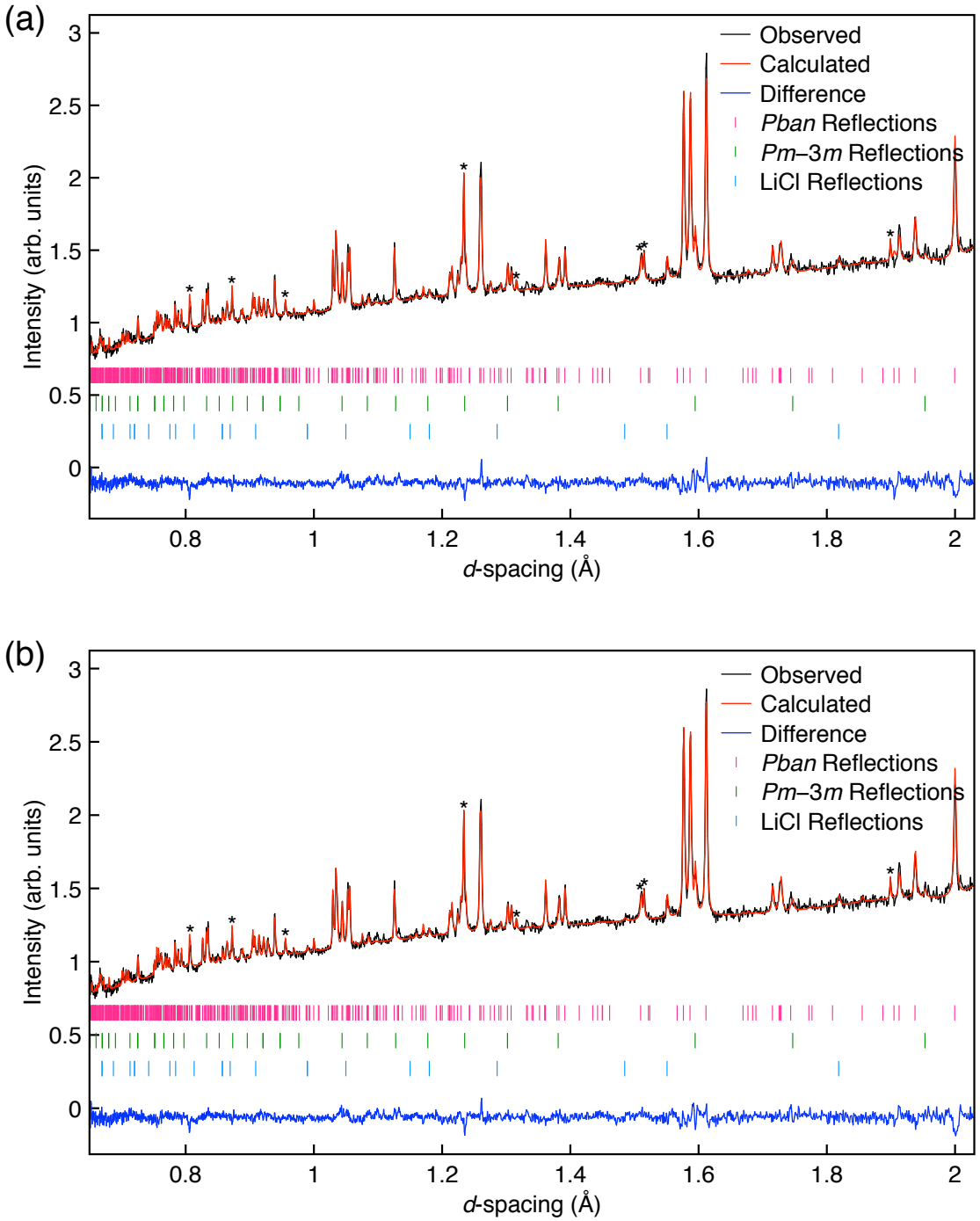

Figure 4.24: Rietveld refinement of the NPD data collected at 20 °C for 322.89 μA using the backscattering bank, for a sample of Li_2ODCl, synthesised using a conventional solid-state reaction, using the *Pban* (Li_2ODCl) structural model adapted from those proposed at (a) 300 and (b) 4 K by Hanghofer *et al.*,[210] the $Pm\bar{3}m$ (Li_2ODCl)[210] and $Fm\bar{3}m$ (LiCl)[199] models. Reflections corresponding to the sample holder were excluded and are denoted by *. (a) χ^2 = 1.83, wR_p = 1.96%, R_p = 1.58%. (b) χ^2 = 1.77, wR_p = 1.93%, R_p = 1.59%.

Table 4.15: Structural parameters for a sample of Li_2ODCl, synthesised using a conventional solid-state reaction, obtained from Rietveld refinement of the NPD data collected at 20 °C using isotropic thermal coefficients. 300 K model: Li_2ODCl: space group *Pban*, a = 7.75000(14) Å, b = 7.99780(11) Å, c = 3.82554(7) Å, V = 237.118(5) Å^3, phase fraction = 96.89(10)%. Li_2ODCl: space group $Pm\bar{3}m$, a = 3.90604(25) Å, V = 59.595(12) Å^3, phase fraction = 2.68(10)%. LiCl: space group $Fm\bar{3}m$, a = 5.14333(57) Å, V = 136.061(45) Å^3, phase fraction = 0.43(2)%. χ^2 = 1.83, wR_P = 1.96%, R_P = 1.58%. 4 K model: Li_2ODCl: space group *Pban*, a = 7.74999(14) Å, b = 7.99783(10) Å, c = 3.82550(7) Å, V = 237.116(5) Å^3, phase fraction = 96.94(10)%. Li_2ODCl: space group $Pm\bar{3}m$, a = 3.90599(25) Å, V = 59.593(11) Å^3, phase fraction = 2.66(10)%. LiCl: space group $Fm\bar{3}m$, a = 5.14339(57) Å, V = 136.066(45) Å^3, phase fraction = 0.41(2)%. χ^2 = 1.77, wR_P = 1.93%, R_P = 1.59%.

Atom	x	y	z	Occ.	U(iso) × 100 (Å^2)
Pban					
300 K					
Li1	0.0237(15)	0.25	0	0.366(17)	2.38(34)
Li2	0.25	−0.0118(325)	0	0.063(7)	2.38(34)
Li3	0.0737(18)	−0.0192(42)	0.4972(177)	0.117(9)	2.38(34)
O1	0	0	0	0.25	0.65(7)
D1	0.0812(13)	0.0145(19)	0.1607(30)	0.106(5)	2.52(26)
D2	0.0502(23)	0.4975(75)	0.1203(56)	0.053(4)	2.52(26)
Cl1	0.25	0.25	0.5	0.25	0.33(5)
Cl2	0.75	0.25	0.5	0.25	0.33(5)
Pm$\bar{3}$m					
Li1	0.5	0	0	0.667	2.5
O1	0	0	0	1	2.5
D1	0.1469(71)	0.1469(71)	0.1469(71)	0.125	2.5
Cl1	0.5	0.5	0.5	1	2.5
Pban					
4 K					
Li1	0.0234(15)	0.25	0	0.355(17)	2.01(35)
Li2	0.25	−0.0117(343)	0	0.052(7)	2.01(35)
Li3	0.0824(24)	−0.0185(47)	0.4886(211)	0.106(10)	2.01(35)
Li4	0.25	0.75	0	0.060(14)	2.01(35)
O1	0	0	0	0.25	0.46(7)
D1	0.0706(32)	0.0044(63)	0.1372(51)	0.098(11)	3.12(79)
D2	0.0736(50)	0.4838(56)	0.1699(78)	0.060(10)	3.12(139)
Cl1	0.25	0.25	0.5	0.25	0.77(22)
Cl2	0.75	0.25	0.5	0.25	0.33(18)

Pm$\bar{3}$m					
Li1	0.5	0	0	0.667	2.5
O1	0	0	0	1	2.5
D1	0.1542(82)	0.1542(82)	0.1542(82)	0.125	2.5
Cl1	0.5	0.5	0.5	1	2.5

0.43(2)% LiCl phase. In general, the new *Pban* 300 K model provides a good fit for the NPD data recorded at 20 °C. However, not being able to refine the thermal coefficients freely suggests that the fit may not be as good as it first appears. Hence, the model may not be fully accurate, which is surprising given that this model provided the best fit for the XRD data (Figure 4.11).

The new *Pban* 4 K model also provides a very good fit with a χ^2 = 1.77 and wR_p = 1.93% (Figure 4.24(b)). Again, all reflections are indexed, and the calculated and observed intensities appear to match quite well. As expected, the lattice parameters obtained are very similar to those obtained using the 300 K model. The atomic coordinates for Li and D atoms were successfully refined, and the values obtained generally agree with those reported by Hanghofer *et al.*[210] However, the coordinates for Li3 are observed to differ noticeably. Hence, the proposed and refined structure are shown in Figure 4.25 for comparison. As with the *Pban* 300 K model, the fractional occupancies for the O and Cl atoms were fixed at 0.25 and, those for the Li and D atoms were refined freely. The occupancy values obtained differ significantly from those obtained from the XRD analysis and suggest a composition of $Li_{2.578}OD_{1.264}Cl$. Again, the formula obtained is not charge-balanced and deviates from the intended composition of Li_2ODCl. Here too, only isotropic thermal coefficients could be obtained, and even then, the coefficients for the Li atoms had to be constrained to be equivalent to avoid negative values. Overall, the values obtained seem quite typical for diffraction data acquired close to room temperature. For the *Pm$\bar{3}$m* phase, the atomic coordinates for D were successfully refined. However, again, the coordinates obtained differ from those reported.[210] As with the earlier refinements, the fractional occupancies for Li and D could not be refined to sensible values. Moreover, the thermal coefficients for all atoms in the *Pm$\bar{3}$m*

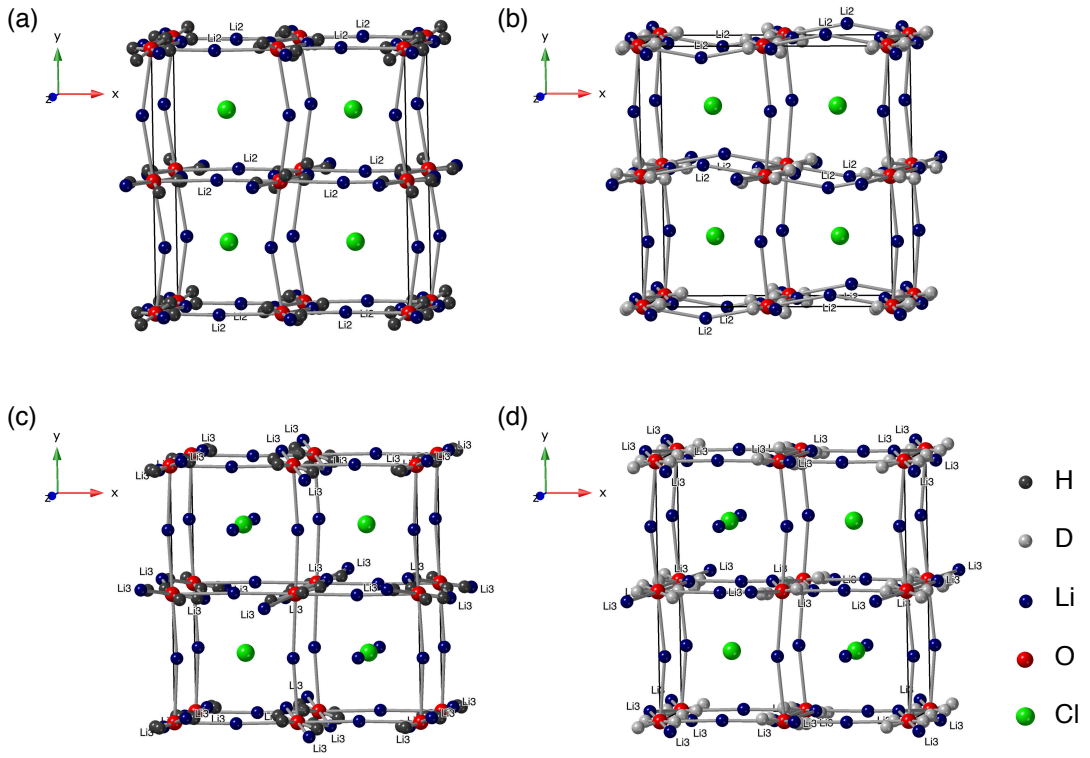

Figure 4.25: The structure of Li_2OHCl in space group *Pban* adapted from the models proposed by Hanghofer and co-workers[210] at (a) 300 and (c) 4 K. Also, shown is the refined structure of Li_2ODCl in space group *Pban* obtained via Rietveld analysis of the NPD data acquired at 20 °C during the current study using the (b) 300 and (d) 4 K models.

and LiCl phases had to be fixed at 2.5×10^{-2} Å^2 as suitable values could not be obtained. Lastly, the phase fractions obtained suggest the sample contains 96.94(10)% *Pban* phase, 2.66(10)% $Pm\bar{3}m$ phase and 0.41(2)% LiCl phase. These ratios are very similar to those determined via the earlier refinement using the *Pban* 300 K model. Overall, the fit appears to be quite good. Thus, suggesting that Li_2OH/DCl very likely exists in an orthorhombic structure in space group *Pban* at room temperature. However, it is difficult to establish the presence of an additional Li site from the current data. Hence, the precise structure of Li_2OH/DCl at room temperature remains to be confirmed.

The High-Temperature Cubic Phase of Li_2OH/DCl

Finally, the NPD patterns acquired at 50 and 150 °C were analysed to investigate the high-temperature cubic ($Pm\bar{3}m$) phase of Li_2OH/DCl. Multi-phase refinements completed using the $Pm\bar{3}m$ (Li_2ODCl)[210] and $Fm\bar{3}m$ (LiCl)[199]

models are shown in Figure 4.26. The corresponding structural parameters are detailed in Table 4.16. A reasonable fit is obtained for the NPD data acquired at 50 °C (χ^2 = 4.45 and wR_p = 3.08%). All reflections have been indexed. However, for some of the reflections, the calculated intensity does not match well with that observed. Inspection of the structural parameters obtained shows that the lattice parameter obtained is in agreement with the value reported in the literature for this phase at ~50 °C.[213] The atomic coordinates for D were successfully refined and are very similar to those originally reported by Hanghofer and co-workers for protons in $Li_{1.84}OH_{1.16}Cl$.[210] Unfortunately, the fractional occupancies for Li and D could not be refined as attempts to do so resulted in an extremely low value for Li and a negative value for D. Thus, the precise stoichiometry of the desired phase could not be determined. This is in contrast to the findings of Hanghofer *et al.*[210] as they were able to successfully refine the fractional occupancies for Li and H in $Li_{1.84}OH_{1.16}Cl$. However, it is noted that the sample investigated by Hanghofer *et al.*,[210] was originally intended to be Li_3OCl and not Li_2OHCl. Isotropic thermal coefficients were also determined and the coefficients for O and D were constrained to be equivalent to avoid an unreasonably large value for D. In general, the coefficients obtained appear reasonable and are in good agreement with those reported by Hanghofer *et al.*[210] However, it is noted that the coefficient obtained for Li is slightly large. As with the earlier refinements, the thermal coefficients for atoms in the LiCl phase could not be refined. Hence, they were fixed at 2.5×10^{-2} Å^2. Lastly, the phase fractions obtained suggest that the sample contains 99.10(11)% Li_2ODCl and 0.90(11)% LiCl. However, these values may not be accurate owing to the quality of fit obtained.

A slightly better fit was obtained for the NPD data acquired at 150 °C data with a χ^2 = 2.93 and wR_p = 2.90%. Again, all reflections are indexed. However, there is still some mismatch between the observed and calculated intensities. As expected, the lattice parameter increases with increasing temperature. Additionally, the atomic coordinates for D are very similar to those obtained earlier at 50 °C and those reported by Hanghofer *et al.*[210] As with the previous refinement, the fractional occupancies for Li and D could not be refined. Any

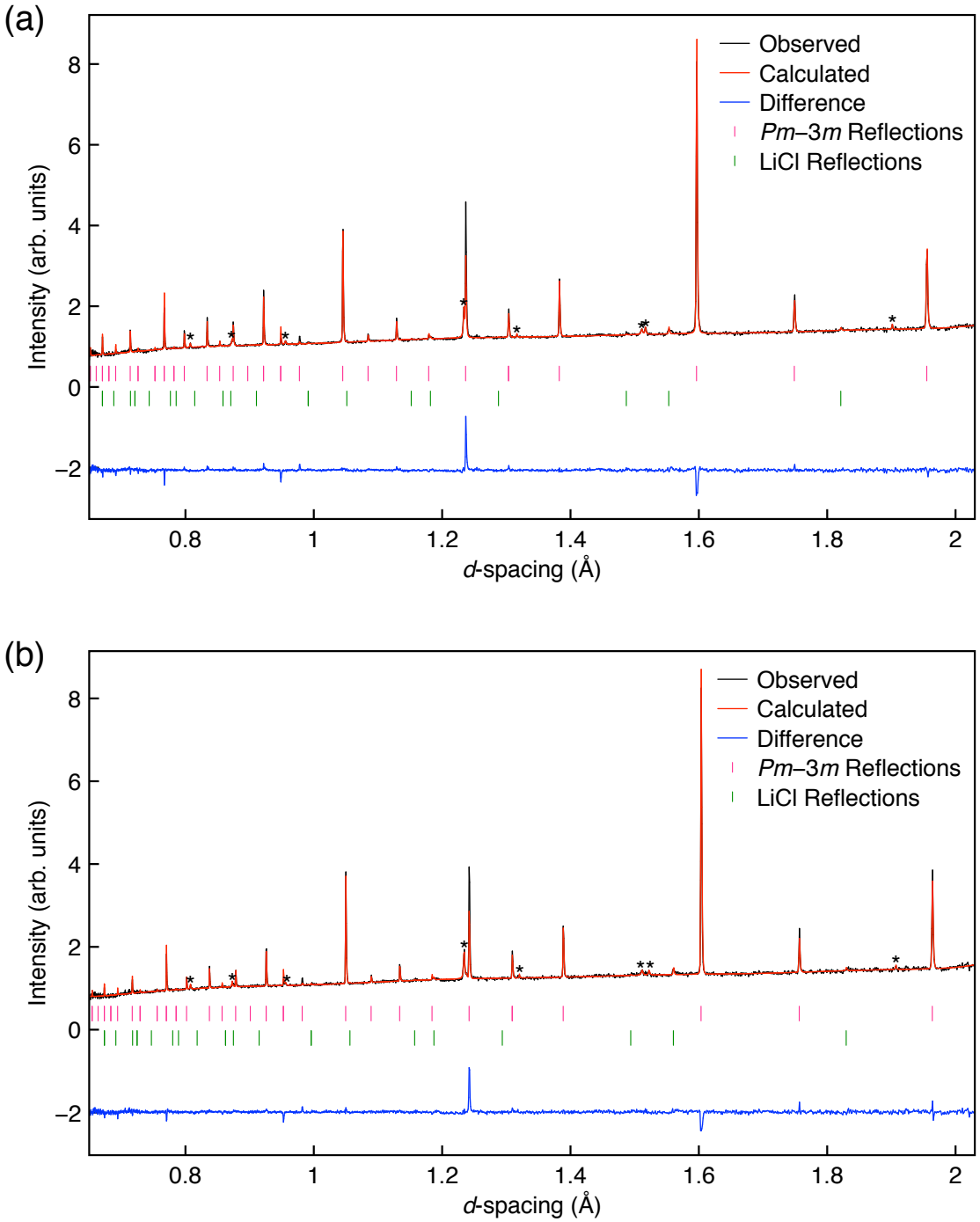

Figure 4.26: Rietveld refinement of the NPD data collected at (a) 50 °C for 320.04 μA and (b) 150 °C for 237.44 μA using the backscattering bank, for a sample of Li_2ODCl, synthesised using a conventional solid-state reaction, using the $Pm\bar{3}m$ (Li_2ODCl) structural model proposed by Hanghofer *et al.*[210] and the $Fm\bar{3}m$ (LiCl)[199] model. Reflections corresponding to the sample holder were excluded and are denoted by *. (a) χ^2 = 4.45, wR_p = 3.08%, R_p = 1.78%. (b) χ^2 = 2.93, wR_p = 2.90%, R_p = 1.88%.

Table 4.16: Structural parameters for a sample of Li_2ODCl, synthesised using a conventional solid-state reaction, obtained from Rietveld refinement of the NPD data collected at 50 and 150 °C using isotropic thermal coefficients. 50 °C: Li_2ODCl: space group $Pm\bar{3}m$, a = 3.91033(2) Å, V = 59.792(1) Å^3, phase fraction = 99.10(11)%. LiCl: space group $Fm\bar{3}m$, a = 5.15109(63) Å, V = 136.677(50) Å^3, phase fraction = 0.90(11)%. χ^2 = 4.45, wR_P = 3.08%, R_P = 1.78%. 150 °C: Li_2ODCl: space group $Pm\bar{3}m$, a = 3.92756(2) Å, V = 60.586(1) Å^3, phase fraction = 99.05(10)%. LiCl: space group $Fm\bar{3}m$, a = 5.17493(53) Å, V = 138.584(43) Å^3, phase fraction = 0.95(10)%. χ^2 = 2.93, wR_P = 2.90%, R_P = 1.88%.

Atom	x	y	z	Occ.	U(iso) × 100 (Å^2)
50 °C					
Li	0.5	0	0	0.667	4.45(22)
O	0	0	0	1	1.23(5)
D	0.1214(8)	0.1214(8)	0.1214(8)	0.125	1.23(5)
Cl	0.5	0.5	0.5	1	1.05(5)
150 °C					
Li	0.5	0	0	0.667	4.85(24)
O	0	0	0	1	1.76(6)
D	0.1211(9)	0.1211(9)	0.1211(9)	0.125	1.76(6)
Cl	0.5	0.5	0.5	1	1.48(5)

attempts to do so resulted in a very low value for Li and a negative coefficient for D. The thermal coefficients were also refined, and the coefficients for O and D were constrained to be equivalent. Again, the coefficients obtained are very similar to those obtained at 50 °C and those reported in the literature.[210] Once again, the thermal coefficients for atoms in the LiCl phase could not be refined and were fixed at 2.5×10^{-2} Å^2. Lastly, the phase fractions obtained suggest that the sample contains 99.05(10)% Li_2ODCl and 0.95(10)% LiCl. This ratio is very similar to that determined at 50 °C for this sample and via the XRD data presented earlier (Figure 4.6).

It is noticed that the quality of fit obtained using the $Pm\bar{3}m$ model is not as good as initially hoped. This is surprising as the high-temperature phase of Li_2OH/DCl has been extensively studied, and all studies unanimously agree that Li_2OHCl exists in a cubic structure in space group $Pm\bar{3}m$ at temperatures

~>35 °C.[213] However, it must be noted that there is a distinct lack of crystallographic information in the literature regarding the proton/deuteron positions in the cubic ($Pm\bar{3}m$) phase of Li_2OH/DCl. Hence, the model reported by Hanghofer *et al.*[210] for a hydrated sample of "Li_3OCl", the composition of which was closer to Li_2OHCl than Li_3OCl, was used during analysis. To date, this is the only model to include structural information regarding the protons. Hence, this model was deemed suitable to analyse the data presented in the current study. However, the discrepancy between the observed and calculated intensities suggests that the structural information regarding the atoms is not entirely accurate. As discussed earlier, sensible fractional occupancies could not be determined for Li and D at 50 or 150 °C. Moreover, the thermal coefficients corresponding to O and D had to be constrained to be equivalent in order to avoid an unusually large coefficient for D. Thus, demonstrating that precise characterisation of Li and D atoms within Li_2ODCl is extremely challenging. Eilbracht *et al.*,[215] described the protons to be statically disordered over four possible positions around the oxygen. Additionally, Li_2OHCl is a known Li-ion conductor in the cubic ($Pm\bar{3}m$) phase.[213] Considering the temperature at which the data was collected (50 and 150 °C), it is very likely that Li_2OHCl exhibits Li-ion mobility. Moreover, it is entirely possible for the OH/OD groups to also exhibit mobility in the forms of rotational movement. Thus, possibly explaining the difficulties encountered during the characterisation of both Li and H/D atoms.

Another possible reason for a poor fit could be that the model used may have been inaccurate. It is well known that deuterons will naturally exchange with protons over time. Due to the hygroscopic nature of LiRAPs, great care was taken when packing and transporting the deuterated Li_2OHCl sample from the laboratory to the HRPD facility at ISIS, Oxford. The sample was carefully sealed and kept under moisture-free conditions. However, it is possible that over the course of the initial measurements (at −263 and 20 °C), which were quite lengthy (20 hrs 45 mins and 8 hrs 46 mins), some or most of the deuterium may have exchanged for protons. In such situations, post-measurement analysis via techniques such as NMR can be beneficial. However, this was not

possible as the sample was heated above its melting point during NPD measurements.

Nevertheless, to examine this possibility, the NPD patterns acquired at 50 and 150 °C were also analysed using the $Pm\bar{3}m$ (Li_2OHCl) model containing H instead of D. The refinements completed are shown in Figure 4.27 and the corresponding structural parameters are listed in Table 4.17. In both cases, the fit obtained appears to be fairly good (50 °C: χ^2 = 1.41 and wR_p = 2.01% and 150 °C: χ^2 = 1.41 and wR_p = 2.02%). It is noticed that the difference between the observed and calculated intensities is considerably reduced when compared to the previous refinements completed using the deuterated model (Figure 4.26). Thus, suggesting that the Li_2OHCl model provides a better fit than Li_2ODCl. Hence, the sample may contain some protons.

An inspection of the structural parameters obtained shows that the lattice parameters obtained are similar to those determined using the Li_2ODCl model (Figure 4.26). However, the atomic coordinates obtained for H, at 50 and 150 °C, vary significantly from those determined for D and those reported in the literature.[210] Unlike the refinements completed using Li_2ODCl, the fractional occupancies for Li and H were refined successfully. The occupancies obtained suggest a composition of $Li_{1.539}OH_{0.84}Cl$ and $Li_{1.383}OH_{1.06}Cl$ at 50 and 150 °C, respectively. Unfortunately, neither of the formulae are charge-balanced. They also differ significantly from each other and the intended composition. Moreover, the thermal coefficients could be refined freely for all atoms in both cases as no constraints were required. The coefficients obtained for O and Cl appear quite reasonable, whereas the coefficients obtained for Li and H are a little high but in agreement with those reported in the literature.[210] Yet again, the thermal coefficients for atoms in the LiCl phase could not be refined and were fixed at 2.5×10^{-2} Å^2. Lastly, according to the phase fractions obtained, the sample consists of 99.08(6)% Li_2OHCl and 0.92(6)% LiCl at 50 °C and 99.05(7)% Li_2OHCl and 0.95(7)% LiCl at 150 °C. The phase fractions obtained are similar to those determined earlier using the Li_2ODCl model (Figure 4.26) and via the XRD data (Figure 4.6).

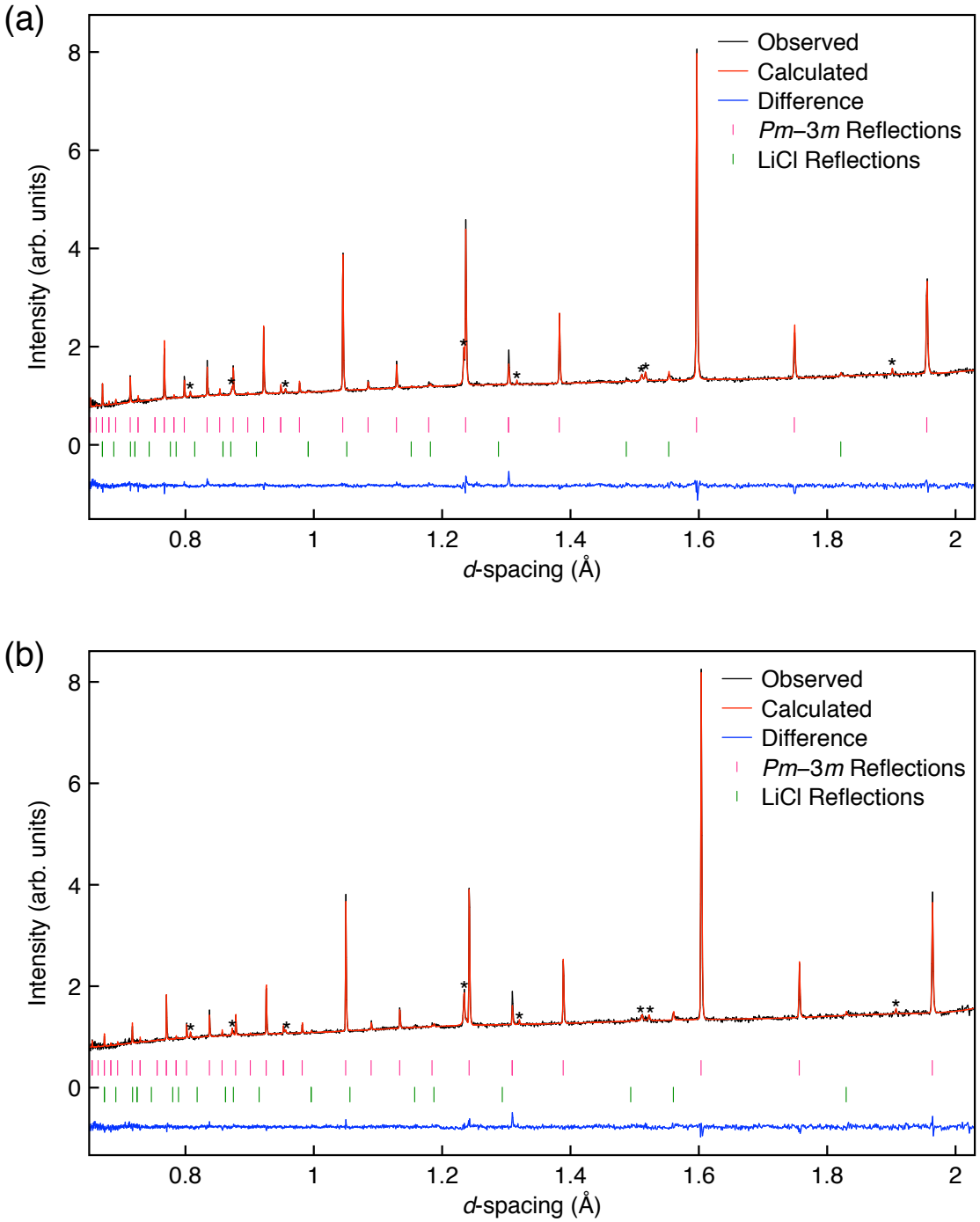

Figure 4.27: Rietveld refinement of the NPD data collected at (a) 50 °C for 320.04 μA and (b) 150 °C for 237.44 μA using the backscattering bank, for a sample of Li_2ODCl, synthesised using a conventional solid-state reaction, using the $Pm\bar{3}m$ (Li_2OHCl) structural model proposed by Hanghofer *et al.*[210] and the $Fm\bar{3}m$ (LiCl)[199] model. Reflections corresponding to the sample holder were excluded and are denoted by *. (a) χ^2 = 1.75, wR_p = 1.94%, R_p = 1.56%. (b) χ^2 = 1.41, wR_p = 2.01%, R_p = 1.67%.

Table 4.17: Structural parameters for a sample of Li_2ODCl, synthesised using a conventional solid-state reaction, obtained from Rietveld refinement of the NPD data collected at 50 and 150 °C using isotropic thermal coefficients. 50 °C: Li_2OHCl: space group $Pm\bar{3}m$, a = 3.91035(1) Å, V = 59.793(0) Å^3, phase fraction = 99.08(6)%. LiCl: space group $Fm\bar{3}m$, a = 5.15094(38) Å, V = 136.666(30) Å^3, phase fraction = 0.92(6)%. χ^2 = 1.75, wR_P = 1.94%, R_P = 1.56%. 150 °C: Li_2OHCl: space group $Pm\bar{3}m$, a = 3.92757(1) Å, V = 60.586(1) Å^3, phase fraction = 99.05(7)%. LiCl: space group $Fm\bar{3}m$, a = 5.17487(36) Å, V = 138.579(29) Å^3, phase fraction = 0.95(7)%. χ^2 = 1.41, wR_P = 2.01%, R_P = 1.67%.

Atom	x	y	z	Occ.	U(iso) × 100 (Å^2)
50 °C					
Li	0.5	0	0	0.513(22)	3.97(33)
O	0	0	0	1	1.59(4)
H	0.1010(17)	0.1010(17)	0.1010(17)	0.105(14)	4.59(114)
Cl	0.5	0.5	0.5	1	0.98(3)
150 °C					
Li	0.5	0	0	0.461(23)	3.50(39)
O	0	0	0	1	2.11(5)
H	0.1102(16)	0.1102(16)	0.1102(16)	0.133(22)	4.96(125)
Cl	0.5	0.5	0.5	1	1.36(4)

Considering both sets of refinements completed with the Li_2ODCl and Li_2OHCl models, it is clear that neither of these models provide particularly good fits for the NPD data acquired at 50 and 150 °C. The Li_2ODCl model does not allow for the fractional occupancies to be refined, meaning the precise composition of the desired phase cannot be determined. The Li_2OHCl model, on the other hand, allows for the fractional occupancies to be refined. However, the composition obtained deviates significantly from Li_2OHCl. Additionally, the compositions determined at 50 and 150 °C do not agree with each other. Overall, it is challenging to determine whether any deuterons have indeed been replaced by protons. Refinements were also attempted using the $Li_2OH_{1-x}D_xCl$ models. However, the structural parameters obtained for H and D were the same as those presented here. As in, the fractional occupancies determined for D were negative, and those for H were similar to those obtained using the Li_2OHCl model. Thus, the relative amounts of H and D

in the sample could not be determined. However, the most likely scenario is that some deuterons may have been exchanged with protons. Hence, the most likely cause of the difficulties encountered during the refinements is the deuteron/proton exchange *and* Li and H mobility within the samples. This also explains the severe lack of crystallographic information for the H/D atoms in the Li_2OH/DCl system in the literature.

4.3.1.4 SSNMR Studies of Li_2OHCl

To further elucidate the structure of Li_2OHCl, both the room- and high-temperature phase were analysed via VT multinuclear SSNMR. The ^1H and ^7Li MAS NMR spectra obtained at 33 and 52 °C, for a sample of Li_2OHCl synthesised via a conventional solid-state route, are shown in Figure 4.28. At 33 °C, a single broad resonance centred around 0 ppm is observed in both cases. In the ^1H MAS NMR spectrum, a resonance with two sets of spinning sidebands is observed, characteristic of hydroxyl groups. Typically, a single resonance is indicative of a single site. However, both the ^1H and ^7Li resonances observed here are relatively broad and may be composed of multiple, overlapped resonances, making it challenging to determine the number of crystallographically distinct H and Li sites present in the sample at 33 °C. At 52 °C, where Li_2OHCl is known to adopt a cubic structure in space group $Pm\bar{3}m$, both resonances narrow and increase in intensity, and the spinning sidebands become less pronounced. The line narrowing observed here is likely due to a decrease in homonuclear dipolar couplings as expected following the phase transition to a higher symmetry structure.

As stated earlier, MAS is an effective technique for removing the effects of anisotropic interactions to achieve narrow lineshapes in NMR spectra. However, static conditions can be beneficial in some instances, *e.g.*, during structural analysis, as the effects of anisotropic NMR interactions can be observed in the spectrum. Hence, Li_2OHCl was also investigated using static ^7Li NMR, and the spectra obtained at 24 and 54 °C are shown in Figure 4.29. At 24 °C, a broad symmetrical resonance with satellite transitions is observed. This is expected for a spin-3/2 nucleus, *i.e.*, a dipolar broadened lineshape at ~0 ppm,

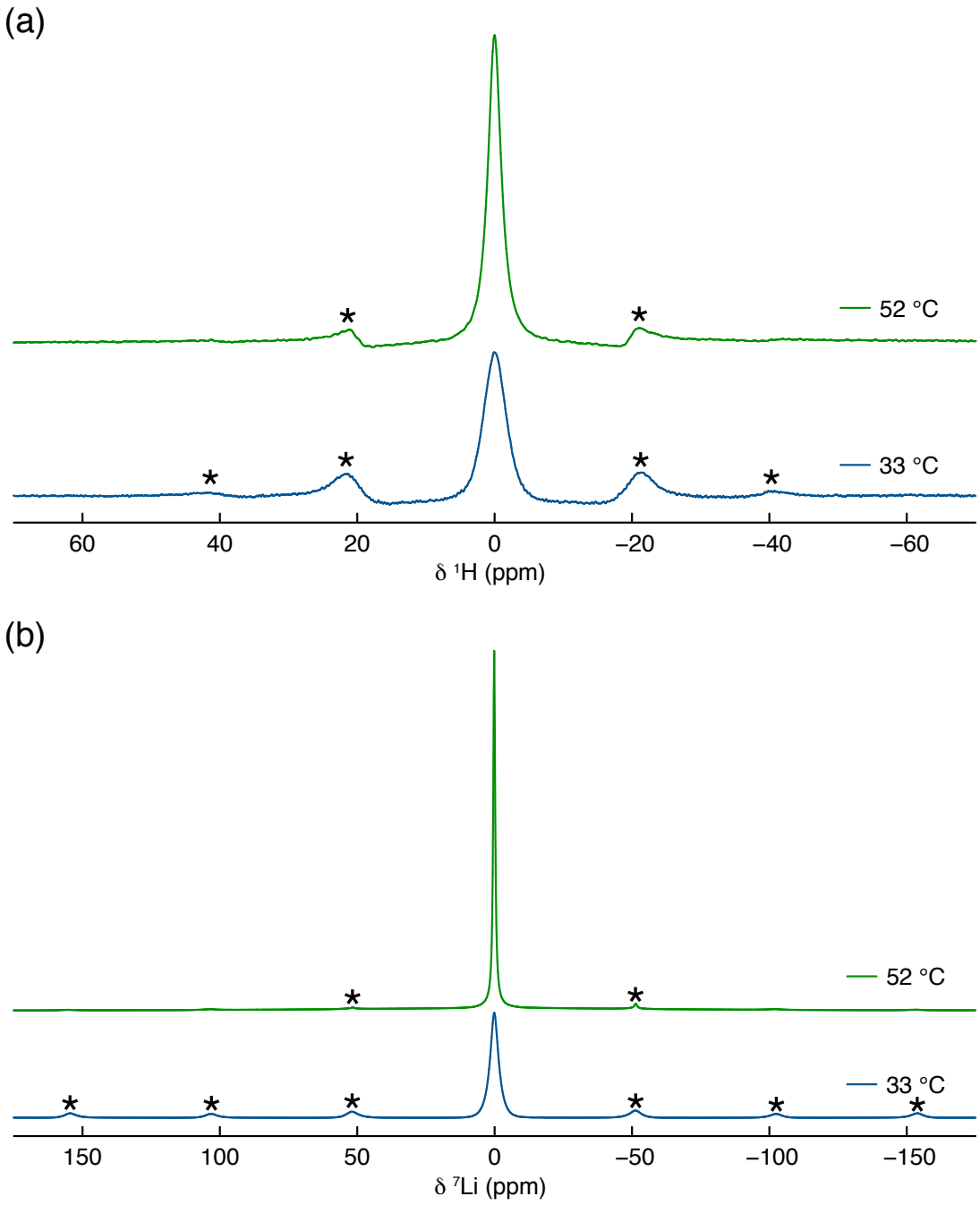

Figure 4.28: (a) ^{1}H and (b) ^{7}Li (11.7 T) MAS NMR spectra acquired at 33 (blue) and 52 °C (green), for a sample of Li_2OHCl prepared via conventional solid-state synthesis inside an Ar-filled glovebox. The MAS rate was 10 kHz and spinning sidebands are denoted by *. A recycle delay of (a) 500 and 60 s was used at 33 and 52 °C and (b) 60 s was used at 33 and 52 °C. In all cases, 4 transients were acquired.

corresponding to the central transition ($+1/2 \longleftrightarrow -1/2$). A broad resonance is also observed, corresponding to the satellite transitions ($3/2 \longleftrightarrow 1/2$ and $-1/2 \longleftrightarrow -3/2$). Broadening of the central transition is due to strong ^{7}Li – ^{7}Li

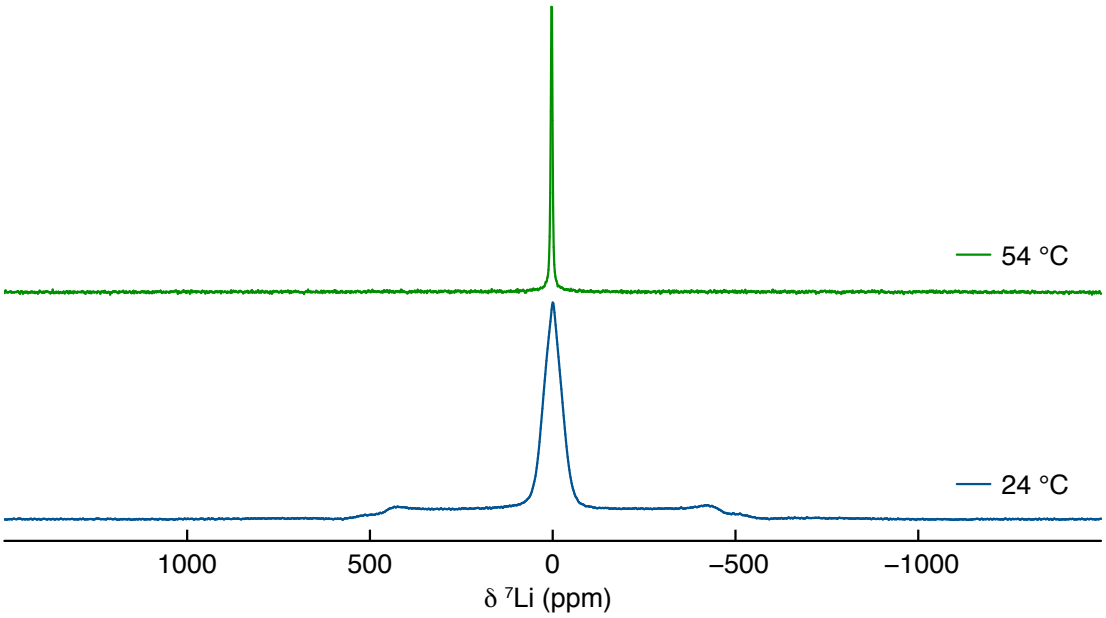

Figure 4.29: Static ^{7}Li (9.4 T) NMR spectra acquired at 24 (blue) and 54 °C (green), for a sample of Li_2OHCl, prepared via conventional solid-state synthesis inside an Ar-filled glovebox. A recycle delay of 65 and 1 s was used at 24 and 54 °C, respectively, to acquire 8 transients.

homonuclear dipolar interactions that are averaged out as the temperature is increased to 54 °C, and a single narrow resonance, indicative of a single site is observed. Unfortunately, it is not possible to differentiate how many distinct Li sites there are at 24 °C because there is considerable overlap.

Li_2OHCl was also studied using VT ^{35}Cl MAS NMR spectroscopy and the spectra acquired at 33 and 63 °C are shown in Figure 4.30. At 33 °C, the lineshape observed appears to be composed of multiple overlapping resonances. It is noted that a signal appears at ~5 ppm which corresponds to LiCl, an impurity phase present in a very small quantity (~0.56%). This is in agreement with the XRD and NPD data (*vide supra*). At 63 °C, following the phase transition to cubic symmetry in space group $Pm\bar{3}m$, the lineshape is different, with a broad asymmetric lineshape observed, with an additional shouldering present. The resonance corresponding to LiCl remains unchanged. Both lineshapes were simulated to determine the number of crystallographically distinct Cl sites present and are shown in Figure 4.31. The corresponding quadrupolar parameters are listed in Table 4.18. The lineshape observed in the spectrum obtained

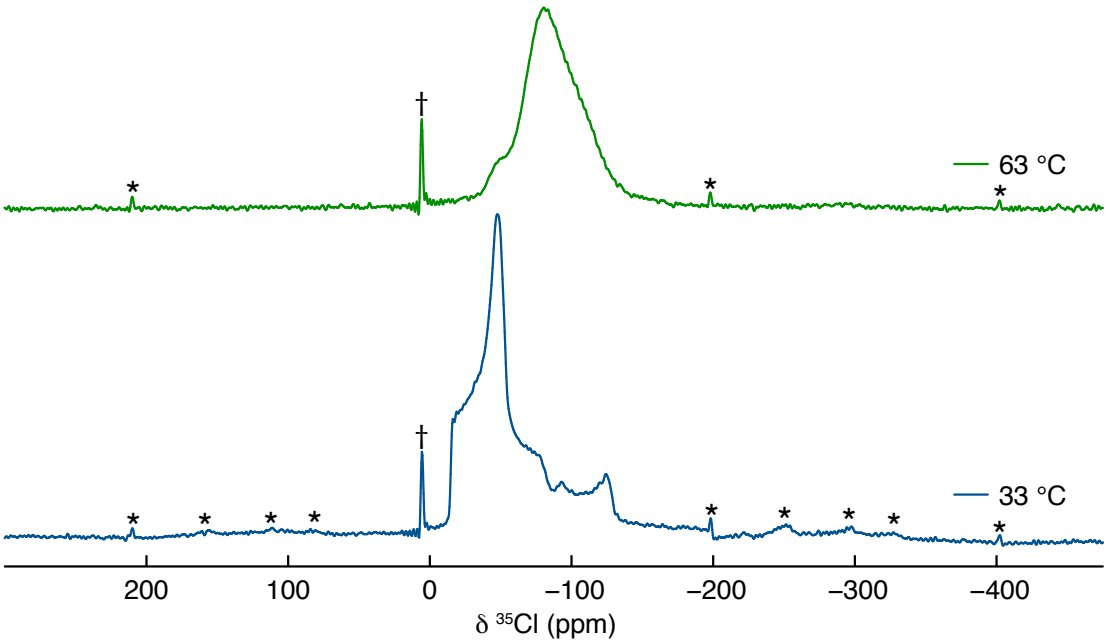

Figure 4.30: ^{35}Cl (11.7 T) MAS NMR spectra acquired at 33 (blue) and 63 °C (green), for a sample of Li_2OHCl prepared via conventional solid-state synthesis inside an Ar-filled glovebox. The MAS rate was 12 kHz and spinning sidebands are denoted by *. In both cases, 2560 transients were acquired using a recycle delay of 5 s. The known LiCl impurity is denoted by †.

at 33 °C could only be simulated using three distinct Cl sites. However, it is noted that none of the proposed structures investigated earlier for the room-temperature phase of Li_2OHCl had three distinct Cl sites. Moreover, two sites were required to simulate the lineshape observed at 63 °C. This is surprising as the high-temperature cubic structure for Li_2OHCl in space group $Pm\bar{3}m$ only has a single Cl site.

As previously discussed in Chapter 2, diffraction techniques are used to investigate the long-range order in a crystalline material, whereas NMR is a local structural probe. Thus, the data presented indicates that whilst there is only one crystallographically distinct Cl site in the high-temperature cubic ($Pm\bar{3}m$) phase of Li_2OHCl, there are two different local Cl environments identified via SSNMR. It is noted that the XRD data presented earlier demonstrated the presence of an unidentified impurity phase in the sample, in addition to the desired phase and residual LiCl. The XRD analysis indicated that the impurity phase is present in a very small quantity when compared

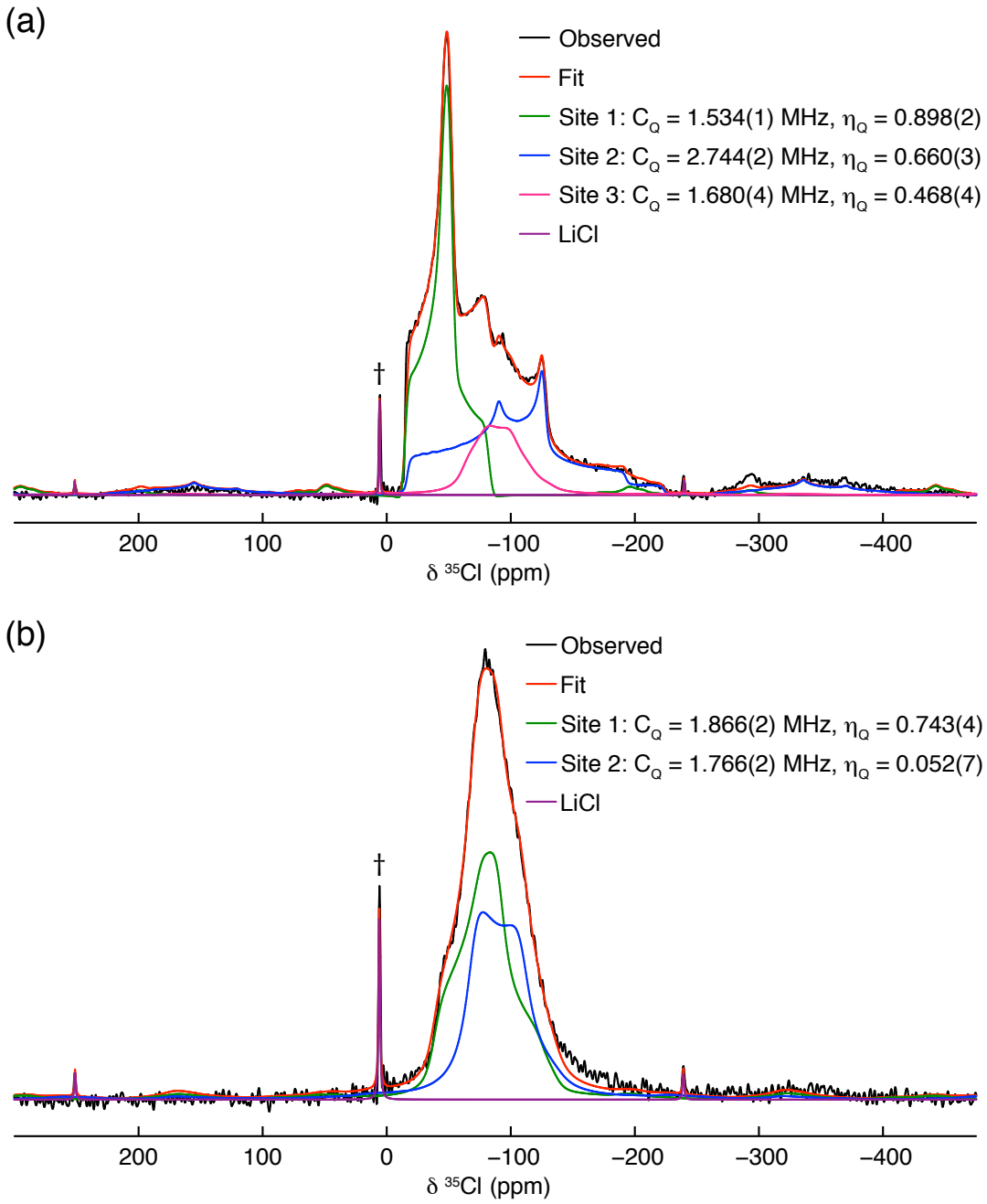

Figure 4.31: Simulations of the ^{35}Cl (11.7 T) MAS NMR spectra acquired at (a) 33 °C and (b) 63 °C for a sample of Li_2OHCl prepared via conventional solid-state synthesis inside an Ar-filled glovebox. The MAS rate was 12 kHz and a recycle delay of 5 s was used to acquire 2560 transients. At 33 °C, three sites were required to fit the lineshape and the corresponding quadrupolar parameters were obtained: Site 1 (C_Q = 1.534(1) MHz and η_Q = 0.898(2)), Site 2 (C_Q = 2.744(2) MHz and η_Q = 0.660(3)), Site 3 (C_Q = 1.680(4) and η_Q = 0.468(4)). At 63 °C, two sites were required to fit the lineshape and the corresponding quadrupolar parameters were obtained: Site 1 (C_Q = 1.866(2) MHz and η_Q = 0.743(4)), Site 2 (C_Q = 1.766(2) MHz and η_Q = 0.052(7)). The known LiCl impurity is denoted by †.

Table 4.18: The ^{35}Cl NMR parameters, δ, C_Q, and η_Q, obtained by simulating the lineshapes observed in the ^{35}Cl MAS NMR spectra obtained at 33 and 63 °C, for a sample of Li_2OHCl prepared via conventional solid-state synthesis inside an Ar-filled glovebox.

Site	δ (ppm)	C_Q (MHz)	η_Q
33 °C			
1	−14.53(1)	1.534(1)	0.898(2)
2	−13.00(7)	2.744(2)	0.660(3)
3	−58.35(8)	1.680(4)	0.468(4)
63 °C			
1	−37.24(5)	1.866(2)	0.743(4)
2	−58.39(6)	1.766(2)	0.052(7)

to the desired Li_2OHCl phase. Furthermore, the corresponding reflections did not change with increasing temperature, suggesting that, unlike Li_2OHCl, the impurity phase does not undergo any structural changes as a function of temperature. As stated earlier, a signal from residual LiCl has been observed in the ^{35}Cl MAS NMR spectra, which remained unchanged between 33 and 63 °C. However, no distinct signal from the impurity phase is observed. It could be argued/suggested that one of the Cl sites simulated corresponds to the impurity phase as only one crystallographically distinct Cl site is expected at 63 °C. However, this is not the case, as the impurity phase does not change with increasing temperature. Therefore, the corresponding ^{35}Cl resonance would also remain unchanged. Thus, further suggesting that Cl exhibits two different local environments in Li_2OHCl at 63 °C, despite occupying only one crystallographically distinct site.

Inspection of the individual Cl sites determined for the room-temperature phase shows that all three sites have a relatively low value of C_Q and a mid to high value of η_Q. Typically, for perfectly cubic systems such as LiCl, NaCl and KCl, C_Q and η_Q are close or equal to 0 for ^{35}Cl,[163] whereas materials with low symmetry, such as transition metal complexes, the values of C_Q can be as high as ~40 MHz for ^{35}Cl.[190] Therefore, the C_Q values determined here are relatively small, suggesting the room-temperature structure of Li_2OHCl is

of high symmetry but not perfectly cubic. Interestingly, the two sites determined for the cubic phase have C_Q = 1.77 and 1.87 MHz and η_Q = 0.743 and 0.052, respectively. It is noted that site 1 appears to be similar to the Cl site 1 identified in the room-temperature phase of Li_2OHCl, with similar values of C_Q and η_Q. Site 2, on the other hand, does not appear to resemble any of the sites in the room-temperature phase. As stated earlier, a perfectly cubic system would have a C_Q and η_Q very close to 0. Thus, the presence of two Cl sites with C_Q and $\eta_Q > 0$ insinuates that the high-temperature phase of Li_2OHCl may not adopt a perfectly cubic structure. Considering these findings and taking them in conjunction with the diffraction data presented earlier, where the high-temperature cubic phase of Li_2OHCl was demonstrated to adopt a cubic phase in space group $Pm\bar{3}m$, it seems that whilst the long-range structure of Li_2OHCl adopts a cubic symmetry, the local structure is of lower symmetry. Such situations can occur in cases of pseudo-symmetry where the unit cell adopts a certain geometrical shape. However, the arrangement of atoms within the unit cell does not exhibit the necessary symmetry elements required for that particular crystal system. Hence, the actual crystal system varies from the one it initially appears to be. Interestingly, the $Li_3OCl_{1-x}Br_x$ system was suggested to be pseudo-cubic by Zhao and Daemen.[124] Hence, the Li_2OHCl system may also be pseudo-cubic. This would explain the presence of two Cl sites in the high-temperature phase of Li_2OHCl. Furthermore, the presence of pseudo-symmetry could also have an influence on the Rietveld analysis presented earlier. However, it is noted that no such suggestions have been made in the literature regarding Li_2OHCl. Moreover, the current findings do not provide conclusive evidence for pseudo-symmetry. Therefore, additional diffraction-based studies would be required to confirm this.

4.3.2 Mechanically-Milled Li_2OHCl

4.3.2.1 Synthesis

The LiRAP samples discussed so far have all been synthesised via conventional solid-state methods. As discussed earlier, additional solid-state techniques such as mechanical milling can be used to aid synthesis and can, in

some cases, access phases that may not be otherwise formed. The usefulness of mechanical milling has been demonstrated in Chapter 3, where it was used to aid the synthesis of Li_3OCl with favourable outcomes. Hence, mechanical milling has also been employed here to investigate an alternative synthetic route for Li_2OHCl. A sample of Li_2OHCl was successfully synthesised via mechanical milling of the reagents, LiCl and LiOH, together at 500 rpm for 9 hrs via a planetary ball mill. The sample produced was analysed via laboratory XRD, and the corresponding diffraction pattern is shown in Figure 4.32. The XRD pattern obtained closely resembles that of the high-temperature cubic phase of Li_2OHCl (Figure 4.5). Thus, suggesting the desired phase in the mechanically-milled sample exists in cubic symmetry at room temperature. It is noted that the reflections observed are relatively broad, which suggests that the particle size of the mechanically-milled sample is considerably smaller than those prepared via conventional solid-state synthesis. In addition to the desired Li_2OHCl, there also appear to be some low intensity reflections corresponding to the starting material, LiCl. These reflections are also quite

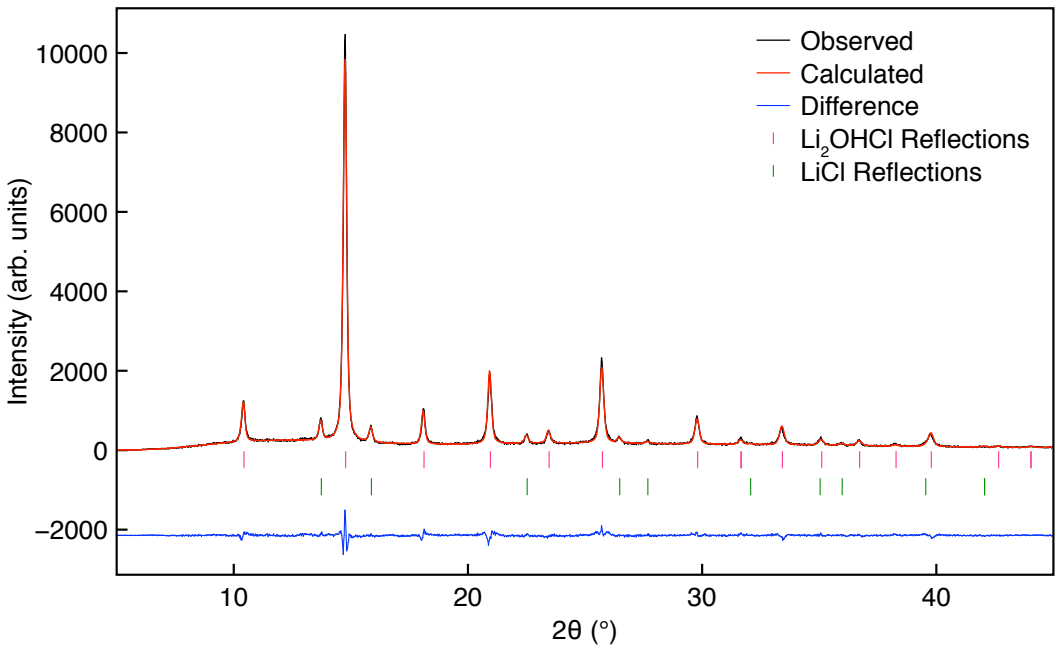

Figure 4.32: Rietveld refinement of the XRD data obtained for the mechanically-milled sample of Li_2OHCl. The sample was prepared via mechanical milling of the reagents together at 500 rpm for 9 hrs via a planetary ball mill. The refinement was completed using the $Pm\bar{3}m$ (Li_2OHCl)[125] and $Fm\bar{3}m$ (LiCl)[199] structural models. χ^2 = 2.08, wR_p = 8.87%, R_p = 6.96%.

broad. However, no reflections corresponding to the other reagent, LiOH, are observed. Similar observations were made for the Li_2OHCl sample prepared via conventional solid-state synthesis, as it was also found to contain residual LiCl, but no LiOH was present. Therefore, the presence of LiCl is likely a feature of the Li_2OHCl system and not solely the preparation method. As mentioned earlier, it has been suggested in the literature that residual LiCl may be indicative of LiCl-based defects in the system.[132,218] Therefore, the same may also be true for the sample prepared via mechanical milling.

The XRD data obtained was analysed via the Rietveld method using the $Pm\bar{3}m$ (Li_2OHCl)[210] and $Fm\bar{3}m$ (LiCl)[199] structural models. The corresponding structural parameters, including the isotropic thermal coefficients, are listed in Table 4.19. The fit appears to be quite good and a χ^2 = 2.08 and wR_p = 8.87% are obtained. The Rietveld analysis confirms initial suggestions that the sample produced via mechanical milling adopts a cubic structure in space group $Pm\bar{3}m$ at room temperature. A lattice parameter of 3.90775(9) Å is obtained, in good agreement with the value previously determined for the high temperature Li_2OHCl phase (*vide supra*) and with that reported in the literature.[213] The presence of residual LiCl suggests the composition of the de-

Table 4.19: Structural parameters for a mechanically-milled sample of Li_2OHCl, obtained from Rietveld refinement of the XRD data, using isotropic thermal coefficients. Li_2OHCl: space group $Pm\bar{3}m$, a = 3.90775(9) Å, V = 59.673(4) Å^3, phase fraction: 97.98(5)%. LiCl: space group $Fm\bar{3}m$, a = 5.14572(1) Å, V = 136.250(48) Å^3, phase fraction: 2.02(5)%. χ^2 = 2.08, wR_p = 8.87%, R_p = 6.96%.

Atom	x	y	z	Occ.	U(iso) × 100 (Å^2)
Li_2OHCl					
Li	0.5	0	0	0.656(19)	8.81(60)
O	0	0	0	1	2.73(7)
H	0.1279	0.1279	0.1279	0.169(8)	2.73(7)
Cl	0.5	0.5	0.5	1	4.05(5)
LiCl					
Li	0	0	0	1	8.05(140)
Cl	0.5	0.5	0.5	1	2.29(22)

sired phase may not be exactly as intended. Hence, in order to determine the exact composition of the desired phase, the fractional occupancies of the Li and H sites were refined. The occupancies obtained indicate a composition of $Li_{1.968}OH_{1.352}Cl$. Unfortunately, the formula is not charge-balanced. This is most likely due to the insufficient resolution of laboratory XRD. Nevertheless, it is close to the intended composition and similar to that determined for the sample synthesised via the conventional solid-state route.

Isotropic thermal coefficients were also determined and, as with the earlier refinements, the coefficients for O and H in Li_2OHCl were constrained to be equivalent. All thermal coefficients appear to be quite large. However, those corresponding to Li in both Li_2OHCl and LiCl are particularly big. The coefficient for Li in LiCl also has a large error. Similar observations were made for the refinement completed using the XRD data for the Li_2OHCl sample prepared via the conventional solid-state route (Figure 4.6). As stated earlier, this is in agreement with the literature as Hanghofer and co-workers also reported unusually large thermal coefficients for Li in this system.[210] Thus, unusually large thermal coefficients for Li appear to be a feature of this system. As discussed earlier, Li_2OHCl is known to exhibit Li-ion mobility in the cubic phase. Typically, Li_2OHCl adopts the cubic phase at elevated temperatures, therefore, it only exhibits Li-ion mobility at increased temperatures. However, in this instance, the cubic phase is present at room temperature. Thus, it is possible for the system to exhibit low levels of ion mobility at room temperature. This could result in a particularly large thermal coefficient for Li as the ion mobility may be interpreted as thermal motion during Rietveld analysis. Such a large thermal coefficient for Li in Li_2OHCl is also likely to affect the one determined for Li in LiCl. In this particular case, the breadth of the reflections, coupled with the low resolution of laboratory XRD, could be making it challenging to accurately determine structural parameters. Moreover, the fractional occupancies determined earlier may be slightly inaccurate, which would influence the corresponding thermal coefficients. Regrettably, it is difficult to determine the exact cause of the unusually large thermal parameters from this data alone.

Overall, the diffraction data presented here is interesting as it demon-

strates that not only can Li_2OHCl be synthesised without applying heat, but the high-temperature phase can be accessed directly at room temperature via solely mechanical milling. Hence, mechanically-milled Li_2OHCl is of great interest as it broadens the scope for further investigation into the LiRAP system.

4.3.2.2 NPD Studies of Mechanically-Milled Li_2ODCl

To further examine the effects of mechanical milling on Li_2OHCl, a deuterated sample was also studied via NPD at HRPD. A sample of Li_2ODCl was prepared by our collaborator using a 5% excess of LiOD to ensure that no residual LiCl remained. The reagent mixture was milled at 500 rpm for 15 hrs, and an XRD pattern corresponding to the sample produced is shown in Figure 4.33. Also shown for comparison is a diffraction pattern corresponding to the non-deuterated Li_2OHCl sample discussed earlier (first shown in Figure 4.32). Both diffraction patterns look very similar, suggesting the deuterated sample has been synthesised successfully. It is noted that no reflections corresponding to LiCl are observed in the XRD pattern corresponding to the deuterated sample. Thus, suggesting a 5% excess of LiOD is quite effective in ensuring that no residual LiCl remains. However, there does appear to be a small additional reflection present at $2\theta = 14.15°$, suggesting the presence of an impurity phase, albeit in a very small quantity. It is to be noted that the pattern is shown here for comparison to the non-deuterated sample. The XRD pattern corresponding to the exact sample analysed via NPD was acquired using a diffractometer with a Co source and is shown in the Appendix.

Initially, the mechanically-milled Li_2ODCl sample was analysed at 20 °C, and the NPD pattern obtained is shown in Figure 4.34(a). It looks very similar to the pattern obtained for the high-temperature cubic phase of Li_2ODCl synthesised via a conventional solid-state route (Figure 4.6). Additionally, in a similar manner to the XRD data, the reflections observed in the NPD pattern are quite broad, suggesting a small particle size. As demonstrated earlier, the Li_2OHCl sample synthesised via a conventional solid-state route undergoes a phase transition upon heating and adopts a cubic structure in space group $Pm\bar{3}m$ at ~40 °C. The mechanically-milled sample of Li_2OH/DCl, on the

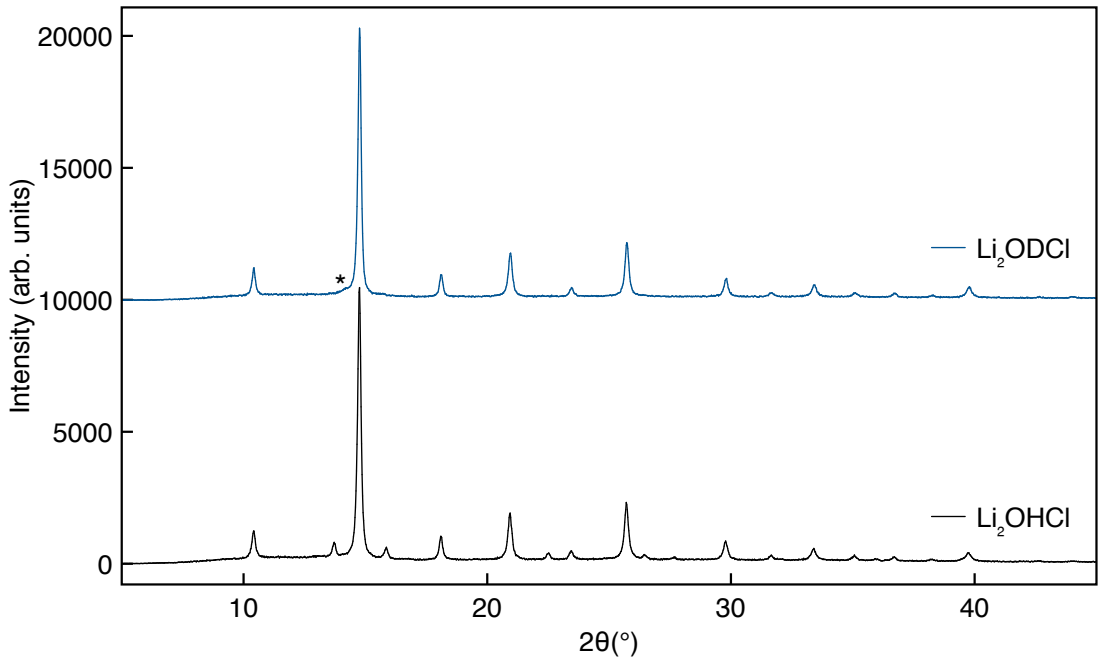

Figure 4.33: X-ray diffraction patterns obtained for the deuterated and non-deuterated samples of Li_2OHCl synthesised via mechanical milling. The deuterated and non-deuterated samples were prepared via mechanical milling of the reagents together at 500 rpm for 15 hrs and 9 hrs, respectively, via a planetary ball mill. The reflection denoted with * is believed to correspond to an impurity phase.

other hand, adopts a cubic structure, also in space group $Pm\bar{3}m$, but at room temperature. Thus, VT NPD experiments were completed to investigate the phase behaviour of the mechanically-milled Li_2ODCl sample. HRPD allows for a much wider temperature range to be explored compared to the laboratory X-ray diffractometers. As such, the sample was cooled to −263 °C (10 K), the lowest temperature that could be achieved using the apparatus available. The diffraction pattern recorded at −263 °C (10 K) is also shown in Figure 4.34(a), and it appears to be different from the one obtained at 20 °C, owing to the presence of multiple additional reflections. Thus, suggesting a phase transition to a structure with lower symmetry at very low temperatures. The diffraction pattern at −263 °C consists of multiple broad reflections that overlap, making it challenging to determine whether this is the same phase as the room-temperature phase of the Li_2OHCl sample discussed earlier. The sample was then reheated to 20 °C, and the corresponding diffraction pattern is shown in Figure 4.34(b). The diffraction pattern looks identical to that observed prior

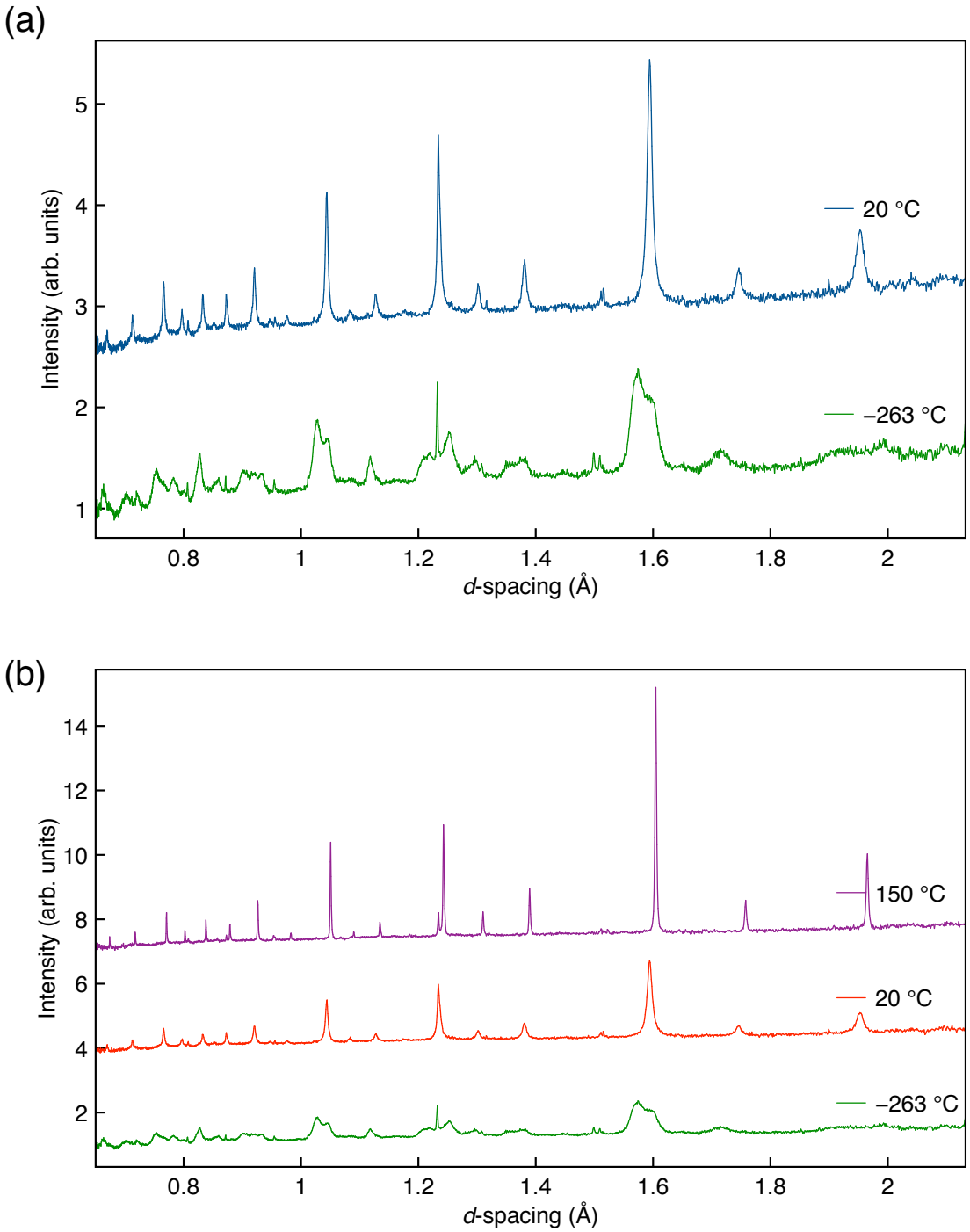

Figure 4.34: (a) Neutron diffraction powder patterns obtained for a sample of mechanically-milled Li_2ODCl at 20 and −263 °C, collected for 320.97 and 320.02 μA, respectively. (b) The sample was then heated to 20 and 150 °C and the data was collected for 278.02 and 250.13 μA, respectively. The diffraction patterns also contain reflections corresponding to the sample holder (1.23, 1.51, 2.14 and 2.35 Å).

to cooling. Thus, demonstrating the reversible nature of the phase transition. A further increase in temperature to 150 °C produces a diffraction pattern that looks very similar to that at 20 °C. However, the reflections observed are much sharper with a concomitant increase in intensity. Thus, suggesting an increase in crystallinity at elevated temperatures. Additionally, the narrower reflections allow some reflections to be observed more clearly due to less overlap.

The NPD data recorded at 20 °C was analysed via the Rietveld method using the $Pm\bar{3}m$ structural model proposed by Hanghofer *et al.*[210] The refinement is shown in Figure 4.35(a), and the corresponding structural parameters, including the isotropic thermal coefficients, are shown in Table 4.20. A $\chi^2 = 3.14$ and $wR_p = 2.48\%$ suggest a very good fit. Inspection of the refinement shows that all reflections corresponding to the sample are successfully indexed, and the observed and calculated intensities match well. As with the earlier NPD refinements, the reflections corresponding to the sample holder were excluded and are denoted by *. A lattice parameter of 3.90389(8) Å is obtained. This is similar to the one determined earlier from the laboratory XRD data and agrees with that reported in the literature for the cubic phase of Li_2OHCl synthesised via conventional solid-state methods.[213] As with the earlier NPD refinements, the thermal motion was treated as isotropic because reliable values could not be obtained for anisotropic thermal coefficients. Also, the coefficients for O and D were constrained to be equivalent to avoid an unrealistically large coefficient for D. Inspection of the thermal coefficients obtained shows that the coefficient corresponding to Li is considerably smaller than that obtained via XRD and is generally more in line with what is expected. Unfortunately, additional structural parameters such as the atomic coordinates for D and the fractional occupancies for Li and D could not be refined. Attempts to refine these parameters did not result in a fully converged refinement. Thus, making it difficult to determine reliable values for these parameters.

The NPD data obtained at −263 °C (10 K) was also analysed via the Rietveld method. The data was refined using the new *Pban* model proposed earlier (Figure 4.19) as it appeared to be the most suitable candidate for the room-temperature orthorhombic phase of Li_2OHCl (*vide supra*). The refine-

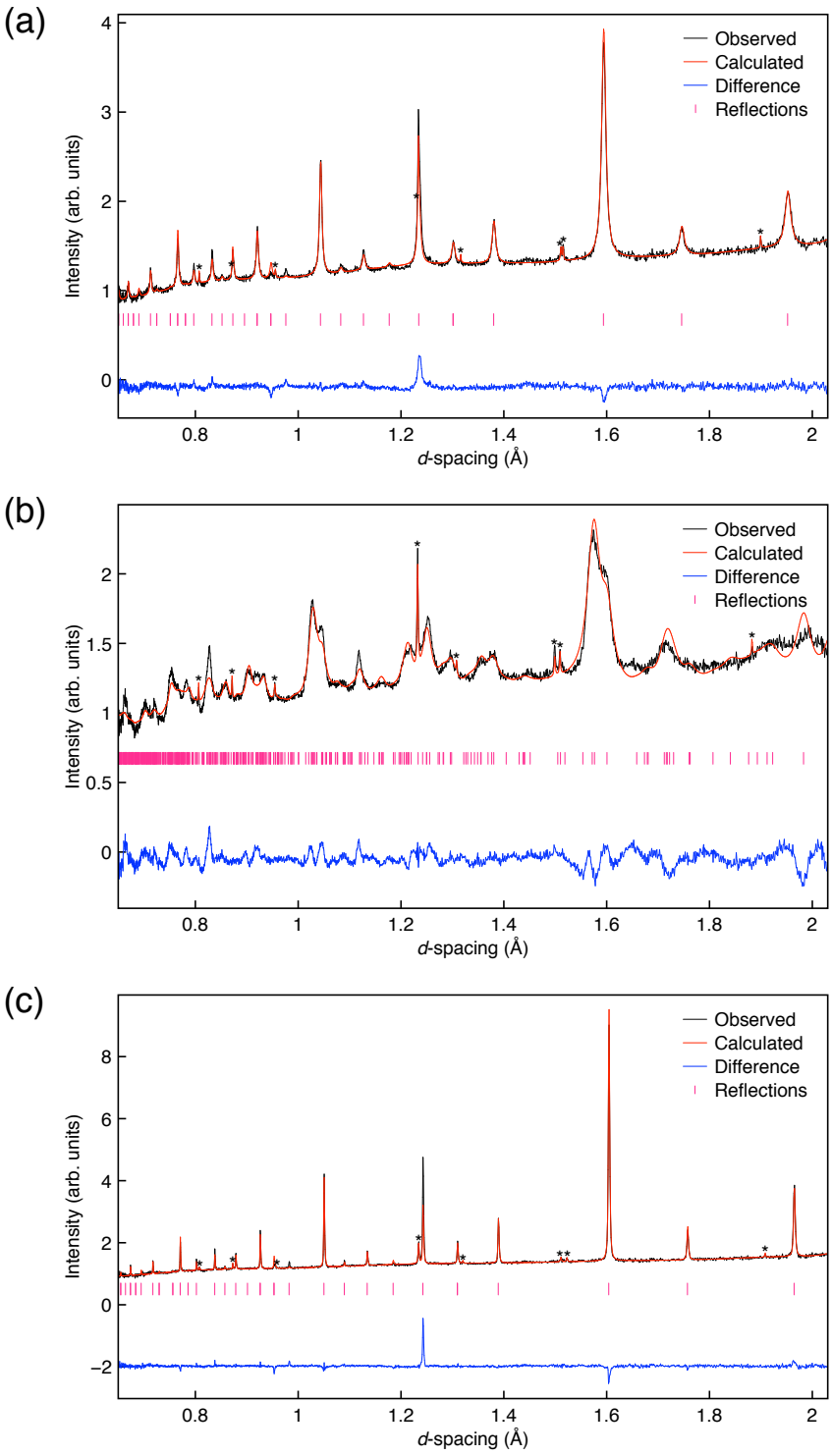

Figure 4.35: Rietveld refinements of the NPD data collected at (a) 20, (b) −263 and (c) 150 °C for 320.07, 320.02 and 250.13 μA, respectively, using the backscattering bank, for a sample of mechanically-milled Li_2ODCl using the (a,c) $Pm\bar{3}m$ (Li_2ODCl) and (b) *Pban* (Li_2ODCl) structural models.[210] The reflections corresponding to the sample holder were excluded and are indicated by *. (a) χ^2 = 3.14, wR_p = 2.48%, R_p = 1.72%. (b) χ^2 = 6.08, wR_p = 3.44%, R_p = 2.85%. (c) χ^2 = 4.58, wR_p = 3.35%, R_p = 1.97%.

Table 4.20: Structural parameters for a sample of mechanically-milled Li_2ODCl, obtained from Rietveld refinement of the NPD data obtained at 20, −263 and 150 °C, using isotropic thermal coefficients. 20 °C: Li_2ODCl: space group $Pm\bar{3}m$, a = 3.90389(8) Å, V = 59.497(4) Å^3. χ^2 = 3.14, wR_p = 2.48%, R_p = 1.72%. −263 °C: Li_2ODCl: space group *Pban*, a = 7.69147(224) Å, b = 7.93179(127) Å, c = 3.82411(95) Å, V = 233.298(52) Å^3. χ^2 = 6.08, wR_p = 3.44%, R_p = 2.85%. 150 °C: Li_2ODCl: space group $Pm\bar{3}m$, a = 3.92909(3) Å, V = 60.656(1) Å^3. χ^2 = 4.58, wR_p = 3.35%, R_p = 1.97%.

Atom	x	y	z	Occ.	U(iso) × 100 (Å^2)
20 °C					
$Pm\bar{3}m$					
Li	0.5	0	0	0.667	3.56(18)
O	0	0	0	1	1.25(5)
D	0.1279	0.1279	0.1279	0.125	1.25(5)
Cl	0.5	0.5	0.5	1	1.22(4)
−263 °C					
Pban					
Li1	0.0371(34)	0.25	0	0.282(14)	2.5
Li2	0.25	0.1714(39)	0	0.168(23)	2.5
Li3	−0.0018(95)	0.0310(22)	0.8356(47)	0.575(66)	2.5
O1	0	0	0	0.25	2.5
D1	0.0451(86)	−0.0130(69)	0.2050(157)	0.073(31)	2.5
D2	0.0534(31)	0.4670(14)	0.1924(56)	0.163(16)	2.5
Cl1	0.25	0.25	0.5	0.25	2.5
Cl2	0.75	0.25	0.5	0.25	2.5
150 °C					
$Pm\bar{3}m$					
Li	0.5	0	0	0.667	5.10(21)
O	0	0	0	1	2.10(5)
D	0.1279	0.1279	0.1279	0.125	2.10(5)
Cl	0.5	0.5	0.5	1	1.98(4)

ment completed is shown in Figure 4.35(b), and the corresponding structural parameters are listed in Table 4.20. A χ^2 = 6.08 and wR_p = 3.44% suggest a relatively good fit, and all relevant reflections are successfully indexed. The observed and calculated intensities match reasonably well, but there are some noticeable differences. Inspection of the structural parameters indicates that

the cell volume is lower than that determined using the NPD data acquired at 20 °C for the Li_2ODCl sample synthesised using a conventional solid-state synthesis (Table 4.15). This is to be expected as a decrease in temperature will cause the unit cell to contract. The cell volume is similar to that determined at −263 °C (10 K) for the Li_2ODCl sample synthesised via a conventional solid-state route. However, the lattice parameters are noted to differ somewhat. For the mechanically-milled sample, the lattice parameter "a" is slightly larger, whereas "b" and "c" are slightly smaller. The parameters determined also have a rather large error which is most likely due to the low crystallinity of the sample. Unlike the cubic phase, the atomic coordinates for Li and D in the orthorhombic phase were successfully refined. An inspection of the coordinates obtained shows that the coordinates for Li1 and D1 do not exhibit any significant change from those in the initial model (Figure 4.12 and Table 4.9). However, those for Li2, Li3 and D2 exhibit a noticeable shift. Figure 4.36 shows the structures of the initial model and that corresponding to the refined structural parameters. There is a noticeable difference between the two structures. In particular, the atomic coordinates for Li2 have shifted considerably. The fractional occupancies for the Li and D atoms were also refined, and the resulting occupancies indicate a composition of $Li_{6.44}OD_{1.888}Cl$. Once again, the formula obtained is not charge-balanced and differs drastically from that expected. This may be due to the poorly refined atomic coordinates, which will affect the fractional occupancy. Moreover, the thermal coefficients could not be refined to sensible values and had to be fixed at 2.5×10^{-2} Å^2 for all atoms. Overall, the data analysis demonstrates that the mechanically-milled sample undergoes a phase transition at lower temperatures. The structure of the low-temperature phase appears to be orthorhombic. However, precise structural parameters could not be obtained.

Lastly, the NPD data acquired at 150 °C was also analysed via the Rietveld method using the $Pm\bar{3}m$ model[210] (Figure 4.35(c) and Table 4.20). A χ^2 = 4.58 and wR_p = 3.53% suggest a relatively good fit. Additionally, all reflections corresponding to the sample are successfully indexed with a good match between the observed and calculated intensities. As expected, the lattice pa-

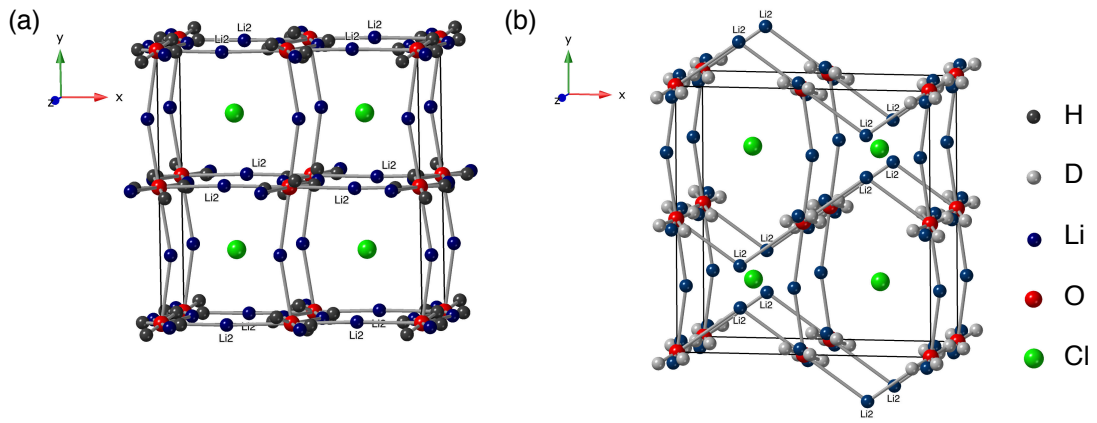

Figure 4.36: (a) The structure of Li_2OHCl in space group *Pban* adapted from the model proposed by Hanghofer and co-workers[210] at 300 K. (b) Also, shown is the refined structure of Li_2ODCl in space group *Pban* obtained via Rietveld analysis of the NPD data acquired at 20 °C during the current study.

rameter exhibits a noticeable increase with increasing temperature. The same is true for the isotropic thermal coefficients. As with the NPD data acquired at 20 °C, the atomic coordinates for D and the fractional occupancies for Li and D could not be refined. Attempts to refine these parameters did not return a fully converged refinement, meaning reliable parameters could not be obtained. Earlier, it was suggested that this might be due to low sample crystallinity and/or ion mobility. At 150 °C, the sample crystallinity appears to have increased. Thus, the issue is likely to be ion mobility.

At the time of this writing, the synthesis of "Li_2OHCl" solely via mechanical milling was reported by Yamamoto and co-workers.[221] The exact composition of the sample is reported to be $Li_{1.88}OH_{1.12}Cl$. Their method involved milling together LiCl and LiOH at 700 rpm for 72 hrs. The sample produced is reported to be cubic in space group $Pm\bar{3}m$ at room temperature with a lattice parameter a = 3.90317(2) Å. Thus, confirming the findings reported in the current study. Yamamoto *et al.*[221] investigated the sample's phase behaviour via VT synchrotron XRD experiments. Upon heating $Li_{1.88}OH_{1.12}Cl$ to 200 °C, Yamamoto *et al.*,[221] also observed an increase in crystallinity as heating allows for the crystal growth to occur. When cooling the sample, the structure remained cubic until 40 °C. At 30 °C, however, a phase transition to orthorhombic symmetry was observed. Yamamoto *et al.*[221] believe the orthorhombic

phase to exist in space group $Pmc2_1$. Around the same time, Yang and co-workers[222] utilised mechanical milling methods to induce the orthorhombic to cubic phase transition in Li_2OHCl. Samples were initially produced via conventional solid-state methods and were subsequently quenched to obtain Li_2OHCl with an orthorhombic structure. Li_2OHCl was then mechanically milled for 30 mins, which resulted in a phase transition from an orthorhombic to cubic symmetry. Thus, further demonstrating the effectiveness of mechanical milling.

More recently, Ni and co-workers[223] have reported the synthesis of Li_2OHCl via wet mechanical milling, a commonly used method to facilitate mixing. The procedure involved milling together LiCl and LiOH along with n-hexane at 400 rpm for 10 hrs. n-hexane was subsequently removed by drying the sample under vacuum for 12 hrs. The resulting sample was reported to exist in a cubic symmetry at room temperature. The sample also exhibited low crystallinity, which is attributed to the stress incurred during milling. VT laboratory XRD experiments indicated a phase transition from cubic to orthorhombic symmetry when cooling from −150 to −200 °C. However, the exact temperature at which the phase transition occurs was not determined. Ni *et al.*[223] also investigated the thermal stability of Li_2OHCl by annealing an already prepared sample at 210 °C for 5 hrs. The heat-treated sample was observed to remain cubic when cooled to 25 °C. These findings contrast with those reported by Yamamoto and co-workers[221] as they observed Li_2OHCl to undergo a phase transition when cooling from 200 to 30 °C. Although, further cooling to −10 °C did result in a phase transition to orthorhombic symmetry. Moreover, reheating the sample to 25 °C did not change the structure to cubic symmetry, and the sample remained orthorhombic.

Ni *et al.*[223] also stated that in an orthorhombic structure, the OH groups are ordered, thus resulting in lattice parameters a = b < c. An increase in temperature increases the kinetic energy of H, and the OH groups become disordered. This changes the lattice parameters to a = b = c, and a transition from an orthorhombic to cubic symmetry occurs. Ni *et al.*[223] suggest that the low crystallinity aids in stabilising the metastable cubic phase at room temperature as

a larger surface energy is likely to reduce the ordering of OH groups. Thus, suppressing the transition to an orthorhombic phase. However, a decrease in temperature will cause the OH groups to become ordered, in turn transforming the unit cell from cubic to orthorhombic. As such, the milled samples were observed to undergo a phase transition at much lower temperatures.

Overall, the findings presented in the current study and the recent literature reports suggest that in a similar manner to the Li_2OHCl samples discussed earlier, the preparation methods used for mechanically-milled Li_2OHCl greatly influence the phase behaviour of the sample. Thus, making mechanically-milled Li_2OHCl a worthy candidate for further exploration.

4.3.2.3 SSNMR Studies of Mechanically-Milled Li_2OHCl

The mechanically-milled Li_2OHCl was also studied via multinuclear SSNMR. The ^{1}H and ^{7}Li MAS NMR spectra obtained are shown in Figure 4.37. In both cases, a single resonance centred around 0 ppm is observed. Both the ^{1}H and ^{7}Li NMR spectra closely resemble those obtained for the high-temperature cubic phase of Li_2OHCl, *i.e.*, the lineshape observed is similar, and the sidebands are not very pronounced. A single resonance is indicative of a single site, and this is to be expected as mechanically-milled Li_2OHCl adopts a cubic structure in space group $Pm\bar{3}m$ with a single H and Li site. The ^{1}H resonance with one set of spinning sidebands is characteristic of hydroxyl groups, and the ^{7}Li resonance with a single set of spinning sidebands indicates a high symmetry environment. These results are in line with what is expected for a cubic structure.

The mechanically-milled Li_2OHCl sample was also analysed via VT ^{35}Cl MAS NMR spectroscopy, and the spectra acquired at −19 and 33 °C are shown in Figure 4.38. The NPD data presented earlier indicated that the mechanically-milled sample undergoes a phase transition upon cooling. Thus, a ^{35}Cl MAS NMR spectrum was also obtained below room temperature at −19 °C, as this was the lowest temperature achievable with the apparatus used. At 33 °C, a single broad resonance with an asymmetric lineshape is observed. In a

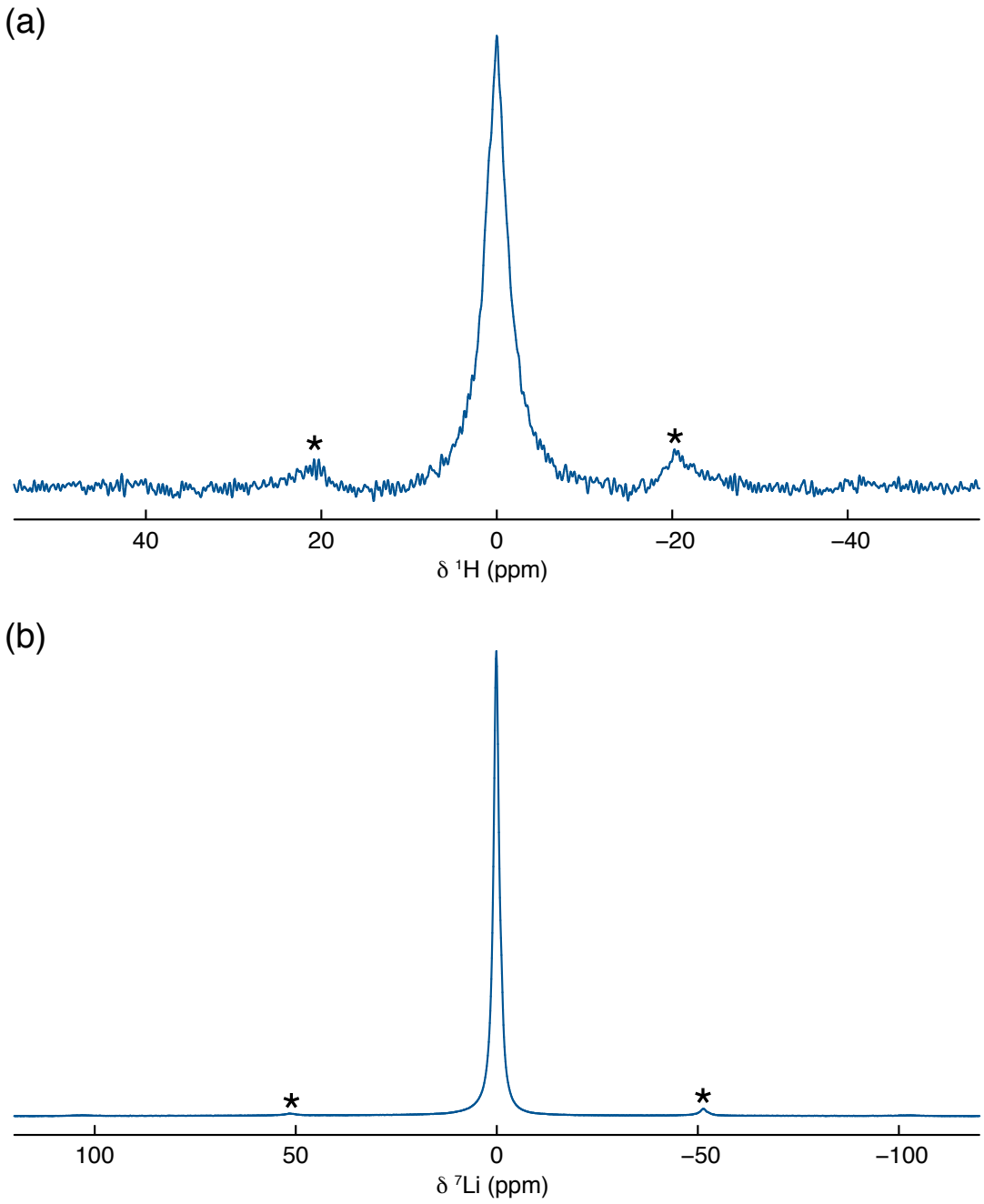

Figure 4.37: (a) ^{1}H and (b) ^{7}Li (11.7 T) MAS NMR spectra obtained for the mechanically-milled sample of Li_2OHCl. The sample was prepared via mechanical milling of the reagents together at 500 rpm for 9 hrs via a planetary ball mill. The MAS rate was 10 kHz and spinning sidebands are denoted by *. A recycle delay of (a) 1500 and (b) 60 s was used to acquire (a) 16 and (b) 4 transients, respectively.

similar manner to the ^{1}H and ^{7}Li NMR data, the lineshape observed resembles that observed earlier for the high-temperature Li_2OHCl sample synthesised via a conventional solid-state route. It is noted that a signal is also observed at

~5 ppm from residual LiCl, which is present in the sample as an impurity. The spectrum acquired at −19 °C (Figure 4.38) exhibits a resonance similar to that observed for the room-temperature Li_2OHCl phase. The lineshape observed appears to be composed of multiple overlapping resonances. It also exhibits less well-defined features when compared to the ^{35}Cl MAS NMR spectra corresponding to the Li_2OHCl sample prepared via conventional solid-state routes (Figure 4.30).

Both spectra were simulated to fit the lineshape observed, as shown in Figure 4.39 and the corresponding quadrupolar parameters are detailed in Table 4.21. In a similar manner to the previous Li_2OHCl sample discussed earlier, two Cl sites were required to fit the spectrum corresponding to the cubic phase in space group $Pm\bar{3}m$. The Cl sites observed at 33 °C for the mechanically-milled sample are slightly different from those observed for the Li_2OHCl sample synthesised via a conventional solid-state route (Figure 4.31). Therefore, the quadrupolar parameters also differ slightly. The C_Q values observed in

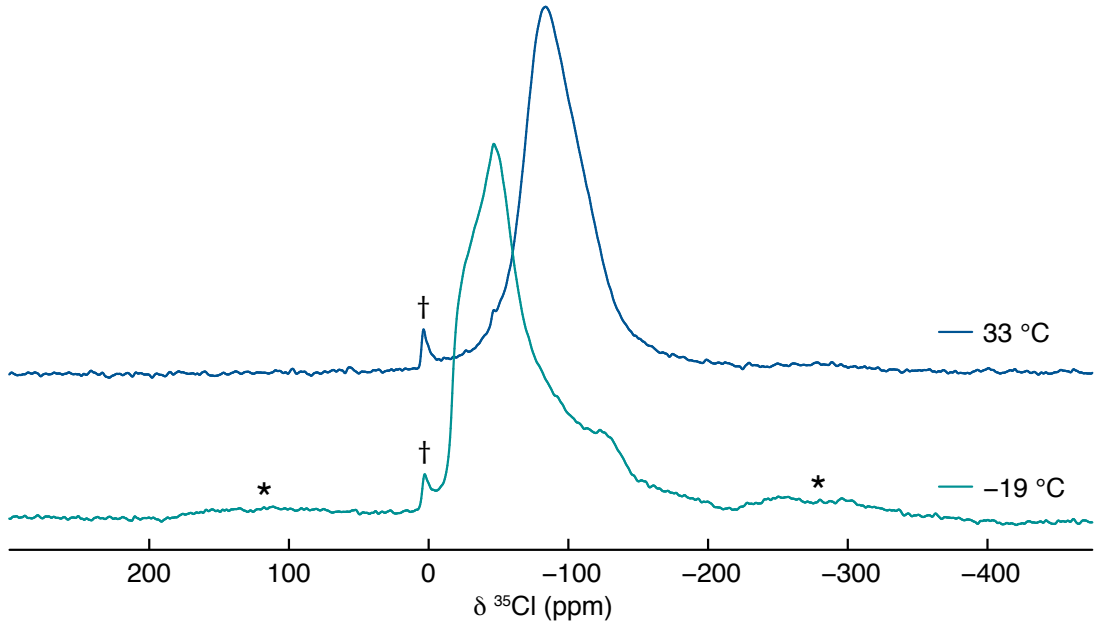

Figure 4.38: ^{35}Cl (11.7 T) MAS NMR spectra obtained for the mechanically-milled sample of Li_2OHCl. The sample was prepared via mechanical milling of the reagents together at 500 rpm for 9 hrs via a planetary ball mill. The MAS rate was 10 kHz and spinning side bands are denoted by *. In both cases, a recycle delay of 1 s was used to acquire 2560 transients. The known LiCl impurity is denoted by †.

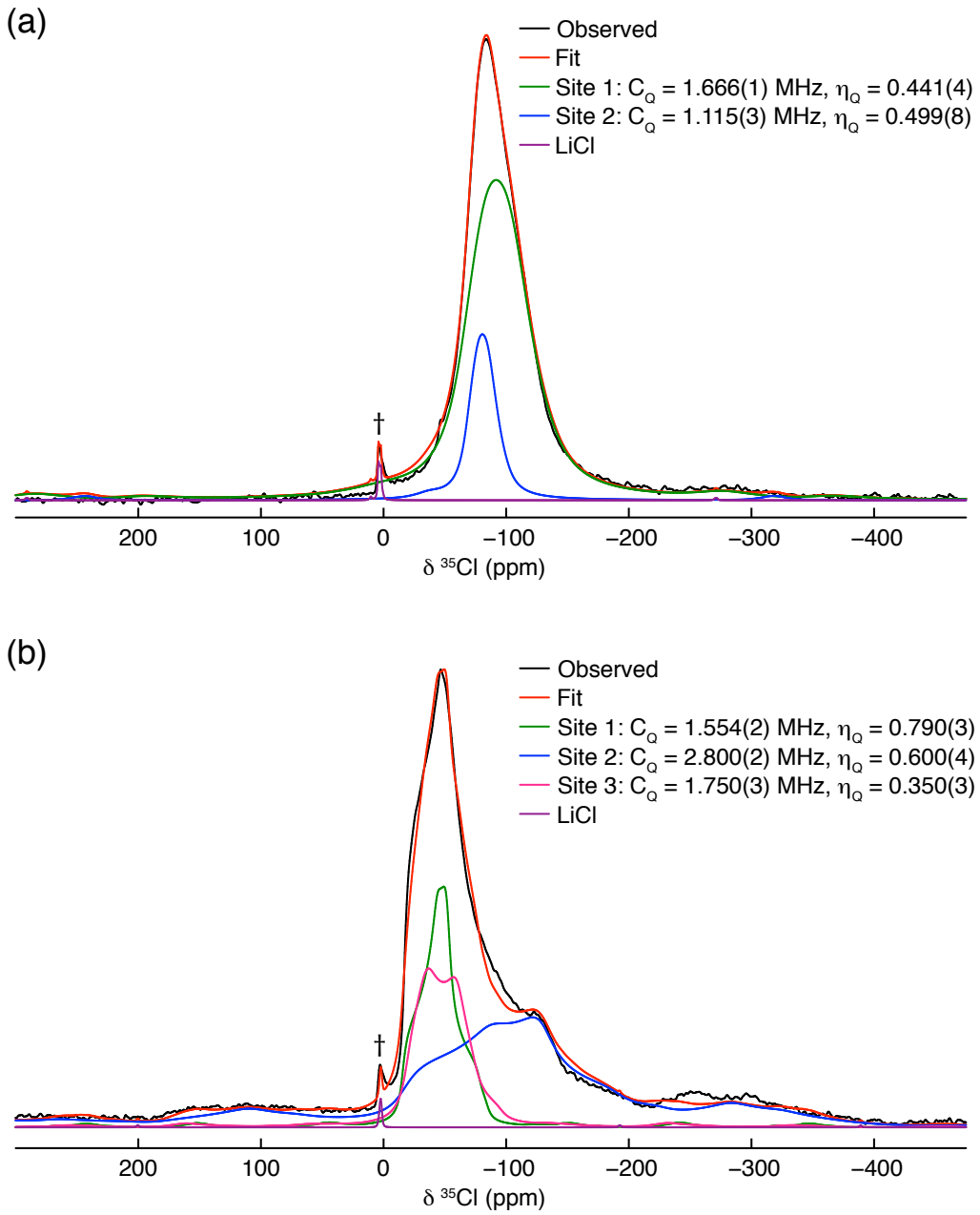

Figure 4.39: Simulated ^{35}Cl (11.7 T) MAS NMR spectra acquired at (a) 33 °C and (b) −19 °C for a sample of mechanically-milled Li_2OHCl. The sample was prepared via mechanical milling of the reagents together at 500 rpm for 9 hrs via a planetary ball mill. The MAS rate was 10 kHz and a recycle delay of 1 s was used to acquire 2560 transients. At 33 °C, two sites were required to fit the lineshape and the corresponding quadrupolar parameters obtained are: Site 1 (C_Q = 1.666(1) MHz and η_Q = 0.441(4)), Site 2 (C_Q = 1.115(3) MHz and η_Q = 0.499(8)). At −19 °C, three sites were required to fit the lineshape the corresponding quadrupolar parameters obtained are: Site 1 (C_Q = 1.554(2) MHz and η_Q = 0.790(3)), Site 2 (C_Q = 2.800(2) MHz and η_Q = 0.600(4)), Site 3 (C_Q = 1.750(3) MHz and η_Q = 0.350(3)). The known LiCl impurity is denoted by †.

Table 4.21: ^{35}Cl NMR parameters, δ, C_Q, and η_Q, obtained by simulating the lineshapes observed in the ^{35}Cl MAS NMR spectra obtained at 33 °C and −19 °C for a sample of mechanically-milled Li_2OHCl.

Site	δ (ppm)	C_Q (MHz)	η_Q
33 °C			
1	−62.78(4)	1.666(1)	0.441(4)
2	−67.20(2)	1.115(3)	0.499(8)
−19 °C			
1	−15.00(15)	1.554(2)	0.790(3)
2	−12.00(28)	2.800(2)	0.600(4)
3	−14.50(8)	1.750(3)	0.350(3)

both cases are similar, but the η_Q values differ considerably. Thus, suggesting that in both samples, Cl experiences two distinct local environments which are similar but not identical. As stated earlier, a Cl site in a perfectly symmetrical environment, *i.e.*, a perfectly cubic system, would have C_Q and η_Q close to 0. However, the parameters obtained here suggest that Cl experiences some EFG. Thus, the low C_Q values indicate a symmetrical structure, but not a perfectly cubic structure. The lineshape observed at −19 °C could only be fitted using at least three sites. The Cl sites observed at −19 °C have similar quadrupolar parameters to those observed for the room-temperature phase of Li_2OHCl and therefore have similar lineshapes. Earlier, analysis of the NPD data obtained at −263 °C (10 K) suggested that the low-temperature phase of the mechanically-milled Li_2OHCl has the same structure as that of the room-temperature phase of the Li_2OHCl sample synthesised via a conventional solid-state route, *i.e.*, mostly likely an orthorhombic structure in space group *Pban*. Thus, the ^{35}Cl NMR data presented here supports the NPD data.

4.4 Conclusions

This chapter focused on the synthesis of Li_2OHCl, which was demonstrated to be considerably easier than that of Li_3OCl. Li_2OHCl was successfully

synthesised via conventional solid-state routes and mechanical milling methods. In both cases, the sample produced contained predominantly the desired phase and only a very small quantity of the starting material LiCl and traces of an additional, as yet unidentified, impurity. The Li_2OHCl sample synthesised via a conventional solid-state route adopted what is believed to be an orthorhombic structure. The sample exhibited a phase transition at ~40 °C to a cubic structure in space group $Pm\bar{3}m$. The diffraction pattern obtained at 50 °C was analysed via Rietveld refinement using the $Pm\bar{3}m$ structural model,[210] and an excellent fit was obtained, thereby confirming that the sample produced is indeed Li_2OHCl. Mechanically-milled Li_2OHCl, on the other hand, existed in a cubic ($Pm\bar{3}m$) phase at room temperature. Thus, exhibiting the usefulness of mechanical milling as it appears to stabilise the cubic phase at room temperature. However, lowering the temperature does result in a phase transition to a structure that seems to be the same as that of the room-temperature phase of Li_2OHCl samples synthesised via conventional solid-state routes. The phase transition was seen to be reversible as an increase in temperature caused the sample to revert to a cubic symmetry. A further increase in temperature resulted in an increased crystallinity.

As stated earlier, the room-temperature structure of Li_2OHCl has been the subject of considerable debate. Several structural models have been proposed, but no single model has been agreed upon. Some models suggested in the literature included sufficient crystallographic information to generate a cif. Thereby allowing to test these models by refining the XRD and NPD data acquired during the current study. It is noted that there were additional structural suggestions which could not be verified as insufficient crystallographic information was reported. The models examined included a tetragonal structure in space group $P4mm$ and orthorhombic structures in space groups $Pmc2_1$ and $Cmcm$ proposed by Howard and co-workers.[216,217] The orthorhombic structures reported by Hanghofer and co-workers[210] were also tested. Interestingly, Hanghofer *et al.*[210] reported the structure of Li_2OHCl at very low temperatures (10 K) to vary from the room-temperature structure, as an additional Li site appears at low temperatures. Hence, they proposed dif-

ferent orthorhombic structures in space groups *Pmmm* and *Pban* at 300 and 4 K.

Initially, these models were evaluated using the laboratory XRD data. The ground state tetragonal structure in space group *P*4*mm* was found to be unsuitable as many of the major reflections observed could not be indexed, and as a result, the refinement could not be completed. In contrast, the orthorhombic models in space groups $Pmc2_1$ and *Cmcm* appeared to be quite promising as most of the major reflections observed were successfully indexed, and reasonably good fits were obtained. However, some of the thermal coefficients for Li atoms were unusually large. Thus, potentially suggesting inaccuracies within the structural models. These could include inaccurate atomic positions. A reasonable fit was also obtained using the *Pmmm* models. However, the thermal coefficients could not be refined using the 300 K model and had to be heavily constrained when using the 4 K model. Thus, making them less promising than the $Pmc2_1$ and *Cmcm* models. Moreover, the presence or absence of an additional Li site could not be determined for certain.

Surprisingly, the *Pban* model reported by Hanghofer *et al.*[210] resulted in an extremely poor fit. Detailed examination of the crystallographic information reported by Hanghofer *et al.*[210] revealed the proposed structure to be invalid, as the reported atomic coordinates for some of the atoms were not in agreement with the assigned Wyckoff positions, as per the guidelines specified for space group *Pban* in the International Tables for Crystallography.[220] Therefore, a refinement could not be completed. In addition, the fractional occupancies reported for the structures in space groups *Pmmm* and *Pban* did not indicate a sample composition of Li_2OHCl. In fact, the sample composition was noted to vary significantly from that intended. Thus, suggesting that the sample investigated by Hanghofer *et al.*[210] did not have the correct stoichiometry. The *Pban* model was modified as per the guidelines detailed in the International Tables for Crystallography[220] to correct the atomic positions. The fit obtained using the new model appeared to be quite promising. Thus, indicating that at room temperature, Li_2OHCl may exist in an orthorhombic structure in space group *Pban*. However, the exact crystallographic details, such as the

precise atomic coordinates, could not be determined using the laboratory XRD data. Moreover, the *Pban* model proposed at 4 K was also altered and tested. The new *Pban* 4 K model also provided a very good fit, although the thermal coefficients for the Li atoms could not be refined freely. Therefore, it can be said to be less promising. However, given the quality of the fit obtained, it was challenging to determine the presence or absence of an additional Li site with any certainty.

Li_2OHCl was analysed further via VT NPD at HRPD, ISIS, using a deuterated sample of Li_2OHCl prepared by our collaborator. The sample produced contained the desired phase, residual LiCl and an unidentified impurity phase. The reaction conditions used to prepare the sample differed from those used for the sample of Li_2OHCl used for XRD studies. As a result of the different reaction conditions used, both the orthorhombic and cubic phases were present at room temperature. For a comprehensive study of Li_2ODCl as a function of temperature, VT NPD experiments were completed at temperatures ranging from −263 (10 K) to 300 °C. As expected, the diffraction patterns corresponding to the room-temperature phase of Li_2ODCl (recorded at −263 °C (10 K) and 20 °C) looked very different from those corresponding to the high-temperature cubic phase of Li_2ODCl (recorded at 50 °C and above). Extremely high temperatures were also probed, and the sample was observed to melt between 290 to 300 °C. In hopes of elucidating the precise structure of the room-temperature phase of Li_2OH/DCl, the diffraction patterns acquired at −263 °C (10 K) and 20 °C were used to test the various models proposed in the literature. These included the $Pmc2_1$ and *Cmcm* models proposed by Howard and co-workers[216,217] and the *Pmmm* models reported by Hanghofer and co-workers[210] at 300 and 4 K. The new *Pban* models adapted from those initially reported by Hanghofer *et al.*[210] at 300 and 4 K were also tested.

Initially, the NPD pattern acquired at −263 °C (10 K) was analysed as it is typically easier to determine precise atomic coordinates at low temperature owing to a lesser degree of thermal motion when compared to ambient temperature. Unfortunately, none of the models mentioned above provided a particularly good fit. The $Pmc2_1$ model resulted in an extremely poor fit, and

structural parameters such as the atomic coordinates, fractional occupancies and thermal coefficients could not be refined. The fit improved when using the *Cmcm* model. However, the overall quality remained moderate. Again, most structural parameters could not be refined to sensible values. The *Pmmm* model proposed at 300 K also provided a moderate fit, and parameters such as the atomic coordinates and the corresponding fractional occupancies were successfully refined. However, the composition obtained deviated significantly from Li_2ODCl. Unfortunately, the quality of the fit declined when using the *Pmmm* model proposed at 4 K. The atomic coordinates for all atoms could be refined. However, the corresponding fractional occupancies could not be determined as a negative occupancy was obtained for Li5, the additional Li site. Moreover, the thermal coefficients could not be refined for either *Pmmm* model. Surprisingly, the new *Pban* models adapted from those proposed at 300 and 4 K did not provide a good fit. Structural parameters such as the atomic coordinates and the corresponding fractional occupancies were successfully refined. However, the compositions indicated by the fractional occupancies deviated considerably from Li_2ODCl, and the thermal coefficients could not be refined at all.

All these models were also tested using the NPD pattern obtained at 20 °C, and the goodness of fit increased in all cases. Unfortunately, the overall quality of fit remained low for the $Pmc2_1$ and *Cmcm* models as several structural parameters could not be refined. Although, the fit obtained using the *Cmcm* model was a little better when compared to the $Pmc2_1$ model. The *Pmmm* model proposed at 300 K provided a very good fit, and all structure parameters, including the isotropic thermal coefficients, were successfully refined. However, the composition determined was shown to deviate from Li_2ODCl. The *Pmmm* model proposed at 4 K also resulted in a similar fit. However, the atomic coordinates for Li5, the additional Li site, could not be refined. Thus, suggesting that this site may not be present at room temperature. The new *Pban* 300 K model also provided a very good fit, albeit the isotropic thermal coefficients had to be heavily constrained to achieve reasonable parameters. Similarly to the *Pmmm* models, the composition corresponding to the de-

sired phase differed significantly from that intended. The new *Pban* 4 K model resulted in a similar fit to the 300 K model. It is unclear whether an additional Li site exists as neither model appears to be favoured over the other. Overall, the fit obtained using the *Pban* models was not as good as initially expected following the analysis of the laboratory XRD data. Thus, the precise structure of the room-temperature phase of Li_2OH/DCl is still not known for certain. However, the findings presented in the current study strongly indicate that, at room temperature, Li_2OH/DCl most likely adopts an orthorhombic structure in space group *Pban*. Moreover, at extremely low temperatures, the structure of Li_2OH/DCl appears to differ somewhat from the room-temperature structure. At 20 °C, the Li_2ODCl sample also contained the cubic $Pm\bar{3}m$ phase of Li_2OH/DCl. This phase was also included during the Rietveld analysis. In some cases, the atomic coordinates of D could be refined. However, the coordinates obtained differed significantly from those reported for H by Hanghofer *et al.*[210] Additional structural parameters such as the fractional occupancies and isotropic thermal coefficients could not be refined at all. Lastly, the residual LiCl phase was also included during analysis. However, thermal coefficients could not be refined in any case for the LiCl phase.

The NPD patterns obtained at 50 and 150 °C were also analysed to investigate the cubic ($Pm\bar{3}m$) phase of Li_2OH/DCl. Interestingly, the high-temperature phase of Li_2OH/DCl was not as easy to characterise as initially expected. The cubic structure of Li_2OH/DCl in space group $Pm\bar{3}m$ has been widely reported. However, specific crystallographic information regarding the H/D atoms, *i.e.*, the atomic coordinates, is severely lacking. Thus, the model reported by Hanghofer *et al.*[210] for a hydrated sample of "Li_3OCl" was used during analysis. As expected, the $Pm\bar{3}m$ model could index all reflections corresponding to Li_2OHCl. However, parameters such as the fractional occupancies for Li and D could not be refined. Thus, the precise composition of the desired phase could not be determined. Additionally, the isotropic thermal coefficients could not be refined freely for all atoms, and the coefficients for O and D had to be constrained to be equivalent to obtain sensible values. Overall, the goodness of fit achieved was a lot lower than expected.

Eilbracht and co-workers[215] suggested that the protons in Li_2OHCl/Br are statically disordered around the oxygen in four possible positions, making precise characterisation difficult. This may be true for the cubic $Pm\bar{3}m$ phase at room temperature and can explain why the parameters such as the fractional occupancies and thermal coefficients could not be determined for D at 20 °C. However, Li_2OHCl is a known Li-ion conductor and is likely to exhibit Li-ion mobility at elevated temperatures (50 and 150 °C). Moreover, OH/OD groups are also capable of exhibiting motion. Typically, OH/OD groups often exhibit rotational motion in solids. Therefore, the inability to freely refine the thermal coefficients for D and obtain fractional occupancies for Li and D may be a consequence of ion mobility within Li_2OH/DCl. Thus, suggesting that precise characterisation of Li and H/D is very challenging. This also explains the lack of crystallographic information in the literature regarding the H/D positions.

Furthermore, the deuterons are likely to exchange with protons over time, making it challenging to obtain a good fit using the Li_2ODCl model. Hence, the NPD patterns obtained at 50 and 150 °C were also analysed using the $Pm\bar{3}m$ (Li_2OHCl) model containing H instead of D. Initially, the fits obtained appeared to be much better. However, the coordinates determined for H atoms did not agree with those reported in the literature.[210] Although, it must be noted that, to date, only one study has reported the coordinates for H in a system close to Li_2OHCl.[210] The fractional occupancies for Li and H were refined successfully. However, the compositions obtained varied drastically from Li_2OHCl. Moreover, the isotropic thermal coefficients for all atoms were freely refined, and the resulting values were in good agreement with those reported in the literature.[210] Overall, neither model appears to be favoured over the other, making the precise characterisation of the high-temperature phase quite challenging. This is most likely due to the H/D exchange and ion mobility occurring in the sample. Hence, refinements were also attempted using a single model containing both H and D. However, the structural parameters determined were the same as those obtained using two separate models, and the relative proportions of H and D could not be determined as the fractional occupancy for D could not be refined successfully.

Mechanically-milled Li_2ODCl, prepared by our collaborator, was also analysed via NPD at HRPD between −263 (10 K) and 150 °C. The patterns obtained at 20 and 150 °C were analysed using the $Pm\bar{3}m$ models. The fits obtained appeared to be quite reasonable. However, in both cases, it was not possible to refine the atomic coordinates for D. The fractional occupancies for Li and D could not be refined either. As stated earlier, this is most likely due to static disorder or ion mobility in this system in the cubic phase, which would make it challenging to determine their precise location and fractional occupancy. The new *Pban* 300 K model was used to analyse the NPD pattern obtained at −263 °C. The fit obtained was moderate. Thus, suggesting that at low temperatures, mechanically-milled Li_2OHCl likely adopts the same orthorhombic structure as that of the sample prepared via conventional solid-state routes.

Furthermore, Li_2OHCl was analysed via multinuclear SSNMR spectroscopy to complement the XRD and NPD data obtained to assist in the elucidation of the room-temperature structure of Li_2OHCl and to gain additional structural information regarding the high-temperature cubic phase of Li_2OHCl. The ^{1}H and ^{7}Li MAS NMR spectra of Li_2OHCl at 33 °C indicated a single, relatively broad resonance, and as such, it was not possible to determine the number of distinct H and Li sites present accurately. In both cases, an increase in temperature resulted in significant line narrowing, as expected following the phase transition to a higher symmetry structure. At 24 °C, the ^{7}Li static NMR spectrum exhibited a dipolar broadened lineshape along with satellite transitions. Again, no distinct Li sites could be determined owing to considerable broadening and overlap. Here too, an increase in temperature to 54 °C resulted in a narrowing of the resonance, as expected following the phase transition to a cubic symmetry.

The ^{35}Cl MAS NMR data obtained indicated the presence of at least three distinct Cl sites in the room-temperature phase of Li_2OHCl. As expected, all sites determined had a relatively low value of C_Q and a mid to high η_Q, indicating a non-symmetrical structure. It is noted that none of the structural models discussed earlier for the room-temperature phase contained three dis-

tinct Cl sites. However, NMR is a local probe and therefore suggests the presence of three distinct Cl sites only locally. Interestingly, the high-temperature cubic phase in space group $Pm\bar{3}m$ has just one crystallographically distinct Cl site. However, two distinct Cl sites were identified via ^{35}Cl MAS NMR. This suggests that Cl possibly experiences two different local environments despite occupying a single crystallographic site. Moreover, Li_3OCl is suggested to be pseudo-cubic. Hence, Li_2OHCl may also be pseudo-cubic, and the actual symmetry may be lower than initially anticipated. Overall, the ^{35}Cl MAS NMR data presented has proven to be extremely valuable as it has provided considerable insight into the local structure of Li_2OHCl, at both room and elevated temperatures.

Mechanically-milled Li_2OHCl was also studied via multinuclear NMR to complement the diffraction studies presented. The ^{1}H and ^{7}Li MAS NMR spectra exhibited single resonances indicative of single H and Li sites. In both cases, the lineshapes observed looked very similar to those obtained for the high-temperature cubic phase of Li_2OHCl synthesised via conventional solid-state methods. VT ^{35}Cl NMR experiments completed at −19 and 33 °C suggested that the mechanically-milled Li_2OHCl undergoes a phase transition to lower symmetry upon decreasing the temperature. As with the ^{1}H and ^{7}Li NMR data, the ^{35}Cl NMR spectrum obtained at 33 °C exhibited a lineshape similar to that observed for the cubic phase of Li_2OHCl synthesised via conventional solid-state methods. Lineshape analysis indicated two distinct Cl sites, which again looked similar to those observed for the high-temperature cubic phase of Li_2OHCl. The lineshape obtained at −19 °C closely resembled that of the room-temperature orthorhombic phase of Li_2OHCl. Additionally, three distinct sites were obtained, which again looked similar to those observed for the room-temperature orthorhombic phase of Li_2OHCl. Thus, supporting the VT NPD studies presented, which demonstrated that the mechanically-milled Li_2OHCl undergoes a phase transition to an orthorhombic phase at lower temperatures.

Overall, the synthesis of Li_2OHCl has been demonstrated both via conventional solid-state routes and mechanical milling. The synthesis methods

and reaction conditions used appear to greatly influence the sample composition and phase obtained, making Li_2OHCl a versatile material.

5 $Li_{3-x}OH_xCl$ (x = 0.25, 0.5 and 0.75)

5.1 Introduction

As demonstrated previously in Chapter 3, synthesising a phase pure sample of Li_3OCl is extremely challenging. However, the synthesis of materials belonging to the series $Li_{3-x}OH_xCl$ has been reported in the literature.[213,218] Thereby indicating that it is possible to produce materials with variable lithium and proton content.

Schwering and co-workers have reported the synthesis of $Li_{2.17}OH_{0.83}Cl$.[213] Unlike Li_2OHCl, $Li_{2.17}OH_{0.83}Cl$ was reported to adopt a cubic structure at room temperature in space group $Pm\bar{3}m$ with a lattice parameter of 3.9035 Å, and Schwering *et al.*,[213] suggested this was due to an increase in the Li content. $Li_{2.17}OH_{0.83}Cl$ was also investigated at lower temperatures, and it was found to undergo a phase transition at −60 °C to tetragonal symmetry. However, no specific structural information was provided.

As discussed earlier, Song and co-workers have investigated the series $Li_{3-x}OH_xCl$ (x = 0.3 – 1).[218] Li_2OHCl was proposed to adopt an orthorhombic structure in space group $Pmmm$ at room temperature and transition to a cubic ($Pm\bar{3}m$) phase via an intermediary tetragonal ($P4/mmm$) phase. The same pattern was observed for $Li_{2.4}OH_{0.6}Cl$, whereas $Li_{2.1}OH_{0.9}Cl$ is reported to transition directly from an orthorhombic to cubic phase. However, detailed crystallographic information was not provided, making it challenging to confirm these claims and evaluate the reported structures.

This chapter details the attempts to modify the structure of Li_2OHCl by varying the Li and consequently the H content to produce samples in the series $Li_{3-x}OH_xCl$ (x = 0.25, 0.5 and 0.75). The samples prepared have been characterised via XRD, NPD and multinuclear SSNMR and the resulting findings are discussed in the following sections.

5.2 Experimental

5.2.1 Synthesis

Samples in the series $Li_{3-x}OH_xCl$, x = 0.25 – 0.75, were synthesised via the Schlenk line method described in Chapter 3. Stoichiometric amounts of LiCl (Alfa Aesar, ultra dry, 99.9%) and LiOH (Acros Organics, anhydrous, 98%) were mixed and ground together in an agate mortar and pestle inside an Ar-filled glovebox. The powdered samples were placed in an alumina crucible that was placed inside a quartz tube. The quartz tube was sealed, removed from the glovebox, connected to a conventional Schlenk line apparatus and evacuated to 10^{-3} mbar for 1 hr. All samples were heated at 350 °C for 30 mins. Once the reaction was complete, the sealed quartz tube was removed from the furnace and allowed to cool to room temperature. Once cooled, the tube was returned to the Ar-filled glovebox, where the product was recovered. A sample of $Li_{2.5}OH_{0.5}Cl$ was deuterated for ^2H NMR and NPD experiments using the Schlenk line procedure, and the deuterated starting reagent LiOD.

5.2.2 X-ray Diffraction

All samples were ground using an agate mortar and pestle and packed into 0.7 mm special glass capillaries, inside an Ar-filled glovebox. All XRD patterns were recorded on a Bruker d8 diffractometer using Mo (λ = 0.71073 Å) radiation. All scans were acquired for 2θ = 5 – 45°, with a step size of 0.01° and a step time of 2 seconds. During all scans, the capillary was continually rotated at 60 rpm to reduce the effects of preferred orientation. VT XRD patterns were also acquired using a Bruker d8 diffractometer, where the temperature was increased at 2 °C per hr from 25 to 50 °C, whilst continuously recording the diffraction pattern. The experimental temperatures were controlled via an Oxford Cryosystems Cryostream and set using the Cryopad control software. Rietveld analysis was performed using the GSAS-II software.[150] Parameters including the background coefficients, lattice parameters, isotropic thermal coefficients and the profile coefficients were refined.

5.2.3 Neutron Powder Diffraction

A deuterated sample of $Li_{2.75}OH_{0.25}Cl$ synthesised via the Schlenk line method described above was analysed using HRPD at ISIS Neutron and Muon Source, Oxford, UK. The sample was packed into a 5 mm aluminium-framed slab can with vanadium windows. The body of the can and fixing screws were masked with Cd foil, and the can was sealed using indium wire. The can was then mounted into a top-loading CCR and a diffraction pattern was recorded at room temperature. Specific details regarding the number of counts acquired are provided in the relevant figure caption. Rietveld analysis was performed using the GSAS-II software.[150] Parameters including the background coefficients, instrumental parameters, lattice parameters, isotropic thermal factors, atomic positional coordinates and the profile coefficients were refined.

5.2.4 Solid-State NMR

All solid-state NMR spectra were acquired using a Bruker 500 Avance III HD spectrometer, equipped with a wide-bore 11.7 T Oxford magnet, using Larmor frequencies of 499.69 MHz for ^{1}H (I = 1/2), 194.20 MHz for ^{7}Li (I = 3/2) and 49.00 MHz for ^{35}Cl (I = 3/2). Powdered samples were packed into conventional 4.0 mm ZrO_2 rotors under an Ar atmosphere and placed into a Bruker 4.0 mm HX probe. ^{1}H chemical shifts were referenced to neat tetramethylsilane, by setting the resonance from a sample of adamantane to δ_{iso} = 1.9 ppm. ^{7}Li and ^{35}Cl chemical shifts were referenced to 1 M $LiCl_{(aq)}$ and 1 M $NaCl_{(aq)}$, respectively. Standard VT ^{1}H, ^{7}Li and ^{35}Cl MAS NMR experiments were completed between 33 and 52 °C using conventional hardware.

^{1}H MAS NMR spectra were acquired using a background suppression (DEPTH)[197] experiment with typical $\pi/2$ and π pulse lengths of 4 and 8 μs, respectively. Conventional ^{7}Li MAS NMR spectra were obtained using a single-pulse experiment with a typical pulse length of 1.5 μs. During acquisition, proton-decoupling was applied using SPINAL-64,[198] with a RF field of 32 kHz. Typical RF fieldstrengths of 62 – 166 kHz were employed. ^{35}Cl MAS NMR spectra were acquired using a hahn-echo ($90°_x$ – τ – $180°_y$ – τ) experi-

ment with a pulse length of 4 μs. Specific details regarding the recycle delays and MAS rates used are provided in the relevant figure captions. In all cases, quoted temperatures have been calibrated and reflect the true temperature of the sample during the experiment. Selected NMR spectra were fitted using the SOLA tool in Topspin 4.0.

5.3 Results and Discussion

5.3.1 Synthesis

In this study, samples of $Li_{3-x}OH_xCl$, x = 0.25, 0.5 and 0.75, were synthesised via the Schlenk line method described in Chapter 3 as follows,

$$LiCl + 2 - xLiOH \longrightarrow Li_{3-x}OH_xCl + 1 - xH_2O\,. \tag{5.1}$$

During synthesis, water is produced as a by-product, and the Schlenk line method allows for water to be removed as it is formed. All samples were prepared using a reaction temperature of 350 °C and a reaction time of 30 mins. The XRD patterns obtained for the samples produced are shown in Figure 5.1(a), and an expanded region between $2\theta = 9 - 25°$ is shown in Figure 5.1(b). Also shown are the XRD patterns for Li_2OHCl at room temperature (first shown in Figure 4.4) and a sample of Li_3OCl synthesised via the Schlenk line method under the same reaction conditions (first shown in Figure 3.5). A simulated diffraction pattern for Li_3OCl in space group $Pm\bar{3}m$ is also shown.

All experimental diffraction patterns look very similar, as they all contain reflections at the same 2θ positions. Thus, suggesting that the same phase observed for Li_2OHCl at room temperature is also observed across the series. Closer inspection of the XRD patterns shows a slight variation in the relative peak intensities. It is noted that the XRD patterns for samples where Li > 2 exhibit additional reflections in places where those for the cubic phase ($Pm\bar{3}m$) would be expected. Thus, suggesting the samples may also contain the cubic phase at room temperature. However, most of the reflections corresponding to the room-temperature and cubic phase will occur at similar positions, resulting in a significant overlap. Hence, it is challenging to identify the phases present from a visual inspection of the data alone. The Li_3OCl samples (dis-

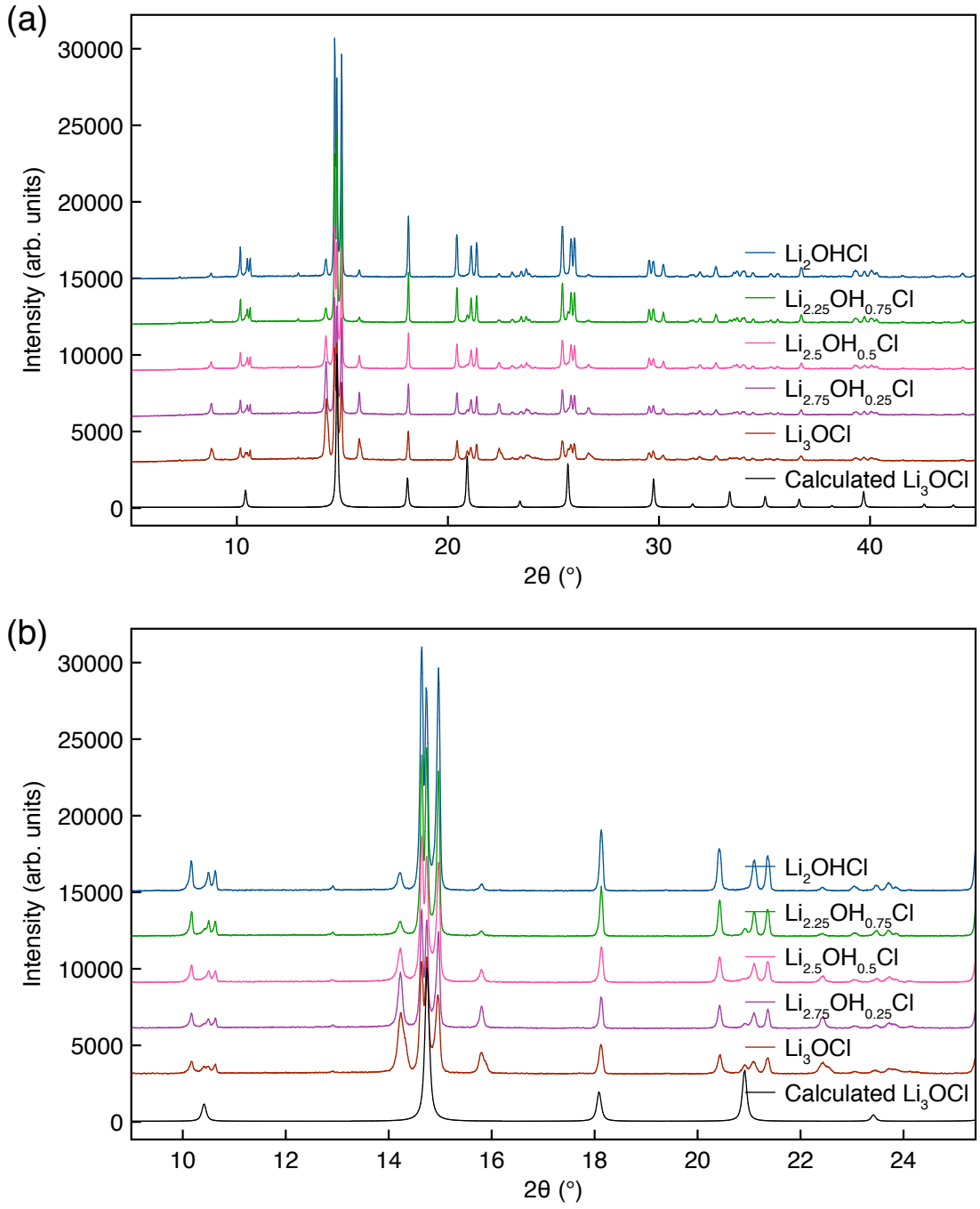

Figure 5.1: X-ray diffraction patterns obtained for the series $Li_{3-x}OH_xCl$ where x = 0, 0.25, 0.5 and 0.75. All samples were synthesised using the Schlenk line method. The reaction temperature was 350 °C and the reaction time was 30 mins. Also shown for comparison is the XRD pattern for Li_2OHCl, synthesised using the muffle furnace method. A simulated diffraction pattern for Li_3OCl in space group $Pm\bar{3}m$ is also shown.

cussed in detail in Chapter 3) synthesised using LiCl and LiOH were observed to contain additional phase(s) along with a small quantity of the desired phase. A comparison of the diffraction pattern corresponding to Li_3OCl with that of

Li_2OHCl shows that some of those additional reflections likely correspond to the hydrated phase, Li_2OHCl. This suggests that a lot of the Li_3OCl samples discussed in Chapter 3 contained Li_2OHCl as an impurity phase. Finally, it is noted that all patterns exhibit additional reflections at 2θ = 8.79, 14.24 and 15.81°, shown more clearly in Figure 5.1(b). Earlier, these reflections were demonstrated to correspond to an unidentified impurity phase (Figure 4.6). These reflections appear to increase in intensity with increasing Li content, suggesting that attempts to increase the Li content in the $Li_{3-x}OH_xCl$ system result in an increased quantity of the impurity phase. This also implies that the actual composition of the desired phase in these samples may vary from that intended as some of the reagents will be used to form the impurity phase.

The diffraction patterns obtained for samples in the $Li_{3-x}OH_xCl$ (x = 0, 0.25, 0.5 and 0.75) series were analysed via the Rietveld method. As discussed earlier, the exact structure of the room-temperature phase of Li_2OHCl is not yet confirmed. However, the orthorhombic structure in space group *Pban*, adapted from the one reported in the literature,[210] has shown the greatest promise. Hence, the new *Pban* model was also used here for the Rietveld analysis, in addition to the $Pm\bar{3}m$ model.[210] The refinements completed are shown in Figure 5.2, and the corresponding structural parameters are listed in Table 5.1. Initial inspection of the refinements shows that the fits obtained are of a reasonable quality. However, the goodness of fit exhibits a steady decline with increasing Li content. This is most likely due to a concomitant increase in the amount of impurity phase produced with increasing Li content. Most reflections are successfully indexed using the *Pban* and $Pm\bar{3}m$ models. Thus, supporting earlier suggestions that both the orthorhombic and cubic phases are present at room temperature. In all cases, the lattice parameters obtained for the *Pban* phase are very similar to the parent material, Li_2OHCl. Thus, demonstrating that variation in the Li content does not result in any significant changes to the lattice parameters. This was also the case for the $Pm\bar{3}m$ phase, as very similar lattice parameters were observed across the series.

As stated earlier, the presence of the impurity phase in the samples implies that the composition of the desired phase may not be as expected. Thus,

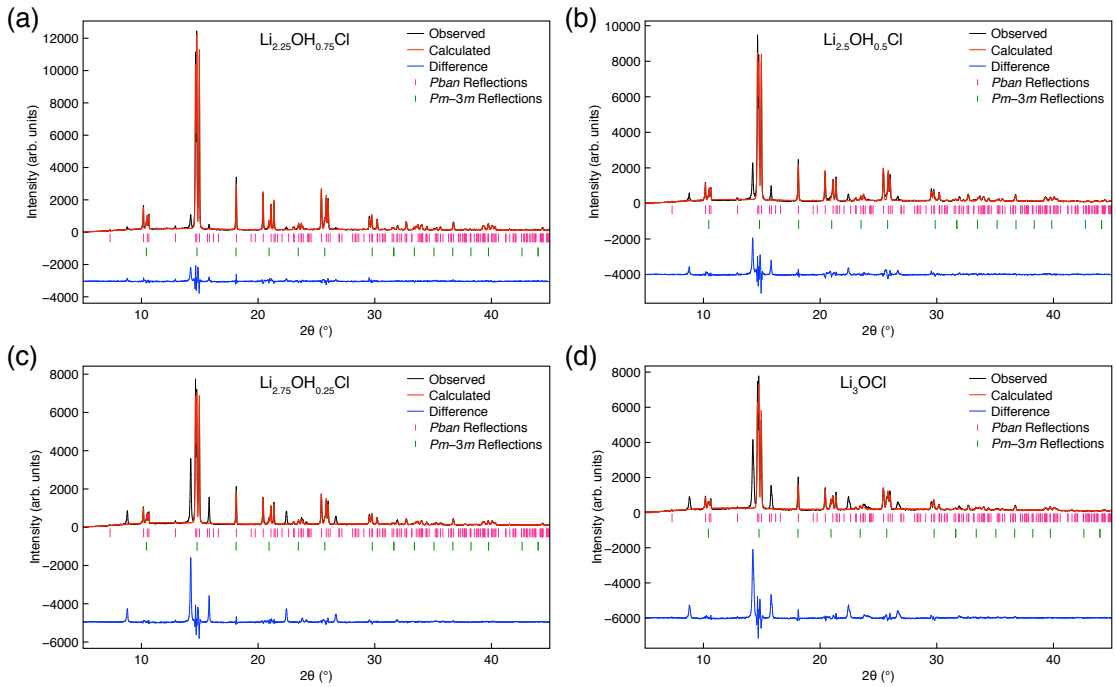

Figure 5.2: Rietveld refinements of the XRD data obtained for samples in the series $Li_{3-x}OH_xCl$ where x = (a) 0.75, (b) 0.5, (c) 0.25 and (d) 0. All samples were synthesised using the Schlenk line method. The reaction temperature was 350 °C and the reaction time was 30 mins. (a) χ^2 = 6.03, wR_p = 14.22%, R_p = 9.17%. (b) χ^2 = 14.15, wR_p = 22.46%, R_p = 14.29%. (c) χ^2 = 19.65, wR_p = 27.35%, R_p = 16.49%. (d) χ^2 = 29.46, wR_p = 31.37%, R_p = 19.87%.

to determine the exact composition of the desired phase, the fractional occupancies of Li and H in the *Pban* phase were refined. It is noted that the laboratory XRD data does not offer sufficient resolution to detect very light elements. However, the *Pban* phase contains multiple Li and H sites and structural details for the system $Li_{3-x}OH_xCl$ ($x < 1$) have not been reported in the literature. Thus, the ideal fractional occupancies for Li and H sites are currently unknown. Hence, it was hoped that refining the corresponding fractional occupancies would at least allow for a rough estimate. The fractional occupancies for O and Cl were fixed at 0.25. In all cases, the fractional occupancies for Li and H were successfully refined. The resulting values suggest a composition of $Li_{2.02}OH_{1.632}Cl$, $Li_{1.656}OH_{2.368}Cl$, $Li_{1.784}OH_{2.112}Cl$ and $Li_{1.588}OH_{2.656}Cl$ for samples in the $Li_{3-x}OH_xCl$ system, where x was intended to be 0.75, 0.5, 0.25 and 0, respectively. Unfortunately, these formulae are not charge-balanced and differ from the intended compositions. Moreover, the fractional occupancies for Li and H in the $Pm\bar{3}m$ phase could not be refined in any case, whereas satisfactory

Table 5.1: Structural parameters for samples in the $Li_{3-x}OH_xCl$ series where x = 0.25, 0.5, 0.75 and 1, obtained from Rietveld refinement of the XRD data using isotropic thermal coefficients. $Li_{2.25}OH_{0.75}Cl$: space group *Pban*, a = 7.75968(17) Å, b = 8.01122(17) Å, c = 3.83280(8) Å, V = 238.264(6) Å^3, phase fraction = 97.14(13)%. Space group $Pm\bar{3}m$, a = 3.91158(22) Å, V = 59.849(10) Å^3, phase fraction = 2.86(13)%. χ^2 = 6.03, wR_p = 14.22%, R_p = 9.17%. $Li_{2.5}OH_{0.5}Cl$: space group *Pban*, a = 7.75937(36) Å, b = 8.01124(34) Å, c = 3.83288(17) Å, V = 238.260(13) Å^3, phase fraction = 98.13(9)%. Space group $Pm\bar{3}m$, a = 3.90099(61) Å, V = 59.364(28) Å^3, phase fraction = 1.87(9)%. χ^2 = 14.15, wR_p = 22.46%, R_p = 14.29%. $Li_{2.75}OH_{0.25}Cl$: space group *Pban*, a = 7.76263(45) Å, b = 8.01064(44) Å, c = 3.83259(22) Å, V = 238.325(16) Å^3, phase fraction = 97.99(14)%. Space group $Pm\bar{3}m$, a = 3.91076(69) Å, V = 59.811(32) Å^3, phase fraction = 2.01(14)%. χ^2 = 19.65, wR_p = 27.35%, R_p = 16.49%. Li_3OCl: space group *Pban*, a = 7.76783(79) Å, b = 8.00718(74) Å, c = 3.83355(37) Å, V = 238.441(28) Å^3, phase fraction = 96.06(23)%. Space group $Pm\bar{3}m$, a = 3.91260(74) Å, V = 59.896(34) Å^3, phase fraction = 3.94(23)%. χ^2 = 29.46, wR_p = 31.37%, R_p = 19.87%.

Atom	x	y	z	Occ.	U(iso) × 100 (Å^2)
$Li_{2.25}OH_{0.75}Cl$					
Pban					
Li1	0.0373	0.25	0	0.256(8)	2.60(60)
Li2	0.25	−0.0049	0	0.082(8)	2.04(145)
Li3	0.0741	0.0037	0.4540	0.083(6)	4.07(150)
O1	0	0	0	0.25	2.16(13)
H1	0.0834	0.0016	0.1296	0.188(22)	2.16(13)
H2	0.0399	0.4681	0.2168	0.016(23)	2.16(13)
Cl1	0.25	0.25	0.5	0.25	2.31(22)
Cl2	0.75	0.25	0.5	0.25	2.08(21)
$Pm\bar{3}m$					
Li	0.5	0	0	0.75	18.71(352)
O	0	0	0	1	0.84(55)
H	0.1279	0.1279	0.1279	0.0938	0.84(55)
Cl	0.5	0.5	0.5	1	3.72(41)
$Li_{2.5}OH_{0.5}Cl$					
Pban					
Li1	0.0373	0.25	0	0.218(7)	2.5
Li2	0.25	−0.0049	0	0.080(7)	2.5
Li3	0.0741	0.0037	0.4540	0.058(5)	2.5
O1	0	0	0	0.25	2.5
H1	0.0834	0.0016	0.1296	0.148(9)	2.5
H2	0.0399	0.4681	0.2168	0.148(9)	2.5

Cl1	0.25	0.25	0.5	0.25	2.5
Cl2	0.75	0.25	0.5	0.25	2.5
Pm$\bar{3}$m					
Li	0.5	0	0	0.833	2.5
O	0	0	0	1	2.5
H	0.1279	0.1279	0.1279	0.062	2.5
Cl	0.5	0.5	0.5	1	2.5
$Li_{2.75}OH_{0.25}Cl$					
Pban					
Li1	0.0373	0.25	0	0.234(10)	2.5
Li2	0.25	−0.0049	0	0.080(10)	2.5
Li3	0.0741	0.0037	0.4540	0.066(7)	2.5
O1	0	0	0	0.25	2.5
H1	0.0834	0.0016	0.1296	0.132(12)	2.5
H2	0.0399	0.4681	0.2168	0.132(12)	2.5
Cl1	0.25	0.25	0.5	0.25	2.5
Cl2	0.75	0.25	0.5	0.25	2.5
Pm$\bar{3}$m					
Li	0.5	0	0	0.917	2.5
O	0	0	0	1	2.5
H	0.1279	0.1279	0.1279	0.031	2.5
Cl	0.5	0.5	0.5	1	2.5
Li_3OCl					
Pban					
Li1	0.0373	0.25	0	0.218(13)	2.5
Li2	0.25	−0.0049	0	0.069(14)	2.5
Li3	0.0741	0.0037	0.4540	0.055(9)	2.5
O1	0	0	0	0.25	2.5
H1	0.0834	0.0016	0.1296	0.166(16)	2.5
H2	0.0399	0.4681	0.2168	0.166(16)	2.5
Cl1	0.25	0.25	0.5	0.25	2.5
Cl2	0.75	0.25	0.5	0.25	2.5
Pm$\bar{3}$m					
Li	0.5	0	0	1	2.5
O	0	0	0	1	2.5
Cl	0.5	0.5	0.5	1	2.5

isotropic thermal coefficients could only be obtained for the "$Li_{2.25}OH_{0.75}Cl$" sample. The coefficients for O and H atoms were constrained to be equivalent, and the coefficients obtained for all atoms in the *Pban* phase appear quite reasonable. However, an unusually high coefficient is obtained for Li in the $Pm\bar{3}m$ phase. For all other samples, it was not possible to obtain sensible thermal coefficients as any attempts at refinement produced several extremely large, negative values. Hence, all thermal coefficients were fixed at 2.5×10^{-2} Å^2. As all of these refinements were completed using two phases, the phase fractions were also determined to identify the relative amounts of each phase present. According to the phase fractions obtained (Table 5.1), all samples are predominantly composed of the *Pban* phase, and the $Pm\bar{3}m$ phase is present in small quantities (<4%). However, it is noted that the exact sample compositions could not be determined, as the samples also contain an unidentified impurity phase which is unaccounted for during the refinements. Hence, these phase fractions can only be used as estimates.

Overall, the findings presented here demonstrate that samples in the series $Li_{3-x}OH_xCl$ (x = 0.25, 0.5 and 0.75) adopt the same orthorhombic phase at room temperature as the parent material, Li_2OHCl. However, a small amount of the high-temperature cubic phase is also formed. Unfortunately, the samples produced are not phase pure. All samples appear to contain the same impurity phase(s), the amount of which appears to increase with increasing Li content. Thus, suggesting that the actual Li and H content of the desired phases will be different from that intended, as some of the reagents will be used to produce the impurity phase. These findings differ from those reported by Schwering *et al.*,[213] who claimed that an increase in the Li content stabilises the cubic structure at room temperature. Thus, the phase transition to a lower symmetry is suppressed. As such, the composition $Li_{2.17}OH_{0.83}Cl$ was reported to exist in a cubic structure in space group $Pm\bar{3}m$ at room temperature. In the current study, samples with a Li content > 2 appear to contain only a very small amount of the cubic phase, suggesting that the observations made by Schwering *et al.*[213] cannot be explained by the higher Li content alone. Hence, the stabilisation of the cubic phase at room temperature must

be due to a combination of the higher Li content (> 2) and the reaction conditions used. Indeed, there is a key difference between the methods used to vary the Li content in $Li_{3-x}OH_xCl$, in this study and by Schwering *et al.*[213] In the current study, the stoichiometry of the reagents was varied to modify the composition of the desired phase. Schwering *et al.*,[213] on the other hand, claim to have doped Li_2OHCl with Li via annealing the as-prepared Li_2OHCl sample with Li metal in an Ag crucible. Thus, it is possible that the cubic phase is stabilised because of the annealing process. Song and co-workers[218] have also studied the $Li_{3-x}OH_xCl$ system where x was varied from 0.3 to 1 and samples of Li_2OHCl, $Li_{2.1}OH_{0.9}Cl$, $Li_{2.4}OH_{0.6}Cl$ and $Li_{2.7}OH_{0.3}Cl$ were synthesised. Their method involved preparing Li_2OHCl using a conventional solid-state synthesis and subsequently using n-butyllithium as a deprotonation agent to adjust the H and, in turn, the Li content. Song *et al.*[218] reported all samples to exist in an orthorhombic phase in space group *Pmmm*. However, no specific crystallographic details were reported. Hence, their claims cannot be verified. However, it appears that the phases observed for samples in the $Li_{3-x}OH_xCl$ system are greatly influenced by the reaction conditions used.

5.3.2 Phase Transition

As demonstrated earlier, the parent material, Li_2OHCl, undergoes a phase transition from orthorhombic to cubic symmetry at around 40 °C (Figure 4.5). Hence, samples in the series $Li_{3-x}OH_xCl$ (x = 0.25, 0.5 and 0.75) were analysed via VT XRD to determine if the same phase transition occurs in these compositions. To do so, each sample was gradually heated from 30 to 50 °C. The corresponding XRD patterns are shown in Figure 5.3. In a similar manner to Li_2OHCl, samples in this series also exhibited a phase transition to cubic symmetry in space group $Pm\bar{3}m$ at ~40 °C. The XRD patterns at 50 °C appear to be very similar to that of the high-temperature cubic phase of Li_2OHCl. Thus, suggesting that these materials also adopt a cubic structure at 50 °C. It is noted that the reflections believed to correspond to an impurity phase remain unchanged. The XRD patterns obtained for all samples at 50 °C were analysed via Rietveld refinement using the $Pm\bar{3}m$ structural model. The refinements are

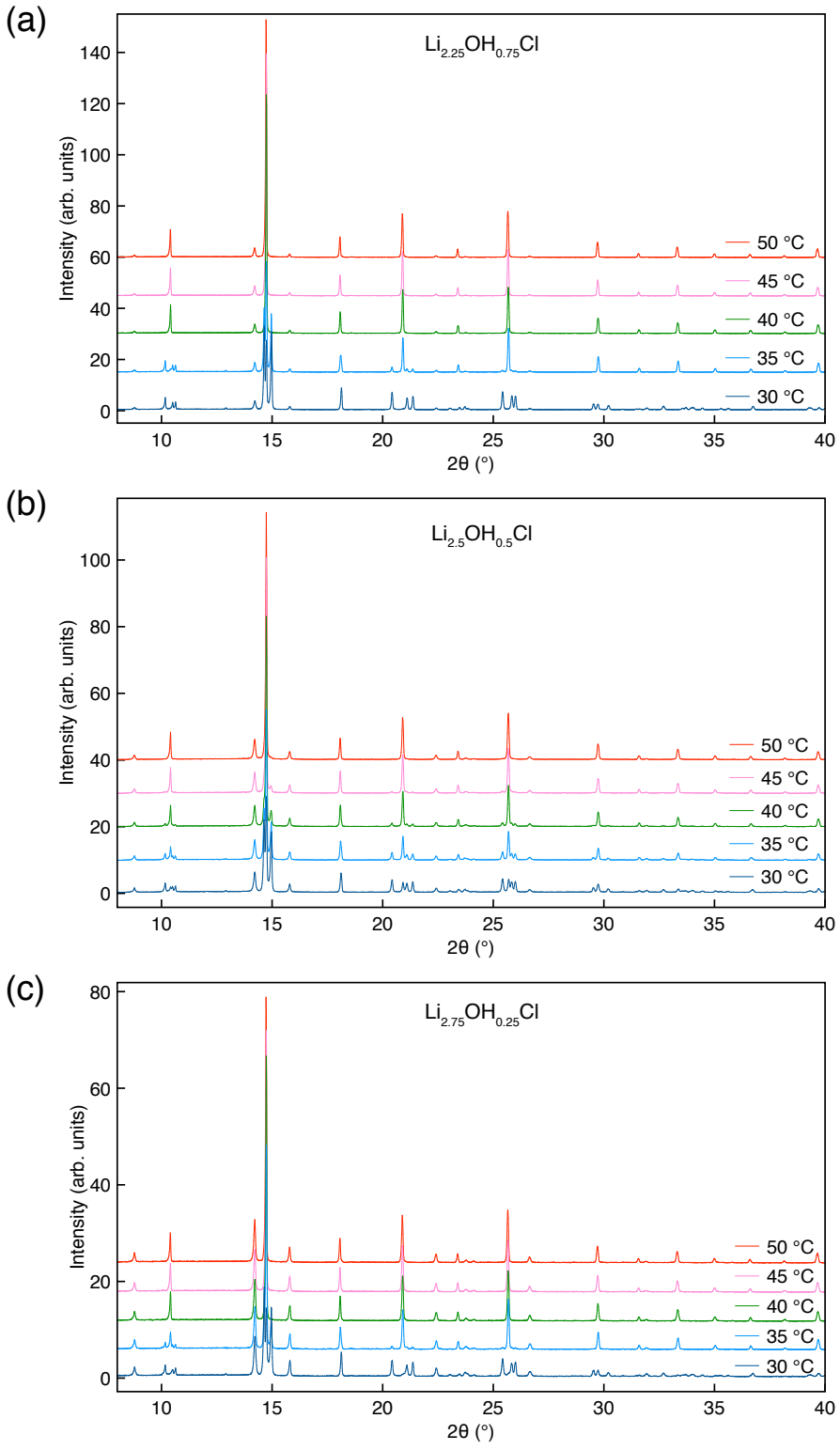

Figure 5.3: X-ray diffraction patterns obtained for samples of (a) $Li_{2.25}OH_{0.75}Cl$ (b) $Li_{2.5}OH_{0.5}Cl$ (c) $Li_{2.75}OH_{0.25}Cl$ during a variable-temperature study in which the temperature was gradually increased from 30 to 50 °C. All samples were synthesised using the Schlenk line method. The reaction temperature was 350 °C and the reaction time was 30 mins.

shown in Figure 5.4, and the corresponding structural parameters obtained are detailed in Table 5.2.

In each case, all major reflections are successfully indexed using the $Pm\bar{3}m$ model. Thus, confirming that the high-temperature phase in these compositions exists in a cubic symmetry in space group $Pm\bar{3}m$. It is noted that some minor reflections are not indexed using the $Pm\bar{3}m$ model. As stated earlier, these reflections are believed to correspond to an impurity phase. A comparison of the diffraction patterns recorded at 50 °C across the series shows that the reflections corresponding to the impurity phase increase in intensity with increasing Li content. Consequently, the goodness of fit achieved decreases with decreasing x in $Li_{3-x}OH_xCl$. As mentioned earlier, the presence of an impurity phase suggests that the composition of the desired phases is not as intended, and the value of x in all the $Li_{3-x}OH_xCl$ samples is likely to be higher than expected. Thus, the fractional occupancies for Li and H were refined in an attempt to determine the exact composition of the desired phase(s). All refined occupancy values are quite similar, suggesting little variation in the composition across the series. The values obtained suggest a composition of $Li_{1.989}OH_{1.09}Cl$, $Li_{1.95}OH_{1.48}Cl$ and $Li_{2.0}OH_{1.208}Cl$ for samples where x is expected to be 0.75, 0.5 and 0.25, respectively. These formulae suggest that the composition of the desired phases is similar to Li_2OHCl. It is noted that none of these formulae are charge-balanced. Moreover, they differ from those obtained earlier using the room-temperature XRD data for the same samples. This is unsurprising as it is extremely difficult to detect light atoms via laboratory XRD. Furthermore, the presence of an unidentified impurity phase makes the analysis difficult owing to multiple overlapping reflections. Thus, the exact composition of the desired phase is very challenging to determine. Isotropic thermal coefficients were also determined, and most coefficients are quite reasonable, except those corresponding to Li, which are unusually large. A similar observation was made earlier for the parent material, Li_2OHCl, where an unusually large isotropic thermal coefficient was determined for Li. However, it was in agreement with the values reported in the literature by Hanghofer *et al.*[210] for a similar composition, $Li_{1.84}OH_{1.16}Cl$. To date, detailed structural

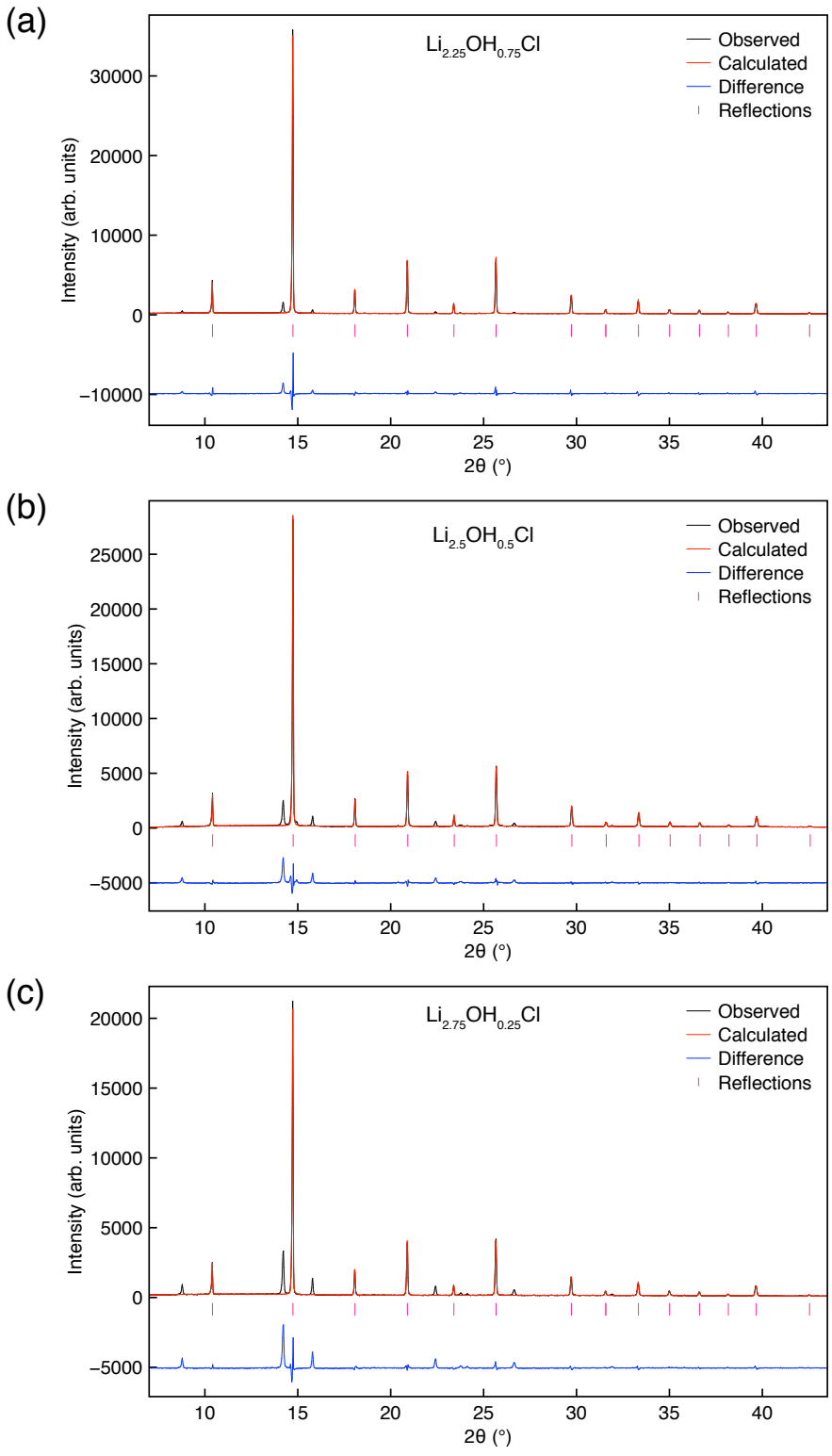

Figure 5.4: Rietveld refinements of the XRD data acquired at 50 °C, for samples of (a) $Li_{2.25}OH_{0.75}Cl$ (b) $Li_{2.5}OH_{0.5}Cl$ (c) $Li_{2.75}OH_{0.25}Cl$, using the $Pm\bar{3}m$ model.[210] All samples were synthesised using the Schlenk line method. The reaction temperature was 350 °C and the reaction time was 30 mins. (a) χ^2 = 8.16, wR_p = 16.12%, R_p = 10.77%. (b) χ^2 = 13.04, wR_p = 21.89%, R_p = 12.90%. (c) χ^2 = 16.29, wR_p = 24.78%, R_p = 14.40%.

Table 5.2: Structural parameters for samples in the $Li_{3-x}OH_xCl$ series where x = 0.25, 0.5 and 0.75 at 50 °C, obtained from Rietveld refinement of the XRD data using isotropic thermal coefficients. $Li_{2.25}OH_{0.75}Cl$: space group $Pm\bar{3}m$, a = 3.91815(5) Å, V = 60.151(2) Å^3. χ^2 = 8.16, wR_p = 16.12%, R_p = 10.77%. $Li_{2.5}OH_{0.5}Cl$: space group $Pm\bar{3}m$, a = 3.91517(7) Å, V = 60.014(3) Å^3. χ^2 = 13.04, wR_p = 21.89%, R_p = 12.90%. $Li_{2.75}OH_{0.25}Cl$: space group $Pm\bar{3}m$, a = 3.91843(10) Å, V = 60.164(4) Å^3. χ^2 = 16.29, wR_p = 24.78%, R_p = 14.40%.

Atoms	x	y	z	Occ.	U(iso) × 100 (Å^2)
$Li_{2.25}OH_{0.75}Cl$					
Li	0.50	0	0	0.663(28)	7.02(77)
O	0	0	0	1	2.52(13)
H	0.1279	0.1279	0.1279	0.136(13)	2.56(13)
Cl	0.5	0.5	0.5	1	2.94(7)
$Li_{2.5}OH_{0.5}Cl$					
Li	0.50	0	0	0.646(35)	6.49(96)
O	0	0	0	1	2.60(16)
H	0.1279	0.1279	0.1279	0.185(17)	2.60(16)
Cl	0.5	0.5	0.5	1	2.93(9)
$Li_{2.75}OH_{0.25}Cl$					
Li	0.50	0	0	0.672(52)	6.77(142)
O	0	0	0	1	2.50(24)
H	0.1279	0.1279	0.1279	0.151(25)	2.50(24)
Cl	0.5	0.5	0.5	1	2.86(14)

parameters have not been reported for compositions in the series $Li_{3-x}OH_xCl$ ($x < 1$). Thus, the thermal coefficients determined in the current study for samples in the series $Li_{3-x}OH_xCl$ (x = 0.25, 0.5 and 0.75) can only be compared to the parent material and those reported for $Li_{1.84}OH_{1.16}Cl$. As discussed earlier, the unusually large thermal coefficient obtained for Li in these compositions is most likely due to inaccurate fractional occupancies and/or Li mobility in the samples.

It must be noted that these findings differ somewhat from those reported by Song *et al.*[218] According to their reports, $Li_{2.4}OH_{0.6}Cl$ transitions from an orthorhombic phase in space group *Pmmm* (at 26 °C) to a cubic phase

in space group $Pm\bar{3}m$ (at 60 °C) via an intermediary tetragonal phase in space group $P4/mmm$ (at 40 °C). A similar pattern was reported for the parent material, Li_2OHCl. However, in that case, the intermediary tetragonal phase was reported to be in space group $P4mm$. $Li_{2.1}OH_{0.9}Cl$, on the other hand, was reported to transition directly from an orthorhombic phase in space group $Pmmm$ (at 26 °C) to cubic symmetry in space group $Pm\bar{3}m$ (at 40 °C). No specific details regarding the phase transition for the composition $Li_{2.7}OH_{0.3}Cl$ were reported. In the current study, all compositions were observed to transition directly from the orthorhombic phase to the cubic phase and no intermediary phases were observed. Moreover, Song *et al.*[218] observed the formation of LiCl when heating the samples to induce a phase change. Interestingly, the formation of LiCl was found to be irreversible, and no Li_2O or LiOH was observed. Thus, the authors concluded that it must be due to the formation of LiCl defects within the structure, as LiCl defects are believed to be more energetically favourable when compared to the Li_2O based defects. Again, the findings presented in the current study differ from those reported by Song *et al.*,[218] as no LiCl was observed when heating the samples. Thus, the claims made by Song *et al.*[218] regarding the phase transition and LiCl formation cannot be supported. It is noted that Schwering *et al.*[213] did not make any comment regarding the formation of LiCl upon heating $Li_{2.17}OH_{0.83}Cl$ either. Considering these literature reports, alongside the findings presented in this study, it appears that variations in the sample preparation method hugely influence the phases present in the samples. Thus, the reaction conditions used to prepare the LiRAP samples are essential for tuning the structure in order to promote Li-ion mobility.

5.3.3 NPD study of $Li_{2.75}OD_{0.25}Cl$

To further investigate the $Li_{3-x}OH_xCl$ system, a deuterated sample of $Li_{2.75}OH_{0.25}Cl$ was prepared for NPD analysis. The XRD pattern obtained for the deuterated sample is shown in Figure 5.5. Also shown for comparison is the XRD pattern for the non-deuterated sample. In the first instance, both patterns appear to be very similar as they exhibit the same reflections. It is noted

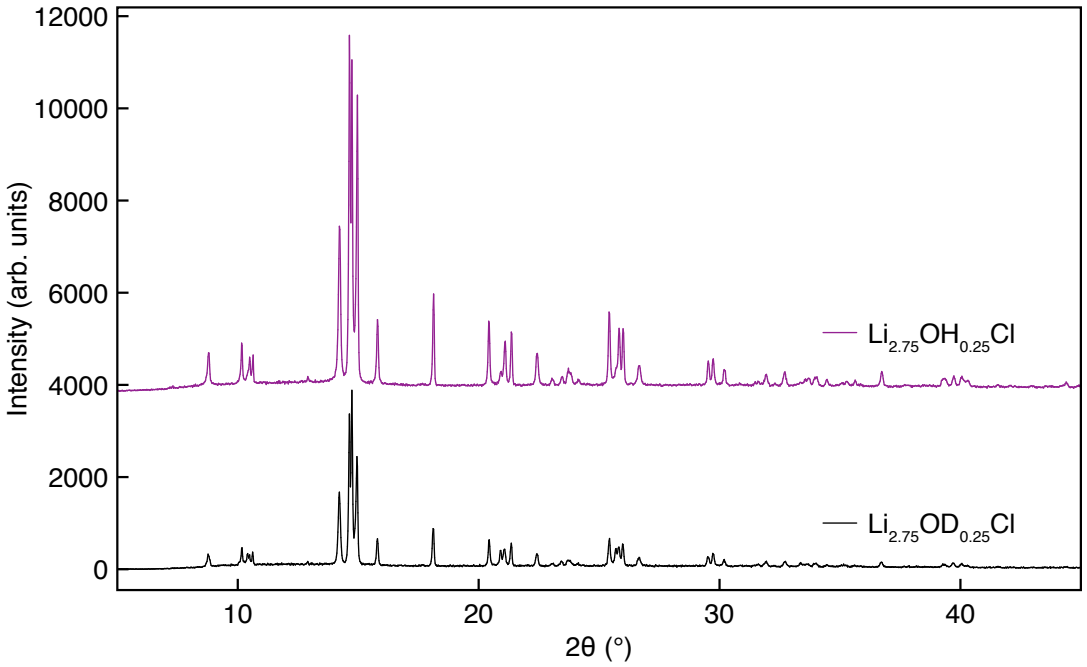

Figure 5.5: X-ray diffraction patterns obtained for the deuterated and non-deuterated samples of $Li_{2.75}OH_{0.25}Cl$ synthesised using the Schlenk line method. The reaction temperature was 350 °C and the reaction time was 30 mins.

that the relative intensity of these reflections differs slightly. Thus, suggesting minor differences between the two samples. These differences could be due to slight variations in the atomic coordinates, fractional occupancies, or the degree of thermal motion exhibited by the atoms.

The NPD pattern obtained for $Li_{2.75}OD_{0.25}Cl$ is shown in Figure 5.6(a). An NPD pattern recorded at 20 °C for the parent material, Li_2ODCl, is also shown for comparison. An initial inspection of the patterns shows a significant difference in the background observed. Both patterns exhibit reflections at the same d-spacings. However, the relative intensities of these reflections vary. This is to be expected given the obvious differences in the sample compositions. The diffraction pattern corresponding to $Li_{2.75}OD_{0.25}Cl$ contains a few additional reflections (d = 0.99, 1.15, 1.18, 1.43, 1.54 and 1.82 Å) that were not present in the pattern corresponding to Li_2ODCl. These are believed to correspond to the impurity phase(s) present in the sample.

Earlier, the new *Pban* and $Pm\bar{3}m$ models were demonstrated to provide a reasonable fit for the laboratory XRD data corresponding to $Li_{2.75}OH_{0.25}Cl$.

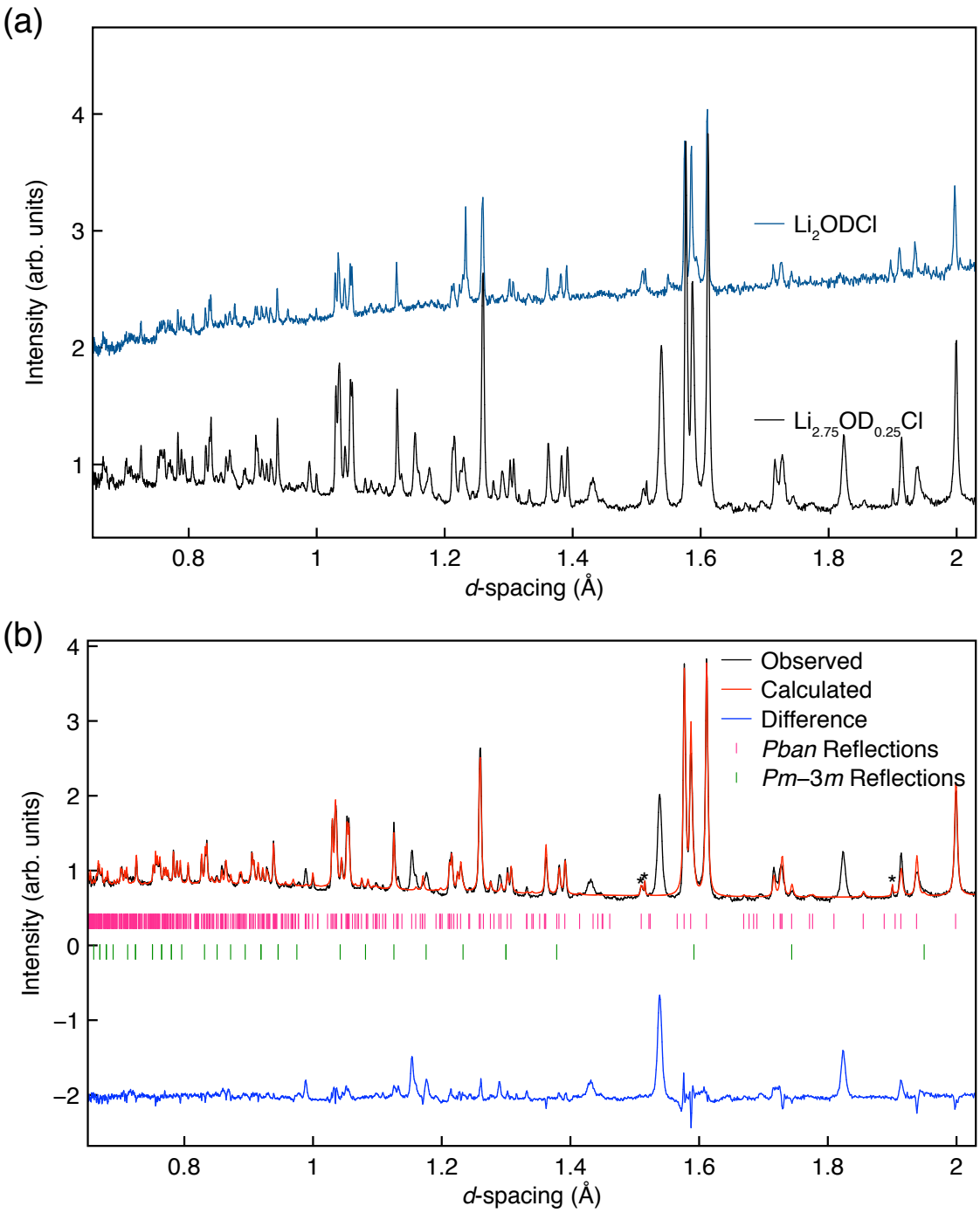

Figure 5.6: (a) NPD patterns obtained for samples of Li_2ODCl (blue) and $Li_{2.75}OD_{0.25}Cl$ (black), synthesised using the muffle furnace and Schlenk line method, respectively. The data was collected at 20 °C for 322.89 (blue) and 492 (black) μA, using the backscattering bank at HRPD. (b) Rietveld refinement of the data acquired for $Li_{2.75}OD_{0.25}Cl$ using the *Pban* and *Pm*$\bar{3}$*m* structural models. Reflections corresponding to the sample holder were excluded and are denoted by *. χ^2 = 42.80, wR_p = 9.05%, R_p = 5.21%.

However, the laboratory XRD data is not suitable for determining accurate atomic coordinates. Thus, it was hoped that the NPD data would enable the atomic coordinates to be refined, in turn, providing an accurate and precise structural model. The Rietveld refinement completed using the new *Pban* and $Pm\bar{3}m$ models is shown in Figure 5.6(b), and the corresponding structural parameters are detailed in Table 5.3. As with the earlier refinements, the reflections corresponding to the sample holder were excluded from the overall fit. This was done by fitting them as background peaks. The fit obtained appears to be of a moderate quality with a χ^2 = 42.80 and wR_p = 9.05%. All major reflections believed to correspond to the desired phase are successfully indexed via the *Pban* and $Pm\bar{3}m$ models. A few reflections that are believed to correspond to the impurity phase have not been indexed. Inspection of the structural parameters indicates that the lattice parameters determined are similar to those obtained earlier via the laboratory XRD data corresponding to $Li_{2.75}OH_{0.25}Cl$. However, there is a noticeable difference between the phase fractions. The deuterated sample appears to contain 99.37(14)% of the *Pban* phase and 0.63(14)% of the $Pm\bar{3}m$ phase. It is noted that the impurity phase

Table 5.3: Structural parameters for a sample of $Li_{2.75}OD_{0.25}Cl$, synthesised using the Schlenk line method, obtained from Rietveld refinement of the NPD data collected at 20 °C using isotropic thermal coefficients. $Li_{2.75}OD_{0.25}Cl$: space group *Pban*: a = 7.75157(33) Å, b = 7.99434(24) Å, c = 3.82694(15) Å, V = 237.150(10) Å^3, phase fraction = 99.37(14)%. Space group: $Pm\bar{3}m$: a = 3.89943(200) Å, V = 59.293(91) Å^3, phase fraction = 0.63(14)%. χ^2 = 42.80, wR_p = 9.05%, R_p = 5.21%.

Atom	x	y	z	Occ.	U(iso) × 100 (Å^2)
Li1	0.0271(22)	0.25	0	0.369(33)	2.09(64)
Li2	0.25	0.0002(336)	0	0.253(81)	10.39(329)
Li3	0.0784(31)	−0.0187(66)	0.5185(224)	0.107(22)	1.35(142)
O1	0	0	0	0.25	0.30(12)
D1	0.0669(39)	0.0049(99)	0.1016(76)	0.068(14)	2.61(108)
D2	0.0825(28)	0.4868(40)	0.1718(57)	0.077(12)	1.42(77)
Cl1	0.25	0.25	0.5	0.25	0.10(9)
Cl2	0.75	0.25	0.5	0.25	0.10(9)

present in the sample is not included during the Rietveld analysis. Therefore, the phase fractions determined do not represent the exact composition of the sample and can only be used as an estimate. However, it is obvious that most of the desired phase adopts an orthorhombic structure in space group *Pban* and the cubic ($Pm\bar{3}m$) phase is present in very small quantities.

Further inspection of the structural parameters indicates that the refined atomic coordinates for Li and D are very similar to those specified initially for the new *Pban* model (Table 4.9). The corresponding fractional occupancies were also determined to identify the exact composition of the desired phase. Unfortunately, the values obtained correspond to a composition of $Li_{3.336}OD_{1.16}Cl$, a formula that is not charge-balanced and deviates considerably from the intended composition of $Li_{2.75}OD_{0.25}Cl$. Moreover, as with the Li_2ODCl sample discussed earlier, here too, the thermal motion had to be treated as isotropic. Attempts to determine anisotropic thermal coefficients resulted in several extremely large and some negative values. Inspection of the isotropic thermal coefficients indicates that most coefficients are reasonable. However, the coefficient for Li2 is unusually large and has a large error. Conversely, the coefficients for the O and Cl atoms are too small. It is noted that, the coefficients for the Cl atoms had to be constrained to be equivalent to avoid a negative value for Cl1. Unfortunately, for the $Pm\bar{3}m$ phase, structural parameters such as the atomic coordinates for D, the fractional occupancies for Li and D and the isotropic thermal coefficients could not be refined to sensible values. Any attempts at refinement resulted in several negative and/or extremely large values for multiple parameters. Thus, the atomic coordinates for D were fixed at x = y = z = 0.1279, as per the details reported in the literature.[210] The fractional occupancies for Li and D were fixed at 0.917 and 0.031, respectively, to indicate a composition of $Li_{2.75}OD_{0.25}Cl$ and the isotropic thermal coefficients were fixed at 2.5×10^{-2} Å^2.

Overall, the new *Pban* and $Pm\bar{3}m$ models appear to provide a reasonable fit for the NPD data. Thus, strongly suggesting that "$Li_{2.75}OD_{0.25}Cl$" also adopts the same orthorhombic phase as the parent material, Li_2OHCl. Additionally, a small amount of the cubic phase in space group $Pm\bar{3}m$ is also present

at room temperature. Unfortunately, some of the structural parameters determined, *e.g.*, the fractional occupancies and the thermal coefficients are not fully reliable, as the values obtained differ drastically from those expected. Moreover, structural parameters for the $Pm\bar{3}m$ phase could not be determined at all. It is possible that the structure of "$Li_{2.75}OH/D_{0.25}Cl$" differs somewhat from the parent material, Li_2OH/DCl. Therefore, the new *Pban* model may not be a truly accurate description of the structure. This, in turn, makes it difficult to determine sensible structural parameters. However, the most probable cause for this is likely to be the presence of an impurity phase in the sample. The laboratory XRD data obtained for samples in the series $Li_{3-x}OH_xCl$ (x = 0.25, 0.5 and 0.75) showed that the amount of the impurity phase produced increases with increasing Li content. Thus, suggesting that a sample of "$Li_{2.75}OH/D_{0.25}Cl$" contains a significant amount of the impurity phase. Therefore, there is likely to be a significant overlap between the reflections corresponding to the desired phase and the as yet unidentified impurity phase, in turn, making precise sample characterisation extremely challenging.

5.3.4 ^{1}H and ^{7}Li NMR Studies of $Li_{3-x}OH_xCl$ (x = 0.25, 0.5 and 0.75)

Samples in the series $Li_{3-x}OH_xCl$ (x = 0.25, 0.5 and 0.75) were also investigated via multinuclear SSNMR, and both the room- and high-temperature phases were analysed. The ^{1}H and ^{7}Li MAS NMR spectra acquired for $Li_{3-x}OH_xCl$ (x = 0.25, 0.5 and 0.75) at 33 and 52 °C are shown in Figure 5.7. In a similar manner to Li_2OHCl, a single relatively broad resonance is observed in all cases. At 33 °C, both the ^{1}H and ^{7}Li resonances are broad with intense spinning sidebands. All ^{1}H spectra exhibit just a few spinning sidebands, typically characteristic of OH groups. At 52 °C, the resonances begin to narrow and the spinning sidebands reduce in intensity. This change in appearance for both the ^{1}H and ^{7}Li NMR spectra can be attributed to the phase transition to a cubic structure in space group $Pm\bar{3}m$. As discussed earlier, a change in structure to higher symmetry results in narrower lines owing to a reduction in the dipolar couplings. Notably, the diffraction data presented earlier clearly demonstrated the presence of multiple phases in the samples, meaning that

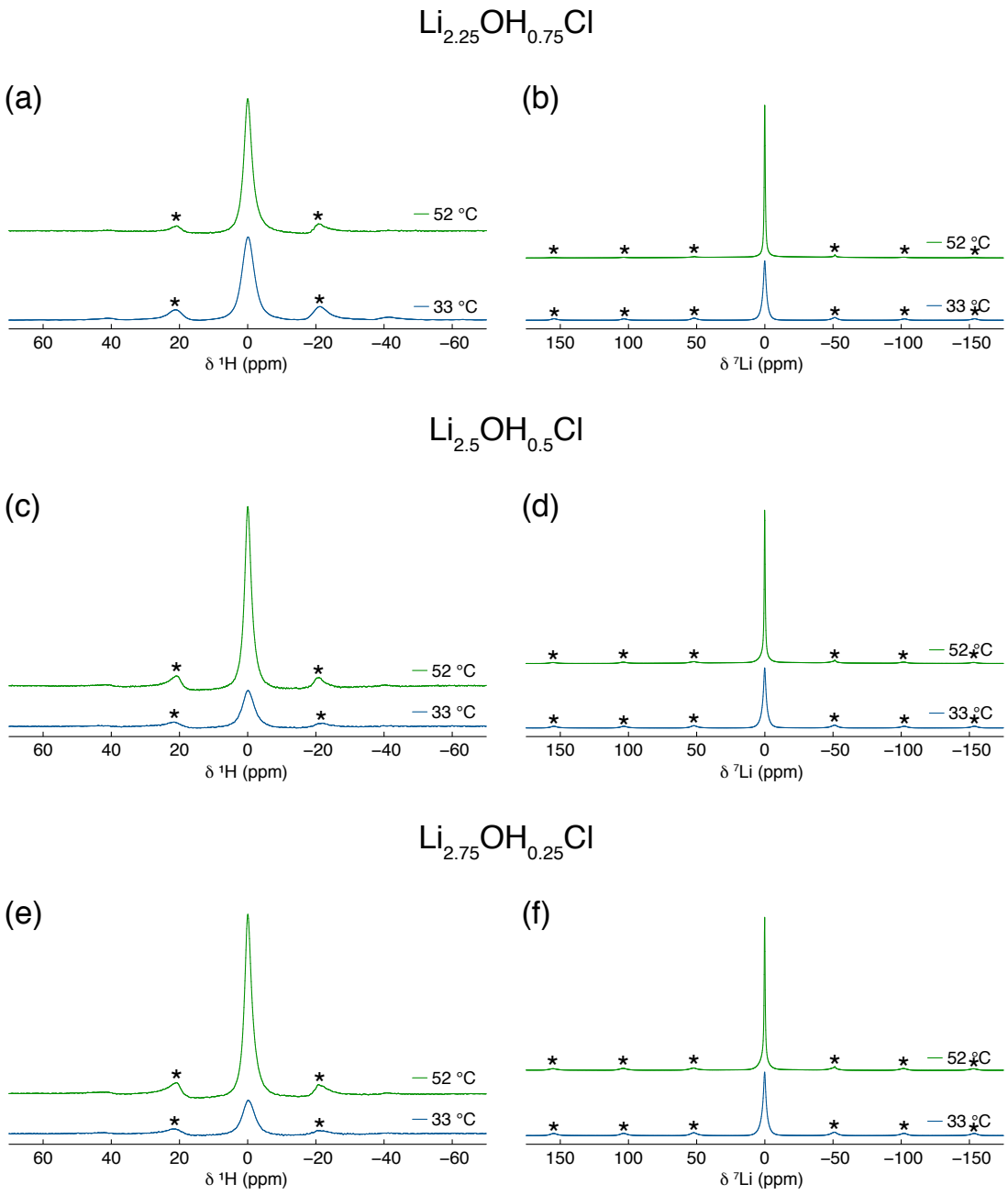

Figure 5.7: ^{1}H and ^{7}Li (11.7 T) MAS NMR spectra for samples of (a,b) $Li_{2.25}OH_{0.75}Cl$, (c,d) $Li_{2.5}OH_{0.5}Cl$ and (e,f) $Li_{2.75}OH_{0.25}Cl$. All samples were prepared via the Schlenk line method. The MAS rate was 10 kHz and spinning sidebands are denoted by *. In all cases, a recycle delay of 60 s was used to acquire 4 transients.

the samples contain multiple H and Li species. However, it has not been possible to identify different H and Li species from the NMR data shown in Figure 5.7. As previously discussed, ^{1}H resonances are typically broad, and ^{7}Li has a very small chemical shift, meaning that signals from different species are often

indistinguishable due to considerable spectral overlap.

5.3.5 ^{35}Cl NMR Studies of $Li_{2.5}OH_{0.5}Cl$

One of the samples in the series, $Li_{2.5}OH_{0.5}Cl$, was analysed further via VT ^{35}Cl MAS NMR and the spectra acquired at 33 and 63 °C are shown in Figure 5.8. The spectrum acquired at 33 °C exhibits a lineshape that appears to be composed of several overlapping resonances. The lineshape is similar to that observed for the parent material, Li_2OHCl. However, it is noted that, unlike Li_2OHCl, this sample does not contain residual LiCl. Hence, the corresponding signal is not observed. Whilst the spectrum acquired at 33 °C for $Li_{2.5}OH_{0.5}Cl$ appears to be similar to that of its parent material, Li_2OHCl, the spectrum acquired following the phase transition at 63 °C is noticeably different. At 63 °C, a broad lineshape exhibiting two very obvious resonances is observed. This is in contrast to the spectrum obtained for Li_2OHCl at 63 °C, where only a single broad resonance was observed. The lineshapes observed were simulated to determine the number of Cl sites present in the sample. The

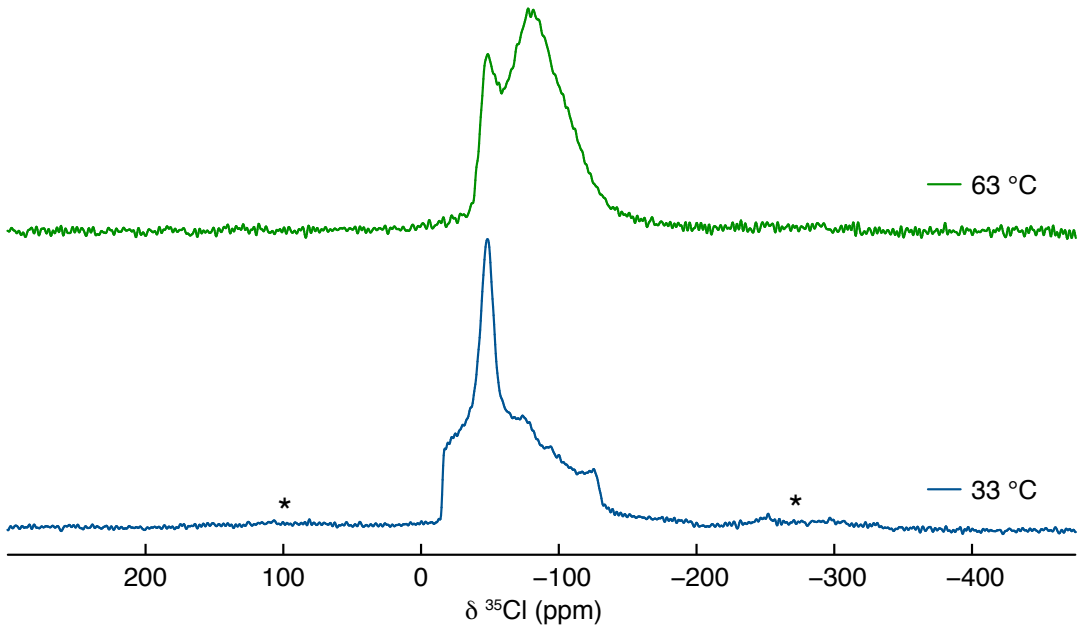

Figure 5.8: ^{35}Cl (11.7 T) MAS NMR spectra acquired at 33 (blue) and 63 °C (green), for a sample of $Li_{2.5}OH_{0.5}Cl$ prepared via the Schlenk line method. The MAS rate was 10 kHz and spinning sidebands are denoted by *. In both cases, a recycle delay of 10 s was used to acquire 2560 transients.

fits obtained are shown in Figure 5.9 and the corresponding quadrupolar parameters are detailed in Table 5.4.

A minimum of three distinct Cl sites were required to simulate the lineshape observed at 33 °C. This is similar to what was observed for Li_2OHCl, and the sites observed appear to have similar quadrupolar parameters. Thus, indicating that Cl experiences similar environments in both samples. This further suggests that $Li_{2.5}OH_{0.5}Cl$ and Li_2OHCl adopt the same structure prior to undergoing a phase transition at ~40 °C. Interestingly, the lineshape observed at 63 °C could only be accurately simulated using three sites. This is in contrast to what was observed for Li_2OHCl, where two sites were required to simulate the corresponding lineshape. It is noted that site 1 has a similar δ and C_Q to site 1 obtained for Li_2OHCl at 63 °C. However, the corresponding η_Q varies considerably. Moreover, sites 2 and 3 do not resemble any site observed for the parent material, Li_2OHCl, at 63 °C. This suggests that, upon increasing the Li content of the sample, the local environment of the Cl changes significantly. All sites have a similar C_Q, which is relatively small. As discussed previously, a perfectly cubic system would have C_Q close to 0. Thus, a small C_Q for these sites indicates a system exhibiting high symmetry, albeit not perfectly cubic. The diffraction data presented earlier indicated the presence of an impurity phase in the sample, albeit in a small quantity when compared to the desired phase. Therefore, one of the sites most likely corresponds to the impurity phase. It is likely to be "site 2" due to its much lower intensity when compared to the other two signals that clearly dominate the lineshape. It is noted that an additional site was not required to simulate the lineshape corresponding to the room-temperature phase. This may be due to the fact that the impurity phase is present in a small quantity, meaning that the corresponding signal has a low intensity. Hence, it may have been overshadowed by the signals arising from the desired phase.

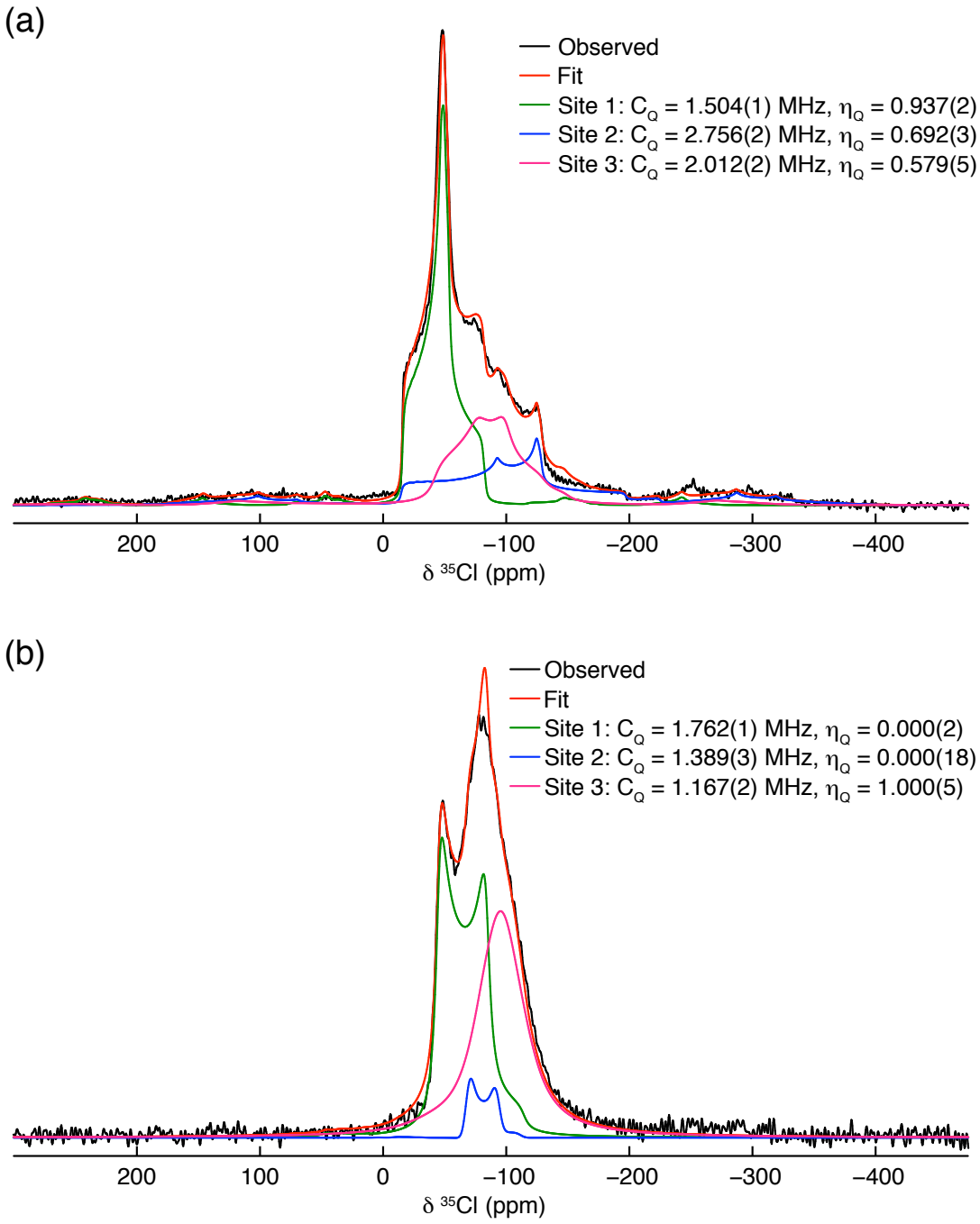

Figure 5.9: Simulations of the ^{35}Cl (11.7 T) MAS NMR spectra acquired at (a) 33 °C and (b) 63 °C for a sample of $Li_{2.5}OH_{2.5}Cl$, prepared via the Schlenk line method. The MAS rate was 10 kHz and a recycle delay of 10 s was used to acquire 2560 transients. At 33 °C, three sites were required to fit the lineshape and the corresponding quadrupolar parameters were obtained: Site 1 (C_Q = 1.504(1) MHz and η_Q = 0.937(2)), Site 2 (C_Q = 2.756(2) MHz and η_Q = 0.692(3)), Site 3 (C_Q = 2.012(2) and η_Q = 0.579(5)). At 63 °C, three sites were required to fit the lineshape and the corresponding quadrupolar parameters were obtained: Site 1 (C_Q = 1.762(1) MHz and η_Q = 0.000(2)), Site 2 (C_Q = 1.389(3) MHz and η_Q = 0.000(18)), Site 3 (C_Q = 1.167(2) MHz and η_Q = 1.000(5)).

Table 5.4: ^{35}Cl NMR parameters, δ, C_Q, and η_Q, obtained by simulating the lineshapes observed in the ^{35}Cl MAS NMR spectra obtained at 33 and 63 °C, for a sample of $Li_{2.5}OH_{0.5}Cl$ prepared via the Schlenk line method.

Site	δ (ppm)	C_Q (MHz)	η_Q
33 °C			
1	−15.60(2)	1.504(1)	0.937(2)
2	−11.53(4)	2.756(2)	0.692(3)
3	−38.98(13)	2.012(2)	0.579(5)
63 °C			
1	−33.57(4)	1.762(1)	0.000(2)
2	−61.55(2)	1.389(3)	0.000(18)
3	−76.63(6)	1.167(2)	1.000(5)

5.4 Conclusions

As demonstrated earlier, a phase pure sample of Li_3OCl cannot be synthesised, predominantly owing to its hygroscopic nature, but its hydrated analogue, Li_2OHCl, is much easier to synthesise. Thus, this chapter focused on the synthesis of samples in the series $Li_{3-x}OH_xCl$ (x = 0.25, 0.5 and 0.75) to determine whether phase pure samples could be produced. The samples produced were analysed via XRD, NPD and multinuclear SSNMR spectroscopy. All samples were found to contain multiple phases. The desired phases were observed to adopt the same structure as the room-temperature phase of Li_2OHCl. A small amount of the cubic phase in space group $Pm\bar{3}m$ was also present. Unfortunately, the samples also contained an unidentified impurity phase, and a comparison of the diffraction patterns for samples in the series $Li_{3-x}OH_xCl$ (x = 0, 0.25, 0.5, 0.75 and 1) indicated that the amount of impurity phase formed increases with increasing Li content. Thus, suggesting the compositions of the desired phases likely differ from those intended. Moreover, a comparison of the diffraction patterns for the end members, Li_2OHCl and Li_3OCl, strongly suggested that the Li_3OCl sample initially prepared also contained some of the hydrated LiRAP. All diffraction patterns were analysed via the Rietveld method using the new *Pban* and $Pm\bar{3}m$ models. The fits obtained were of

reasonable quality. However, the goodness of fit decreased steadily with increasing Li content. This is believed to be due to a concomitant increase in the amount of the impurity phase produced.

Samples in the series $Li_{3-x}OH_xCl$ (x = 0.25, 0.5 and 0.75) were also analysed via VT XRD, and the same phase transition to cubic symmetry ($Pm\bar{3}m$) observed for Li_2OHCl was also observed for these samples. The reflections corresponding to an unknown impurity phase were more clearly observed in the diffraction patterns acquired at 50 °C. It appears that as the stoichiometric amount of LiOH added increases, *i.e.*, as the composition is pushed closer to Li_3OCl, the amount of the impurity phase formed also increases. Hence, the samples produced are unlikely to have the desired composition, and the true value of x in $Li_{3-x}OH_xCl$ must be higher than expected as a proportion of the starting materials must be used to form the impurity phase. To determine the precise compositions of the desired phases, the fractional occupancies for both Li and H were refined using the diffraction data acquired both at room temperature and 50 °C. In all cases, the formulae obtained deviated from those intended. Moreover, the formulas determined for the same samples at room temperature and 50 °C were not in agreement. It is noted that the laboratory XRD data does not offer sufficient resolution to accurately determine the corresponding occupancies for light atoms such as Li and H. Thus, the results obtained are not highly reliable. Thus, it was not possible to determine the true value of x from the diffraction data presented in the $Li_{3-x}OH_xCl$ samples synthesised.

To further investigate the $Li_{3-x}OH_xCl$ system, a deuterated sample of "$Li_{2.75}OH_{0.25}Cl$" was synthesised and analysed via NPD at HRPD. The diffraction pattern obtained was similar to that of the parent material, Li_2ODCl. However, there were some noticeable differences in the relative peak intensities. A few additional reflections, believed to correspond to the impurity phase, were also present. Rietveld analysis of the diffraction pattern was completed using the new *Pban* and $Pm\bar{3}m$ models. The sample was found to consist predominantly of the orthorhombic phase in space group *Pban*, with small amounts of the cubic phase. Structural parameters such as atomic coordinates, frac-

tional occupancies and isotropic thermal coefficients could be refined for the *Pban* phase. However, no structural parameters could be refined for the $Pm\bar{3}m$ phase. It is also noted that the composition dictated by the fractional occupancies for the *Pban* phase deviated from that intended. Moreover, the isotropic thermal coefficients obtained did not appear to be very sensible. This is likely due to the unidentified impurity phase because the reflections corresponding to the desired phase will overlap with those for the impurity phase. However, the impurity phase is not included in the refinement. Thus, the analysis is completed on the assumption that all reflections correspond to the desired phase. This makes it challenging to determine accurate structural parameters.

Samples in the series $Li_{3-x}OH_xCl$ (x = 0.25, 0.5 and 0.75) were also analysed via SSNMR spectroscopy. The NMR analysis has shown similar results to those observed for the parent material, Li_2OHCl. More specifically, the ^1H and ^7Li MAS NMR spectra for all samples exhibited a single resonance that narrowed following the phase transition, likely owing to a reduction in dipolar couplings. The diffraction analysis presented indicated the presence of additional phases in the samples. However, multiple species could not be identified using the ^1H and ^7Li NMR data. A sample of $Li_{2.5}OH_{0.5}Cl$ was further analysed via ^{35}Cl MAS NMR spectroscopy, and the corresponding spectrum for the room-temperature phase closely resembled that of the parent material, Li_2OHCl. Specifically, three different Cl sites with similar quadrupolar parameters were observed. Conversely, the spectrum corresponding to the high–temperature cubic phase of $Li_{2.5}OH_{0.5}Cl$ was significantly different from that of Li_2OHCl. Here, three different Cl sites were observed, whereas only two were observed for Li_2OHCl. The third site is believed to correspond to the as yet unidentified impurity phase present in the sample.

Overall, synthesising samples with varied Li and H content appears to be more challenging than initially envisaged. Samples produced exhibited the same phase behaviour as the parent material, Li_2OHCl. However, the precise composition of the desired phases is yet to be confirmed.

6 Li_2OHCl: Probing Ion Mobility

6.1 Introduction

As previously discussed, Li_2OHCl is a potential solid electrolyte material for Li-ion batteries, as it has been reported to exhibit a high Li-ion conductivity. However, in order for it to be successfully used in practical applications, it is imperative to gain information regarding the ion mobility mechanisms taking place within such a system.

One of the first reports regarding ion conductivity in LiRAPs was by Schwering and co-workers.[213] They studied Li_2OHCl via EIS and VT static ^1H and ^7Li SSNMR. A narrowing of the resonances was observed for both ^1H and ^7Li with increasing temperature, which is suggestive of ion mobility in the system. ^7Li T_1 measurements were also completed for the $Li_{3-x}OH_xCl$ (x = 0.83 – 2) series, and a reduction in T_1 values was observed with increasing temperature. ^7Li T_1 measurements were used to determine an E_a of 0.36 eV for Li_2OHCl. However, the E_a determined from EIS was ~0.56 eV. It has been suggested that the difference between the E_a values determined from NMR and EIS is due to the fact that NMR is a local probe and only detects motion in the bulk of a material. Whereas, EIS can detect the motional processes at both the grain boundaries and in the bulk material. Schwering *et al.* noted that the ionic conductivity of Li_2OHCl increases sharply following the phase transition.[213] This observation led to suggestions that the cubic symmetry is a prerequisite for high ion conductivity in Li_2OHCl. It was theorised that in the cubic phase, the freely rotating OH^- groups allow for Li-ion mobility, meaning that the two processes are correlated. Static OH^- groups, on the other hand, would restrict the movement of Li-ions. It was further suggested that the phase transition in Li_2OHCl from orthorhombic to cubic symmetry is, in fact, a consequence of the onset of Li movement.

Hood *et al.* have also explored Li_2OHCl as a potential solid electrolyte system via EIS (*vide supra*).[214] As stated earlier, they synthesised Li_2OHCl via both fast and slow cooling methods and reported that fast cooled Li_2OHCl

exhibited a higher ionic conductivity and lower activation energy at elevated temperatures. An ionic conductivity of 2.8×10^{-3} S cm^{-1} was reported at 195 °C, with an E_a of 0.56 eV, which is in agreement with that reported by Schwering *et al.* via EIS.[213]

The ionic conductivities of $Li_{3-x}OH_xCl$ (x = 0.3 – 1) have been measured as a function of proton concentration via EIS by Song and co-workers.[218] Despite specific conductivity values not being reported for any of the compositions, it was stated that conductivities on the order of 10^{-4} S cm^{-1} were measured at 110 °C. They also performed MD simulations to investigate the Li-ion motion, where it was suggested that the Li-ions move via Frenkel defects and it is the rotation of the OH^- groups in the cubic structure that provides access to lower-energy pathways.

Finally, the dynamics of the Li_2OHCl/Br system have also been studied via ^2H NMR of deuterated samples. Eilbracht and co-workers reported a dynamical orientational disordering of the OD^- groups.[215] However, specific details regarding the motion of the OD^- groups or Li-ions were not provided.

In the current study, VT ^1H, ^2H and ^7Li MAS and static ^7Li NMR spectroscopy has been used to study Li-ion mobility in Li_2OHCl and the related series $Li_{3-x}OH_xCl$ (x = 0.25 – 0.75). The feasibility of proton transport has also been evaluated. AIMD calculations have also been completed by our collaborators, which support our experimental findings. Finally, VT ^{35}Cl MAS NMR spectroscopy has also been used to investigate the corresponding structural changes in the $Li_{3-x}OH_xCl$ (x = 0.25 – 1) series.

6.2 Experimental

6.2.1 Synthesis

The synthesis of all samples discussed in this chapter has been described earlier in Chapter 4. Samples of Li_2OH/DCl were synthesised via the muffle furnace method and the samples $Li_{2.25}OH_{0.75}Cl$, $Li_{2.5}OH/D_{0.5}Cl$ and $Li_{2.75}OH_{0.25}Cl$ were synthesised via the Schlenk line method.

6.2.2 Solid-State NMR

All solid-state NMR spectra were acquired using a Bruker 500 Avance III HD spectrometer, equipped with a wide-bore 11.7 T Oxford magnet, using Larmor frequencies of 499.69 MHz for ^{1}H (I = 1/2), 76.77 MHz for ^{2}H (I = 1), 194.20 MHz for ^{7}Li (I = 3/2) and 49.00 MHz for ^{35}Cl (I = 3/2). Powdered samples were packed into conventional 4.0 mm ZrO_2 rotors under an Ar atmosphere and placed into a Bruker 4.0 mm HX probe. A MAS rate of 10 kHz was employed, unless stated otherwise. ^{1}H chemical shifts were referenced to neat tetramethylsilane, by setting the resonance from a sample of adamantane to δ_{iso} = 1.9 ppm. ^{7}Li chemical shifts were referenced to 1 M $LiCl_{(aq)}$. ^{2}H chemical shifts were referenced to $(CD_3)_4Si$ using a sample of $CDCl_3$, δ_{iso} = 7.24 ppm. ^{35}Cl chemical shifts were referenced to 1 M $NaCl_{(aq)}$. VT static ^{7}Li NMR experiments, completed over the temperature range −65 to 230 °C, were undertaken using a Bruker 400 Avance III HD spectrometer, equipped with a wide-bore 9.4 T magnet, using a Larmor frequency of 155.5 MHz for ^{7}Li. The sample was packed into a 5.0 mm ceramic rotor inside an Ar-filled glovebox and placed into a Bruker 5.0 mm static-HX probe.

Standard VT ^{1}H, ^{2}H and ^{7}Li MAS NMR experiments were completed over the temperature range −19 to 110 °C using conventional hardware. All ^{1}H MAS NMR spectra were acquired using a background suppression (DEPTH)[197] experiment with typical $\pi/2$ and π pulse lengths of 4 and 8 μs, respectively. Conventional ^{7}Li MAS NMR spectra were obtained using a single-pulse experiment with a typical pulse length of 1.5 μs. During the acquisition, proton-decoupling was applied using SPINAL-64,[198] with a RF field of 32 kHz. For ^{1}H and ^{7}Li MAS NMR experiments, typical RF field strengths of 62 – 166 kHz were employed. Static ^{7}Li NMR spectra were acquired using a solid-echo ($90°_x - \tau - 90°_y - \tau$) experiment with a typical pulse length of 1 μs. ^{1}H and ^{7}Li T_1 values were measured using a saturation recovery experiment. Static and MAS ^{2}H NMR spectra were obtained using a solid-echo ($90°_x - \tau - 90°_y - \tau$) experiment with a typical pulse length of 4 μs and a RF field of 62.5 kHz.

VT ^{35}Cl MAS NMR spectra were acquired between 33 – 109 °C, using a hahn-echo ($90°_x - \tau - 180°_y - \tau$) experiment with a pulse length of 4 μs and a RF field of 62.5 kHz. ^{35}Cl EXSY spectra were acquired using a standard $\pi_{90} - t_1 - \pi_{90} - \tau_{mix} - \pi_{90}$ pulse sequence, with t_1 = 1 s and τ_{mix} = 0.1 s. For all ^{35}Cl NMR experiments MAS rates of 10 or 12 kHz were employed. Specific details regarding the recycle delays used and the number of transients acquired are provided in the relevant figure captions. In all cases, quoted temperatures have been calibrated and reflect the true temperature of the sample during the experiment. Selected NMR spectra were fitted using the SOLA tool in Topspin 4.0.

6.2.3 PFG-NMR Spectroscopy

^{7}Li PFG-NMR experiments were performed in collaboration with Professor Clare P. Grey and Mr Steffen P. Emge at the University of Cambridge, using a Bruker Diff50 PFG probe equipped with a Z-gradient and an enhanced variable temperature (EVT) ^{7}Li saddle coil in a 7.046 T magnet. Spectra were acquired using a stimulated diffusion pulse sequence (Figure 2.20) and varying gradient strengths. The effective gradient length, δ, was set to 5 ms and a maximum gradient strength of 1800 G cm^{-1} was used. The diffusion time, Δ, was kept constant and set to either 100, 175 or 250 ms. Diffusion coefficients were obtained by fitting the decaying signal. All acquisitions were performed at an elevated temperature of 100 °C. All samples were sealed into glass tubes under an Ar atmosphere.

^{1}H PFG-NMR experiments were completed in collaboration with Professor Laurent Le Polles and Dr Claire Roiland at Université De Rennes, Rennes, France, using the stimulated diffusion pulse sequence (Figure 2.20) on a Bruker AV 300 spectrometer equipped with a PFG Bruker probe (30 T m^{-1}). The gradient strengths were varied from 0 to 1450 G cm^{-1} and from 0 to 3000 G cm^{-1}, at room temperature and 100 °C, respectively.

6.2.4 *Ab initio* Simulations

All *ab initio* simulations were carried out by our collaborators Professor Saiful Islam and Dr James Dawson at the University of Bath. All calculations were performed using DFT based on the Vienna *ab initio* simulation package (VASP).[224] A plane-wave cut-off energy of 400 eV, the projector augmented wave method[225] and the PBEsol exchange–correlation functional were employed. This particular functional was selected because it has been used in previous successful studies of Li-ion battery materials.[226–228] The *k*-space was sampled with a *k*-point mesh spacing smaller than 0.05 $Å^{-1}$ and the gamma–point only for the reaction enthalpy and AIMD calculations, respectively. Structural optimisation was performed until the residual force on each atom was smaller than 0.03 eV $Å^{-1}$. AIMD simulations were carried out to examine Li^+ ion diffusion in $Li_{3-x}OH_xCl$, (x = 0 – 1.06), with $4 \times 4 \times 4$ supercells containing 320 atoms. Each composition was first equilibrated for 10 ps. Statistical properties were then obtained from the following 50 ps simulations using the NVT ensemble with a Nose–Hoover thermostat.[229] The AIMD calculations were carried out at 600, 700, 800, 900 and 1000 K, with a short time step of 1 fs due to the presence of hydrogen. Self-diffusion data for Li were obtained from the mean square displacement (MSD) according to,

$$r_i^2(t) = 6D_{\mathrm{Li}}t \ , \tag{6.1}$$

where $r_i^2(t)$ is the MSD, D_{Li} is the diffusion coefficient for Li and t is time. The diffusion coefficients were then converted to conductivities using the Nernst-Einstein relationship,

$$\frac{\sigma}{D_{\mathrm{Li}}} = H_{\mathrm{R}}\frac{nq^2}{k\mathrm{T}} \ , \tag{6.2}$$

where n is the number of charge carriers per unit volume, q is the electron charge, k is the Boltzmann constant, T is the temperature and H_{R} is the Haven ratio. A Haven ratio of one was used in our calculations.

6.3 Results and Discussion

6.3.1 Probing Proton and Li-ion Mobility in Li_2OHCl

In this study, VT SSNMR spectroscopy has been used extensively to monitor ion dynamics, in particular lithium and proton mobility. This chapter is focused on exploring ion mobility in Li_2OHCl and its related compositions. The ^1H MAS NMR spectra acquired over the temperature range −19 – 106 °C for a sample of Li_2OHCl synthesised via a conventional solid-state route are shown in Figure 6.1(a). In all cases, a single resonance is observed. The resonance observed in the spectra obtained between −19 and 33 °C corresponds to the room-temperature orthorhombic phase of Li_2OHCl and is relatively broad. As the temperature is increased to 52 °C, a narrowing of the lineshape is observed. As discussed in Chapter 4, the ^1H resonance narrows considerably following the phase transition to cubic symmetry. The lineshape continues to narrow until 106 °C. A corresponding plot of the FWHM vs. temperature is shown in Figure 6.1(b), which confirms a narrowing of the lineshape with increasing temperature. Between −19 and 33 °C, there is minimal change in the linewidth, suggesting there is no change in the local H environment, *i.e.*, the protons are static and not moving. As the temperature is increased to 52 °C, there is a sudden decrease in linewidth, believed to correspond to the known phase transition to the cubic $Pm\bar{3}m$ phase. There is a further, more gradual, reduction in linewidth above 52 °C, believed to correspond to the movement or mobility of protons within the Li_2OHCl structure, likely the rotation or free movement of the OH^- groups. However, the precise nature of the movement cannot be discerned from this data alone. It is also noted that between 33 and 52 °C, it is challenging to accurately differentiate the precise contribution of the phase transition versus the mobility of the OH^- groups to the observed change in linewidth.

The ^7Li MAS NMR spectra acquired over the temperature range −19 – 106 °C for a sample of Li_2OHCl synthesised via a conventional solid-state route are shown in Figure 6.2(a). In a similar manner to the ^1H MAS NMR, a single resonance is observed. Between −19 and 33 °C, where Li_2OHCl is known to

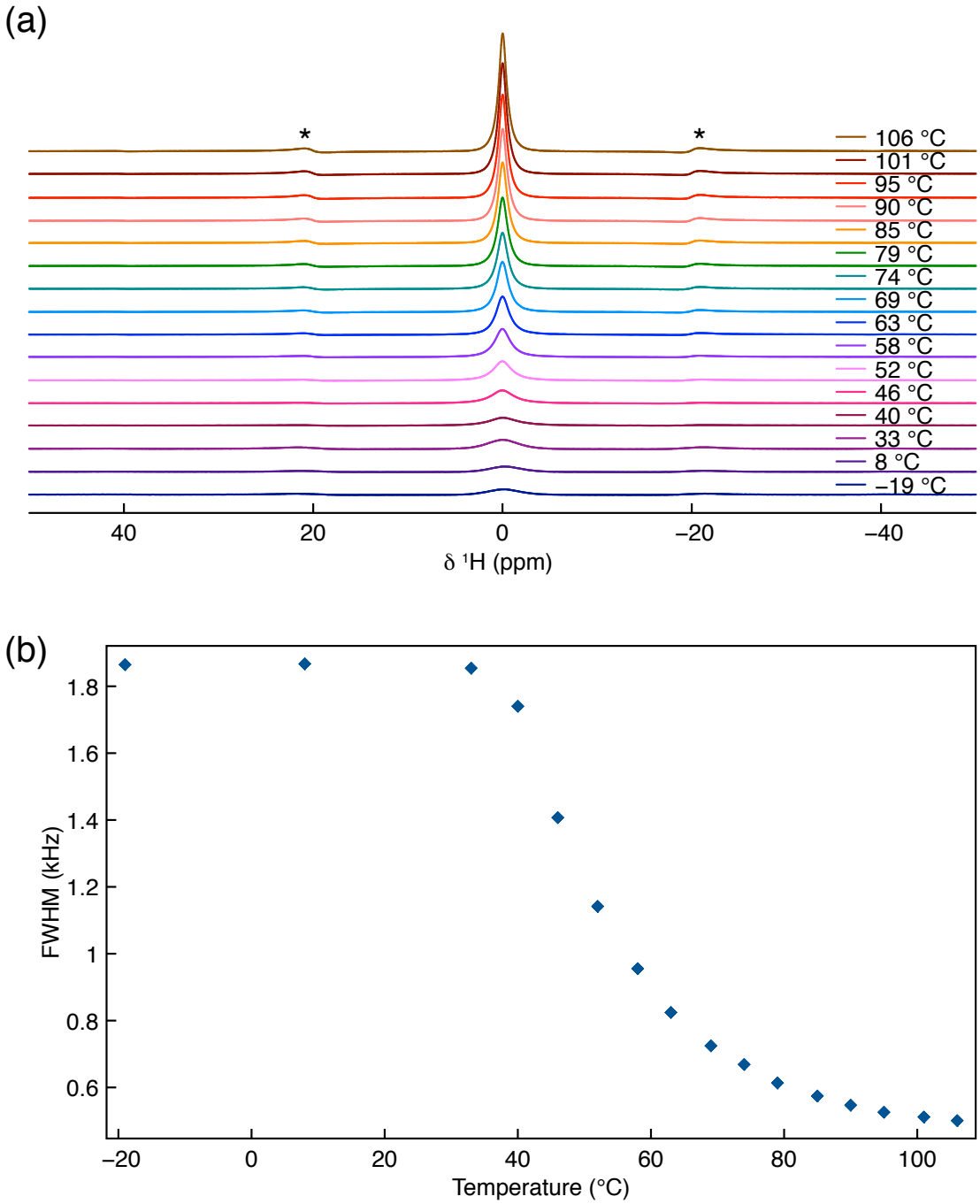

Figure 6.1: (a) VT ^{1}H (11.7 T) MAS NMR spectra acquired between −19 and 106 °C for a sample of Li_2OHCl synthesised via a conventional solid-state route. The MAS rate was 10 kHz and spinning sidebands are denoted by *. A recycle delay of 500 and 60 s was used between −19 – 33 °C and 40 – 106 °C, respectively. In all cases, 4 transients were acquired. (b) The corresponding variation in the FWHM as a function of temperature.

adopt the room-temperature orthorhombic structure, the ^{7}Li resonance is fairly broad. Between 33 and 40 °C, a sudden narrowing of the resonance is observed

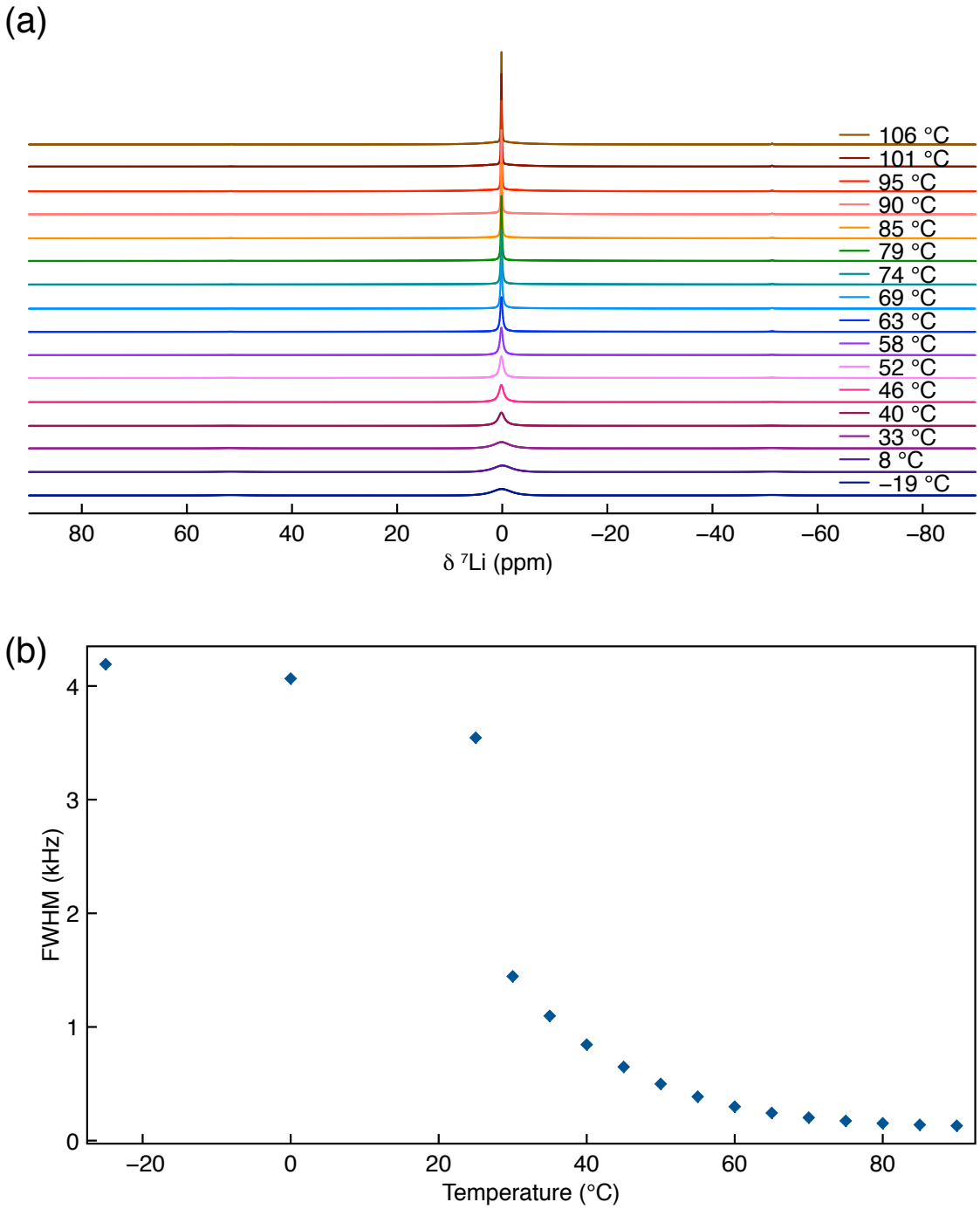

Figure 6.2: (a) VT ^{7}Li (11.7 T) MAS NMR spectra acquired between −19 and 106 °C for a sample of Li_2OHCl synthesised via a conventional solid-state route. The MAS rate was 10 kHz. In all cases, a recycle delay of 60 s was used to acquire 4 transients. (b) The corresponding variation in the FWHM as a function of temperature.

and a further increase in temperature results in continuous line narrowing. The corresponding FWHM between −19 and 106 °C is shown in Figure 6.2(b). The line narrowing in the VT ^{7}Li MAS NMR data is similar to that observed for the

VT ^{1}H MAS NMR data. Between −19 and 33 °C, there is a small variation in the linewidth and between 33 and 40 °C, a considerable reduction in linewidth is observed owing to the known phase transition to cubic symmetry. As the temperature is increased incrementally to 106 °C, further line narrowing is observed. This gradual reduction in linewidth is believed to be due to mobile Li species within the structure. It is noted that the degree of line narrowing observed for ^{7}Li is greater than that observed for ^{1}H, suggesting Li exhibits greater mobility in Li_2OHCl when compared to ^{1}H (*vide infra*).

Li_2OHCl was also analysed via VT static ^{7}Li NMR and the spectra acquired over the temperature range −65 – 230 °C are shown in Figure 6.3. Between −65 and 24 °C, the static ^{7}Li NMR spectra exhibit a dipolar broadened lineshape at ~0 ppm, corresponding to the central transition ($1/2 \longleftrightarrow -1/2$). A broad resonance corresponding to the satellite transitions is also observed ($3/2 \longleftrightarrow 1/2$ and $-1/2 \longleftrightarrow -3/2$). All spectra obtained at 54 °C and above exhibit a single sharp resonance, corresponding to the cubic phase of Li_2OHCl. The lineshapes observed at 24 and 54 °C, corresponding to the room-

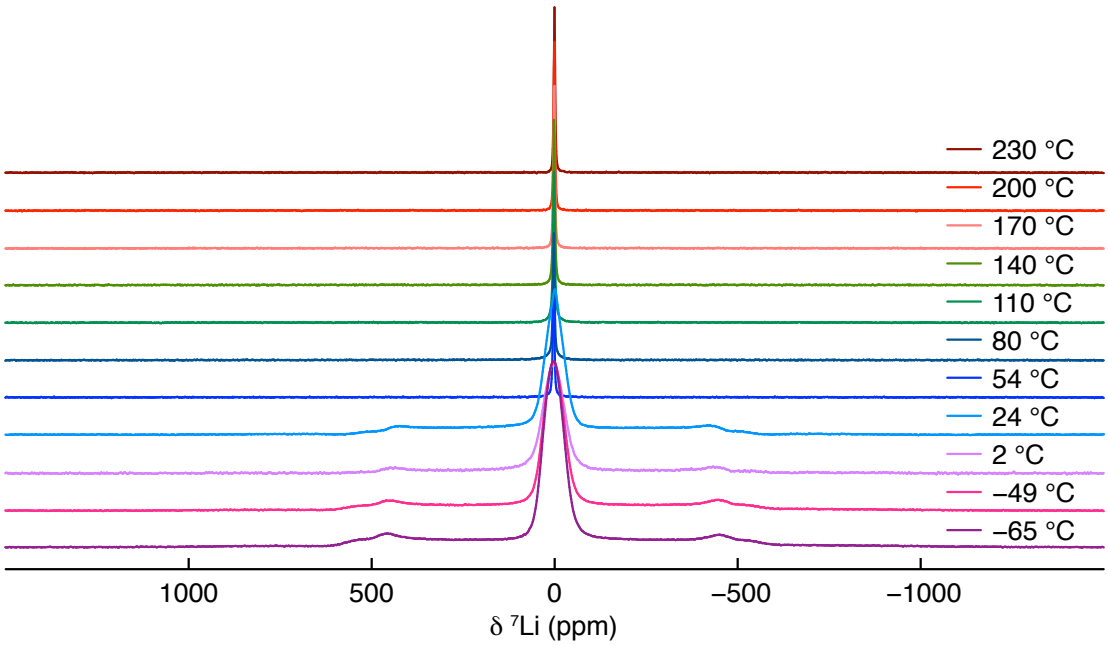

Figure 6.3: Static VT ^{7}Li (9.4 T) NMR spectra obtained between −65 and 230 °C for a sample of Li_2OHCl synthesised via a conventional solid-state route. A recycle delay of 300, 65 and 1 s was used at −65 – 2 °C, 24 °C and 54 – 230 °C, respectively, to acquire 8 transients.

temperature and high-temperature phase of Li_2OHCl, respectively, have been discussed in detail in Chapter 4. Hence, here the discussion will focus predominantly on ion mobility. In a similar manner to the ^{7}Li MAS NMR data (Figure 6.2), the static ^{7}Li NMR data exhibits line narrowing, as demonstrated in the corresponding FWHM plot vs. temperature, shown in Figure 6.4(a). Below room temperature, little variation in the FWHM is observed, whereas, a dramatic decrease is observed between 24 and 54 °C. This reduction in FWHM is attributed to the phase transition, as the transition to cubic symmetry averages out the ^{7}Li homonuclear dipolar couplings and thus a narrower resonance is observed. A further increase in temperature results in a very gradual reduction in linewidth, as observed for the spectra acquired between 54 and 230 °C. This is indicative of Li-ion mobility, as ion mobility would result in motional narrowing of the NMR linewidths. This gradual change is challenging to observe in Figure 6.4(a). Hence, for clarity, an expansion of the data obtained between 54 and 230 °C is shown in Figure 6.4(b).

To gain further insight into proton and Li-ion mobility within Li_2OHCl, ^{1}H and ^{7}Li T_1 values were measured. As stated in Chapter 2, T_1 values are dependent on the environment of the nucleus under investigation and, therefore, will change with any structural changes, *i.e.*, phase transitions, mobility etc. ^{1}H and ^{7}Li T_1 values were measured over the temperature range −19 – 116 °C and are shown in Figure 6.5(a,b). In both cases, the T_1 values at low temperatures, *e.g.*, −19 and 8 °C, are quite similar, followed by a rapid change between 8 and ~60 °C. This change is believed to correspond to the expected phase change from what is believed to be orthorhombic to cubic symmetry. A more gradual change in ^{1}H T_1 is observed between 70 and 100 °C, where the value is on the order of seconds. This is in contrast to the ^{7}Li T_1 measurements, where there is a gradual but significant change. Comparison of the ^{1}H and ^{7}Li T_1 values obtained at 116 °C exhibits an order of magnitude difference between the two. Such a difference in the value of T_1 suggests that Li is the more mobile species in Li_2OHCl, and protons only exhibit limited mobility. To further probe the Li-ion mobility, additional static ^{7}Li NMR experiments were completed at a lower field strength between 54 and 230 °C. The ^{7}Li T_1 values obtained are

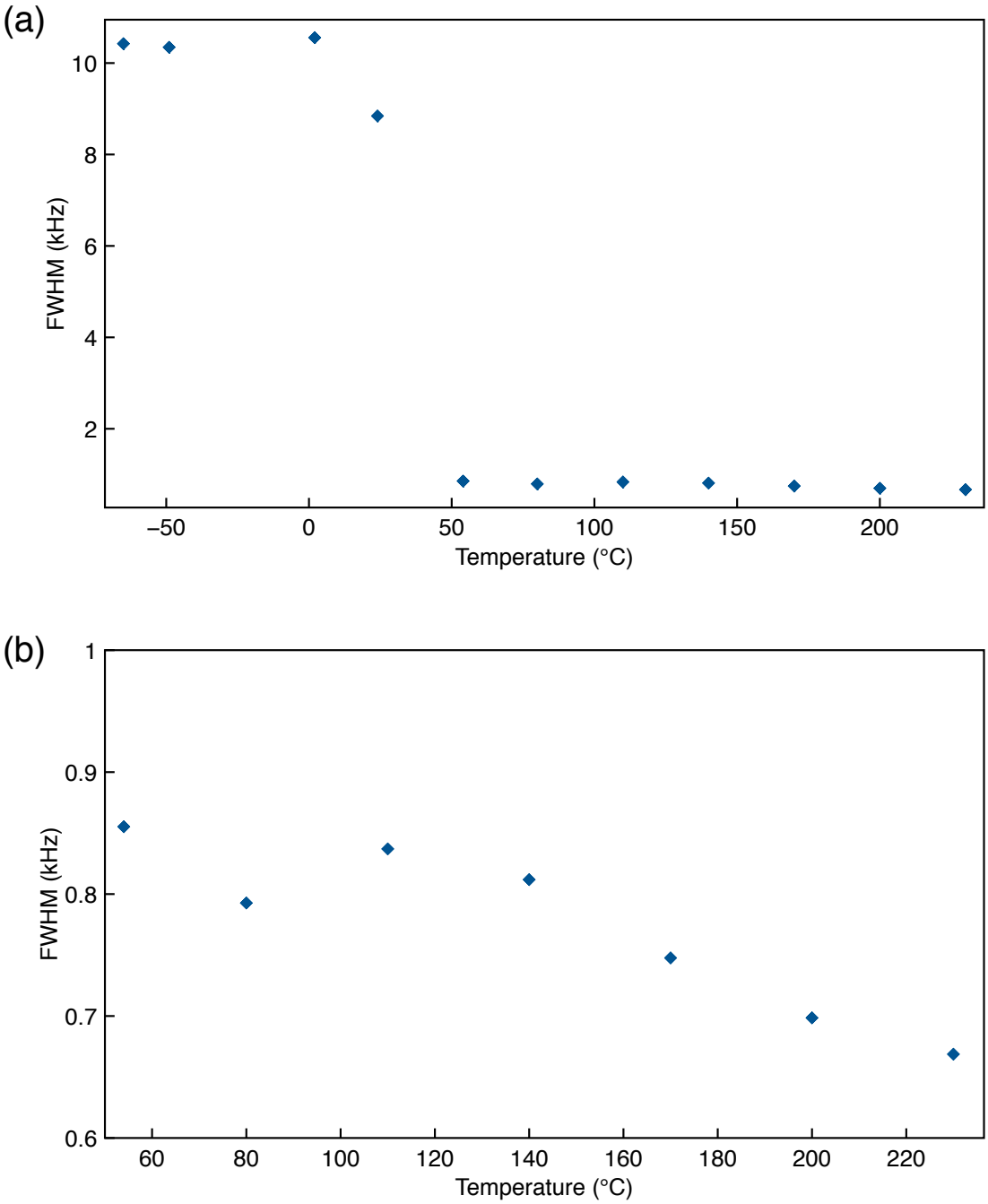

Figure 6.4: (a) Variation in the ^{7}Li FWHM as a function of temperature obtained from the VT static ^{7}Li (9.4 T) NMR spectra acquired between −65 and 230 °C for a sample of Li_2OHCl synthesised via a conventional solid-state route. (b) An expansion of the region between 54 and 230 °C.

shown in Figure 6.5(c). Interestingly, the T_1 values exhibit a continuous decrease with increasing temperature, and at 230 °C, a T_1 of ~0.007 s is obtained. This suggests an increased degree of Li-ion mobility with increasing temper-

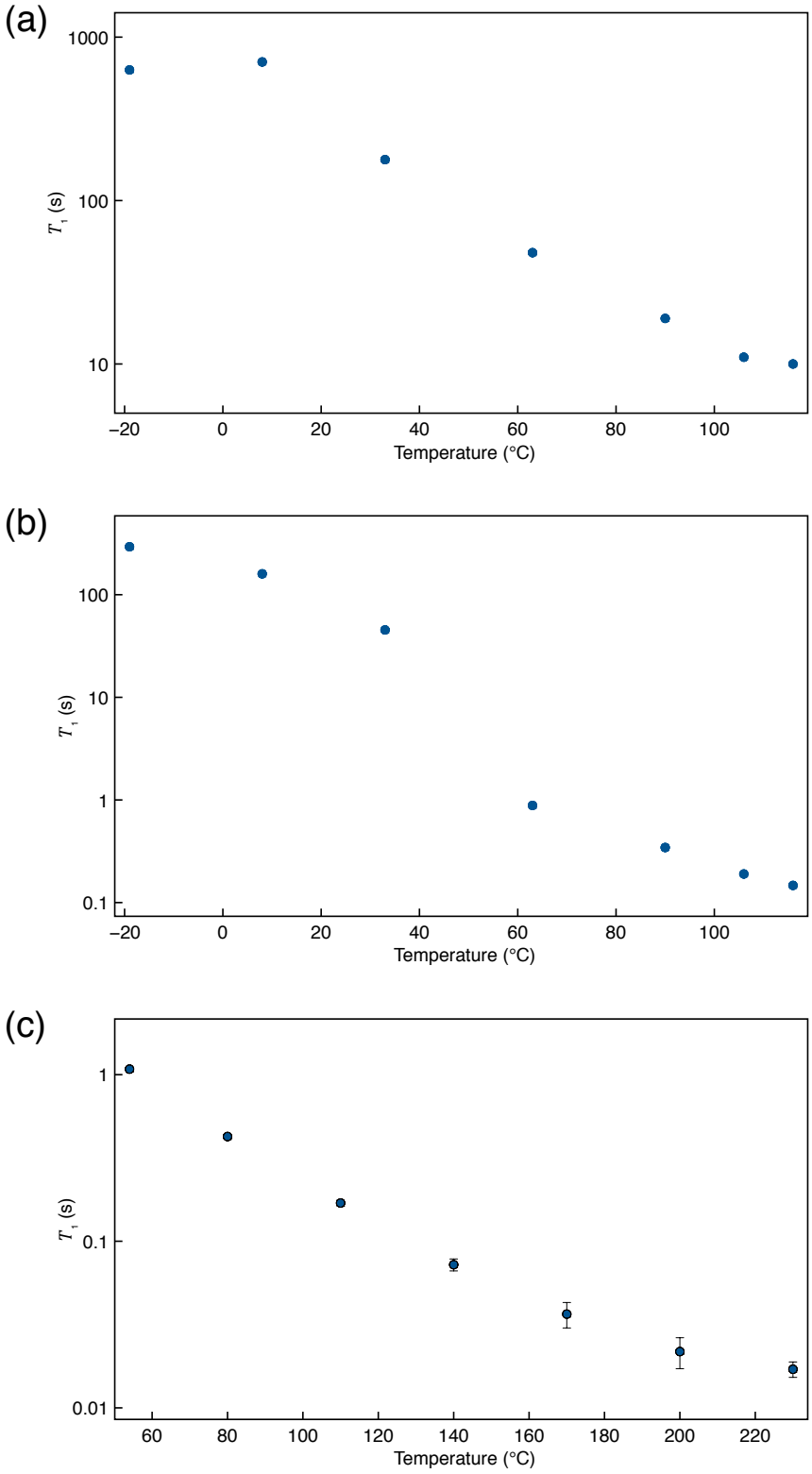

Figure 6.5: (a) ^{1}H and (b) ^{7}Li (11.7 T) T_1 values obtained between −19 – 106 °C and (c) ^{7}Li (9.4 T) T_1 values obtained between 54 – 230 °C, for a sample of Li_2OHCl synthesised via a conventional solid-state route. In most cases, the estimated error bars are smaller than the symbols used and are therefore not shown.

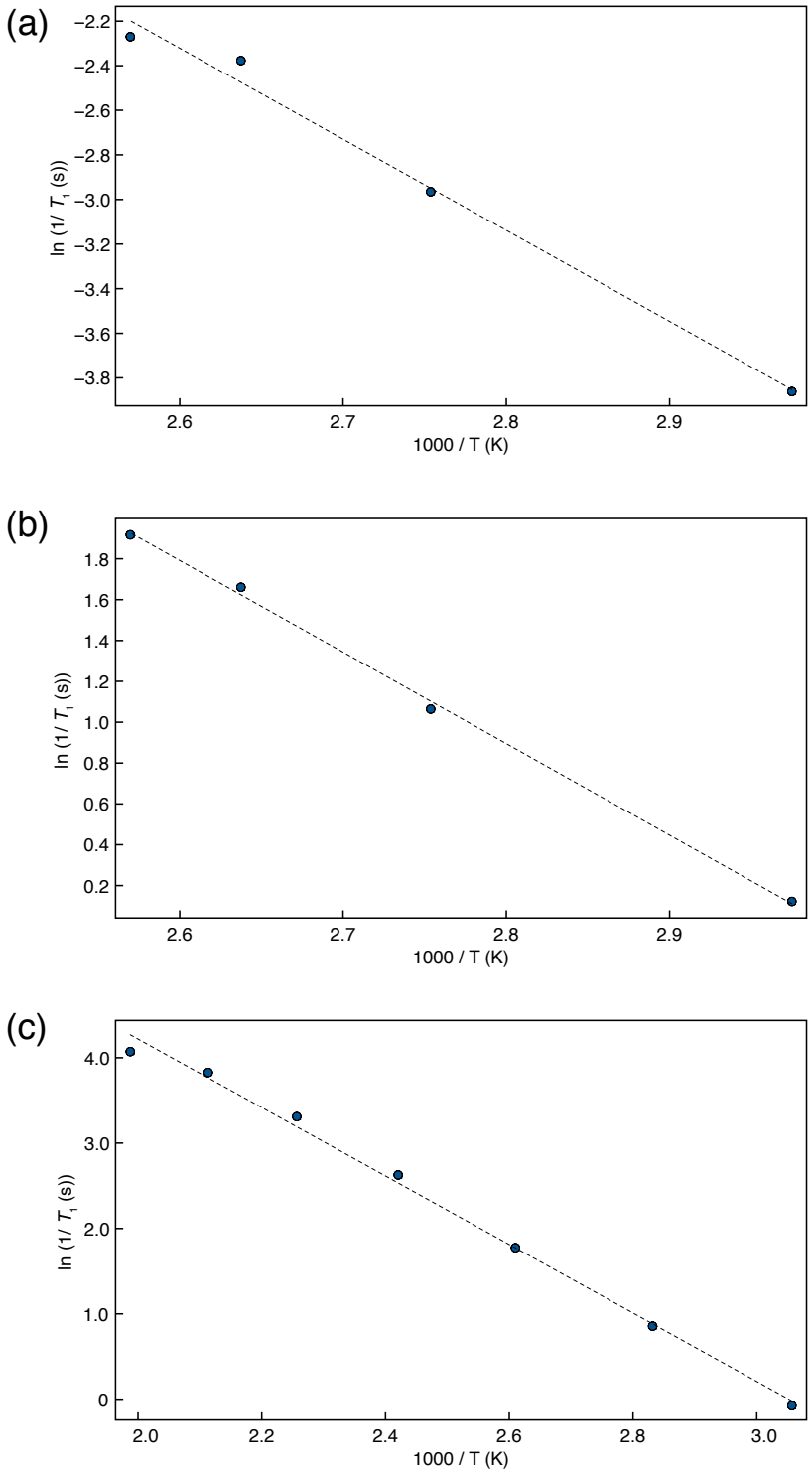

Figure 6.6: An Arrhenius plot of the (a) ^{1}H, (b) ^{7}Li (11.7 T) and (c) ^{7}Li (9.4 T) T_1 data obtained for a sample of Li_2OHCl synthesised via a conventional solid-state route, over a temperature range of (a,b) 63 – 116 °C and (c) 54 – 230 °C. In all cases, a linear fit is obtained with gradients (a) −4.08(28), (b) −4.48(13) and (c) −4.01(12), and R^2 = (a) 0.9906, (b) 0.9984 and (c) 0.9952. Activation energies of (a) 0.35(2) eV, (b) 0.39(1) eV and (c) 0.35(1) eV were calculated.

ature. Based on the data presented, it is likely that the protons are only locally mobile, *i.e.*, rotating or flipping around a localised point, whereas the Li can move freely throughout the structure.

The T_1 data shown here can be used to determine E_a for both ^{1}H and ^{7}Li motion using an Arrhenius plot. A plot of $\ln(1/T_1)$ vs. inverse temperature will have a gradient that is proportional to E_a, as follows,

$$\ln\left(\frac{1}{T_1}\right) = \ln(A) - \frac{E_a}{RT}\,, \tag{6.3}$$

where A is a constant, R is the gas constant (8.314 kJ mol^{-1}) and T is the temperature in unit Kelvin. The corresponding plots for the ^{1}H and ^{7}Li NMR data corresponding to the cubic phase, are shown in Figure 6.6. In all cases, a linear fit is achieved with R^2 = 0.9906 and 0.9984 for ^{1}H and ^{7}Li T_1 experiments completed between 63 and 116 °C. An R^2 = 0.9952 is obtained for ^{7}Li T_1 experiments completed between 54 and 230 °C. R^2 is a parameter used to determine the goodness of fit. It has values ranging from 0 to 1, with R^2 = 1 indicating a perfect fit. Thus, the R^2 values obtained here indicate an excellent fit. E_a values of 0.35(2) eV and 0.39(1) eV are calculated for ^{1}H and ^{7}Li motion, respectively, between 63 and 116 °C. Thus, indicating a lower energy barrier for proton mobility when compared to ^{7}Li mobility. For the ^{7}Li T_1 experiments completed at a lower field strength between 54 and 230 °C, an E_a 0.35(1) eV is obtained. A drop in the E_a at higher temperature suggests that it becomes easier for the Li-ions to exhibit movement with increasing temperature. The value of E_a determined for ^{7}Li in the current study via static ^{7}Li NMR is in agreement with that initially reported by Schwering *et al.* (0.36 eV), who also used static NMR conditions.[213] Overall, the T_1 data analysis presented here suggests that both the protons and Li ions exhibit mobility. However, the nature of the motion taking place cannot be confirmed solely from the current data.

6.3.2 ^{2}H NMR Studies of Li_2OHCl

To further investigate the local environment and mobility of the OH^- groups in Li_2OHCl, a sample was deuterated using LiOD and studied via ^{2}H SSNMR spectroscopy. The room temperature XRD pattern obtained for

the deuterated sample of Li_2OHCl (Li_2ODCl) is shown in Figure 6.7. Diffraction patterns corresponding to the parent material, Li_2OHCl and the reagent, LiCl, are also shown for comparison. The diffraction pattern for the deuterated sample closely resembles that of Li_2OHCl, indicating that the desired phase has been successfully synthesised. It is noted that the reflections corresponding to the starting material LiCl have higher intensity in the XRD pattern for Li_2ODCl than Li_2OHCl, suggesting that the deuterated sample contains a slightly higher quantity of residual LiCl.

VT ^2H MAS NMR data was acquired for Li_2ODCl over the temperature range −19 – 110 °C, and is shown in Figure 6.8. Between −19 and 63 °C, a classic, axially symmetric lineshape, with a large manifold of spinning sidebands is observed. It is well documented within the literature that this type of lineshape indicates an absence of motion, and, thus corresponds to static OH^-/OD^- groups.[158] The MAS lineshape obtained at 33 °C was simulated and fitted (Figure 6.9) to obtain the quadrupolar NMR parameters, C_Q = 259(1) kHz and η_Q = 0.0(1), which are also in good agreement with those reported for

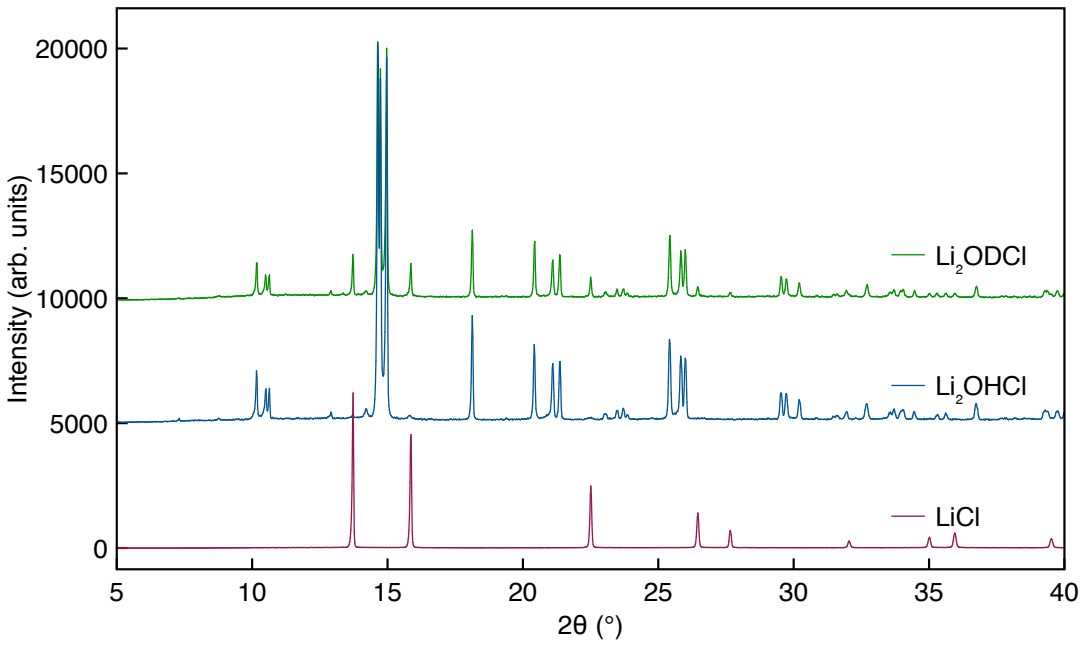

Figure 6.7: XRD patterns obtained for samples of Li_2OHCl and Li_2ODCl synthesised inside an Ar-filled glovebox via a conventional solid-state route. The reaction temperature was 350 °C and the reaction time was 30 mins. Also shown is a diffraction pattern for the starting material, LiCl.

static ^{2}H environments.[215] The known phase transition from, what is believed to be, orthorhombic to cubic symmetry occurs at ~35 – 40 °C. Interestingly, the ^{2}H NMR data presented indicates that even at 63 °C, when Li_2ODCl is known to be in the cubic phase, the OH^-/OD^- groups are still static. Thus, indicating that even though the phase transition has occurred, the OH^-/OD^- groups are not yet mobile. Hence, the phase transition alone is not responsible for the mobility of the OH^-/OD^- groups. This is in direct contrast to previous reports in the literature that stated the phase transition alone is responsible for the enhanced ion conduction capabilities of Li_2OHCl.[213]

At 69 °C, there is a very noticeable change in the appearance of the ^{2}H MAS NMR spectrum (Figure 6.8). The spectrum contains a broad central resonance, in addition to the axially symmetric lineshape observed at low temperatures. The broad resonance is believed to correspond to the mobile OH^-/OD^- groups. Therefore, the spectrum acquired at 69 °C indicates the presence of two different OH^-/OD^- environments simultaneously, *i.e.*, both static and mobile OH^-/OD^- groups. As the temperature is increased to 95 °C, the axially symmetric lineshape corresponding to the static OH^-/OD^- groups decreases in intensity, whilst the broad resonance narrows and increases in intensity. This indicates that, at 95 °C, the majority of OH^-/OD^- groups are mobile. Finally, at 110 °C, a single resonance is observed, with the axially symmetric lineshape also present, albeit at very low intensities. Hence, at 110 °C almost all of the OH^-/OD^- groups are now mobile.

It is well documented that for fast-moving deuterons, a single, sharp "solution-like" lineshape (*e.g.*, ca. 20 Hz), with very high intensity, will be observed in the ^{2}H MAS NMR spectrum, owing to complete averaging of the quadrupolar tensor.[230] Such a sharp, narrow resonance is characteristic of a deuteron dissociating and moving freely throughout the structure.[230,231] Here, however, the linewidth of the resonance is still relatively large (ca. 2.7 kHz), suggesting movement of the OD^- group rather than that of a free deuteron, *i.e.*, likely rotation of the H/D around the oxygen (*vide infra*). This is unsurprising as the OH bond is quite difficult to break. It is also noted that at high temperatures (95 and 110 °C) the manifold of spinning sidebands remains (albeit

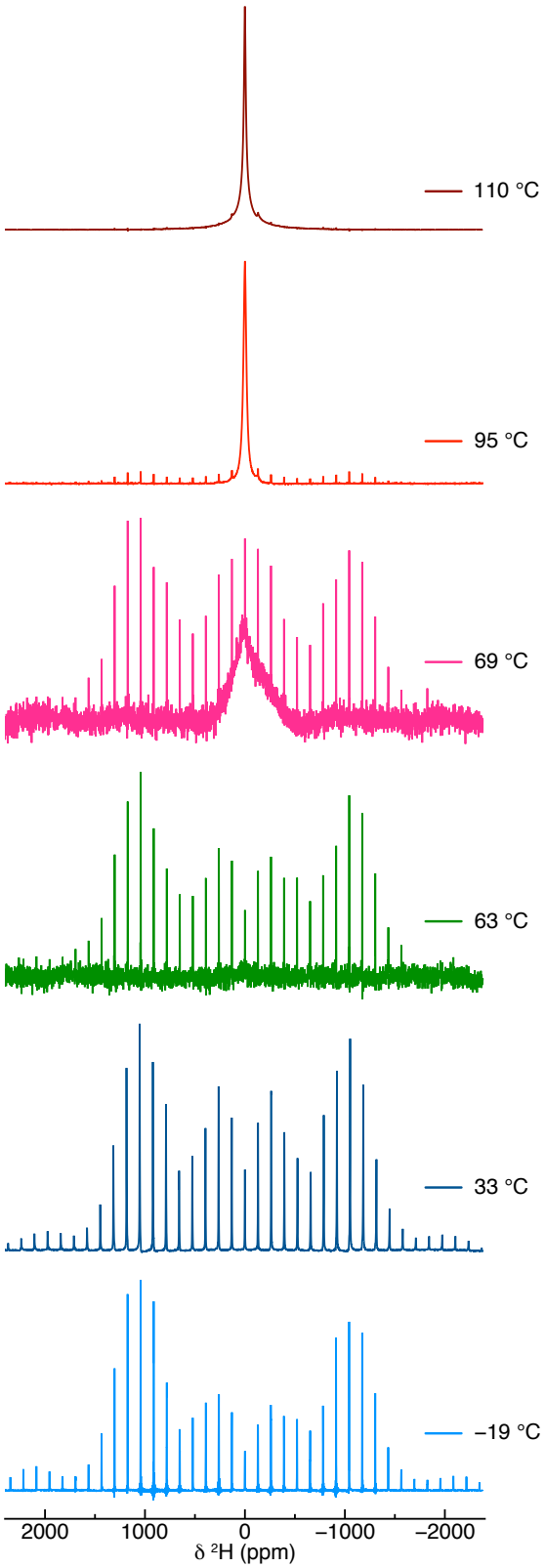

Figure 6.8: VT ^{2}H (11.7 T) MAS NMR spectra acquired at −19, 33, 63, 69, 95 and 110 °C for a sample of Li_2ODCl synthesised via a conventional solid-state route. The MAS rate was 10 kHz. In all cases, a recycle delay of 5 s was used to acquire 3200 transients.

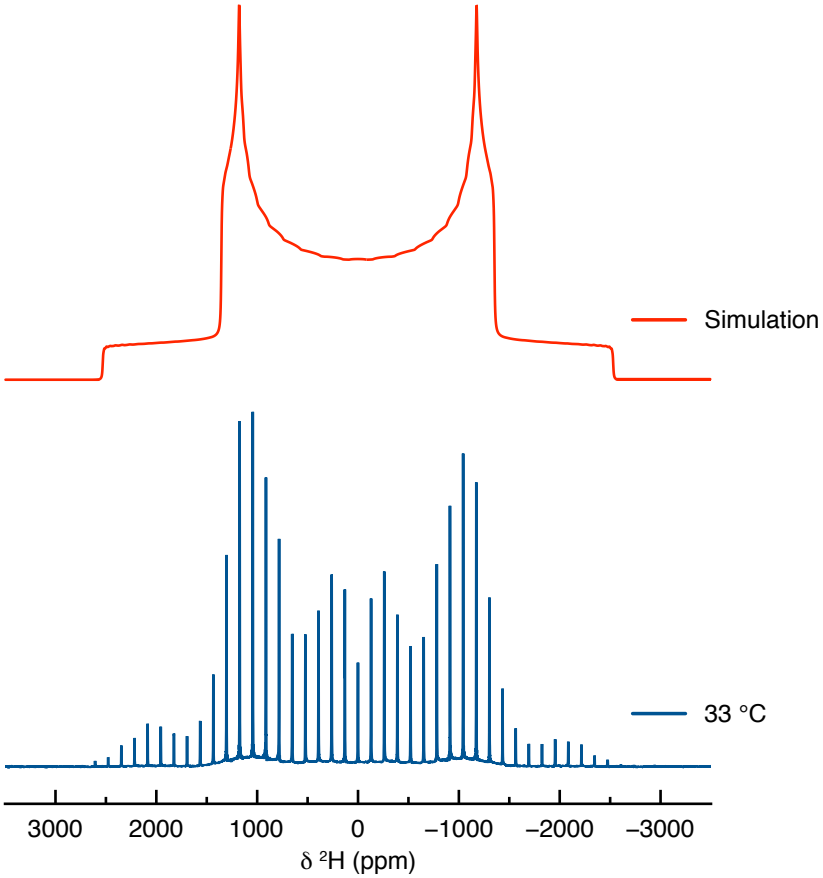

Figure 6.9: Simulation of the ^{2}H (11.7 T) MAS NMR spectrum of Li_2ODCl acquired at 33 °C for a sample synthesised via conventional solid-state routes. The MAS rate was 10 kHz. A recycle delay of 5 s was used to acquire 3200 transients. The spectrum was simulated to obtain the corresponding quadrupolar parameters, C_Q = 259(1) kHz and η_Q = 0.0(1).

at very low intensities), indicating the continued presence of static OH^-/OD^- groups. Hence, it appears that two different OH^-/OD^- environments are consistently present in the cubic phase of Li_2ODCl, both static and locally rotating OH^-/OD^- groups (*vide infra*).

Li_2ODCl was also analysed via static ^{2}H NMR and the spectra acquired at −19, 69 and 110 °C are shown in Figure 6.10. In a similar manner to the ^{2}H MAS NMR spectrum, an axially symmetric lineshape is observed at −19 °C. The lineshape observed resembles that of the simulated spectrum shown in Figure 6.9. Again, this lineshape corresponds to static OH^-/OD^- groups, thus further confirming the absence of motion. An increase in temperature to 69 °C results in a single relatively broad resonance which corresponds to mo-

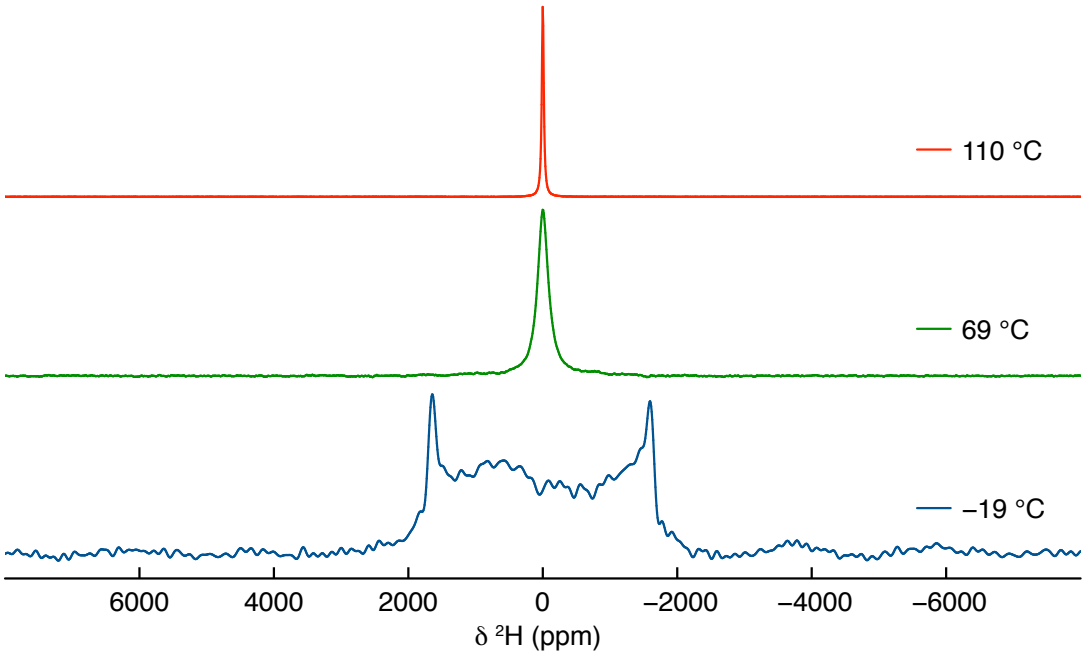

Figure 6.10: VT static ^{2}H (11.7 T) NMR spectra acquired at −19, 69 and 110 °C for a sample of Li_2ODCl synthesised via a conventional solid-state route. In all cases, a recycle delay of 5 s was used to acquire 3200 transients.

bile OH^-/OD^- groups. Here, unlike the ^{2}H MAS NMR spectra, the resonance corresponding to the static OH^-/OD^- groups, is not visible. Finally, at 110 °C a narrow resonance is observed, confirming that the majority of OH^-/OD^- groups are mobile.

Considering these findings alongside the ^{1}H and ^{7}Li NMR data presented earlier, it is believed that the mobility of the Li ions in Li_2ODCl is intimately connected to the position of the OH^-/OD^- groups within the structure. As stated earlier, Schwering *et al.*,[213] claimed that the cubic symmetry is a prerequisite for mobility and the phase transition in Li_2OHCl is, in fact, a consequence of the onset of Li-ion mobility. This is in direct contrast with the findings presented here, where the phase transition from orthorhombic to cubic symmetry does not result in mobile OH^-/OD^- groups. Hence, the phase transition *alone* is not responsible for ion mobility. As demonstrated by our VT studies, additional thermal energy is required to facilitate both proton and Li-ion mobility. Hence, both an increase in temperature *and* the phase transition to cubic symmetry are needed for enhanced ion mobility.

6.3.3 PFG-NMR Spectroscopy of Li_2OHCl

To probe the Li-ion mobility further and confirm our initial findings from the ^{1}H and ^{7}Li T_1 studies, PFG-NMR experiments were completed. To determine the diffusion coefficient of Li, D_{Li}, in Li_2OHCl, the ^{7}Li echo signal intensity was obtained as a function of the magnetic field gradient, g, as shown in Figure 6.11(a). The signal shows a decrease in intensity, I, with increasing gradient strength, and the decay in intensity appears to be faster at longer diffusion times. Thus, indicating Li-ion mobility and diffusion. Plotting the normalised natural logarithm of the intensity I against b (a summary of constants and parameters is detailed in Equation 2.35), the diffusion coefficient, D_{Li}, can be obtained from a linear fit of Equation 2.35. The fits obtained for the data are shown in Figure 6.11(b), and the extracted diffusion coefficients are summarised in Table 6.1. ^{7}Li PFG-NMR measurements appear to confirm initial suggestions that there is long-range Li diffusion at 100 °C. This is in good agreement with the ^{7}Li MAS NMR and T_1 data presented earlier. In restricted systems (*e.g.*, pores or finite-sized particles) diffusion coefficients often exhibit a decrease at longer diffusion times. This appears to be the case for Li_2OHCl at 100 °C, as shown in Figure 6.12. In order to precisely determine the factors affecting Li diffusion within Li_2OHCl, additional analysis is needed. In particular, a comprehensive structural understanding of Li_2OHCl is needed, which is currently ongoing.

Similar ^{1}H diffusion measurements were also completed for Li_2OHCl using PFG-NMR methods. In the ^{1}H PFG-NMR measurements, no signal attenuation as a function of the gradient strength was observed, as demonstrated in Figure 6.13. Typically, as is the case for the ^{7}Li PFG-NMR measurements already discussed, the signal intensity is plotted as a function of the gradient strength. However, in this particular case, this is not feasible, as there is significant dephasing between the first and last spectrum of the two-dimensional dataset acquired. Hence, the first and last raw datasets of the two-dimensional spectra were extracted to determine any changes occurring in the signal intensity. When this is done, the magnitude of the signal remains the same both with

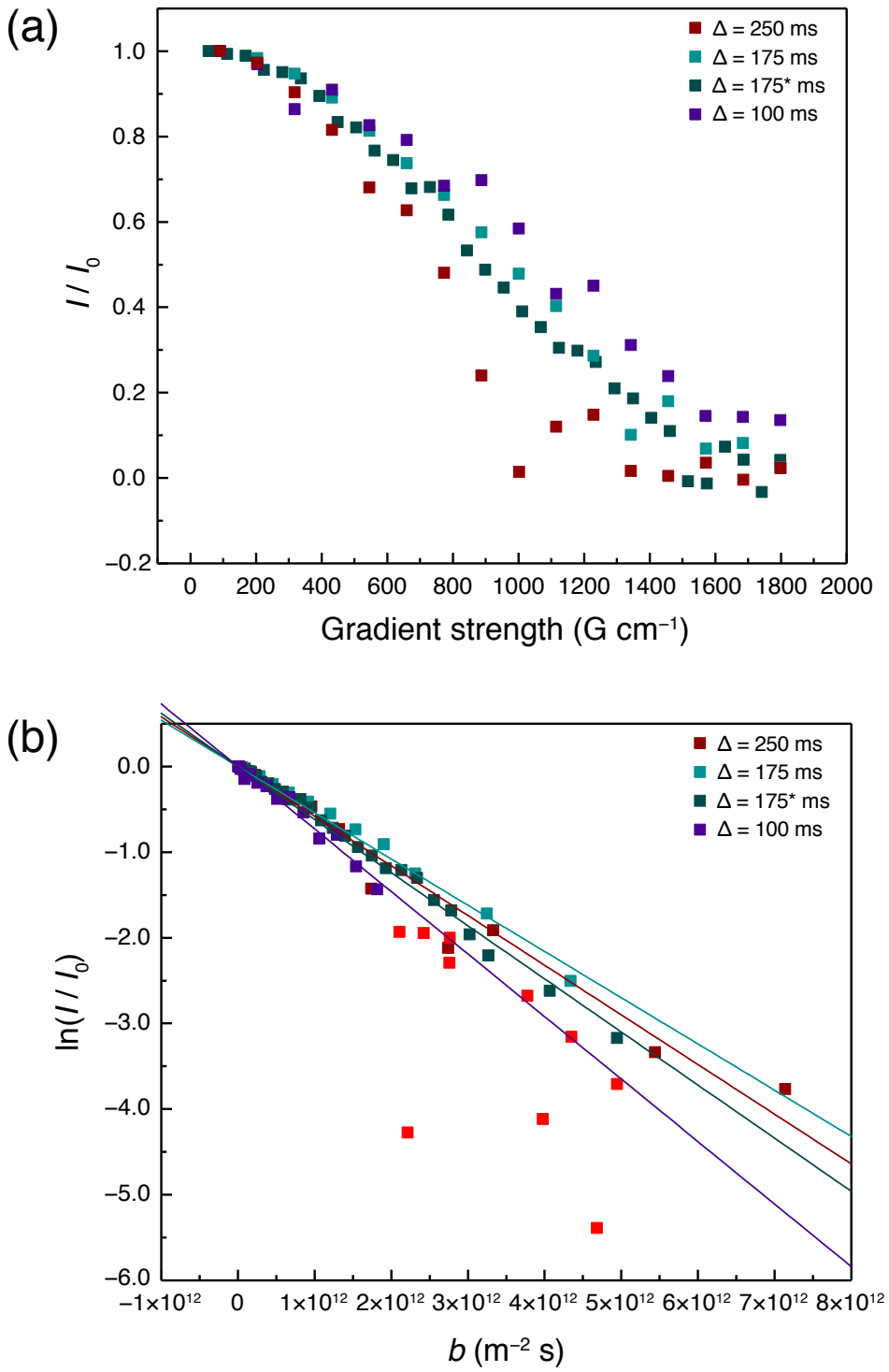

Figure 6.11: (a) The decaying ^{7}Li signal intensity, I/I_0, plotted against the applied gradient strength at 100 °C for a range of diffusion times, Δ, for a sample of Li_2OHCl synthesised via a conventional solid-state route. (b) Natural logarithm of the intensity I/I_0 plotted against *b* at 100 °C for a sample of Li_2OHCl synthesised via a conventional solid-state route. The data points in red were considered as outliers and have not been included in the fits.

Table 6.1: Summary of the Li diffusion coefficients, D_{Li}, obtained at 100 °C for a sample of Li_2OHCl synthesised via a conventional solid-state route, extracted from the ^7Li PFG-NMR data obtained at gradient strengths ranging from 0 to 1800 G cm^{-1}. (* used 32 different gradient strengths instead of 16)

Δ (ms)	D_{Li} (m^2 s^{-1})
250	$5.8 \times 10^{-13} \pm 2.4 \times 10^{-14}$
175	$5.4 \times 10^{-13} \pm 1.2 \times 10^{-14}$
175*	$6.2 \times 10^{-13} \pm 7.3 \times 10^{-15}$
100	$7.3 \times 10^{-13} \pm 2.4 \times 10^{-14}$

and without gradient pulses at room temperature. Hence, as no signal attenuation is observed as a function of the gradient strength, there is no evidence for proton diffusion at room temperature. Similar experiments were completed at 100 °C, this time under the application of a much higher gradient, 3000 G cm^{-1}. At present, this is the highest commercially available gradient. Under these conditions, again, no signal attenuation is observed. Hence, there is also no diffusion at 100 °C. These findings are in good agreement with the ^1H and ^2H MAS NMR data presented earlier. Hence, all of the data presented thus

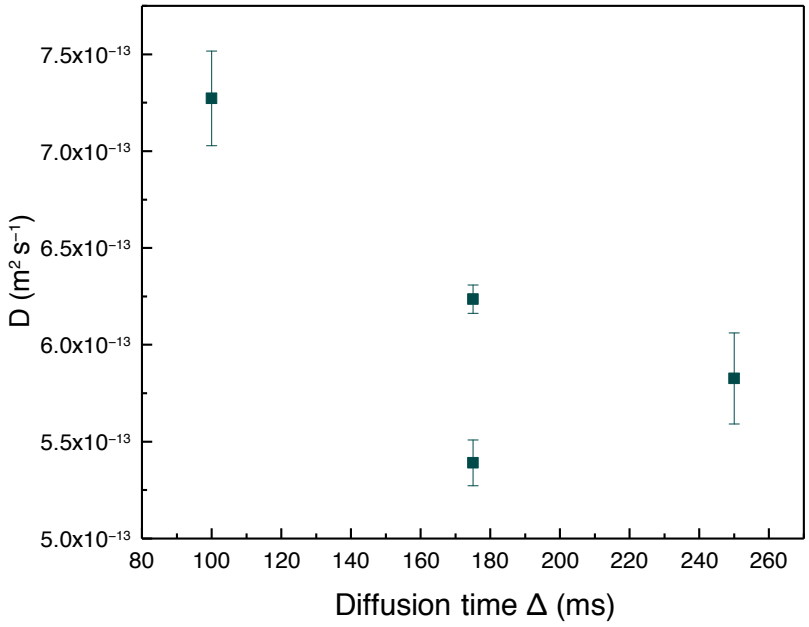

Figure 6.12: Trend in Li diffusion coefficients at 100 °C as a function of diffusion time for a sample of Li_2OHCl synthesised via a conventional solid-state route.

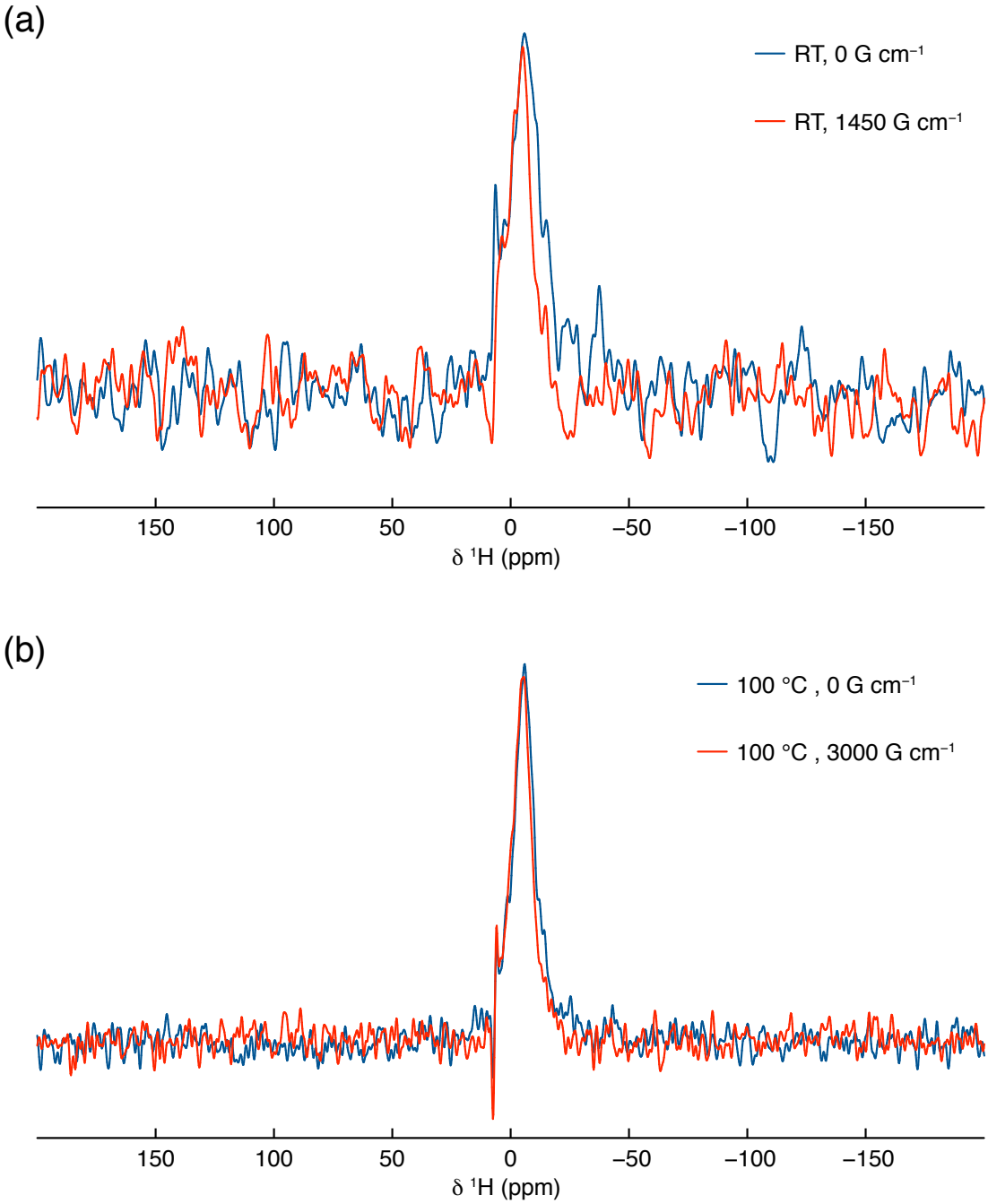

Figure 6.13: ^{1}H PFG-NMR spectra acquired at (a) room temperature (RT) and (b) 100 °C for a sample of Li_2OHCl synthesised via a conventional solid-state route. In both cases, spectra were extracted from two-dimensional datasets and represent the first (0 G cm^{-1}) and last (1450 or 3000 G cm^{-1}) spectrum obtained in the dataset. In both cases, no change in intensity is observed, indicating an absence of ^{1}H diffusion.

far appears to confirm restricted proton mobility within Li_2OHCl, *i.e.*, local rotations of the OH^-/OD^- groups.

6.3.4 $Li_{3-x}OH_xCl$ (x = 0.25, 0.5 and 0.75)

Samples in the $Li_{3-x}OH_xCl$ (x = 0.25, 0.5 and 0.75) series were also analysed via VT ^1H and ^7Li MAS NMR spectroscopy to determine whether they exhibited similar proton and Li mobility to that of their parent material, Li_2OHCl. The VT ^1H and ^7Li MAS NMR spectra obtained for $Li_{2.25}OH_{0.75}Cl$, $Li_{2.5}OH_{0.5}Cl$ and $Li_{2.75}OH_{0.25}Cl$ are shown in Figures 6.14, 6.15 and 6.16, respectively. The spectra obtained appear to be very similar to those corresponding to Li_2OHCl. In all cases, the spectra acquired between −19 and 33 °C, contain a single relatively broad resonance with well-pronounced spinning sidebands. As the temperature is increased to 40 °C, a significant narrowing of the resonance and a reduction in the intensity of the spinning sidebands is observed. Further increases in temperature result in a gradual narrowing of the lineshape. The corresponding variation in FWHM, as a function of temperature, for both ^1H and ^7Li for all samples and the parent material Li_2OHCl is shown in Figure 6.17. For ^1H, there is little change in the linewidth between −19 and 33 °C. This is consistent with previous studies for Li_2OHCl and the presence of static OH^- groups. Upon increasing the temperature, the linewidth exhibits a gradual decrease. For ^7Li, the linewidth remains similar between −19 and 8 °C and then starts to decrease with increasing temperature. The changes observed in FWHM for all samples are similar to the parent material, Li_2OHCl. The diffraction data presented in Chapter 4, indicated that samples in the $Li_{3-x}OH_xCl$ (x = 0.25, 0.5 and 0.75) series undergo the same phase transition as the parent material, Li_2OHCl. Thus, suggesting that both a phase change and ion mobility contribute to the line narrowing observed between 33 and 52 °C. After 52 °C, however, the phase transition is complete, meaning that the line narrowing is solely due to ion mobility. The changes observed are similar to those previously observed for Li_2OHCl, suggesting that both the protons and Li ions are mobile at temperatures >52 °C. Furthermore, it appears that small compositional changes have little effect on the FWHM across this temperature range, as a similar reduction in linewidth is consistently observed across the series.

From this series, $Li_{2.5}OH_{0.5}Cl$ was selected for further analysis, with

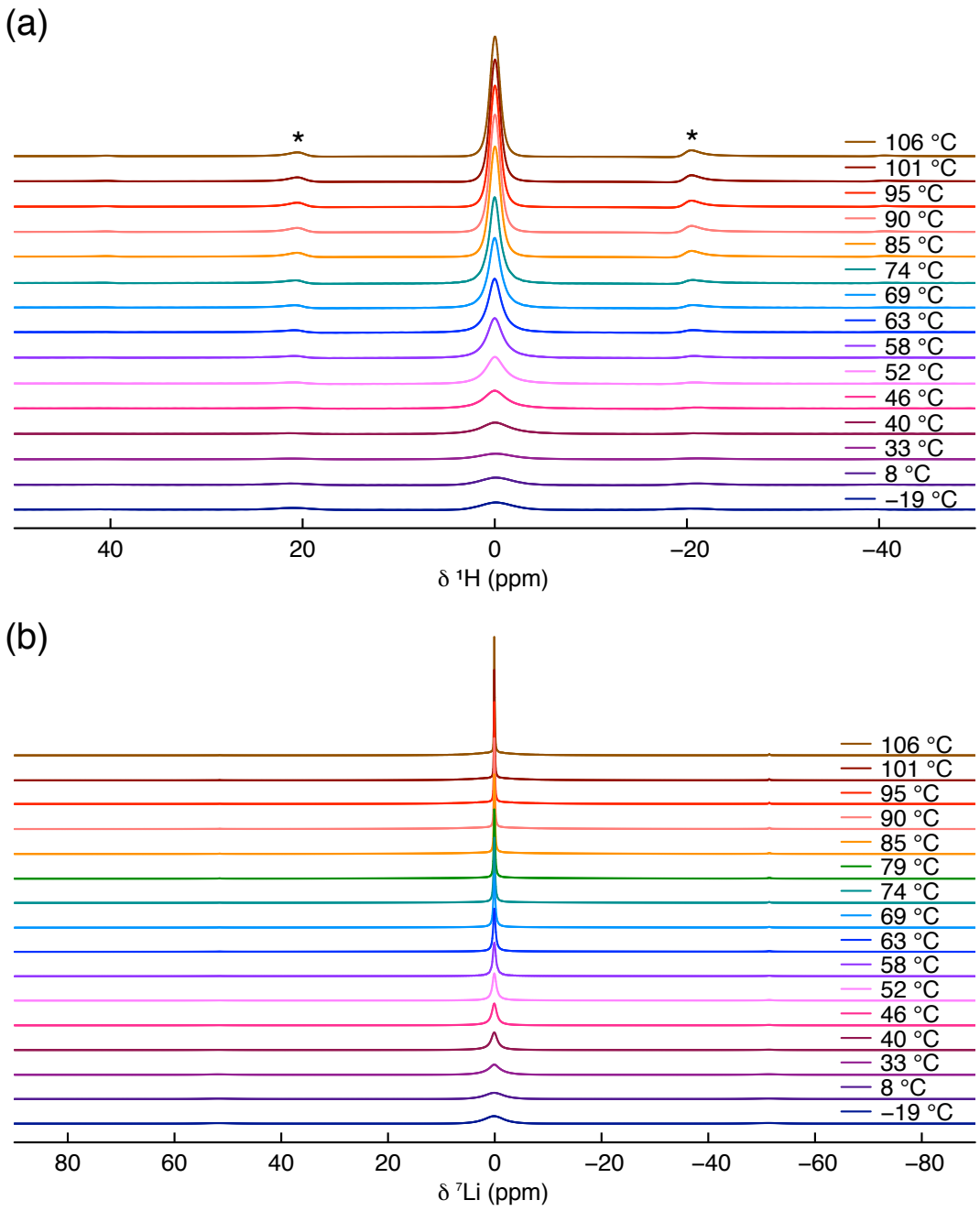

Figure 6.14: VT (a) ^{1}H and (b) ^{7}Li (11.7 T) MAS NMR spectra obtained between −19 and 106 °C for a sample of $Li_{2.25}OH_{0.75}Cl$ synthesised via the Schlenk line method. The MAS rate was 10 kHz and spinning sidebands are denoted by *. A recycle delay of (a,b) 60 s was used to acquire 4 transients, except for the spectra in (a) acquired at −19 and 8 °C, where a recycle delay of 500 s was used.

^{1}H and ^{7}Li T_1 measurements completed between −19 and 116 °C to gain additional information regarding ion mobility. The data obtained is shown in Figure 6.18. Initially, the ^{1}H T_1 values show little variation between −19 and

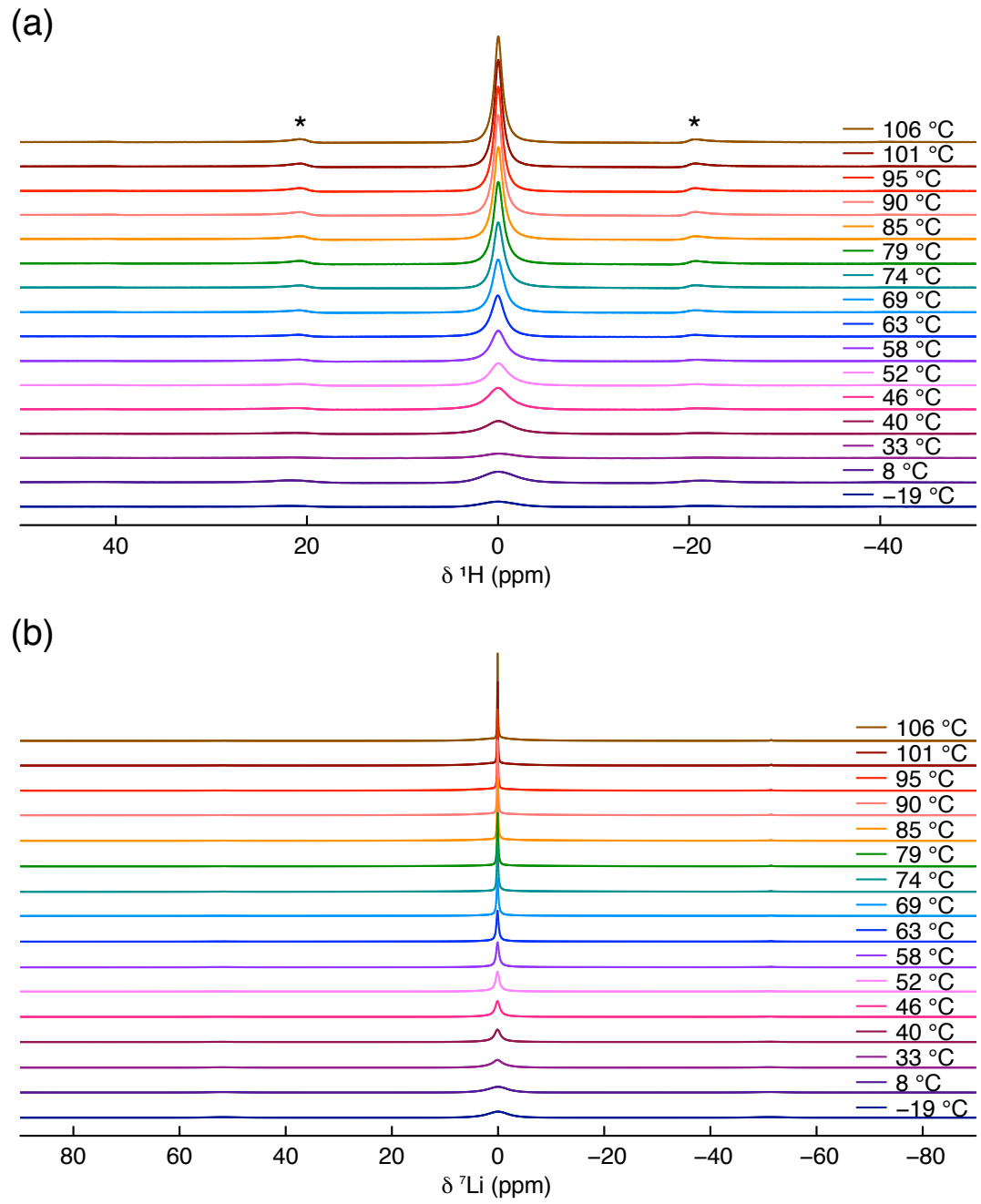

Figure 6.15: VT (a) ^{1}H and (b) ^{7}Li (11.7 T) MAS NMR spectra obtained between −19 and 106 °C for a sample of $Li_{2.5}OH_{0.5}Cl$ synthesised via the Schlenk line method. The MAS rate was 10 kHz and spinning sidebands are denoted by *. A recycle delay of (a,b) 60 s was used to acquire 4 transients, except for the spectra in (a) acquired at −19 and 8 °C, where a recycle delay of 500 s was used.

33 °C. An increase in temperature from 33 to 106 °C results in a decrease in T_1. At 116 °C, the T_1 for ^{1}H is ~10 s. For ^{7}Li, a slight decrease in T_1 is observed from −19 to 33 °C, and a further increase in temperature results in a sharp

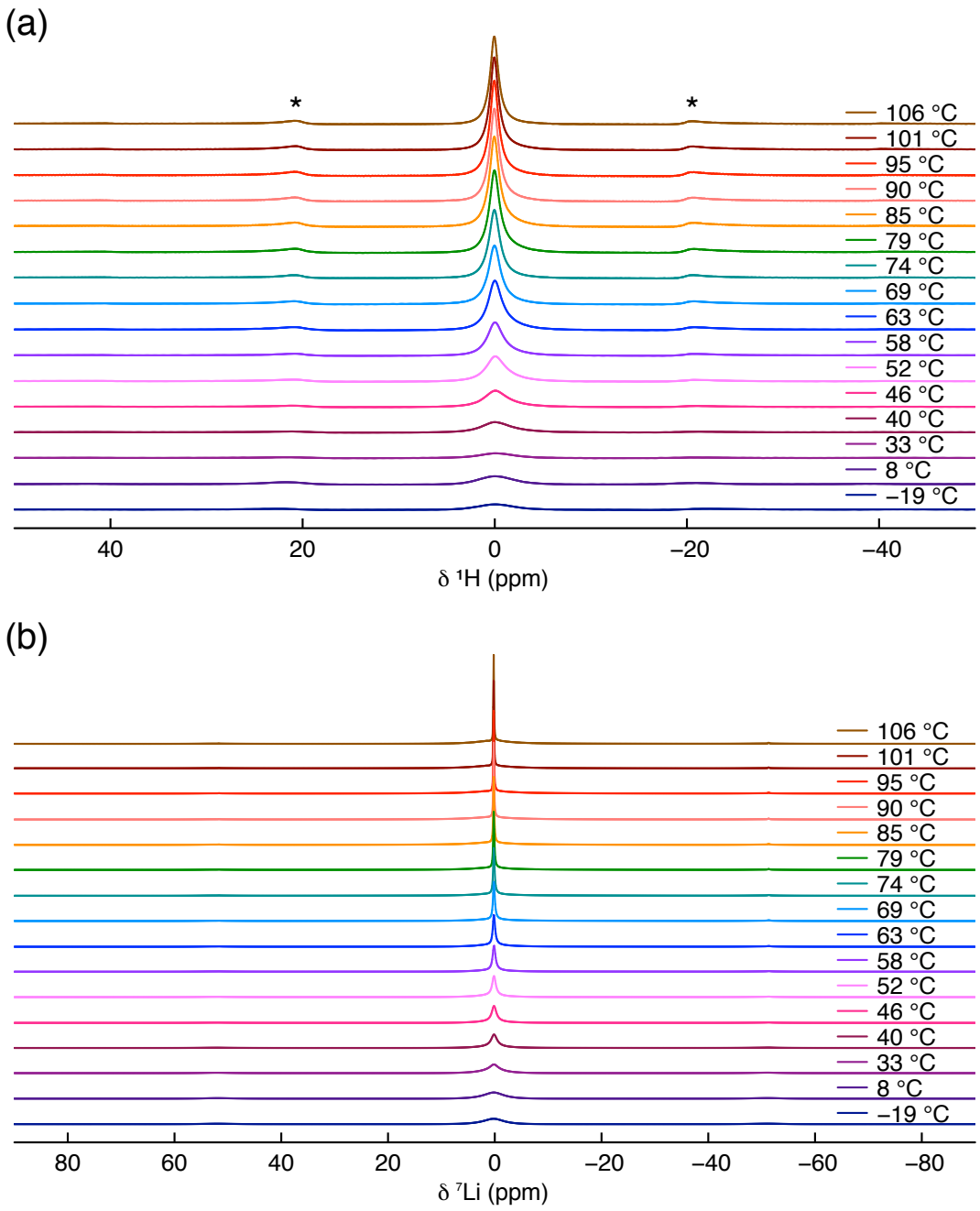

Figure 6.16: VT (a) ^{1}H and (b) ^{7}Li (11.7 T) MAS NMR spectra obtained between −19 and 106 °C for a sample of $Li_{2.75}OH_{0.25}Cl$ synthesised via the Schlenk line method. The MAS rate was 10 kHz and spinning sidebands are denoted by *. A recycle delay of (a,b) 60 s was used to acquire 4 transients, except for the spectra in (a) acquired at −19 and 8 °C, where a recycle delay of 500 s was used.

decrease. The ^{7}Li T_1 at 116 °C is approximately 0.1 s, which is considerably lower than the ^{1}H T_1 at the same temperature. These findings indicate that in $Li_{2.5}OH_{0.5}Cl$, the Li ions exhibit a greater degree of mobility than the protons.

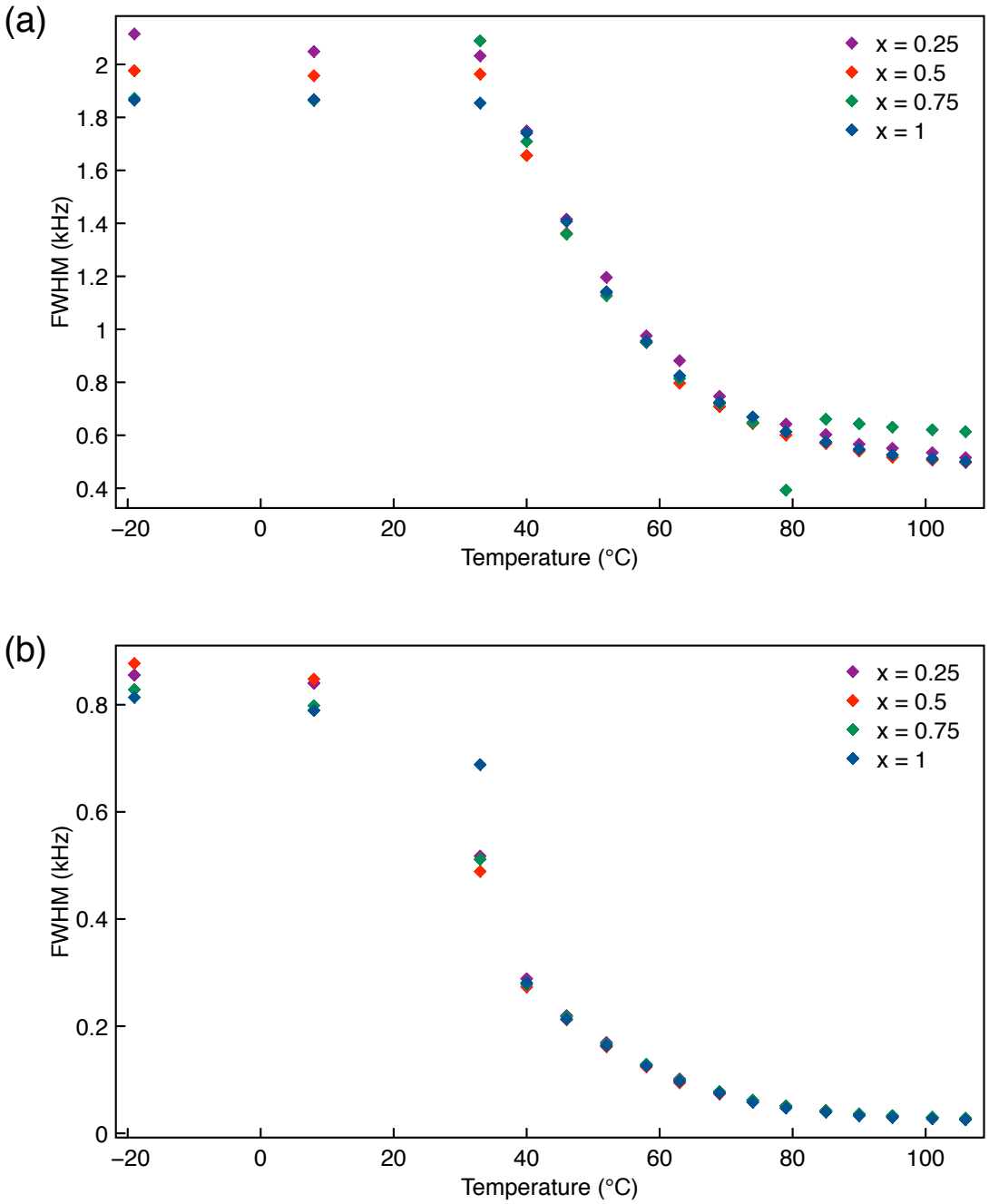

Figure 6.17: Variation in the (a) ^{1}H and (b) ^{7}Li FWHM as a function of temperature from the ^{1}H and ^{7}Li (11.7 T) MAS NMR spectra acquired between −19 and 106 °C for samples in the series $Li_{3-x}OH_xCl$ where x = 0.25, 0.5, 0.75 and 1.

Both the ^{1}H and ^{7}Li T_1 values for $Li_{2.5}OH_{0.5}Cl$ are similar to those reported for Li_2OHCl, suggesting a similar degree of ion mobility in both samples. The T_1 data obtained between 63 and 116 °C, for both ^{1}H and ^{7}Li, was further analysed to determine the corresponding activation energies. Arrhenius plots for

both the ^{1}H and ^{7}Li T_1 data are shown in Figure 6.19 and, in both cases, a linear fit is obtained. Activation energies of 0.39(6) and 0.38(1) eV are obtained for ^{1}H and ^{7}Li, respectively. These values are very similar, indicating a similar energy barrier for the movement of both species. A comparison of these values to those obtained for Li_2OHCl, indicates a minor increase in the E_a for ^{1}H in $Li_{2.5}OH_{0.5}Cl$ and a small decrease for ^{7}Li. Thus, suggesting that an increase in the Li content of the sample results in a marginally lower energy barrier for Li mobility. The proton mobility, on the other hand, faces a greater energy barrier.

To further understand ion mobility in $Li_{2.5}OH_{0.5}Cl$, a deuterated sample was studied via VT ^{2}H MAS NMR between −13 and 110 °C. The corresponding spectra are shown in Figure 6.20. The spectra obtained between −13 and 69 °C appear to be similar in lineshape although there is a noticeable reduction in the signal observed. In each case, an axially symmetric lineshape is observed, indicating an absence of motion. The spectrum obtained at 33 °C was simulated to extract the corresponding quadrupolar parameters. The simulated lineshape is shown in Figure 6.21 and the quadrupolar NMR parameters, C_Q = 259(1) kHz and η_Q = 0.0(1), were obtained. As stated earlier, these values indicate the presence of static OH^-/OD^- groups. At 69 °C, an additional broad resonance, albeit of very low intensity, is observed. As stated earlier, this broad resonance is believed to correspond to mobile OH^-/OD^- groups, more specifically, free rotation of these groups. As the temperature is increased to 79 °C, the broad component increases in intensity and becomes the dominant species, whilst the intensity of the manifold of sidebands corresponding to the static OH^-/OD^- groups decreases. This indicates that an increase in temperature leads to an increase in the proportion of freely rotating OH^-/OD^- groups. At 110 °C, the signal corresponding to the mobile OH^-/OD^- groups increases considerably, whereas the opposite is true for the signal arising from the static OH^-/OD^- groups. Thus, suggesting that a large proportion of the OH^-/OD^- groups are mobile at this temperature.

A comparison of this data to that obtained for the parent material, Li_2OHCl, (Figure 6.8) indicates a number of differences. Most importantly, the resonance corresponding to the mobile species becomes apparent at 79 °C

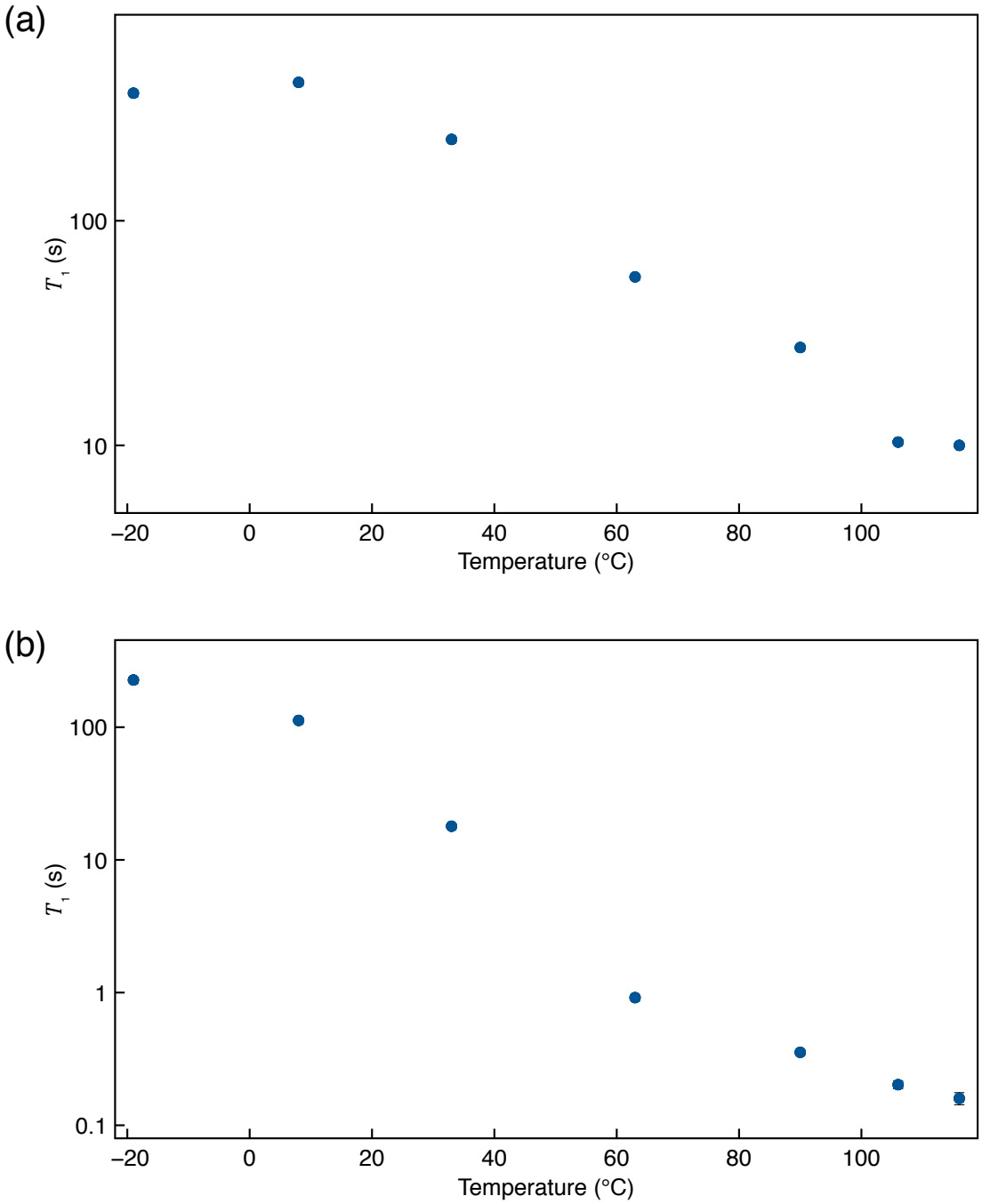

Figure 6.18: (a) ^{1}H and (b) ^{7}Li (11.7 T) T_1 values obtained between −19 and 116 °C for a sample of $Li_{2.5}OH_{0.5}Cl$ synthesised via the Schlenk line method. The estimated error bars are smaller than the symbols used and are therefore not shown.

rather than 69 °C for Li_2OHCl. Additionally, at 110 °C, the ^{2}H MAS NMR spectrum of Li_2OHCl indicates that almost all of the OH^-/OD^- groups are mobile whereas, in $Li_{2.5}OH_{0.5}Cl$, there are still a considerable number of static OH^-/OD^- groups. This indicates that, in $Li_{2.5}OH_{0.5}Cl$, the OH^-/OD^- groups

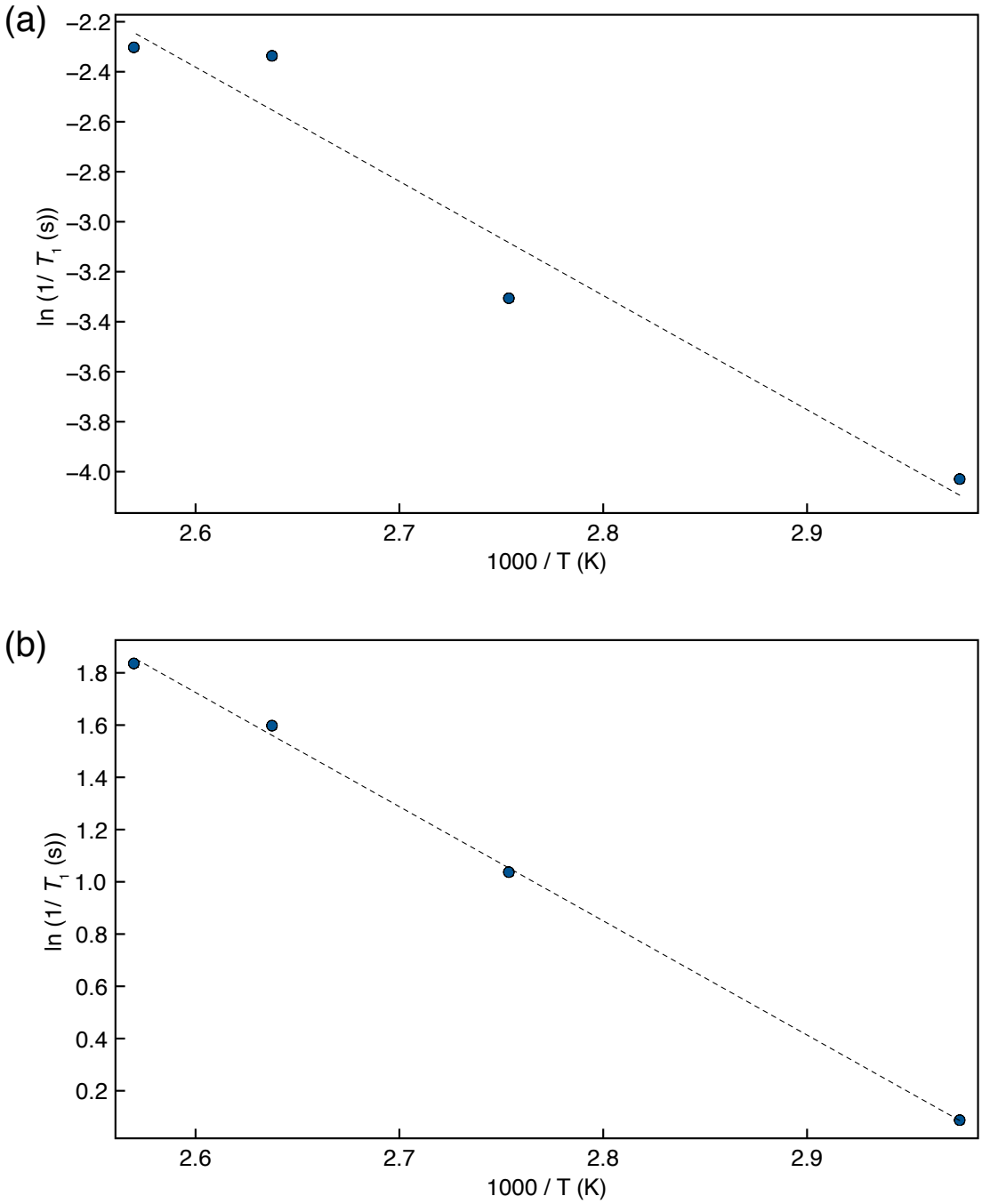

Figure 6.19: An Arrhenius plot of (a) ^{1}H and (b) ^{7}Li (11.7 T) T_1 data obtained for a sample of $Li_{2.5}OH_{2.5}Cl$ synthesised via the Schlenk line method, over a temperature range of 63 – 116 °C. In both cases, a linear fit is obtained with gradients (a) −4.57(74) and (b) −4.37(10) and R^2 = (a) 0.9500 and (b) 0.9989. Activation energies of (a) 0.39(6) eV and (b) 0.38(1) eV were calculated.

become mobile much later and they do not become the dominant species until higher temperatures. As discussed earlier, the movement of the OH^-/OD^- groups is intimately connected to the movement of Li ions. The ^{2}H MAS NMR

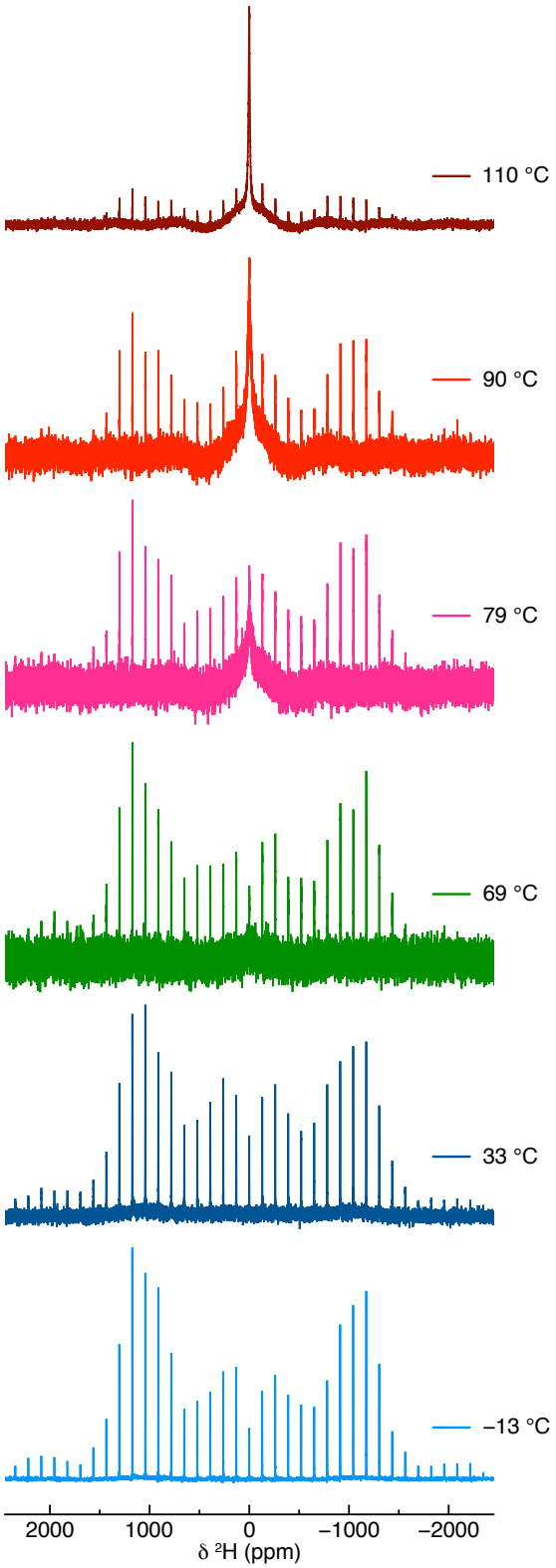

Figure 6.20: VT ^{2}H (11.7 T) MAS NMR spectra acquired between −13 and 110 °C for a sample of $Li_{2.5}OD_{0.5}Cl$ synthesised via the Schlenk line method. The MAS rate was 10 kHz. In all cases, a recycle delay of 15 s was used to acquire 48 transients.

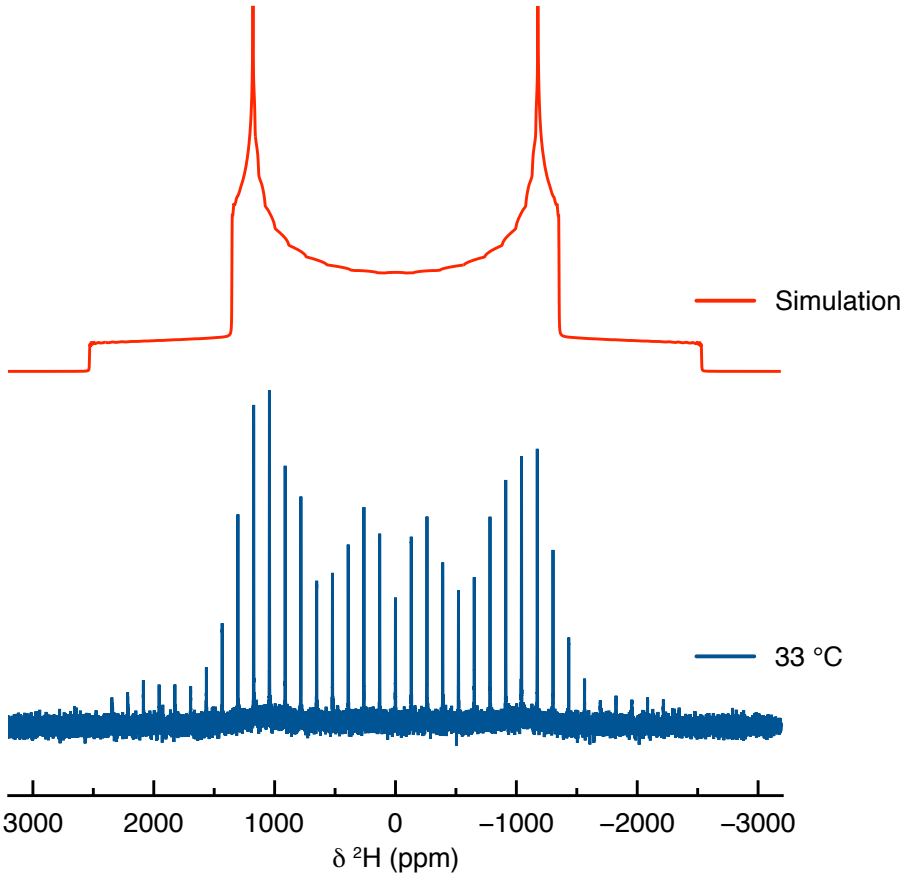

Figure 6.21: Simulation of the ^{2}H (11.7 T) MAS NMR spectrum acquired for $Li_{2.5}OH_{0.5}Cl$ at 33 °C for a sample synthesised via the Schlenk line method. A recycle delay of 15 s was used to acquire 48 transients. The spectrum was simulated to obtain the corresponding quadrupolar parameters, C_Q = 259(1) kHz and η_Q = 0.0(1).

data presented here for $Li_{2.5}OH_{0.5}Cl$ (Figure 6.20) indicates that, when compared to the parent material, Li_2OHCl, the OH^-/OD^- groups become mobile at higher temperatures, *i.e.*, at 79 °C. Thus, suggesting that in $Li_{2.5}OH_{0.5}Cl$, the Li ions also become mobile at a higher temperature. This data also agrees with the ^{1}H E_a previously determined, where the ^{1}H E_a was marginally higher than that for the parent material, Li_2OHCl. Overall, the data appears to suggest that an increase in the Li content results in proton mobility at higher temperatures, which, in turn, suggests lower Li-ion mobility at lower temperatures.

6.3.5 *Ab Initio* Molecular Dynamics Simulations

To support our experimental findings, AIMD simulations were completed by our collaborators. The NMR data presented for Li_2OHCl indicated that protons exhibit localised mobility, such as free rotation of the OH^- groups.

Li, on the other hand, exhibits long-range mobility, *i.e.*, movement throughout the structure. To confirm this, mean square displacements were obtained for each element in Li_2OHCl from AIMD simulations completed at 800 K. The simulations were run for 50 ps and the data obtained is shown in Figure 6.22. The MSD for Li increases linearly from 0 to ~6 Å over the simulated time. Thus, indicating long-range Li-ion diffusion. However, this is not the case for proton transport, as the proton MSD begins to flatten before the end of the simulation. Furthermore, the proton MSD never exceeds 2 Å, which is far below the O–O distance of 3.91 Å in the high-temperature cubic phase of Li_2OHCl.[213] Thus, again suggesting that protons do not partake in long-range diffusion and, instead, exhibit only localised motion. It is noted that the MSDs corresponding to O and Cl do not exhibit any change over the simulated time. Thus, suggesting that these two species do not exhibit any mobility.

The AIMD simulations completed for Li_2OHCl also produce diffusion density maps for Li and H, shown in Figure 6.23. These maps are a sum of all of the trajectories of Li and H accumulated over the length of the simulation. It can be seen for both Li and H that the largest densities are located around the corresponding crystallographic sites with considerable local oscillation. More-

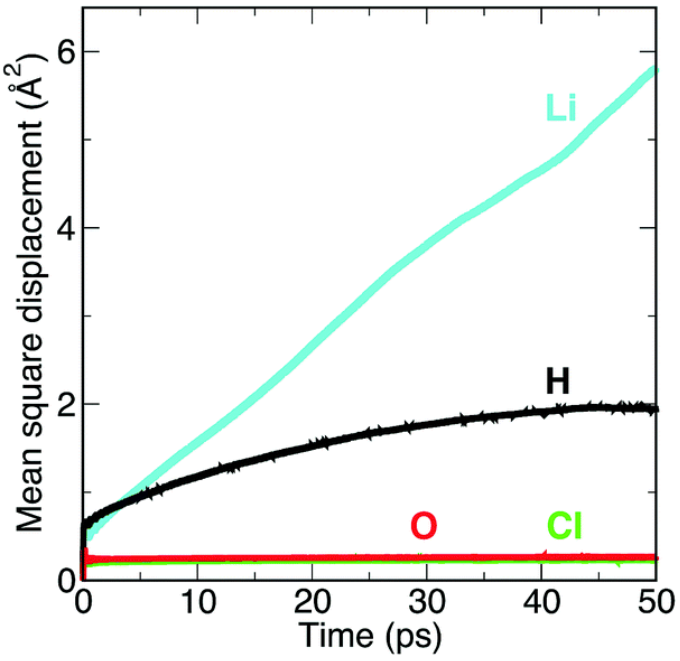

Figure 6.22: MSD plots for each element in Li_2OHCl at 800 K.

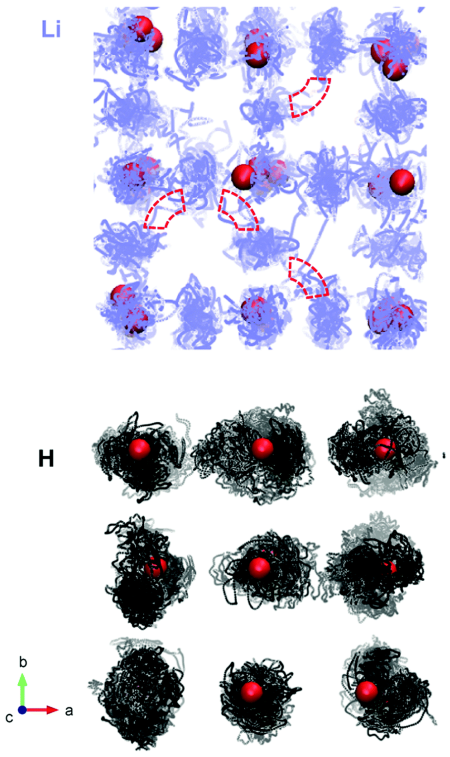

Figure 6.23: Density plots of trajectories for lithium ions (blue) and protons (black) in Li_2OHCl at 800 K. Oxygen positions are given in red. Chlorine ions are omitted for clarity. Examples of local Li-ion jumps are highlighted with red dashed lines.

over, these maps suggest that significant Li-ion diffusion occurs via a vacancy mechanism, in which Li ions diffuse to adjacent vacant sites both diagonally and laterally to create long-range diffusion pathways. In contrast, there are no long-range proton diffusion pathways identified, with only O–H rotational motion observed. This is perhaps unsurprising when the O–O distance of 3.91 Å is considered in these materials and compared to proton-conducting perovskite oxides, such as $BaZrO_3$ (with an O–O separation of 2.97 Å).[232] Clearly, the large O–O distances in these anti-perovskite systems will inhibit significant proton hopping transport.

The findings presented here (Figure 6.22 and 6.23) are in good agreement with the VT ^{1}H and ^{7}Li NMR data presented (Figures 6.1 and 6.2). As the temperature is increased, line narrowing is observed in both the ^{1}H and ^{7}Li NMR data. Hence, both the H and Li are, to some extent, mobile within the system. However, the changes observed in both the ^{1}H T_1 values and the FWHM indicate that the protons are not as mobile as Li. Higher ^{1}H T_1 values

and reduced line narrowing indicate proton mobility is limited to rotation of the OH^- groups. This is further validated by the ^2H MAS NMR data shown. Coupling these findings with the ^1H, ^2H and ^7Li NMR data presented, it is believed that the mobility of the Li ions in Li_2OH/DCl is very intimately connected to the position of the OH^-/OD^- groups within the structure. Based on both the experimental and computational data presented, it is believed that a change to cubic symmetry alone is not sufficient to increase the ionic conductivity of Li_2OHCl. The AIMD calculations presented indicate that, in the cubic phase of Li_2OHCl, the OH^-/OD^- groups point towards a Li vacancy and, as the temperature is increased, the Li ions become mobile, starting to "hop" into the Li vacancies and moving through the structure. As the temperature is increased further, the Li ions start to hop at a faster rate. Since the OH^-/OD^- groups point directly towards a Li vacancy, the movement of the Li-ions will directly influence the position of the OH^-/OD^- groups, *i.e.*, when a Li vacancy is filled, the H/D will rotate around the oxygen, repositioning itself so that it is always pointing towards a vacancy, as it will therefore have the greatest degree of freedom and movement. Essentially, whatever the position of a Li vacancy, the OH^-/OD^- groups will reorient themselves to ensure they always point in the direction of a vacancy. To demonstrate this, a schematic representation of the cubic structure and the movement of Li ions is shown in Figure 6.24.

Interestingly, in the AIMD calculations, O atoms were identified that were coordinated to different numbers of Li ions, namely, three, four or five. For oxygen atoms coordinated to three Li ions, the proton movement is faster as it has more space to rotate into (because there are effectively three vacant sites). Conversely, for O atoms coordinated to five Li-ions, the movement is more restricted and hence the OH^- groups are limited in the spaces they can rotate into. Hence, the presence of multiple coordination environments in the supercell calculations appears to correlate well with the ^2H NMR findings, and the presence of both static and mobile OH^-/OD^- groups.

In order to study the effect of different H and Li content on ion mobility, AIMD simulations were also completed for the $Li_{3-x}OH_xCl$ (x = 0 to 1.06) system. The representative MSD plots obtained for Li in different composi-

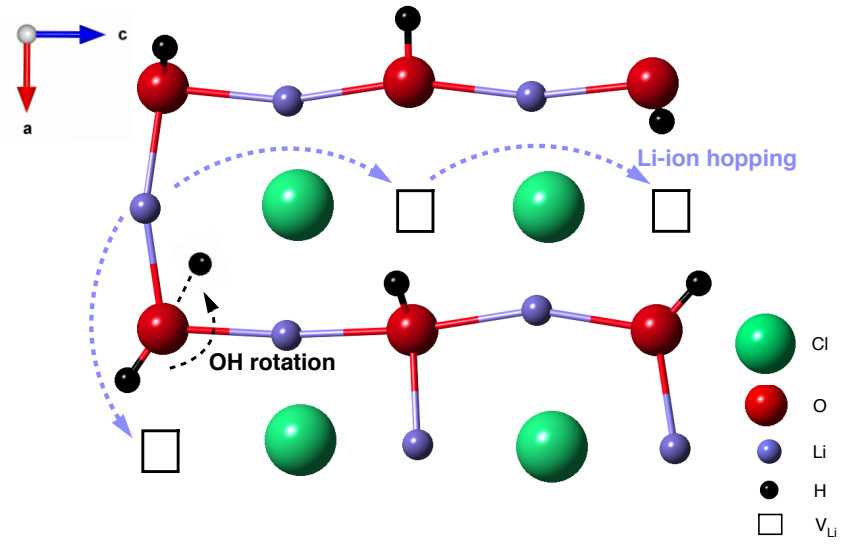

Figure 6.24: Schematic representation of the Li-ion hopping mechanism in the cubic $Pm\bar{3}m$ phase of Li_2OHCl. The OH^- groups point towards Li vacancies. Li-ion hopping occurs via these vacancies, denoted by the blue dashed arrows. Rotation of the OH^- groups occurs as a result of a nearby Li ion hopping to an adjacent site, denoted by the black dashed arrow.

tions, $Li_{3-x}OH_xCl$ (x = 0, 0.5, 0.56, 1 and 1.06) at 800 K, are shown in Figure 6.25. Several key points emerge from these plots. First, it is clear that with increasing proton concentration, there is a concomitant increase in Li-ion diffusion at 800 K. This is perhaps unsurprising given the increase in Li vacancy concentration as a result of hydration. It is well known that Li vacancies are the dominant charge carriers in anhydrous Li_3OCl with defects.[59,129,132,226] These results reinforce the fact that there is a strong correlation between Li-ion transport and proton concentration.

Second, the increase in Li-ion diffusion extends beyond x = 1, *i.e.*, Li_2OHCl. This indicates that the formation of water molecules at low concentrations does not hinder Li-ion transport and the increasing Li vacancy concentration still dominates. For large proton concentrations (x = 2), it is known experimentally that $LiOH_2Cl$ (or $LiCl{\cdot}H_2O$) is orthorhombic in space group *Cmcm*.[213] This is indicative of Li ordering, as confirmed by single-crystal XRD studies,[233] and a reduction in Li-ion mobility. The poor Li-ion conductivity of $LiCl{\cdot}H_2O$ was confirmed by Schwering *et al.*, with values dropping below the levels of detection ($<10^{-8}$ S cm^{-1}) of the impedance analyser.[213]

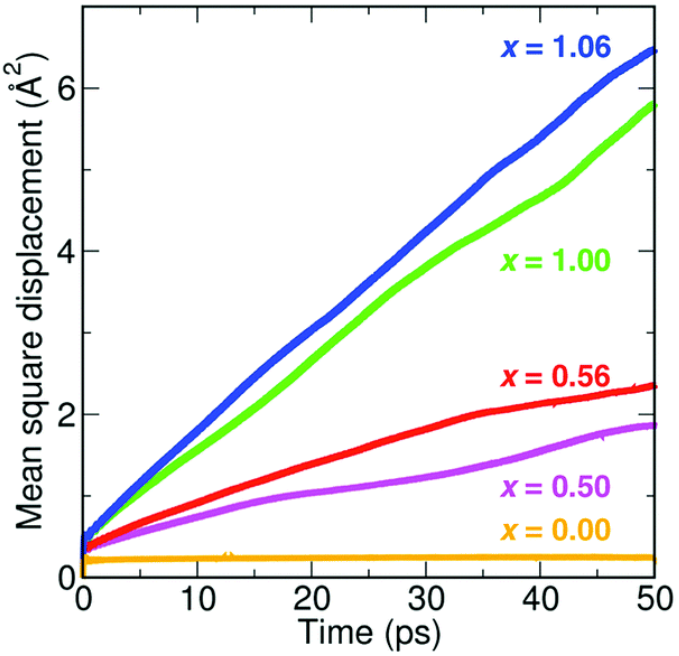

Figure 6.25: MSD plots of Li^+ in five different compositions of $Li_{3-x}OH_xCl$ (x = 0, 0.5, 0.56, 1 and 1.06) at 800 K, showing increased Li-ion diffusion with increasing proton concentration.

Third, in Li_3OCl (x = 0), there is no Li diffusion due to the lack of Li vacancies. It is well known that perfect crystals are not good ion conductors as there are no pathways for ion transport. Hence, a certain amount of disorder is required for ion conduction. Disorder is usually introduced into this system via LiCl Schottky defect pairs, as found experimentally and computationally.[132,135] The calculations presented here indicate that proton incorporation can provide an alternative mechanism for introducing disorder in the anti-perovskite material.

The self-diffusion coefficients for Li were converted into Li-ion conductivities and are presented as an Arrhenius plot in Figure 6.26. The conductivity data for compositions x = 0.5, 0.56, 1.0 and 1.06 can be divided into two main groups. For low proton concentrations, x = 0.50 and 0.56, low activation barriers of 0.32 and 0.30 eV are obtained, respectively. Whereas, for high proton concentrations (x = 1.00 and 1.06) slightly higher activation barriers of 0.41 and 0.42 eV are observed, respectively. It is clear from the calculations presented that although the Li-ion conductivities of Li_2OHCl and $Li_{1.94}OH_{1.06}Cl$ are higher than those of $Li_{2.5}OH_{0.5}Cl$ and $Li_{2.44}OH_{0.56}Cl$ at high temperatures (>550 K), they are significantly lower at typical solid-state battery operating

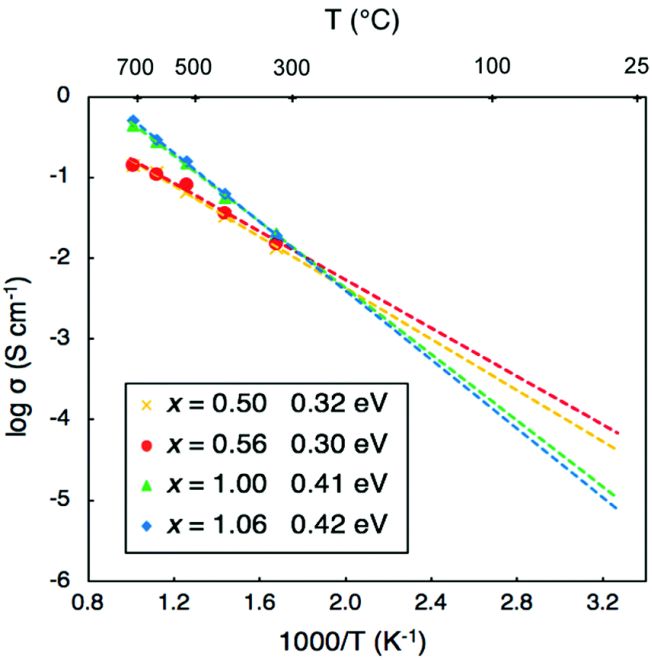

Figure 6.26: Li-ion conductivities and activation energies of $Li_{3-x}OH_xCl$ (x = 0.5, 0.56, 1.0 and 1.06) derived from AIMD simulations.

temperatures (~270 – 400 K). These results suggest that compositions with low proton concentrations (x = ~0.5) will have superior Li-ion transport properties in practical battery applications when compared to compositions with high levels of protons. We can compare our conductivity values to experiment by extrapolating our calculated values to lower temperatures. Hood *et al.*[214] obtained a conductivity of ~1 × 10^{-4} S cm^{-1} at 373 K for fast-cooled Li_2OHCl, which is in excellent agreement with our extrapolated value of ~1.7 × 10^{-4} S cm^{-1}.

Our calculated E_a of 0.41 eV for Li mobility in Li_2OHCl is in good agreement with the value obtained from the ^{7}Li T_1 data (0.39 eV). It is noted that slightly higher values of 0.56 and 0.52 eV were determined by Hood *et al.*[214] and Li *et al.*,[234] respectively, using EIS. As mentioned earlier, there is typically a discrepancy between the E_a values determined via NMR and EIS. This is because NMR is a local probe and only detects the motional processes in the bulk of the materials, whereas, EIS can detect motion both in the bulk of the material and at the grain boundaries. The calculations demonstrated that E_a decreases with increasing Li content, and an E_a of 0.32 eV was calculated for $Li_{2.5}OH_{0.5}Cl$. This is also in agreement with our NMR data, where an E_a

of 0.38 eV was determined for $Li_{2.5}OH_{0.5}Cl$, which is slightly lower than the parent material, Li_2OHCl.

6.3.6 ^{35}Cl MAS NMR Spectroscopy

To gain a greater structural understanding of this system, Li_2OHCl was also studied via VT ^{35}Cl MAS NMR spectroscopy. The spectra acquired at 33, 63, 79 and 106 °C are shown in Figure 6.27. The spectrum acquired at 33 °C corresponds to the room-temperature phase of Li_2OHCl and, as the temperature is increased to 63 °C, the lineshape changes owing to the phase transition to cubic symmetry. The ^{35}Cl MAS NMR data obtained at 33 and 63 °C have been discussed in Chapter 4 and, as such, will not be discussed in any great detail here. Instead, they will be discussed in the context of a comparison with the VT ^{35}Cl MAS NMR data obtained. As the temperature is increased to 79 °C the lineshape is similar to that acquired at 63 °C. However, there is a significant reduction in the observed signal intensity. At 106 °C, there is a further decrease in the signal, making it difficult to obtain a good quality spectrum. Following

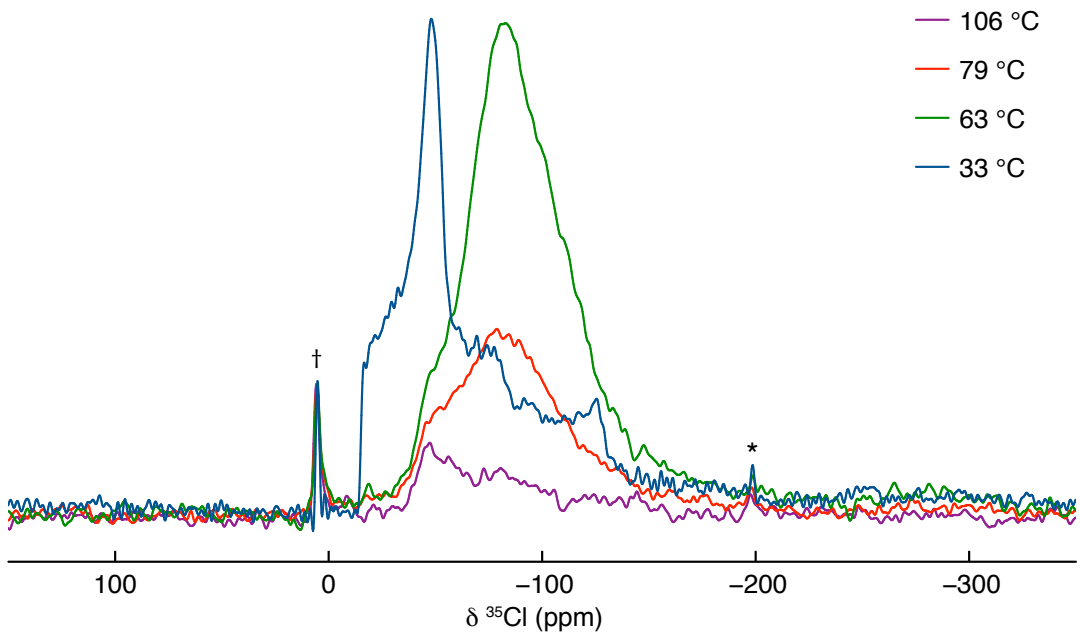

Figure 6.27: VT ^{35}Cl (11.7 T) MAS NMR spectra acquired at 33, 63, 79 and 106 °C for a sample of Li_2OHCl synthesised via a conventional solid-state route. The MAS rate was 12 kHz and spinning sidebands are denoted by *. In all cases, a recycle delay of 5 s was used to acquire 2560 transients. The resonance corresponding to LiCl is denoted by †.

the phase transition, the lineshape corresponding to Li_2OHCl appears at the same chemical shift, but its intensity gradually decreases with increasing temperature. It is noted that a signal pertaining to LiCl (present as an impurity) is also observed. The signal from LiCl remains unchanged at all temperatures, indicating that the signal reduction is related to a change in the local environment of the Cl in Li_2OHCl and not the experimental conditions employed.

At present, it is not clear why this reduction in signal intensity occurs. Following the phase transition to cubic symmetry at ~35 – 40 °C, Li_2OHCl exists in the cubic phase until it melts. Hence, the decrease in signal observed cannot be attributed to any significant structural changes within the sample. It has already been demonstrated that, as the temperature increases, Li ions become mobile throughout the structure, and protons undergo rapid rotational motion. Hence, it is possible that the movement of these species causes the local environment of Cl to change, which could have a significant impact on the NMR parameters observed and, consequently, the signal observed. However, it is noted that the local environment of the species exhibiting mobility (H and Li) also changes rapidly, but no such signal reduction was observed in ^{1}H and ^{7}Li NMR spectra. Another possibility is that Cl could be exhibiting some motion. Cl could display a high degree of thermal motion within the unit cell or perhaps exchange between the two ^{35}Cl sites observed in the spectrum corresponding to the cubic phase. However, translational motion, similar to H and Li, is unlikely as line narrowing would likely be observed in such instances. Here, no line narrowing is observed. Instead, a progressive drop in the signal intensity is observed.

If Cl were to move from one site to another, this could be monitored/observed via ^{35}Cl EXSY. Hence, EXSY experiments were completed at 33, 63 and 79 °C, and the resulting spectra are shown in Figure 6.28. Unfortunately, it was not feasible to obtain a spectrum of reasonable quality at 106 °C owing to a distinct lack of signal. All of the EXSY spectra obtained exhibit a signal solely on the diagonal, corresponding to the ^{35}Cl MAS NMR spectrum for Li_2OHCl. If the nucleus under observation was to take part in an exchange process from one site to another, then "cross-peaks" would be observed between the two

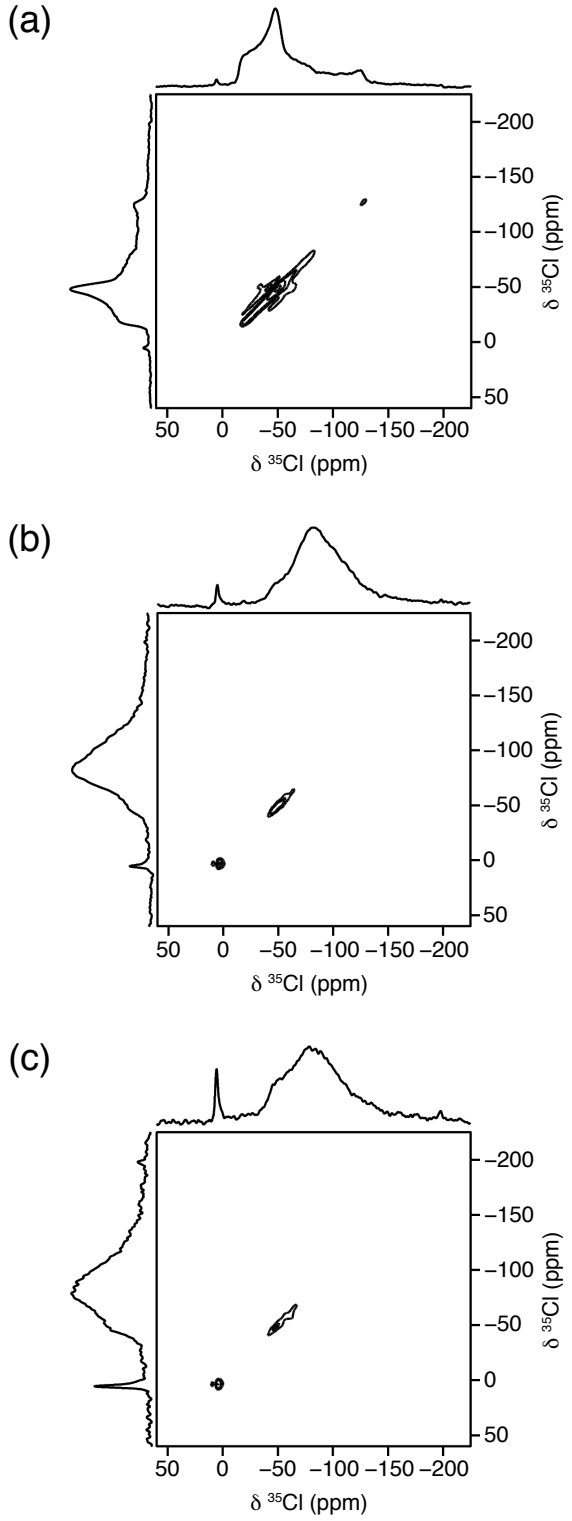

Figure 6.28: ^{35}Cl (11.7 T) EXSY spectra acquired at (a) 33, (b) 63 and (c) 79 °C for a sample of Li_2OHCl synthesised via a conventional solid-state route. The MAS rate was 12 kHz. In all cases, a mixing time of 0.1 s was used and a recycle delay of 1 s was used to acquire (a) 96, (b) 480 and (c) 384 transients.

sites involved. Here, however, no such cross-peaks are observed, indicating that no exchange has taken place on the timescale investigated. This is in agreement with the AIMD simulations presented (Figure 6.22), where the MSD plots for Li_2OHCl indicated Cl does not exhibit any motion.

These findings therefore suggest that the gradual disappearance of the ^{35}Cl signal with increasing temperature is unlikely to be caused by Cl mobility. It is more likely that the reduction in signal with increasing temperature is the result of changes in the local Cl environment caused by movement of surrounding Li and H species, as they undergo translational and local mobility, respectively. The NMR data presented earlier demonstrated that an increase in temperature results in an increase in proton and Li-ion mobility. This coincides with the gradual drop in the ^{35}Cl signal. Thus, it is possible that these changes could cause the EFG experienced by the Cl to change, making it less feasible to observe the Cl. Therefore, as the temperature is increased, the signal diminishes in intensity. It is noted that, these suggestions cannot be confirmed from the current data alone. Thus, the exact cause of the diminishing ^{35}Cl signal with increasing temperature remains unclear.

A sample of $Li_{2.5}OH_{0.5}Cl$ was also analysed via VT ^{35}Cl MAS NMR spectroscopy and the spectra obtained at 33, 63 and 106 °C are shown in Figure 6.29. The spectra acquired at 33 and 63 °C correspond to the room-temperature and the high-temperature phase, respectively. It is noted that they have been discussed in detail in Chapter 4 and are only shown here for comparison. As stated earlier, the lineshape changes significantly following the phase transition from the room-temperature structure to the cubic phase in space group $Pm\bar{3}m$. The lineshape observed at 33 and 63 °C was simulated, and three distinct Cl sites were observed in both cases. The Cl sites observed at 33 °C appeared to be similar to those observed for the parent material, Li_2OHCl. At 63 °C, Li_2OHCl exhibited two distinct Cl sites. However, the $Li_{2.5}OH_{0.5}Cl$ sample was observed to have three distinct Cl sites. The additional site observed at 63 °C was attributed to the impurity phase present in the sample. As the temperature is increased to 106 °C, the lineshape of the ^{35}Cl resonance observed for $Li_{2.5}OH_{0.5}Cl$ changes significantly. In a similar manner to Li_2OHCl a drop in

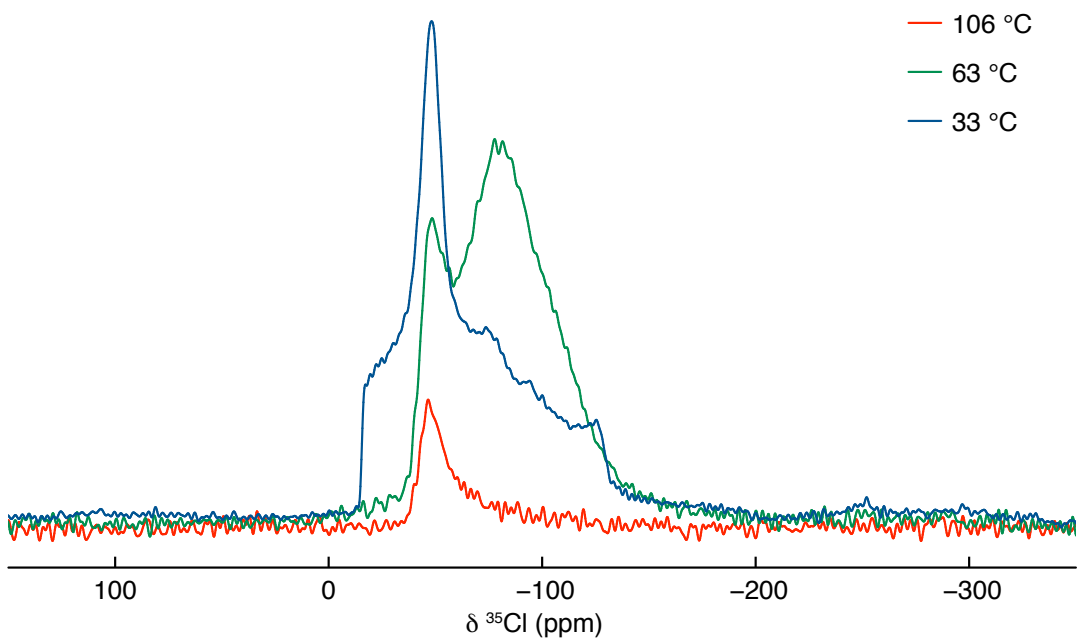

Figure 6.29: VT ^{35}Cl (11.7 T) NMR spectra acquired at 33, 63 and 106 °C for a sample of $Li_{2.5}OH_{0.5}Cl$ synthesised via the Schlenk line method. The MAS rate was 10 kHz. In all cases, a recycle delay of 10 s was used to acquire 2560 transients.

the intensity of the signal is observed. However, in this instance, signal is still observable at 106 °C, whereas for Li_2OHCl, the signal was barely visible. This sample also contains an impurity phase, as discussed in Chapter 4. Hence, it is difficult to determine whether the signal corresponding to $Li_{2.5}OH_{0.5}Cl$ has disappeared completely or not. As discussed earlier, the precise cause of a reduction in the ^{35}Cl signal is unclear. It was suggested that this could be an indirect consequence of proton and Li-ion mobility as the movement of these species will lead to rapid changes in the EFG experienced by Cl. This, in turn, could make the signal unobservable. Earlier, the $^{1/2}$H and ^{7}Li NMR data presented for $Li_{2.5}OH/D_{0.5}Cl$ demonstrated proton and Li-ion mobility. Therefore, the same could also be true for $Li_{2.5}OH_{0.5}Cl$.

6.4 Conclusions

This chapter was dedicated to investigating ion dynamics in Li_2OHCl synthesised via a conventional solid-state reaction and samples in the related series $Li_{3-x}OH_xCl$ (x = 0.25, 0.5 and 0.75) synthesised via the Schlenk line method. VT ^{1}H and ^{7}Li MAS NMR experiments were completed for all sam-

ples between −19 – 106 °C. In all cases, a single resonance was observed and the lineshape narrowed as a function of temperature, indicating that both the protons and Li ions exhibit mobility in these samples. VT static ^{7}Li NMR experiments were also completed for Li_2OHCl over the temperature range −65 – 230 °C. Here, the resonance corresponding to the room- and high-temperature phase exhibited a different lineshape. As with the ^{7}Li MAS NMR data, here too, an increase in temperature resulted in a narrowing of the resonance, suggesting mobility. To confirm proton and Li-ion mobility, ^{1}H and ^{7}Li T_1 measurements were completed for samples of Li_2OHCl and $Li_{2.5}OH_{0.5}Cl$. Both samples were observed to exhibit proton and Li-ion mobility and the data obtained suggested that, in both cases, Li ions exhibit greater mobility. The E_a calculated from the ^{1}H, and ^{7}Li T_1 data indicated that, in Li_2OHCl, the Li-ions face a higher energy barrier when compared to the protons. In $Li_{2.5}OH_{0.5}Cl$, however, the energy for both proton and Li-ion movement is similar and the E_a for protons is higher than for Li_2OHCl, and for Li-ions it is slightly lower than for Li_2OHCl. Whilst the ^{1}H and ^{7}Li NMR data obtained demonstrated that both species are mobile, the nature of the movement of these species, however, could not be discerned from this data alone. To probe this further, Li_2OHCl was analysed via VT ^{2}H NMR spectroscopy under static and MAS conditions. The sample was shown to contain static OH^-/OD^- groups from −19 to 63 °C. At 69 °C, some of the OH^-/OD^- groups became mobile, meaning that the sample contained both static and mobile OH^-/OD^- groups. An increase in temperature led to an increase in the proportion of the mobile OH^-/OD^- groups present in the sample and at 110 °C, almost all of the OH^-/OD^- groups appear to be mobile. The linewidths obtained in the ^{2}H MAS NMR spectra at high temperatures (95 and 110 °C) strongly suggest that the protons are undergoing a rotational motion rather than long-range motion, *i.e.*, dissociating and moving throughout the structure. Interestingly, in $Li_{2.5}OH_{0.5}Cl$, the OH^-/OD^- groups were observed to become mobile at higher temperatures (79 °C) relative to Li_2OHCl. The parent system, Li_2OHCl, was also analysed via ^{1}H and ^{7}Li PFG-NMR spectroscopy. The data obtained confirmed Li-ion diffusion throughout the structure, whereas the protons did not undergo any

long-range motion.

AIMD simulations were completed to support the NMR findings. The MSDs plotted for each element in Li_2OHCl at 800 K and the diffusion density maps extracted, indicated that Li ions indeed exhibit diffusion throughout the structure, whereas the protons only exhibit localised motion. Thus, confirming the experimental findings. The AIMD simulations, in conjunction with the NMR data, have been used to propose a mechanism for Li-ion and proton movement. The AIMD calculations indicated that there were O atoms coordinated to three, four or five Li-ions and the proton movement was faster for O atoms connected to three Li-ions. This is because there are more sites for it to rotate into. It appears that the OH^-/OD^- groups point directly towards a Li vacancy and, when a Li vacancy is filled, the H/D rotates around the O to point towards another vacancy. Thus, explaining the influence of Li-ion movement on the OH^-/OD^- position. Li MSDs for $Li_{3-x}OH_xCl$ (x = 0, 0.5, 1 and 1.06) indicated that an increase in Li concentration results in a decrease in Li-ion diffusion. This is in agreement with the ^2H MAS NMR data because in $Li_{2.5}OH_{0.5}Cl$ the OH^-/OD^- groups became mobile at higher temperatures when compared to Li_2OHCl, in turn suggesting that Li-ions in $Li_{2.5}OH_{0.5}Cl$ also become mobile at higher temperatures when compared to Li_2OHCl. The E_a determined for Li mobility in $Li_{3-x}OH_xCl$ (x = 0, 0.5, 1 and 1.06) via AIMD calculations were in agreement with those determined via NMR. In general, the energy barriers were found to decrease with increasing Li concentration. Interestingly, the Li-ion conductivities obtained at high temperatures such as >550 K suggested that samples with a lower Li concentration, conversely a higher proton concentration, will have a higher Li-ion conductivity. However, the Li-ion conductivities were significantly lower at typical operating temperatures (~270 – 400 K) for solid-state batteries. Thus, suggesting that an increase in Li concentration will produce samples with higher Li-ion conductivities.

Finally, samples of Li_2OHCl and $Li_{2.5}OH_{0.5}Cl$ were also analysed via VT ^{35}Cl MAS NMR spectroscopy. Interestingly, in both cases, the signal obtained exhibited a significant decrease in intensity with increasing temperature. The reason for this reduction in signal remains unclear. It was thought

that Cl could be exhibiting mobility. However, no line narrowing was observed in the ^{35}Cl MAS NMR spectra. Li_2OHCl was also analysed via VT ^{35}Cl EXSY, and no cross-peaks were observed at any temperature. Thus, indicating that no inter-site exchange takes place in Li_2OHCl. Moreover, the MSD for Cl in Li_2OHCl obtained from AIMD simulations did not exhibit any change during the simulation. Therefore, the gradual reduction in signal is unlikely to be due to Cl mobility as no motion is detected on the NMR timescale. It was also suggested that the signal reduction could be an indirect consequence of the proton and Li-ion mobility. As demonstrated earlier, the protons and Li ions in both samples become increasingly mobile with increasing temperature. Therefore, as the movement of these species speeds up, the EFG experienced by the Cl starts to change, which, in turn, causes the signal to become unobservable. However, the exact cause of the progressive signal reduction observed for both samples is yet to be confirmed.

7 Probing Compositional Changes in Li_2OHCl

7.1 Introduction

In a similar manner to perovskites, anti-perovskites are known to exhibit extreme structural flexibility. Hence, various types of structural modifications via cation and/or anion substitution are possible. Such structural changes will affect the ionic conductivity and other physical properties of the material. In fact, the composition of the material can be fine-tuned to produce a material with a very high ionic conductivity. Hence, there is considerable motivation for altering the composition of anti-perovskites, as it could result in a high-performance solid electrolyte material.

Recently, Li and co-workers reported that partially substituting OH^- in Li_2OHX (X = Cl or Br) with F^- produces a promising solid electrolyte, as the material exhibits high ionic conductivity.[234] EIS measurements indicated that $Li_2(OH)_{0.9}F_{0.1}Cl$ exhibits a conductivity of 3.5×10^{-5} S cm^{-1} at 25 °C, which increases to 1.9×10^{-3} S cm^{-1} at 100 °C. An activation energy of 0.52 eV was determined via EIS, and $Li_2(OH)_{0.9}F_{0.1}Cl$ was found to be stable on contact with metallic Li. They reported that partially substituting OH^- with F^- produces a cubic phase at room temperature. This is interesting as the cubic structure is believed to be better suited for Li-ion mobility when compared to the orthorhombic structure of the parent material, Li_2OHCl. They also propose that the absence of H reduces steric hindrance and thus promotes Li-ion mobility. Hanghofer *et al.* recently suggested that fluorine substitution is likely to replace Cl^- instead of OH^-.[210] However, no experimental evidence was provided to support this hypothesis.

More recently, Effat and co-workers studied Li_2OHCl and its fluorinated analogues, $Li_2(OH)_{0.9}F_{0.1}Cl$ and $Li_2OHCl_{0.9}F_{0.1}$, via computational methods.[235] DFT calculations and AIMD simulations were completed to assess the stability of these materials and their suitability as Li-ion conductors. All three LiRAPs were found to have similar formation energies that are much more favourable when compared to Li_3OCl, meaning their synthesis should be eas-

ier when compared to Li_3OCl. However, in a similar manner to Li_3OCl and Li_2OHCl, the fluorinated LiRAPs are metastable and may decompose to form LiCl, LiF and $Li_4(OH)_3Cl$. The AIMD simulations identified Li as the only species to exhibit long-range motion within Li_2OHCl and its fluorinated analogues, $Li_2(OH)_{0.9}F_{0.1}Cl$ and $Li_2OHCl_{0.9}F_{0.1}$. The movement of Li-ions is believed to be mediated via vacancies. The calculated ionic conductivities and activation energies suggest that fluorine doping is an appropriate method for improving the ion conductivity of Li_2OHCl. As such, $Li_2(OH)_{0.9}F_{0.1}Cl$ is predicted to exhibit an ion conductivity of 0.05×10^{-3} S cm^{-1} at 25 °C, which is expected to increase to 0.94×10^{-3} S cm^{-1} at 100 °C, with an E_a of 0.40 eV. $Li_2OHCl_{0.9}F_{0.1}$, on the other hand, is expected to be an even better Li-ion conductor with an ion conductivity of 0.38×10^{-3} S cm^{-1} at 25 °C, which increases to 4.78×10^{-3} S cm^{-1} at 100 °C. A lower E_a of 0.35 eV was also calculated for $Li_2OHCl_{0.9}F_{0.1}$.

The composition of Li_2OHCl can also be modified via halide mixing, *e.g.*, substituting Cl^- with Br^- to produce $Li_2OHCl_{1-x}Br_x$ (x = 0 – 1). As stated earlier, the end member of this series, Li_2OHBr, has been studied by Schwering *et al.* and is reported to adopt a cubic structure at room temperature, in space group $Pm\bar{3}m$.[213] No phase transition was observed between room temperature and −50 °C, indicating Li_2OHBr remained cubic. Li_2OHBr was investigated via static VT ^{7}Li NMR and the resonance was observed to narrow with increasing temperature. ^{7}Li T_1 measurements were also completed, and an activation energy of 0.37 eV was determined. Li_2OHBr has also been deuterated and studied via neutron diffraction and ^{2}H NMR by Eilbracht *et al.*[215] They report a phase transition in Li_2OHBr without a symmetry change due to a discontinuity of the thermal expansion of the lattice parameter and cell volume at ~60 °C. However, detailed crystallographic information was not reported.

This chapter describes attempts to modify the composition and, hence, the structure of Li_2OHCl via fluorine doping to form $Li_2(OH)_{0.9}F_{0.1}Cl$, and halide mixing to produce samples in the series $Li_2OHCl_{1-x}Br_x$ (x = 0.1 – 1). In a similar manner to Li_2OHCl, the samples discussed in this chapter were prepared via air-sensitive methods and studied via a combination of diffrac-

tion and NMR techniques to observe any structural changes occurring upon substitution and to understand the subsequent effects these may have on their physical properties.

7.2 Experimental

7.2.1 Synthesis

Samples of $Li_2(OH)_{0.9}F_{0.1}Cl$ and $Li_2OHCl_{1-x}Br_x$ (x = 0.1 – 1), were synthesised via the muffle furnace method described in Chapter 3, using LiCl (Alfa Aesar, ultra dry, 99.9%), LiOH (Acros Organics, anhydrous, 98%), LiF (Acros Organics, anhydrous, 99.98%) and LiBr (Alfa Aesar, ultra dry, 99.9%) as precursors. The powdered samples were placed in an alumina or zirconia crucible and heated at 350 °C for 30 mins in a muffle furnace located inside an Ar-filled glovebox. Once the reaction was complete, the furnace was allowed to cool to room temperature and the sample was recovered. Samples of $Li_2(OH)_{0.9}F_{0.1}Cl$, Li_2OHBr and $Li_2OHCl_{0.4}Br_{0.6}$ were deuterated using LiOD as a precursor and the synthetic procedures outlined above. The preparation method for LiOD is described in Chapter 4.

7.2.2 X-ray Diffraction

All samples were ground using an agate mortar and pestle and packed into 0.7 mm special glass capillaries, inside an Ar-filled glovebox. All XRD patterns were recorded on a Bruker d8 diffractometer using Mo (λ = 0.71073 Å) radiation. All scans were acquired for 2θ = 5 – 40°, with a step size of 0.01° and a step time of 2 seconds. During all scans, the capillary was continually rotated at 60 rpm to reduce the effects of preferred orientation. VT XRD patterns were also acquired for Li_2OHBr on the Bruker d8 diffractometer, where the temperature was increased at 10 °C per hour from −163 to 77 °C, whilst continuously recording the diffraction pattern. The experimental temperatures were controlled via an Oxford Cryosystems Cryostream and set using the Cryopad control software. Rietveld refinements were completed using the GSAS-II software.[150] Parameters including the background, unit cell size, isotropic thermal

coefficients, and the peak profile coefficients were refined.

7.2.3 Solid-State NMR

All solid-state NMR spectra were acquired using a Bruker 500 Avance III HD spectrometer, equipped with a wide-bore 11.7 T Oxford magnet, using Larmor frequencies of 499.69 MHz for ^{1}H (I = 1/2), 76.77 MHz for ^{2}H (I = 1), 194.20 MHz for ^{7}Li (I = 3/2), 49.00 MHz for ^{35}Cl (I = 3/2) and 125.30 MHz for ^{79}Br (I = 3/2). Powdered samples were packed into conventional 4.0 mm ZrO_2 rotors under an Ar atmosphere and placed into a Bruker 4.0 mm HX probe. A MAS rate of 10 kHz was employed, unless otherwise stated. ^{1}H chemical shifts were referenced to neat tetramethylsilane, by setting the resonance from a sample of adamantane to δ_{iso} = 1.9 ppm. ^{7}Li chemical shifts were referenced to 1 M $LiCl_{(aq)}$. ^{2}H chemical shifts were referenced to $(CD_3)_4Si$ using a sample of $CDCl_3$, δ_{iso} = 7.24 ppm. ^{35}Cl chemical shifts were referenced to 1 M $NaCl_{(aq)}$. ^{79}Br chemical shifts were referenced to 1 M NaBr in D_2O using a sample of KBr, δ_{iso} = 0 ppm.

Standard VT ^{1}H, ^{2}H and ^{7}Li MAS NMR experiments were completed between −19 and 110°C using conventional hardware. All ^{1}H MAS NMR spectra were acquired using a background suppression (DEPTH)[197] experiment with typical $\pi/2$ and π pulse lengths of 4 and 8 μs, respectively. Conventional ^{7}Li MAS NMR spectra were obtained using a single pulse experiment with a typical pulse length of 1.5 μs. During the acquisition, proton decoupling was applied using SPINAL-64,[198] with a RF field of 32 kHz. Typical RF field strengths of 62 – 166 kHz were employed. ^{1}H and ^{7}Li T_1 values were measured using a saturation recovery experiment. Static and MAS ^{2}H NMR spectra were obtained using a solid-echo ($90°_x - \tau - 90°_y - \tau$) experiment with a pulse length of 4 μs and RF field of 62.5 kHz.

VT ^{35}Cl MAS NMR spectra were acquired between 33 – 109 °C using a hahn-echo ($90°_x - \tau - 180°_y - \tau$) experiment with a pulse length of 4 μs and RF field of 62.5 kHz. ^{79}Br MAS NMR spectra were acquired across the temperature range −14 – 106 °C using a single pulse experiment with a pulse length of 3 μs

and RF field of 83.3 kHz.

VT ^{19}F MAS NMR experiments were completed over the temperature range −14 to 106 °C using a Bruker 400 Avance III HD spectrometer, equipped with a wide-bore 9.4 T magnet, using a Larmor frequency of 376.50 MHz for ^{19}F (I = 1/2). Chemical shifts were referenced to trichlorofluoromethane (CCl_3F). The sample was packed into a 3.2 mm ZrO_2 rotor inside an Ar-filled glovebox and placed into a Bruker 3.2 mm HFX probe. A MAS rate of 20 kHz was employed for all ^{19}F MAS NMR experiments. VT ^{19}F MAS NMR spectra were acquired using a hahn-echo ($90°_x - \tau - 180°_y - \tau$) experiment with a pulse length of 3 μs and RF field of 83.3 kHz. ^{19}F T_1 values were measured using a saturation recovery experiment.

Specific details regarding the recycle delays used are provided in the relevant figure captions. In all cases, quoted temperatures have been calibrated and reflect the true temperature of the sample during the experiment. Selected NMR spectra were fitted using the SOLA tool in Topspin 4.0.

7.3 Results and Discussion

7.3.1 $Li_2(OH)_{0.9}F_{0.1}Cl$

7.3.1.1 Synthesis

As stated earlier, the composition of Li_2OHCl can be altered via fluorine doping, and a fluorine-doped analogue of Li_2OHCl, $Li_2(OH)_{0.9}F_{0.1}Cl$, is reported to exhibit a much higher ion conductivity than Li_2OHCl.[234] In order to understand the ion dynamics in $Li_2(OH)_{0.9}F_{0.1}Cl$, a sample was prepared and studied extensively via multinuclear VT SSNMR. The synthesis was completed using the same reaction conditions as Li_2OHCl prepared via the muffle furnace method (*vide supra*). Here, OH^- is being partially replaced by F^-. Even though fluorine is a halide, it is expected to occupy the OH^- site rather than the Cl^- site, based on their similar ionic radii ($r_{ion}F^-$ = 1.33 Å and $r_{ion}OH^-$ = 1.37 Å).[11] The XRD pattern obtained for the sample synthesised is shown in Figure 7.1(a). Also shown are the diffraction patterns obtained for the reagents,

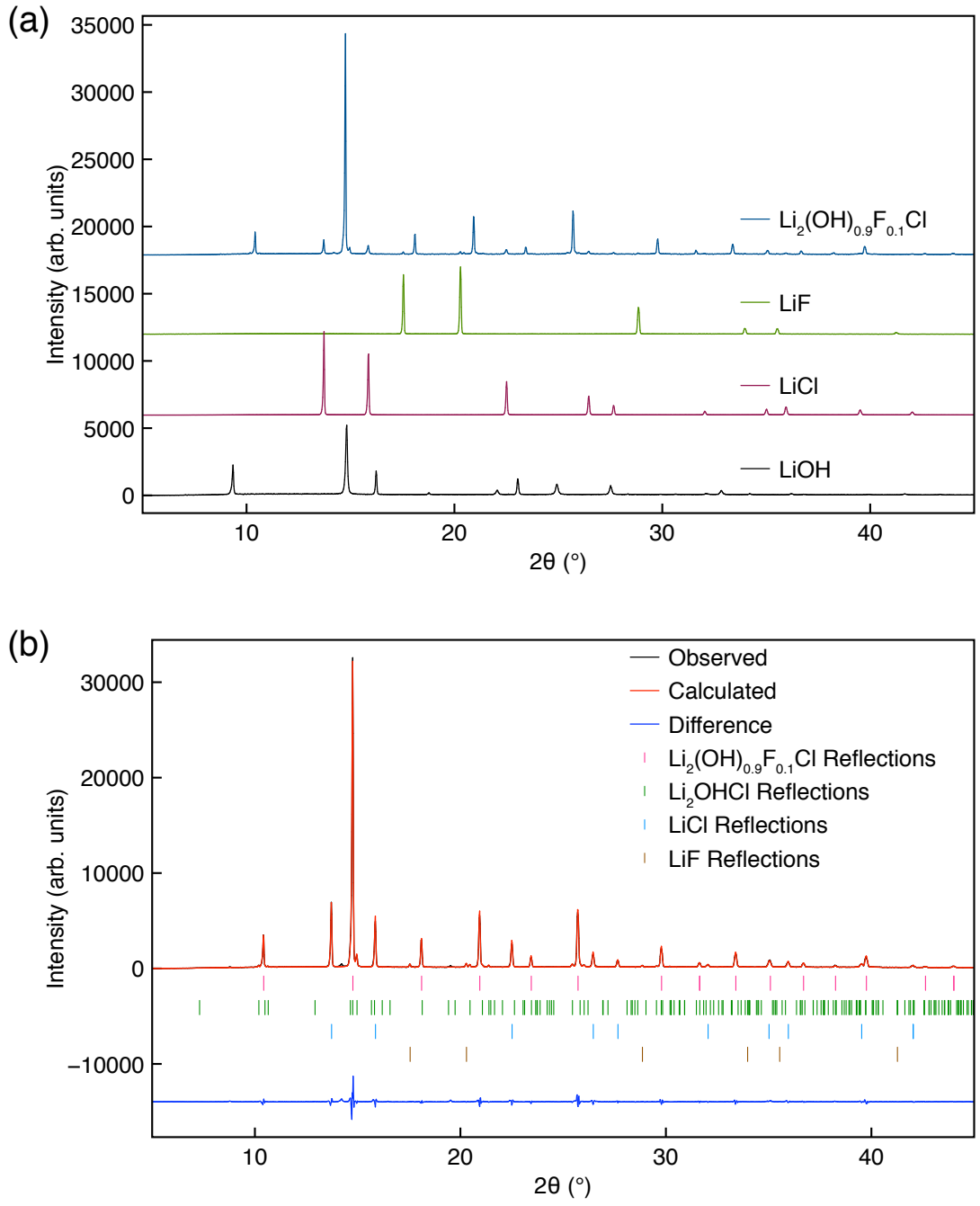

Figure 7.1: (a) X-ray diffraction pattern obtained for a sample of $Li_2(OH)_{0.9}F_{0.1}Cl$ synthesised via a conventional solid-state reaction completed inside an Ar-filled glovebox. The reaction temperature was 350 °C and the reaction time was 30 mins. Also shown for comparison are the diffraction patterns obtained for the reagents, LiF, LiCl and LiOH. (b) Rietveld refinement of the XRD data for $Li_2(OH)_{0.9}F_{0.1}Cl$ using the $Pm\bar{3}m$ ($Li_2(OH)_{0.9}F_{0.1}Cl$), *Pban* (Li_2OHCl) and $Fm\bar{3}m$ (LiCl and LiF) structural models.[199,236] χ^2 = 4.19, wR_P = 11.15%, R_P = 8.57%.

LiF, LiCl and LiOH. The diffraction pattern obtained for $Li_2(OH)_{0.9}F_{0.1}Cl$ appears to resemble that of the high-temperature phase of Li_2OHCl, suggesting a cubic phase in space group $Pm\bar{3}m$ has been formed. There also appear to be reflections corresponding to LiCl and LiF, suggesting the presence of residual starting materials. However, there are no reflections to indicate the presence of LiOH. Similar observations were made for the parent material, Li_2OHCl.

Rietveld analysis was completed using the XRD data and the $Pm\bar{3}m$ ($Li_2(OH)_{0.9}F_{0.1}Cl$), *Pban* (Li_2OHCl) and $Fm\bar{3}m$ (LiCl and LiF)[199,236] structural models. The refinement is shown in Figure 7.1(b), and the corresponding structural parameters, including the isotropic thermal coefficients, are detailed in Table 7.1. At first glance, the fit obtained appears to be of a very good quality with a $\chi^2 = 4.19$ and $wR_p = 11.15\%$. All major reflections are indexed using the

Table 7.1: Structural parameters obtained for a sample of $Li_2(OH)_{0.9}F_{0.1}Cl$ synthesised via a conventional solid-state reaction completed inside an Ar-filled glovebox, from Rietveld refinement of the XRD data using isotropic thermal coefficients. $Li_2(OH)_{0.9}F_{0.1}Cl$: space group $Pm\bar{3}m$, a = 3.91029(4) Å, V = 59.790(2) Å^3, phase fraction = 64.28(34)%. Li_2OHCl: space group *Pban*, a = 7.77402(82) Å, b = 8.00049(71) Å, c = 3.82989(37) Å, V = 238.204(27) Å^3, phase fraction = 28.34(35)%. LiCl: space group $Fm\bar{3}m$, a = 5.14850(9) Å, V = 136.471(7) Å^3, phase fraction = 6.07(6)%. LiF: space group $Fm\bar{3}m$, a = 4.03374(36) Å, V = 65.633(17) Å^3, phase fraction = 1.31(11)%. $\chi^2 = 4.19$, $wR_P = 11.15\%$, $R_P = 8.57\%$.

Atom	x	y	z	Occ.	U(iso) × 100 (Å^2)
$Li_2(OH)_{0.9}F_{0.1}Cl$					
Li	0.5	0	0	0.667	7.6(3)
O	0	0	0	0.9	2.5(17)
H	0.1279	0.1279	0.1279	0.113	2.5(17)
F	0	0	0	0.1	3.0(141)
Cl	0.5	0.5	0.5	1	2.9(1)
LiCl					
Li	0.0	0.0	0.0	1	3.7(4)
Cl	0.5	0.5	0.5	1	2.2(1)
LiF					
Li	0.5	0.5	0.5	1	1.1(10)
F	0.0	0.0	0.0	1	1.5(8)

models included in the refinement, and there is an excellent match between the observed and calculated reflection intensities. The refinement confirms that $Li_2(OH)_{0.9}F_{0.1}Cl$ exists in a cubic structure in space group $Pm\bar{3}m$. Thus, indicating that fluorine doping stabilises the cubic phase at room temperature. These findings are in agreement with those reported by Li *et al.*,[234] who reasoned that fluorine substitution increases the tolerance factor (Equation 1.3) of the material, and therefore, the sample produced adopts a cubic structure. A lattice parameter of 3.91029(4) Å is obtained for $Li_2(OH)_{0.9}F_{0.1}Cl$, which agrees with the values previously reported in the literature for the high-temperature cubic phase of Li_2OHCl. Unfortunately, Li *et al.*[234] did not report any crystallographic information for $Li_2(OH)_{0.9}F_{0.1}Cl$. Therefore, a direct comparison of structural parameters is not possible.

It is noted that there are two reflections of very low intensity at 2θ = 14.23 and 19.54°, that do not correspond to any of the expected phases. Thus, suggesting the presence of an impurity phase. Earlier, the diffraction pattern corresponding to Li_2OHCl was also observed to exhibit an additional reflection at 2θ = 14.21°. This suggests that the impurity phase(s) present in the Li_2OHCl sample may also be present in this sample. The $Li_2(OH)_{0.9}F_{0.1}Cl$ sample also contains residual LiCl and LiF, suggesting that not all the F^- added was successfully incorporated into the structure. Consequently, the exact value of x in $Li_2(OH)_{1-x}F_xCl$ likely differs somewhat from 0.1, meaning the composition of the desired phase is not exactly as intended. Unfortunately, the fractional occupancies cannot be refined to obtain reliable values due to the low resolution of laboratory XRD data. Thus, the precise composition of the desired phase cannot be determined using this data alone. Hence, the fractional occupancies for atoms in the $Pm\bar{3}m$ phase were fixed to reflect the intended composition of $Li_2(OH)_{0.9}F_{0.1}Cl$. Furthermore, inspection of the thermal coefficients obtained for atoms in $Li_2(OH)_{0.9}F_{0.1}Cl$ indicates an unusually large value for Li. This is similar to the observations made for all of the LiRAP samples discussed thus far and agrees with the literature.[210] Earlier, it was suggested that it is most likely due to discrepancies in the structural model, *i.e.*, inaccurate atomic coordinates and/or occupancies or ion mobility in the samples. This could also be

the case for this sample as the occupancy values used in the model most likely differ in reality, as evidenced by the presence of residual LiCl and LiF.

As stated earlier, the sample also appears to contain the parent material, Li_2OHCl. Thus, the new *Pban* model proposed and discussed in Chapter 4 (Figure 4.12 and Table 4.9) was included in the Rietveld analysis. The reflections believed to correspond to Li_2OHCl are successfully indexed using the *Pban* model. However, the fractional occupancies for Li and H could not be refined to sensible values as attempts at refinement consistently resulted in a negative fractional occupancy for Li2. Hence, the fractional occupancies were fixed to the values determined earlier for Li_2OHCl (Table 4.9). Additionally, attempts to refine the thermal coefficients produced several unrealistically large values. Thus, the thermal coefficients for all atoms in Li_2OHCl were fixed at 2.5×10^{-2} Å^2. Moreover, the thermal coefficient obtained for Li in LiCl is somewhat larger than expected, whereas the coefficients for both Li and F in LiF are quite small but have relatively large errors. As mentioned earlier, these issues are likely due to slight inaccuracies in some of the models used. It is possible that inaccuracies in the $Li_2(OH)_{0.9}F_{0.1}Cl$ and Li_2OHCl models also influence the structural parameters obtained for LiCl and LiF.

Lastly, the phase fractions were refined to determine the relative quantities of each phase present in the sample. The sample appears to contain 64.28(34)% $Li_2(OH)_{0.9}F_{0.1}Cl$, 28.34(35)% Li_2OHCl, 6.07(6)% LiCl and 1.31(11)% LiF. It is noted that this is not the precise composition of the sample owing to the presence of an unknown impurity phase, albeit in a very small quantity. The phase fractions determined are also likely to be affected by the structural parameters that could not be refined to sensible values. Nevertheless, the values stated above provide a reasonable indication of the actual sample composition. It appears that most of the sample consists of the desired phase. However, a sizeable amount of the parent material, Li_2OHCl, is also produced. The starting materials, on the other hand, are present in relatively low quantities. Interestingly, as with Li_2OHCl, only the lithium halides are leftover. No LiOH is detected. Earlier, it was suggested that this could be due to lithium halide-based defects in the structure. These defects may also be present in

the fluorine-doped sample. Hence, the presence of residual LiCl and LiF. In addition, Effat and co-workers[235] have suggested that $Li_2(OH)_{0.9}F_{0.1}Cl$ is a metastable phase that is likely to decompose to form LiCl, LiF and $Li_4(OH)_3Cl$. This could explain the presence of residual LiCl and LiF and a small impurity phase. Moreover, Effat and co-workers[235] proposed $Li_2OHCl_{0.9}F_{0.1}$ as a viable composition with a formation energy similar to Li_2OHCl and $Li_2(OH)_{0.9}F_{0.1}Cl$. Thus, it is possible that some of the F^- could have occupied the Cl sites. This could explain the presence of residual LiCl and the difficulties in obtaining sensible structural parameters during refinement. However, these suggestions cannot be confirmed for certain via laboratory XRD data. High-resolution diffraction studies would need to be completed for a thorough characterisation of $Li_2(OH)_{0.9}F_{0.1}Cl$.

7.3.1.2 SSNMR Studies of $Li_2(OH)_{0.9}F_{0.1}Cl$

^{1}H MAS NMR Spectroscopy

$Li_2(OH)_{0.9}F_{0.1}Cl$ was analysed via VT SSNMR spectroscopy for further characterisation and to study ion dynamics within the sample. The ^{1}H MAS NMR spectra acquired between −19 and 106 °C are shown in Figure 7.2(a). In all cases, a single resonance is observed. The spectrum acquired below room temperature is very similar to that obtained for the room-temperature phase of Li_2OHCl, *i.e.*, a relatively broad resonance with two sets of spinning sidebands. As previously discussed, this is characteristic of OH groups. At 33 °C, the resonance maintains its broad lineshape. However, the spinning sidebands are reduced in intensity, and the resonance exhibits an increase in intensity. The spectrum appears to resemble that of the high-temperature cubic phase of Li_2OHCl. Further increases in temperature to 63 and then 106 °C result in considerably narrower lineshapes with greater intensities.

The corresponding variation in FWHM is shown in Figure 7.2(b). Here, the trend differs from that observed for the parent material, Li_2OHCl. In fact, the trend observed is somewhat unusual. The linewidth increases slightly between −19 to 33 °C, and from then on, the lineshape narrows significantly with

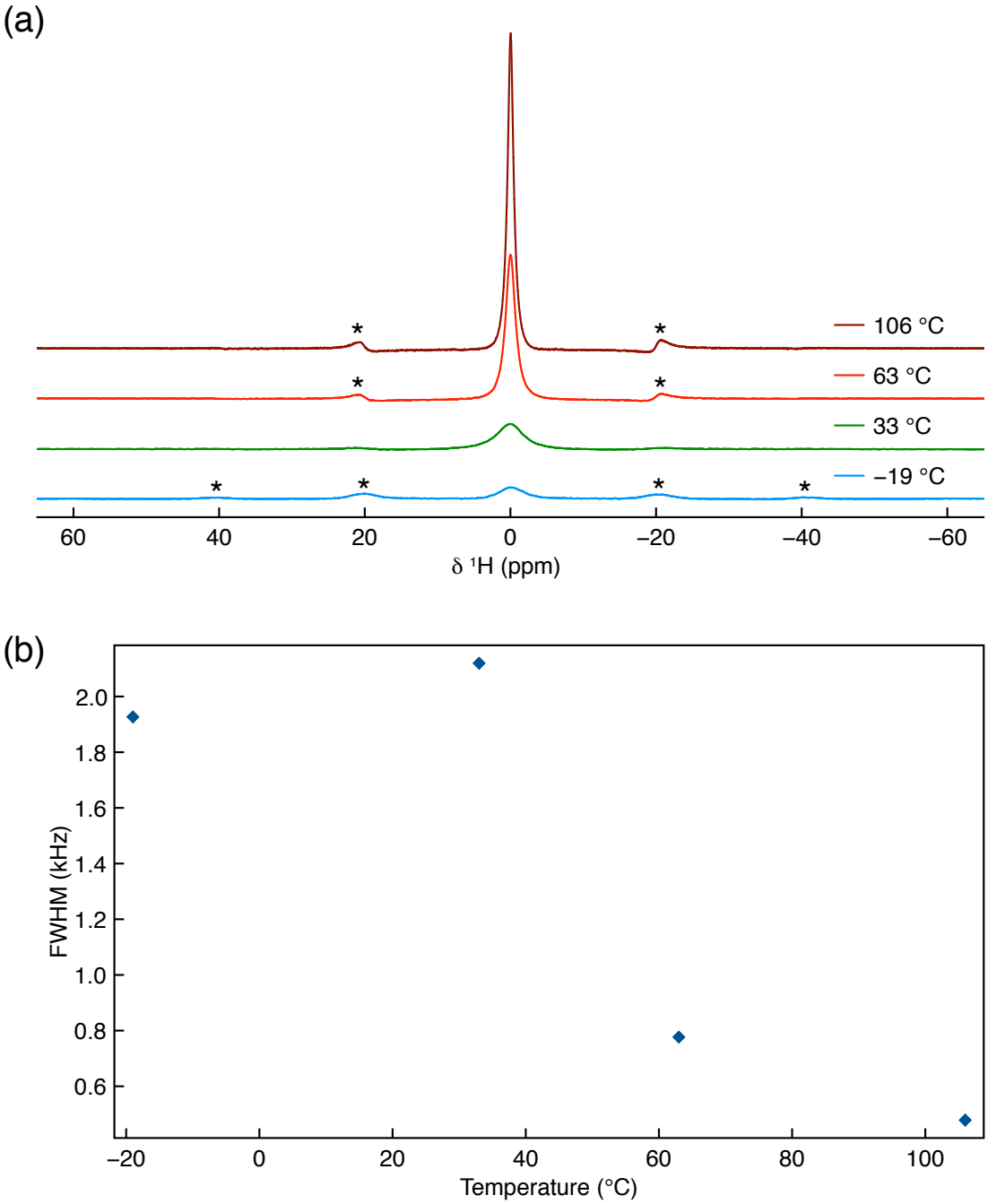

Figure 7.2: (a) VT ^{1}H (11.7 T) MAS NMR spectra acquired between −19 and 106 °C for a sample of $Li_2(OH)_{0.9}F_{0.1}Cl$ synthesised via a conventional solid-state reaction completed inside an Ar-filled glovebox. The MAS rate was 10 kHz and spinning sidebands are denoted by *. In all cases, a recycle delay of 60 s was used to acquire 4 transients. (b) The corresponding variation in FWHM as a function of temperature.

increasing temperature. As discussed in Chapter 2, changes in the linewidth are typically indicative of structural changes or ion mobility within the sample. As observed earlier for Li_2OHCl, ion mobility results in a gradual line

narrowing, as it does here between 33 and 106 °C. Thus, suggesting that the protons in $Li_2(OH)_{0.9}F_{0.1}Cl$ become mobile between 33 and 106 °C. However, the broadening of the lineshape from −19 to 33 °C suggests a different type of structural change, perhaps a phase transition. Unfortunately, the exact nature of the structural change is unclear at present.

^{7}Li MAS NMR Spectroscopy

The VT ^{7}Li MAS NMR spectra acquired for $Li_2(OH)_{0.9}F_{0.1}Cl$ over the temperature range −19 to 106 °C are shown in Figure 7.3(a). Below room temperature, at −19 and 8 °C, a broad lineshape with multiple spinning sidebands is observed. Again, this is similar to that observed for the room-temperature phase of Li_2OHCl. At 33 °C, the resonance narrows, and the spinning sidebands are barely visible. This is similar to the high-temperature cubic phase of Li_2OHCl. This change is also similar to that observed earlier for ^{1}H NMR. This suggests that the structure of $Li_2(OH)_{0.9}F_{0.1}Cl$ may exhibit significant changes at lower temperatures. Increasing the temperature to 63 and then 106 °C results in a continuous line narrowing.

Closer inspection of the lineshapes obtained (Figure 7.3(b)) suggests two distinct resonances are present. One is centred around 0 ppm, and the other around −1.5 ppm. From diffraction, it is evident that four distinct phases are present in the sample, $Li_2(OH)_{0.9}F_{0.1}Cl$, Li_2OHCl, LiCl and LiF. Both starting materials, LiCl and LiF, are reported to exhibit a ^{7}Li chemical shift of −1.1 ppm.[212] The resonance for LiCl is reportedly sharp and narrow, whereas that of LiF is slightly broader. Hence, the resonance at ∼−1.5 ppm likely corresponds to the starting materials. The lineshape observed is similar to that reported for LiF, but it is most likely composed of two overlapping resonances. The resonance at ∼0 ppm is believed to correspond to both the desired phase and Li_2OHCl because it occurs at the same shift as the resonance observed for Li_2OHCl in Chapter 4 (Figure 4.28). However, unfortunately, it is not possible to distinguish between the two owing to considerable spectral overlap. It is noted that the resonance corresponding to the desired phase changes with increasing temperature, whereas those corresponding to the starting materials

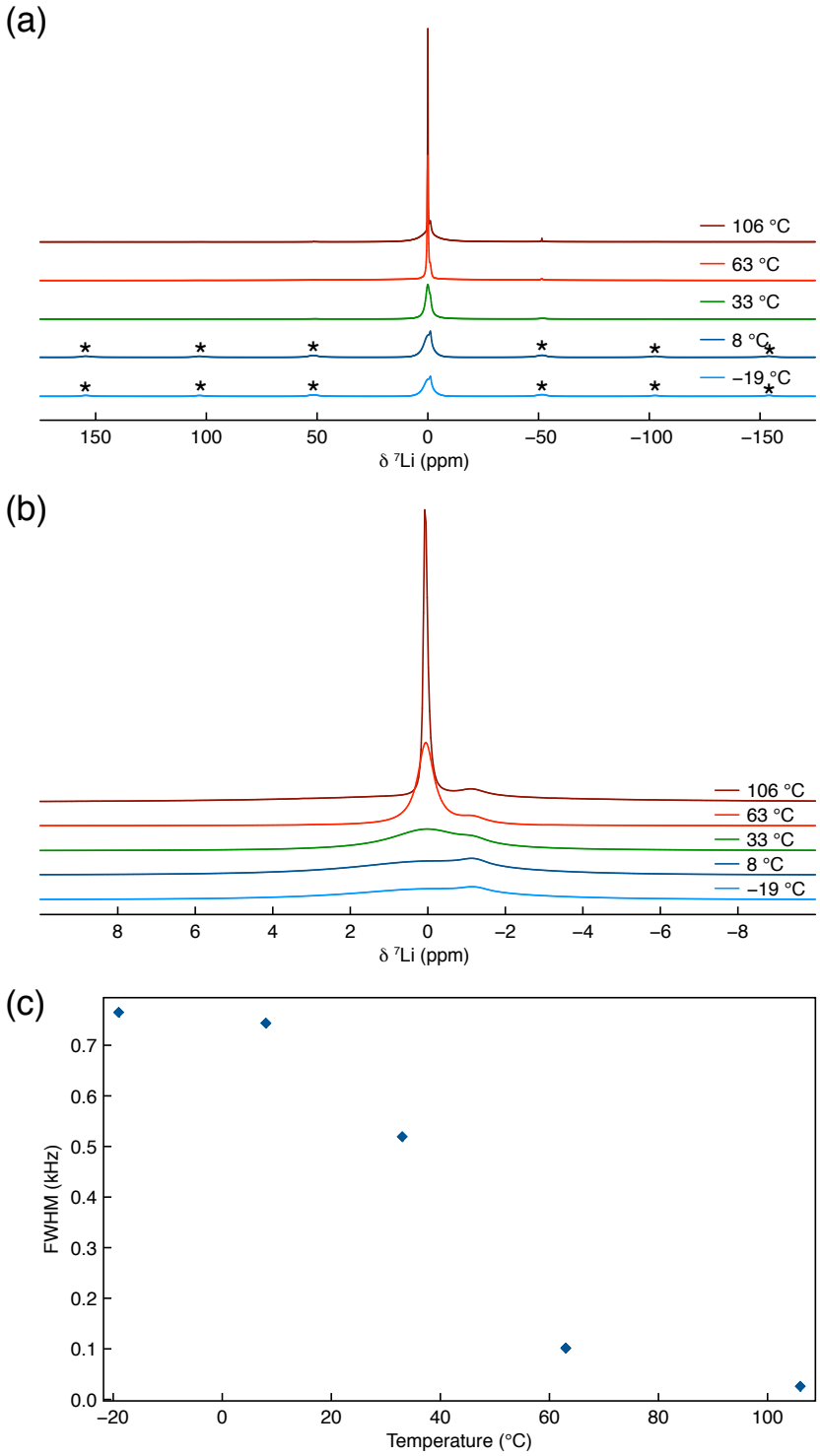

Figure 7.3: (a) VT ^{7}Li (11.7 T) MAS NMR spectra acquired between −19 and 106 °C for a sample of $Li_2(OH)_{0.9}F_{0.1}Cl$ synthesised via a conventional solid-state reaction completed inside an Ar-filled glovebox. The MAS rate was 10 kHz and spinning sidebands are denoted by *. In all cases, a recycle delay of 60 s was used to acquire 4 transients. (b) Expansion of the VT ^{7}Li MAS NMR spectra and (c) the corresponding variation in FWHM as a function of temperature.

remains the same.

The variation in linewidth observed for the dominant resonance, corresponding to the desired phase, is shown as a plot of the FWHM vs. temperature in Figure 7.3(c). Here, the linewidth decreases gradually with increasing temperature. As previously discussed, gradual line narrowing typically suggests ion mobility. Thus, it appears that, in a similar manner to Li_2OHCl, $Li_2(OH)_{0.9}F_{0.1}Cl$ also exhibits Li-ion mobility. This is in agreement with predictions made by Effat and co-workers.[235] A comparison to the FWHM presented earlier for ^1H suggests that Li-ions become mobile much earlier than the protons. Moreover, comparing the trend in FWHM to that observed for Li_2OHCl indicates that $Li_2(OH)_{0.9}F_{0.1}Cl$ exhibits mobility at lower temperatures than Li_2OHCl.

^{2}H MAS NMR Spectroscopy

To gain an understanding of the mobility of the protons or, more specifically the OH^- groups, a sample of $Li_2(OH)_{0.9}F_{0.1}Cl$ was deuterated and analysed via ^2H MAS NMR spectroscopy. The XRD pattern corresponding to the deuterated sample is shown in Figure 7.4. Also shown for comparison is the diffraction pattern for the non-deuterated sample. Both diffraction patterns look identical, suggesting the deuterated sample was synthesised successfully. The ^2H MAS NMR spectra obtained at temperatures ranging from −19 to 106 °C are shown in Figure 7.5. At lower temperatures (−19 and 8 °C), the lineshapes observed are similar to those obtained for the room-temperature phase of Li_2OHCl, an axially symmetric lineshape composed of multiple spinning sidebands indicative of static OH^-/OD^- groups. It is noted that the lineshape observed at 8 °C is less intense, suggesting some loss of signal. The lineshape observed at −19 °C was simulated to extract the corresponding quadrupolar parameters (Figure 7.6). A C_Q = 256(1) kHz and η_Q = 0.06(1) were obtained, which are very close to those obtained for the room-temperature phase of Li_2OHCl. Thus, confirming the presence of static OH^-/OD^- groups. Surprisingly, as the temperature is increased to 33 °C, the ^2H signal vanishes completely. A further increase in temperature to 69 °C produces little change as

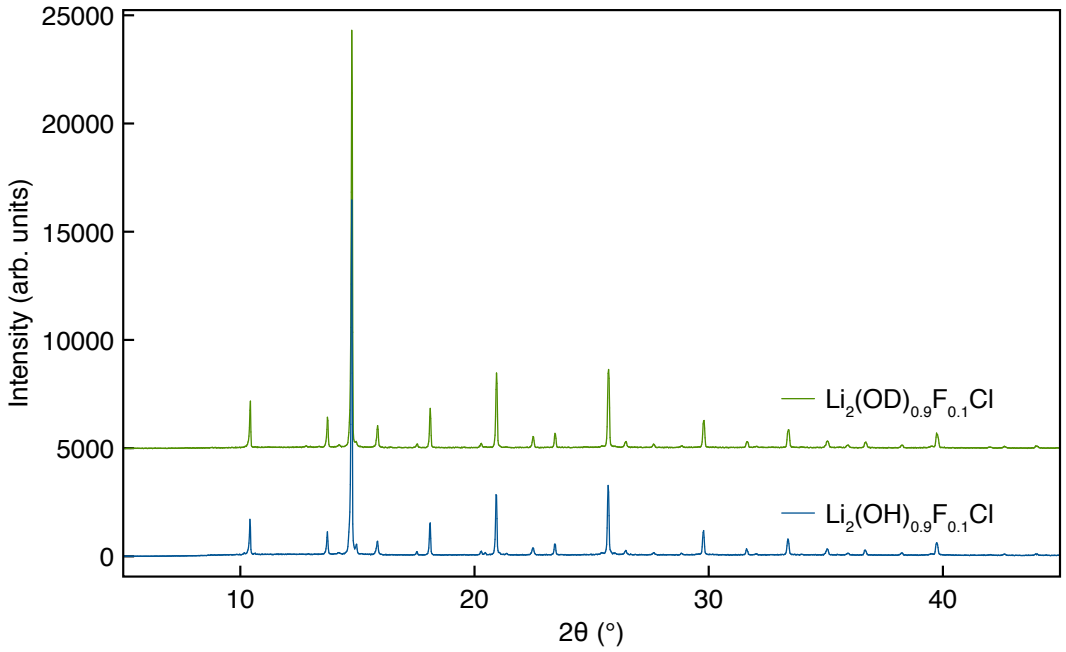

Figure 7.4: X-ray diffraction patterns corresponding to $Li_2(OD)_{0.9}F_{0.1}Cl$ and $Li_2(OH)_{0.9}F_{0.1}Cl$ synthesised via a conventional solid-state reaction inside an Ar-filled glovebox. The reaction temperature was 350 °C and the reaction time was 30 mins.

barely any signal is observed. It is noted that the ^2H MAS NMR spectra presented for Li_2OHCl and $Li_{2.5}OH_{0.5}Cl$ also exhibited a lower signal to noise ratio with increasing temperatures. However, the signal was still observable. Finally, at 106 °C, a single, resonance is observed. Based on similar data obtained for Li_2OHCl and $Li_{2.5}OH_{0.5}Cl$, this resonance is believed to indicate mobile or freely rotating OH^-/OD^- groups.

To investigate the signal disappearance at 33 and 69 °C, additional spectra were acquired with a greater number of transients (Figure 7.7). In both cases, signal is now detectable, but the signal to noise is extremely poor. At 33 °C, a lineshape indicative of static OH^-/OD^- groups is observed, whereas at 69 °C, two distinct resonances can be differentiated. One is similar to that observed between −19 and 33 °C and is believed to correspond to the static OH^-/OD^- groups. The other is broad and believed to correspond to mobile OH^-/OD^- groups. Thus, suggesting that at 69 °C, both species are present simultaneously. The ^2H MAS NMR data shown here is extremely interesting and informative. Firstly, considering the ^2H MAS NMR in conjunction with the ^1H and ^7Li MAS NMR presented earlier, it appears that $Li_2(OH)_{0.9}F_{0.1}Cl$

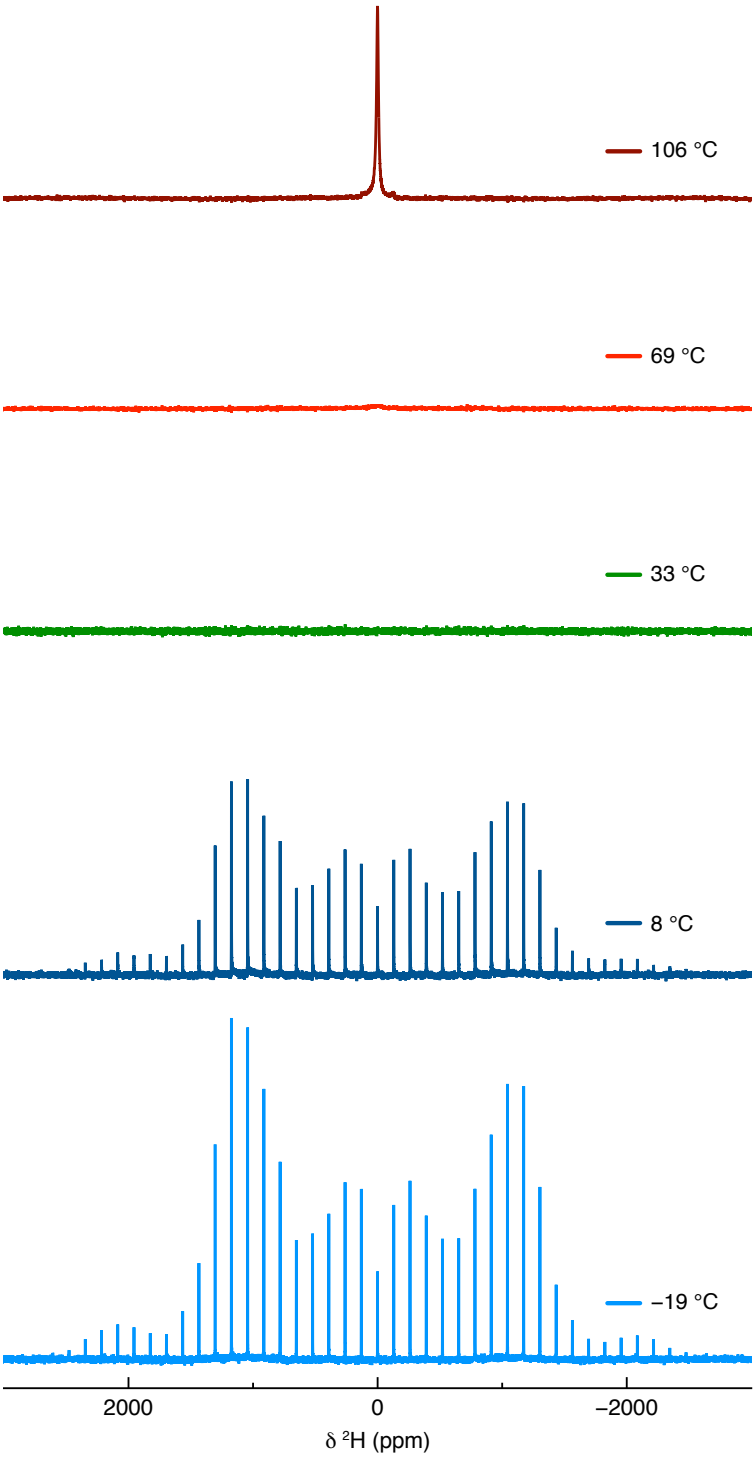

Figure 7.5: VT ^{2}H (11.7 T) MAS NMR spectra acquired between −19 and 106 °C for a sample of $Li_2(OH)_{0.9}F_{0.1}Cl$ synthesised via a conventional solid-state reaction completed inside an Ar-filled glovebox. The MAS rate was 10 kHz. In all cases, a recycle delay of 15 s was used to acquire 80 transients.

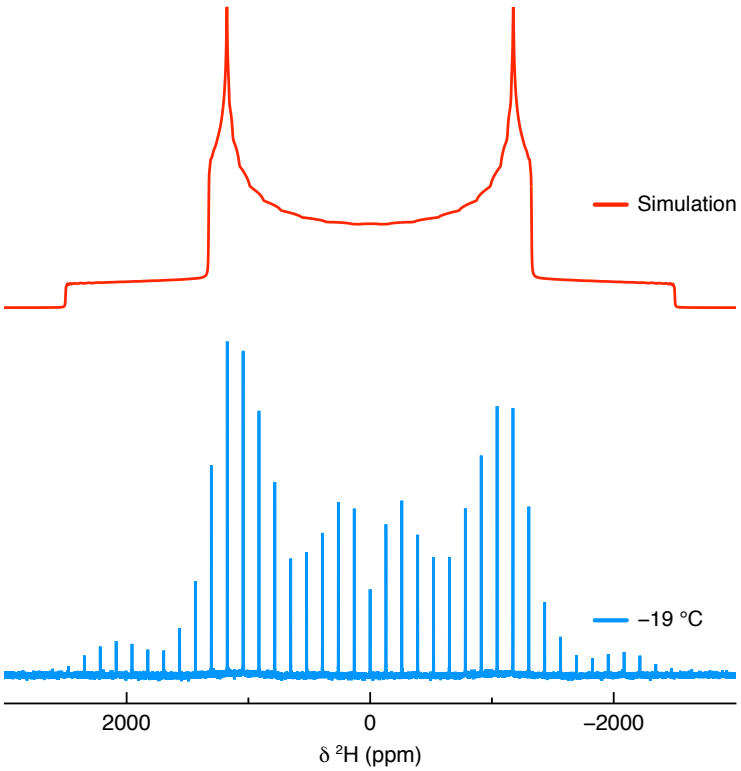

Figure 7.6: The ^{2}H (11.7 T) MAS NMR spectrum obtained at −19 °C for a sample of $Li_2(OH)_{0.9}F_{0.1}Cl$ synthesised via a conventional solid-state reaction completed inside an Ar-filled glovebox. The MAS rate was 10 kHz. A recycle delay of 15 s was used to acquire 80 transients. The spectrum was simulated to obtain the corresponding quadrupolar parameters, C_Q = 256(1) kHz and η_Q = 0.06(1).

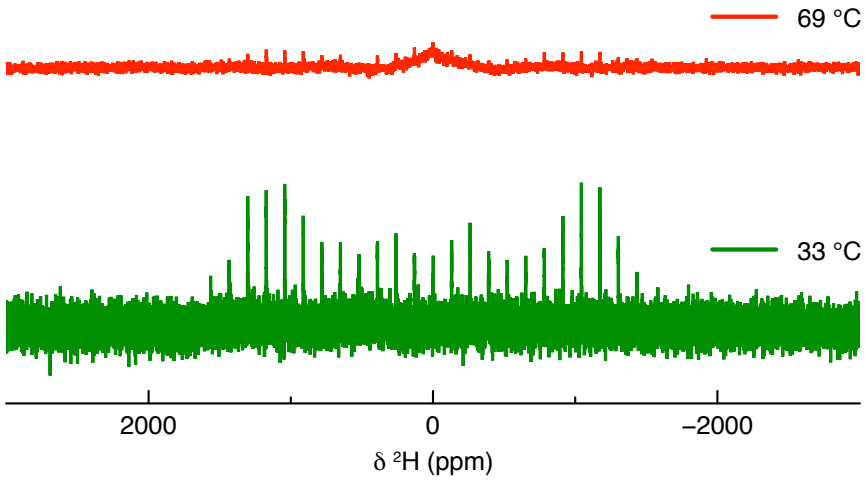

Figure 7.7: VT ^{2}H (11.7 T) MAS NMR spectra acquired at 33 and 69 °C for a sample of $Li_2(OH)_{0.9}F_{0.1}Cl$ synthesised via a conventional solid-state reaction completed inside an Ar-filled glovebox. The MAS rate was 10 kHz. A recycle delay of 15 s was used to acquire 3200 and 400 transients at 33 and 69 °C, respectively.

may be undergoing a phase transition as there is a clear difference between the spectra acquired above and below room temperature. Secondly, the fact that the ^{2}H signal almost disappears and then re-appears at higher temperatures indicates some significant structural changes to the local ^{2}H environment. At present, it is not known precisely what structural changes are causing the removal of signal from the ^{2}H MAS NMR spectrum. As such, additional studies are needed.

^{35}Cl MAS NMR Spectroscopy

To understand this system further, the $Li_2(OH)_{0.9}F_{0.1}Cl$ sample was analysed via VT ^{35}Cl MAS NMR spectroscopy, and the spectra acquired between −19 and 106 °C are shown in Figure 7.8. Below room temperature, at −19 and 8 °C, a broad resonance is observed, which appears to indicate multiple overlapped sites. The lineshape obtained is similar to that observed for the room-temperature phase of Li_2OHCl. It is noted that a signal corresponding to LiCl, which is present in the sample as an impurity, is also observed. At 33 °C, the lineshape observed changes significantly, as many of the distinct features of the lineshape disappear and a broad resonance centred around −100 ppm, similar to that of the high-temperature cubic phase of Li_2OHCl in space group $Pm\bar{3}m$, is observed. As the temperature is increased further to 63 °C, the lineshape remains unchanged. However, the intensity of the signal observed decreases. Finally, at 106 °C, a severe drop in intensity is observed, and the resonance is barely visible. A similar trend was observed for Li_2OHCl and $Li_{2.5}OH_{0.5}Cl$. This phenomenon was discussed in detail in Chapter 5. It was suggested that the EFG experienced by Cl could constantly be changing, making the signal unobservable. This could occur by the movement of Cl itself, or the movement of the surrounding species such as H and Li. ^{35}Cl EXSY experiments, in conjunction with MSD plots obtained via AIMD simulations, indicated that Cl does not exhibit any motion in Li_2OHCl. Thus, it was suggested that the reduction of the Cl signal is likely due to increased proton and Li-ion mobility at higher temperatures, causing the EFG experienced by Cl to change rapidly. As such, this makes it challenging to observe the ^{35}Cl NMR

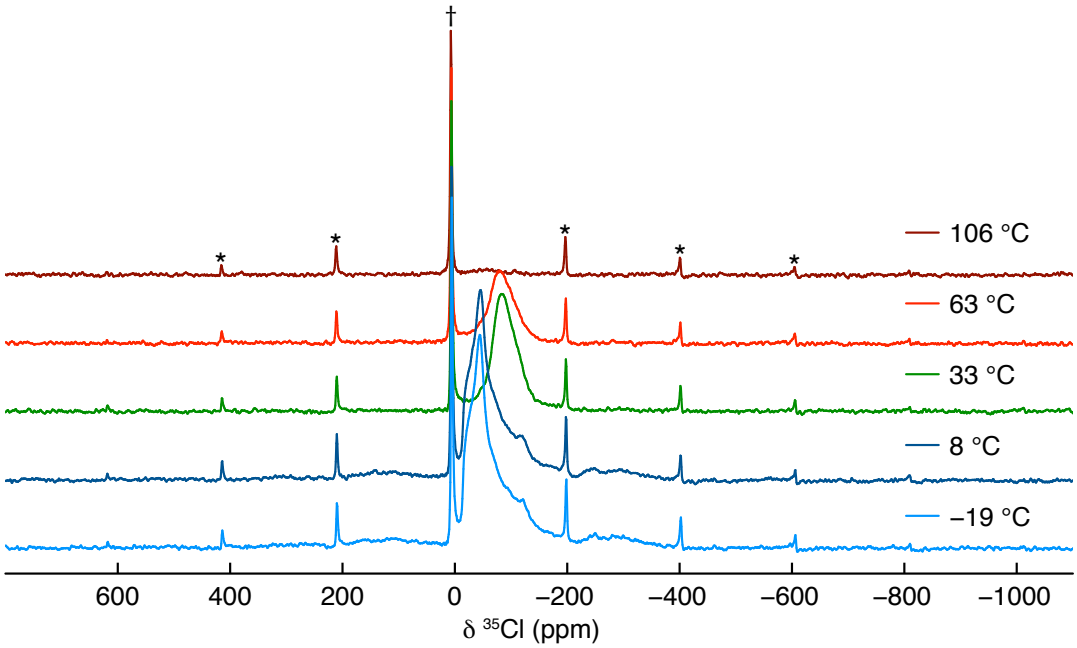

Figure 7.8: VT ^{35}Cl (11.7 T) MAS NMR spectra acquired between −19 and 106 °C for a sample of $Li_2(OH)_{0.9}F_{0.1}Cl$ synthesised via a conventional solid-state reaction completed inside an Ar-filled glovebox. The MAS rate was 10 kHz and spinning sidebands are denoted by *. In all cases, a recycle delay of 5 s was used to acquire 320 transients. LiCl impurity is denoted by †.

signal.

The lineshapes observed at 33 and −19 °C have been simulated to determine the number of distinct Cl sites present and extract the corresponding quadrupolar parameters. The simulated lineshapes with individual Cl sites are shown in Figure 7.9, and the corresponding quadrupolar parameters are detailed in Table 7.2. At 33 °C, two distinct Cl sites are observed with relatively low values of C_Q (Figure 7.9(a)). This was also the case for the high-temperature cubic phase of Li_2OHCl. However, it is noted that the values of η_Q differ from those obtained for the cubic phase of Li_2OHCl. This is unsurprising as the composition of this sample differs from Li_2OHCl. Thus, the EFG experienced by Cl will also differ slightly, resulting in different quadrupolar parameters. As discussed previously, for perfectly cubic systems, C_Q and η_Q will be close to or equal to 0. Thus, the parameters obtained here suggest a fairly symmetrical environment for Cl, but it does not seem perfectly cubic. Earlier, it was suggested that, similar to Li_3OCl, Li_2OHCl may be pseudo-cubic. Thus,

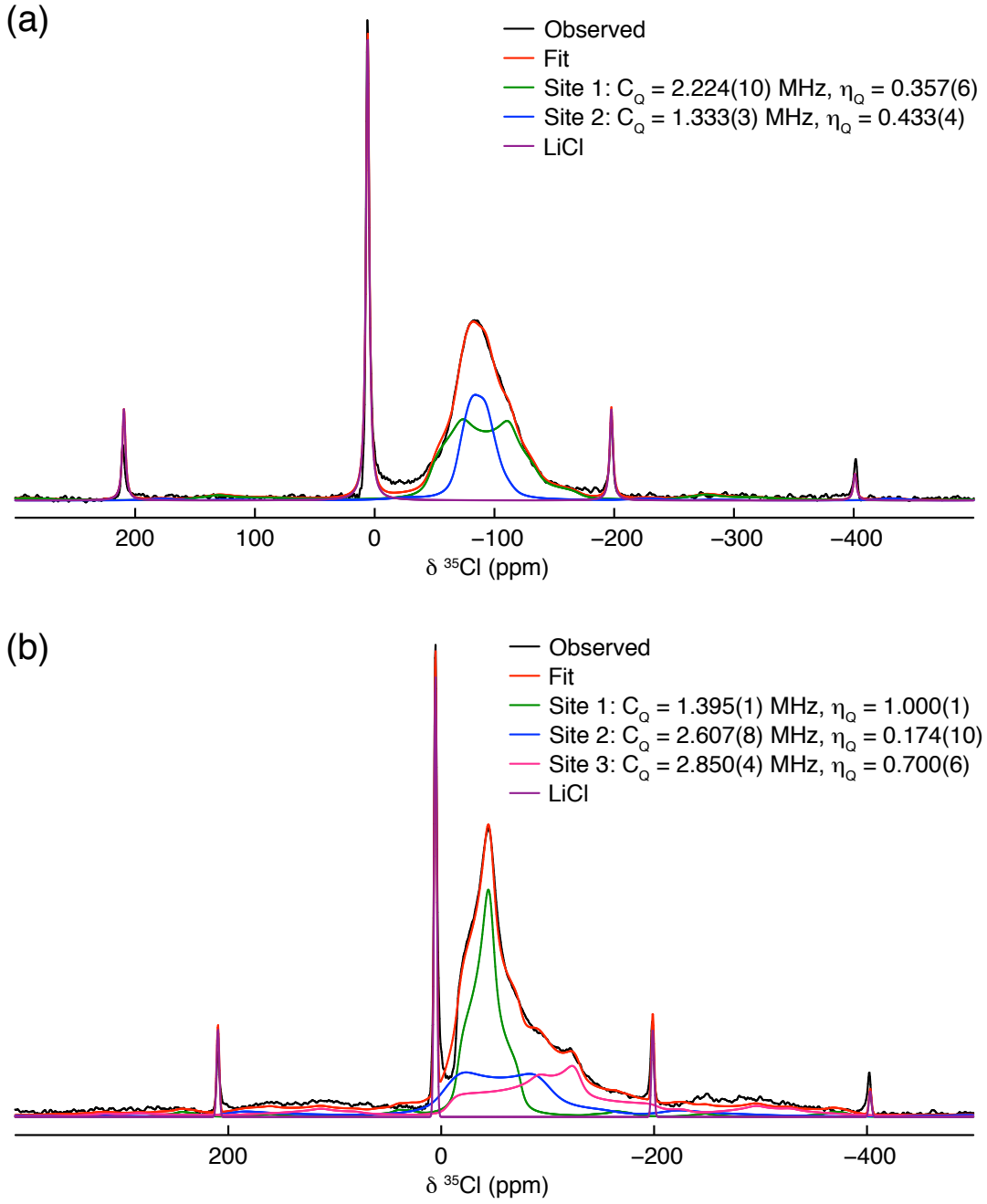

Figure 7.9: Simulations of the ^{35}Cl (11.7 T) MAS NMR spectra acquired at (a) 33 °C and (b) −19 °C for a sample of $Li_2(OH)_{0.9}F_{0.1}Cl$ prepared via conventional solid-state synthesis inside an Ar-filled glovebox. The MAS rate was 10 kHz and a recycle delay of 5 s was used to acquire 320 transients. At 33 °C, two sites were required to fit the lineshape and the corresponding quadrupolar parameters are: Site 1 (C_Q = 2.224(10) MHz and η_Q = 0.357(6)), Site 2 (C_Q = 1.333(3) MHz and η_Q = 0.433(4)). At −19 °C, three sites were required to fit the lineshape and the corresponding quadrupolar parameters are: Site 1 (C_Q = 1.395(1) MHz and η_Q = 1.000(1)), Site 2 (C_Q = 2.607(8) MHz and η_Q = 0.174(10)), Site 3 (C_Q = 2.850(4) MHz and η_Q = 0.700(6)).

Table 7.2: ^{35}Cl NMR parameters, δ, C_Q, and η_Q, obtained at 33 and −19 °C, for a sample of $Li_2(OH)_{0.9}F_{0.1}Cl$ prepared via conventional solid-state synthesis inside an Ar-filled glovebox.

Site	δ (ppm)	C_Q (MHz)	η_Q
33 °C			
1	−39.04(2)	2.224(10)	0.357(6)
2	−67.30(8)	1.333(3)	0.433(4)
−19 °C			
1	−15.50(7)	1.395(1)	1.000(1)
2	15.89(80)	2.607(8)	0.174(10)
3	−4.00(7)	2.850(4)	0.700(6)

it is possible that the fluorinated analogue of Li_2OHCl may also be pseudo-cubic. Alternatively, the long-range structure of $Li_2(OH)_{0.9}F_{0.1}Cl$ may indeed be cubic with a single crystallographic Cl site, but locally the Cl experiences two distinct Cl environments. At −19 °C, three distinct Cl sites were used to fit the spectrum accurately. This is similar to the room-temperature phase of Li_2OHCl. The lineshapes corresponding to these sites are, again, similar to those simulated for the room-temperature Li_2OHCl phase and have similar quadrupolar parameters. As with the $^{1/2}$H and ^{7}Li NMR data presented earlier, the ^{35}Cl NMR data also suggests that $Li_2(OH)_{0.9}F_{0.1}Cl$ likely undergoes a phase transition to adopt a different structure below room temperature.

^{19}F MAS NMR Spectroscopy

Finally, $Li_2(OH)_{0.9}F_{0.1}Cl$ was also analysed via VT ^{19}F MAS NMR spectroscopy, and the spectra acquired at temperatures ranging from −14 to 106 °C, are shown in Figure 7.10(a). In all cases, two distinct resonances centred around δ_{iso} = −178 and −205 ppm are observed. The diffraction data presented earlier indicated the presence of the desired phase, $Li_2(OH)_{0.9}F_{0.1}Cl$, and the starting material, LiF, in the sample. Hence, the presence of two distinct ^{19}F resonances is to be expected. To accurately assign the two resonances, a ^{19}F MAS NMR spectrum of LiF was acquired and is also shown in Figure 7.10(a)

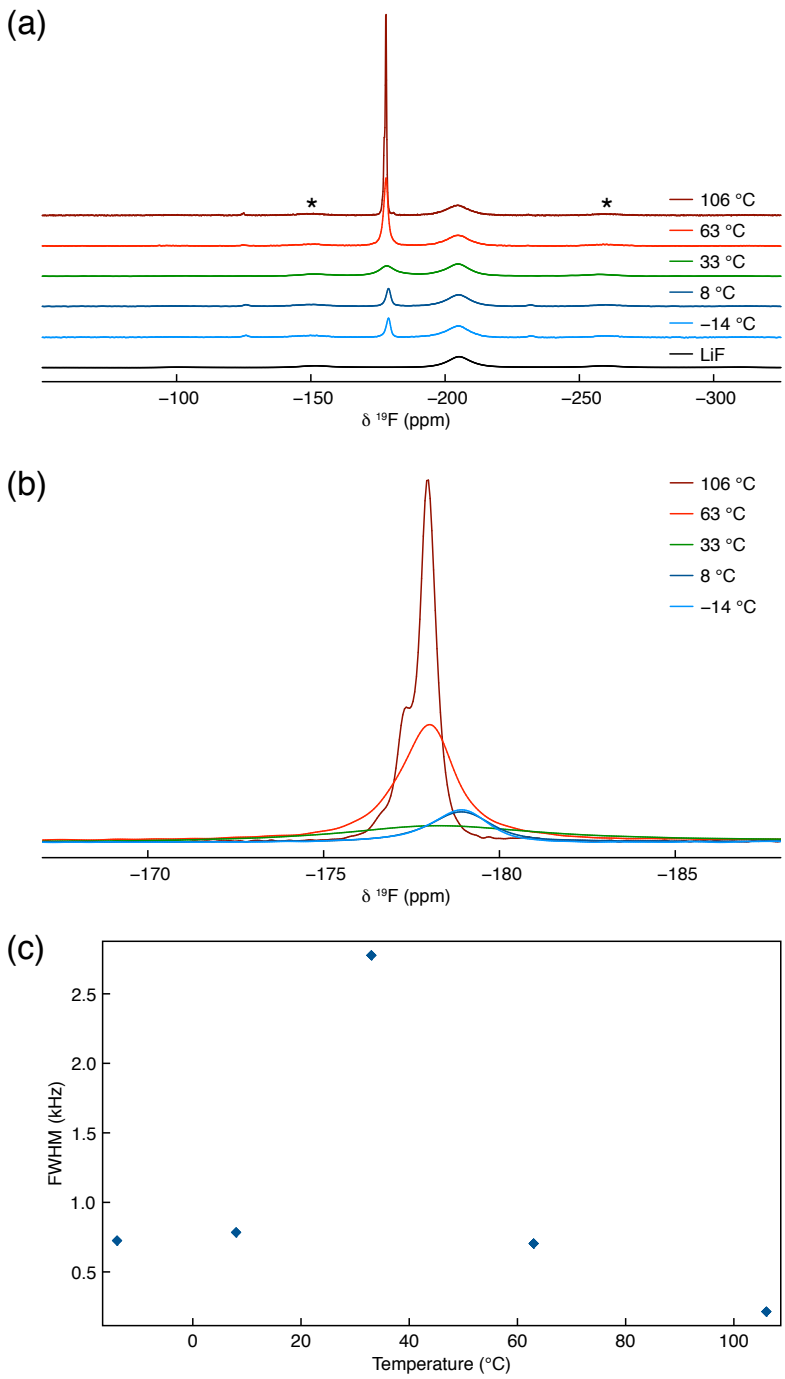

Figure 7.10: (a) VT ^{19}F (9.4 T) MAS NMR spectra acquired between −14 to 106 °C for a sample of $Li_2(OH)_{0.9}F_{0.1}Cl$ synthesised via a conventional solid-state reaction completed inside an Ar-filled glovebox. The MAS rate was 20 kHz and spinning sidebands are denoted by *. In all cases, a recycle delay of 60 s was used to acquire 32 transients. Also shown is the ^{19}F (9.4 T) MAS NMR spectrum acquired for LiF where a recycle delay of 60 s was used to acquire 16 transients. (b) An overlay of the VT spectra obtained to highlight the resonance corresponding to $Li_2(OH)_{0.9}F_{0.1}Cl$ and (c) the corresponding variation in FWHM as a function of temperature.

for comparison. A single broad resonance around $\delta_{iso} = -205$ ppm is observed, thereby, identifying that resonance as LiF. Hence, the resonance at $\delta_{iso} = -178$ ppm must correspond to the desired phase. It is noted that the linewidth of the resonance corresponding to $Li_2(OH)_{0.9}F_{0.1}Cl$ varies with changing temperature, whereas the LiF resonance remains unchanged at all temperatures. To demonstrate the changes in linewidth more clearly, an expansion of the spectra is shown in Figure 7.10(b). Here, the spectra have been overlaid, making it easier to see the variation in both the intensity and linewidth of the resonance. Below room temperature (−14 and 8 °C), the resonance corresponding to $Li_2(OH)_{0.9}F_{0.1}Cl$ is relatively broad and is centred around $\delta_{iso} = -178.90$ ppm. At 33 °C, the resonance exhibits additional broadening, alongside a slight increase in chemical shift to −177.90 ppm. There is a concurrent decrease in the intensity as well. An increase in temperature to 63 °C results in significant line narrowing along with an increase in intensity. This trend appears to continue with increasing temperature, and at 106 °C, the line narrows further, and the resonance observed has a greater intensity. Here, two distinct overlapping sites are observed at $\delta_{iso} = -177.33$ and −177.94 ppm. This is surprising as only one crystallographic site is expected for F in the cubic structure of $Li_2(OH)_{0.9}F_{0.1}Cl$ in space group $Pm\bar{3}m$. However, as discussed earlier, Effat and co-workers[235] have proposed two different fluorine analogues for Li_2OHCl. It was suggested that fluorine could occupy the OH or Cl site to form $Li_2(OH)_{0.9}F_{0.1}Cl$ and $Li_2OHCl_{0.9}F_{0.1}$, respectively. Both compositions are calculated to have similar formation energies, meaning the synthesis of both materials is feasible. Hence, it is possible that in this instance, fluorine may have been incorporated onto both the OH and Cl sites, resulting in two different fluorine environments/sites. Interestingly, this could also, in part, explain the presence of residual LiCl in the sample.

The change in linewidth can be seen more clearly in a plot of the FWHM vs. temperature, shown in Figure 7.10(c). Below room temperature (−14 and 8 °C), the linewidth is similar. However, an increase in temperature to 33 °C results in substantial line broadening. From then onwards, increasing the temperature results in significant line narrowing. Overall, the resonance cor-

responding to the desired phase undergoes two distinct changes. Firstly, the chemical shift of the resonance changes as the temperature increases from 8 to 33 °C. The resonance also exhibits significant line broadening. Secondly, from 33 °C onwards, the resonance narrows considerably. As previously demonstrated in Chapters 4 and 5 for Li_2OHCl, changes in linewidth typically occur due to structural changes such as a phase transition or ion mobility. A change in the chemical shift along with line broadening from 8 to 33 °C indicates a change in the ^{19}F environment. Thus, considering the ^{19}F NMR data in conjunction with the $^{1/2}H$, ^{7}Li and ^{35}Cl NMR data presented earlier, it is very likely that $Li_2(OH)_{0.9}F_{0.1}Cl$ undergoes a phase transition below rom temperature. The NMR data acquired between −19 and 8 °C appear very similar to that corresponding to the room-temperature phase of Li_2OHCl. This suggests that $Li_2(OH)_{0.9}F_{0.1}Cl$ likely adopts an orthorhombic structure below room temperature.

Moreover, the continuous narrowing of the resonance observed between 33 and 106 °C is suggestive of mobility. In the previous chapter, the parent material, Li_2OHCl, exhibited both proton and Li-ion mobility. The protons were shown to exhibit localised motion, *i.e.*, rotational/re-orientational motion around the O. The Li-ions, on the other hand, exhibited long-range diffusion. Interestingly, in the fluorine-doped sample, OH^- is partially substituted by F^-. Therefore, it is possible for the F^- to display localised motion as it is located on the OH^- site. It could also exhibit long-range motion as it sits in the structure as an isolated anion. To probe this further, ^{19}F T_1 measurements were completed between 8 and 106 °C, and are shown in Figure 7.11. It is noted that the sample comprised two fluorine-containing phases, $Li_2(OH)_{0.9}F_{0.1}Cl$ and LiF. Thus, these T_1 values may not be exact. Nonetheless, they are a helpful guide as the sample predominantly consists of the desired phase. The T_1 data presented here is very interesting. Initially, from 8 to 33 °C T_1 decreases then increases slightly from 33 to 63 °C. An increase in temperature to 106 °C results in a sharp drop from ~28 to ~2 s. Such a significant decrease in T_1 is suggestive of mobility. Interestingly, the computational study reported by Effat and co-workers[235] identified Li as the only mobile species

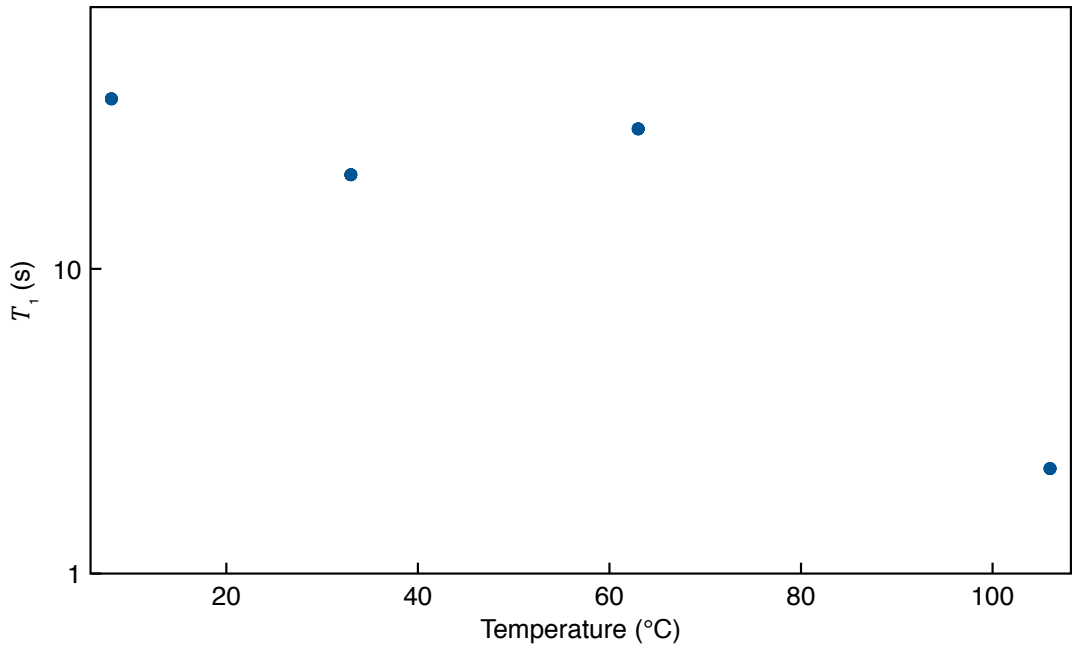

Figure 7.11: ^{19}F (9.4 T) T_1 values obtained between 8 – 106 °C for a sample of $Li_2(OH)_{0.9}F_{0.1}Cl$ synthesised via a conventional solid-state route.

in $Li_2(OH)_{0.9}F_{0.1}Cl$. No fluorine mobility was suggested. However, it is noted that whilst the VT ^{19}F NMR data presented here strongly suggests that ^{19}F exhibits mobility in $Li_2(OH)_{0.9}F_{0.1}Cl$, it does not explain the precise nature of the F^- motion. Additional detailed studies, specifically PFG-based experiments, are needed to determine the precise nature of any fluorine mobility present.

7.3.2 $Li_2OHCl_{1-x}Br_x$ (x = 0.1 – 1)

The composition of Li_2OHCl can also be modified via halide mixing. In the current study, this was done by substituting Cl^- with Br^- to produce samples in the series $Li_2OHCl_{1-x}Br_x$, where x varies from 0.1 to 1. All samples were synthesised using the same reaction conditions used for Li_2OHCl via the muffle furnace method described earlier. The XRD patterns obtained for the samples synthesised are shown in Figure 7.12. Initial inspection of the data indicates that all diffraction patterns appear very similar to that of the high-temperature cubic phase of Li_2OHCl in space group $Pm\bar{3}m$, suggesting that the samples produced also adopt a cubic structure in space group $Pm\bar{3}m$. It is noted that all reflections shift to lower 2θ angles with increasing x. Thus, suggesting an increase in the lattice parameter with increasing Br concentration.

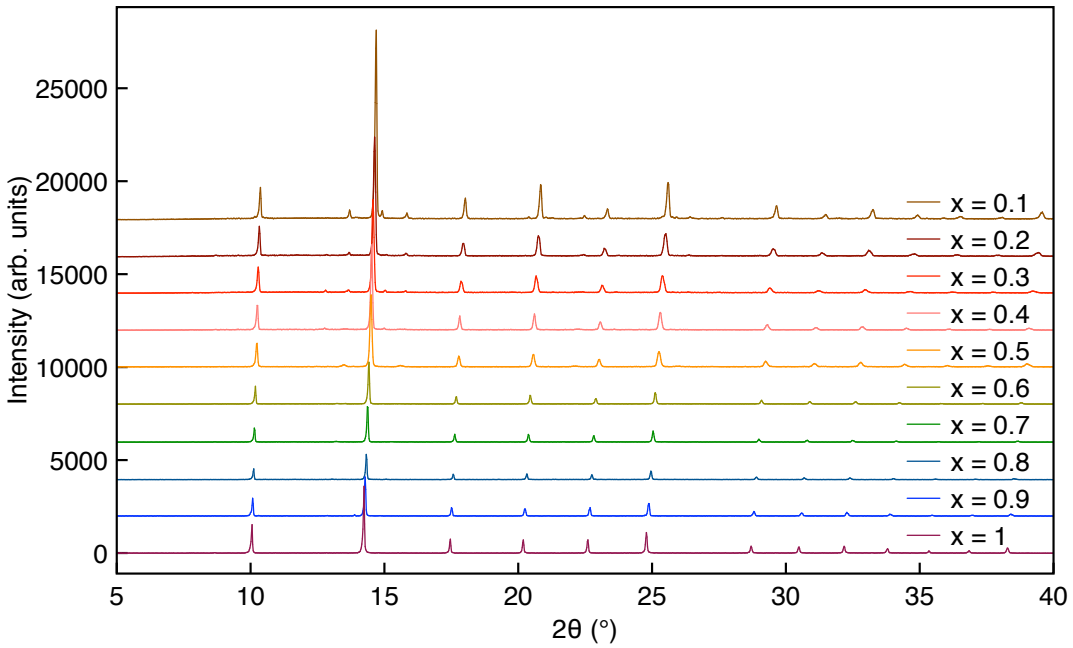

Figure 7.12: X-ray diffraction patterns obtained for samples of $Li_2OHCl_{1-x}Br_x$, (x = 0.1 – 1), synthesised via conventional solid-state reactions completed inside an Ar-filled glovebox. In all cases, the reaction temperature was 350 °C and the reaction time was 30 mins.

This is to be expected as Br has a larger ionic radius than Cl ($r_{ion}Br^-$ = 1.96 Å and $r_{ion}Cl^-$ = 1.81 Å).[11]

All of the diffraction patterns shown in Figure 7.12 were analysed via Rietveld refinement using the reported $Pm\bar{3}m$ structural model.[210] The refinements are shown in Figure 7.13, and the corresponding structural parameters are listed in Table 7.3. The diffraction pattern for the $Li_2OHCl_{0.9}Br_{0.1}$ sample suggested the presence of a second phase which appears to be the room-temperature Li_2OHCl phase and residual LiCl. Hence, the corresponding XRD data was refined using the $Pm\bar{3}m$ structural model for Li_2OHBr with appropriate occupancy values for Li, Cl and Br, and the *Pban* and $Fm\bar{3}m$ structural models for Li_2OHCl and LiCl, respectively.[199] The fractional occupancies for atoms in the Li_2OHCl phase were specified to be the same as those determined earlier via Rietveld analysis of the XRD data for Li_2OHCl (Figure 4.13). The diffraction pattern for $Li_2OHCl_{0.8}Br_{0.2}$ suggested the presence of residual LiCl. Thus, the corresponding XRD data was refined using the $Pm\bar{3}m$ and $Fm\bar{3}m$ structural models for $Li_2OHCl_{0.8}Br_{0.2}$ and LiCl, respectively.[199] The diffraction patterns for the rest of the samples in the series $Li_2OHCl_{1-x}Br_x$ (x = 0.3 – 1) were refined

using the $Pm\bar{3}m$ structural model alone. In all cases, the fractional occupancies for Cl and Br in the $Pm\bar{3}m$ structural model were varied to reflect the intended phase composition.

It is noted that, unlike Li_2OHCl, no structural information regarding the protons was included in the Rietveld analysis. This is because the lattice parameters will change with the gradual substitution of Cl, and it is difficult to predict how this will affect the proton positions. Interestingly, at the time of writing this thesis, the synthesis of Li_2OHBr was reported by Deng and co-workers.[237] A deuterated sample of Li_2OHBr was analysed via NPD, and it is suggested that H/D occupy two different positions in the cubic structure of Li_2OHBr in space group $Pm\bar{3}m$. Moreover, Sugumar and co-workers have explored the $Li_{3-x}OH_xBr$ (x = 0.6 – 1.5) system and have analysed Li_2OHBr via NPD.[238] They have reported a single crystallographic site for the protons, thereby disagreeing with Deng *et al.*[237] These reports are interesting as it appears that locating the precise proton positions in this system is quite challenging. It also means that Li_2OHBr is a good contender for further characterisation to confirm the corresponding crystallographic information. Unfortunately, the current study has not focused on determining the exact coordinates for protons in Li_2OHBr as high-resolution diffraction data would be required to do so. Instead, Li_2OHBr has been analysed to study the ion dynamics, which have then been compared to Li_2OHCl.

Inspection of the structural parameters indicates that, in all cases, the χ^2 and wR_p values obtained suggest a good fit. A closer look at the refinement for $Li_2OHCl_{0.9}Br_{0.1}$ shows that the sample contains 66.14(53)% $Li_2OHCl_{0.9}Br_{0.1}$, 32.53(54)% Li_2OHCl and 1.33(3)% LiCl. In the case of $Li_2OHCl_{0.8}Br_{0.2}$, the phase fractions obtained suggest the sample contains 98.66(5)% $Li_2OHCl_{0.8}Br_{0.2}$ and 1.34(5)% LiCl. The rest of the samples, with the exception of $Li_2OHCl_{0.4}Br_{0.6}$ and the end member Li_2OHBr, appear to contain small amounts of impurities, as the diffraction patterns contain reflections that do not correspond to either the desired phase or the starting reagents. However, it is noted that the quantity of the impurity phase present appears to be very low, thereby making it quite challenging to identify them accurately.

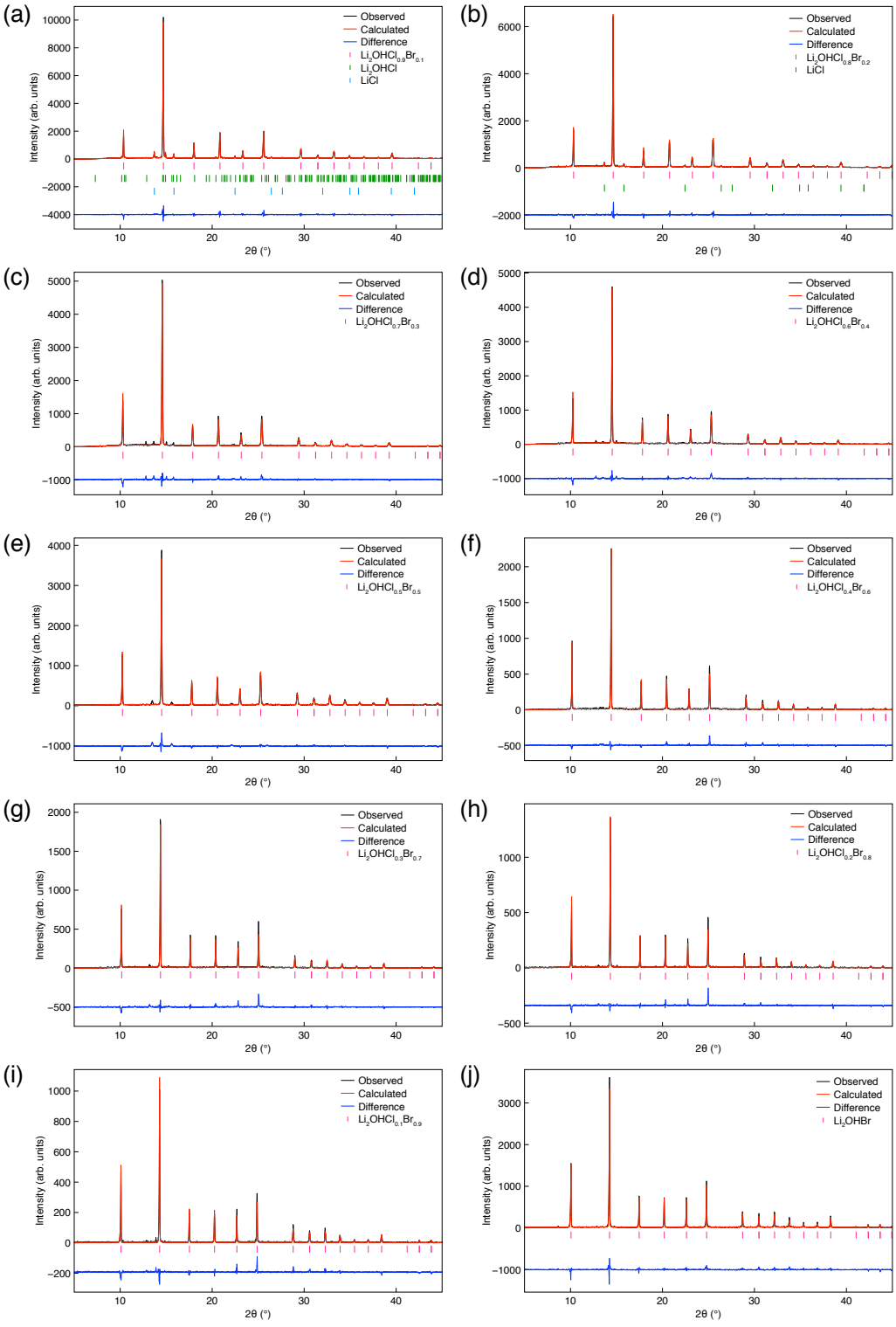

Figure 7.13: Rietveld refinement of the XRD data obtained for samples in the series $Li_2OHCl_{1-x}Br_x$ (x = 0.1 – 1) synthesised via the muffle furnace method, using the $Pm\bar{3}m$ ($Li_2OHCl_{1-x}Br_x$), *Pban* (Li_2OHCl) and $Fm\bar{3}m$ (LiCl) structural models.[125,199] The corresponding χ^2, wR_P and R_P values are listed in Table 7.3.

Table 7.3: Structural parameters obtained for samples in the series $Li_2OHCl_{1-x}Br_x$ (x = 0.1 – 1) synthesised via the muffle furnace method, from Rietveld refinement of the XRD data using isotropic thermal coefficients. $Li_2OHCl_{0.9}Br_{0.1}$: space group $Pm\bar{3}m$, a = 3.92871(5) Å, V = 60.639(2) Å^3, phase fraction = 66.14(53)%. Li_2OHCl: space group *Pban*, a = 7.7835(11) Å, b = 8.0243(10) Å, c = 3.8456(5) Å, V = 240.184(39) Å^3, phase fraction = 32.53(54)%. LiCl: space group $Fm\bar{3}m$, a = 5.15484(35) Å, V = 136.997(28) Å^3, phase fraction = 1.33(3)%. χ^2 = 2.10, wR_P = 13.87%, R_P = 10.73%. $Li_2OHCl_{0.8}Br_{0.2}$: space group $Pm\bar{3}m$, a = 3.94284(6) Å, V = 61.295(3) Å^3, phase fraction = 98.66(5)%. LiCl: space group $Fm\bar{3}m$, a = 5.16379(74) Å, V = 137.691(59)Å^3, phase fraction = 1.34(5)%. χ^2 = 1.87, wR_P = 14.76%, R_P = 10.83%. $Li_2OHCl_{0.7}Br_{0.3}$: space group $Pm\bar{3}m$, a = 3.95834(8) Å, V = 62.021(4) Å^3. χ^2 = 2.09, wR_P = 18.49%, R_P = 13.27%. $Li_2OHCl_{0.6}Br_{0.4}$: space group $Pm\bar{3}m$, a = 3.97212(7) Å, V = 62.671(3) Å^3. χ^2 = 1.82, wR_P = 19.14%, R_P = 13.64%. $Li_2OHCl_{0.5}Br_{0.5}$: space group $Pm\bar{3}m$, a = 3.97926(8) Å, V = 63.010(4) Å^3. χ^2 = 2.00, wR_P = 19.93%, R_P = 13.69%. $Li_2OHCl_{0.4}Br_{0.6}$: space group $Pm\bar{3}m$, a = 4.00145(7) Å, V = 64.070(3) Å^3. χ^2 = 1.52, wR_P = 26.56%, R_P = 18.63%. $Li_2OHCl_{0.3}Br_{0.7}$: space group $Pm\bar{3}m$, a = 4.01431(8) Å, V = 64.689(4) Å^3. χ^2 = 1.57, wR_P = 29.54%, R_P = 20.90%. $Li_2OHCl_{0.2}Br_{0.8}$: space group $Pm\bar{3}m$, a = 4.02710(8) Å, V = 65.310(4) Å^3. χ^2 = 1.39, wR_P = 33.20%, R_P = 23.38%. $Li_2OHCl_{0.1}Br_{0.9}$: space group $Pm\bar{3}m$, a = 4.04035(8) Å, V = 65.956(4) Å^3. χ^2 = 1.22, wR_P = 35.39%, R_P = 24.97%. Li_2OHBr: space group $Pm\bar{3}m$, a = 4.05372(5) Å, V = 66.613(3) Å^3. χ^2 = 1.91, wR_P = 22.59%, R_P = 16.69%.

Atom	x	y	z	Occ.	U(iso) × 100 (Å^2)
$Li_2OHCl_{0.9}Br_{0.1}$					
Li	0.5	0	0	0.667	6.7(3)
O	0	0	0	1	2.2(1)
Cl	0.5	0.5	0.5	0.9	2.5(7)
Br	0.5	0.5	0.5	0.1	2.9(18)
$Li_2OHCl_{0.8}Br_{0.2}$					
Li	0.5	0	0	0.667	6.5(4)
O	0	0	0	1	2.7(1)
Cl	0.5	0.5	0.5	0.8	2.9(11)
Br	0.5	0.5	0.5	0.2	3.3(14)
$Li_2OHCl_{0.7}Br_{0.3}$					
Li	0.5	0	0	0.667	7.7(5)
O	0	0	0	1	3.8(2)
Cl	0.5	0.5	0.5	0.7	4.8(23)
Br	0.5	0.5	0.5	0.3	3.7(17)
$Li_2OHCl_{0.6}Br_{0.4}$					
Li	0.5	0	0	0.667	6.8(5)
O	0	0	0	1	3.7(2)

Cl	0.5	0.5	0.5	0.6	4.0(27)
Br	0.5	0.5	0.5	0.4	4.1(18)
$Li_2OHCl_{0.5}Br_{0.5}$					
Li	0.5	0	0	0.667	4.7(5)
O	0	0	0	1	1.9(2)
Cl	0.5	0.5	0.5	0.5	4.0(22)
Br	0.5	0.5	0.5	0.5	1.8(11)
$Li_2OHCl_{0.4}Br_{0.6}$					
Li	0.5	0	0	0.667	3.8(6)
O	0	0	0	1	3.8(3)
Cl	0.5	0.5	0.5	0.4	3.9(103)
Br	0.5	0.5	0.5	0.6	3.5(24)
$Li_2OHCl_{0.3}Br_{0.7}$					
Li	0.5	0	0	0.667	4.6(7)
O	0	0	0	1	4.3(3)
Cl	0.5	0.5	0.5	0.3	3.6(80)
Br	0.5	0.5	0.5	0.7	4.4(10)
$Li_2OHCl_{0.2}Br_{0.8}$					
Li	0.5	0	0	0.667	2.5(7)
O	0	0	0	1	3.5(3)
Cl	0.5	0.5	0.5	0.2	6.1(40)
Br	0.5	0.5	0.5	0.8	3.2(6)
$Li_2OHCl_{0.1}Br_{0.9}$					
Li	0.5	0	0	0.667	2.3(7)
O	0	0	0	1	3.3(4)
Cl	0.5	0.5	0.5	0.1	8.0(34)
Br	0.5	0.5	0.5	0.9	2.5(4)
Li_2OHBr					
Li	0.5	0	0	0.667	5.6(8)
O	0	0	0	1	1.8(2)
Br	0.5	0.5	0.5	1	2.2(1)

Furthermore, the thermal coefficients obtained for Li in the desired phase for the x = 0.1 – 0.4 samples are a little high. This is similar to what has been observed previously for Li_2OHCl. An increase in x results in more

reasonable thermal coefficients. In addition, the thermal coefficients for the halides in the x = 0.1 – 0.9 samples are larger than expected and have relatively large errors. As discussed in previous chapters, these issues are most likely due to the occupancy values used during the refinements. In reality, the occupancies must differ somewhat as some of the starting materials go on to form the impurity phases present in these samples. Moreover, Li is known to exhibit mobility in the LiRAPs when they exist in a cubic structure. Hence, Li may be exhibiting some mobility in these samples at room temperature. This could influence the thermal coefficients as low levels of mobility may be interpreted as thermal motion. Thus, resulting in unusually large thermal coefficients for Li. It is noted that the thermal coefficients for all atoms in the Li_2OHCl and LiCl phase in the x = 0.1 and 0.2 samples were fixed at 2.5×10^{-2} Å^2, as attempts to refine them resulted in some unrealistically large and negative values. Overall, the refinements presented here (Figure 7.13) confirm that all samples in the $Li_2OHCl_{1-x}Br_x$ (x = 0.1 – 1) series adopt a cubic structure in space group $Pm\bar{3}m$ at room temperature. Thus, indicating that halide mixing is a suitable method for stabilising the cubic structure at room temperature.

Earlier, based on the XRD data presented in Figure 7.12, it was suggested that an increase in the Br concentration in $Li_2OHCl_{1-x}Br_x$ results in an increase in the lattice parameter. Rietveld analysis of the XRD data of all samples in the $Li_2OHCl_{1-x}Br_x$ series (x = 0.1 – 1) enabled the lattice parameter to be determined for each composition. The variation in lattice parameter with respect to the composition is shown in Figure 7.14. There appears to be a linear relationship between the lattice parameter and the relative concentrations of Cl and Br. The lattice parameter gradually increases from 3.92871(5) to 4.05372(5) Å as x increases from 0.1 to 1. This follows Vegard's law[239] and is to be expected as Br^- has a larger ionic radius than Cl^-. The lattice parameter obtained for Li_2OHBr is in agreement with that reported in the literature.[213] Moreover, the gradual change in lattice parameter with changing Br concentration also confirms that halide mixing has taken place as intended.

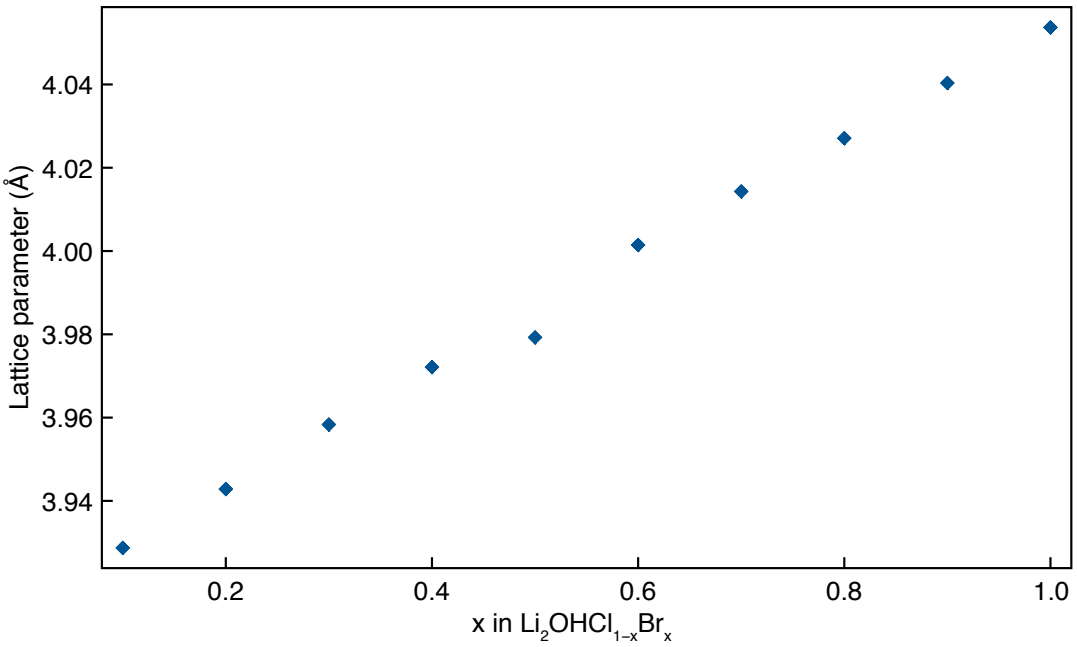

Figure 7.14: Variation in lattice parameter of samples in the $Li_2OHCl_{1-x}Br_x$ series, where x varied from 0.1 to 1.

7.3.2.1 Li_2OHBr

The diffraction data presented earlier indicated that the end member of the $Li_2OHCl_{1-x}Br_x$ series, Li_2OHBr, adopts a cubic structure in space group $Pm\bar{3}m$ at room temperature. It is noted that the mechanically milled Li_2OHCl sample also adopted a cubic structure at room temperature. However, VT NPD experiments indicated that the sample undergoes a phase transition at low temperatures. Similarly, the VT NMR data acquired for the fluorine-doped sample, $Li_2(OH)_{0.9}F_{0.1}Cl$, also suggested a phase transition at lower temperatures. Moreover, Eilbracht and co-workers reported that Li_2OHBr undergoes a phase transition without a change in symmetry at ~60 °C, as a discontinuity of the thermal expansion of the lattice parameter and cell volume was observed.[215] To probe these changes further, Li_2OHBr was studied via VT XRD over the temperature range −163 – 77 °C. The diffraction patterns recorded are shown in Figure 7.15. The sample was first cooled to −163 °C, the lowest temperature that could be reached via the instrumental setup used. The sample was then gradually heated to 77 °C. Upon reaching −163 °C, the diffraction pattern obtained appears similar to that obtained at room temperature, *i.e.*,

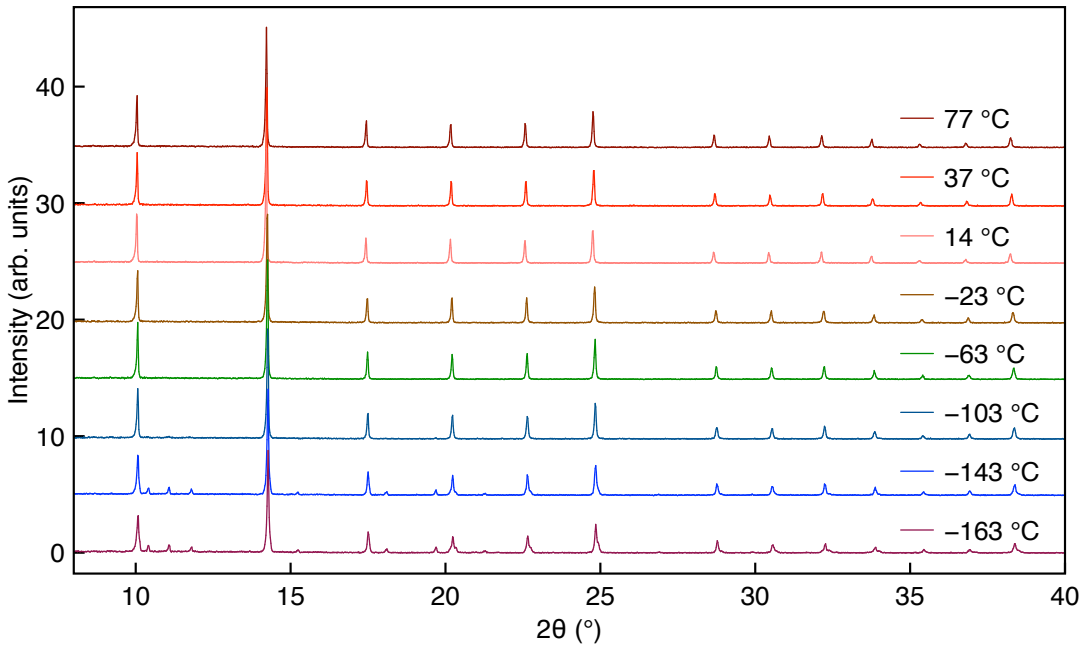

Figure 7.15: VT X-ray diffraction patterns obtained for Li_2OHBr between −163 and 77 °C. The sample was synthesised via a conventional solid-state reaction completed inside an Ar-filled glovebox. The reaction temperature was 350 °C and the reaction time was 30 mins.

it contains reflections corresponding to the cubic $Pm\bar{3}m$ phase. However, a number of additional reflections are also observed, suggesting the presence of an additional phase in the sample. However, it is noted that these additional peaks are of very low intensity. Thus, possibly suggesting the start of a phase transition, although it is clear that a complete transition has not taken place as the diffraction pattern predominantly consists of reflections corresponding to the known $Pm\bar{3}m$ phase. Thus, indicating that at −163 °C, the $Pm\bar{3}m$ phase is still the dominant phase present in the sample. The diffraction pattern obtained at −143 °C appears to be identical to that at −163 °C, suggesting no structural change occurs between −163 and −143 °C. As the temperature is increased to −103 °C, the additional reflections initially observed disappear, indicating a reversal of the phase transition. The diffraction pattern now solely contains reflections corresponding to the $Pm\bar{3}m$ phase. Subsequent incremental increases in temperature to 77 °C do not result in any change in the diffraction pattern, indicating that, between −103 and 77 °C, the sample remains in the cubic phase in space group $Pm\bar{3}m$. Moreover, the reflections in all patterns appear at similar 2θ angles and do not suggest any discontinuity in the lattice

parameters. This is in contrast to the findings of Eilbracht and co-workers.[215] Unfortunately, owing to technical and hardware limitations, temperatures below −163 °C could not be explored. Hence, it was not possible to fully investigate the possible phase transition. It is noted that, to date, no phase transitions at low temperatures have been reported for Li_2OHBr.

7.3.2.2 SSNMR Studies of Li_2OHBr

^1H and ^7Li MAS NMR Spectroscopy

Li_2OHBr was further investigated via multinuclear VT SSNMR spectroscopy to study ion dynamics within the sample. The ^1H MAS NMR spectra obtained between −19 and 106 °C are shown in Figure 7.16(a). In all cases, a single resonance believed to be indicative of a single site is observed. This is in agreement with the majority of literature reports, where the cubic $Pm\bar{3}m$ structure for Li_2OHX (X = Cl and Br) is believed to have a single H site.[125,201,213,215] It also agrees with recent reports by Sugumar and co-workers[238] who have reported a single H site specifically for Li_2OHBr. However, these findings contrast with those reported by Deng *et al.*,[237] who proposed two H sites in Li_2OHBr. Closer inspection of the spectra obtained indicates that, at −19 °C, a relatively broad resonance with well-defined spinning sidebands is observed. Again, this is characteristic of OH groups. An increase in temperature to 8 and then 33 °C, results in a broadening of the resonance and less intense spinning sidebands. The subsequent increase in temperature, from 33 to 106 °C, results in a gradual narrowing of the resonance. The line narrowing can be seen more clearly as a function of temperature in Figure 7.16(b), where the variation in FWHM is shown. At first, the resonance broadens from −19 to 33 °C, after which there is a steady reduction in the linewidth with increasing temperature. As discussed previously for Li_2OHCl and the related compositions, the gradual narrowing of the lineshape with increasing temperature is suggestive of mobility. This suggests that in Li_2OHBr, the protons exhibit some type of movement between 33 and 106 °C. The gradual broadening of the resonance observed between −19 and 33 °C is very interesting because it indicates

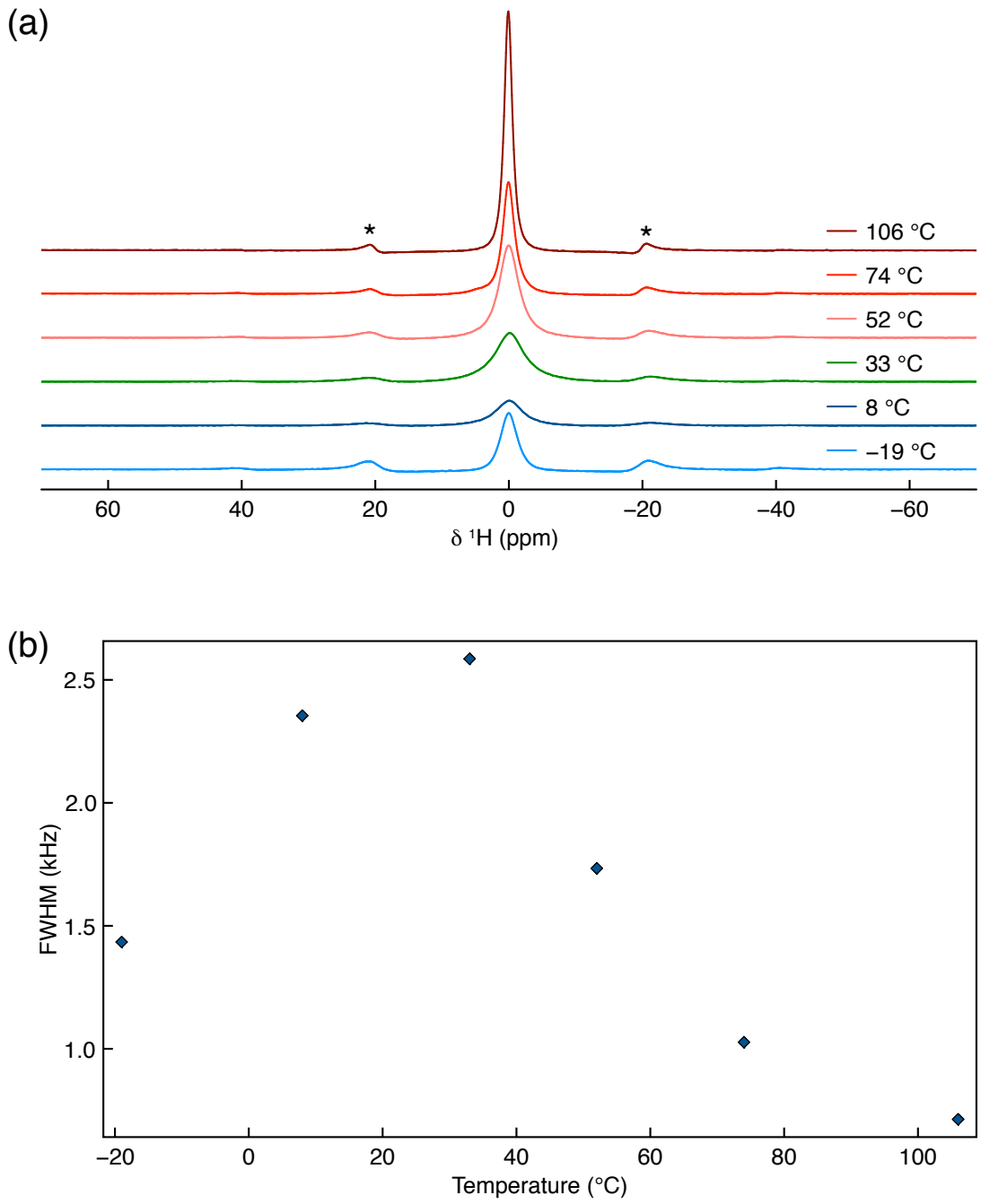

Figure 7.16: (a) VT ^{1}H (11.7 T) MAS NMR spectra acquired between −19 and 106 °C for a sample of Li_2OHBr synthesised via a conventional solid-state reaction completed inside an Ar-filled glovebox. The MAS rate was 10 kHz and spinning sidebands are denoted by *. A recycle delay of 1175 and 400 s was used between −19 and 52 °C and 74 and 106 °C, respectively. In all cases, 4 transients were acquired. (b) The corresponding variation in FWHM as a function of temperature.

a change in the local environment of the protons. However, the VT XRD shown earlier did not indicate any structural changes in Li_2OHBr between −19 and 33

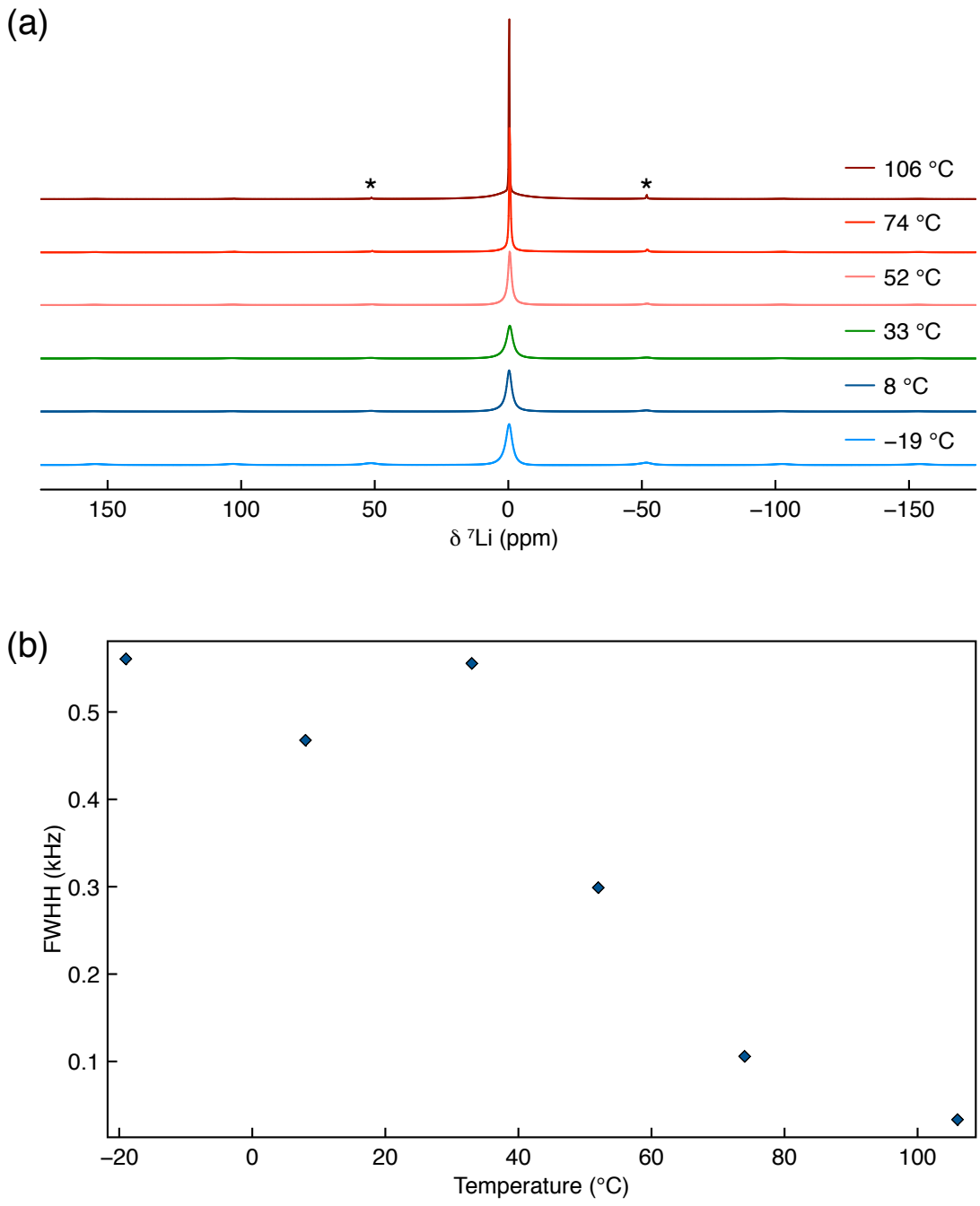

Figure 7.17: (a) VT ^{7}Li (11.7 T) MAS NMR spectra acquired between −19 and 106 °C for a sample of Li_2OHBr synthesised via a conventional solid-state reaction completed inside an Ar-filled glovebox. The MAS rate was 10 kHz and spinning sidebands are denoted by *. A recycle delay of 60 and 30 s was used between −19 and 52 °C and 74 and 106 °C, respectively. In all cases, 4 transients were acquired. (b) The corresponding variation in FWHM as a function of temperature.

°C. Thus, making it difficult to ascertain how and why the local environment of the protons changes from the current data alone.

The ^{7}Li MAS NMR spectra acquired for Li_2OHBr between −19 and 106 °C are shown in Figure 7.17(a). A single resonance, indicative of a single site, is observed at all temperatures. This is to be expected for a cubic structure in space group $Pm\bar{3}m$ and is in agreement with the XRD analysis presented earlier (Figure 7.13). At −19 °C, several spinning sidebands are observed, the intensity of which decreases with increasing temperature. An increase in temperature also appears to produce narrower resonances with a concomitant increase in intensity. The variation in linewidth can be seen more clearly in the corresponding plot of FWHM vs. temperature, shown in Figure 7.17(b). Interestingly, the linewidth decreases from −19 to 8 °C and then increases again at 33 °C. From then on, a steady decrease is observed between 33 and 106 °C. As discussed earlier, a gradual reduction in FWHM is suggestive of mobility. Therefore, the data suggests that Li_2OHBr exhibits Li-ion mobility between 33 and 106 °C. As with the protons, it appears that Li also experiences a change in its local environment between −19 and 33 °C. Hence, the ^{1}H and ^{7}Li NMR data suggest a structural change below room temperature. Although, the precise nature of this structural change is currently unknown.

To probe the H and Li mobility in greater detail in Li_2OHBr, ^{1}H and ^{7}Li T_1 measurements were completed over the temperature range −19 – 116 °C. The data obtained is shown in Figure 7.18. Between −19 and 19 °C there appears to be little variation in the ^{1}H T_1 data. However, it is noted that the T_1 increases by ~10 s from −19 to −3 °C. It then decreases again at 8 °C and remains the same until 19 °C. A subsequent increase in temperature from 19 to 116 °C results in a gradual decrease in ^{1}H T_1. At 116 °C, a ^{1}H T_1 value of ~15 s was measured, whereas, for Li_2OHCl it was ~10 s. Thus, suggesting that, in this sample, the protons are not as mobile as those in Li_2OHCl. In contrast to the ^{1}H T_1 data, the ^{7}Li T_1 decreases across the entire temperature range (−19 to 116 °C). At 116 °C, a T_1 value of 0.260 s is observed for Li, whereas, in Li_2OHCl it was 0.147 s. Thus, suggesting a lower degree of Li-ion mobility in Li_2OHBr when compared to Li_2OHCl. Also, this is considerably lower than the ^{1}H T_1 value, suggesting that in Li_2OHBr, Li-ions exhibit greater mobility than protons. This is in good agreement with the findings presented earlier for

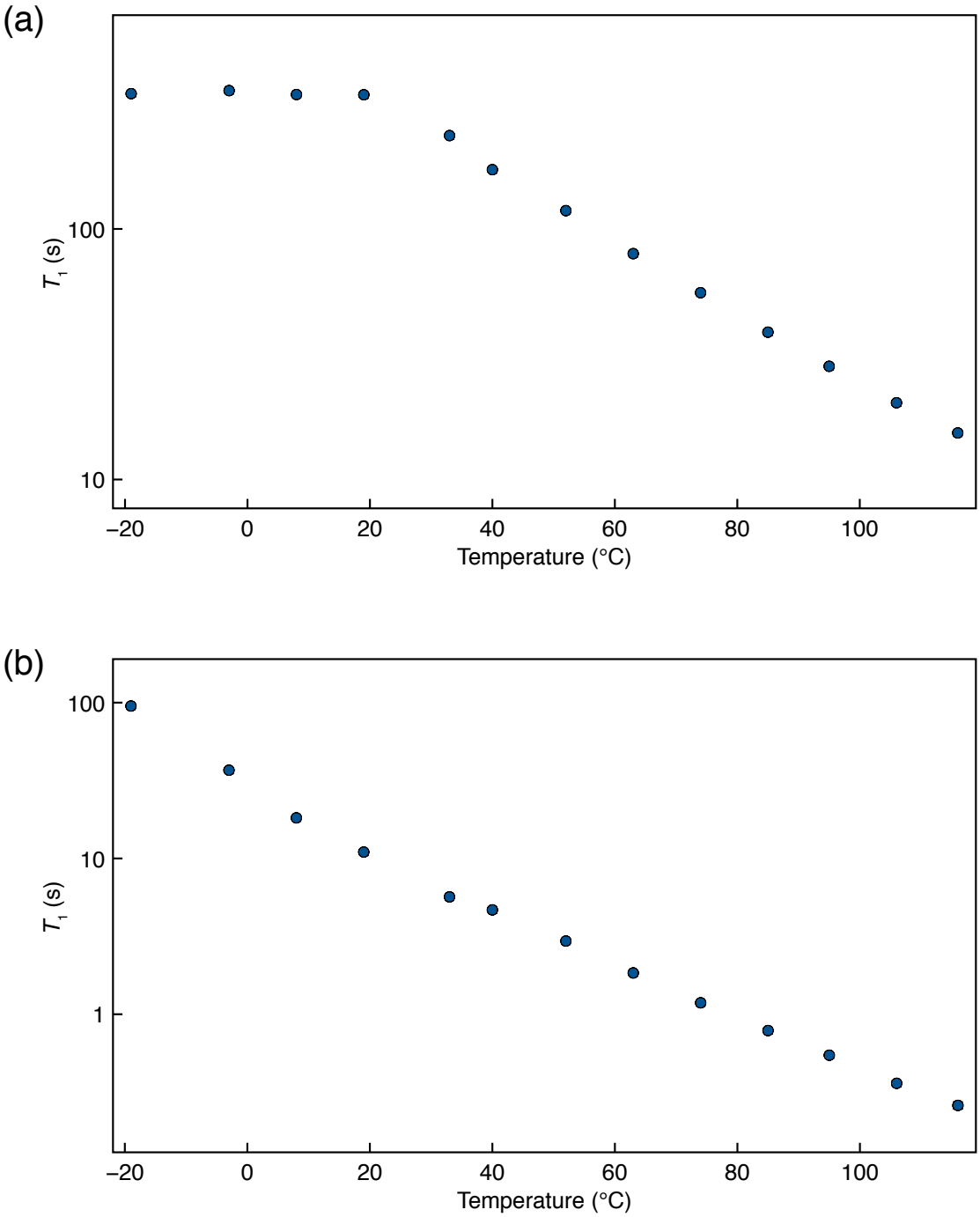

Figure 7.18: (a) ^{1}H and (b) ^{7}Li (11.7 T) T_1 data obtained over the temperature range −19 – 116 °C, for a sample of Li_2OHBr synthesised via a conventional solid-state reaction completed inside an Ar-filled glovebox. In all cases, the estimated error bars are smaller than the symbols used and are therefore not shown.

Li_2OHCl.

The ^{1}H and ^{7}Li NMR T_1 data obtained for Li_2OHBr has been used

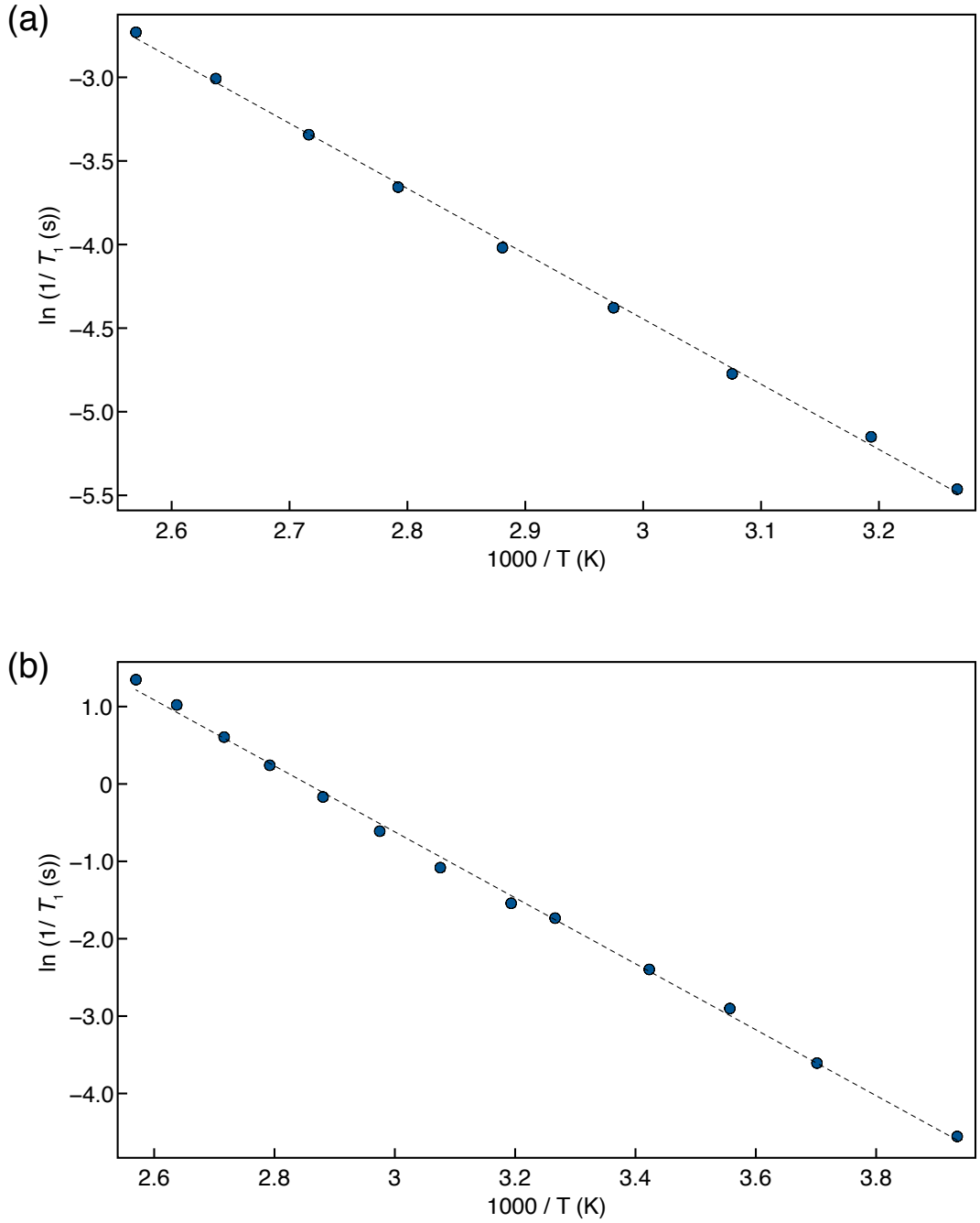

Figure 7.19: Arrhenius plots of (a) ^{1}H and (b) ^{7}Li (11.7 T) T_1 data obtained over the temperature range (a) 33 – 116 °C and (b) −19 – 116 °C, for a sample of Li_2OHBr synthesised via a conventional solid-state reaction completed inside an Ar-filled glovebox. In both cases, a linear fit is obtained, with gradients (a) −3.90(5) and (b) −4.26(6) and (a) R^2 = 0.9988 and (b) 0.9980. The corresponding activation energies of 0.34(1) and 0.37(1) eV were obtained for ^{1}H and ^{7}Li, respectively.

to extract the corresponding activation energies, owing to the Arrhenius relationship between the temperature and T_1 values. The Arrhenius plots of the

^{1}H and ^{7}Li T_1 data acquired over the temperature range 33 – 116 °C and −19 – 116 °C, respectively, are shown in Figure 7.19. In both cases, a linear fit is obtained with R^2 = 0.9988 and 0.9980 for ^{1}H and ^{7}Li, respectively. As stated earlier, the gradient of an Arrhenius plot is proportional to E_a, and E_a = 0.34(1) and 0.37(1) eV were obtained for ^{1}H and ^{7}Li, respectively. Thus, indicating that the energy barrier for Li-ion movement is higher than for protons. The E_a for Li-ion movement in Li_2OHBr is in excellent agreement with that reported in the literature by Schwering *et al.*[213] A similar observation was made for the parent material, Li_2OHCl, where the E_a for Li motion was higher than for H. It is noted that the value of E_a obtained for both species is lower in Li_2OHBr when compared to Li_2OHCl. Thus, suggesting that ion mobility should be favoured in the Br analogue. This is surprising given the T_1 values obtained, which suggest a higher degree of ion mobility in Li_2OHCl than Li_2OHBr.

^{2}H MAS NMR Spectroscopy

To probe ion dynamics further, a sample of Li_2OHBr was deuterated for analysis via VT ^{2}H MAS NMR spectroscopy. The ^{2}H MAS NMR spectra acquired over the temperature range 8 – 110 °C are shown in Figure 7.20. The spectra acquired at 8 and 69 °C closely resemble those obtained for Li_2OHCl between −19 and 63 °C, *i.e.*, an axially symmetric lineshape, comprising a large manifold of spinning sidebands is observed. The spectrum acquired at 69 °C was simulated (Figure 7.21) to determine the corresponding quadrupolar parameters, C_Q = 255(1) kHz and η_Q = 0.060(10). As stated earlier, these values are characteristic of static ^{2}H environments. Thus, indicating the presence of static OH^-/OD^- groups in Li_2OHBr, between 8 and 69 °C. At 79 °C, a broad signal is observed, in addition to the signal corresponding to the static OH^-/OD^- groups. The broad signal is believed to correspond to mobile or freely rotating OH^-/OD^- groups. Thus, indicating that, at 79 °C, both static and mobile OH^-/OD^- groups are present in the sample simultaneously. The intensity of this broad signal increases with increasing temperature, whilst the opposite is observed for the signal corresponding to the static OH^-/OD^- groups. A similar pattern was observed for the parent material, Li_2OHCl.

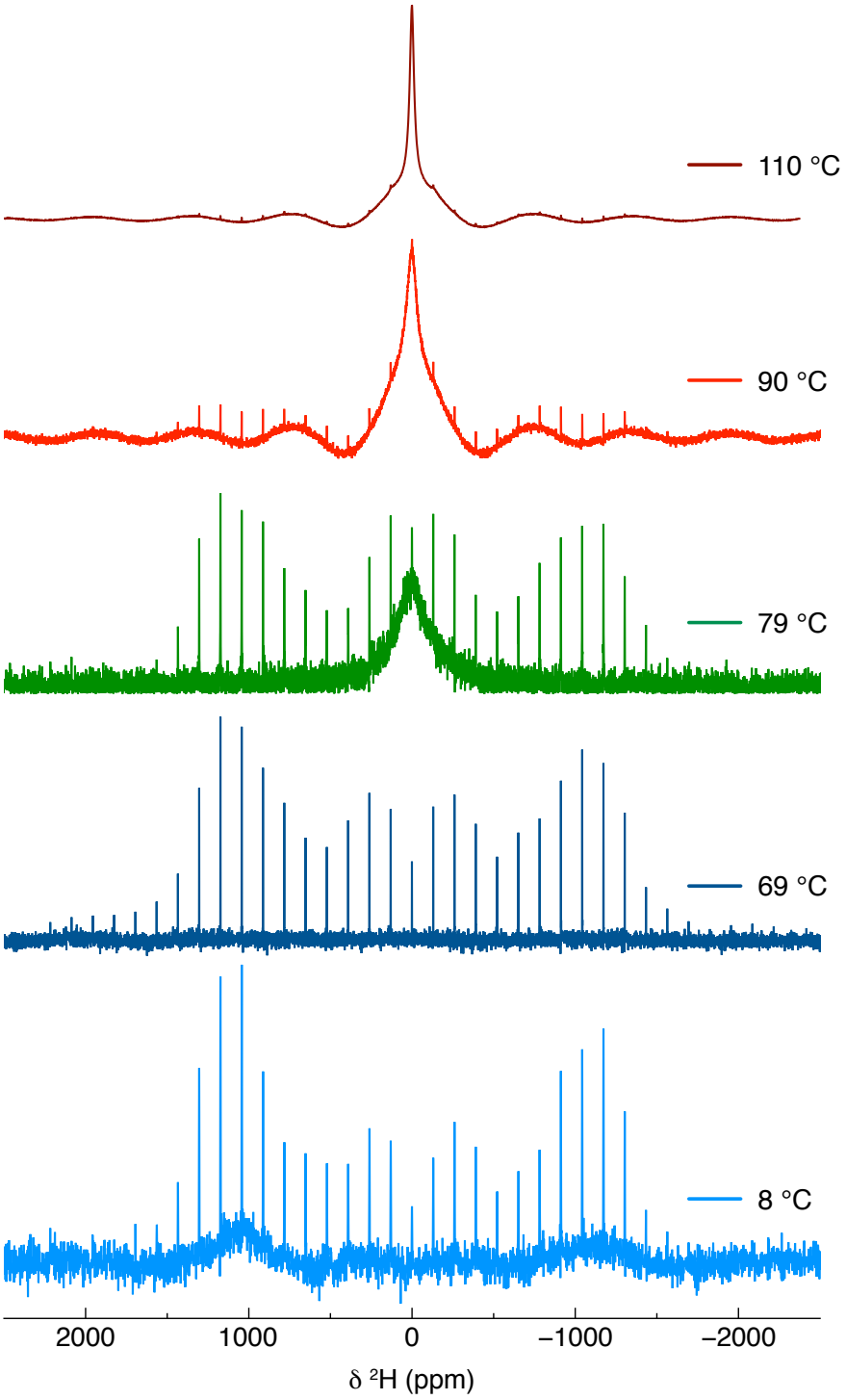

Figure 7.20: ^{2}H (11.7 T) MAS NMR spectra acquired over the temperature range 8 – 110 °C, for a sample of Li_2ODBr synthesised via a conventional solid-state reaction completed inside an Ar-filled glovebox. In all cases, the MAS rate was 10 kHz and a recycle delay of 15 s was used to acquire 4000 transients.

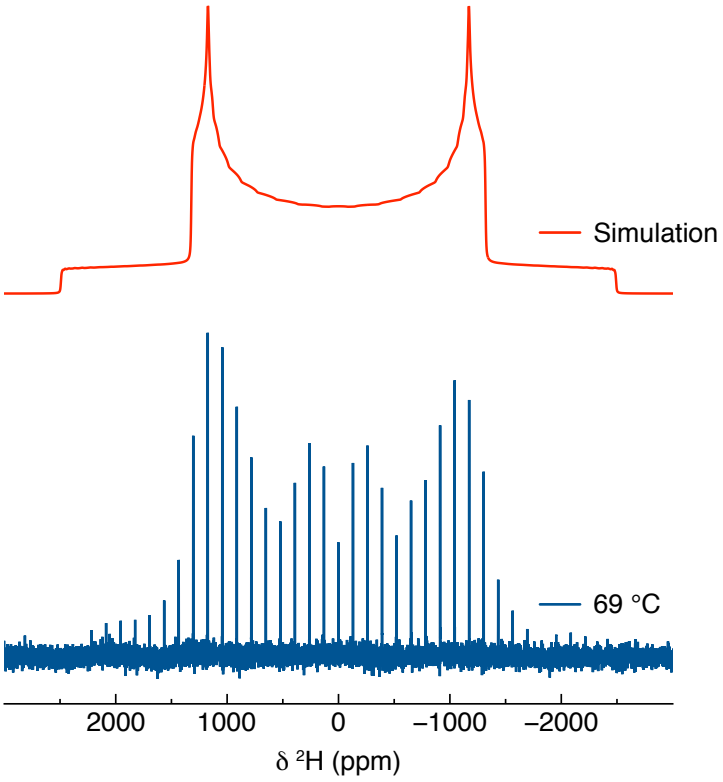

Figure 7.21: The ^{2}H (11.7 T) MAS NMR spectrum acquired at 69 °C for a sample of Li_2ODBr synthesised via a conventional solid-state route. The MAS rate was 10 kHz and a recycle delay of 15 s was used to acquire 4000 transients. The spectrum was simulated to obtain the corresponding quadrupolar parameters, C_Q = 255(1) kHz and η_Q = 0.060(10).

However, for Li_2OHCl, the broad resonance appeared at a lower temperature (63 °C). Thus, in Li_2OHBr, the OH^-/OD^- groups become mobile at higher temperatures when compared to Li_2OHCl. As previously demonstrated, the OH^-/OD^- movement is closely related to the Li-ion mobility. Therefore, the data presented here suggests that in Li_2OHBr Li-ion mobility may also be occurring at a higher temperature when compared to Li_2OHCl.

^{79}Br MAS NMR Spectroscopy

Finally, Li_2OHBr was analysed via VT ^{79}Br MAS NMR spectroscopy, and the spectra obtained between −19 and 106 °C are shown in Figure 7.22(a). In all cases, a single resonance centred around 65 ppm, indicative of a single site, with multiple spinning sidebands is observed. This is in agreement with the diffraction data shown earlier (Figure 7.13), where Li_2OHBr was shown to adopt a cubic structure, in space group $Pm\bar{3}m$, with a single Br site. For clarity,

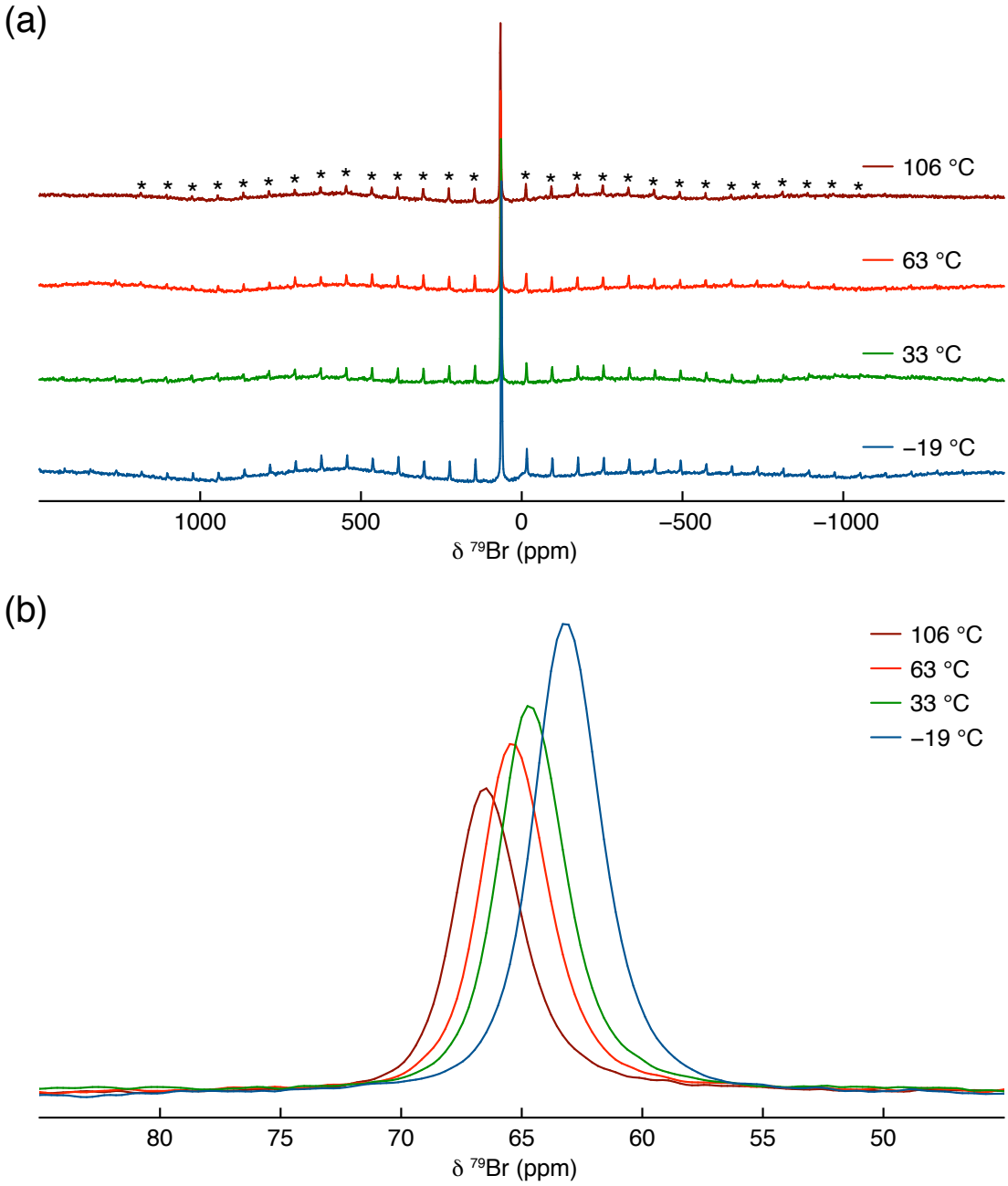

Figure 7.22: (a) ^{79}Br (11.7 T) MAS NMR spectra acquired over the temperature range −19 to 106 °C, for a sample of Li_2OHBr synthesised via a conventional solid-state reaction completed inside an Ar-filled glovebox. The MAS rate was 10 kHz. A recycle delay of 1 s was used to acquire 800 transients. (b) An overlay of the central transition shown in (a).

an expansion of the resonance is shown in Figure 7.22(b), where the spectra have been overlaid. It appears that an increase in temperature results in a gradual increase in chemical shift from 63.30 to 66.47 ppm, along with a drop in intensity. These changes in intensity and the chemical shift are continual,

suggesting a gradual change to the Br environment with increasing temperature. It is evident from the VT XRD data presented earlier that Li_2OHBr retains its cubic structure in space group $Pm\bar{3}m$ over the temperature range −103 to 77 °C. Also, Li_2OHBr has not been reported to undergo a phase transition to a different symmetry in the literature. Therefore, any changes occurring in the local environment of ^{79}Br are not due to major structural changes, *i.e.*, no phase transition is occurring. It is noted that the ^{35}Cl MAS NMR spectra acquired for Li_2OHCl also exhibited a reduction in signal intensity with increasing temperature and the signal was barely noticeable at 106 °C (Figure 6.27). Thus, it was suggested that Cl could be exhibiting some motion in Li_2OHCl. Alternatively, the movement of proton and Li-ions causes the EFG experienced by Cl to vary continuously, making it difficult to observe the ^{35}Cl signal. Interestingly, the AIMD simulations completed for Li_2OHCl did not indicate Cl mobility, and no motion was detected via ^{35}Cl EXSY experiments. Thus, it was suggested that the signal reduction is most likely an indirect consequence of the proton and Li-ion movement. The same could also be true for the Br analogue, Li_2OHBr, as the ^{1}H and ^{7}Li NMR data presented earlier suggested that Li_2OHBr also exhibits proton and Li-ion mobility. It is noted that the ^{79}Br NMR data shown here does not suggest Br mobility as the resonance does not narrow with increasing temperature. However, the possibility of Br motion cannot be ruled for certain from the current data alone. Additional work such as T_1 measurements, EXSY and PFG experiments are required to probe Br mobility. Interestingly, the degree of signal reduction is not as severe as that observed for ^{35}Cl. Thus, suggesting that ^{35}Cl is much more sensitive to the changes in the EFG when compared to ^{79}Br.

7.3.2.3 SSNMR Studies of $Li_2OHCl_{0.4}Br_{0.6}$

^{1}H and ^{7}Li MAS NMR Spectroscopy

A sample from the series $Li_2OHCl_{1-x}Br_x$ (x = 0 – 1) was analysed further via multinuclear VT SSNMR in order to study the influence of halide mixing on ion mobility within the sample and its effects on the local environment

of the halides. $Li_2OHCl_{0.4}Br_{0.6}$ was deemed a suitable candidate as the sample produced did not contain any impurities. The ^{1}H MAS NMR spectra acquired for this sample between −14 and 106 °C are shown in Figure 7.23(a). In all cases, a single relatively broad resonance centred around 0 ppm, indicative of a single site, is observed. This is in agreement with the diffraction data presented earlier, as $Li_2OHCl_{0.4}Br_{0.6}$ adopts a cubic structure in space group $Pm\bar{3}m$, where a single H site is expected. Interestingly, the resonance is observed to broaden from −14 to 33 °C. Thus, suggesting a change in the local environment of the protons. The variation in linewidth as a function of temperature is shown more clearly in Figure 7.23(b). The trend is similar to that observed for Li_2OHBr. Thus, suggesting that, below room temperature, $Li_2OHCl_{0.4}Br_{0.6}$ exhibits similar structural changes to Li_2OHBr. An increase in temperature to 106 °C results in a considerable narrowing of the resonance with a concomitant increase in intensity. This suggests that, in a similar manner to the end members of the series (Li_2OHCl and Li_2OHBr), $Li_2OHCl_{0.4}Br_{0.6}$ also exhibits proton mobility at elevated temperatures.

The ^{7}Li MAS NMR spectra acquired over the temperature range −14 and 106 °C are shown in Figure 7.24. Here too, a single resonance centred around 0 ppm is observed. This is in agreement with the XRD data presented earlier and is in line with what is expected for a cubic structure in space group $Pm\bar{3}m$. As with the ^{1}H NMR data, the ^{7}Li NMR data obtained for $Li_2OHCl_{0.4}Br_{0.6}$ resembles that obtained for the end member Li_2OHBr. At first, the resonance narrows significantly between −14 and −3 °C and then broadens again at 8 °C. As stated earlier, this suggests a structural change below room temperature. A subsequent increase in temperature to 106 °C produces a considerable narrowing of the resonance, which is suggestive of Li-ion mobility.

To further probe the proton and Li-ion mobility in $Li_2OHCl_{0.4}Br_{0.6}$, ^{1}H and ^{7}Li T_1 values were measured between −14 and 106 °C. The corresponding data is shown in Figure 7.25. In both cases, the trend observed is similar to that of Li_2OHBr. The ^{1}H T_1 values exhibit little variation between −14 and −3 °C. However, an increase in temperature to 106 °C results in a gradual reduction in T_1. At 106 °C, a ^{1}H T_1 of ~16 s is measured. This is midway between the

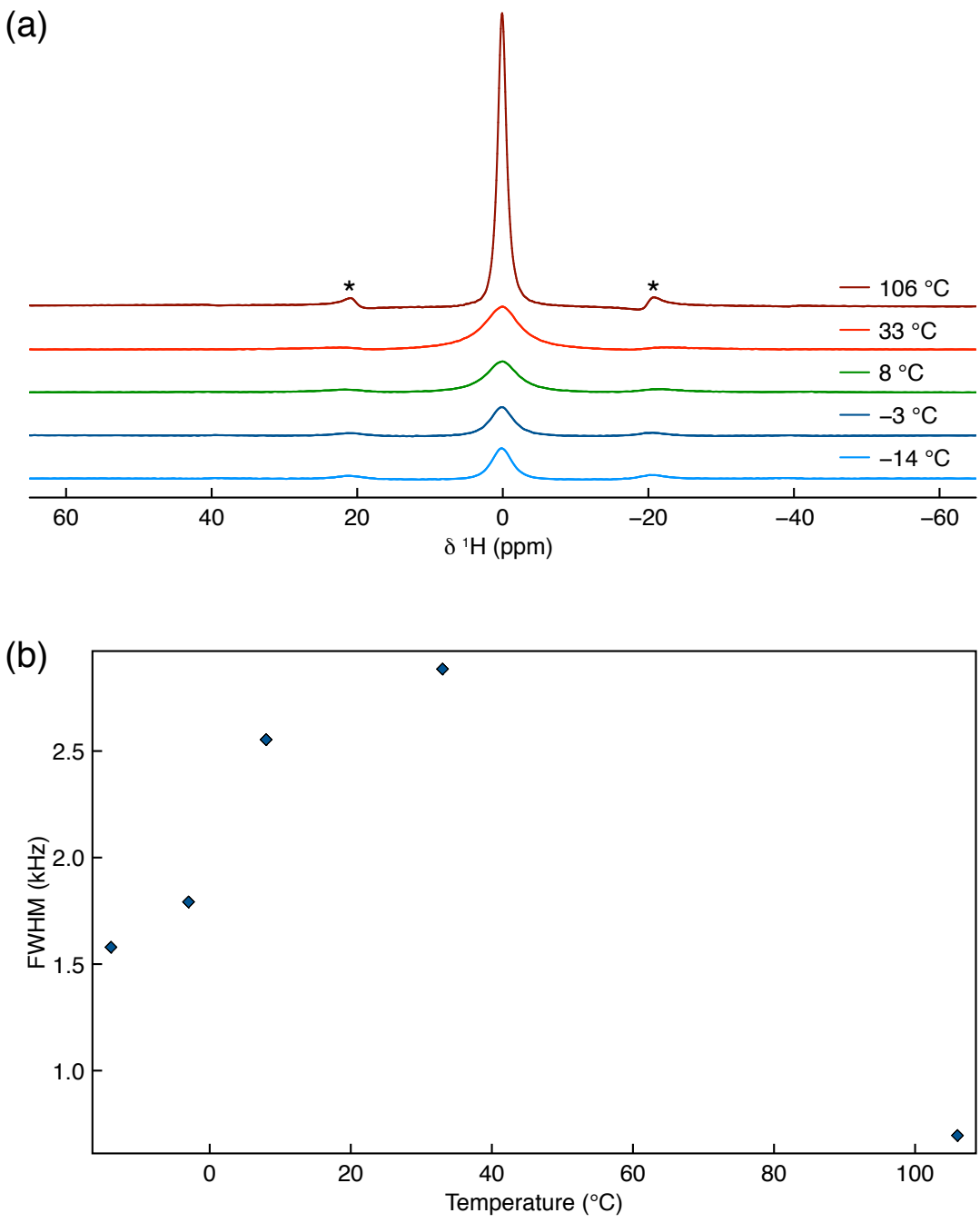

Figure 7.23: (a) ^{1}H (11.7 T) MAS NMR spectra acquired between −14 and 106 °C, for a sample of $Li_2OHCl_{0.4}Br_{0.6}$ synthesised via a conventional solid-state reaction completed inside an Ar-filled glovebox. The MAS rate was 10 kHz and spinning sidebands are denoted by *. A recycle delay of 200 s was used at 33 °C. In all other cases, a recycle delay of 2000 s was used. In all cases, 4 transients were acquired. (b) The corresponding variation in FWHM as a function of temperature.

^{1}H T_1 of ~11 and ~20 s observed for the end members, Li_2OHCl and Li_2OHBr, respectively, at 106 °C. Conversely, the ^{7}Li T_1 values exhibit a steady decrease

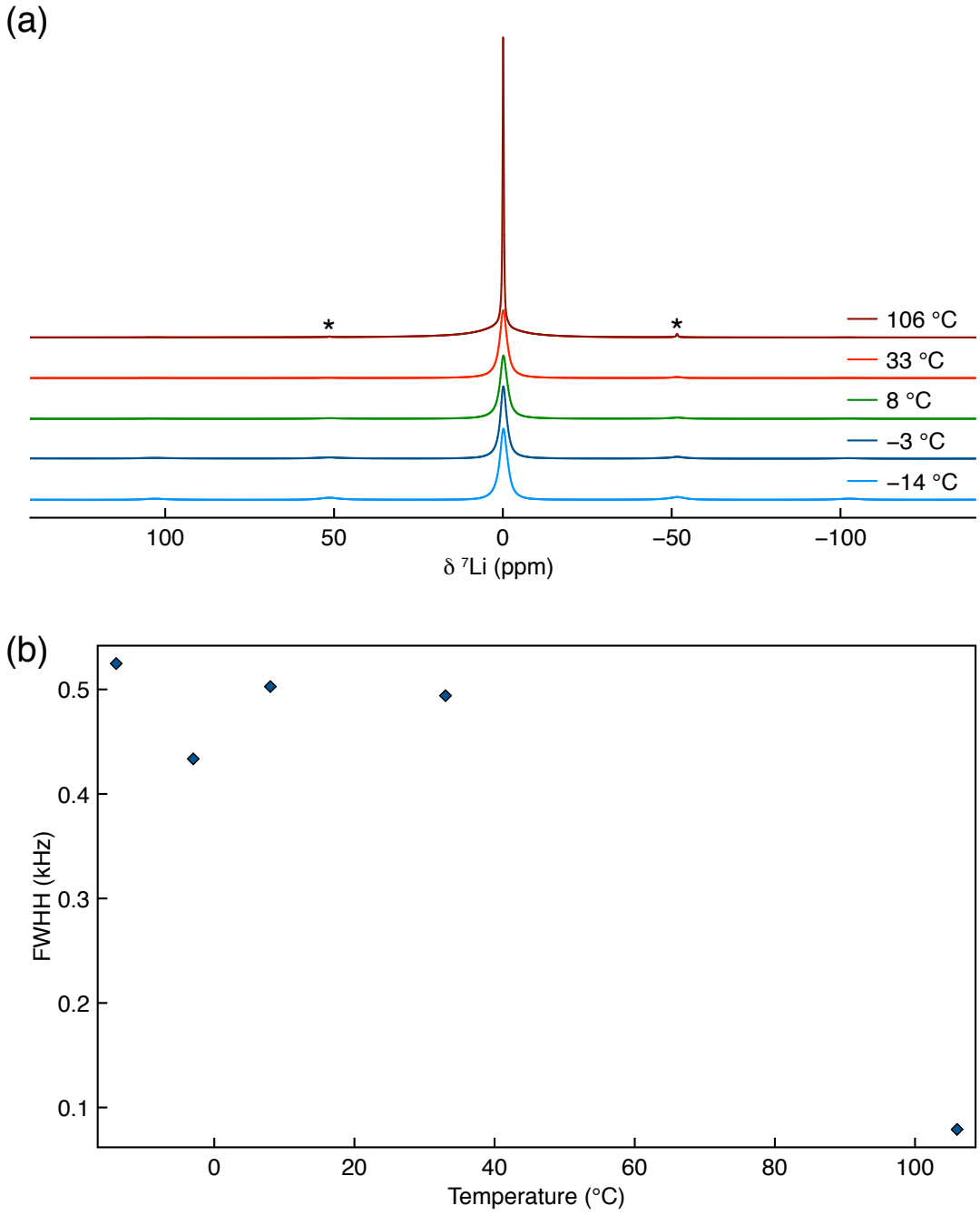

Figure 7.24: (a) ^{7}Li (11.7 T) MAS NMR spectra acquired between −14 and 106 °C, for a sample of $Li_2OHCl_{0.4}Br_{0.6}$ synthesised via a conventional solid-state reaction completed inside an Ar-filled glovebox. The MAS rate was 10 kHz and spinning sidebands are denoted by *. In all cases, a recycle delay of 10 s was used to acquire 4 transients. (b) The corresponding variation in FWHM as a function of temperature.

across the whole temperature range. At 106 °C, a ^{7}Li T_1 of ~0.26 s is obtained. Interestingly, this is also approximately midway between the T_1 of ~0.19 and ~0.36 s obtained at 106 °C for Li_2OHCl and Li_2OHBr, respectively. The ^{1}H and

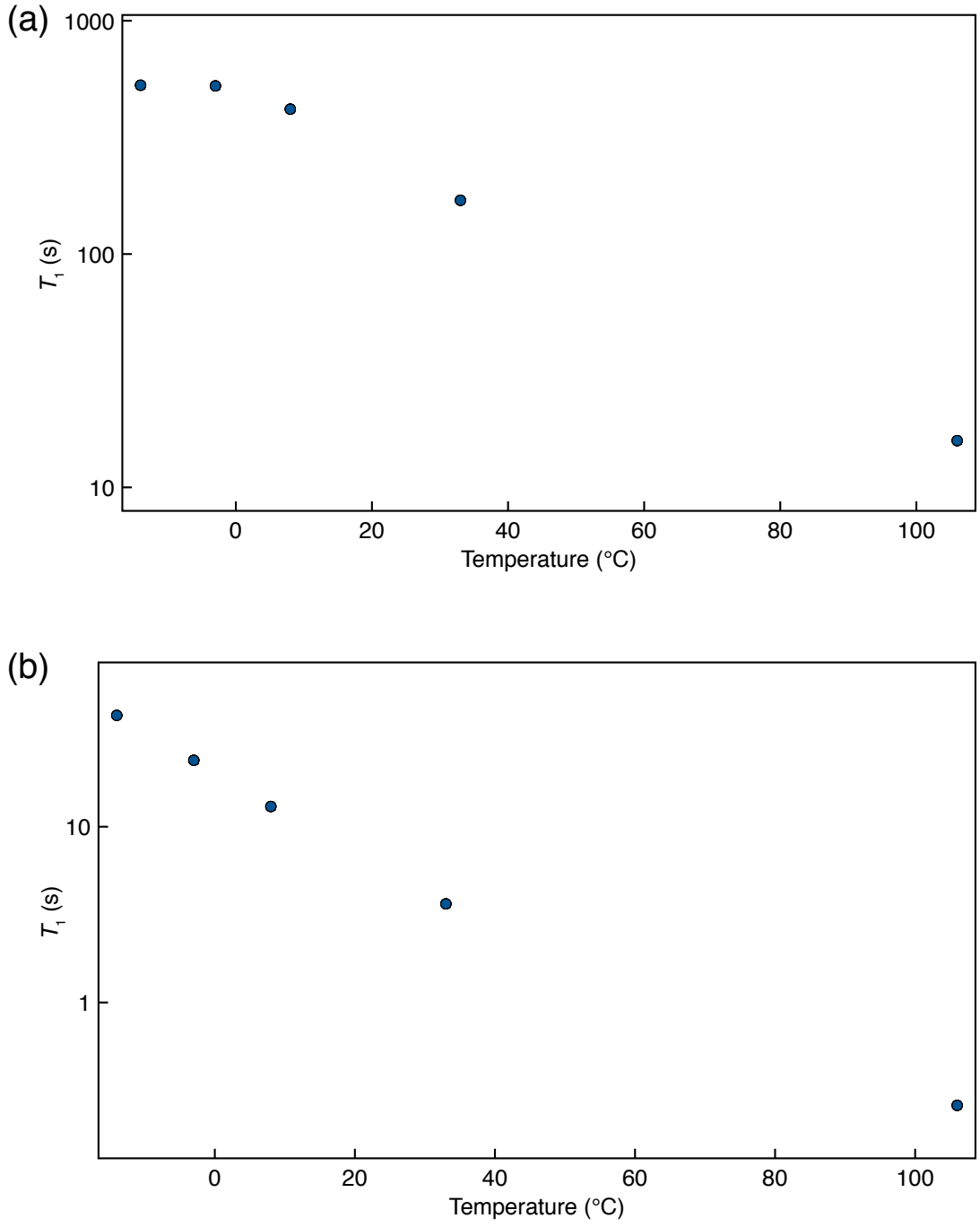

Figure 7.25: (a) ^{1}H and (b) ^{7}Li (11.7 T) T_1 values obtained between −14 – 106 °C, for a sample of $Li_2OHCl_{0.4}Br_{0.6}$ synthesised via a conventional solid-state route. In all cases, the estimated error bars are smaller than the symbols used and are therefore not shown.

^{7}Li data presented here suggests that the degree of proton and Li-ion mobility exhibited by $Li_2OHCl_{0.4}Br_{0.6}$ is higher than Li_2OHBr but lower than Li_2OHCl. This is somewhat surprising as Zhao and Daemen[124] proposed that LiRAPs with a mixed halide composition such as $Li_3OCl_{0.5}Br_{0.5}$ exhibit superior ion

conductivity compared to the end members (Li_3OCl and Li_3OBr). However, this does not appear to be the case for the hydrated analogues. Instead, the ^1H and ^7Li T_1 data presented appears to suggest that T_1 values likely vary linearly as a function of x in the $Li_2OHCl_{1-x}Br_x$ system. It is noted that additional experiments are needed to confirm this suggestion. More specifically, the rest of the samples in the series will also need to be analysed via VT multinuclear SSNMR. In general, the NMR data presented here is very insightful as it demonstrates that the degree of mobility exhibited in the $Li_2OHCl_{1-x}Br_x$ system can be readily tuned via compositional doping.

^2H MAS NMR Spectroscopy

As with the end members of the $Li_2OHCl_{1-x}Br_x$ (x = 0 and 1) series, a sample of $Li_2OHCl_{0.4}Br_{0.6}$ was deuterated and analysed via VT ^2H MAS NMR spectroscopy. The ^2H MAS NMR spectra acquired between −19 and 116 °C are shown in Figure 7.26. Between −19 and 69 °C, an axially symmetric lineshape consisting of multiple spinning sidebands is observed. As mentioned earlier, this lineshape corresponds to static OH^-/OD^- groups. Thus, indicating that in $Li_2OHCl_{0.4}Br_{0.6}$, the OH^-/OD^- groups do not exhibit any motion between −19 and 69 °C. The lineshape observed at 33 °C was simulated to determine the corresponding quadrupolar parameters, and a C_Q = 257(1) kHz and η_Q = 0.065(1) were obtained (Figure 7.27). These values are similar to those obtained for both Li_2OHCl and Li_2OHBr and those reported in the literature for static ^2H species.[215] Thus, confirming the presence of static OH^-/OD^- groups in the sample. At 116 °C, there is a broad signal around 0 ppm, believed to correspond to freely rotating OH^-/OD^- groups. However, the spectrum is dominated by the signal corresponding to the static OH^-/OD^- groups. Thus, indicating that only a very small proportion of OH^-/OD^- groups are exhibiting motion. It is noted that in $Li_2OHCl_{0.4}Br_{0.6}$, this broad signal appears much later, at 116 °C, when compared to Li_2OHCl and Li_2OHBr, where this signal was first observed at 69 and 79 °C, respectively. Also, in Li_2OHCl and Li_2OHBr, this broad component became the dominant signal at ~110 °C. However, in $Li_2OHCl_{0.4}Br_{0.6}$, its intensity is considerably lower when com-

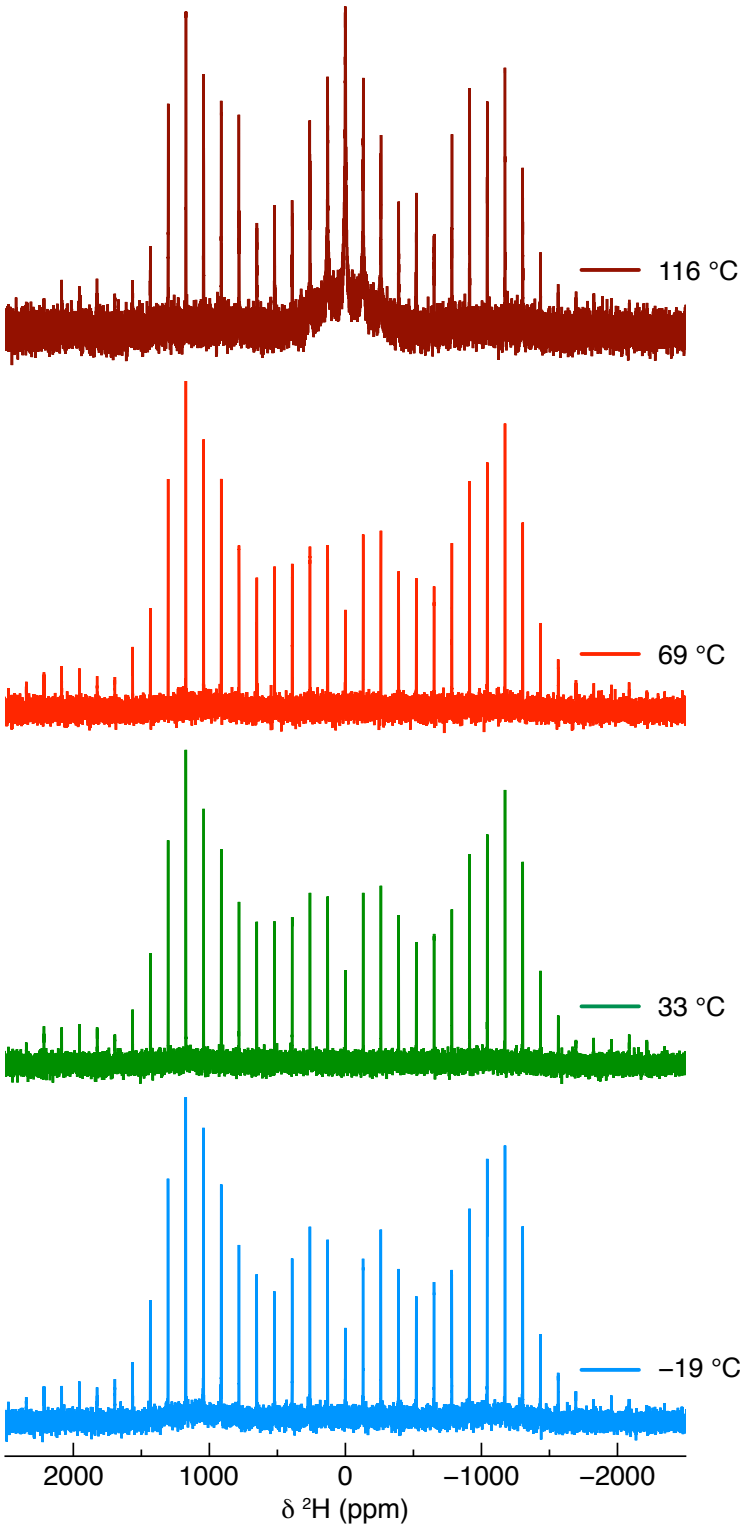

Figure 7.26: ^{2}H (11.7 T) MAS NMR spectra acquired over the temperature range −19 – 116 °C, for a sample of $Li_2OHCl_{0.4}Br_{0.6}$ synthesised via a conventional solid-state reaction completed inside an Ar-filled glovebox. The MAS rate was 10 kHz and a recycle delay of 15 s was used to acquire 80 transients.

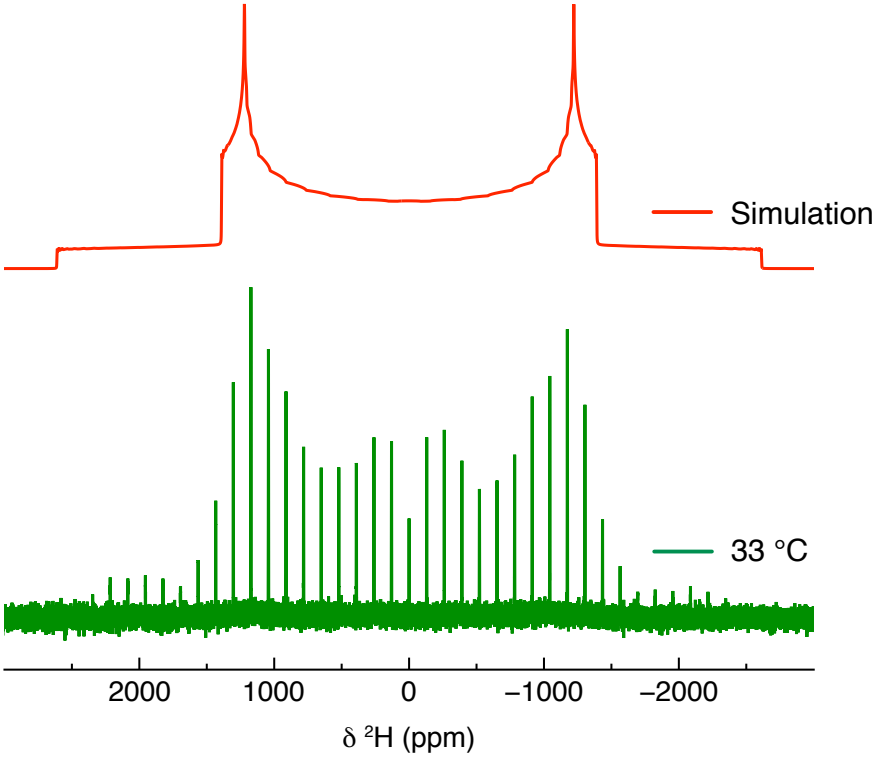

Figure 7.27: ^{2}H (11.7 T) MAS NMR spectrum acquired at 33 °C, for a sample of $Li_2OHCl_{0.4}Br_{0.6}$ synthesised via a conventional solid-state reaction completed inside an Ar-filled glovebox. The MAS rate was 10 kHz and a recycle delay of 15 s was used to acquire 80 transients. The spectrum was simulated to obtain the corresponding quadrupolar parameters, C_Q = 257(1) kHz and η_Q = 0.065(1).

pared to the signal corresponding to the static environments. Thus, suggesting that halide mixing may not be a suitable method for promoting ion mobility in Li_2OHCl/Br samples, as it appears to limit or restrict the free rotation of OH^-/OD^- groups. Moreover, temperatures over 100 °C are required in order to observe any movement of the OH^-/OD^- groups. Again, this is in contrast to Zhao and Daemen's[124] suggestion that LiRAPs with mixed halide compositions exhibit much higher ionic conductivities than the end members. As discussed previously, the OH^-/OD^- movement is believed to be closely connected to the Li-ion movement. Thus, the ^{2}H NMR data presented here suggests that the OH^-/OD^- groups in $Li_2OHCl_{0.4}Br_{0.6}$ may hinder the Li-ion mobility because they remain static over a large temperature range. These findings also indicate that a cubic structure is not the only criteria for ion mobility in LiRAPs. Additional factors such as the halides present in the sample and their concentration are also important, as well as the temperature.

^{35}Cl MAS NMR Spectroscopy

A sample of $Li_2OHCl_{0.4}Br_{0.6}$ was also analysed via VT ^{35}Cl MAS NMR spectroscopy, and the spectra acquired at 33, 63 and 106 °C are shown in Figure 7.28. At 33 °C, an asymmetric lineshape is observed. A signal is also observed around 5 ppm, corresponding to LiCl (*vide supra*). However, the diffraction pattern obtained for this sample (Figure 7.13) did not show any evidence of residual LiCl. Hence, LiCl must be present in an extremely small quantity. An increase in temperature to 63 °C does not appear to have any noticeable effects on the spectrum observed, as it remains unchanged. However, a further increase to 106 °C results in significant narrowing of the resonance, but there is no concurrent increase in the intensity. Thus, implying a reduction in the amount of signal obtained.

The lineshapes observed in the spectra acquired at 33 and 106 °C were simulated to try and determine the number of distinct Cl sites present in each case. The simulated lineshapes, along with the distinct Cl sites required for

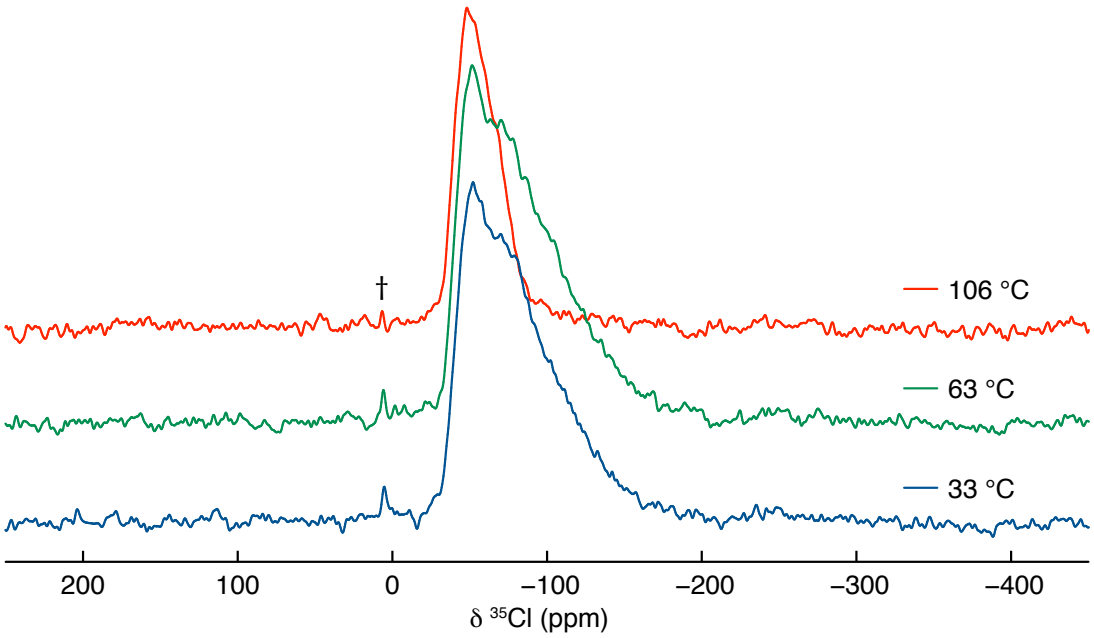

Figure 7.28: ^{35}Cl (11.7 T) MAS NMR spectra acquired over the temperature range 33 – 106 °C, for a sample of $Li_2OHCl_{0.4}Br_{0.6}$ synthesised via a conventional solid-state reaction completed inside an Ar-filled glovebox. In all cases, the MAS rate was 10 kHz and a recycle delay of 5 s was used to acquire 2560 transients. The signal corresponding to LiCl is denoted by †.

the fit, are shown in Figure 7.29, and the corresponding quadrupolar parameters are detailed in Table 7.4. At 33 °C, three sites were required to simulate the overall lineshape, whereas, at 106 °C, only two sites were required. The XRD analysis of this sample indicated that $Li_2OHCl_{0.4}Br_{0.6}$ adopts a cubic structure in space group $Pm\bar{3}m$ with a single halide site. Therefore, the presence of multiple Cl sites at 33 and 106 °C is somewhat surprising. However, as discussed earlier, NMR is a local probe, and therefore, only provides information regarding the local environment of a nucleus and not the crystal structure as a whole. Thus, the ^{35}Cl NMR data presented here indicates that whilst $Li_2OHCl_{0.4}Br_{0.6}$ contains one crystallographically distinct Cl site, various local Cl environments are present in the sample. The corresponding quadrupolar parameters obtained indicate a highly symmetrical environment for all Cl sites but it is not perfectly cubic. Interestingly, the ^{35}Cl MAS NMR data obtained for the cubic phases of Li_2OHCl also exhibited multiple sites with similar quadrupolar parameters.

Moreover, the VT ^{35}Cl NMR data acquired for Li_2OHCl exhibited a severe reduction in the observable signal with increasing temperature. Here, however, a moderate drop is observed. Earlier it was suggested that the reduction in the ^{35}Cl signal with increasing temperature is likely an indirect consequence of proton and Li-ion mobility, or perhaps Cl could also be exhibiting some local movement. However, it is noted that no Cl motion was detected in Li_2OHCl on the NMR timescale via ^{35}Cl EXSY. Thus, ^{35}Cl NMR signal reduction is likely due to the proton and Li-ion mobility. As mentioned earlier, the ^{1}H and ^{7}Li NMR data obtained for $Li_2OHCl_{0.4}Br_{0.6}$ suggested a lesser degree of H and Li mobility when compared to Li_2OHCl. Additionally, the ^{2}H NMR data demonstrated that the OH^-/OD^- groups in $Li_2OHCl_{0.4}Br_{0.6}$ become mobile much later (>100 °C) compared to Li_2OHCl. This appears to correlate well with the fact that the signal reduction observed for ^{35}Cl in $Li_2OHCl_{0.4}Br_{0.6}$ is much lower than for Li_2OHCl. Thus, the two processes may be linked. However, the current data does not provide conclusive proof for this and further investigation is still needed.

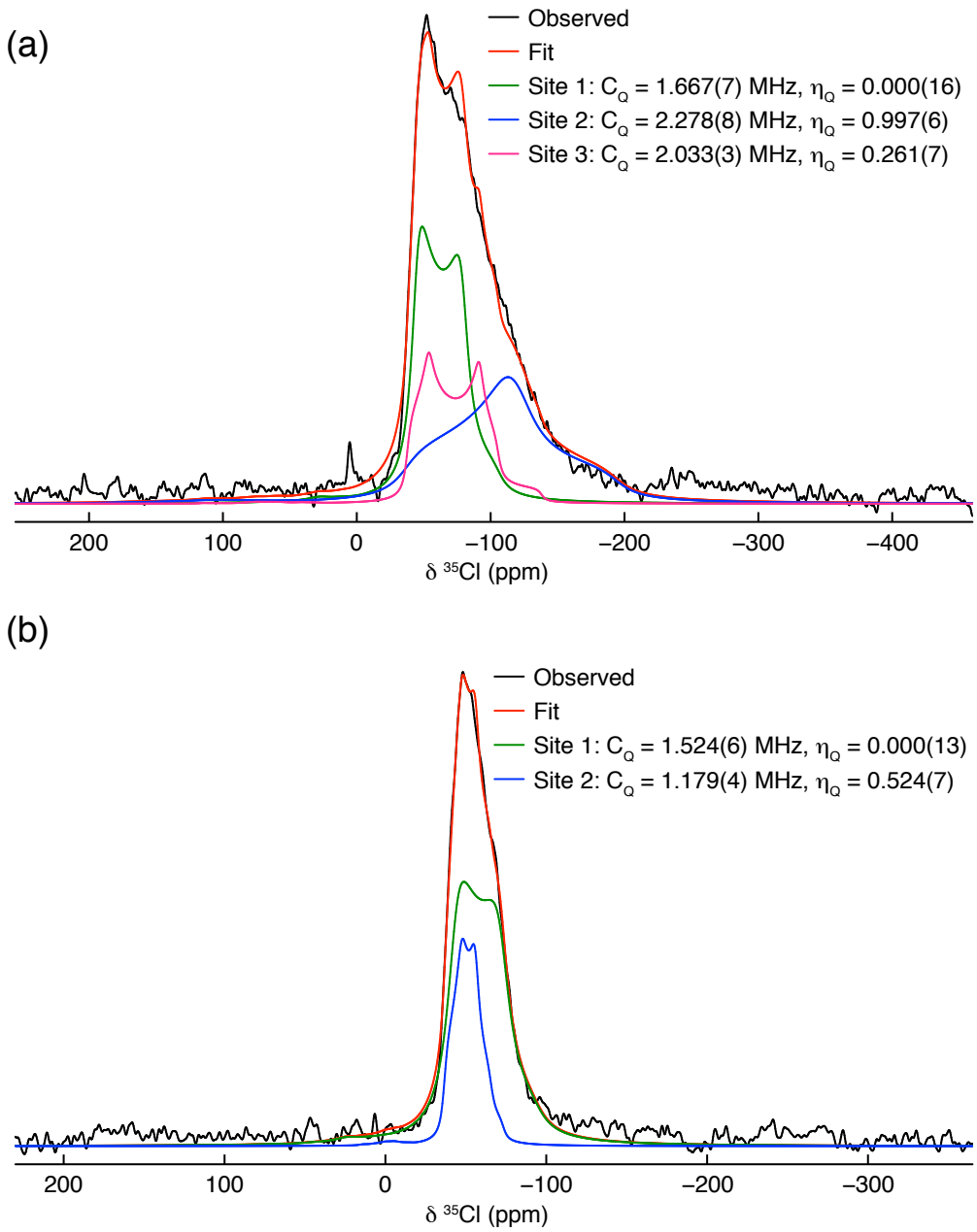

Figure 7.29: Simulations of the ^{35}Cl (11.7 T) MAS NMR spectra acquired at (a) 33 °C and (b) 106 °C for a sample of $Li_2OHCl_{0.4}Br_{0.6}$ synthesised via a conventional solid-state reaction completed inside an Ar-filled glovebox. The MAS rate was 10 kHz and a recycle delay of 5 s was used to acquire 2560 transients. At 33 °C, three sites were required to fit the lineshape and the corresponding quadrupolar parameters are: Site 1 (C_Q = 1.667(7) MHz and η_Q = 0.000(16)), Site 2 (C_Q = 2.278(8) MHz and η_Q = 0.997(6)), Site 3 (C_Q = 2.033(3) and η_Q = 0.261(7)). At 106 °C, two sites were required to fit the lineshape and the corresponding quadrupolar parameters are: Site 1 (C_Q = 1.524(6) MHz and η_Q = 0.000(13)), Site 2 (C_Q = 1.179(4) MHz and η_Q = 0.524(7)).

Table 7.4: ^{35}Cl NMR parameters, δ, C_Q, and η_Q, obtained by simulating the lineshapes observed in the ^{35}Cl MAS NMR spectra obtained at 33 and 106 °C, for a sample of $Li_2OHCl_{0.4}Br_{0.6}$ prepared via conventional solid-state synthesis inside an Ar-filled glovebox.

Site	δ (ppm)	C_Q (MHz)	η_Q
33 °C			
1	−34.20(5)	1.667(7)	0.000(16)
2	−36.51(22)	2.278(8)	0.997(6)
3	−29.15(13)	2.033(3)	0.261(7)
106 °C			
1	−34.40(17)	1.524(6)	0.000(13)
2	−35.44(8)	1.179(4)	0.524(7)

^{79}Br MAS NMR Spectroscopy

Finally, $Li_2OHCl_{0.4}Br_{0.6}$ was also analysed via VT ^{79}Br MAS NMR spectroscopy and the spectra acquired at 33, 63 and 106 °C are shown in Figure 7.30. At 33 °C, a single relatively broad resonance centred around 64.87 ppm is observed. Again, this is expected for a cubic structure in space group $Pm\bar{3}m$, which has a single halide site. An increase in temperature to 63 and 106 °C results in a gradual decrease in the signal intensity and a change in chemical shift, first to 65.60 and then to 66.58 ppm. Also, the linewidth of the resonance observed does not exhibit any noticeable changes. This trend is similar to that observed for Li_2OHBr (*vide supra*).

In the case of Li_2OHBr, the gradual change in the ^{79}Br NMR data was compared to the ^{35}Cl NMR data acquired for Li_2OHCl. As both systems are analogues, similar trends are expected. It was suggested that the change in the ^{79}Br resonance might be an influenced of the proton and Li-ion mobility occurring in the sample. However, the two halides exhibit different trends in this mixed halide sample. The ^{35}Cl NMR spectra did not exhibit any change between 33 and 63 °C, whereas the ^{79}Br NMR spectra exhibits a gradual change across the whole temperature range. Thus, suggesting that the two halides may be experiencing different effects. This is surprising because Cl and Br are

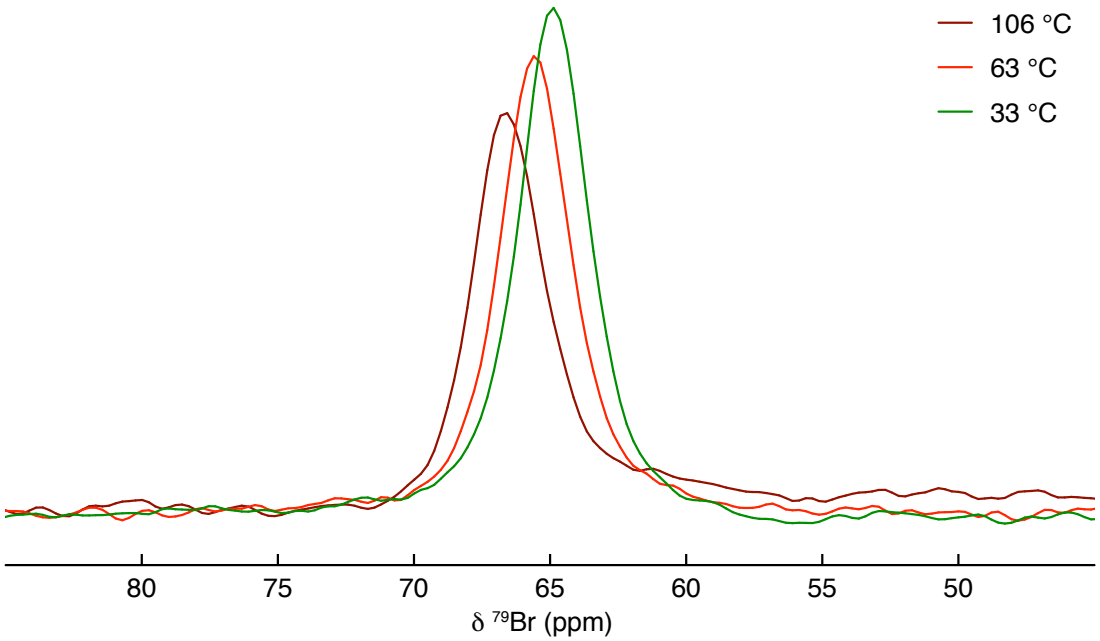

Figure 7.30: ^{79}Br (11.7 T) MAS NMR spectra acquired over the temperature range 33 – 106 °C, for a sample of $Li_2OHCl_{0.4}Br_{0.6}$ synthesised via a conventional solid-state reaction completed inside an Ar-filled glovebox. The MAS rate was 10 kHz and a recycle delay of 1 s was used to acquire 800 transients, in all cases.

expected to occupy the same site in the cubic structure in space group $Pm\bar{3}m$. Therefore, it remains unclear as to why this occurs.

Overall, the ^{35}Cl and ^{79}Br NMR data presented has proven to be particularly useful, as it highlights the need for further research into these systems. In particular, a comprehensive characterisation of the halide environments in LiRAPs is needed to understand this system fully and determine the role or influence of the halide(s).

7.4 Conclusions

This chapter focused on probing compositional changes in Li_2OHCl via fluorine doping and halide mixing. All samples were synthesised via the muffle furnace method described earlier using the same reaction conditions as Li_2OHCl. The samples produced were characterised using laboratory XRD and SSNMR methods to investigate the structural changes occurring and ion mobility as a function of composition. A fluorinated analogue of Li_2OHCl was

synthesised via partial substitution of OH^- by F^- to produce $Li_2(OH)_{0.9}F_{0.1}Cl$. Fluorine doping was observed to stabilise the cubic structure at room temperature, owing to an increase in the tolerance factor. Thus, the sample produced adopted a cubic structure in space group $Pm\bar{3}m$ at room temperature. The sample produced was not entirely phase pure as the parent material, Li_2OHCl, was also present, as well as, residual amounts of starting reagents, LiCl and LiF. However, most of the sample consisted of the desired phase, making the synthesis successful.

The $Li_2(OH)_{0.9}F_{0.1}Cl$ sample was analysed via VT ^1H and ^7Li MAS NMR spectroscopy over a temperature range of −19 to 106 °C to probe ion dynamics within the sample. In a similar manner to Li_2OHCl, $Li_2(OH)_{0.9}F_{0.1}Cl$ also exhibited proton and Li-ion mobility with increasing temperature. A deuterated sample studied via ^2H MAS NMR spectroscopy indicated the presence of static OH^-/OD^- groups between −19 and 8 °C, and at 106 °C, a large majority of the OH^-/OD^- groups were identified as being mobile. Determining the state of OH^-/OD^- groups at 33 and 69 °C proved quite difficult as the ^2H MAS NMR signal disappeared upon increasing the temperature to 33 °C before re-appearing at 106 °C. Hence, additional ^2H MAS NMR spectra were acquired with a greater number of transients at 33 and 69 °C to see if a signal could be observed. Despite an extremely poor signal to noise ratio, the data obtained confirmed the presence of static OH^-/OD^- groups at 33 °C. At 69 °C, the static and mobile OH^-/OD^- groups were present simultaneously. Similar observations were made for Li_2OHCl, where the OH^-/OD^- also became mobile at 69 °C. However, for Li_2OHCl, a ^2H NMR signal was observable across the whole temperature range investigated. At present, the exact reasons for the disappearance of the ^2H NMR signal are not fully understood.

The VT ^{35}Cl MAS NMR spectrum obtained for $Li_2(OH)_{0.9}F_{0.1}Cl$ at 33 °C closely resembled that observed for the high-temperature cubic phase of Li_2OHCl. Here too, two local environments were identified for Cl in the cubic structure, and an increase in temperature resulted in a gradual reduction in the signal observed. At 106 °C, the resonance was barely visible. Again, it is not clear why this occurs. However, it was suggested that the EFG experienced by

Cl could constantly be changing, which could make the signal unobservable. This could occur either due to Cl motion or the proton and Li-ion mobility in the sample. However, no Cl motion was detected in the parent material on the NMR timescale. Thus, it was suggested that the signal reduction may indirectly result from the proton and Li-ion movement. However, this cannot be confirmed solely from the data presented.

Finally, $Li_2(OH)_{0.9}F_{0.1}Cl$ was analysed via VT ^{19}F MAS NMR spectroscopy over the temperature range −14 to 106 °C. In all cases, two distinct resonances corresponding to $Li_2(OH)_{0.9}F_{0.1}Cl$ and LiF were observed. The resonance corresponding to $Li_2(OH)_{0.9}F_{0.1}Cl$ exhibited significant line narrowing with a concurrent increase in intensity with increasing temperature. Thus, suggesting that fluorine may also be exhibiting mobility. The corresponding ^{19}F T_1 values exhibited a significant decrease with increasing temperature, further suggesting fluorine mobility. However, the current data does not allow for the precise nature of the fluorine movement to be determined, *i.e.*, it could not be discerned whether fluorine exhibits short- or long-range motion. Lastly, at 106 °C, where the ^{19}F resonance narrows considerably, two distinct F sites were observed. Thus, suggesting two distinct local environments for fluorine. However, the cubic structure has only one crystallographically distinct fluorine site. Thus, it was suggested that fluorine could possibly be occupying both the OH and Cl sites as both configurations are reported to have similar formation energies.[235]

Interestingly, all VT NMR data acquired for $Li_2(OH)_{0.9}F_{0.1}Cl$ exhibited significant differences above and below room temperature. Thus, suggesting a phase transition below room temperature. However, this phase transition was not investigated in great detail, as the primary focus of this study was to probe ion mobility in the LiRAP samples. As such, the cubic phase of $Li_2(OH)_{0.9}F_{0.1}Cl$ was deemed more important as the cubic structure allows for ion mobility, whereas no ion mobility was observed at lower temperatures.

The composition of Li_2OHCl was also modified via halide mixing, where Cl^- was partially replaced by Br^- to produce samples in the series

$Li_2OHCl_{1-x}Br_x$ (x = 0.1 – 1). The Br concentration was increased gradually in 0.1 increments to eventually produce Li_2OHBr. All samples in this series adopted a cubic structure in space group $Pm\bar{3}m$. Thus, demonstrating that, in addition to fluorine doping, halide mixing is also a suitable method for stabilising the desired cubic structure at room temperature. The lattice parameter increased linearly with increasing Br concentration, owing to the relative sizes of the halide ions. The samples produced predominantly consisted of the desired phase. However, the $Li_2OHCl_{0.9}Br_{0.1}$ sample also contained some Li_2OHCl, and both the $Li_2OHCl_{0.9}Br_{0.1}$ and $Li_2OHCl_{0.8}Br_{0.2}$ samples contained residual LiCl. The remaining samples, with the exceptions of $Li_2OHCl_{0.4}Br_{0.6}$ and Li_2OHBr, contained trace amounts of impurity phases, most likely non-stoichiometric hydrated phases based on the desired phase. The end member of the series, Li_2OHBr, was analysed via VT XRD over the temperature range −163 to 77 °C. At −163 °C, there were initial signs of a phase transition. However, a complete transition was not observed owing to the technical limitations of the equipment used. This structural change was observed to be reversible with increasing temperature.

Li_2OHBr was studied via VT multinuclear NMR spectroscopy over the temperature range −19 to 106 °C. The VT ^1H and ^7Li NMR spectra obtained suggested that Li_2OHBr also exhibits proton and Li-ion mobility. ^1H and ^7Li T_1 data indicated that protons exhibit less mobility than Li-ions, and both species were less mobile when compared to Li_2OHCl. Additionally, the energy barrier calculated for Li-ion mobility was a little higher than for protons. However, the energy barrier for both species was lower in Li_2OHBr compared to Li_2OHCl. The ^2H MAS NMR data obtained for Li_2OHBr demonstrated the presence of static OH^-/OD^- groups between 8 – 69 °C. The OH^-/OD^- groups were observed to become mobile at 79 °C, and further increases in temperature resulted in an increase in the proportion of mobile OH^-/OD^- groups and thus a decrease in the static groups. Almost all of the OH^-/OD^- groups were mobile at 110 °C. A similar trend was observed for Li_2OHCl, although in Li_2OHCl, the OH^-/OD^- groups became mobile at lower temperatures (69 °C). Li_2OHBr was also analysed via VT ^{79}Br MAS NMR spectroscopy over a temperature

range of −19 to 106 °C. A single resonance indicative of a single site was observed. The resonance exhibited a gradual decrease in intensity, along with an increase in the chemical shift, with increasing temperature. This was likened to the decrease in signal observed for ^{35}Cl NMR signal in Li_2OHCl. However, the precise cause for this remains unclear.

Lastly, a mixed halide sample, $Li_2OHCl_{0.4}Br_{0.6}$, was also selected to be studied via multinuclear VT SSNMR spectroscopy. The ^{1}H and ^{7}Li MAS NMR data obtained for $Li_2OHCl_{0.4}Br_{0.6}$ suggested that, in a similar manner to Li_2OHCl/Br, it also exhibits proton and Li-ion mobility. Interestingly, the ^{1}H and ^{7}Li T_1 values obtained were midway between those obtained for Li_2OHCl and Li_2OHBr. Thus, suggesting that the mobility exhibited may decrease linearly with increasing x in $Li_2OHCl_{1-x}Br_x$. However, the ^{2}H MAS NMR data acquired for a deuterated sample indicated that all OH^-/OD^- groups were static between −19 and 69 °C. Only a small proportion of the OH^-/OD^- groups become mobile at 116 °C. Thus, indicating much lower proton and, consequently, Li-ion mobility in the mixed halide sample. VT ^{35}Cl MAS NMR experiments were also completed for the $Li_2OHCl_{0.4}Br_{0.6}$ sample between 33 – 106 °C. At 33 °C, three distinct Cl sites were observed, and at 106 °C, two distinct Cl sites were observed. At 106 °C, a noticeable reduction in the signal was also observed, but the signal was still observable. Finally, the sample was also analysed via VT ^{79}Br MAS NMR spectroscopy between 33 and 106 °C. A similar trend to that observed for Li_2OHBr was also observed here, *i.e.*, a single resonance exhibiting a small but gradual decrease in intensity with increasing temperature was observed. The resonance also exhibited a change in chemical shift to higher ppm values. Interestingly, Cl and Br are expected to occupy the same site in this sample. Thus, they are expected to exhibit similar behaviour. However, this was not the case as the ^{35}Cl signal did not change until 106 °C, whereas the ^{79}Br signal changed across the whole temperature range.

Overall, the data presented in this chapter demonstrates that Li_2OHCl is a promising material that exhibits good structural flexibility. Its composition can be easily modified via fluorine doping and halide mixing to access the high-temperature cubic phase at room temperature. Moreover, the sam-

ple composition was demonstrated to influence the proton and Li-ion mobility greatly. Thus, fine-tuning the composition of Li_2OHCl can be useful in producing materials capable of exhibiting very high Li-ion conductivities.

8 Conclusions and Future Work

8.1 Conclusions

The primary focus of this thesis was to synthesise and characterise a series of LiRAPs, including Li_3OCl, Li_3OBr, their hydrated analogues, Li_2OHCl, Li_2OHBr and probe compositional changes in Li_2OHCl via fluorine doping and halide mixing. Owing to their extremely hygroscopic nature, a series of air-sensitive techniques were used to prepare each LiRAP. Each sample was analysed extensively via laboratory XRD, NPD and multinuclear SSNMR spectroscopy. Particular emphasis was placed on probing ion mobility within LiRAPs as they have been proposed as candidate solid electrolyte materials. AIMD simulations were also completed by our collaborators to support our experimental findings.

Initial investigations began with attempts to synthesise phase pure samples of Li_3OCl and Li_3OBr. Samples were synthesised using LiCl, LiBr, LiOH and Li_2O as precursors via the Schlenk link or the muffle furnace method. Numerous reaction temperatures and times were tested to optimise the reaction conditions. Li_3OCl and Li_3OBr were successfully produced, but the success was limited as the samples prepared were not phase pure. Attempts to increase phase purity included preparing the reagent mixture under an inert atmosphere, regrinding and reheating the sample and using methods such as pellet pressing and mechanical milling. However, producing phase pure samples remained a challenge. The samples synthesised using LiCl, LiBr, and LiOH always contained impurity phase(s), believed to be non-stoichiometric hydrates or non-hydrated phases based on Li_3OCl and Li_3OBr. Conversely, the reactions carried out using LiCl, LiBr, and Li_2O never reached completion as Li_3OCl and Li_3OBr are believed to be metastable phases and are reported to readily decompose to form LiCl, LiBr and Li_2O. Overall, the Schlenk line method resulted in more favourable outcomes when compared to the muffle furnace method, as more of the desired phase was produced for both Li_3OCl and Li_3OBr. However, the numerous experiments detailed in this study sat-

isfactorily demonstrate that the prospects of forming phase pure samples of Li_3OCl and Li_3OBr are extremely low. This is in agreement with recent literature reports and brings Zhao and Daemen's findings into serious question and doubt.[124,196,218]

The inability to form a phase pure sample of Li_3OCl shifted the focus of this study towards its hydrated analogue, Li_2OHCl. The synthesis of which proved to be a much easier task. Li_2OHCl was successfully synthesised using two different methods, a conventional solid-state reaction and solely via mechanical milling, both of which were again completed under air-sensitive conditions. Li_2OHCl is known to exist in two different phases, a room-temperature phase believed to be orthorhombic and a high-temperature cubic phase in space group $Pm\bar{3}m$. The findings presented in the current study demonstrate that the synthesis method greatly influences the phase obtained at room temperature. The sample synthesised via a conventional solid-state route adopted what is believed to be an orthorhombic structure, whereas mechanical milling produced a sample that contained a cubic phase in space group $Pm\bar{3}m$ at room temperature. Thus, highlighting the usefulness of mechanical milling, as the high-temperature phase can be accessed at room temperature.

The room-temperature phase of Li_2OHCl has been a subject of considerable debate within the literature in recent years, as a suitable and complete structure is yet to be agreed upon. Hence, considerable efforts were dedicated to elucidating the room-temperature structure of Li_2OHCl. Several structural models proposed in the literature, including a tetragonal structure in space group $P4mm$ and numerous orthorhombic structures, in space groups $Pmc2_1$, $Cmcm$, $Pmmm$ and $Pban$, were assessed using the XRD and NPD data. Some structural suggestions reported in the literature could not be evaluated owing to a lack of crystallographic information required to generate a model. However, of the models proposed and evaluated, the orthorhombic structures in space groups $Pmc2_1$, $Cmcm$, and $Pmmm$ appeared to be the most suitable candidates. Conversely, the crystallographic information reported in the literature for the $Pban$ model was identified as being incorrect, as it was not in line with the guidelines specified in the International Tables for Crystallography.[220] In-

terestingly, correcting this information produced a structural model that appears to be an excellent candidate structure for the room-temperature phase of Li_2OHCl. Moreover, ^{35}Cl NMR studies proved highly informative, as the data obtained indicated that Cl exhibits at least three distinct local environments in the room-temperature phase and two distinct environments in the high-temperature cubic ($Pm\bar{3}m$) phase. However, none of the room-temperature structures investigated contained three crystallographic sites for Cl, and the high-temperature cubic ($Pm\bar{3}m$) phase is known to have a single crystallographic Cl site. NMR is a local probe that provides information regarding the local structure as opposed to the long-range structure. Thus, it appears that the number of local Cl environments varies from the number of crystallographic sites proposed by diffraction-based methods, which highlights the importance of using multiple, complementary characterisation techniques.

In a similar manner to the perovskite structure, the anti-perovskite structure exhibits extreme structural flexibility. Consequently, the composition of Li_2OHCl is easily altered. In the current study, the composition of Li_2OHCl was modified by varying the Li and, in turn, the H content to produce samples in the series $Li_{3-x}OH_xCl$ (x = 0.25, 0.5 and 0.75). Fluorine doping also was used to prepare $Li_2(OH)_{0.9}F_{0.1}Cl$, and halide mixing was used to produce $Li_2OHCl_{1-x}Br_x$ (x = 0.1 – 1). All samples in the series $Li_{3-x}OH_xCl$ (x = 0.25, 0.5 and 0.75) adopted the same structure as the room-temperature phase of Li_2OHCl and, upon heating, exhibited a phase transition to cubic symmetry in space group $Pm\bar{3}m$. Conversely, $Li_2(OH)_{0.9}F_{0.1}Cl$ and samples in the series $Li_2OHCl_{1-x}Br_x$ (x = 0.1 – 1) adopted a cubic structure in space group $Pm\bar{3}m$ at room temperature. Thus, demonstrating that the structure of Li_2OHCl can be controlled via doping. Interestingly, ^{19}F NMR data acquired for $Li_2(OH)_{0.9}F_{0.1}Cl$ at high temperatures indicated two distinct fluorine environments in the sample. It is suspected that fluorine occupies both the OH and Cl sites in the structure. However, this is particularly challenging to prove or confirm with solely the current data and further investigation is therefore needed. Moreover, all VT NMR datasets acquired for $Li_2(OH)_{0.9}F_{0.1}Cl$, Li_2OHBr and $Li_2OHCl_{0.4}Br_{0.6}$ suggest significant structural changes below room

temperature. The data suggests that these samples may be undergoing a phase transition below room temperature to adopt the same structure as that of the room-temperature phase of Li_2OHCl.

Li_2OHCl was extensively investigated via VT multinuclear SSNMR methods to probe ion mobility within LiRAPs. The ^1H and ^7Li NMR data obtained suggested that both species exhibit mobility. This was confirmed via ^1H and ^7Li T_1 measurements, and the corresponding energy barriers obtained were in agreement with those reported in the literature.[213] The ^2H NMR experiments completed for a deuterated sample indicated that the protons/deuterons exhibit reorientational/rotational motion around the oxygen rather than free movement throughout the structure. Moreover, the OH^-/OD^- groups do not appear to exhibit any motion until much higher temperature, *i.e.*, following the phase transition. Thus, temperature was determined to play a key role in the mobility of OH^-/OD^- groups. ^1H and ^7Li PFG-NMR spectroscopy confirmed that protons do not display any diffusion, whereas Li-ions exhibit diffusion and are therefore capable of moving throughout the structure. The experimental findings were supported by AIMD simulations completed by our collaborators. The MSD plots generated for each element in Li_2OHCl and the diffusion maps obtained indicate that Li exhibits long-range motion, whereas proton mobility is limited. The calculations also indicated a highly correlated movement of protons and Li-ions, as the protons always point towards a Li-ion vacancy. Thus, the movement of Li-ions causes the protons to reorient in order to ensure they are always pointing towards a vacancy.

Samples in the series $Li_{3-x}OH_xCl$ (x = 0.25, 0.5 and 0.75), $Li_2OHCl_{1-x}Br_x$ (x = 0.1 – 1) and the fluorinated sample, $Li_2(OH)_{0.9}F_{0.1}Cl$, were also studied via ^1H and ^7Li NMR to investigate proton and Li-ion mobility. In a similar manner to Li_2OHCl, these samples also exhibited proton and Li-ion mobility. Deuterated samples of $Li_{2.5}OH_{0.5}Cl$, $Li_2(OH)_{0.9}F_{0.1}Cl$, Li_2OHBr and $Li_2OHCl_{0.4}Br_{0.6}$ were analysed via VT ^2H NMR spectroscopy. Similar to Li_2OHCl, in $Li_2(OH)_{0.9}F_{0.1}Cl$, the OH^-/OD^- groups became mobile at 69 °C. However, in $Li_{2.5}OH_{0.5}Cl$ and Li_2OHBr, the OH^-/OD^- groups become mobile at 79 °C, whereas in $Li_2OHCl_{0.4}Br_{0.6}$, only a small proportion of OH^-/OD^- groups became mobile at much

higher temperatures (116 °C). Surprisingly, while analysing the $Li_2(OH)_{0.9}F_{0.1}Cl$ sample, the ^2H NMR signal disappeared between 33 and 69 °C. At present, it is not clear why this occurs.

The LiRAPs investigated in the current study all contain halides. Thus, VT ^{35}Cl and ^{79}Br NMR spectroscopy was also utilised. The data obtained was particularly informative, as it reveals many new avenues of investigation into these systems. For Li_2OHCl, the ^{35}Cl resonance observed exhibited a significant decrease in intensity with increasing temperature and eventually became unobservable. This decrease in signal intensity was also observed for $Li_{2.5}OH_{0.5}Cl$ and $Li_2(OH)_{0.9}F_{0.1}Cl$. However, the degree of signal reduction was markedly lower for $Li_2OHCl_{0.4}Br_{0.6}$. A similar trend was also observed in the VT ^{79}Br NMR data acquired for samples of Li_2OHBr and $Li_2OHCl_{0.4}Br_{0.6}$. Here, the resonance exhibited a gradual decrease in signal alongside a change in the chemical shift. This behaviour was suggested to be linked to the mobility exhibited in the sample, but the exact cause is yet to be confirmed.

In conclusion, the current study has demonstrated that phase pure samples of Li_3OCl and Li_3OBr cannot be synthesised, whilst their hydrated analogues, Li_2OHCl and Li_2OHBr, are relatively easy to synthesise. Li_2OHCl was observed to exhibit localised proton mobility and long-range Li-ion diffusion, and the experimental findings were supported by AIMD simulations. Overall, Li_2OHCl has been demonstrated to be a versatile material, the composition of which can be readily altered by varying the Li and H content, fluorine doping and halide mixing to influence both the structure and ion mobility. This makes Li_2OHCl and its related compositions worthy contenders to be tested for use as solid electrolytes in ASSBs.

8.2 Future Work

The primary objective of this study was to synthesise LiRAP samples and probe ion mobility within the samples. Several LiRAP samples were synthesised and demonstrated to exhibit localised proton mobility and long-range Li-ion movement. However, the versatility of LiRAP system means it can be

researched further, with many potential areas of interest yet to be explored.

The experiments completed to synthesise phase pure samples of Li_3OCl and Li_3OBr tested a wide range of reaction conditions and techniques commonly used during solid-state synthesis. However, phase pure samples could not be produced. There are additional experiments that can be attempted to try and optimise the reaction conditions further and increase the amount of the desired phase produced. They include mechanically milling the reagents for longer, *i.e.*, greater than the 1 hr attempted in this study. In a similar manner to Li_2OHCl, the synthesis of Li_3OCl and Li_3OBr could be attempted solely via mechanical milling. Moreover, ultra-high vacuums could be utilised in conjunction with the Schlenk line method to potentially reduce the number of impurity phases produced. Furthermore, cation and anion doping and halide mixing can be attempted to aid synthesis and increase phase purity. The results presented for the hydrated analogue, Li_2OHCl, in this study are quite promising. Hence, this is a possible avenue for further investigation. Moreover, the samples discussed in the current study could be further analysed and characterised using techniques such as inductively coupled plasma mass spectrometry (ICP-MS) and X-ray fluorescence (XRF) for quantitative analysis of sample composition. This would be extremely useful in identifying the impurity phases present in the samples and, in turn, allowing for a deeper understanding of the reactions taking place. However, it is noted that their air-sensitive nature may make such analysis challenging.

The deuterated sample of Li_2OHCl analysed via NPD was found to contain a small amount of the cubic ($Pm\bar{3}m$) phase at room temperature. This was attributed to the slightly different reaction conditions used to prepare the sample. Hence, it may be possible to increase the proportion of the cubic ($Pm\bar{3}m$) phase or even produce a sample consisting solely of the desirable cubic phase by optimising the reaction conditions further. The mechanically-milled Li_2OHCl was analysed extensively via VT NPD. The sample was initially cooled to −263 °C and then heated gradually to 150 °C, where the sample crystallinity was observed to increase. Additional VT NPD experiments could be completed to investigate the effects of subsequent cooling on the sample.

Recently, mechanically-milled Li_2OHCl was reported to undergo a phase transition to an orthorhombic structure when cooled after annealing at high temperatures.[221,223] However, the exact temperature for the phase transition seems to depend on the method of sample preparation and the duration of annealing. Thus, VT NPD experiments will be instrumental in studying this possible phase transition. Moreover, additional VT $^{1/2}H$ and ^{7}Li NMR experiments can also be completed to probe ion mobility within the sample as a function of temperature. VT ^{35}Cl MAS NMR experiments will also be helpful, and the findings can be compared with those obtained for the Li_2OHCl sample synthesised via conventional solid-state methods. Moreover, the XRD and NPD data obtained for Li_2OHCl samples indicated that different synthesis methods, conventional solid-state methods and mechanical milling produce samples with different crystallite sizes. Techniques such as scanning electron microscopy (SEM) and transmission electron microscopy (TEM) can be utilised to investigate the differences in sample morphologies. However, it is noted that the analysis is likely to be difficult as Li_2OHCl is extremely hygroscopic.

Furthermore, samples in the series $Li_{3-x}OH_xCl$ (x = 0.25, 0.5 and 0.75) were found to contain an unidentified impurity phase that was also present in the Li_3OCl samples. Hence, these samples could be analysed via VT NPD to determine the precise composition of both the desired phases and the identity of the impurity phase. Obtaining NPD patterns for the high-temperature cubic phases will be advantageous as the cubic phases will produce fewer reflections. In turn, there will be less overlap between reflections corresponding to the desired phase and the impurities. This will aid in obtaining accurate fractional occupancies during Rietveld analysis and allow for accurate determination of the compositions for the desired phases. Additional experiments can also be completed to optimise the reaction conditions to increase phase purity. These can include varying the reaction temperature, time and heating and cooling rates. In the current study, only the $Li_{2.5}OH_{0.5}Cl$ sample was analysed via VT ^{2}H and ^{35}Cl NMR spectroscopy. The other samples in the $Li_{3-x}OH_xCl$ series could also be analysed via VT ^{2}H and ^{35}Cl NMR spectroscopy to probe the proton mobility and Cl environments as a function of composition and

temperature. Moreover, ^{1}H and ^{7}Li PFG-NMR experiments could also be undertaken to confirm the precise nature of proton and Li-ion mobility in these samples.

The fluorinated analogue of Li_2OHCl, $Li_2(OH)_{0.9}F_{0.1}Cl$, was observed to exist in a cubic ($Pm\bar{3}m$) phase at room temperature. However, the VT multinuclear NMR data acquired for the sample suggested a phase transition below room temperature. Hence, a comprehensive structural characterisation of $Li_2(OH)_{0.9}F_{0.1}Cl$ can be completed using VT XRD and NPD methods to explore the possible phase transition. Moreover, the VT ^{19}F MAS NMR indicated the presence of two distinct fluorine environments at 106 °C. Therefore, complementary high-resolution XRD and NPD will be extremely useful in determining the precise location and number of crystallographically distinct fluorine sites present in the sample. Moreover, two fluorine environments were only observed at 106 °C, when the resonance had narrowed considerably. Therefore, additional NMR experiments can be completed using faster MAS rates to determine whether multiple fluorine environments are present at all temperatures or whether they only appear at higher temperatures. ^{1}H and ^{7}Li T_1 and PFG-NMR experiments can also be completed to probe the proton and Li-ion mobility. The VT ^{19}F NMR data and preliminary ^{19}F T_1 measurements suggested that fluorine may also be exhibiting motion. This can be further investigated by completing additional ^{19}F T_1 measurements to acquire more data points across a greater temperature range. Moreover, ^{19}F EXSY and PFG-NMR experiments can also provide valuable insight into any fluorine dynamics within these LiRAPs.

Furthermore, VT XRD studies of the Br analogue, Li_2OHBr, suggested a phase transition at very low temperatures. However, this phase transition could not be fully observed owing to technical limitations. Hence, additional VT diffraction experiments could be completed using NPD at HRPD or synchrotron XRD, as these techniques allow a much larger temperature range to be explored. Similar to Li_2OHCl, Li_2OHBr can also be analysed via ^{1}H and ^{7}Li PFG-NMR spectroscopy to determine the precise nature of any proton and Li-ion motion. Moreover, VT ^{79}Br NMR data presented in the current study in-

dicated a gradual change in the Br environment with increasing temperature. The reasons for this are currently unclear. One of the suggestions included Br mobility. Therefore, Br mobility can be investigated via ^{79}Br T_1 and PFG-based methods. A more comprehensive study of Li_2OHBr could include ^{81}Br NMR studies. It would be interesting to see if VT ^{81}Br NMR data exhibits the same trend as that observed via ^{79}Br NMR spectroscopy. Recently, the synthesis of Li_2OHBr prepared solely via mechanical milling and samples in the series $Li_{3-x}OH_xBr$ (x = 0.6 – 1.5) were reported in the literature.[238,240] However, extensive analysis of the samples via NMR spectroscopy is not yet reported. Hence, future research could include the synthesis, deuteration and analysis of these materials via multinuclear VT NMR spectroscopy. Thus, allowing for a direct comparison with the data presented for Li_2OHCl in the current study.

In a similar manner to Li_2OHBr, the VT NMR data acquired for a mixed halide sample, $Li_2OHCl_{0.4}Br_{0.6}$, suggested significant structural changes when the sample was cooled below room temperature. Hence, these changes could be further explored via VT XRD and NPD methods. Moreover, all samples in the series $Li_2OHCl_{1-x}Br_x$ (x = 0.1 – 1) can be studied via VT ^{1}H and ^{7}Li NMR to observe the effects of gradual changes in the composition on proton and Li-ion mobility. VT ^{1}H and ^{7}Li T_1 measurements will be particularly useful to determine whether there is a correlation between the T_1 values and sample composition. Moreover, all samples can be deuterated and studied via VT ^{2}H NMR spectroscopy to probe any variations in the H/D mobility varied as a function of Cl and, in turn, Br concentration. Additionally, the mixed halide samples can be investigated via VT ^{35}Cl and ^{79}Br NMR spectroscopy to gain information regarding the local halide environments and analyse the influence of variations in the relative halide concentrations.

The compositional doping of Li_2OHCl investigated in this study demonstrates the highly flexible nature of Li_2OHCl. However, only anion doping was explored in the current study. Cation doping can also be used to partially substitute Li with several cations, including but not limited to Na^+, Mg^{2+}, Ca^{2+}, and Al^{3+}. Moreover, cation doping can be combined with F^- doping and/or halide mixing to produce a wide range of compositions. Hence, the composi-

tion of LiRAPs can be customised to achieve very high ionic conductivity.

It is noted that all samples discussed in this study contain oxygen. However, no ^{17}O NMR experiments were undertaken due to its extremely low natural abundance (0.038%). Therefore, additional research into the LiRAP system could include analysis via ^{17}O NMR spectroscopy following enrichment of the samples with ^{17}O. The AIMD simulations completed for Li_2OHCl indicated multiple O environments due to different Li coordination during Li-ion diffusion. These could be explored in detail via ^{17}O NMR spectroscopy. Thus, allowing an insight into the influence of ion dynamics in the system on O. Moreover, ^{17}O NMR studies of the fluorinated analogue and the mixed halide samples could prove to be very helpful in analysing the influence of dopants on the O environment.

Finally, the techniques used during this work, including XRD, NPD and SSNMR spectroscopy, have proved instrumental in investigating the structure of LiRAPs and probing ion dynamics within the samples. Thus, demonstrating the usefulness of these techniques. However, it is noted that the ion conductivity exhibited by the LiRAP samples has not been measured quantitatively. Therefore, future studies can focus on analysing the LiRAP samples via EIS to measure ion conductivities as a function of temperature and composition. Doing so can identify favoured compositions. In turn, the synthesis can be tailored to produce samples with very high ion conductivities.

References

1. F. Barbir, T. Veziroğlu and H. Plass, *Int. J. Hydrog. Energy*, 1990, **15**, 739–749.

2. Met Press Office, *Faster CO_2 rise expected in 2019*, https://www.metoffice.gov.uk/about-us/press-office/news/weather-and-climate/2019/2019-carbondioxide-forecast, (accessed February 2020).

3. R. Ruan, Y. Zhang, P. Chen, S. Liu, L. Fan, N. Zhou, K. Ding, P. Peng, M. Addy, Y. Cheng, E. Anderson, Y. Wang, Y. Liu, H. Lei and B. Li, *Biofuels: Alternative Feedstocks and Conversion Processes for the Production of Liquid and Gaseous Biofuels*, Academic Press, Cambridge, Massachusetts, 2019.

4. E. S. Rubin, H. Mantripragada, A. Marks, P. Versteeg and J. Kitchin, *Prog. Energy Combust. Sci.*, 2012, **38**, 630–671.

5. N. Panwar, S. Kaushik and S. Kothari, *Renewable Sustainable Energy Rev.*, 2011, **15**, 1513–1524.

6. R. M. Dell and D. A. J. Rand, *Understanding Batteries*, The Royal Society of Chemistry, London, 2001.

7. R. Dell, *Solid State Ion.*, 2000, **134**, 139–158.

8. T. B. Reddy, *Linden's handbook of batteries*, Mcgraw-hill, New York, 2011.

9. P. Ruetschi, *J. Power Sources*, 1977, **2**, 3–120.

10. J. Xie and Y. Lu, *Nat. Commun.*, 2020, **11**, 2499.

11. D. Shriver, M. Weller, T. Overton, J. Rourke and F. Armstrong, *Inorganic Chemistry*, Oxford University Press, Oxford, 2010.

12. M. R. Palacín, *Chem. Soc. Rev.*, 2009, **38**, 2565–2575.

13. Y. Nishi, *Chem. Rec.*, 2001, **1**, 406–413.

14. M. S. Whittingham, *Chem. Rev.*, 2004, **104**, 4271–4302.

15. K. Mizushima, P. Jones, P. Wiseman and J. Goodenough, *Mater. Res. Bull.*, 1980, **15**, 783–789.

16. K. Wang, J. Wan, Y. Xiang, J. Zhu, Q. Leng, M. Wang, L. Xu and Y. Yang, *J. Power Sources*, 2020, **460**, 228062.

17. M. Holzapfel, C. Haak and A. Ott, *J. Solid State Chem.*, 2001, **156**, 470–479.

18. J. Reimers and J. Dahn, *J. Electrochem. Soc.*, 1992, **139**, 2091–2097.

19. I. D. Scott, Y. S. Jung, A. S. Cavanagh, Y. Yan, A. C. Dillon, S. M. George and S. H. Lee, *Nano Lett.*, 2011, **11**, 414–418.

20. N. Nitta, F. Wu, J. T. Lee and G. Yushin, *Mater. Today*, 2015, **18**, 252–264.

21. M. Broussely, F. Perton, P. Biensan, J. Bodet, J. Labat, A. Lecerf, C. Delmas, A. Rougier and J. Pérès, *J. Power Sources*, 1995, **54**, 109–114.

22. T. Ohzuku, A. Ueda and M. Nagayama, *J. Electrochem. Soc.*, 1993, **140**, 1862.

23. A. Rougier, P. Gravereau and C. Delmas, *J. Electrochem. Soc.*, 1996, **143**, 1168.

24. M. Gu, I. Belharouak, J. Zheng, H. Wu, J. Xiao, A. Genc, K. Amine, S. Thevuthasan, D. R. Baer, J.-G. Zhang, N. D. Browning, J. Liu and C. Wang, *ACS Nano*, 2013, **7**, 760–767.

25. S. Komaba, N. Kumagai, R. Kumagai, N. Kumagai and H. Yashiro, *Solid State Ion.*, 2002, **152–153**, 319–326.

26. M. Wohlfahrt-Mehrens, C. Vogler and J. Garche, *J. Power Sources*, 2004, **127**, 58–64.

27. H. Zheng, Q. Sun, G. Liu, X. Song and V. S. Battaglia, *J. Power Sources*, 2012, **207**, 134–140.

28. A. Wang, S. Kadam, H. Li, S. Shi and Y. Qi, *Npj Comput. Mater.*, 2018, **4**, 15.

29. Y. I. Jang, B. Huang, Y. M. Chiang and D. R. Sadoway, *Electrochem. Solid State Lett.*, 1998, **1**, 13–16.

30. M. M. Thackeray, L. A. de Picciotto, A. de Kock, P. J. Johnson, V. A. Nicholas and K. T. Adendorff, *J. Power Sources*, 1987, **21**, 1–8.

31. M. M. Thackeray, *J. Am. Ceram. Soc.*, 1999, **82**, 3347–3354.

32. K. S. Yoo, N. W. Cho and Y. J. Oh, *Solid State Ion.*, 1998, **113–115**, 43–49.

33. I. Bloom, S. A. Jones, V. S. Battaglia, G. L. Henriksen, J. P. Christophersen, R. B. Wright, C. D. Ho, J. R. Belt and C. G. Motloch, *J. Power Sources*, 2003, **124**, 538–550.

34. Y. Itou and Y. Ukyo, *J. Power Sources*, 2005, **146**, 39–44.

35. E. Rossen, C. D. W. Jones and J. R. Dahn, *Solid State Ion.*, 1992, **57**, 311–318.

36. N. Yabuuchi and T. Ohzuku, *J. Power Sources*, 2003, **119**, 171–174.

37. K. Kang, Y. S. Meng, J. Bréger, C. P. Grey and G. Ceder, *Science*, 2006, **311**, 977–980.

38. A. Yamada, S. C. Chung and K. Hinokuma, *J. Electrochem. Soc.*, 2001, **148**, A224–A229.

39. D. Choi, D. Wang, I. T. Bae, J. Xiao, Z. Nie, W. Wang, V. V. Viswanathan, Y. J. Lee, J. G. Zhang, G. L. Graff, Z. Yang and J. Liu, *Nano Lett.*, 2010, **10**, 2799–2805.

40. C. Delacourt, L. Laffont, R. Bouchet, C. Wurm, J. B. Leriche, M. Morcrette, J. M. Tarascon and C. Masquelier, *J. Electrochem. Soc.*, 2005, **152**, A913–A921.

41. J. J. Biendicho and A. R. West, *Solid State Ion.*, 2011, **203**, 33–36.

42. S. B. Chikkannanavar, D. M. Bernardi and L. Liu, *J. Power Sources*, 2014, **248**, 91–100.

43. F. Schipper, E. M. Erickson, C. Erk, J. Y. Shin, F. F. Chesneau and D. Aurbach, *J. Electrochem. Soc.*, 2016, **164**, A6220–A6228.

44. D. Lin, Y. Liu and Y. Cui, *Nat. Nanotechnol.*, 2017, **12**, 194–206.

45. J. B. Goodenough and K. S. Park, *J. Am. Chem. Soc.*, 2013, **135**, 1167–1176.

46. D. Aurbach, B. Markovsky, I. Weissman, E. Levi and Y. Ein-Eli, *Electrochim. Acta*, 1999, **45**, 67–86.

47. N. A. Kaskhedikar and J. Maier, *Adv. Mater.*, 2009, **21**, 2664–2680.

48. G. N. Zhu, Y. G. Wang and Y. Y. Xia, *Energy Environ. Sci.*, 2012, **5**, 6652–6667.

49. Z. Chen, I. Belharouak, Y. K. Sun and K. Amine, *Adv. Funct. Mater.*, 2013, **23**, 959–969.

50. M. Wagemaker, D. Simon, E. Kelder, J. Schoonman, C. Ringpfeil, U. Haake, D. Lützenkirchen-Hecht, R. Frahm and F. Mulder, *Adv. Mater.*, 2006, **18**, 3169–3173.

51. J. F. Colin, V. Godbole and P. Novák, *Electrochem. commun.*, 2010, **12**, 804–807.

52. M. Nakayama, Y. Ishida, H. Ikuta and M. Wakihara, *Solid State Ion.*, 1999, **117**, 265–271.

53. S. Zhang, K. Xu and T. Jow, *J. Solid State Electrochem.*, 2003, **7**, 147–151.

54. P. Knauth, *Solid State Ion.*, 2009, **180**, 911–916.

55. F. Zheng, M. Kotobuki, S. Song, M. O. Lai and L. Lu, *J. Power Sources*, 2018, **389**, 198–213.

56. J. F. M. Oudenhoven, L. Baggetto and P. H. L. Notten, *Adv. Energy Mater.*, 2011, **1**, 10–33.

57. J. G. Kim, B. Son, S. Mukherjee, N. Schuppert, A. Bates, O. Kwon, M. J. Choi, H. Y. Chung and S. Park, *J. Power Sources*, 2015, **282**, 299–322.

58. A. Aboulaich, R. Bouchet, G. Delaizir, V. Seznec, L. Tortet, M. Morcrette, P. Rozier, J. M. Tarascon, V. Viallet and M. Dollé, *Adv. Energy Mater.*, 2011, **1**, 179–183.

59. A. Emly, E. Kioupakis and A. Van der Ven, *Chem. Mater.*, 2013, **25**, 4663–4670.

60. H. F. Kay and P. C. Bailey, *Acta Crystallogr.*, 1957, **10**, 219–226.

61. V. M. Goldschmidt, *Naturwissenschaften*, 1926, **14**, 477–485.

62. A. R. West, *Solid State Chemistry and Its Applications*, Wiley, Hoboken, New Jersey, 2014.

63. Y. Sun, P. Guan, Y. Liu, H. Xu, S. Li and D. Chu, *Crit. Rev. Solid State Mater. Sci.*, 2019, **44**, 265–282.

64. S. Stramare, V. Thangadurai and W. Weppner, *Chem. Mater.*, 2003, **15**, 3974–3990.

65. V. Thangadurai and W. Weppner, *Ionics*, 2006, **12**, 81–92.

66. J. Ibarra, A. Várez, C. León, J. Santamara, L. Torres-Martnez and J. Sanz, *Solid State Ion.*, 2000, **134**, 219–228.

67. Y. Inaguma, L. Chen, M. Itoh and T. Nakamura, *Solid State Ion.*, 1994, **70–71**, 196–202.

68. O. Bohnke, *Solid State Ion.*, 2008, **179**, 9–15.

69. V. Thangadurai, A. K. Shukla and J. Gopalakrishnan, *Chem. Mater.*, 1999, **11**, 835–839.

70. C. Chen, S. Xie, E. Sperling, A. Yang, G. Henriksen and K. Amine, *Solid State Ion.*, 2004, **167**, 263–272.

71. B. Huang, B. Xu, Y. Li, W. Zhou, Y. You, S. Zhong, C.-A. Wang and J. B. Goodenough, *ACS Appl. Mater. Interfaces*, 2016, **8**, 14552–14557.

72. Z. Jian, Y.-S. Hu, X. Ji and W. Chen, *Adv. Mater.*, 2017, **29**, 1601925.

73. N. Anantharamulu, K. K. Rao, G. Rambabu, B. V. Kumar, V. Radha and M. Vithal, *J. Mater. Sci.*, 2011, **46**, 2821–2837.

74. R. M. Hazen, L. W. Finger, D. K. Agrawal, H. A. McKinstry and A. J. Perrotta, *J. Mater. Res.*, 1987, **2**, 329–337.

75. J. Goodenough, H. Y. P. Hong and J. Kafalas, *Mater. Res. Bull.*, 1976, **11**, 203–220.

76. K. Arbi, J. M. Rojo and J. Sanz, *J. Eur. Ceram. Soc.*, 2007, **27**, 4215–4218.

77. E. Dashjav and F. Tietz, *Z. Anorg. Allg. Chem.*, 2014, **640**, 3070–3073.

78. J. Fu, *Solid State Ion.*, 1997, **104**, 191–194.

79. M. Illbeigi, A. Fazlali, M. Kazazi and A. H. Mohammadi, *Solid State Ion.*, 2016, **289**, 180–187.

80. J. Feng, L. Lu and M. Lai, *J. Alloys Compd.*, 2010, **501**, 255–258.

81. E. Zhao, F. Ma, Y. Guo and Y. Jin, *RSC Adv.*, 2016, **6**, 92579–92585.

82. H. Y. P. Hong, *Mater. Res. Bull.*, 1978, **13**, 117–124.

83. P. G. Bruce and A. R. West, *J. Electrochem. Soc.*, 1983, **130**, 662–669.

84. B. Wang, B. Chakoumakos, B. Sales, B. Kwak and J. Bates, *J. Solid State Chem.*, 1995, **115**, 313–323.

85. S. Song, J. Lu, F. Zheng, H. M. Duong and L. Lu, *RSC Adv.*, 2015, **5**, 6588–6594.

86. J. Kuwano and A. R. West, *Mater. Res. Bull.*, 1980, **15**, 1661–1667.

87. Y. W. Hu, I. D. Raistrick and R. A. Huggins, *J. Electrochem. Soc.*, 1977, **124**, 1240.

88. V. Thangadurai and W. Weppner, *J. Solid State Chem.*, 2006, **179**, 974–984.

89. L. van Wüllen, T. Echelmeyer, H. W. Meyer and D. Wilmer, *Phys. Chem. Chem. Phys.*, 2007, **9**, 3298–3303.

90. V. Thangadurai and W. Weppner, *Adv. Funct. Mater.*, 2005, **15**, 107–112.

91. E. J. Cussen, *Chem. Commun.*, 2006, 412–413.

92. R. Murugan, V. Thangadurai and W. Weppner, *Angew. Chem. Int. Ed.*, 2007, **46**, 7778–7781.

93. S. Ohta, T. Kobayashi and T. Asaoka, *J. Power Sources*, 2011, **196**, 3342–3345.

94. B. Wang, B. S. Kwak, B. C. Sales and J. B. Bates, *J. Non-Cryst. Solids*, 1995, **183**, 297–306.

95. J. B. Bates, N. J. Dudney, G. R. Gruzalski, R. A. Zuhr, A. Choudhury, C. F. Luck and J. D. Robertson, *J. Power Sources*, 1993, **43**, 103–110.

96. N. Suzuki, T. Inaba and T. Shiga, *Thin Solid Films*, 2012, **520**, 1821–1825.

97. G. Li, M. Li, L. Dong, X. Li and D. Li, *Int. J. Hydrogen Energ.*, 2014, **39**, 17466–17472.

98. Y. Hamon, A. Douard, F. Sabary, C. Marcel, P. Vinatier, B. Pecquenard and A. Levasseur, *Solid State Ion.*, 2006, **177**, 257–261.

99. D. H. Gregory, P. M. O'Meara, A. G. Gordon, J. P. Hodges, S. Short and J. D. Jorgensen, *Chem. Mater.*, 2002, **14**, 2063–2070.

100. B. A. Boukamp and R. A. Huggins, *Phys. Lett. A*, 1976, **58**, 231–233.

101. R. A. Huggins, *Electrochim. Acta*, 1977, **22**, 773–781.

102. K. Kitahama, Y. Furukawa, S. Kawai and O. Nakamura, *Solid State Ion.*, 1981, **3–4**, 335–339.

103. S. Hatake, J. Kuwano, M. Miyamori, Y. Saito and S. Koyama, *J. Power Sources*, 1997, **68**, 416–420.

104. H. Yamane, S. Kikkawa and M. Koizumi, *Solid State Ion.*, 1985, **15**, 51–54.

105. E. Narimatsu, Y. Yamamoto, T. Nishimura and N. Hirosaki, *J. Ceram. Soc. Jpn.*, 2010, **118**, 837–841.

106. E. Narimatsu, Y. Yamamoto, T. Takeda, T. Nishimura and N. Hirosaki, *J. Mater. Res.*, 2011, **26**, 1133–1142.

107. M. Tatsumisago and A. Hayashi, *Int. J. Appl. Glass Sci.*, 2014, **5**, 226–235.

108. M. Murayama, R. Kanno, Y. Kawamoto and T. Kamiyama, *Solid State Ion.*, 2002, **154–155**, 789–794.

109. N. Kamaya, K. Homma, Y. Yamakawa, M. Hirayama, R. Kanno, M. Yonemura, T. Kamiyama, Y. Kato, S. Hama, K. Kawamoto and A. Mitsui, *Nat. Mater.*, 2011, **10**, 682–686.

110. R. Kanno, T. Hata, Y. Kawamoto and M. Irie, *Solid State Ion.*, 2000, **130**, 97–104.

111. R. Kanno and M. Murayama, *J. Electrochem. Soc.*, 2001, **148**, A742.

112. F. Mizuno, A. Hayashi, K. Tadanaga and M. Tatsumisago, *Adv. Mater.*, 2005, **17**, 918–921.

113. A. Hayashi, S. Hama, H. Morimoto, M. Tatsumisago and T. Minami, *J. Am. Ceram. Soc.*, 2001, **84**, 477–479.

114. A. Hayashi, S. Hama, H. Morimoto, M. Tatsumisago and T. Minami, *Chem. Lett.*, 2001, **30**, 872–873.

115. Y. Seino, T. Ota, K. Takada, A. Hayashi and M. Tatsumisago, *Energy Environ. Sci.*, 2014, **7**, 627–631.

116. H. Deiseroth, S. Kong, H. Eckert, J. Vannahme, C. Reiner, T. Zaiß and M. Schlosser, *Angew. Chem. Int. Ed.*, 2008, **47**, 755–758.

117. M. A. Kraft, S. P. Culver, M. Calderon, F. Böcher, T. Krauskopf, A. Senyshyn, C. Dietrich, A. Zevalkink, J. Janek and W. G. Zeier, *J. Am. Chem. Soc.*, 2017, **139**, 10909–10918.

118. O. Pecher, S. T. Kong, T. Goebel, V. Nickel, K. Weichert, C. Reiner, H. J. Deiseroth, J. Maier, F. Haarmann and D. Zahn, *Chem. Eur. J.*, 2010, **16**, 8347–8354.

119. V. Epp, O. Gün, H. J. Deiseroth and M. Wilkening, *J. Phys. Chem. Lett.*, 2013, **4**, 2118–2123.

120. S. Boulineau, M. Courty, J. M. Tarascon and V. Viallet, *Solid State Ion.*, 2012, **221**, 1–5.

121. Z. Zhang, L. Zhang, Y. Liu, C. Yu, X. Yan, B. Xu and L. M. Wang, *J. Alloys Compd.*, 2018, **747**, 227–235.

122. M. O'Keeffee and J. O. Bovin, *Science*, 1979, **206**, 599–600.

123. A. Yoshiasa, D. Sakamoto, H. Okudera, M. Sugahara, K. Ota and A. Nakatsuka, *Z. Anorg. Allg. Chem*, 2005, **631**, 502–506.

124. Y. Zhao and L. L. Daemen, *J. Am. Chem. Soc.*, 2012, **134**, 15042–15047.

125. P. Hartwig, A. Rabenau and W. Weppner, *J. Less-Common Met.*, 1981, **78**, 227–233.

126. O. Reckeweg, B. Blaschkowski and T. Schleid, *Z. Anorg. Allg. Chem.*, 2012, **638**, 2081–2086.

127. Y. Zhang, Y. Zhao and C. Chen, *Phys. Rev. B*, 2013, **87**, 134303.

128. J. Zhang, J. Han, J. Zhu, Z. Lin, M. H. Braga, L. L. Daemen, L. Wang and Y. Zhao, *Inorg. Chem. Commun.*, 2014, **48**, 140–143.

129. R. Mouta, M. Á. B. Melo, E. M. Diniz and C. W. A. Paschoal, *Chem. Mater.*, 2014, **26**, 7137–7144.

130. M. H. Chen, A. Emly and A. Van der Ven, *Phys. Rev. B*, 2015, **91**, 214306.

131. Z. Deng, B. Radhakrishnan and S. P. Ong, *Chem. Mater.*, 2015, **27**, 3749–3755.

132. Z. Lu, C. Chen, Z. M. Baiyee, X. Chen, C. Niu and F. Ciucci, *Phys. Chem. Chem. Phys.*, 2015, **17**, 32547–32555.

133. R. Mouta, E. M. Diniz and C. W. A. Paschoal, *J. Mater. Chem. A*, 2016, **4**, 1586–1590.

134. X. Lü, G. Wu, J. W. Howard, A. Chen, Y. Zhao, L. L. Daemen and Q. Jia, *Chem. Commun.*, 2014, **50**, 11520–11522.

135. X. Lü, J. W. Howard, A. Chen, J. Zhu, S. Li, G. Wu, P. Dowden, H. Xu, Y. Zhao and Q. Jia, *Adv. Sci.*, 2016, **3**, 1500359.

136. M. H. Braga, J. A. Ferreira, V. Stockhausen, J. E. Oliveira and A. El-Azab, *J. Mater. Chem. A*, 2014, **2**, 5470–5480.

137. R. Wortmann, S. Sitta and H. Sabrowsky, *Z. Naturforsch. B*, 1989, **44**, 1348–1350.

138. J. Zhu, S. Li, Y. Zhang, J. W. Howard, X. Lü, Y. Li, Y. Wang, R. S. Kumar, L. Wang and Y. Zhao, *Appl. Phys. Lett.*, 2016, **109**, 101904.

139. W. Clegg, *X-ray Crystallography*, Oxford University Press, Oxford, 2015.

140. W. Massa, *Crystal Structure Determination*, Springer Berlin, Heidelberg, 2000.

141. U. Shmueli, *Theories and Techniques of Crystal Structure Determination*, Oxford University Press, Oxford, 2007.

142. P. Atkins and J. de Paula, *Atkins' Physical Chemistry*, Oxford University Press, Oxford, 2009.

143. G. L. Squires, *Introduction to the Theory of Thermal Neutron Scattering*, Dover Publications, New York, 1996.

144. ISIS Neutron and Muon Source, *High Resolution Powder Diffractometer*, https://www.isis.stfc.ac.uk/Pages/hrpd.aspx, (accessed May 2020).

145. R. M. Ibberson, W. I. F. David and K. S. Knight, *The High Resolution Neutron Powder Diffractometer (HRPD) at ISIS – A User Guide Report RAL-92-031*, 1992.

146. R. A. Young, *The Rietveld Method*, Oxford University Press, Oxford, 1996.

147. H. M. Rietveld, *J. Appl. Crystallogr.*, 1969, **2**, 65–71.

148. H. M. Rietveld, *Acta Crystallogr.*, 1966, **20**, 508–513.

149. A. Albinati and B. T. M. Willis, *Journal of Applied Crystallography*, 1982, **15**, 361–374.

150. B. H. Toby and R. B. Von Dreele, *J. Appl. Crystallogr.*, 2013, **46**, 544–549.

151. P. J. Hore, *Nuclear Magnetic Resonance*, Oxford University Press, Oxford, 2015.

152. P. J. Hore, J. A. Jones and S. Wimperis, *NMR The Toolkit: How Pulse Sequences Work*, Oxford University Press, Oxford, 2015.

153. M. H. Levitt, *Spin Dynamics: Basics of Nuclear Magnetic Resonance*, John Wiley & Sons, Ltd, Chichester, 2008.

154. J. A. Iggo and K. V. Luzyanin, *NMR Spectroscopy in Inorganic Chemistry*, Oxford University Press, Oxford, 2020.

155. A. Abragam, *Principles of Nuclear Magnetism*, Oxford Science Publications, Oxford, 1961.

156. C. P. Slichter, *Principles of Magnetic Resonance*, Springer Verlag, Berlin, 1990.

157. J. Keeler, *Understanding NMR Spectroscopy*, John Wiley & Sons, Ltd, Chichester, 2010.

158. M. J. Duer, *Introduction to Solid-State NMR Spectroscopy*, John Wiley & Sons, Ltd, Chichester, 2004.

159. D. W. Bruce, D. O'Hare and R. I. Walton, *Local Structural Characterisation*, John Wiley & Sons, Ltd, Chichester, 2013.

160. D. C. Apperley, R. K. Harris and P. Hodgkinson, *Solid-State NMR: Basic Principles and Practice*, Momentum Press, New York, 2012.

161. S. E. Ashbrook, *Phys. Chem. Chem. Phys.*, 2009, **11**, 6892–6905.

162. S. E. Ashbrook, J. M. Griffin, and K. E. Johnston, *Annu. Rev. Anal. Chem.*, 2018, **11**, 485–508.

163. K. J. D. Mackenzie and M. E. Smith, *Multinuclear Solid-State Nuclear Magnetic Resonance of Inorganic Materials*, Pergamon, Oxford, 2002.

164. S. P. Brown and H. W. Spiess, *Chem. Rev.*, 2001, **101**, 4125–4156.

165. C. Vinod Chandran and P. Heitjans, *Annu. Rep. NMR Spectrosc*, 2016, **89**, 1–102.

166. G. Pagès, V. Gilard, R. Martino and M. Malet Martino, *Analyst*, 2017, **142**, 3771–3796.

167. P. Hodgkinson, *Modern Methods in Solid-State NMR: A Practitioner's Guide*, The Royal Society of Chemistry, London, 2018.

168. G. H. Sørland, *Dynamic Pulsed-Field-Gradient NMR*, Springer Berlin, Heidelberg, 2014.

169. T. Parella, *Magn. Reson. Chem.*, 1998, **36**, 467–495.

170. A. C. Forse, J. M. Griffin, C. Merlet, J. C. Gonzalez, A. R. O. Raji, N. M. Trease and C. P. Grey, *Nat. Energy*, 2017, **2**, 16216.

171. E. O. Stejskal and J. E. Tanner, *J. Chem. Phys.*, 1965, **42**, 288–292.

172. C. Karunakaran, P. Santharaman and M. Balamurugan, *Spin Resonance Spectroscopy*, Elsevier, Netherlands, 2018.

173. J. P. Yesinowski and H. Eckert, *J. Am. Chem. Soc.*, 1987, **109**, 6274–6282.

174. J. P. Yesinowski, H. Eckert and G. R. Rossman, *J. Am. Chem. Soc.*, 1988, **110**, 1367–1375.

175. M. Fait, D. Heidemann and H. J. Lunk, *Z. Anorg. Allg. Chem*, 1999, **625**, 530–538.

176. S. Odedra and S. Wimperis, *J. Magn. Reson.*, 2012, **221**, 41–50.

177. Y. J. Lee, T. Murakhtina, D. Sebastiani and H. W. Spiess, *J. Am. Chem. Soc.*, 2007, **129**, 12406–12407.

178. A. E. Aliev, K. D. Harris and D. C. Apperley, *Chem. Phys. Lett.*, 1994, **226**, 193–198.

179. C. M. Gall, T. A. Cross, J. A. DiVerdi and S. J. Opella, *PNAS*, 1982, **79**, 101–105.

180. J. Stebbins, Z. Xu and D. Vollath, *Solid State Ion.*, 1995, **78**, L1–L8.

181. K. Nairn, M. Forsyth, M. Greville, D. MacFarlane and M. Smith, *Solid State Ion.*, 1996, **86–88**, 1397–1402.

182. Y.-X. Xiang, G. Zheng, G. Zhong, D. Wang, R. Fu and Y. Yang, *Solid State Ion.*, 2018, **318**, 19–26.

183. R. Böhmer, K. Jeffrey and M. Vogel, *Prog. Nucl. Magn. Reson. Spectrosc.*, 2007, **50**, 87–174.

184. R. K. Harris and P. Jackson, *Chem. Rev.*, 1991, **91**, 1427–1440.

185. J. M. Miller, *Prog. Nucl. Magn. Reson. Spectrosc.*, 1996, **28**, 255–281.

186. A. T. Kreinbrink, C. D. Sazavsky, J. W. Pyrz, D. G. Nelson and R. S. Honkonen, *J. Magn. Reson.*, 1990, **88**, 267–276.

187. P. Jain, S. Kim, R. E. Youngman and S. Sen, *J. Phys. Chem. Lett.*, 2010, **1**, 1126–1129.

188. X. Zhang, Q. Xing, L. Liao and Y. Han, *Crystals*, 2020, **10**, 3.

189. D. L. Bryce and G. D. Sward, *Magn. Reson. Chem.*, 2006, **44**, 409–450.

190. K. E. Johnston, C. A. O'Keefe, R. M. Gauvin, J. Trébosc, L. Delevoye, J.-P. Amoureux, N. Popoff, M. Taoufik, K. Oudatchin and R. W. Schurko, *Chem. Eur. J.*, 2013, **19**, 12396–12414.

191. H. Hamaed, J. M. Pawlowski, B. F. Cooper, R. Fu, S. H. Eichhorn and R. W. Schurko, *J. Am. Chem. Soc.*, 2008, **130**, 11056–11065.

192. C. M. Widdifield and D. L. Bryce, *J. Phys. Chem. A*, 2010, **114**, 2102–2116.

193. C. M. Widdifield, R. P. Chapman and D. L. Bryce, *Annu. Rep. NMR Spectrosc.*, 2009, **66**, 195–326.

194. T. Kanda, *J. Phys. Soc. Jpn.*, 1955, **10**, 85–88.

195. S. Hayashi and K. Hayamizu, *J. Phys. Chem. Solids*, 1992, **53**, 239–248.

196. S. Li, J. Zhu, Y. Wang, J. W. Howard, X. Lü, Y. Li, R. S. Kumar, L. Wang, L. L. Daemen and Y. Zhao, *Solid State Ion.*, 2016, **284**, 14–19.

197. D. G. Cory and W. M. Ritchey, *J. Magn. Reson.*, 1988, **80**, 128–132.

198. B. M. Fung, A. K. Khitrin and K. Ermolaev, *J. Magn. Reson.*, 2000, **142**, 97–101.

199. G. I. Finch and S. Fordham, *Proc. Phys. Soc.*, 1936, **48**, 85–94.

200. Physical Sciences Data-science Service, *Inorganic Crystal Structure Database*, https://www.psds.ac.uk/icsd, (accessed June 2022).

201. D. J. Schroeder, A. A. Hubaud and J. T. Vaughey, *Mater. Res. Bull.*, 2014, **49**, 614–617.

202. H. J. Fecht, G. Han, Z. Fu and W. L. Johnson, *J. Appl. Phys.*, 1990, **67**, 1744–1748.

203. E. Gaffet, C. Louison, M. Harmelin and F. Faudot, *Mater. Sci. Eng. A*, 1991, **134**, 1380–1384.

204. J. Huot, G. Liang, S. Boily, A. Van Neste and R. Schulz, *J. Alloys Compd.*, 1999, **293**, 495–500.

205. M. S. El-Eskandarany, M. Banyan and F. Al-Ajmi, *RSC Adv.*, 2018, **8**, 32003–32008.

206. P. N. Kuznetsov, L. I. Kuznetsova, A. M. Zhyzhaev, G. L. Pashkov and V. V. Boldyrev, *Appl. Catal. A: Gen*, 2002, **227**, 299–307.

207. K. Hara, E. Yamasue, H. Okumura and K. Ishihara, *J. Phys. Conf. Ser*, 2009, **144**, 012021.

208. J. L. Do and T. Friščić, *ACS Cent. Sci.*, 2017, **3**, 13–19.

209. A. Watanabe, G. Kobayashi, N. Matsui, M. Yonemura, A. Kubota, K. Suzuki, M. Hirayama and R. Kanno, *Electrochemistry*, 2017, **85**, 88.

210. I. Hanghofer, G. J. Redhammer, S. Rohde, I. Hanzu, A. Senyshyn, H. M. R. Wilkening and D. Rettenwander, *Chem. Mater.*, 2018, **30**, 8134–8144.

211. J. A. Dawson, T. S. Attari, H. Chen, S. P. Emge, K. E. Johnston and M. S. Islam, *Energy Environ. Sci.*, 2018, **11**, 2993–3002.

212. B. Meyer, N. Leifer, S. Sakamoto, S. Greenbaum and C. P. Grey, *Electrochem. Solid-State Lett.*, 2005, **8**, A145.

213. G. Schwering, A. Hönnerscheid, L. van Wüllen and M. Jansen, *ChemPhysChem*, 2003, **4**, 343–348.

214. Z. D. Hood, H. Wang, A. Samuthira Pandian, J. K. Keum and C. Liang, *J. Am. Chem. Soc.*, 2016, **138**, 1768–1771.

215. C. Eilbracht, W. Kockelmann, D. Hohlwein and H. Jacobs, *Phys. B: Condens. Matter*, 1997, **234–236**, 48–50.

216. J. Howard, Z. D. Hood and N. A. W. Holzwarth, *Phys. Rev. Mater.*, 2017, **1**, 075406.

217. J. Howard and N. A. W. Holzwarth, *Phys. Rev. B*, 2019, **99**, 014109.

218. A. Y. Song, Y. Xiao, K. Turcheniuk, P. Upadhya, A. Ramanujapuram, J. Benson, A. Magasinski, M. Olguin, L. Meda, O. Borodin and G. Yushin, *Adv. Energy Mater.*, 2018, **8**, 1700971.

219. C. Ammann, P. Meier and A. Merbach, *J. Magn. Reson.*, 1982, **46**, 319–321.

220. *International Tables for Crystallography, Volume A: Space Group Symmetry*, ed. T. Hahn, Springer Dordrecht, Netherlands, 2002.

221. T. Yamamoto, H. Shiba, N. Mitsukuchi, M. K. Sugumar, M. Motoyama and Y. Iriyama, *Inorg. Chem.*, 2020, **59**, 11901–11904.

222. Y. Yang, J. Han, M. DeVita, S. S. Lee and J. C. Kim, *Front. Chem.*, 2020, **8**, 562549.

223. D. X. Ni, Y. D. Liu, Z. Deng, D. C. Chen, X. X. Zhang, T. Wang, S. Li and Y. S. Zhao, *Chin. Phys. Lett.*, 2022, **39**, 028201.

224. G. Kresse and J. Furthmüller, *Phys. Rev. B*, 1996, **54**, 11169–11186.

225. J. P. Perdew, A. Ruzsinszky, G. I. Csonka, O. A. Vydrov, G. E. Scuseria, L. A. Constantin, X. Zhou and K. Burke, *Phys. Rev. Lett.*, 2008, **100**, 136406.

226. S. Stegmaier, J. Voss, K. Reuter and A. C. Luntz, *Chem. Mater.*, 2017, **29**, 4330–4340.

227. B. J. Morgan and P. A. Madden, *Phys. Rev. B*, 2012, **86**, 035147.

228. J. A. Dawson, A. J. Naylor, C. Eames, M. Roberts, W. Zhang, H. J. Snaith, P. G. Bruce and M. S. Islam, *ACS Energy Lett.*, 2017, **2**, 1818–1824.

229. L. J. Miara, S. P. Ong, Y. Mo, W. D. Richards, Y. Park, J. M. Lee, H. S. Lee and G. Ceder, *Chem. Mater.*, 2013, **25**, 3048–3055.

230. G. Kim, F. Blanc, Y. Y. Hu and C. P. Grey, *J. Phys. Chem. C*, 2013, **117**, 6504–6515.

231. R. E. Wasylishen, S. E. Ashbrook and S. Wimperis, *NMR of Quadrupolar Nuclei in Solid Materials*, John Wiley & Sons, Ltd, Chichester, 2012.

232. J. A. Dawson, J. A. Miller and I. Tanaka, *Chem. Mater.*, 2015, **27**, 901–908.

233. A. Hönnerscheid, J. Nuss, C. Mühle and M. Jansen, *Z. Anorg. Allg. Chem*, 2003, **629**, 312–316.

234. Y. Li, W. Zhou, S. Xin, S. Li, J. Zhu, X. Lü, Z. Cui, Q. Jia, J. Zhou, Y. Zhao and J. B. Goodenough, *Angew. Chem. Int. Ed.*, 2016, **55**, 9965–9968.

235. M. B. Effat, J. Liu, Z. Lu, T. H. Wan, A. Curcio and F. Ciucci, *ACS Appl. Mater. Interfaces.*, 2020, **12**, 55011–55022.

236. V. A. Streltsov, V. Tsirelson, R. P. Ozerov and O. Golovanov, *Kristallografiya*, 1988, **33**, 90–97.

237. Z. Deng, M. Ou, J. Wan, S. Li, Y. Li, Y. Zhang, Z. Deng, J. Xu, Y. Qiu, Y. Liu, C. Fang, Q. Li, L. Huang, J. Zhu, S. Han, J. Han and Y. Zhao, *Chem. Mater.*, 2020, **32**, 8827–8835.

238. M. K. Sugumar, T. Yamamoto, K. Ikeda, M. Motoyama and Y. Iriyama, *Inorg. Chem.*, 2022, **61**, 4655–4659.

239. L. Vegard, *Z. Physik*, 1921, **5**, 17–26.

240. M. K. Sugumar, T. Yamamoto, M. Motoyama and Y. Iriyama, *Solid State Ion.*, 2020, **349**, 115298.

Appendix

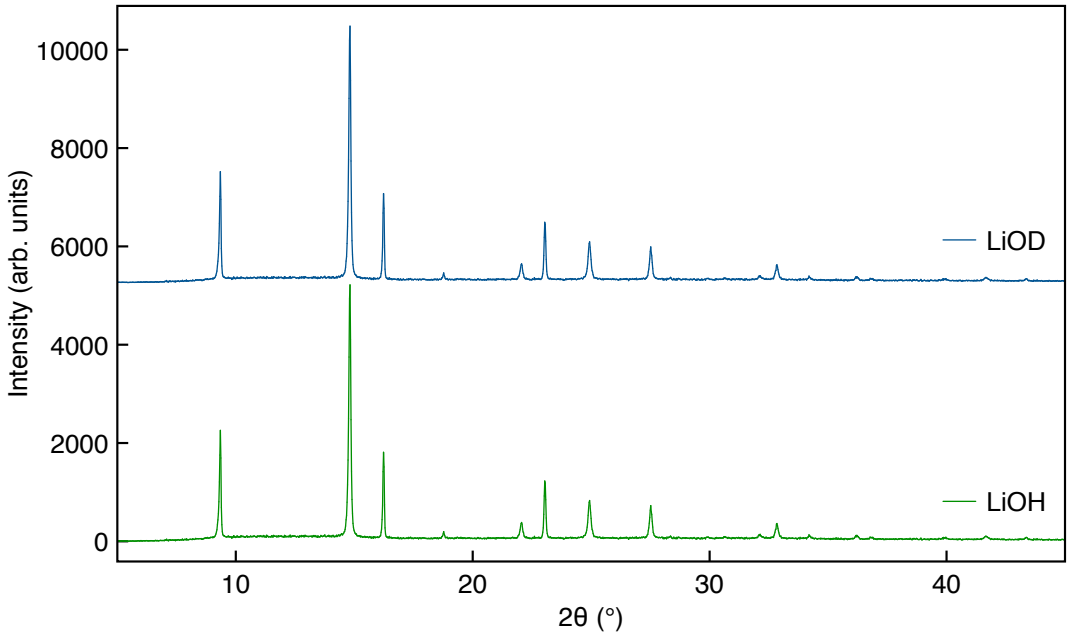

Figure A1: X-ray diffraction pattern obtained for LiOD. Also shown for comparison is the diffraction pattern obtained for LiOH.

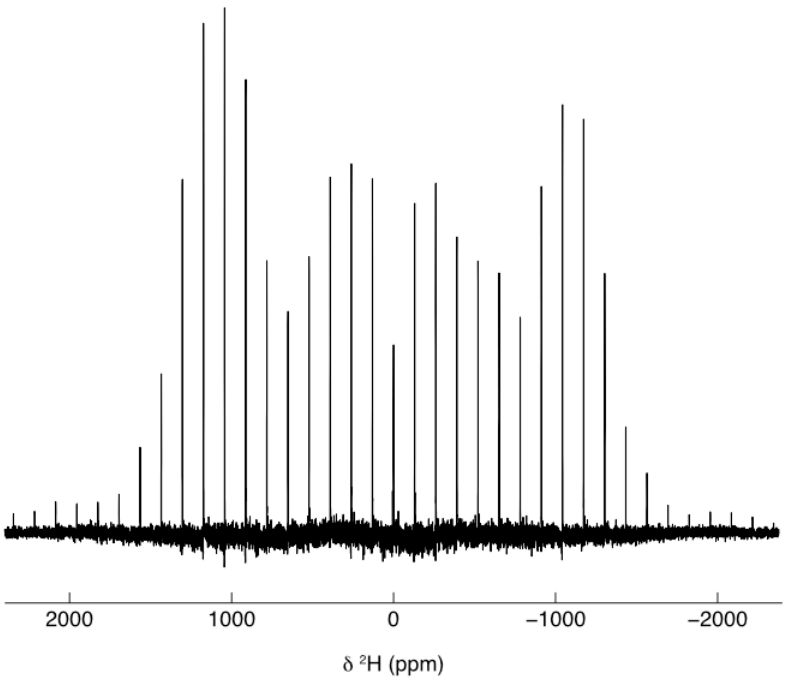

Figure A2: ^{2}H (11.7 T) MAS NMR spectrum obtained for LiOD. The MAS rate was 10 kHz. A recycle delay of 5 s was used to acquire 4 transients.

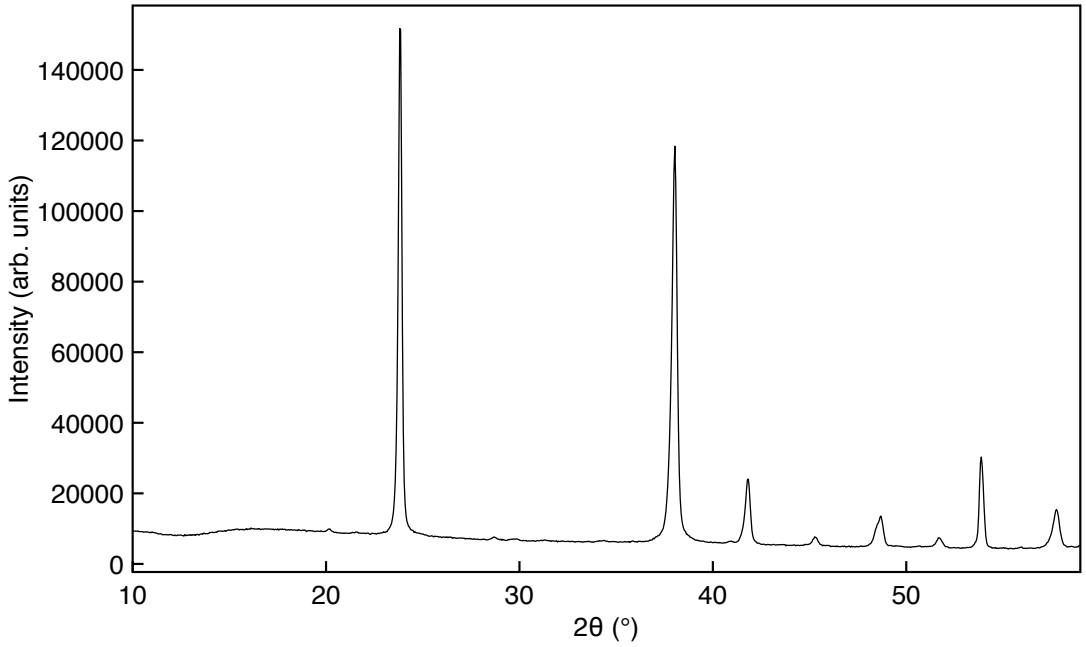

Figure A3: X-ray diffraction pattern obtained for LiOD. The diffraction pattern was recorded using a Co source through Be windows. Reflections corresponding to Be (~54°) and BeO (45.4, 48.5, 51.9°) are also observed.

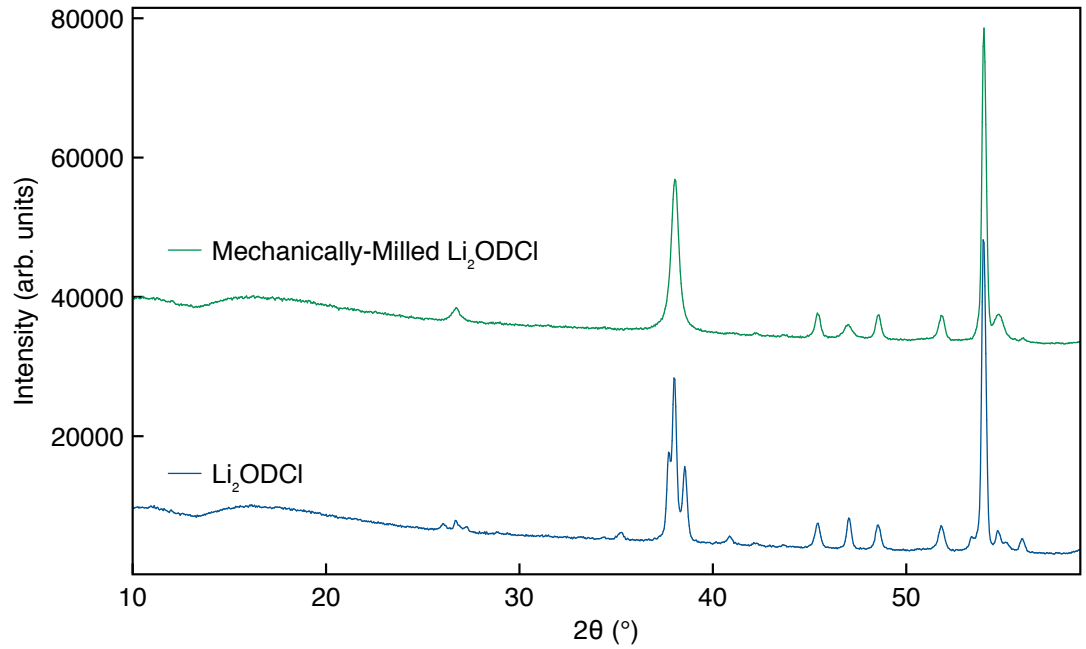

Figure A4: X-ray diffraction patterns obtained for samples of Li_2ODCl synthesised via conventional solid-state routes (blue) and mechanical milling (green). The diffraction patterns were recorded using a Co source through Be windows. Reflections corresponding to Be (~54°) and BeO (45.4, 48.5, 51.9°) are also observed.

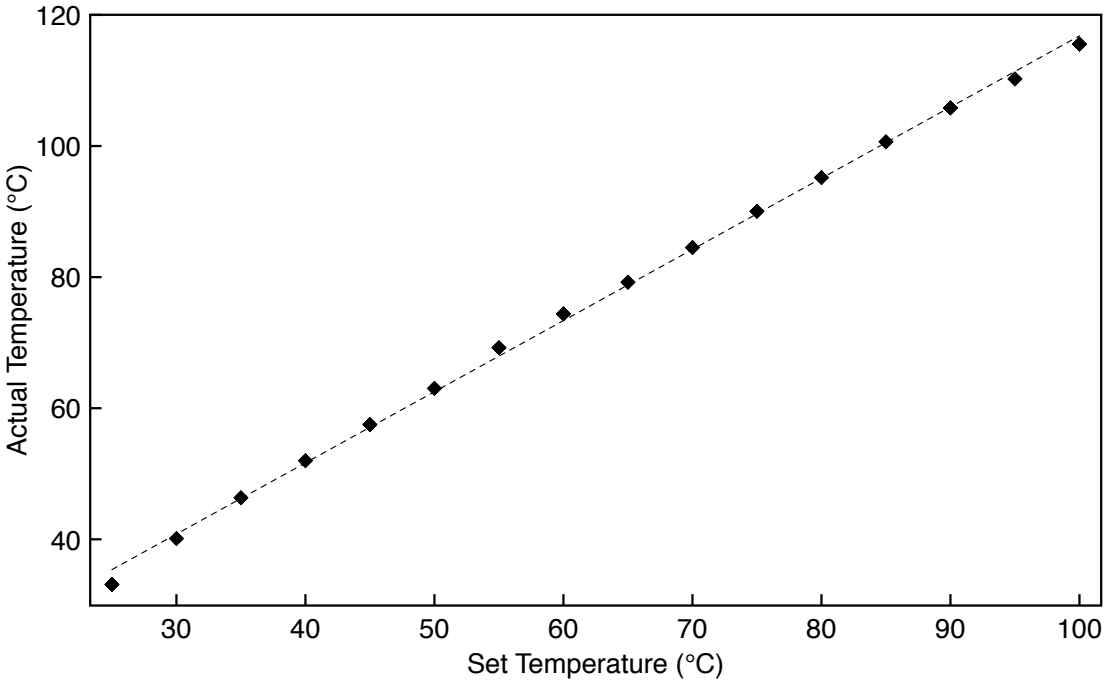

Figure A5: Temperature calibration data obtained for the 4 mm probe at 10 kHz using neat methanol.